



HAL
open science

Développement de nouveaux fluorophores pour le marquage site-spécifique de l'ADN : applications à la détection fluorogénique des acides nucléiques

Steve Vincent

► To cite this version:

Steve Vincent. Développement de nouveaux fluorophores pour le marquage site-spécifique de l'ADN : applications à la détection fluorogénique des acides nucléiques. Chimie organique. Université Côte d'Azur, 2022. Français. NNT : 2022COAZ4069 . tel-04801051

HAL Id: tel-04801051

<https://theses.hal.science/tel-04801051v1>

Submitted on 25 Nov 2024

HAL is a multi-disciplinary open access archive for the deposit and dissemination of scientific research documents, whether they are published or not. The documents may come from teaching and research institutions in France or abroad, or from public or private research centers.

L'archive ouverte pluridisciplinaire **HAL**, est destinée au dépôt et à la diffusion de documents scientifiques de niveau recherche, publiés ou non, émanant des établissements d'enseignement et de recherche français ou étrangers, des laboratoires publics ou privés.



$$\rho \left(\frac{\partial v}{\partial t} + v \cdot \nabla v \right) = -\nabla p + \nabla \cdot T + f$$

$$e^{i\pi} + 1 = 0$$

THÈSE DE DOCTORAT

Développement de nouveaux fluorophores pour le marquage site-spécifique de l'ADN

Applications à la détection fluorogénique des acides
nucléiques

Steve VINCENT

Institut de Chimie de Nice (ICN)

Présentée en vue de l'obtention
du grade de docteur en Chimie
de l'Université Côte d'Azur

Dirigée par : Pr. Alain Burger
Co-dirigée par : Dr Benoît Michel

Soutenue le : 23 Novembre 2022

Devant le jury, composé de :

Yves Mély, Professeur, Université de
Strasbourg

Jean-Marc Escudier, Directeur de recherche
CNRS, Université Paul Sabatier Toulouse

Nadia Patino, Professeure, Université Côte
d'Azur

Julie Karpenko, Docteure, Université de
Strasbourg

Développement de nouveaux fluorophores pour le marquage site-spécifique de l'ADN

Applications à la détection fluorogénique des acides nucléiques

Rapporteurs :

Yves MÉLY, Professeur, Université de Strasbourg

Jean-Marc ESCUDIER, Directeur de recherche CNRS, Université Paul Sabatier
Toulouse

Examinatrices :

Nadia PATINO, Professeure, Université Côte d'Azur

Julie KARPENKO, Docteure, Université de Strasbourg

Directeur de thèse :

Alain BURGER, Professeur, Université Côte d'Azur

Co-directeur de thèse :

Benoît MICHEL, Maître de conférences, Université Côte d'Azur

Résumé :

La conception de nouveaux fluorophores est aujourd'hui essentielle pour le développement de l'imagerie des systèmes biologiques et plus particulièrement des acides nucléiques afin de mieux comprendre leurs implications dans le vivant. Ce type de sonde exige des paramètres photophysiques précis comme des longueurs d'onde d'absorption et d'émission décalées vers le rouge ainsi qu'une bonne photostabilité. Aujourd'hui les sondes fluorogéniques font partie des systèmes les plus prometteurs pour l'imagerie des acides nucléiques. Les systèmes permettant de passer d'un simple brin d'acide nucléique non-fluorescent à un duplexe fluorescent après l'hybridation permet de réduire considérablement le bruit de fond tout en gardant un système peu complexe. Dans cette thèse, nous rapportons le développement et la caractérisation de 14 nouvelles sondes fluorogéniques qui ont été liées par des réactions de CuAAC à de multiples séquences d'ADN. Celles-ci nous ont permis d'étudier les amplifications fluorogéniques après hybridation du simple brin à sa cible. Plusieurs stratégies ont été utilisées pour accroître ces amplifications. Nous avons étudié plusieurs familles de molécules utilisant des mécanismes fluorogéniques variés. Il s'est révélé que les sondes dérivées de la Miami Green répondent au mieux au cahier des charges que nous nous étions fixé. Ses longueurs d'ondes d'absorption et d'émission sont fortement décalées vers le rouge tout en gardant un très large déplacement de Stokes et une bonne photostabilité. Par-dessus tout, ces sondes ont permis l'obtention d'amplifications de fluorescence les plus importantes avec un facteur allant jusqu'à 30 lors de la formation d'un duplexe d'ADN. Ces résultats très prometteurs offrent de nouvelles perspectives pour des applications en imagerie classique ou de super résolution.

Mots-clés : Fluorophore, détection fluorogénique, acides nucléiques, hybridation fluorogénique.

Abstract:

The design of new fluorophores is now essential for the development of imaging of biological systems and more particularly of nucleic acids in order to better understand their implications in life. This type of probe requires precise photophysical parameters such as red-shifted absorption and emission wavelengths as well as good photostability. Today, fluorogenic probes are among the most promising systems for nucleic acid imaging. Systems that allow to switch from a single strand of non-fluorescent nucleic acid to a fluorescent duplex after hybridization allow to reduce considerably the background noise while keeping a low complexity system. In this thesis, we report the development and characterization of 14 novel fluorogenic probes that were linked by CuAAC reactions to multiple DNA sequences. These allowed us to study fluorogenic amplifications after hybridization of the single strand to its target. Several strategies were used to increase these amplifications. We studied several families of molecules using various fluorogenic mechanisms. It turned out that the probes derived from Miami Green best meet the specifications we had set ourselves. Its absorption and emission wavelengths are strongly red-shifted while keeping a very large Stokes shift and exhibiting good photostability. Above all, these probes have allowed us to obtain fluorescence amplification higher than a factor of 30 during the formation of a DNA duplex. These promising results offer new perspectives for classical and super-resolution imaging applications.

Keywords: Fluorophore, fluorogenic sensing, nucleic acids, fluorogenic hybridization.

Remerciements

Je tiens tout d'abord à remercier l'entièreté du jury : le Pr. Yves Mély, le Dr. Jean-Marc Escudier, la Dr. Julie Karpenko et la Pr. Nadia Patino. Je vous remercie de l'intérêt que vous portez à mon sujet et du temps que vous avez consacré à l'étude de mon manuscrit.

Je suis très reconnaissant d'avoir travaillé sur ce sujet complet comprenant de nombreux domaines. Merci à mon directeur de thèse, le Pr. Alain Burger et à mon co-directeur Dr. Benoît Michel de m'avoir offert cette opportunité. Je leur suis reconnaissant des conseils qu'ils ont pu me donner tout au long de ces années.

Je remercie les membres de mon comité de thèse, Dr. Nicolas Baldovini et Dr. Anthony Martin pour les discussions partagées et leurs implications.

Je souhaite également remercier chaleureusement Nadia pour son aide qui a été sans défaut. Merci beaucoup d'avoir été présente dans des moments compliqués. Je suis très heureux que tu aies accepté de faire partie de mon jury pour clôturer avec moi ces années de recherche.

Merci à tous les étudiants de l'équipe. Merci à Ngoan de m'avoir aidé au labo et à surmonter toutes ces chromones. Merci à Guillaume pour beaucoup trop de choses. Tu as réussi à rendre agréables toutes ces ~~matinées~~ matinées, après-midis et nuits de travail. C'est digne d'un grand pogueur. Merci à Suman, tu as su m'aider dans un moment-clé de ma thèse. Je te serai toujours reconnaissant pour cela.

Pognow. Membre de la pogne, maintenant tous docteurs, je vous remercie. Pendant maintenant plus de 3 ans, Raph el Presidente, Adri le président d'honneur et Guigui le trésorier, vous avez toujours répondu à l'appel. Toujours là, à la table, pour discuter de tout. Toutes ces conversations resteront inoubliables. On n'oubliera pas toutes ces parties de poker qui nous ont rendus fous, toutes ces histoires de Kambing, de Mamienergie et de philosophie pognique.



Merci à tous les autres avec qui j'ai pu partager des bons moments, merci au trio de choc Lou, Chloé, Céline. Merci à notre apprentie pogueuse Sarah, qui nous a permis de faire de très belles balades et de sacrées parties de volley. Merci à tous ceux du 5^{ème} qui ont permis d'avoir cette superbe ambiance, Mauro, Mathilde, Kevin, Pascal, Rost, Zak, Julie. Mais aussi tous les autres étudiants, Marco, Sylvain, Maurine, Philippe, Aurélien, Simon, Laure, Marie, Kim, Maeva, Adèle, Max, Guillaume, Vanessa, Jana mais aussi à tous les autres que j'ai oubliés, désolé...

Je veux remercier du fond du cœur toute ma famille, elle a toujours été là pour me soutenir. Merci beaucoup papa et maman de m'avoir fait confiance immanquablement. J'y suis enfin arrivé et c'est grâce à vous.

Cette thèse vous est dédiée.

Table des matières

LISTE DES FIGURES	10
LISTE DES SCHEMAS	12
LISTE DES TABLEAUX.....	13
ABRÉVIATIONS.....	14
INTRODUCTION GENERALE	16
CHAPITRE 1 : ÉTAT DE L'ART	20
I. SPECTROSCOPIE DE FLUORESCENCE	21
<i>I.1. Principe</i>	<i>21</i>
I.1.1. Absorption.....	21
I.1.2. Emission	22
<i>I.2. Caractéristiques de la fluorescence.....</i>	<i>24</i>
I.2.1. Déplacement de Stokes.....	24
I.2.2. Rendement quantique	25
I.2.3. Brillance	25
II. SONDES SENSIBLES AUX CHANGEMENTS ENVIRONNEMENTAUX	26
<i>II.1. Processus à un seul partenaire</i>	<i>27</i>
II.1.1 Transfert de charge intramoléculaire (ICT).....	27
II.1.2. Transfert de proton intramoléculaire.....	30
II.1.3. Changement de conformation	32
II.1.4. Isomérisation à l'état fondamental	33
II.1.5. Sensibilité au pH.....	34
<i>II.2. Processus à plusieurs partenaires.....</i>	<i>34</i>
II.2.1. Agrégation.....	35
II.2.2. PET	37
II.2.3. FRET.....	39
II.2.4. DRET	41
III. LES ACIDES NUCLEIQUES	43

<i>III.1. Rappels</i>	43
III.1.1 Composition	43
III.1.2 Structure des acides nucléiques.....	44
<i>III.2. Marquage fluorescent des acides nucléiques (AN)</i>	50
III.2.1. Marquages non-covalents.....	50
III.2.2. Marquages covalents.....	52
<i>III.3. Détection des acides nucléiques (AN)</i>	62
III.3.1. Techniques basées sur l'ingénierie cellulaire.....	63
III.3.2. Techniques d'hybridation directe	65
IV. MICROSCOPIE	76
<i>IV.1. Contexte</i>	76
IV.1.1. Phénomène de diffraction	77
IV.1.2. Ouverture numérique et résolution.....	77
<i>IV.2. DNA-PAINT, technique de super-résolution des acides nucléiques</i>	79
IV.2.1. Principe du DNA-PAINT	80
PRESENTATION DU PROJET DE RECHERCHE	83
CHAPITRE 2 : HYBRIDATION FLUOROGENIQUE PAR SONDE PUSH- PULL	85
I. STRATEGIE PAR FRET : HYDROXYCHROMONES.....	86
<i>Publication 1</i>	86
II. STRATEGIE DIRECTE : METHOXYCHROMONES	106
<i>Publication 2</i>	106
CONCLUSION	132
CHAPITRE 3 : HYBRIDATION FLUOROGENIQUE PAR MOLECULAR ROTOR	133
I. CHROMONE ROTOR	134
<i>Publication 3</i>	134
II. MALACHITE GREEN.....	145

<i>II.1. Introduction</i>	145
<i>II.2. Résultats et discussion</i>	147
II.2.1. Synthèse	147
II.2.2. Hybridation fluorogénique	149
II.2.3. DRET.....	149
II.2.4. G-quadruplexes.....	151
II.2.5. Interaction avec des protéines	154
CONCLUSION	155
CHAPITRE 4 : SONDAS MIAMI – LIGAND ET INTERCALANT	156
I. INTRODUCTION	157
II. RESULTATS ET DISCUSSION.....	159
<i>II.1. Synthèse</i>	159
II.1.1. Synthèse des intermédiaires communs azoture 3 & alcyne 5	159
II.1.2. Synthèse des sondes click.....	160
<i>II.2. Caractérisations photophysiques des sondes dérivées de MG et MY</i>	162
<i>II.3. Caractérisations Photophysiques des ODNs marqués</i>	165
II.3.1. Etude de l'hybridation d'ODNs	165
II.3.2. Etude sur une cible ARN.....	173
CONCLUSION & PERSPECTIVE	178
CHAPITRE 5 : PARTIE EXPERIMENTALE.....	183
I. PUBLICATION 1.....	184
II. PUBLICATION 2.....	208
III. PUBLICATION 3.....	227
IV. MALACHITE GREEN.....	234
V. MIAMI.....	249
ANNEXES	274
PUBLICATION 4	275
PUBLICATION 5	291

PUBLICATION 6	303
REFERENCES BIBLIOGRAPHIQUES	314

Liste des figures

Figure 1. Phénomènes d'absorption et de relaxation.....	22
Figure 2. Diagramme de Jablonski.....	23
Figure 3. Représentation du déplacement de Stokes.	25
Figure 4. Mécanismes mis en jeu dans un système fluorogénique. (Adapté de la ref ³).....	27
Figure 5. Construction des sondes Push-Pull.....	27
Figure 6. Exemples de sondes push-pull classiques (en vert est indiqué le groupement donneur, en rouge l'accepteur).....	28
Figure 7. Diagramme énergétique des sondes push-pull sous l'influence de solvant.	29
Figure 8. Diagramme énergétique du phénomène de TICT. ⁷	30
Figure 9. Exemples de sondes push-pull qui présentent un mécanisme ESIPT.....	31
Figure 10. Réaction ESIPT et origine de l'émission duale sur la sonde 3-HC. (BPT : Back Proton Transfert) ⁸	32
Figure 11. Exemples de sondes à changement de conformation.	32
Figure 12. Schéma du fonctionnement des sondes d'isomérisation avec les rhodamines.	33
Figure 13. Exemples de sondes fluorogéniques utilisées pour sonder le pH.	34
Figure 14. A) Structure de la sonde YOYO-1. B) Les deux types d'ACQ : intra- et intermoléculaire.	35
Figure 15. Propriétés électroniques suivant l'arrangement en H ou J-agrégats. ²⁸	36
Figure 16. A) Structure des dérivés de TPE. B) Fonctionnement du phénomène d'AIE. ³⁴	37
Figure 17. Mécanismes de transfert de proton photoinduit A) Oxydatif B) Réductif.	37
Figure 18. Effet d'extinction de fluorescence par PET du pyrène par la nucléobase T. ³⁷	38
Figure 19. A) Structure d'un motif fluorogénique ligand de l'ADN formé par une fluoescéine (en vert) et de bis-benzamidine (en bleu) relié par une courte chaîne (en noir). B) Fonctionnement de la sonde d'hybridation par PET. A gauche, la ligation au double brin induit le turn-on. A droite, l'orientation spatiale de la structure dans son état éteint. ⁴¹	39
Figure 20. A) Diagramme énergétique simplifié montrant les 3 étapes clés du mécanisme FRET. B) Représentation de la distance nécessaire entre un donneur et un accepteur pour effectuer du FRET (en vert).	40
Figure 21. Représentation de l'aire de recouvrement entre le spectre d'émission normalisé du donneur et le spectre d'absorption normalisé de l'accepteur. ⁴³	41
Figure 22. Comparaison entre le système FRET et DRET avec un faible/fort déplacement de Stokes. ⁴⁶	42
Figure 23. Vue schématique d'un acide nucléique.....	43
Figure 24. Structure des nucléosides et nucléotides (nucléoside lié à un ou plusieurs groupements phosphate).....	44
Figure 25. A) Structure chimique d'un simple brin d'ADN. B) Appariement des paires de bases de type Watson-Cricks. C) Paramètres de la double hélice en conformation B. ⁴⁸	45
Figure 26 : ADN A, B et Z ⁴⁹	45
Figure 27. A) Conformation des nucléosides B) Exemple de liaisons de Watson-Crick ou de Hoogsteen sur les bases A-U.	46
Figure 28. Modèle des structures tertiaires de a) l'ADN-A et b) l'ADN-B. ⁵¹	47
Figure 29. Liste non-exhaustive des structures non-canoniques de l'ADN. ⁵³	48
Figure 30. Représentation de la structure et orientation du i-motif. ^{55,56,57}	48
Figure 31. Différentes représentations du motif G-quadruplexe. ⁶⁴	49
Figure 32. Structures d'intercalants de l'ADN.	51
Figure 33. Structures de ligands fluorogéniques du petit sillon.	52
Figure 34 : Exemples de sondes intramoléculaires A) Intercalant inorganique complexe de Ru ^{II} . B) Sonde organique oxazole yellow. C) Sonde organique thiazole orange (TO).	52
Figure 35. Représentation conceptuelle de l'approche post-synthétique.	57
Figure 36. Les deux voies synthétiques en compétition pour la réaction de CuAAC ⁷⁹	60

Figure 37. Exemples de ligands du cuivre pour la CuAAC.....	60
Figure 38. Types de synthons fonctionnalisés pour la CuAAC post-synthétique A) Lien court azoture incompatible avec la synthèse en chimie phosphoramidite sur support solide. B) Lien court alcyne compatible avec la synthèse sur support solide. C) Exemple de lien long azoture.....	62
Figure 39. Principe de fonctionnement de la stratégie MS2. ¹⁰⁷	63
Figure 40. Principe de fonctionnement des aptamères. Exemple de l'aptamère Mango.	64
Figure 41. Imagerie des ARN par FISH via des sondes non-fluorogénique. A) Technique simple utilisant de nombreux petit ODN marqués pour allumer la cible ARN. B) Technique RNAscope : Liaison séquentielle des sondes Z, des préamplificateurs puis des amplificateurs pour créer des sites de liaisons de plusieurs sondes génératrices de signaux.	66
Figure 42. Mécanisme fluorogénique par PET du fluorophore avec la base guanine A) Activation du PET à l'hybridation. B) Désactivation du PET à l'hybridation.....	67
Figure 43. Mécanisme d'hybridation fluorogénique des sondes FIT.....	67
Figure 44. Structure des acides nucléiques et acides nucléiques modifiés.	68
Figure 45. Structure de la 2AP , thA , thG , 3-MI , BPP , NPP , ^{MD}A , ^{MDI} , ^{C^{hpp}} et boP^{hp}C en série désoxyribose.....	70
Figure 46. Structure du pyrène de l'anthracène et du fluorène.	71
Figure 47. Stratégies pour le marquage covalent des ANs <i>via</i> des liens flexibles A) en 3' / 5' B) ou en position interne une approche amidite. C) <i>Via</i> des liens très court pour augmenter la rigidité. D) Exemple de mimique de bases et nucléobases fluorescente par extension de conjugaison ³⁷	72
Figure 48. Représentation schématique des stratégies FRET appliquées aux ANs. A) Stratégie FRET linéaire. B) Stratégie <i>molecular beacon</i> et C) double <i>molecular beacon</i>	73
Figure 49. A) Description d'une lumière cohérente, non cohérente, ou polarisée. B) Comportement d'une lumière cohérente sur une ouverture. C) Représentation de l'effet de diffraction d'une ouverture linéaire. D) Représentation de l'effet de diffraction d'une ouverture circulaire ¹⁴⁸	77
Figure 50. Description de d'épaulement de deux disques de Airy définissant la résolution d'un microscope optique. A gauche, les deux disques sont résolus alors qu'à droite, ils sont indiscernables. Au milieu se trouve la zone limite de discernement définie par la limite de Rayleigh ¹⁴⁸	78
Figure 51. Comparaison de la technique d'imagerie classique <i>wide field</i> avec une imagerie confocale ¹⁴⁸	79
Figure 52. Représentation schématique du fonctionnement de la microscopie en molécule unique (gauche) méthode classique d'imagerie par STORM. ¹⁵⁵	80
Figure 53. A) Principe du DNA-PAINT. B) Représentation schématique d'un origami d'ADN contenant trois sites de liaison (un brin d'ADN par zone rouge), séparés de 80 nm. C) Données expérimentales brutes suite à l'ajout du brin complémentaire de l'origami et localisation des zones d'accumulation. Après soustraction du bruit de fond, seules les zones d'accumulation sont visibles et correspondent aux origamis.....	81
Figure 54 : Principe de fonctionnement d'une sonde fluorogénique d'hybridation de l'ADN. Le simple brin d'ADN en vert est le brin imageur (avec le fluorophore). Le simple brin d'ADN en bleu est la cible.	83
Figure 55. Types de modification utilisée dans ce projet de recherche pour les études d'hybridations fluorogéniques des ANs.....	84
Figure 56. Dérivés de 3HC utilisés dans ce travail.....	86
Figure 57. Structures des analogues nucléosidique M3HF et TdEAF.....	87
Figure 58. Développement de la méthode FRET des sondes à motif 3HC.....	89
Figure 59. Développement des ODN marqué par des dérivés de méthoxychromone 3-MC à partir de la référence dEAF	107
Figure 60. Structure du nucléoside marqué AIMF-Nu.....	108
Figure 61. Structure des liens clicks sur l'ODN.....	109
Figure 62. A) Représentation schématique de l'hybridation fluorogénique de l'ODN. B) Effet de rotation du groupement thiophène suite à l'intercalation pour retrouver une planéité et ainsi de la fluorescence.....	134

Figure 63. Structure des liens click sur l'ODN.....	135
Figure 64. Exemples de triarylméthane.	145
Figure 65. Méthode d'utilisation des molécules FAP spécifiques d'une protéine (<i>tag protein</i>) pour l'imagerie d'une cible (TM : <i>Targeting molecules</i>). ¹⁶⁹	145
Figure 66. Différence de degrés de liberté entre les FAP Malachite Green et Thiazole Orange.....	146
Figure 67. Un exemple de l'effet non-fluorogénique de la MG entre un simple et double brin d'ODN.	149
Figure 68. Spectre d'absorption et d'émission de Cy5 et de la MG dans le PBS.....	150
Figure 69. Exemple d'un spectre de DRET fluorogénique avec la séquence marqué TXT couplé au brin complémentaire Cy5 comparé au spectre de Cy5 seule obtenu par excitation directe à 440 nm.	150
Figure 70. Complexe formé entre la MG (en vert) et une structure G-quadruplexe (représentée en gris).....	151
Figure 71. Spectres de dichroïsme circulaire le la séquence XGG avant (vert) et après ajout de sel, Na ⁺ (bleu).	153
Figure 72. Exemple de la titration de la séquence 5'XGG : A) Spectres d'absorption de la titration en potassium. B) Spectres d'émission de la titration en potassium. C) Spectres d'absorption de la titration en sodium. D) Spectres d'émission de la titration en sodium.	154
Figure 73. Exemple d'interaction du simple brin CXC avec la protéine ligand des ADNss. A) en absorption. B) en émission.	155
Figure 74. A) Structure des sondes Miami Green et Miami Yellow. B) Méthode d'interaction des sondes avec l'ADNs, par interaction avec le petit sillon (gauche) ou par intercalation (droite) ¹⁸⁵	157
Figure 75. Structures asymétriques contenant une seule double liaison A) dérivés de Miami Green, B) dérivés de Miami Yellow. Structures symétriques contenant deux doubles liaisons C) dérivés de Miami Green, D) dérivés de Miami Yellow.	158
Figure 76. A) Spectres d'absorption (gauche) et d'émission (droite) de la sonde pyrimidique 8 , suite à l'augmentation du pourcentage d'eau dans le THF. B) Spectres d'absorption (gauche) et d'émission (droite) de la sonde organoboré 12 suite à l'augmentation du pourcentage d'eau dans le THF.	163
Figure 77. Titration pH, dans le PBS, par addition de NaOH (1M) ou HCl (1M). A) de la sonde pyrimidique 8 B) de la sonde organoborée 12	164
Figure 78. Représentation des spectres d'absorption et d'émission des ODN marqués par la sonde 8/9 ou 12/13	167
Figure 79. Spectres d'absorption (gauche) et d'émission (droite) du simple et double brin marqué par 8 sur la séquence A) AWA B) TST, avec $\lambda_{Ex} = 510nm$	171
Figure 80. Spectres d'absorption (gauche) et d'émission (droite) du simple et double brin marqué par 12 sur la séquence AWA, avec $\lambda_{Ex} = 610nm$	172
Figure 81. Image de la cible ARNm <i>oskar</i> dans la cellule œuf de la drosophile résultant de l'empilement de coupes confocales en utilisant des sondes binaires d'hybridation reposant sur un système DRET.	173
Figure 82. Séquences ARN Oskar, cADN Oskar et brins complémentaires marquées avec la sonde de la section visée de Oskar.....	174
Figure 83 : Chronologie du développement des sondes au cours de la thèse.....	179
Figure 84 : Résumé des propriétés principales des sondes envers les objectifs du projet pour des applications futures.	182

Liste des schémas

Schéma 1. Synthèse sur support solide d'ADN	54
Schéma 2. Exemples de réactions post-synthétiques A) Diels-Alder post-synthétique ⁸⁶ , B) Ligation de Staudinger ⁸⁷	58
Schéma 3. Exemples de réactions post-synthétiques sans utilisation de métal: A) SPAAC ⁹⁶ B) Conjugaison entre un alcène contraint et un tétrazine ⁹³ C) Photoclick entre un alcène et un tetrazole ⁹⁵	59
Schéma 4. Retrosynthèse de la malachite green clickable.....	147
Schéma 5. Synthèse de la malachite green alcyne.	147
Schéma 6. Synthèse de la malachite green azoture.....	148

Schéma 7. Rétrosynthèse des dérivés click de Miami.....	159
Schéma 8. Synthèse de l'intermédiaire azoture 3	160
Schéma 9. Synthèse de l'intermédiaire alcyne 5	160
Schéma 10. Préparation des produits finaux pyrimidiques 8 et 9	161
Schéma 11. Préparation des produit finaux organoborés 12 et 13	161

Liste des tableaux

Tableau 1. Paramètres structuraux des conformations de l'ADN.....	47
Tableau 2. Exemples de dérivés phosphoramidites fluorescents utilisés en synthèse en phase solide pour une approche pré-synthétique - positions de marquage.....	56
Tableau 3. Descriptif des séquences pour les réactions « click » post-synthétiques.....	148
Tableau 4. Descriptif des séquences G-quadruplex pour les réactions de post-synthétique.....	152
Tableau 5. Effet des solvants sur les caractéristiques photophysiques des sondes pyrimidique 8 et organoborée 12	162
Tableau 6. Description des séquences d'ODNs fonctionnalisés utilisées pour les réactions CuAAC avec les dérivés de Miami.....	166
Tableau 7. Etude spectroscopique, dans le PBS, des ODNs marqués par un lien azoture et des duplexes après hybridation avec le brin complémentaire dans le PBS.....	167
Tableau 8. Etude spectroscopique, dans le PBS, des ODNs marqués par un lien alcyne et des duplexes après hybridation avec le brin complémentaire dans le PBS.....	168
Tableau 9. Effet de l'hybridation sur la brillance, le rapport d'absorption et l'amplification de fluorescence pour deux longueurs d'onde d'excitation.....	169
Tableau 10. Description des séquences utilisés pour l'analyse <i>in-vitro</i>	175
Tableau 11. Comparaison des études spectroscopiques concernant les simples-brins et les duplexes ARN:ADN et ADN:ADN, marqués par les sondes 8 et 9	176
Tableau 12. Comparaison des études spectroscopiques concernant les simples-brins et les duplexes ARN:ADN et ADN:ADN marqués par les sondes 12 et 13	176

Abréviations

3-HC	3-hydroxychromone
3-MC	3-méthoxychromone
A	Absorbance
a.u	Arbitrary unit
ACN	Acétonitrile
ACQ	Aggregation-caused quenching
ADN	Acide désoxyribonucléique
ADNss	Acide désoxyribonucléique <i>single strand</i>
ADNds	Acide désoxyribonucléique <i>double strand</i>
A	Adénine
AN	Acide Nucléique
ARN	Acide ribonucléique
ARNm	ARN messenger
AIE	Aggregation-induced emission
C	Concentration / cytosine
<i>c</i>	Vitesse de la lumière dans le vide
CD	Circular dichroism (dichroïsme circulaire)
cm	Centimètre
CPG	Controlled pore glass
CuAAC	Copper(I)-catalyzed alkyne-azide cycloaddition
DAPI	4',6-diamidino-2-phénylindole
DCE	Dichloroéthane
DCM	Dichlorométhane
DIEA (ou DIPEA)	<i>N,N</i> -diisopropyléthylamine
DMF	Diméthylformamide
DMSO	Diméthylsulfoxyde
DMTr	4,4'-diméthoxytrityle
DRET	Dark resonance energy transfer
E	Energie / efficacité de transfert
EtOAc	Acétate d'éthyle
ESIPT	Excited-state intramolecular proton transfer
EtOH	Ethanol
ETT	5-(Ethylthio)-1 <i>H</i> -tetrazole
eV	Electron Volt
ϵ	Coefficient d'absorption molaire
FRET	Förster Resonance Energy Transfer
G	Guanine
GFP	Green fluorescent protein
<i>h</i>	Constante de Planck
liaison H	Liaison hydrogène
HOMO	Highest occupied molecular orbital
HPLC	High-performance liquid chromatography
I	Intensité de fluorescence
ICT	Intramolecular charge transfer
IR	Infrarouge
<i>J</i>	Intégrale de recouvrement
k_r	Constante de vitesse radiative
k_{nr}	Constante de vitesse non radiative
k_{FRET}	Constante de vitesse du FRET
LUMO	Lowest unoccupied molecular orbital

M	Multiplicité de spin
MeOH	Méthanol
MW	Microwave
N*	Forme normale excitée
nm	Nanomètre
nM	Nanomolaire
ODN	Oligodésoxynucléotide
ODN _{ss}	Oligodésoxynucléotide <i>single strand</i>
ODN _{ds}	Oligodésoxynucléotide <i>double strand</i>
ORN	Oligoribonucléotide
PAINT	Point Accumulation in Nanoscale Topography
PALM	Photoactivated localization microscopy
PBS	Phosphate-buffered saline
pb	Paire de base
PCR	Polymerase chain reaction
Ph	Phényle
pH	Potentiel hydrogène
PET	Photoinduced electron transfer
rt	Room temperature
s	Seconde / spin électronique
S	Etat singulet
S ₀	Etat fondamental
S ₁	Etat excité singulet
SIM	Structured illumination microscopy
SMLM	Single-molecule localization microscopy
SNP	Single-nucleotide polymorphism
STED	Stimulated-emission-depletion microscopy
STORM	Stochastic optical reconstruction microscopy
T	Etat triplet / thymine
T*	Forme tautomère excitée
TA	Température Ambiante
THF	Tétrahydrofurane
TICT	Twisted intramolecular charge transfer
Tol	Toluole
TO	Thiazole orange
U	Uracile
UV-Vis	Ultraviolet-visible
vs.	Versus
YO	Yellow oxazole
Å	Angström
$\Delta\lambda$	Déplacement de Stokes
ν	Nombre d'onde
λ	Longueur d'onde
λ_{Abs}	Longueur d'onde d'absorption
λ_{Ex}	Longueur d'onde d'excitation
λ_{Em}	Longueur d'onde d'émission
μ_E et μ_G	Moment dipolaire de l'état excité et fondamental
τ	Temps de vie
Φ	Rendement quantique

Introduction générale

Depuis des siècles, le phénomène de fluorescence a été maintes fois observé et a longtemps été un objet de fascination pour les hommes et les scientifiques, jusqu'à l'arrivée de Sir George Gabriel Stokes et de sa fameuse publication « On the Refrangibility of Light », en 1852. Après cela, et pendant plus d'un siècle, la fluorescence a été considérablement étudiée et, au début des années 1990, le clonage du gène de la protéine fluorescente verte (*GFP* en anglais) et l'étude de son expression dans des bactéries ont conduit à sa large application en microscopie de fluorescence, en particulier dans le domaine biologique.

La « Fluorescence » et ses applications en recherche constituent un domaine particulier de la science. Ce dernier s'appuie sur de nombreuses disciplines interdépendantes, telles que la chimie de synthèse, la chimie computationnelle, la biologie/biochimie, la photophysique, la biophotonique et l'imagerie. De nos jours, l'instrumentation dans le domaine de la fluorescence est devenue facile d'accès et peu onéreuse grâce à de grandes avancées telles que la « microscopie confocale » ou, plus récemment, de nouvelles techniques, telles que la « microscopie à molécule unique », récompensée par un prix Nobel en 2014.

La fluorescence représente un outil d'analyses très puissant. Ses applications sont très larges, en particulier dans les domaines des sciences médicales et pharmaceutiques. Elles s'étendent à l'analyse environnementale (détection de traces d'espèces chimiques dans le milieu environnant), au diagnostic (de cancer par exemple, par le biais de puces à ADN), à la visualisation et détection de biomolécules dans les cellules et l'imagerie du vivant (microscopie de fluorescence).

Pour l'analyse de milieux biologiques telles que les cellules vivantes, la fluorescence est la technique la plus sensible, permettant de détecter des biomolécules telles que des protéines ou des acides nucléiques. Pour ce type d'études, les sondes fluorescentes utilisent, des « fluorophores » qui doivent permettre une résolution spatiale et temporelle très élevée, avec un haut degré de précision, et doivent être non-invasives dans les cellules vivantes.

Dans ce cadre, il est crucial de disposer d'un large éventail de fluorophores, spécifiques à chaque type d'analyses et au milieu dans lequel ils sont utilisés.

La conception de nouveaux fluorophores est essentielle et permet aujourd'hui l'émergence de nouvelles applications dans le domaine de la fluorescence. Ces sondes doivent respecter un cahier des charges particulier, en accord avec les caractéristiques liées à l'imagerie, elles doivent posséder les propriétés adéquates en photophysique, ainsi que la possibilité d'introduire des substituants nécessaires pour une bioconjugaison, tout comme le réglage de la solubilité.

Respecter un cahier des charges si exigeant est un défi en soi. Pour une application particulière, les chimistes en charge de synthétiser ces sondes vont alors développer une chimiothèque de fluorophores, étudier leurs propriétés physiques et photophysiques puis identifier la sonde adéquate à l'application donnée.

Dans notre cas, nous nous sommes penchés sur la détection des acides nucléiques (AN). Ces derniers jouent des rôles prépondérants dans le stockage de l'information génétique ainsi que dans la régulation des processus biologiques. Au vu de leurs fonctions complexes, il est nécessaire de pouvoir les localiser afin de mieux comprendre leur implication dans le fonctionnement des cellules vivantes. La fluorescence est une technique de choix, permettant à la fois leur détection, leur quantification et leur visualisation dans leur environnement naturel (la cellule).

De nos jours, de nombreux fluorophores existent mais leur mode de fluorescence peut différer. On peut les séparer en deux catégories, les traceurs et les capteurs pour la détection dans des milieux biologiques. Les capteurs diffèrent des traceurs par leurs propriétés de fluorescence qui sont variables en fonction des paramètres physico-chimiques du milieu environnant, ce qui leur vaut le nom de sondes fluorogéniques.

Dans le cadre de cette thèse, les objectifs qui m'ont été confiés ont consisté à développer de nouvelles sondes fluorogéniques adaptées à la détection spécifique de séquences primaires d'acides nucléiques (AN). Peu de sondes commerciales ou décrites dans la littérature sont capables d'une telle spécificité et il est donc alors nécessaire d'en développer de nouvelles. Notre équipe de recherche, « Sondes Fluorescentes », est spécialisée dans le développement de sondes fluorogéniques, en particulier de type *Push-Pull*. Leur intensité de fluorescence

ainsi que leurs longueurs d'ondes d'absorption et/ou d'émission varient en fonction de la nature du solvant et, plus généralement, de l'environnement qui les entoure.

D'un autre côté, l'intention générale de cette thèse est de faire progresser le développement de nouveaux fluorophores répondant à un cahier des charges photophysique rigoureux, pour une application biologique ayant trait aux acides nucléiques.

L'ensemble de mes travaux de thèse est décrit dans 5 chapitres :

Le chapitre 1 est un chapitre bibliographique, rappelant les différents concepts liés à la spectroscopie de fluorescence et ceux liés aux acides nucléiques.

Après la présentation des objectifs de cette thèse, le chapitre 2 concerne le développement de deux sondes fluorescentes de type *Push-Pull*, dérivant de la chromone, et leur application à la détection directe ou par FRET d'AN spécifiques. Ces travaux ayant été publiés, ils sont brièvement résumés et les publications correspondantes sont données à la suite.

Le chapitre 3 décrit la synthèse et l'étude photophysique de nouvelles sondes de type « *molecular rotor* » et leur application en tant que sondes fluorogéniques lors de l'hybridation des AN. Une première partie concerne un dérivé de chromone, le 6-EMT. Les travaux s'y référant ont fait l'objet d'une publication, qui est jointe au manuscrit. Une deuxième partie concerne l'élaboration de dérivés de « Malachite Green » et leur application à la détection des AN par de multiples mécanismes.

Le chapitre 4 concerne la synthèse de dérivés de type Miami Green et Yellow, qui combinent à la fois les propriétés *Push-Pull* et *molecular rotor*, et leur application à la détection directe de séquences d'ADN ainsi qu'à celle d'un ARN cible dérivant de l'ARNm oskar.

Le chapitre 5 rassemble les données expérimentales des 3 publications insérées dans le manuscrit ainsi que celles des chapitres 3 et 4.

Par ailleurs et à la suite, dans une partie « Annexe », sont rajoutées trois publications concernant des projets de recherche auxquels j'ai participé et qui ne font pas partie du sujet de ma thèse, mais y sont tout de même corrélés.

Les références bibliographiques sont rassemblées à la fin du manuscrit.

Chapitre 1 : État de l'art

I. Spectroscopie de Fluorescence

La luminescence traduit le phénomène d'émission de lumière à partir d'un état excité de la matière (atome, molécule, cristal). Le processus d'excitation peut être de différentes natures : réaction chimique (chimioluminescence) ou biochimique (bioluminescence), transfert d'énergie thermique (thermoluminescence), absorption de la lumière (photoluminescence), etc...

La photoluminescence englobe deux termes qui sont la fluorescence et la phosphorescence.

I.1. Principe

La lumière est considérée comme une entité duale onde-corpuscule. Plus précisément, elle présente les caractéristiques d'une onde avec une longueur d'onde λ (en nm) ou un nombre d'onde ν (en cm^{-1}) mais également d'une particule, appelée photon, ayant une énergie E . L'énergie du photon est corrélée à sa longueur d'onde par la relation de Planck-Einstein (**Équation 1**) :

$$E = h\nu = h\frac{c}{\lambda}$$

Équation 1. Relation de Planck-Einstein.

Avec h : la constante de Planck ($h \approx 6,63 \times 10^{-34}$ J.s) et c : la célérité de la lumière dans le vide ($c = 3,0 \times 10^8$ m.s⁻¹).

Toute molécule capable d'absorber de la lumière dans la région UV/Visible est appelée chromophore. Dans le cas particulier où elle présente des propriétés de fluorescence, elle sera appelée fluorophore. Le phénomène de fluorescence est composé de 2 étapes clés : l'absorption et l'émission.

I.1.1. Absorption

En l'absence de source d'excitation, toute molécule organique est présente dans son état fondamental appelé S_0 (**Figure 2**). Dans cet état S_0 , deux électrons sont présents dans l'orbitale appelé HOMO (*Highest Occupied Molecular Orbital*), contrairement à la LUMO

(*Lowest Unoccupied Molecular Orbital*) qui, par définition, est vide (**Figure 1**). Dans le cas général, sous l'effet de l'apport d'une énergie lumineuse (laser ou lampe), les électrons sont capables de passer de l'état S_0 à des états d'énergie supérieurs S_1 , S_2 etc...

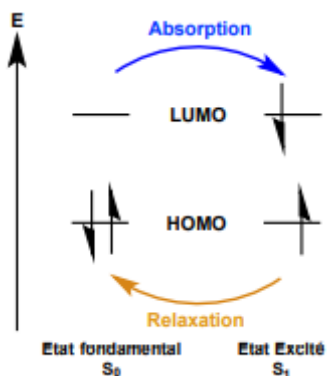


Figure 1. Phénomènes d'absorption et de relaxation.

Généralement, dans le cas de fluorophores organiques, l'écart énergétique HOMO - LUMO correspond à des longueurs d'ondes comprises entre 200-800 nm. Le phénomène d'absorption est étudié à l'aide d'un spectromètre UV/Visible. Le spectre obtenu donne les valeurs d'absorbance du chromophore à chaque longueur d'onde. Cette dernière est reliée au coefficient d'absorption molaire (ϵ) et à la concentration, suivant la relation de Beer-Lambert (**Équation 2**) :

$$A = \epsilon l C$$

Équation 2. Loi de Beer-Lambert.

A est l'absorbance ; ϵ est le coefficient d'absorption molaire ($M^{-1}.cm^{-1}$) ; l la longueur du trajet lumineux (cm) ; C la concentration du soluté à analyser en solution (M).

I.1.2. Emission

A la suite de la transition électronique, le composé organique se retrouve dans un état énergétique plus élevé (par exemple S_1). Il va alors tout d'abord chercher à libérer l'excédent énergétique emmagasiné en réalisant une série de cascades vibrationnelles, afin de se retrouver dans l'état vibrationnel le plus stable de l'état excité (état excité relaxé) (**Figure 2**).

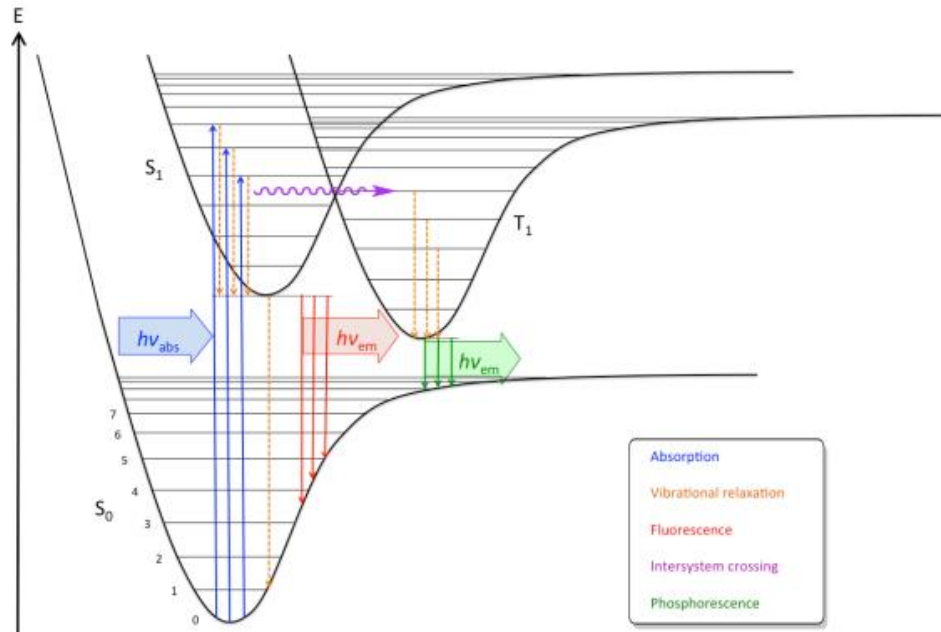


Figure 2. Diagramme de Jablonski.

Le temps de vie (τ) d'un fluorophore dans cet état excité relaxé est très court (compris en général entre 10^{-8} à 10^{-11} s) et dépend des différents facteurs de décroissance (k_r et k_{nr}) (Équation 3) :

$$\tau = \frac{1}{k_r + k_{nr}}$$

Équation 3. Temps de vie d'un fluorophore.

où k_r correspond à la constante de vitesse radiative (fluorescence) et k_{nr} à la constante de vitesse non-radiative. Cette valeur de temps de vie peut être obtenue par le biais d'analyses spectroscopiques en temps de vie. Cette relation nous montre que lorsque le k_r augmente, le temps de vie du fluorophore dans l'état excité relaxé est plus court.

Le phénomène de fluorescence correspond au retour à l'état fondamental qui s'accompagne de l'émission d'un photon (k_r). L'énergie de ce photon émis sera généralement inférieure à celui du photon absorbé, en raison des cascades de relaxations vibrationnelles. Si l'on suit alors la relation de Planck-Einstein (Équation 1), l'évolution de l'énergie est inversement proportionnelle à la longueur d'onde, soit $E_{abs} > E_{em}$ conduit alors à $\lambda_{abs} < \lambda_{em}$.

Le retour à l'état fondamental peut aussi s'effectuer par un mécanisme non-radiatif (k_{nr}) de conversion interne, résultant en une transition vibronique (changement d'état électronique et vibrationnel), ou également provenir de nombreux processus alternatifs (*vide infra*).

I.2. Caractéristiques de la fluorescence

Un fluorophore est caractérisé par un ensemble de paramètres photophysiques.

I.2.1. Déplacement de Stokes

La différence entre le maximum d'absorption et le maximum d'émission d'un fluorophore est appelée déplacement de Stokes (*Stokes Shift*, **Équation 4**, **Figure 3**). Elle correspond à la différence des maxima d'absorption et d'émission exprimée soit à partir de des nombres d'onde soit à partir des longueurs d'onde :

$$\Delta\nu_{ss} = \nu_{abs} - \nu_{em}$$

$$\Delta\lambda_{ss} = \lambda_{em} - \lambda_{abs}$$

Équation 4. Déplacement de Stokes.

avec ν_{abs} et ν_{em} les nombres d'onde, en cm^{-1} , correspondant respectivement aux maxima d'absorption et d'émission du fluorophore

avec λ_{em} et λ_{abs} , les longueurs d'onde, en nm, correspondant respectivement aux maxima d'émission et d'absorption du fluorophore.

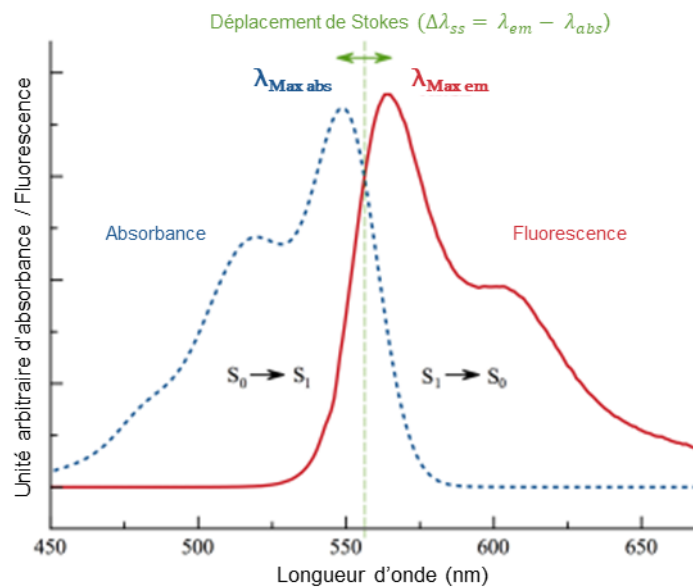


Figure 3. Représentation du déplacement de Stokes.

I.2.2. Rendement quantique

Le rendement quantique correspond au rapport entre le nombre de photons émis et le nombre de photons absorbés (Équation 5). Il est égal au rapport entre la constante de vitesses radiative et la somme des constantes de vitesse radiative et non-radiative. Il peut être également décrit comme le produit de la constante radiative par le temps de vie.

$$\Phi = \frac{\text{photons émis}}{\text{photons absorbés}} = \frac{k_r}{k_r + k_{nr}} = k_r \times \tau$$

Équation 5. Rendement quantique.

I.2.3. Brillance

La brillance est le produit du rendement quantique et du coefficient d'extinction molaire du fluorophore. Cette donnée caractérise la sensibilité du fluorophore et sa limite de détection (Équation 6) :

$$B = \varepsilon \times \Phi$$

Équation 6. Brillance d'un fluorophore.

B est la brillance ($M^{-1}.cm^{-1}$) ; ε le coefficient d'extinction molaire ($M^{-1}.cm^{-1}$) ; Φ le rendement quantique.

II. Sondes sensibles aux changements environnementaux

Il existe deux catégories de sondes fluorescentes. La première regroupe les fluorophores, appelés traceurs. Ces derniers sont insensibles aux changements d'environnement, impliquant que leurs propriétés photophysiques restent constantes. Ils sont caractérisés par un signal stable et une très forte brillance, leur permettant d'être facilement employés pour de la microscopie de fluorescence ou du diagnostic. C'est le cas notamment des sondes Cyanines (c.f. Chap. 1 : II.2.2.). Elles peuvent, par exemple, remplacer le phosphore radioactif dans des applications de séquençage.

La seconde catégorie comprend les molécules fluorescentes sensibles à leur environnement, elles sont appelées capteurs. Ce manuscrit se concentre uniquement sur cette seconde catégorie et, plus précisément, sur les petites molécules organiques fluorogéniques ou ratiométriques.

Le terme fluorogénique définit un changement d'état de fluorescence¹. Le passage d'un état non-fluorescent à un second état fluorescent est appelé *turn-on*. Le phénomène inverse est appelé *turn-off*². Le changement d'état de fluorescence permet de caractériser un évènement. Il peut notamment être induit par des modifications des paramètres physico-chimiques du solvant (polarité, viscosité, pH), par des processus photophysiques intervenant à l'état excité (PET, FRET, ICT...) ou, également, par un changement de conformation du fluorophore. Ces mécanismes fluorogéniques impliquent un ou plusieurs fluorophores.

II.1. Processus à un seul partenaire

Dans cette partie, 5 types de mécanismes de fluorescence seront décrits : le transfert de charge, le transfert de proton, le changement de conformation, l'isomérisation à l'état fondamentale et le phénomène d'agrégation (Figure 4).

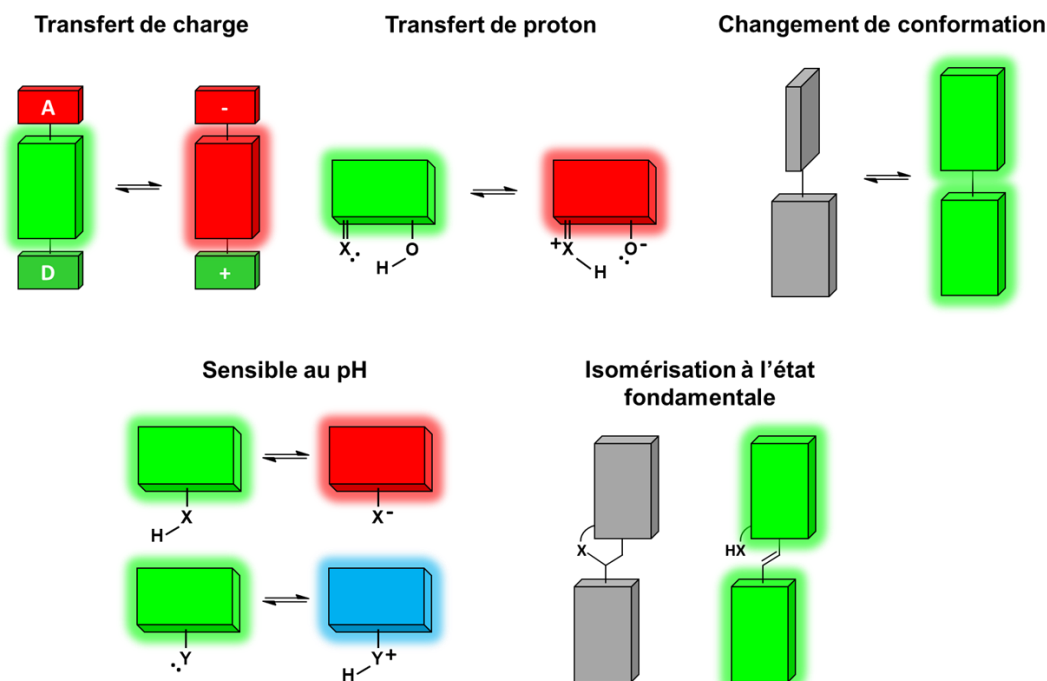


Figure 4. Mécanismes mis en jeu dans un système fluorogénique. (Adapté de la ref³).

II.1.1 Transfert de charge intramoléculaire (ICT)

i. Principe

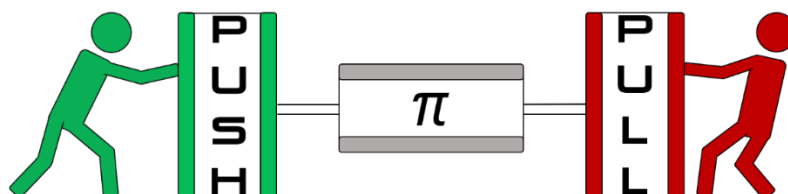


Figure 5. Construction des sondes Push-Pull.

Le transfert de charge intramoléculaire s'opère au sein de fluorophores dits « push-pull ». Au niveau structural, les sondes push-pull sont constituées d'un groupement électrodonneur conjugué, généralement par un système π , à un groupement électroattracteur (Figure 5). Dans la majorité des cas, le système peut être ordonné de plusieurs manières :

- D- π -A (dipolaire)
- D- π -A- π -D ou A- π -D- π -A (quadrupolaire)
- (D- π)₃-A, (D- π)₄-A, etc... (Octupolaire)

Le système π est couramment composé de noyaux aromatiques, hétéroaromatiques (thiophène, pyrrole, furane...) et/ou d'un système aliphatique insaturé (alcène ou alcyne). Le groupement donneur (D) est principalement une fonction simple mésomère donneur : OH, NH, OR, NR₂... Inversement, le groupement accepteur (A) est mésomère et/ou inductif attracteur : CN, CHO ou même des noyaux hétérocycliques électroniquement déficients comme les (di)azines, benzothiazoles ou imidazoles.

En termes de diversité structurale, la famille des sondes push-pull est celle qui est la plus représentée dans la littérature. Les plus communes d'entre elles sont présentées dans la Figure 6.

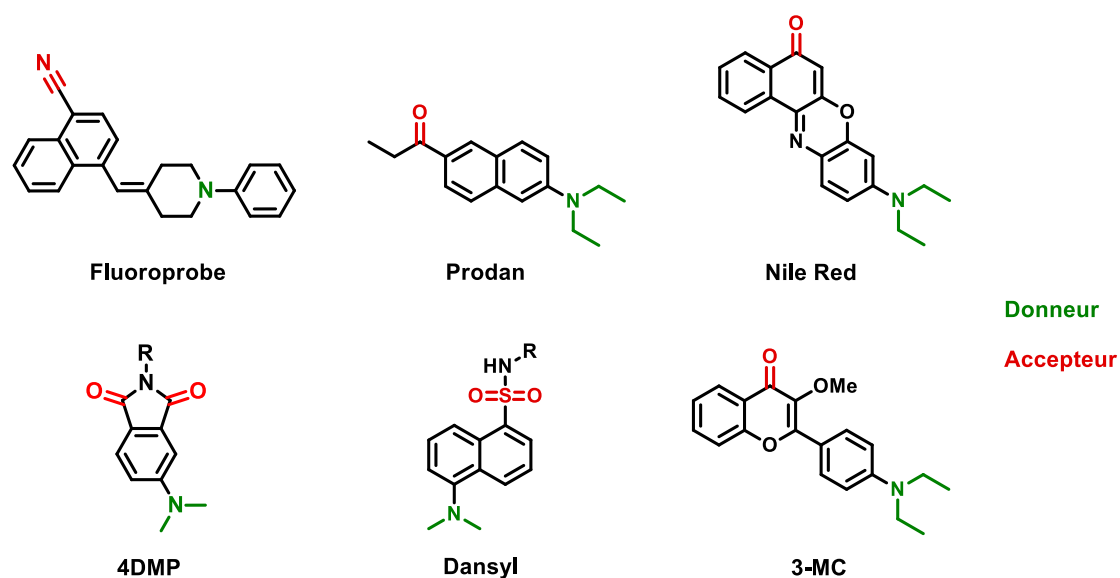


Figure 6. Exemples de sondes push-pull classiques (en vert est indiqué le groupement donneur, en rouge l'accepteur).

Le transfert de charge intramoléculaire photo-induit (ICT – *Intramolecular charge transfert*) fait référence au transfert de charge, à l'état excité, s'opérant du groupement électrodonneur vers le groupement électroattracteur⁴. Dans la plupart des cas, le fluorophore présente alors un moment dipolaire plus important, ce qui lui confère des propriétés photophysiques singulières, en particulier à l'état excité.

Les sondes push-pull sont très sensibles à la polarité du solvant et à sa proticité lorsqu'elles ont des groupements accepteurs sensibles aux liaisons hydrogène (ex. cétone, aldéhyde). Cette sensibilité au solvant se traduit par un déplacement vers le rouge du maximum d'émission (*red-shift*) pour une augmentation de la polarité du solvant. Ce déplacement bathochrome d'émission est induit par un écart énergétique plus faible entre les niveaux d'énergie S_1 et S_0 (**Figure 7**). À la suite du transfert de charge à l'état excité (S_1), les molécules de solvant environnantes vont alors se réorienter afin de stabiliser le dipôle du fluorophore (S_1'). Plus la polarité du solvant est élevée, plus cette stabilisation va être grande. Simultanément, lors du retour à l'état fondamental le solvant, toujours orienté, conduira à une déstabilisation de l'état S_0 appelé transitoire S_0' .

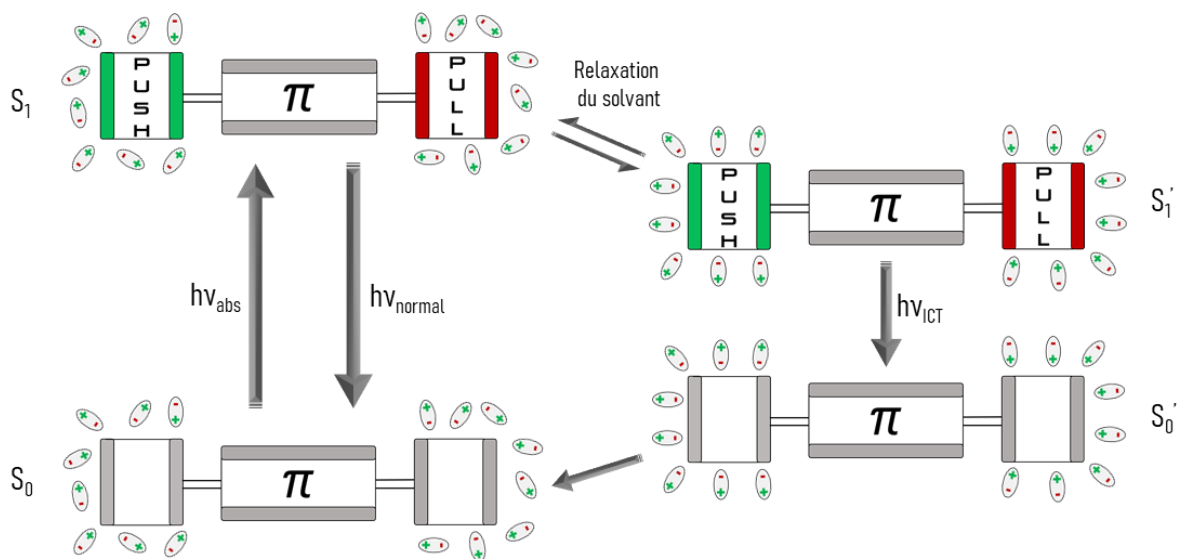


Figure 7. Diagramme énergétique des sondes push-pull sous l'influence de solvant.

En addition de l'effet de stabilisation apporté par les solvants polaires, la formation de liaisons hydrogène entre le solvant et le soluté est observée dans le cas des solvants protiques. Ce type de liaison confère une stabilisation supplémentaire de l'état excité et ainsi amplifie l'effet bathochrome des solvants polaires. Résultant de ces fortes diminutions énergétiques de l'état S_1 , la probabilité d'une désexcitation non-radiative par un mécanisme de conversion interne est fortement accrue. Ceci est observé lors de la présence, sur les sondes, d'un groupement accepteur de liaison hydrogène de type « C=O » (oxygène plus basique à l'état excité). Par conséquent, les solvants les plus polaires protiques induisent une

neutralisation du signal de fluorescence (*quenching*). Cette propriété confère aux sondes push-pull une grande sensibilité aux changements environnementaux. Elles ont été utilisées, par exemple, pour étudier la structure et la dynamique des biomembranes ainsi que les interactions qui s'y établissent⁵.

En complément, certaines sondes *push-pull* peuvent présenter un état torsadé appelé TICT (*Twisted Intermolecular Charge Transfert*)^{6,7} également fortement éteint.

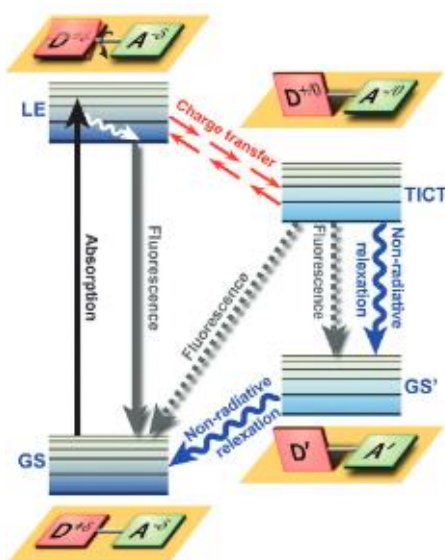


Figure 8. Diagramme énergétique du phénomène de TICT.⁷

Le TICT est le résultat de la rotation hors du plan des groupements donneur et accepteur à l'état excité qui permet de maximiser la séparation de charge entre D et A. Cet état torsadé est favorisé dans les milieux polaires. Il se traduit par un déplacement du maximum d'émission encore plus marqué vers le rouge qui est dû à une réduction accrue de la différence énergétique entre la S_1 et la S_0 (Figure 8). La réduction très prononcée du rendement quantique est principalement due au fait que les deux groupements sont positionnés orthogonalement.

II.1.2. Transfert de proton intramoléculaire

Le mécanisme d'ESIPT (*Excited-State Intramolecular Proton Transfert*) est mis en jeu pour des fluorophores dans lesquels un transfert de proton intramoléculaire a lieu à l'état excité. La sonde ESIPT est composée d'un groupement possédant un proton échangeable

(souvent hydroxyle) et d'un accepteur de proton (souvent carbonyle ou amine), les deux groupements étant proches dans l'espace (systèmes à 5 ou 6 centres, voir **Figure 9** pour des exemples). Cette proximité va conduire à l'échange du proton entre ces deux fonctions. Parmi les exemples les plus courants, on retrouve les sondes **3-HC** (3-hydroxychromone) et leurs aza-analogues (**3-HQ**) ainsi que les **HBON** (2-(2'-hydroxy-4'-diméthylaminophényl)-benzoxazole) (**Figure 9**).

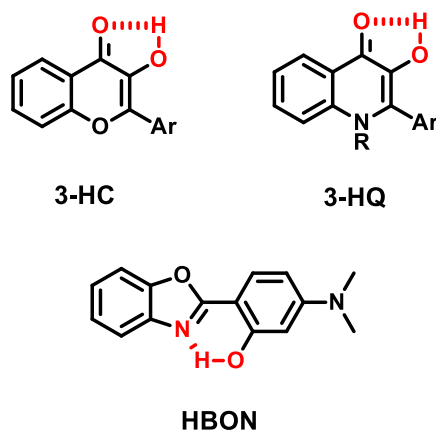


Figure 9. Exemples de sondes push-pull qui présentent un mécanisme ESIPT.

L'émission de fluorescence de ces sondes ESIPT est composée de deux bandes séparées, la bande normale (N^*) et la bande tautomérique (T^*) très décalée vers le rouge (**Figure 10**). L'ESIPT est fortement influencé par la nature électrodonneuse ou électroattractrice de ses substituants. Par exemple dans le cas des 3-HC possédant un groupement aryle mésomère donneur fort (ex. *p*-diméthylaminophényl), les 3-HC se comportent comme des sondes *push-pull* pour le déplacement du maximum d'émission de la bande N^* vers le rouge dans les solvants polaires et ratiométriques pour le rapport d'intensité des deux bandes d'émission N^* et T^* (N^*/T^*). Elles sont ainsi très sensibles aux changements environnementaux. Ici, c'est le rapport entre la bande N^* et T^* qui est le facteur le plus sensible. Celui-ci va être modifié en fonction de la polarité et de la proticité du solvant. Le N^*/T^* augmentera parallèlement avec l'augmentation de la polarité et proticité du solvant. En présence de solvant apolaire aprotique, l'ESIPT sera favorisé avec l'émission dominante de la forme tautomère (**Figure 10**). L'inconvénient majeur des sondes ESIPT concerne leur faible photostabilité.

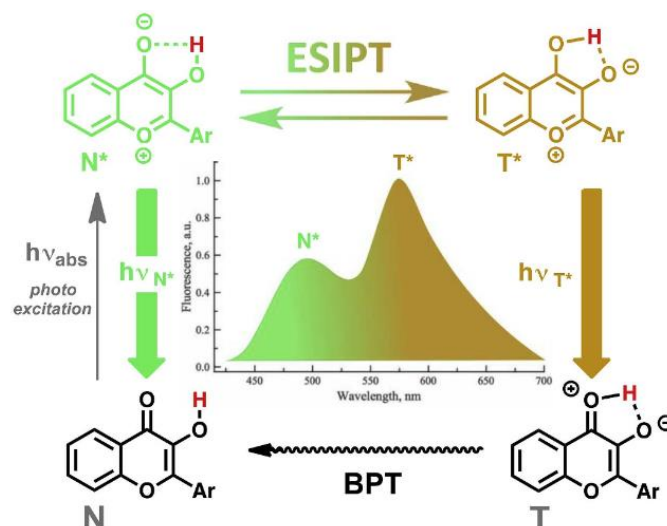


Figure 10. Réaction ES IPT et origine de l'émission duale sur la sonde 3-HC. (BPT : Back Proton Transfert)⁸

L'exploitation de cette émission duale a permis d'observer et quantifier plus facilement certaines interactions biomoléculaires⁹ (hybridation de l'ADN¹⁰, interaction peptide-protéine¹¹ et, peptide-membrane lipidique¹²) mais également de créer des senseurs ioniques¹³ (cations métalliques, anions inorganiques ou petites molécules neutre).

II.1.3. Changement de conformation

La planéité est une des caractéristiques principales requises pour la plupart des molécules fluorescentes. En réalité, lorsqu'une molécule fluorescente perd sa planéité, elle favorise les relaxations non-radiatives et ainsi le retour à l'état fondamental sans émission de photon. Cette propriété a permis d'engendrer les sondes fluorogéniques appelées *molecular rotor*.

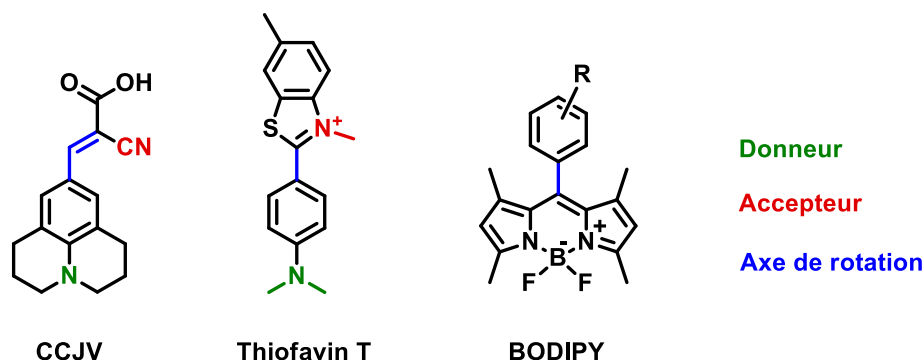


Figure 11. Exemples de sondes à changement de conformation.

Dans un environnement visqueux ou restreint (intercalation, basse température), la rotation de ce type de molécules est ralentie, ce qui leur permet d'émettre de la fluorescence. Par

contre, l'émission de fluorescence en solution est très faible. Les sondes de ce type les plus connues sont (**Figure 11**) :

- Les dérivés de CCVJ (dérivés de julolidine)^{14,15}, utilisés pour étudier des interactions protéine-protéine, observer la microviscosité intracellulaire ou même utilisés en science du polymère.
- La Thiofavin T¹⁶, couramment utilisée pour des tests biomédicaux, notamment en *drug discovery*¹⁷.
- Les dérivés de BODIPY (bore-dipyrrrométhène)¹⁸, pouvant être utilisés en imagerie en temps de vie de fluorescence pour observer la viscosité des membranes cellulaires¹⁹.

II.1.4. Isomérisation à l'état fondamental

A l'état fondamental, certains fluorophores peuvent, par isomérisation, rompre la conjugaison de leur système π , ce qui annihile leur capacité de fluorescence. Très peu de sondes fonctionnent suivant ce phénomène, nous y retrouvons principalement les dérivés de xanthènes (**Figure 12**).

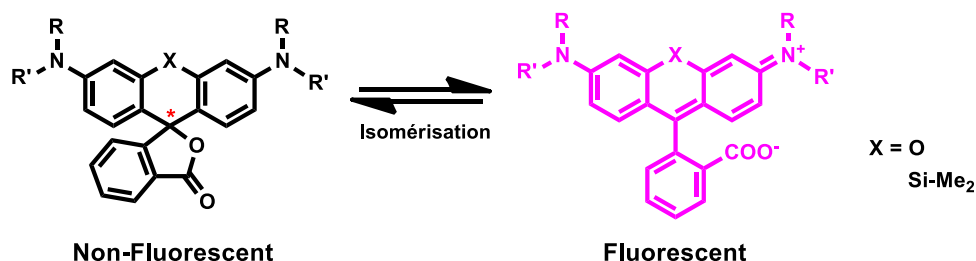


Figure 12. Schéma du fonctionnement des sondes d'isomérisation avec les rhodamines.

Ainsi, dans le cas des rhodamines de type B, il existe un équilibre entre l'ouverture et la fermeture de la forme spirolactone, qui possède un carbone asymétrique. Du fait de cet équilibre, on observe une racémisation de la spirolactone. Cette isomérisation dépend de la polarité du solvant ainsi que du pH en solution aqueuse. Si l'isomérisation est bien contrôlée, la différence de brillance entre la forme ouverte et fermée est considérable, puisque la spirolactone n'émet pas de fluorescence. Grâce à cette propriété, et par l'utilisation de sila-rhodamine²⁰ (SIR), des protéines cibles ont pu être imagées par SIM²¹ (*Structured*

Illumination Microscopy) et des images super-résolues ont pu être obtenues ^{21,22} (dSTORM ou STED, c.f. p.76.).

II.1.5. Sensibilité au pH

De nombreux fluorophores sont sensibles à la variation du pH. En jouant sur la structure du fluorophore, il est possible d'obtenir un *turn on/off* dans des milieux basiques, neutres ou acides²³. De nombreuses sondes à pH ont été décrites. On y retrouve, par exemple, les dérivés de fluorescéine ou de cyanine (**Figure 13**).

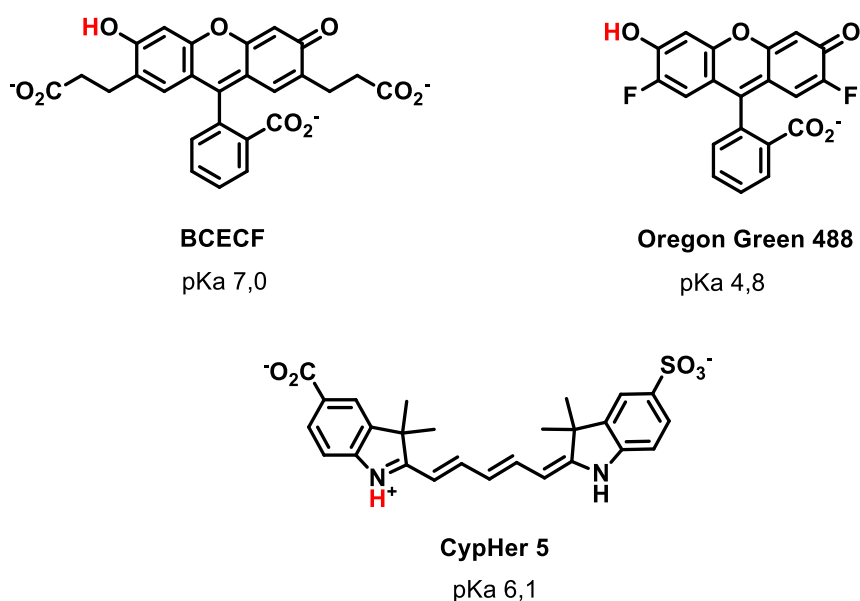


Figure 13. Exemples de sondes fluorogéniques utilisées pour sonder le pH.

En règle générale, toute sonde fluorescente existant en équilibre acido-basique est une sonde fluorogénique de pH, ce qui regroupe la quasi-totalité des sondes fluorescentes²³.

II.2. Processus à plusieurs partenaires

Il existe plusieurs méthodes pour obtenir un système fluorogénique faisant intervenir au minimum 2 partenaires. Dans cette partie, nous allons décrire quatre mécanismes, l'**agrégation**, le **PET**, le **FRET** et le **DRET**. Pour ces trois dernières méthodes, la distance entre les partenaires est un des paramètres clés pour le développement du système fluorogénique.

II.2.1. Agrégation

i. ACQ

Un phénomène couramment rencontré avec les fluorophores organiques (rhodamines, fluorescéines, ou BODIPY²⁴) est leur propension à former des agrégats non émissifs ou ACQ²⁵ (*Aggregation-Caused Quenching*).

Ces fluorophores organiques possèdent des systèmes π planaires peu solubles dans les milieux polaires/protiques. Dans ces milieux, les sondes, en général hydrophobes, s'empilent (π -*stacking*), ce qui génère un effet entropique favorable, augmentant la stabilité thermodynamique. Deux modèles de systèmes fluorogéniques existent, basés sur l'agrégation intramoléculaire ou intermoléculaire (**Figure 14B**).

L'agrégation intramoléculaire a été employée pour la détection de l'ADN double brin. Le dimère formé par les dérivés YOYO en solution est rompu après interaction avec le duplexe d'ADN, permettant ainsi de restaurer sa fluorescence (**Figure 14A**).

En règle générale, lorsque ces fluorophores s'agrègent, leur rendement quantique s'atténue fortement. Or, certaines applications requièrent l'utilisation d'une forte concentration en sonde, par exemple dans le cadre d'études à l'état solide. La majorité des fluorophores ne sont donc pas compatibles avec cette exigence (travailler à haute concentration).

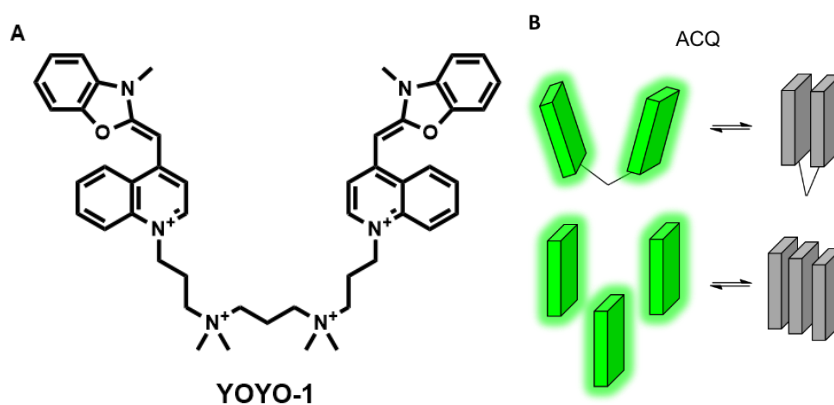


Figure 14. A) Structure de la sonde YOYO-1. B) Les deux types d'ACQ : intra- et intermoléculaire.

Pour les agrégats ordonnés, nous différencions généralement deux types d'agrégation : les H-agrégats et les J-agrégats. Ces deux agrégats se distinguent au niveau de

leur structuration géométrique²⁶. Dans le cas des H-agrégats, un empilement parallèle est observé et conduit à un état excité de plus haute énergie (effet hypsochrome du maximum d'absorption) (**Figure 15**). Pour les J-agrégats, un arrangement de type tête-à-queue est observé. Contrairement aux H-agrégats, cet arrangement provoque un abaissement énergétique de l'état excité et donc un effet bathochrome du maximum d'absorption²⁷. Cette différence de structuration mène à une modification contraire de la constante radiative k_r . Dans la majorité des cas, les J-agrégats conduisent à une valeur de k_r plus haute et ainsi à une forte émission (*turn-on*) contrairement aux H-agrégats, qui seront éteints (*turn-off*). Les H-agrégats sont donc non-fluorescents alors que les J-agrégats le sont.

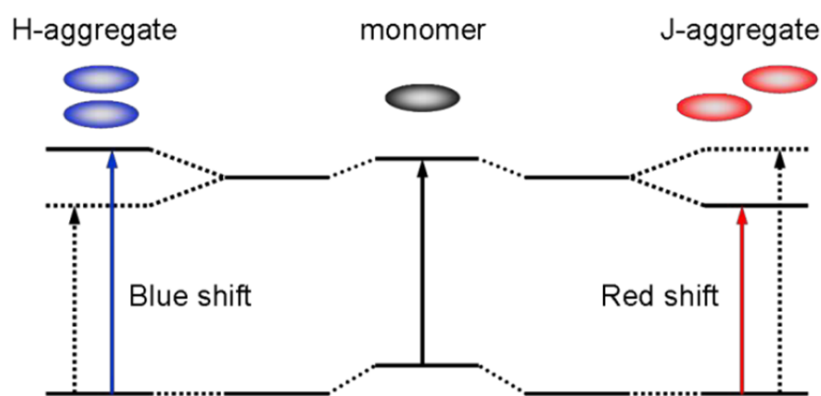


Figure 15. Propriétés électroniques suivant l'arrangement en H ou J-agrégats.²⁸

ii. AIE

Dans certains cas, des monomères non fluorescents en solution peuvent conduire à des agrégats fluorescents. Ils sont le résultat d'un phénomène appelé AIE²⁹ (*Aggregation-Induced Emission*). La compréhension des mécanismes qui régissent l'AIE reste l'objet de recherches intenses. Différents mécanismes ont été proposés pour expliquer certains processus d'AIE comme la restriction de la rotation intramoléculaire (RIR), la restriction des vibrations intramoléculaires (RIV), l'agrégation J, l'aplanissement de la conformation, l'isomérisation *E/Z*, le transfert de charge intramoléculaire torsadé (TICT), le transfert de protons intramoléculaire à l'état excité (ESIPT), etc³⁰. Ces phénomènes fluorogéniques ont été exploités pour de nombreuses applications³¹.

Les exemples les plus courants reposent sur des *molecular rotor* (cf. **Chap. 1 : II.1.3.**, p. 32). C'est le cas de l'exemple historique le tétraphényléthylène (TPE) et de ses dérivés (**Figure**

16A). Suite à son agrégation, il a été proposé que l'émission de fluorescence de TPE repose sur la restriction des mouvements intramoléculaires (RIM) qui inclut les contributions dues aux rotations (RIR) et vibrations (RIV)^{32,33}. Lorsque les molécules sont non-agrégées, le retour à l'état fondamental est dominé par les transitions non-radiatives. Au contraire, une fois agrégées, les contraintes stériques sont amplement augmentées. Elles permettent alors de limiter drastiquement rotations et vibrations favorisant ainsi la désexcitation radiative (Figure 16B).

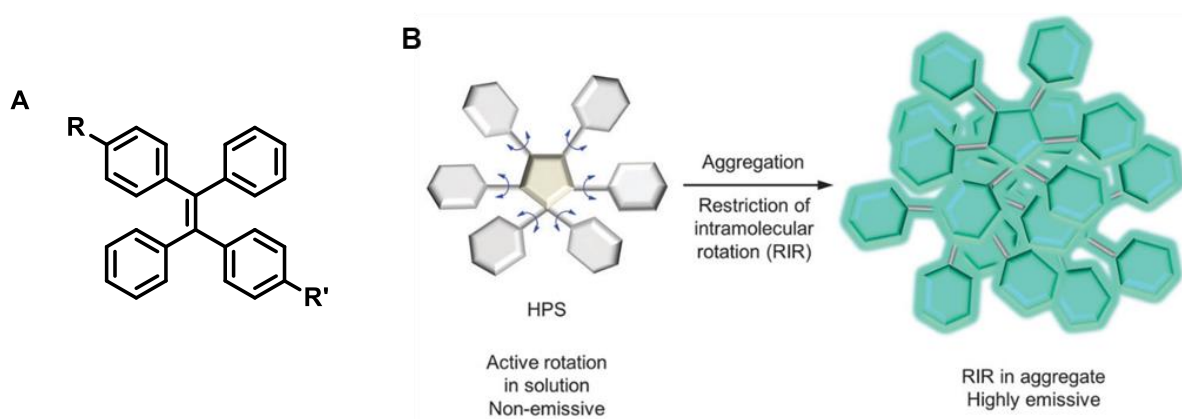


Figure 16. A) Structure des dérivés de TPE. B) Fonctionnement du phénomène d'AIE.³⁴

II.2.2. PET

Le Transfert d'Electron Photoinduit (PET pour *Photoinduced Electron Transfert*) est un processus faisant intervenir les propriétés oxydo-réductrices d'un fluorophore à l'état excité³⁵. Ce mécanisme peut intervenir de manière intra ou intermoléculaire

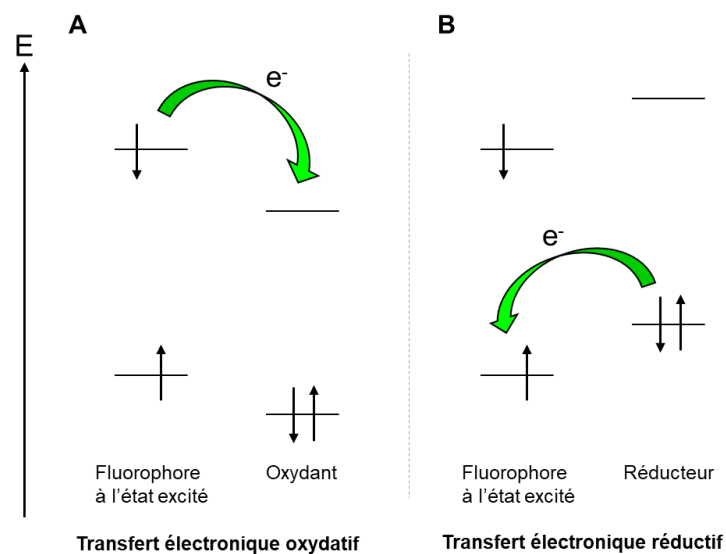


Figure 17. Mécanismes de transfert de proton photoinduit A) Oxydatif B) Réductif.

Le PET peut procéder selon 2 mécanismes différents (**Figure 17**), conduisant soit à l'oxydation soit à la réduction du fluorophore à l'état excité. Dans le cas du transfert électronique oxydatif, l'électron du fluorophore présent sur sa LUMO est transféré à la LUMO de l'espèce oxydante (**Figure 17A**). Ce premier cas peut être observé lors de l'interaction de fluorophores comme le pyrène avec la nucléobase thymine (T)³⁶. En effet, celle-ci possède le potentiel de réduction le plus bas des bases nucléiques et est connue pour être la meilleure acceptrice d'électron. Cette propriété a été mise à profit pour développer des senseurs sensibles à l'activité d'exo et endonucléases (**Figure 18**)³⁷. Dans le second cas, le réducteur possède une HOMO plus haute en énergie que celle du fluorophore. Un transfert entre le réducteur et le fluorophore s'opère pour combler le trou électronique de la sonde (**Figure 17B**). Ce second cas est couramment observé lors de l'interaction de composés fluorescents, telle la rhodamine, avec la nucléobase guanine (G). En effet, celle-ci possède le potentiel d'oxydation le plus bas des bases nucléiques et est connue pour être la meilleure donneuse d'électron³⁸. Dans les deux cas, ces processus conduisent à l'extinction de fluorescence (*quenching*) de nombreux fluorophores organiques. Pour que ce mécanisme soit réalisable, il est nécessaire que les deux espèces soient proches spatialement³⁹. La capacité des fluorophores à être éteints par les nucléobases a été mise à profit dans différentes applications en recherche fondamentale et appliquées. Le BODIPY a été plusieurs fois utilisé en raison de son potentiel réducteur élevé⁴⁰.

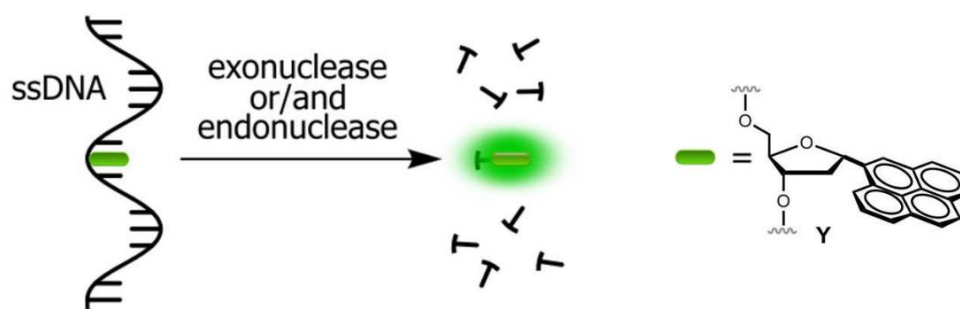


Figure 18. Effet d'extinction de fluorescence par PET du pyrène par la nucléobase T.³⁷

Des systèmes à deux partenaires intramoléculaires ont également été développés pour la détection d'ADN⁴¹. Ces systèmes sont composés d'un ligand de l'ADN et d'une sonde fluorescente. En cas d'une proximité spatiale entre les deux partenaires, un mécanisme PET s'effectue (*turn-off*). Cet effet est un exemple de ce qui est appelé « *contact quenching* ». La

liaison à l'ADN permet de séparer le « quencher » du fluorophore, le système devient alors fluorescent (*turn-on*) (**Figure 19**).

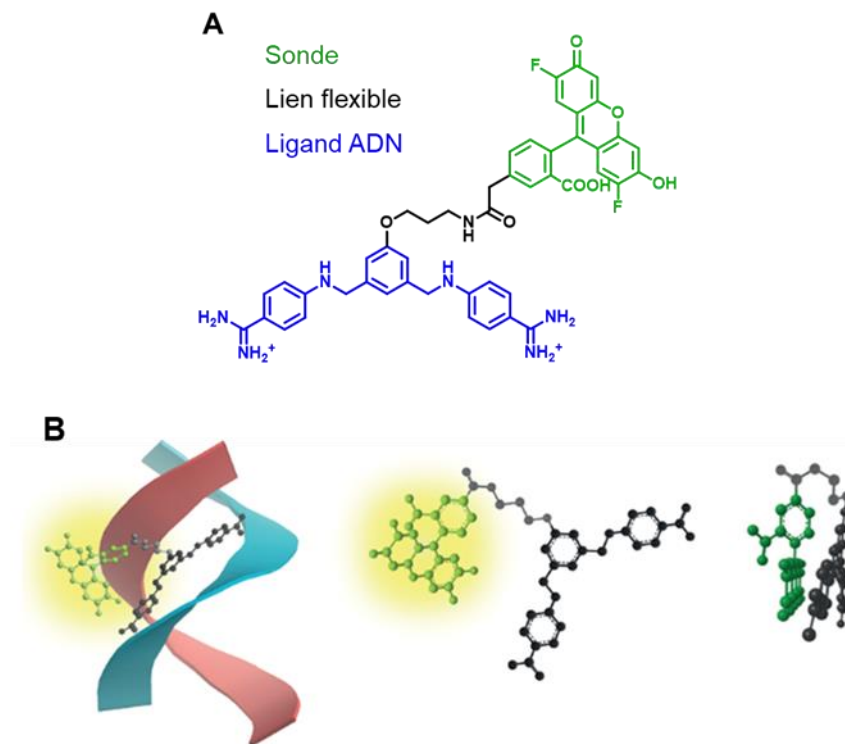


Figure 19. A) Structure d'un motif fluorogénique ligand de l'ADN formé par une fluorescéine (en vert) et de bis-benzamidine (en bleu) relié par une courte chaîne (en noir). B) Fonctionnement de la sonde d'hybridation par PET. A gauche, la ligation au double brin induit le *turn-on*. A droite, l'orientation spatiale de la structure dans son état éteint.⁴¹

II.2.3. FRET

Le FRET (*Förster Resonance Energy Transfer*) est un mécanisme faisant intervenir deux fluorophores (ou plus), l'un jouant le rôle de donneur et l'autre d'accepteur. Ce processus photophysique est un transfert d'énergie non-radiatif. Le FRET se déroule en trois étapes (**Figure 20A**)⁴² :

- ① Passage à l'état excité du donneur à la suite d'une irradiation lumineuse.
- ② Transfert d'énergie par résonance du donneur vers l'accepteur.
- ③ Retour à l'état fondamental de l'accepteur de façon radiative et/ou non-radiative.

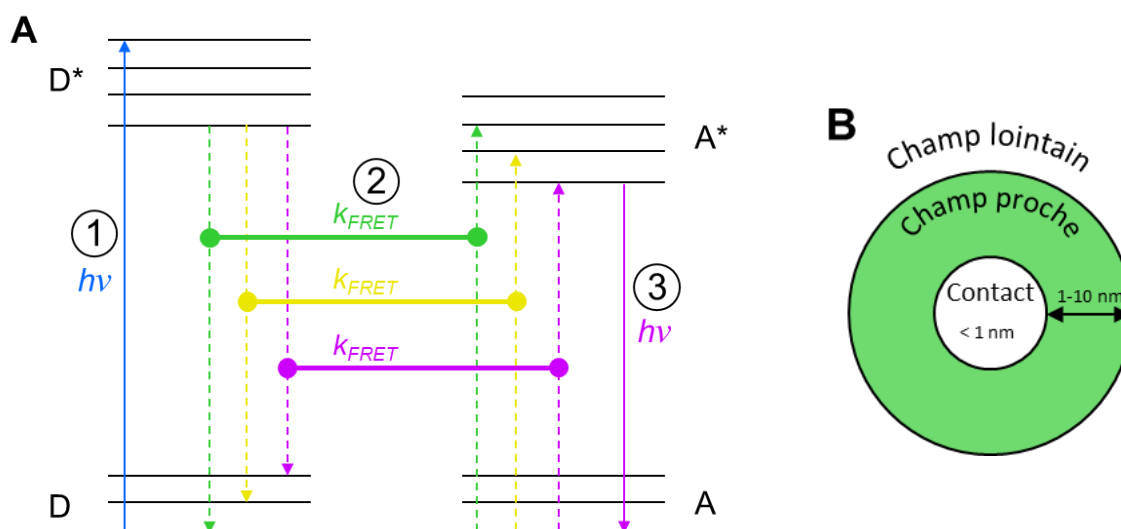


Figure 20. A) Diagramme énergétique simplifié montrant les 3 étapes clés du mécanisme FRET. B) Représentation de la distance nécessaire entre un donneur et un accepteur pour effectuer du FRET (en vert).

Dans le schéma précédent, grandement simplifié, ne sont représentées que les 3 étapes permettant d'obtenir le mécanisme FRET. Les transitions radiatives du donneur et les transitions non-radiatives de l'accepteur ne sont pas dessinées.

La seconde étape du mécanisme de FRET est capitale. Au cours de celle-ci, le donneur entre en résonance avec l'accepteur. Pour que le transfert d'énergie puisse se faire, la distance requise entre les deux fluorophores, nommée par Förster « Champ proche », se situe entre 1 et 10 nm (**Figure 20B**). La zone inférieure à 1 nm correspond à la « zone de contact », où la collision entre le donneur et l'accepteur a lieu et où le mécanisme de Dexter intervient, entraînant une dissipation de l'énergie non-radiative.

Au cours de la résonance, l'énergie entre la transition $D^* \rightarrow D$ et $A \rightarrow A^*$ est similaire. Cela signifie qu'il est nécessaire d'avoir un recouvrement du spectre d'émission du donneur et d'absorption de l'accepteur, appelé aire de recouvrement $J(\lambda)$ (**Figure 21**).

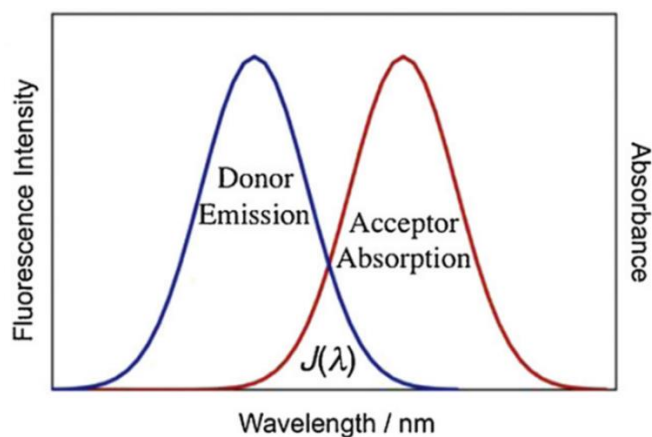


Figure 21. Représentation de l'aire de recouvrement entre le spectre d'émission normalisé du donneur et le spectre d'absorption normalisé de l'accepteur.⁴³

Il existe une multitude de paires FRET, la plus connue étant le couple de sondes Cyanines Cy3/Cy5. On retrouve également des systèmes composés de plusieurs donneurs et/ou accepteurs. De nombreux guides sont disponibles dans la littérature, un large éventail de couples donneurs/accepteurs commerciaux y sont recensés⁴⁴.

II.2.4. DRET

Contrairement au FRET, le DRET (*Dark Resonance Energy Transfer*) est un système fluorogénique très peu exploré. La littérature concerne principalement du DRET intramoléculaire (10 publications). Le premier exemple a été publié en 2002 et décrit un FRET à partir d'un donneur éteint⁴⁵. Pour ce qui est du DRET intermoléculaire, seule une publication récente (2021) traite de ce sujet (c.f. p.363)⁴⁶.

Le principe du DRET est identique à celui du FRET, à la différence de la nature du donneur qui, dans le cas du FRET, est émissif. Dans le cas du DRET, un donneur éteint est utilisé : il possède donc une constante de vitesse non-radiative bien plus élevée que sa constante radiative. Néanmoins, le phénomène de transfert d'énergie par résonance est un processus non-radiatif extrêmement rapide (picoseconde). Par conséquent, il est tout de même possible qu'un transfert d'énergie se produise entre deux espèces.

Suivant ce concept, l'association d'un donneur très peu émissif (espèce noire) et d'un accepteur très brillant conduit à un système fluorogénique. A l'exception de cette différence, les autres propriétés photophysiques du DRET restent similaires au FRET : un

recouvrement spectral (donneur-accepteur) ainsi qu'une distance préférentielle sont essentiels. L'atout majeur de la version, qui a été conçue et étudiée, est l'augmentation très importante du potentiel fluorogénique, résultant d'un fort déplacement de Stokes, et de la réduction de l'excitation (*cross-excitation*) et l'émission croisées (*cross-emission*) (Figure 22 D à comparer avec A-C).

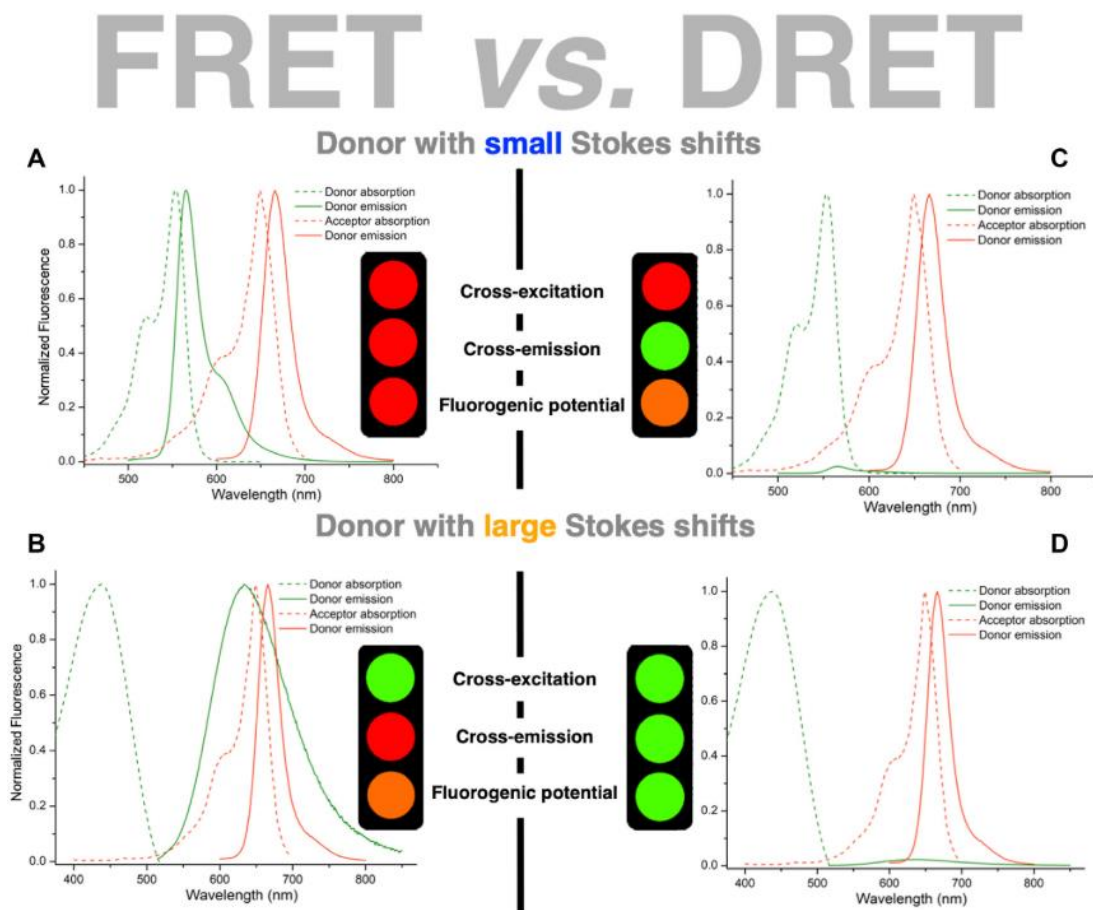


Figure 22. Comparaison entre le système FRET et DRET avec un faible/fort déplacement de Stokes.⁴⁶

III. Les acides nucléiques

III.1. Rappels

III.1.1 Composition

Les acides nucléiques (AN) sont des macromolécules biologiques formées de la polymérisation de plusieurs nucléotides. Suivant la nature de ces nucléotides, on obtient de l'ADN (acide désoxyribonucléique) ou de l'ARN (acide ribonucléique).

Les acides nucléiques sont composés de trois parties distinctes (**Figure 23**) :

- La nucléobase
- Le noyau (désoxy)ribose
- Les groupements phosphates

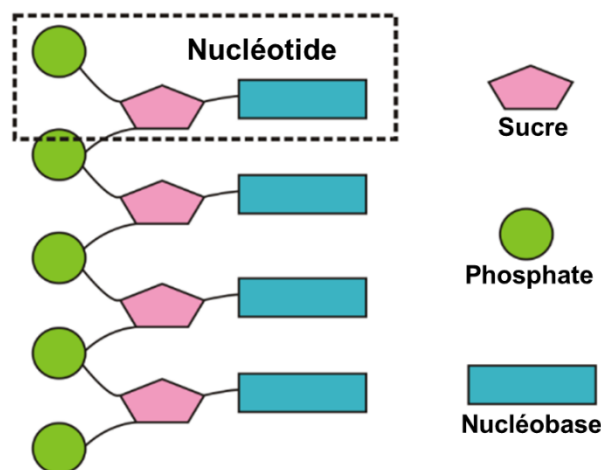


Figure 23. Vue schématique d'un acide nucléique.

La nomenclature (numérotation) des bases et des sucres est représentée dans la **Figure 24**. Les atomes de carbone et d'azote des bases sont numérotés normalement (1,2,3...) alors que les (désoxy)riboses sont numérotés avec un prime en exposant (1',2',3'...). L'ADN et l'ARN sont différents structurellement en deux points. Tout d'abord, le sucre est un 2'-désoxyribose pour l'ADN et un ribose pour l'ARN (**Figure 24**), c'est-à-dire que ce dernier contient un groupement hydroxyle en position 2'. Par ailleurs, la nature des bases nucléiques diffère légèrement : les bases puriques Adénine (A) et Guanine (G) sont présentes à la fois dans

l'ADN et l'ARN. En ce qui concerne les bases pyrimidiques, la cytosine (C) est commune aux deux, par contre la Thymine et l'Uracile sont respectivement spécifiques de l'ADN et de l'ARN (**Figure 24**).

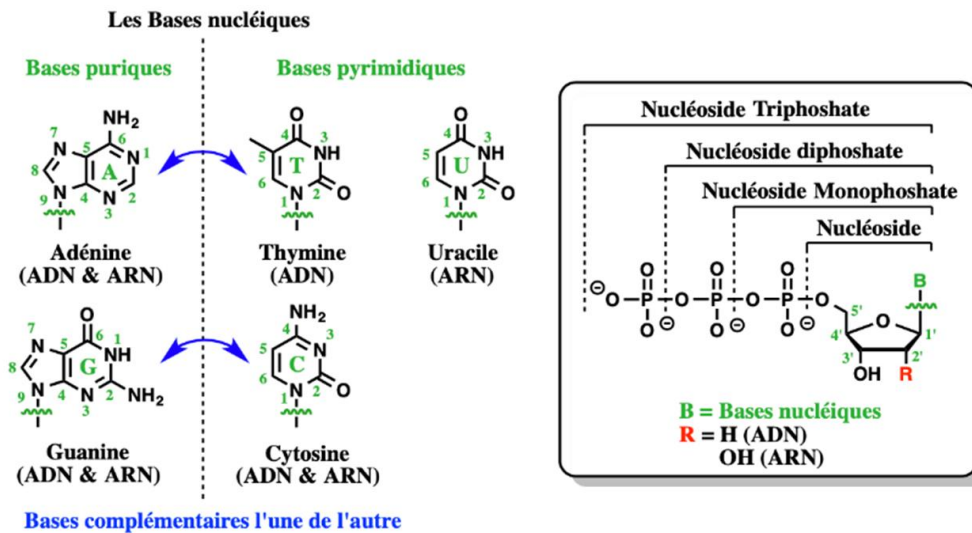


Figure 24. Structure des nucléosides et nucléotides (nucléoside lié à un ou plusieurs groupements phosphate).

III.1.2 Structure des acides nucléiques

a) Structure de l'ADN

L'ADN se présente le plus généralement sous la forme d'un duplexe, dans lesquels deux simple-brins d'ADN (**Figure 25A**) complémentaires sont en position antiparallèle. En fonction des conditions (concentration saline, nature des ions, composition en bases nucléiques, hydratation, etc.), ce double-brin peut adopter différentes conformations hélicoïdales en solution. La plus connue est la structure en double hélice B de l'ADN⁴⁷ (**Figure 25C**). La complémentarité contribue bien évidemment à la stabilité de la structure, grâce aux liaisons H établies entre les paires de bases A-T et G-C (interactions de Watson-Crick, **Figure 25B**), mais les interactions de Van der Waals notamment par recouvrement π (π -stacking) qui s'établissent entre les plateaux de bases y participent aussi largement ainsi que l'élimination d'un grand nombre de molécules d'eau.

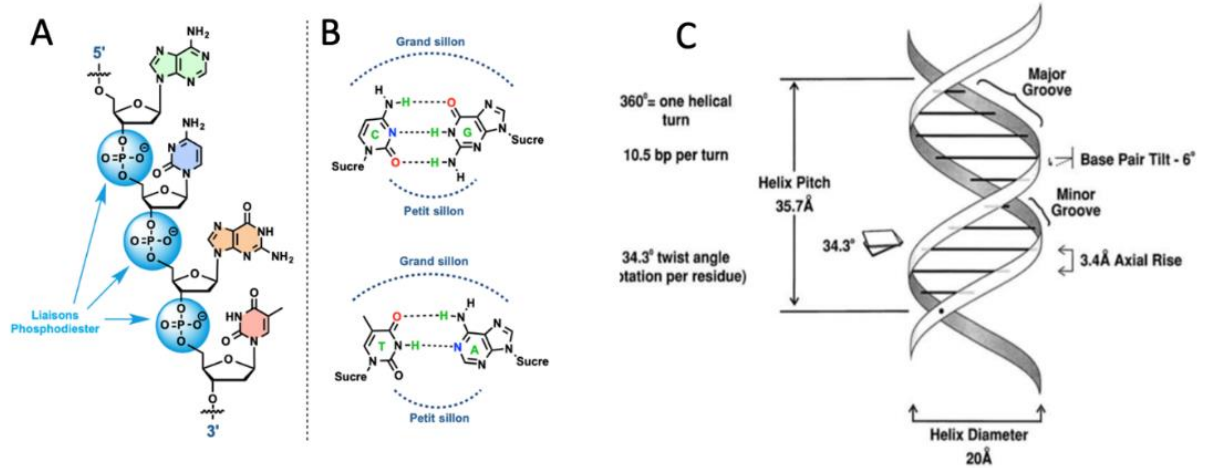


Figure 25. A) Structure chimique d'un simple brin d'ADN. B) Appariement des paires de bases de type Watson-Cricks. C) Paramètres de la double hélice en conformation B.⁴⁸

En dehors de la forme B, l'ADN double-brin peut adopter 2 autres conformations, les conformations A et Z (**Figure 26**).

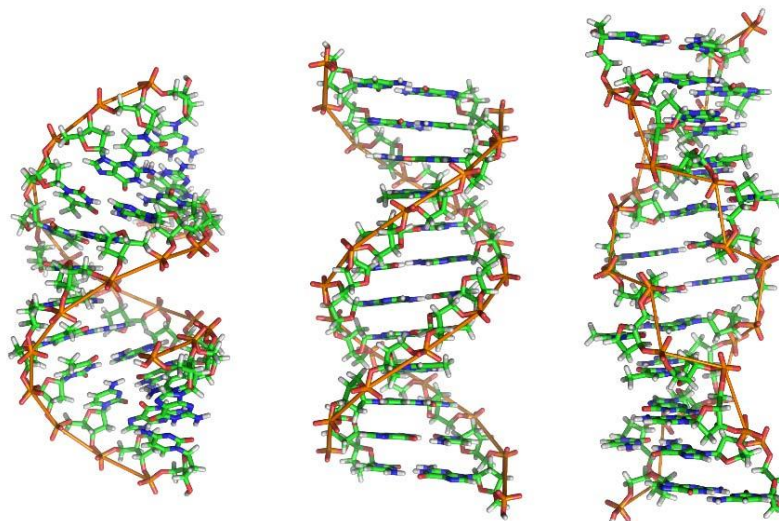


Figure 26 : ADN A, B et Z⁴⁹.

De nombreux paramètres permettent de définir le type d'hélicité adopté par l'ADN :

- Le sens de rotation de l'hélice (droite pour les formes B et A, gauche pour la forme Z).
- Le tour d'hélice, qui correspond au nombre de bases nécessaires pour faire une rotation complète (360°) de l'hélice (*Residues per turn*).
- La distance séparant 2 plateaux de bases (ADN-B \approx 3,4 Å) (*Axial rise*).

- Le pas de l'hélice, correspondant à la longueur d'une rotation complète de l'hélice (ADN-B = 35,7 Å) (*Helix pitch*).
- L'inclinaison entre le plan des bases et l'axe de l'hélice, (-6° pour l'ADN-B) (*Base pair tilt*).
- Le diamètre de l'hélice (de 20 Å pour la forme B).
- L'angle entre deux paires de bases adjacentes, souvent noté h (36° pour la forme ADN-B) (*Rotation per residue* ou *Twist angle*).

Ces paramètres structuraux sont en relation étroite avec les conformations adoptées par la base et le sucre (Figure 27A).

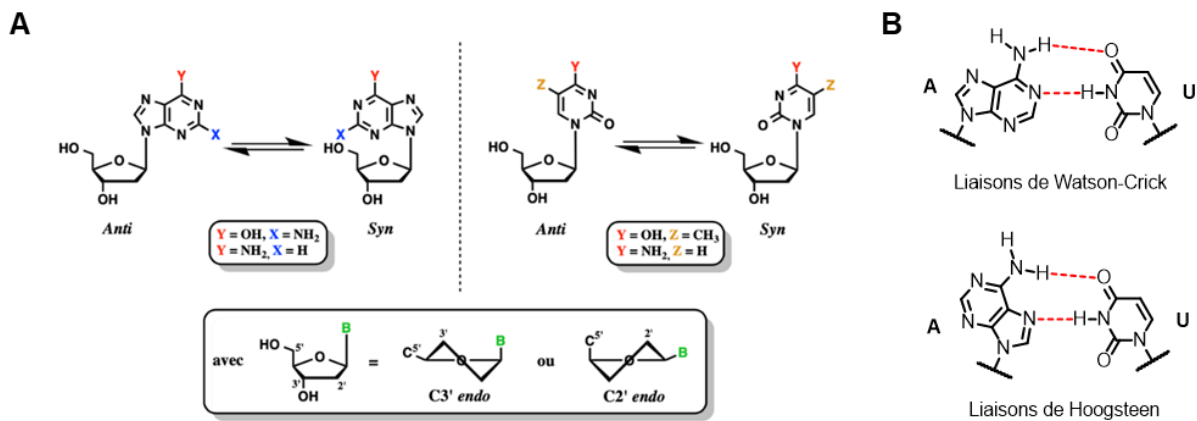


Figure 27. A) Conformation des nucléosides B) Exemple de liaisons de Watson-Crick ou de Hoogsteen sur les bases A-U. Les bases peuvent adopter deux conformations, *anti* ou *syn*, par rapport au sucre. Contrairement aux bases pyrimidiques, les conformations *anti* et *syn* sont énergétiquement proches pour les bases puriques. Des appariements classiques de type Watson-Crick s'établissent lorsque les quatre bases sont en conformation *anti*, alors que des appariements de type Hoogsteen se forment lorsque les bases sont en conformation *syn*⁵⁰ (Figure 27B). Les sucres, quant à eux, peuvent également adopter deux conformations principales, C3'-*endo* ou C2'-*endo*, dans lesquelles le carbone C3' ou C2', pointe vers le haut par rapport au plan du sucre, respectivement. Dans le cas de l'ADN en conformation B, le sucre est de type C2'-*endo*. Ceci conduit à un grand sillon large et un petit sillon fin et profond (Figure 28). L'ADN double-brin riche en paires G-C peut également adopter une forme A, dans certaines

conditions (faible taux d'hydratation, concentration saline élevée). Dans ce cas, le sucre est *C3'-endo*.

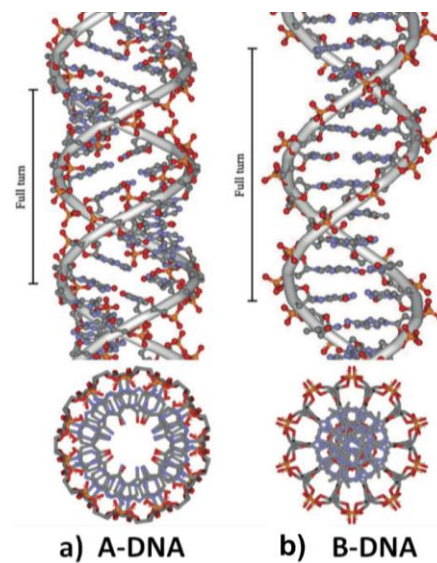


Figure 28. Modèle des structures tertiaires de a) l'ADN-A et b) l'ADN-B.⁵¹

Les paramètres structuraux des deux conformations principales de l'ADN (A et B) sont résumés dans le tableau suivant (Tableau 1)^{48,52} :

Tableau 1. Paramètres structuraux des conformations de l'ADN.

	ADN-A	ADN-B
Sens de l'hélice	Droite	Droite
Paires de bases par tour d'hélice	11	10,5
Distance entre 2 plateaux	2,55 Å	3,4 Å
Pas de l'hélice	28,2 Å	34 Å
Inclinaison des bases par rapport à l'hélice	20°	-6°
Angle entre deux paires adjacentes	32,7°	34,3°
Diamètre	23 Å	20 Å
Configuration des bases <i>dA</i> , <i>dT</i> , <i>dC</i>	<i>Anti</i>	<i>anti</i>
Configuration de la base <i>dG</i>	<i>Anti</i>	<i>anti</i>
Configuration des sucres <i>dA</i> , <i>dT</i> , <i>dC</i>	<i>C3' endo</i>	<i>C2' endo</i>
Configuration du sucre <i>dG</i>	<i>C3' endo</i>	<i>C2' endo</i>

Dans le paragraphe précédent, nous avons discuté des deux formes (hélices A et B) les plus classiques rencontrées dans l'ADN double-brins. Il existe cependant d'autres structures non-canoniques pour l'ADN, telles que les triplexes (ADN-H), les tige-boucles, les renflements, les cruciformes. Certaines structures, telles que les i-motifs et les G-quadruplexes,

s'établissent uniquement lorsque certaines bases prédominent, *via* l'association de un, deux, trois ou quatre brins d'ADN (**Figure 29**).

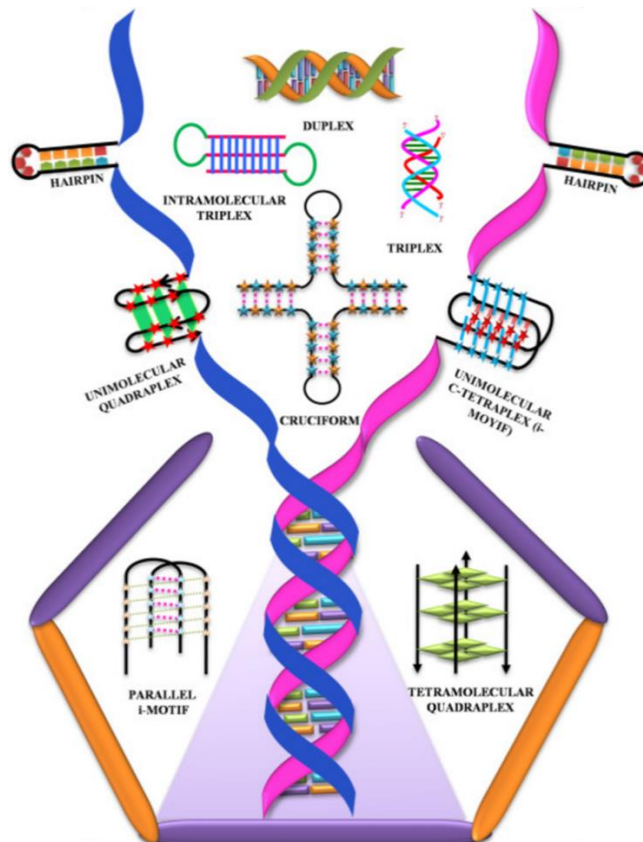


Figure 29. Liste non-exhaustive des structures non-canoniques de l'ADN.⁵³

La structure « i-motif » est constituée majoritairement de bases Cytosine, formant des liaisons Cytosine-Cytosine⁺ héli-protonée (C-C⁺), correspondant à des liaisons non-canoniques de Hoogsteen (**Figure 30**)⁵⁴. Ce motif est favorisé par un pH légèrement acide.

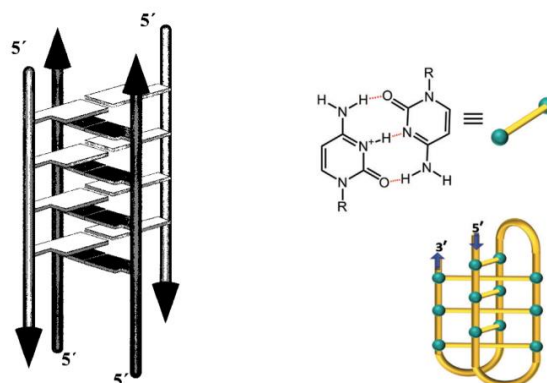


Figure 30. Représentation de la structure et orientation du i-motif.^{55,56,57}

Tout comme le « i-motif », la structure « G-quadruplexe » est favorisée lorsque la séquence ADN est riche en résidus Guanine (G). Contrairement à la plupart des autres structures de

l'ADN, ce ne sont pas des plateaux de deux bases liées par des liaisons H de type Watson–Crick (*base-pairing*) qui sont formés, mais ce que l'on appelle des quartettes de G (*G-quartet* ou *G-tetrad*), à savoir des plateaux de quatre bases liées par des liaisons H de type Hoogsteen^{58,59}, l'ensemble étant stabilisé par un cation (souvent potassium ou sodium) (**Figure 31A**)⁶⁰. Il existe un grand nombre de structures G-quadruplexes, dépendantes à la fois de la séquence de nucléotides, de l'orientation des brins, des conformations *syn/anti* ou même du cation (**Figure 31B et C**). Contrairement à ce que l'on pourrait penser, ce motif n'est pas inhabituel. En réalité, on le retrouve en particulier dans l'ADN humain télomérique ou dans la région promotrice des oncogènes^{60,61,62,63}.

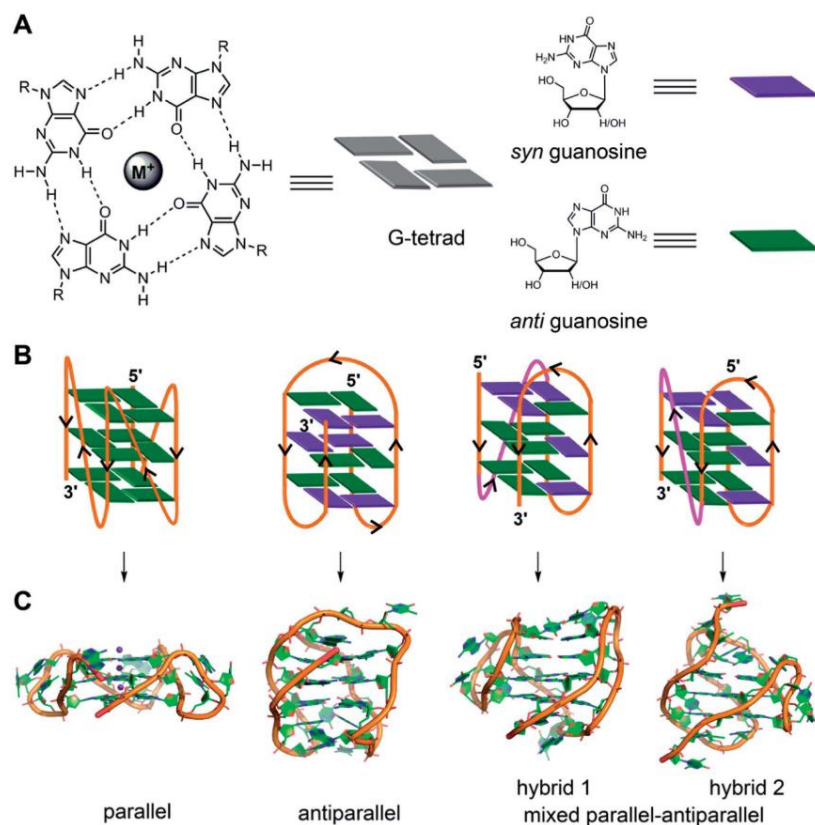


Figure 31. Différentes représentations du motif G-quadruplexe.⁶⁴

b) Structure de l'ARN

Contrairement à l'ADN, l'ARN existe sous forme d'un simple brin qui se replie sur lui-même, en formant des régions hélicoïdales et des régions non appariées (bulge, loops..., **Figure 29**). La présence sur le sucre du groupement hydroxyle en 2' fixe la conformation des régions hélicoïdales en hélice A (**Figure 28**). La conformation C3'-endo

des sucres de l'hélice entraîne une réduction de la distance entre les phosphates adjacents, menant à une structure plus compacte que celle de l'ADN B. Ceci induit un rétrécissement du grand sillon et un élargissement du petit sillon de l'hélice (**Figure 28**).

III.2. Marquage fluorescent des acides nucléiques (AN)

Parmi les différentes techniques permettant la détection des acides nucléiques (AN), la fluorescence est prédominante. Les autres méthodes, comme le marquage radioactif, sont trop contraignantes et ne possèdent pas les avantages majeurs de la fluorescence. Celle-ci est plus facile d'accès, rapide, non-invasive et extraordinairement sensible (à l'échelle de la molécule unique, c.f. p.79). Cependant, les bases nucléiques canoniques sont peu fluorescentes. Il est alors nécessaire d'effectuer le marquage de l'AN par le biais de l'utilisation d'un fluorophore plus brillant. Il existe deux façons de marquer les acides nucléiques, une méthode utilisant des fluorophores non-covalents, la seconde des fluorophores covalents.

III.2.1. Marquages non-covalents

Le marquage fluorescent non-covalent est la méthode la plus simple pour la détection d'acide nucléique. En effet, ce marquage ne nécessite pas la modification de l'AN et peut-être réalisé rapidement par l'ajout d'une concentration voulue de fluorophore au simple ou double brin d'AN. Le point négatif de cette méthode est la non-spécificité de la détection. Dans ce marquage, les fluorophores se lient de manière non-covalente à tous les doubles-brins d'AN présents, quelle que soit leur séquence.

III.2.1.1. Les intercalants

Les intercalants sont des molécules fluorescentes qui vont aller se positionner entre deux plateaux de bases d'une double-hélice d'AN. Ces composés possèdent une structure planaire, capable d'établir des interactions de type *π -stacking* avec les paires de bases et sont souvent chargés positivement à pH physiologique. Cette charge permet d'augmenter la stabilité des complexes formés, via des interactions électrostatiques avec les groupements phosphates de l'AN. Dans la majorité des cas, lors de l'intercalation, le phénomène de

fluorescence est amplifié (système fluorogénique). Cette amplification peut être due à de multiples facteurs (cf. **Chapitre 1 : II.1.** p.27). Dans le cas du bromure d'éthyldium (**BET**), ce fluorophore est fortement éteint au contact de l'eau mais devient très brillant lorsqu'il s'intercale entre les paires de bases de l'AN (ICT, c.f. **Chapitre 1 : II.1.1.** p.27)⁶⁵. Les sondes thiazole orange (**TO**) vont, quant à elles, s'aplanir suite à l'intercalation (*molecular rotor*, c.f. **Chapitre 1 : II.1.3.** p.32). Dû à la formation d'un H-dimère, le bis-intercalant **YOYO** (*vide infra*) donne la sonde la plus éteinte (c.f. **Chapitre 1 : II.2.1.** p.35) dans l'eau et le signal de fluorescence le plus intense après liaison à l'ADN (**Figure 32**)^{66,67}.

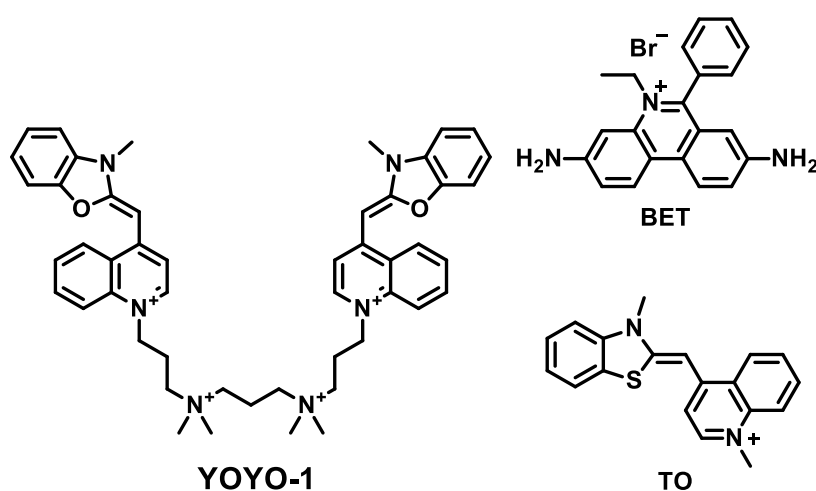


Figure 32. Structures d'intercalants de l'ADN.

III.2.1.2. Les ligands du petit sillon de l'ADN

Les ligands du petit sillon se lient, par le biais de liaisons Hydrogène, dans le petit sillon de l'ADN. Leur caractère hydrophobe permet d'amplifier cette liaison, puisque le petit sillon agit comme une « poche » hydrophobe (effet d'écrantage de l'eau). De plus, ce sillon étant très fin, l'encombrement stérique permet de bloquer le fluorophore à l'intérieur. Ainsi le microenvironnement apolaire et la flexibilité réduite du ligand en interaction avec le petit sillon de l'ADN seraient à l'origine de l'exaltation de fluorescence⁶⁸. Les ligands les plus utilisés pour ce type d'interaction sont les dérivés du DAPI et du Hoescht (**Figure 33**)⁶⁹ qui émettent dans le bleu. De nouveaux ligands émettant dans le rouge et proche infrarouge sont désormais également accessibles⁷⁰.

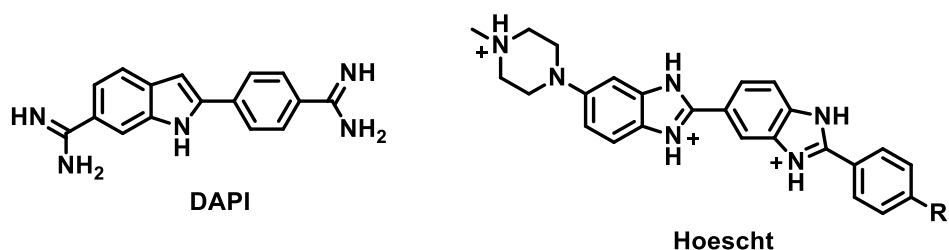


Figure 33. Structures de ligands fluorogéniques du petit sillon.

III.2.2. Marquages covalents

Le marquage covalent des acides nucléiques (AN), consistant à lier la molécule fluorescente à une séquence spécifique d'ADN, est une méthode plus complexe mais qui permet la détection spécifique d'un AN cible. Plusieurs groupes ont utilisé cette méthode pour obtenir une amplification de fluorescence lors de l'hybridation de deux brins d'ADN. C'est le cas des sondes à intercalation forcée (sondes FIT), introduites par O. Seitz⁷¹, qui tirent parti de la sensibilité à la viscosité des noyaux cyanines pour augmenter la fluorescence dans les milieux rigides (Figure 34C). C'est aujourd'hui l'une des sondes fluorogéniques les plus connues et performantes pour le marquage covalent des AN. Avant lui, cette technique avait été utilisée avec un intercalant inorganique⁷² (Figure 34A) mais également avec la sonde organique oxazole yellow⁷³ (Figure 34B). Le fluorophore peut être lié à l'AN à l'une de ses extrémités 5' ou 3' (Figure 34A), au niveau d'un groupement phosphate (Figure 34B), via un espaceur, ou directement au niveau d'un sucre (Figure 34C).

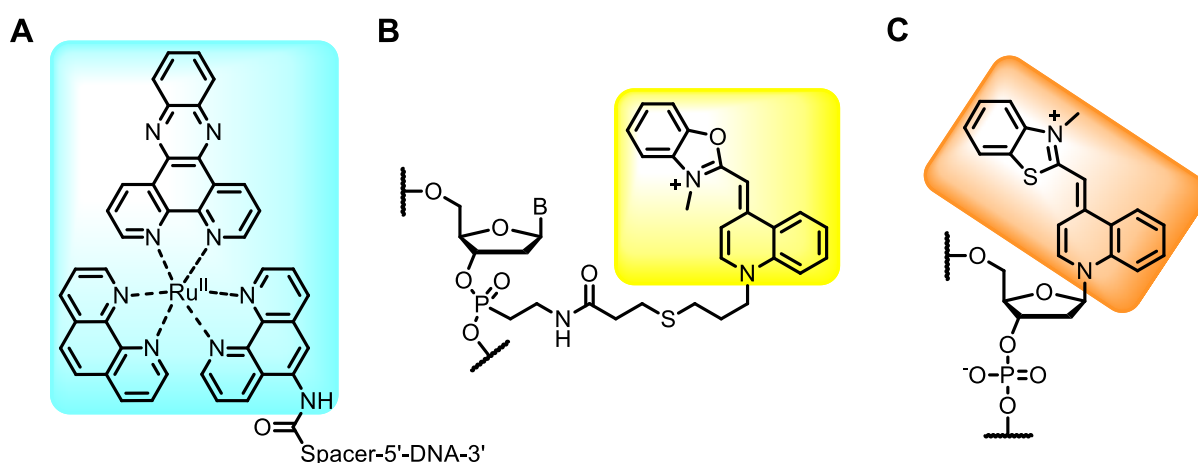


Figure 34 : Exemples de sondes intramoléculeaires A) Intercalant inorganique complexe de Ru^{II}. B) Sonde organique oxazole yellow. C) Sonde organique thiazole orange (TO).

Pour réaliser ce marquage covalent deux méthodes peuvent être mise en œuvre :

- Marquage pré-synthétique : le fluorophore est ajouté pendant la synthèse de l'AN.
- Marquage post-synthétique : le fluorophore est ajouté après la synthèse de l'AN.

Ces deux types de marquage nécessitent la synthèse d'oligonucléotides (ODN : petite séquence d'ADN ou ORN : petite séquence d'ARN). ODN ou ORN sont communément synthétisés en phase solide. Cependant, une autre alternative de synthèse existe, c'est la synthèse enzymatique. Cette dernière est moins versatile quant à la nature et à la position de marquage du fluorophore pouvant être introduit mais permet la formation de longs brins d'ADN ou d'ARN (10^4 nt)^{74,75}.

Seule la synthèse en phase solide d'ODN sera présentée dans ce travail.

III.2.2.1. Synthèse sur support solide d'ODN

La synthèse d'ODN sur support solide est représentée dans le **Schéma 1**.

Le support solide est appelé CPG (*Controlled Pore Glass*). Un premier nucléoside, protégé en position 5' par un groupement diméthoxytrityle, est relié au support *via* son groupement 3'-OH. L'élongation de l'ON va donc se poursuivre dans le sens 3'-5'.

La méthode de couplage la plus répandue est appelée « approche phosphoramidite »⁷⁶. Suivant cette stratégie, les nucléotides utilisés lors des étapes de couplage sont des dérivés phosphoramidites protégés au niveau des nucléobases, et au niveau des groupements hydroxyle en 5' par un groupement diméthoxytrityle. Quatre étapes sont répétées dans un processus cyclique (**Schéma 1**) :

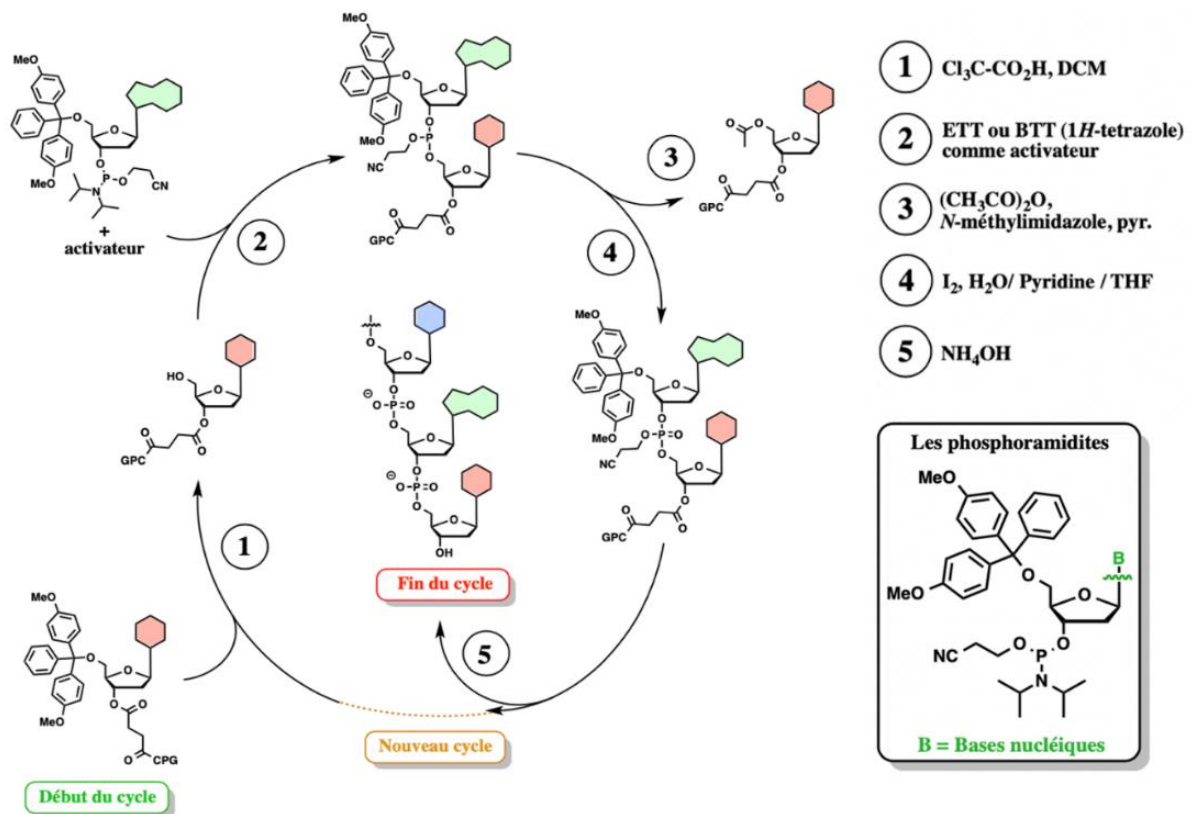


Schéma 1. Synthèse sur support solide d'ADN

- ① Clivage (détritylation) du groupement diméthoxytrityle (DMT) de l'hydroxyle en position 5' du sucre, au moyen d'acide trichloroacétique (TCA).
- ② Couplage d'un deuxième nucléoside phosphoramidite protégé, en présence d'un dérivé acide de 1-*H*-tétrazole : ETT ou BTT).
- ③ Acétylation (« capping ») de tous les 5'-OH libres n'ayant pas réagi lors de la réaction de couplage précédente, au moyen d'anhydride acétique et de *N*-méthylimidazole.
- ④ Oxydation du groupement phosphite (instable), en présence d'iode. Le motif cyanoéthyle agit comme protecteur du groupement phosphotriester, empêchant des réactions indésirables de se produire.

A la fin de la quatrième étape, le cycle recommence à l'étape une, par la déprotection du 5'-OH du dernier nucléotide ajouté.

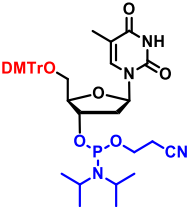
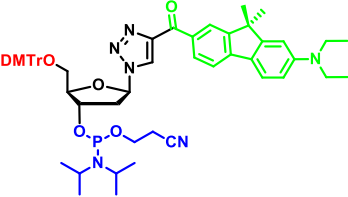
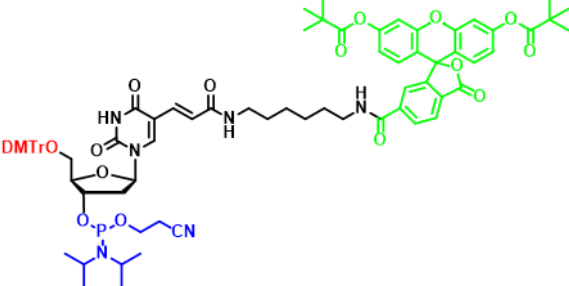
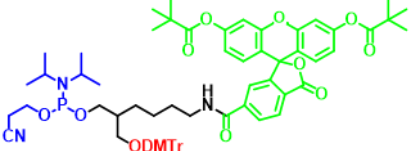
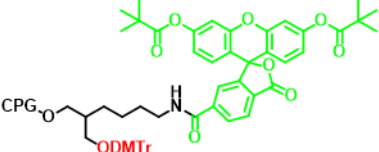
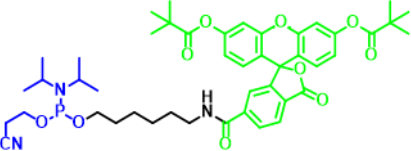
A la fin de l'élongation, l'acide nucléique est clivé du support solide au moyen d'une solution d'ammoniaque à 30%. Ce traitement permet aussi le clivage simultanée de tous les groupements protecteurs des phosphates et nucléobases^{77,78}.

III.2.2.2 Approche pré-synthétique

Dans le cadre de la synthèse des AN marqués par des sondes fluorescentes, l'approche pré-synthétique est basée sur l'incorporation, dans la chaîne d'AN en cours d'élongation, de nucléotides fluorescents. Suivant cette approche, le nucléotide marqué par le fluorophore peut être positionné à l'endroit désiré de la séquence de l'AN à savoir, au milieu ou en position 5' ou 3' de l'AN. La sonde fluorogénique peut être liée à une nucléobase naturelle, au groupement phosphate (*backbone modification*) ou encore, elle peut remplacer la nucléobase (voir **Tableau 2** pour des exemples). Suivant cette stratégie, la partie fastidieuse siège dans la synthèse du nucléoside fluorescent 3'-phosphoramidite.

Cependant, il faut noter que par le biais de cette méthode, toute sonde fluorescente ne peut pas être incorporée. En effet, si l'on se réfère aux conditions utilisées dans la synthèse sur support solide, la dernière étape consiste en une déprotection de l'AN au moyen d'une base forte (ammoniaque 30%). Certaines sondes sont instables dans de telles conditions. Il est alors nécessaire de protéger, si possible, les fonctions pouvant être instables lors de la synthèse, d'utiliser des conditions plus douces de clivage et de déprotection des ANs ou alors d'utiliser une autre méthode de marquage des acides nucléiques (partie suivante).

Tableau 2. Exemples de dérivés phosphoramidites fluorescents utilisés en synthèse en phase solide pour une approche pré-synthétique - positions de marquage.

Type de modification	Structure	Position de marquage
Phosphoramidite non-modifié		Site-spécifique pour une T
Substitution de la base		Site-spécifique, n'importe quelle position
Modification de la base		Site-spécifique, à la place d'une T
Modification du squelette		Site-spécifique, n'importe quelle position
Modification du squelette		Ajout en 3' uniquement
Modification du squelette		Ajout en 5' uniquement

III.2.2.3. Approche post-synthétique

L'approche post-synthétique offre une bien plus grande facilité de synthèse comparée à l'approche pré-synthétique⁷⁹. Il s'agit tout d'abord de synthétiser un AN incorporant, en une position choisie, un synthon fonctionnalisé par un groupement réactif.

Après l'élongation, le fluorophore, lui-même fonctionnalisé, est couplé directement sur l'AN, au niveau du synthon contenant le groupement réactif (**Figure 35**). Suivant cette approche, la réaction de couplage entre le fluorophore et le synthon fonctionnalisé de l'ODN se doit d'être spécifique. Elle doit être simple à mettre en œuvre mais doit surtout être compatible avec la nature chimique des ODNs.

Contrairement à l'approche pré-synthétique, cette stratégie permet, à partir d'un même AN fonctionnalisé, d'obtenir plusieurs AN marqués par différentes sondes fluorescentes.

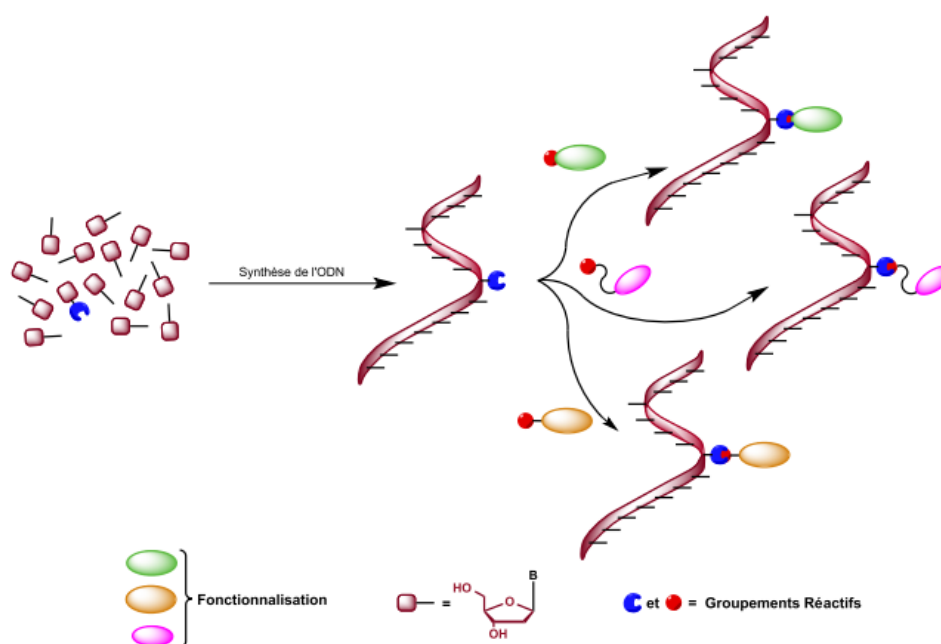


Figure 35. Représentation conceptuelle de l'approche post-synthétique.

i. Types de réactions post-synthétiques

La méthode post-synthétique est aujourd'hui largement répandue, en raison de la simplicité des réactions mises en œuvre, de leurs rendements élevés et de leur versatilité.

La première réaction possible, la plus classique, est la formation d'une liaison amide entre le fluorophore et l'AN, *via* la réaction d'une amine avec un réactif électrophile tel qu'un ester activé, un thiocyanate ou un halogénure d'acide⁸⁰. Une seconde méthode consiste à utiliser un composé thiol que l'on peut faire réagir, de façon orthogonale, sur différentes fonctions chimiques : haloacétyles, maleinimides, ou disulfures activés⁸⁰. Une autre approche plus sélective repose sur la ligation bioorthogonale⁸¹ comme la cycloaddition de

Diels-Alder⁸² (**Schéma 2A**) ou la ligation de Staudinger⁸³ (**Schéma 2B**). Ces réactions sont sélectives vis-à-vis des groupes fonctionnels portés par les composants cellulaires et peuvent être réalisées dans l'eau à pH physiologique avec une constante de vitesse élevée à température ambiante sans catalyseur^{84,85}.

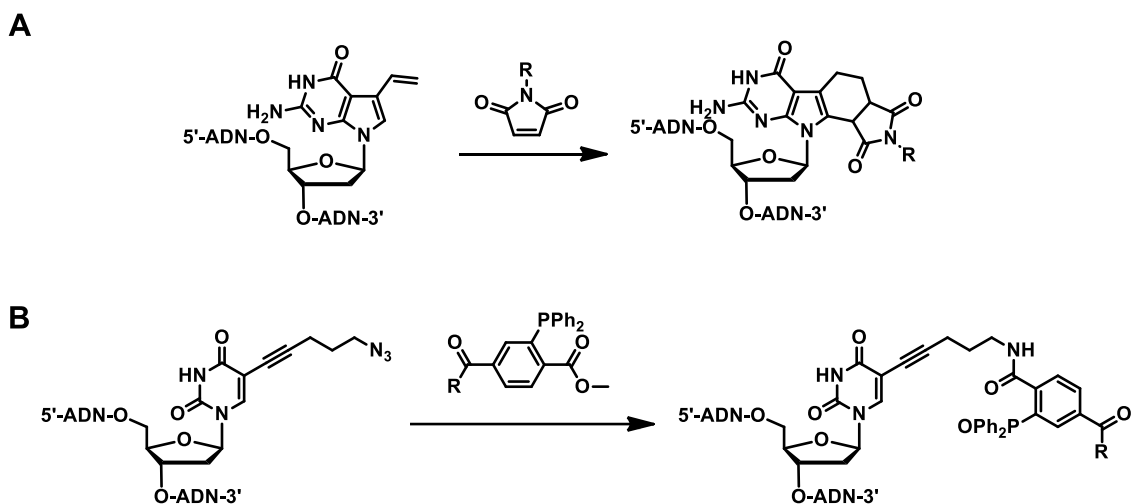


Schéma 2. Exemples de réactions post-synthétiques A) Diels-Alder post-synthétique⁸⁶, B) Ligation de Staudinger⁸⁷.

Ces qualités sont proches de celles de la chimie click introduite par Sharpless⁸⁸. La chimie click a été abondamment décrite et utilisée dans la chimie des acides nucléiques et, particulièrement, la cycloaddition de Huisgen⁸⁹. Cette dernière utilise un métal comme catalyseur. Lorsque ce métal est du cuivre, la réaction est appelée CuAAC (*Copper-catalyzed Azide-Alkyne Cyloaddition*). Plus récemment, en raison de la toxicité et/ou interférence métabolique des métaux, de nouvelles méthodes sans métal ont été développées. Dans celles-ci, on retrouve entre autres les SPAAC (*Strain Promoted Azide-Alkyne Cyloadditions*)^{90,91} aussi connues sous le nom de *Copper-free Azide-Alkyne cycloadditions*, l'équivalent avec les sydnone⁹², les réactions d'hétéro-Diels-Alder entre un alcène contraint et un tétrazine^{93,94} et les réactions de « photoclick » alcène-tétrazole⁹⁵ (**Schéma 3**).

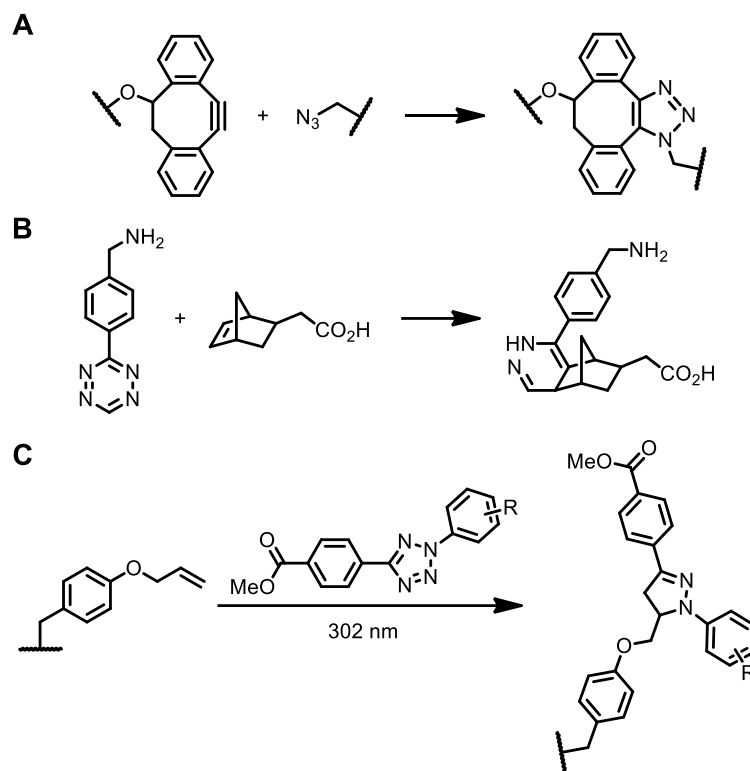


Schéma 3. Exemples de réactions post-synthétiques sans utilisation de métal: A) SPAAC⁹⁶ B) Conjugaison entre un alcène contraint et un tétrazine⁹³ C) Photoclick entre un alcène et un tétrazole⁹⁵.

Dans ce manuscrit, nous nous sommes principalement orientés vers la réaction CuAAC. En effet, celle-ci ne requiert pas l'utilisation de substrats complexes, contrairement aux réactions sans métaux (systèmes contraints ou noyaux hétéroaromatiques, voir **Schéma 3**). Dans ce cadre, le couplage AN/fluorophore doit s'effectuer via une fonction azoture et une fonction alcyne, chacune étant positionnée soit sur l'AN soit sur le fluorophore. Suivant cette méthode, il convient alors de réaliser la synthèse du fluorophore fonctionnalisé soit par l'azoture soit par l'alcyne. Ce choix est bien souvent dicté par la fonction présente sur l'ODN. Cette dernière sera discutée dans la sous-partie suivante (*ii. Diversité des liens*, p.61). Très récemment, une revue de T. Brown *et al.* (2021) a recensé toutes les réactions de *Click-Chemistry* appliquées aux acides nucléiques, ainsi que leurs applications et biocompatibilités⁷⁹.

La réaction de CuAAC peut se dérouler suivant deux voies (**Figure 36**). La première (voie A), la plus lente, implique un complexe mononucléaire CuL où L est un ligand. La seconde (voie B), plus rapide, implique un complexe dinucléaire Cu₂L et est cent fois plus rapide que la voie A.

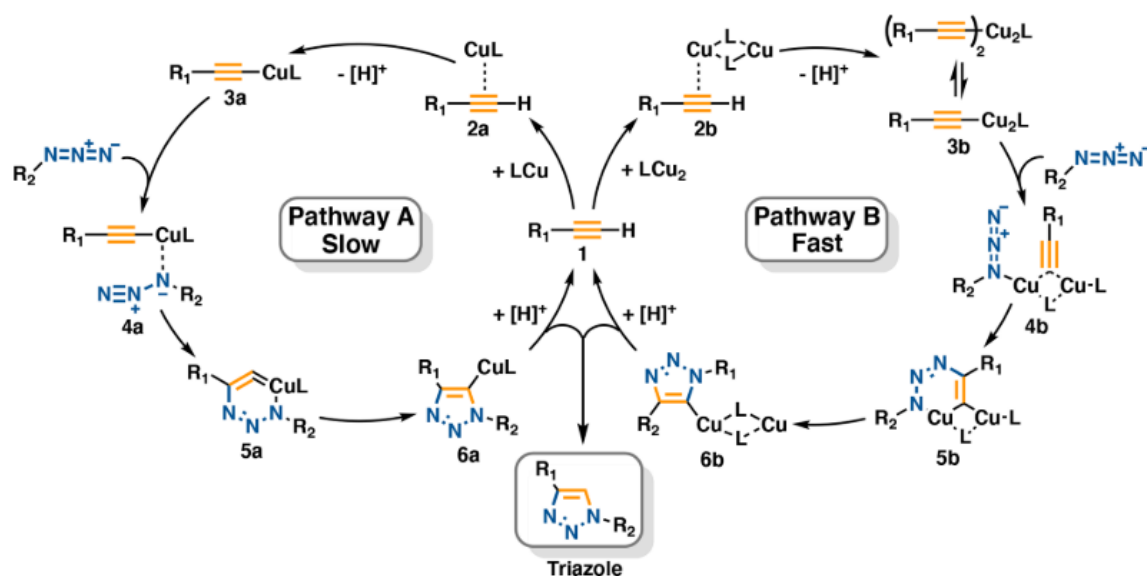


Figure 36. Les deux voies synthétiques en compétition pour la réaction de CuAAC⁷⁹.

La voie B est préférentiellement suivie en présence de ligands permettant la formation et la protection de l'espèce active Cu(I). En effet, le faible potentiel redox entre le couple $\text{Cu}^{2+}/\text{Cu}^+$ ($E_{\text{Cu}^{2+}/\text{Cu}^+} = 0,15 \text{ V}$) tend vers un passage du Cu(I) réactif en Cu(II) non-réactif, en solution aqueuse. Ces ligands sont en général de type tris(triazolyl)amine (Figure 37).

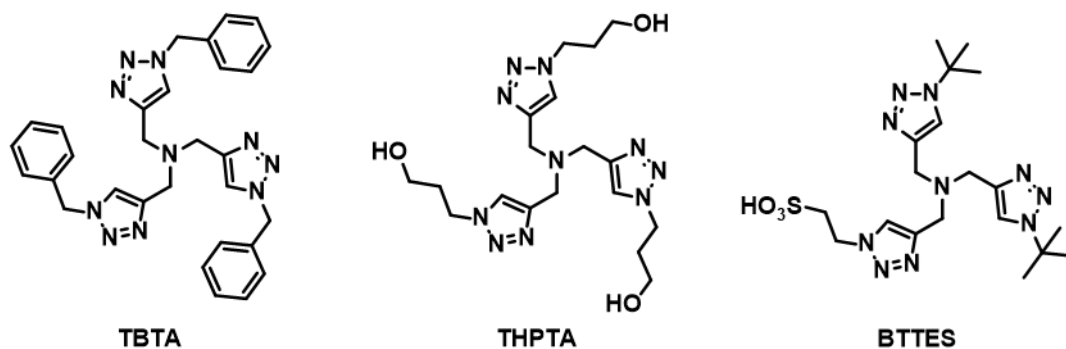


Figure 37. Exemples de ligands du cuivre pour la CuAAC.

A l'origine, le TBTA a été utilisé dans des milieux organique. Puis, son analogue soluble dans l'eau, le THPTA, l'a remplacé⁹⁷. Récemment, des ligands dérivés d'acides sulfoniques (BTTES) ont été développés et confèrent de meilleurs rendements, en raison de leur meilleure solubilité dans l'eau⁹⁸ (Figure 37). De surcroît, ils agissent également comme capteurs de ROS (*reactive oxygen species*), formés lors de la réaction entre les ions cuivre libres, l'ascorbate (réducteur dans la CuAAC) et le dioxygène, dans une réaction similaire à

celle de Fenton. Utilisés en excès dans des cycloadditions impliquant des biomolécules, les BTTES permettent de préserver ces dernières d'une potentielle oxydation⁹⁹.

Les conditions réactionnelles des CuAAC sont très spécifiques et requièrent des quantités très précises de chaque réactif, en fonction du solvant ou des substrats (alcène et azoture). Par exemple, le ratio [L]:[Cu] entre le ligand et le cuivre doit être contrôlé et ajusté en fonction des solvants utilisés, faute de quoi, un complexe inactif de Cu₂L₂ peut se former. La présence de base doit être également évitée, pour ne pas inhiber l'étape finale de protonation du produit cyclisé organocuivreux, conduisant à la libération du dérivé de triazole et au recyclage du complexe de cuivre initial¹⁰⁰.

ii. Diversité des liens

Dans le cas particulier d'une approche post-synthétique par CuAAC, on peut envisager d'incorporer, à un endroit précis de la séquence ADN, un synthon contenant une fonction azoture ou alcyne. Ce synthon peut être par exemple un sucre fonctionnalisé en position 1' (**Figure 38A et B**). Cependant, la présence d'un groupement azoture en position 1' d'un sucre peut entraîner des réactions secondaires de Staudinger lors de la préparation du phosphoramidite et de l'élongation de l'AN en phase solide¹⁰¹. C'est pourquoi on lui préfère en général un sucre possédant un groupement alcyne en 1' plus facile à manipuler. On peut également incorporer un dérivé nucléotidique dont la base nucléique est reliée à une fonction azoture ou alcyne par un bras de longueur choisie (**Figure 38C**). Dans tous les cas, la complémentarité alcyne/azoture permet alors d'élaborer une grande diversité de conjugués d'acides nucléiques et de fluorophores, reliés par des liens de nature et de longueur différente. En règle générale, un lien court (**Figure 38B**) conduira à un rapprochement structural du fluorophore et de l'ODN, contrairement à un lien plus long et plus flexible (**Figure 38C**).

De la même manière que lors d'une approche pré-synthétique, le synthon (sucre ou nucléotide) fonctionnalisé azoture ou alcyne est intégré à l'endroit désiré dans l'ODN (3', 5', ou interne) sous sa forme phosphoramidite. Aujourd'hui, il existe un large panel de

conjugués d'ODN et de fluorophores commerciaux, obtenus *via* des fonctionnalisations post-synthétiques diverses⁷⁸.

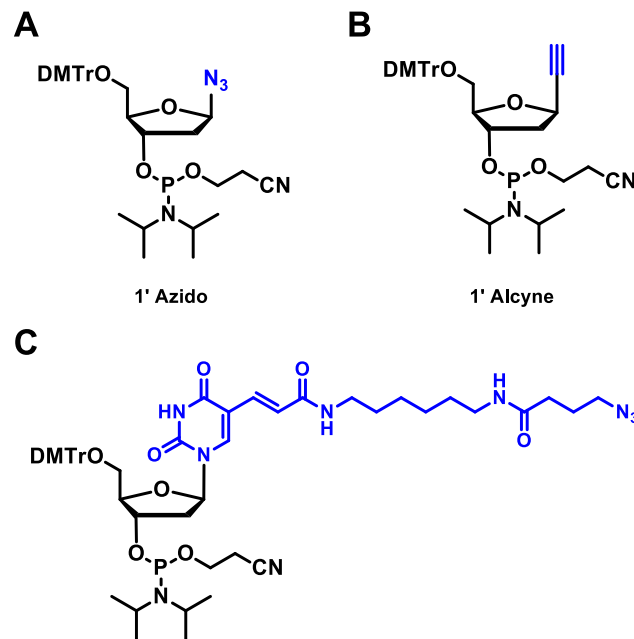


Figure 38. Types de synthons fonctionnalisés pour la CuAAC post-synthétique A) Lien court azoture incompatible avec la synthèse en chimie phosphoramidite sur support solide. B) Lien court alcyne compatible avec la synthèse sur support solide. C) Exemple de lien long azoture.

III.3. Détection des acides nucléiques (AN)

L'ARN joue un rôle essentiel en tant que messager de l'information du génotype (ADN) au phénotype (protéines), ainsi qu'en tant que molécule régulatrice (ARN non codants). Toutes les étapes du parcours de l'ARN, depuis sa synthèse (transcription), son épissage, son transport, sa localisation, sa traduction, jusqu'à sa dégradation finale, comprennent des étapes importantes de l'expression des gènes, contrôlant ainsi le destin de la cellule. Ce cycle de vie concerne la majorité des ARNs. L'imagerie de ces processus dans des cellules fixes et dans des cellules vivantes est un outil essentiel pour une meilleure compréhension des étapes de régulation du parcours des ARNs^{102,103}. Les techniques d'imagerie unicellulaire et unimoléculaire permettent une compréhension beaucoup plus approfondie de la biologie cellulaire qui n'est pas accessible lorsqu'elle est réalisée avec de l'ARN isolé d'un grand nombre de cellules. Par exemple il a été démontré que la localisation de l'ARNm est importante dans de nombreuses situations. Par exemple lors de la croissance d'un ovocyte de drosophile, un ARNm localisé de façon asymétrique produit un gradient

localisé de protéine qui spécifie la polarité antérieure-postérieure de la larve en développement¹⁰⁴. Il existe de nombreuses méthodes reposant sur différents concepts, allant des sondes d'hybridation, aux protéines de liaison à l'ARN et au marquage fluorogénique site spécifique de l'ARN. Ces méthodes présentent différents avantages et limites. Ce chapitre a pour but de présenter les principales techniques et de souligner leurs avantages et limites.

III.3.1. Techniques basées sur l'ingénierie cellulaire

III.3.1.1. La stratégie MS2

Un certain nombre de protéines de liaison à l'ARN dérivées de bactériophages ont été utilisées pour marquer l'ARN dans les cellules. Le plus remarquable d'entre eux est le système MS2 (MS2-MCP) (**Figure 39**). Il comprend deux plasmides qui seront transfectés. L'un d'entre eux code pour la protéine fluorescente verte (GFP) accolée à la protéine de liaison du bactériophage MS2 afin de fixer spécifiquement les GFP sur la séquence cible (exprimée par le second plasmide) par l'intermédiaire de portions en conformation tige boucle accolée à l'ARN ciblé¹⁰⁵. Récemment, le système MS2 a été utilisé pour visualiser des molécules uniques d'ARNm dans des cellules de souris vivantes¹⁰⁶.

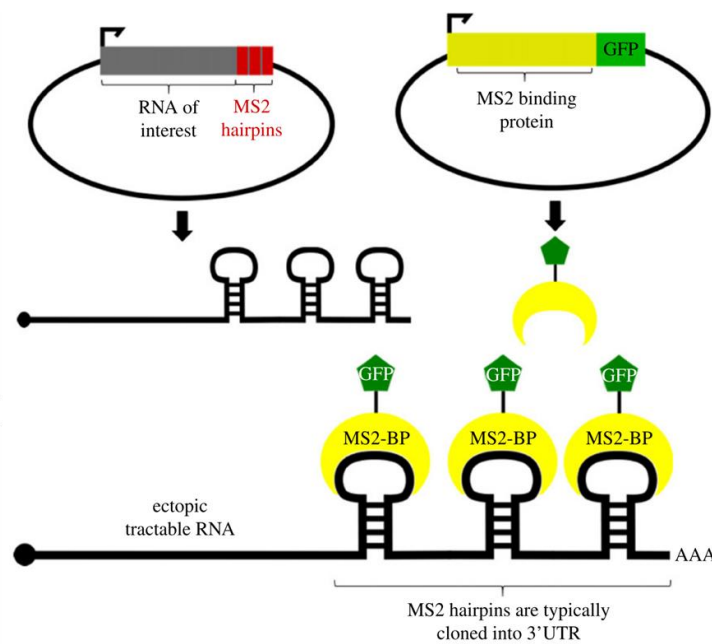


Figure 39. Principe de fonctionnement de la stratégie MS2.¹⁰⁷

Le gros avantage de cette stratégie réside dans le fait que la séquence tige-boucle MS2 ne perturbe pas le site de liaison de l'ARN à visualiser avec sa cible. De plus, une structure secondaire complexe de cet ARN ou des interactions avec des protéines ne gênent pas sa détection et sa localisation. En contrepartie, la grande taille de l'étiquette fluorescente ainsi que les appendices de l'ARN peuvent interférer avec la fonction ou la localisation normale de l'ARN¹⁰⁸. De plus, la quantité élevée de MS2 permettant la saturation de l'ARN cible conduit à l'augmentations importante du bruit de fond¹⁰⁹.

III.3.1.2. Les aptamères

Les aptamères sont des oligonucléotides courts et simple brin capables de se lier spécifiquement à une molécule par l'intermédiaire de leurs structures secondaires. Ils sont généralement sélectionnés *in vitro* par la méthode SELEX¹¹⁰. La spécificité de certains aptamères pour certains ligands est telle, qu'elle égale la performance de leurs équivalents protéiques, les anticorps. Lorsque le ligand spécifique de l'aptamère est un fluorophore, il est alors possible de le visualiser en imagerie et ainsi de suivre l'ARN auquel il est accolé (Figure 40).

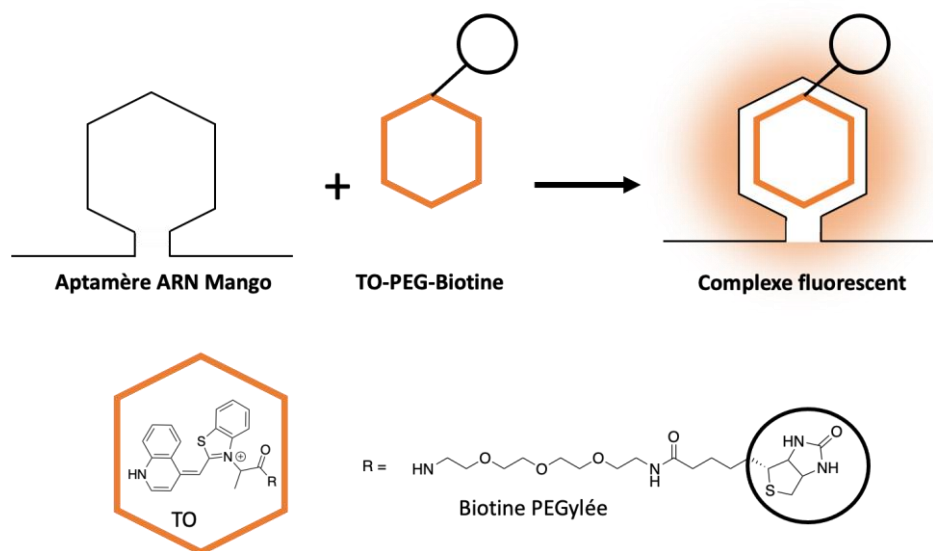


Figure 40. Principe de fonctionnement des aptamères. Exemple de l'aptamère Mango.

Afin de réduire considérablement le bruit de fond lors de l'utilisation de cette méthode, il est nécessaire d'utiliser une sonde générant un effet fluorogénique lors de sa ligation avec l'aptamère. C'est le cas de l'aptamère Spinach qui reconnaît spécifiquement le DFHBI

(chromophore de la **GFP**)^{111,112}. En solution, en raison des divers axes de libre rotations présents dans son squelette, ce colorant est peu fluorescent. A la suite de sa liaison à l'aptamère Spinach, l'augmentation de l'encombrement stérique autour du fluorophore permet d'accroître considérablement sa fluorescence. Par ailleurs, un aptamère permettant la ligation spécifique de la sonde Thiazole Orange (**TO**) a été identifié. Il s'agit de l'aptamère Mango (**Figure 40**). Les propriétés fluorogéniques de ce *molecular rotor* présentant une affinité au nanomolaire pour cet aptamère font de cette combinaison un outil puissant pour localiser des ARN d'intérêts^{113,114}¹¹⁴.

Tout comme la stratégie MS2, les aptamères peuvent perturber le trajet des ARN auxquels ils sont associés. De plus, il est difficile de maintenir leur conformation intacte au sein de la cellule, provoquant ainsi une baisse de sensibilité de la détection. En complément des méthodes d'ingénierie moléculaire, des stratégies de détection basées sur l'utilisation de sondes oligonucléotides antisens ont été développées.

III.3.2. Techniques d'hybridation directe

La séquence d'ARN peut également être ciblée directement dans la cellule par des sondes oligonucléotidiques antisens marquées capables de se lier spécifiquement par appariement de bases Watson-Crick (par complémentarité des bases). Ces techniques sont connues sous le nom de FISH (*Fluorescence in situ hybridization*). Différentes stratégies ont été développées en fonction des propriétés photophysiques du ou des marqueurs.

III.3.2.1. Stratégie simple marquage

La première méthode FISH la plus simple est d'utiliser un marqueur avec une fluorescence similaire sur et en dehors de la cible. Dans ce cas précis, comme pour le système MS2, il est nécessaire d'augmenter le nombre de séquences marquées pour obtenir un signal de fluorescence supérieur au bruit de fond (**Figure 41A**). Cependant, la fixation d'un grand nombre de sondes ne peut convenir qu'aux ARN les plus longs. Pour permettre d'imager des petits ARN (miRNA, siRNA, ...) l'arrangement linéaire juxtaposé ne convient plus, par contre une construction par empilement de sondes sur l'ARN cible est mieux adaptée. Pour ce faire, des stratégies telles que les *HCR* et *RNAscope* ont été conçues (**Figure 41B**).

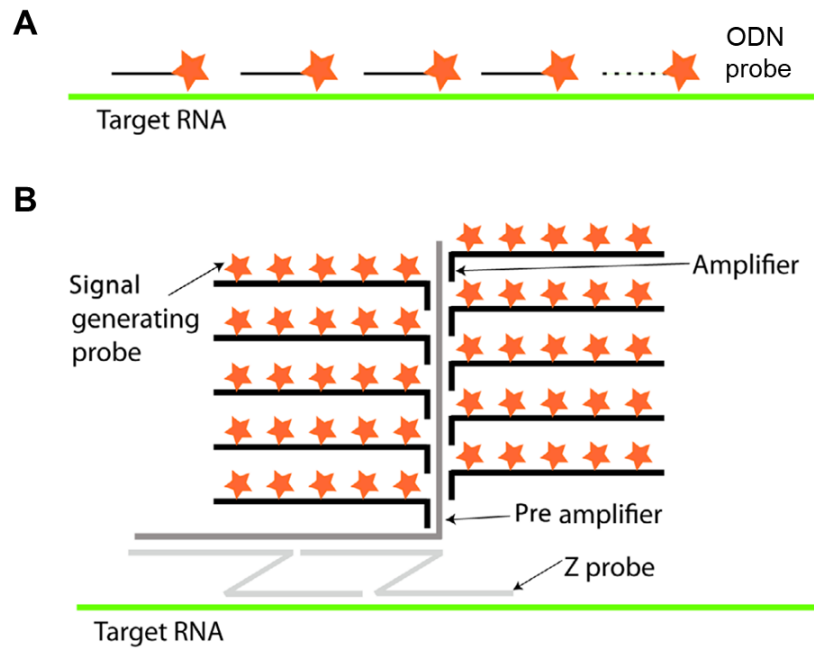


Figure 41. Imagerie des ARN par FISH via des sondes non-fluorogénique. A) Technique simple utilisant de nombreux petit ODN marqués pour allumer la cible ARN. B) Technique RNAscope : Liaison séquentielle des sondes Z, des préamplificateurs puis des amplificateurs pour créer des sites de liaisons de plusieurs sondes génératrices de signaux.

Néanmoins, ces tactiques nécessitent de nombreuses hybridations successives et sont difficiles à mettre en œuvre au sein de la cellule. Afin de simplifier le processus de localisation, il est judicieux de réduire le nombre de sondes employées. Il est alors indispensable d'utiliser une sonde portant un fluorophore capable d'accroître sa fluorescence à la suite de l'hybridation.

i. Sondes fluorogéniques : G-quenching

L'extinction de la fluorescence entre un résidu guanine et un fluorophore est une observation courante en raison du caractère donneur PET de cette base. Comme décrit dans une partie précédente, la guanine est la base avec le potentiel d'oxydation le plus bas, elle est ainsi une très bonne donneuse d'électrons (p.38). Il existe deux façons d'utiliser cette propriété, soit l'hybridation conduit à l'extinction de la fluorescence par un rapprochement avec une G ou, à l'inverse, l'hybridation permet d'accroître la distance entre la G et le fluorophore afin de restaurer sa fluorescence (**Figure 42**)^{115,116}.

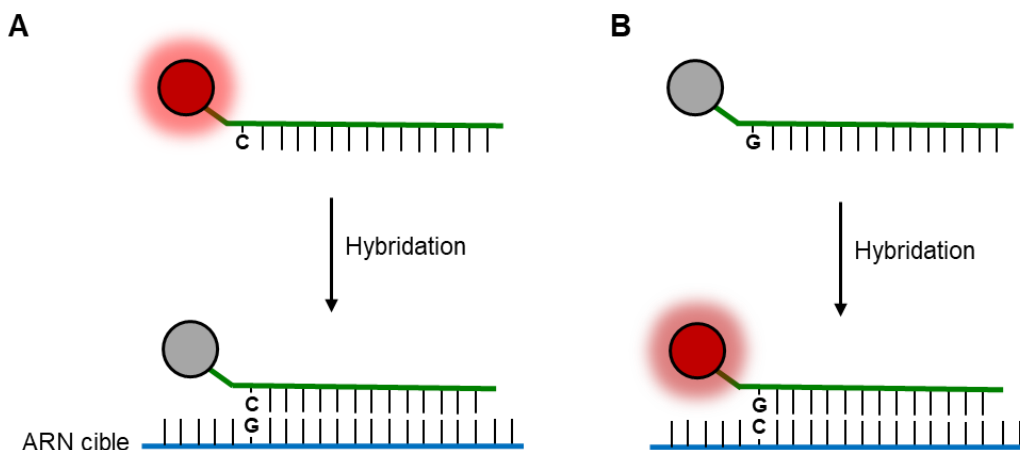


Figure 42. Mécanisme fluorogénique par PET du fluorophore avec la base guanine A) Activation du PET à l'hybridation. B) Désactivation du PET à l'hybridation.

ii. *Sonde fluorogénique : Sondes FIT*

Une autre approche consiste à utiliser des sondes FIT (*Forced Intercalation*). Ces sondes sont composées d'un court brin d'ADN, d'un PNA (*Peptide Nucleic Acid*) ou d'un LNA (*Locked Nucleic Acid*) marqué par un analogue de nucléoside fluorescent. Ceux-ci sont capables lors de l'hybridation avec leur brin complémentaire, d'amplifier leurs signaux de fluorescence une fois intercalé entre des paires de bases *via* la restriction de leurs mouvements (**Figure 43**). Il s'agit de sondes de type *molecular rotor* (*vide infra* p.32 et p.50).

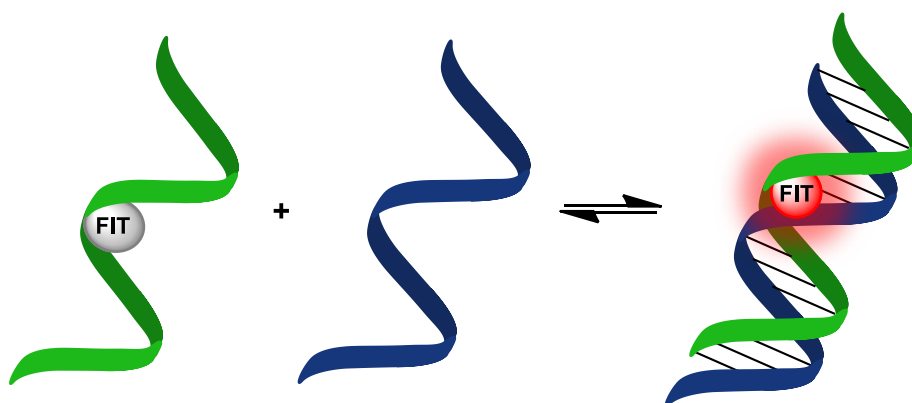


Figure 43. Mécanisme d'hybridation fluorogénique des sondes FIT.

Dans la grande majorité des cas, les sondes FIT utilisées pour la détection des AN sont des dérivées de cyanines comme l'oxazole yellow (YO) ou encore le thiazole orange (TO) (**Figure 44A**). Lorsque la sonde TO est utilisée sur un brin d'ADN, c'est-à-dire pour former un duplexe ADN:ADN, des facteurs d'amplification de 9 entre le simple brin d'ADN et le

duplexe peuvent être observés¹¹⁷. Avec l'utilisation de LNA ce facteur augmente et dans le cas de l'utilisation d'un PNA marqué au TO, le duplexe PNA:DNA formé entraîne des facteurs d'amplification bien plus conséquents, jusqu'à 28 fois supérieur au simple brin^{118,119}.

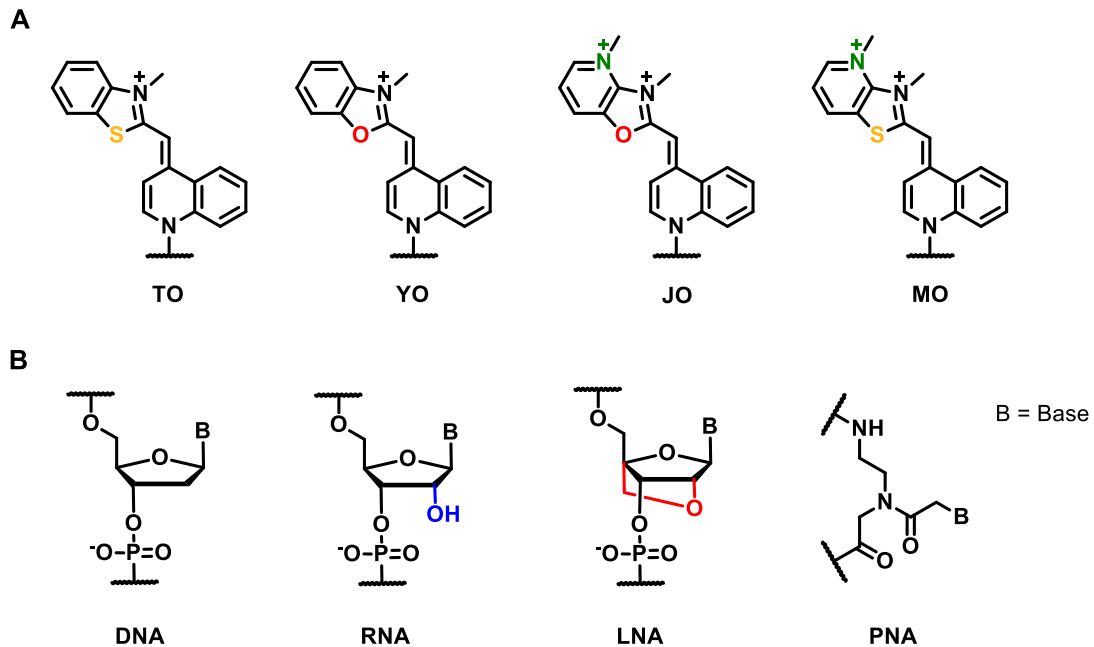


Figure 44. Structure des acides nucléiques et acides nucléiques modifiés.

Ces différences d'amplifications sont fonctions de la structure du duplexe formé. Un LNA est un sucre dont la structure est bloquée dans une conformation C3'-endo (Figure 44B). Cette augmentation de rigidité s'accompagne d'une diminution du pas de l'hélice du duplexe. L'espace disponible entre les paires de base est réduit et accroît ainsi le rendement quantique du *molecular rotor*¹¹⁸. Les PNA quant à eux sont de structure entièrement différente de l'ADN et possèdent un squelette pseudo-peptidique (Figure 44B). Ils se lient à l'ADN et à l'ARN avec une grande spécificité donnant même des duplexes PNA:DNA et PNA:RNA plus stables que les duplexes d'AN correspondant (meilleure stabilité thermique). Toutes ces propriétés peuvent être attribuées au manque de charge sur les squelettes PNA. En effet, la répulsion électrostatique est moindre entre un PNA neutre et de l'ADN chargé négativement qu'entre deux ADN¹¹⁹.

La sonde TO développée par le groupe de Seitz a par la suite été complexifiée par Okamoto et collaborateurs dans une version dimérique connue sous le nom de sonde ECHO¹²⁰ afin d'accroître ses capacités fluorogéniques. En plus des propriétés de la sonde FIT, ce système

démontre des amplifications fluorogéniques bien plus importantes que la sonde seule dues au fait que le dimère dans le simple brin est bien plus éteint (contact quenching) permettant ainsi de réduire de manière plus marquée le bruit de fond (cf. p.35).

iii. Sonde fluorogénique : Analogue de nucléobase fluorescent

Ces composés sont structurellement proches des bases naturelles. Ils ont été en particulier utilisés pour étudier *in vitro* le polymorphisme structural et conformationnel des ANs, leur variabilité et dynamique, et leurs interactions avec les protéines, les métabolites et les drogues les ciblant. La 2-aminopurine (**2AP**) constitue l'exemple historique de nucléobase fluorescente. Analogue de l'adénine, elle maintient la complémentarité avec la thymine mais forme également une paire de type *wobble* (*wobble pairing*) avec la cytosine. Individuellement, elle possède un grand rendement quantique mais sa fluorescence est fortement réduite lors de l'interaction avec les bases¹²¹ ce qui limite son utilisation. De nombreux groupes se sont alors penchés sur le développement d'analogues de nucléobase fluorescents comme celui de Tor qui a introduit la thiénoadénine (th**A**) et la thiénoguanine (th**G**), des mimes plus performants de l'adénine et de la guanine^{122,123,124}.

Le groupe de Hawkins a développé une sonde (**3-MI**) qui lors de l'hybridation avec la cible va former un bulge menant à une augmentation significative de la fluorescence jusqu'à un facteur 27 suivant la séquence utilisée. Au travers de ces résultats, ils ont été capables d'utiliser cet analogue pour détecter des produits PCR positifs à l'aide d'un système de détection du VIH-1¹²⁵.

Les analogues de nucléobase fluorescents ont beaucoup été développés pour la détection des SNP ou l'altération de l'ARN. En effet, grâce à leurs grandes sensibilités aux bases complémentaires, leurs réponses en fluorescence est foncièrement différente. L'équipe de Saito a conçu la benzopyridopyrimidine (**BPP**) comme analogue de base et formant des paires stables de type Watson-Crick avec la G et *wobble* avec la A¹²⁶. En revanche, le rendement quantique observé pour un appariement ODN(**BPP**)/ODN(G) est 20 fois inférieur que celui de ODN(**BPP**)/ODN(A). C'est pourquoi cette sonde est efficace pour discerner la mutation d'un seul nucléotide A/G (SNP) ou l'altération de l'ARN¹²⁷. Des études

et résultats du même ordre ont été observé avec de nombreuses autres sondes comme la **NPP**, **^{MDA}**, **^{MDI}**, **^{C^{hpp}}** ou **boPhpC** (**Figure 45**)^{128,129,130,131}. Cependant l'utilisation de ces dérivés dans les milieux biologiques est limitée. Leurs longueurs d'ondes d'absorption et d'émission sont dans le domaine de l'UV ou ne sont que très peu déplacées vers le rouge avec des λ proches de 400 nm. Ceci limite leurs applications, car de nombreux composés biologiques absorbent vers ces longueurs d'onde, contribuant ainsi fortement au bruit de fond.

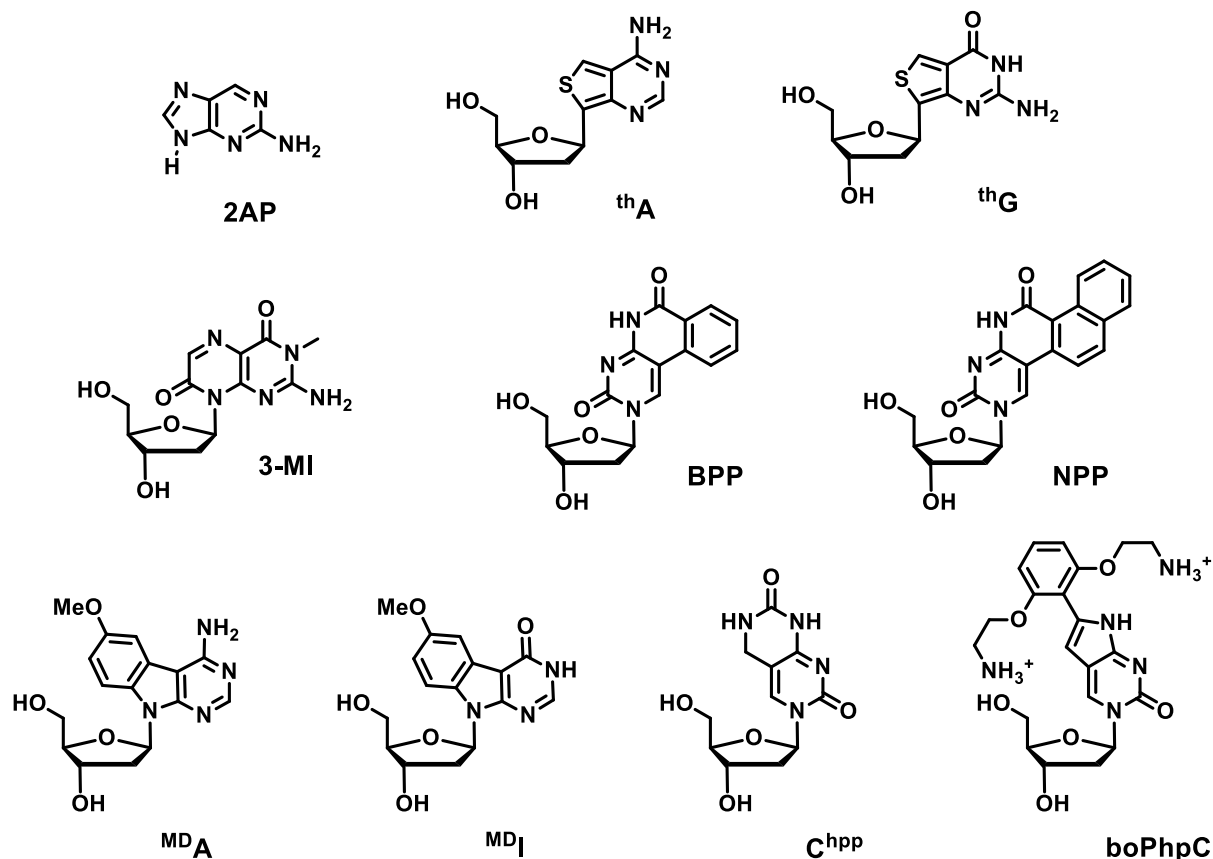


Figure 45. Structure de la 2AP, ^{thA}, ^{thG}, 3-MI, BPP, NPP, ^{MDA}, ^{MDI}, ^{C^{hpp}} et boPhpC en série désoxyribose.

iv. Sonde fluorogénique : Structure aromatique apolaire

Les structures possédant un grand nombre de conjugaison sont souvent de bons fluorophores. Dans cette catégorie on retrouve des enchainements de cycles aromatiques saturés comme dans l'exemple du pyrène, de l'anthracène ou encore du fluorène (**Figure 46**)

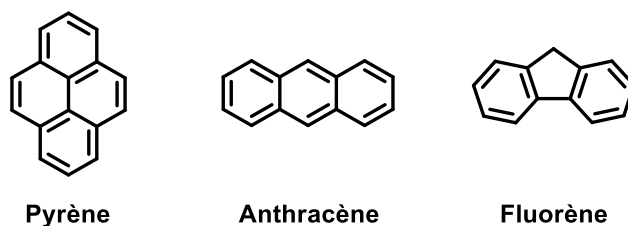


Figure 46. Structure du pyrène de l'anthracène et du fluorène.

Le groupe de Wagenknecht a développé des pyrimidines et purines conjuguées par le biais d'une triple liaison au 1-éthynylpyrène. Lors de l'étude photophysique de ces séquences marquées avec leurs brin complémentaire il obtient sur certaines séquences des amplifications de fluorescence d'un facteur 40¹³². Lors de l'hybridation la sonde va alors s'insérer entre les paires de bases pour former du π -stacking et ainsi augmenter sa stabilité. De nombreuses publications exposent d'importantes amplifications de fluorescences en utilisant ces types de noyaux. C'est le cas d'autres études faites sur le pyrène^{133,134} ou le fluorène¹³⁵.

En revanche, ces noyaux aromatiques souffrent de nombreux désavantages pour de réelles applications dans les milieux biologiques. Leurs structures, bien que conjuguées, ne possèdent pas ou peu de moment dipolaire et ne possèdent ainsi que de très petits déplacements de Stokes. Également, leurs longueurs d'ondes d'absorption et d'émission souffrent des mêmes limites que les analogues de nucléobase fluorescents. Pour ce faire, il est alors nécessaire de développer des sondes avec des moments dipolaires plus élevés telles que les sondes *push-pull*.

v. *Sonde fluorogénique : Sensible au microenvironnement.*

Il existe un très grand nombre de sondes fluorescentes utilisant leur microenvironnement (polarité, viscosité, pH, ...) comme système fluorogénique (cf. p.27). Dans cette catégorie de sonde on y retrouve alors les sondes FIT puisqu'elles exacerbent leurs fluorescences en fonction de leur encombrement stérique. Également, les sondes *push-pull* sont capables de tels changements grâce à un changement de la polarité du système. Dans cette catégorie on y retrouve par exemple les fluorènes *push-pull*¹³⁶ ou les sondes ESIPT^{137,8} (*vide infra* p.27 à 34).

Une revue réalisée en partie par l'équipe « Sondes Fluorescente » décrit en détail l'utilisation des sondes sensibles à l'environnement pour la détection des acides nucléiques (**Figure 47**)³⁷.

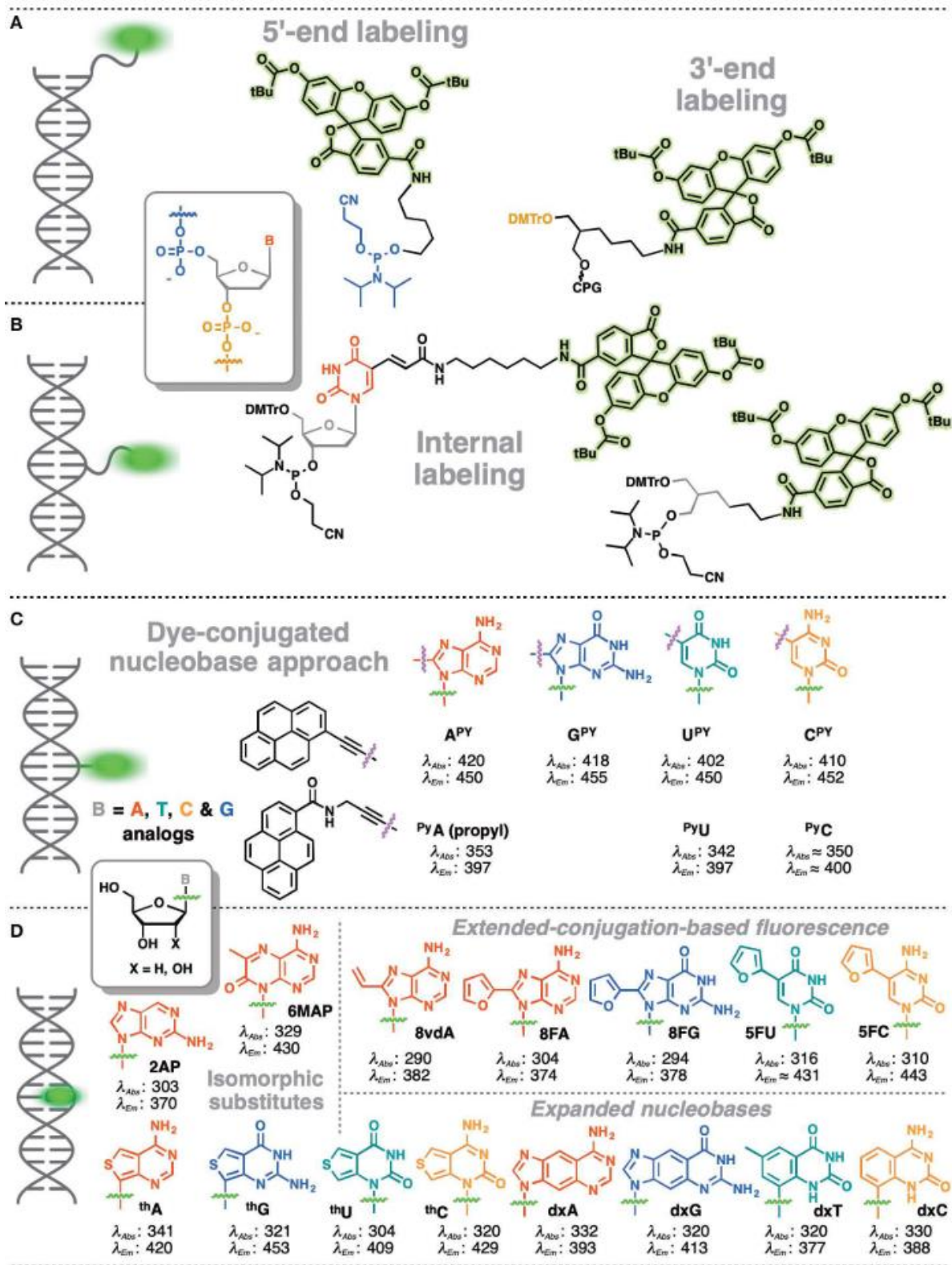


Figure 47. Stratégies pour le marquage covalent des ANs *via* des liens flexibles A) en 3' / 5' B) ou en position interne une approche amidite. C) *Via* des liens très court pour augmenter la rigidité. D) Exemple de mimique de bases et nucléobases fluorescente par extension de conjugaison³⁷.

III.3.2.2. Stratégie par marquage multiple : FRET

La capacité des marqueurs fluorescents à transférer leur énergie par résonance (FRET) à un marqueur voisin ou à une autre molécule est également utilisée pour l'imagerie des ARN. L'objectif principal est d'améliorer la sensibilité des sondes d'hybridation (marquage simple). Le FRET peut être utilisé de différentes manières (**Figure 48**).

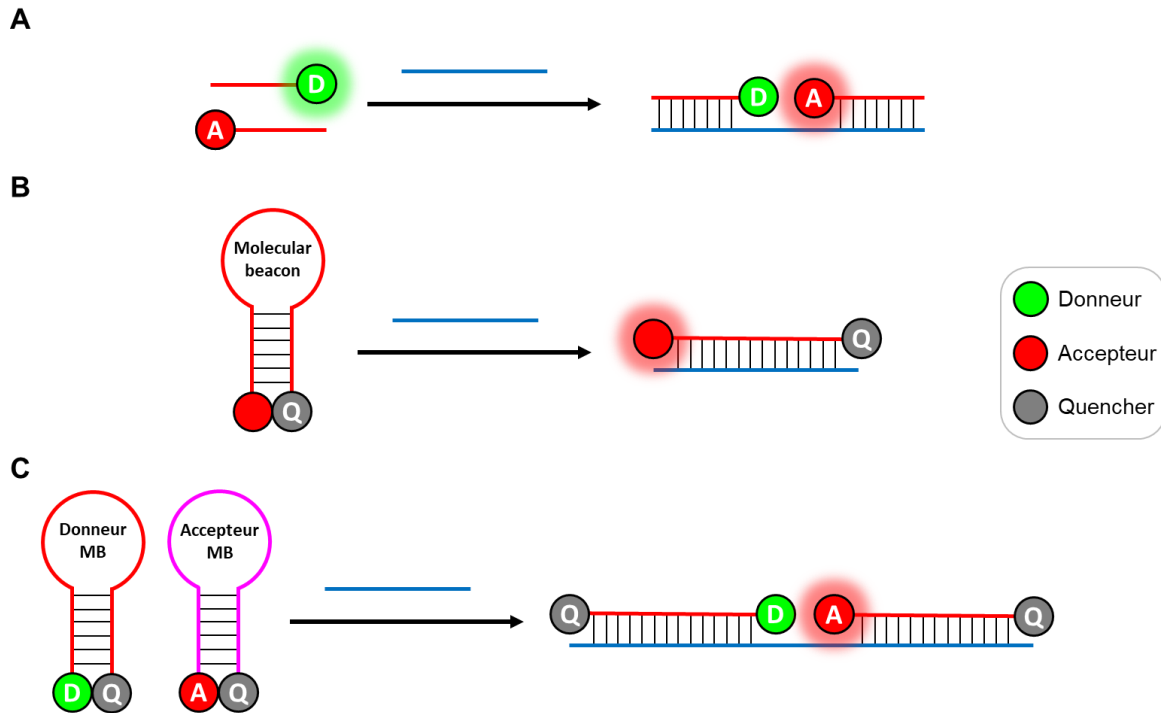


Figure 48. Représentation schématique des stratégies FRET appliquées aux ANs. A) Stratégie FRET linéaire. B) Stratégie *molecular beacon* et C) double *molecular beacon*.

i. FRET linéaire

Cette première approche simple, a été utilisée pour imager l'ARNm c-Fos dans des cellules vivantes^{138,139}. Celle-ci utilise deux sondes et ainsi elle bénéficie d'une meilleure sélectivité puisque la détection du signal spécifique nécessite la liaison des deux sondes. Par rapport aux sondes FIT et ECHO, ces sondes réduisent considérablement le risque de faux positifs car lorsqu'elles sont dégradées, l'accepteur n'est plus stimulé par FRET. En contrepartie, on observe des problèmes liés aux chevauchements spectraux des deux partenaires (*cross-excitation* de l'accepteur et *cross-emission*) qui réduisent la sensibilité de leur performance.

ii. Molecular beacon

Les balises moléculaires (*molecular beacons*) sont de simples brins d'AN structurés en conformation tige-boucle fonctionnalisés sur les 2 positions terminales par un donneur et un quencher. La liaison du molecular beacon à sa cible AN permet de séparer le donneur du quencher et ainsi de restaurer le signal de fluorescence (turn on). Les molecular beacons ont été impliquées dans un grand nombre d'études de détection des ARNm^{140,141} et des petits ARN non codants (ARNnc) dans les cellules vivantes¹⁴². De nombreux fluorophores ont été utilisés dans ces sondes comme par exemple des dérivés de fluorescéine, rhodamine, BODIPY ou coumarine¹⁴³. Dans le rôle de quencher de ces dérivés, le DABCYL permet l'extinction presque totale de leurs fluorescences. C'est aussi le cas des BHQ™ (Black Hole Quencher), qui neutralise la fluorescence des sondes sur une gamme pouvant aller du violet au proche IR¹⁴⁴.

Cependant, le système de *molecular beacon* est compliqué à mettre en œuvre dans des études en « multiplexing » car il est nécessaire de pouvoir trouver des couples FRET dont les domaines de longueurs d'onde sont compatibles^{145,146}. De même, l'utilisation de structures en tige boucle entraînent de nombreuses difficultés dont la principale est le contrôle de l'ouverture des beacons. C'est-à-dire que lorsque le molecular beacon ne s'ouvre pas à l'approche de la cible ou inversement, si celui-ci s'ouvre sans la présence de la cible, l'information est polluée par de faux-positifs. L'utilisation de ce type de système, n'est pas compatible pour des expériences en molécule unique pour du DNA-PAINT (*vide infra*) du fait de la liaison trop lente du molecular beacon à sa cible¹⁴⁷.

iii. Double molecular beacon

La stratégie de double molecular beacon est une manière d'associer le simple beacon et le FRET linéaire. Cette approche permet d'éliminer le problème lié à la sélectivité du marquage mais ajoute un degré supplémentaire dans la complexité du système à mettre en œuvre avec deux molecular beacons et 4 sites de marquage. Ce système plus complexe ne permet pas pour autant d'augmenter les facteurs d'amplification qui restent similaires à ceux obtenus avec un simple molecular beacon.

En tenant compte des différentes techniques pour la détection des acides nucléiques, les plus simples et celles offrant les possibilités les plus prometteuses pour des applications en molécule unique sont les stratégies de mono-marquage. Dans cette catégorie, nous nous concentrerons sur du marquage fluorogénique sensible à l'environnement. Ces dernières possèdent des structures simples pour des applications en imagerie des ANs en particulier dans les techniques d'imagerie super résolutive les plus récentes comme la microscopie à molécule unique DNA-PAINT.

IV. Microscopie

IV.1. Contexte

Au cours des dernières décennies, la microscopie photonique a été largement utilisée, principalement pour son côté non-invasif. La plupart des connaissances acquises en biologie cellulaire et subcellulaire l'ont été grâce à la possibilité d'observer directement les biomolécules dans la cellule.

La microscopie de fluorescence est une des techniques les plus utilisées pour deux principales raisons : la capacité d'observer en temps réel, ainsi que la multitude de sondes fluorescentes disponibles, capables d'interagir spécifiquement avec une cible désignée. Ainsi, il est possible d'obtenir des images de plusieurs cibles simultanément, par le biais d'un marquage multicoloré basé sur différents fluorophores. De plus, en utilisant une mise au point à différents niveaux de profondeur, il est possible de générer une image en 3 dimensions d'une ou de plusieurs cibles.

Néanmoins, la microscopie de fluorescence souffre d'un problème majeur de résolution spatiale. Tout comme les autres microscopies photoniques, la résolution est limitée par la diffraction de la lumière. Cette limite est connue et est d'environ 200 nm en direction latérale (sur un plan 2D) et de 500 nm en direction axiale (en utilisation 3D). En conséquence, de nombreuses structures subcellulaires ne peuvent être observées en détail par microscopie de fluorescence, contrairement à d'autres techniques comme la microscopie électronique (ME), qui possède une plus grande résolution. Pour pallier ce problème de limite de diffraction et ainsi obtenir des images plus précises, des techniques dites de « super-résolution » ont été développées. Grâce à celles-ci, il devient possible d'obtenir des images précises (20 nm de résolution latérale) tout comme avec la ME, mais avec un marquage ciblé et la possibilité d'observer un milieu vivant et donc dynamique. Il existe 3 différentes techniques super-résolutives : Le SSIM, le STED, et les SMLM^{148,149}.

IV.1.1. Phénomène de diffraction

Principale source de limitation du pouvoir de résolution d'un microscope optique, la diffraction est un phénomène physique fondamental. Il est facilement observable et se révèle lors d'une expérience où un laser traverse une fente plus petite que la longueur d'onde du laser. Des phénomènes d'interférences destructives et constructives ont alors lieu, engendrant des motifs de diffraction de type rayures (**Figure 49B**). Si l'on remplace la fente par un trou circulaire, des disques de diffraction, appelés disques de Airy, sont plutôt observés (**Figure 49C et D**).

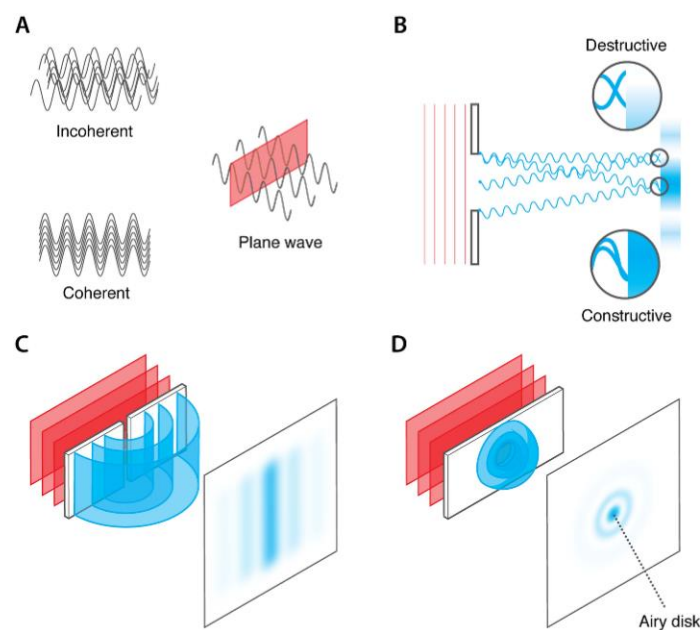


Figure 49. A) Description d'une lumière cohérente, non cohérente, ou polarisée. B) Comportement d'une lumière cohérente sur une ouverture. C) Représentation de l'effet de diffraction d'une ouverture linéaire. D) Représentation de l'effet de diffraction d'une ouverture circulaire¹⁴⁸.

IV.1.2. Ouverture numérique et résolution

Dans le cas du microscope, la lentille va se comporter comme un diaphragme et, analogiquement à l'expérience précédente, provoquera la création de disques de Airy, aussi appelés « Point Spread Function » (PSF). La résolution du microscope est alors fonction de la taille du PSF et, surtout, de la possibilité de différencier deux points proches dans l'espace. Cette valeur, variable, dépend de la longueur d'onde utilisée et elle est calculable par la relation (**Équation 7**) :

$$d = \frac{0,61\lambda}{NA}$$

Équation 7. Relation permettant de calculer la résolution d'un microscope.

Ici, d est la distance minimale entre deux points, λ la longueur d'onde de la lumière utilisée et NA, l'ouverture numérique (*Numerical Aperture*). NA (sans dimension) est définie par l'objectif du microscope, suivant la relation : $NA = \eta \sin(\theta)$, avec η l'indice de réfraction du milieu et θ le demi-angle d'ouverture. Pour la majorité des microscopes, la lentille est immergée dans de l'huile ($\eta \approx 1,45$) et conduit à un $NA \approx 1,40$. Avec cette valeur et l'utilisation d'un laser visible ($\lambda \approx 550 \text{ nm}$), on obtient une résolution maximale d'environ 200 nm (latérale). La résolution axiale est, quant à elle, 2 à 3 fois supérieure, soit environ 500 nm (**Figure 50**).

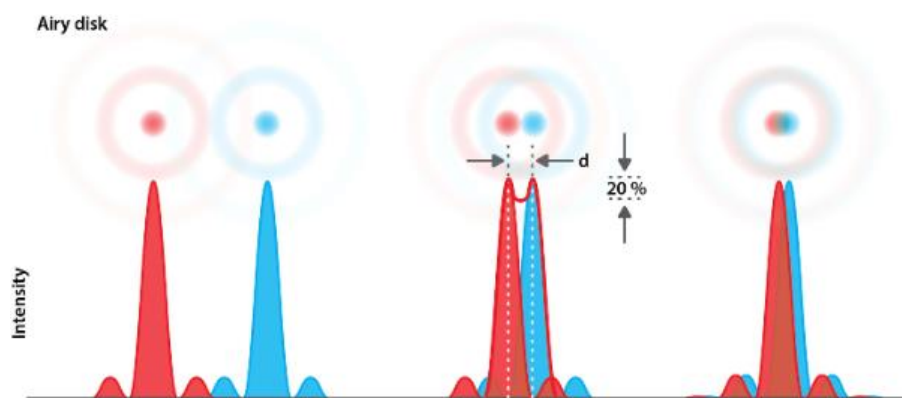


Figure 50. Description de l'épaulement de deux disques de Airy définissant la résolution d'un microscope optique. À gauche, les deux disques sont résolus alors qu'à droite, ils sont indiscernables. Au milieu se trouve la zone limite de discernement définie par la limite de Rayleigh¹⁴⁸.

Cette résolution maximale est restée longtemps la même, jusqu'à l'utilisation du microscope confocal. Au lieu de réaliser une illumination complète de l'échantillon, le microscope procède à un balayage de la cible en plaçant un sténopé (*pinhole*) devant le détecteur, ce qui permet d'obtenir uniquement les photons émis du plan focal désiré (**Figure 51**). Ces deux modifications ont permis une légère augmentation de la résolution des microscopes optiques d'un facteur $\sqrt{2}$.

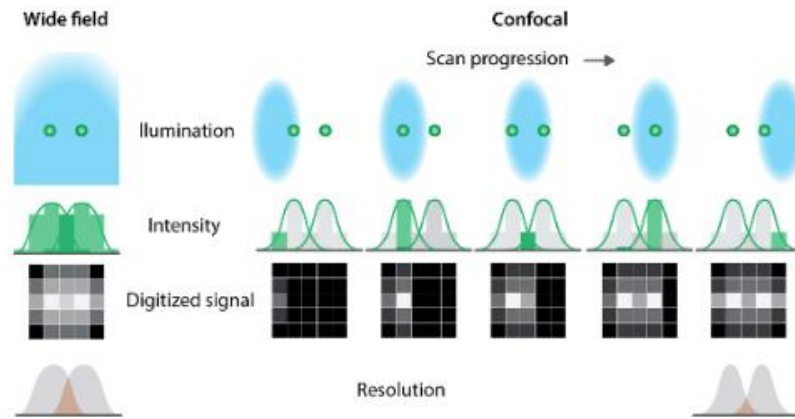


Figure 51. Comparaison de la technique d'imagerie classique *wide field* avec une imagerie confocale¹⁴⁸.

IV.2. DNA-PAINT, technique de super-résolution des acides nucléiques

Les technologies de microscopie super-résolutive sont relativement récentes et ont permis de révolutionner les techniques d'imagerie du vivant, *via* le contournement des problèmes de diffraction. Les avancées qu'ont permis ces techniques, dans le cadre de l'observation du vivant, ont été récompensées par l'attribution du prix Nobel de chimie en 2014 à Stefan Hell, Eric Betzig et William Moerner, pour leurs travaux sur le développement des techniques d'imagerie STED et en molécule unique (STORM/PALM).

Plusieurs techniques sont dites de super-résolution et chacune d'entre elles utilisent des propriétés physiques distinctes :

- **SSIM** (*Saturated Structured Illumination Microscopy*) : amélioration de la technique SIM se basant sur l'étude de phénomènes physiques et l'utilisation de calculs mathématiques complexes^{148,150,151}.
- **STED** (*Stimulated emission depletion*) : diminue la taille de la PSF (*Point and Spread Function*) par l'utilisation d'une émission stimulée^{152,153,154}.
- **SMLM** (*Single molecule localization microscopy*) : correspond à plusieurs techniques utilisant le clignotement d'une sonde fluorescente. Dans cette catégorie sont retrouvés le STORM/dSTORM^{155,156,157,158}, le PALM/FPALM¹⁴⁸ et le DNA-PAINT.

La technique de DNA-PAINT (*DNA-Point Accumulation for Imaging in Nanoscale Topography*) s'applique en particulier à la détection des acides nucléiques.

IV.2.1. Principe du DNA-PAINT

Le principe de fonctionnement classique des techniques de localisation en molécule unique (SMLM) se base sur le passage d'un état allumé/éteint (*turn on/off*) d'un fluorophore, que l'on appelle clignotement.

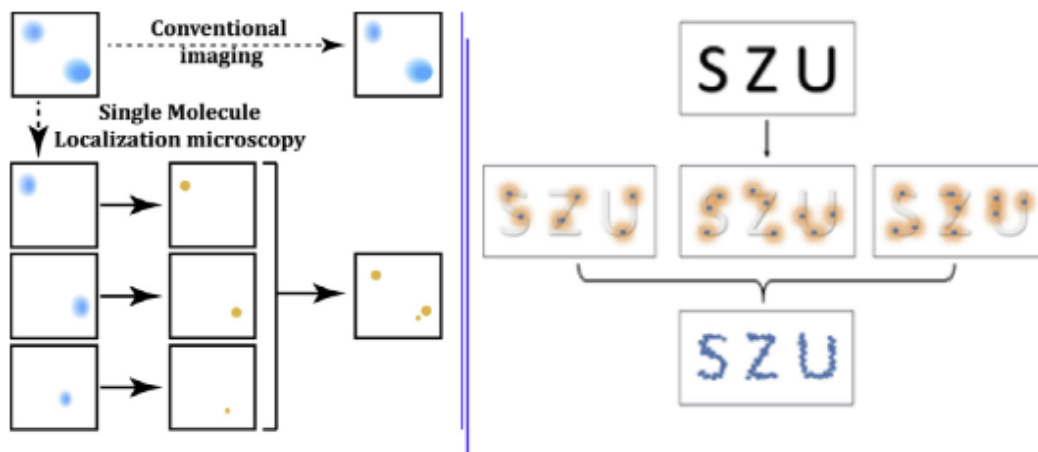


Figure 52. Représentation schématique du fonctionnement de la microscopie en molécule unique (gauche) méthode classique d'imagerie par STORM.¹⁵⁵

Dans le cas où ce clignotement n'existe pas, les sondes sont alors simultanément « allumées » et un phénomène de recouvrement (*overlapping*) s'opère (Figure 52). Toutefois, ce problème peut être évité si deux fluorophores émettent successivement et non simultanément. Alors, un algorithme de localisation et l'application d'une méthode d'ajustement (*fitting*) Gaussien va permettre de déterminer la position exacte, en un point, du fluorophore. Il s'agit du principe de SMLM (Figure 52).

Dans la méthode de DNA-PAINT, la localisation n'est pas créée à la suite du passage d'un état allumé à éteint du fluorophore, mais par l'hybridation transitoire programmable de courts brins d'ADN fluorescents (brins d'ADN imageurs) avec un brin complémentaire (étiquette d'ADN), lié à une cible. Les brins d'ADN imageurs sont des ODN courts (8-10mères), marqués de façon covalente avec un fluorophore organique (Chapitre 1 : III.2. p.50), qui diffusent librement dans l'échantillon. Les brins d'ODN imageurs diffusent trop rapidement pour générer des spots fluorescents, à moins qu'ils ne soient liés au brin

d'amarrage complémentaire. L'ODN imageur lié de manière transitoire au brin d'ancrage génère des salves fluorescentes localisées qui contrastent avec le fond fluorescent résiduel des molécules diffusant au plan focal (**Figure 53A**).

Les nombreuses preuves de concept publiées montrant l'efficacité et le potentiel de cette méthode utilisent des Origami d'ADN^{159,160,161} et comme cible cellulaire les microtubules qui constituent un étalon de référence¹⁶². Elle est basée sur le phénomène d'accumulation de photons au niveau de la cible (**Figure 53 B et C**).

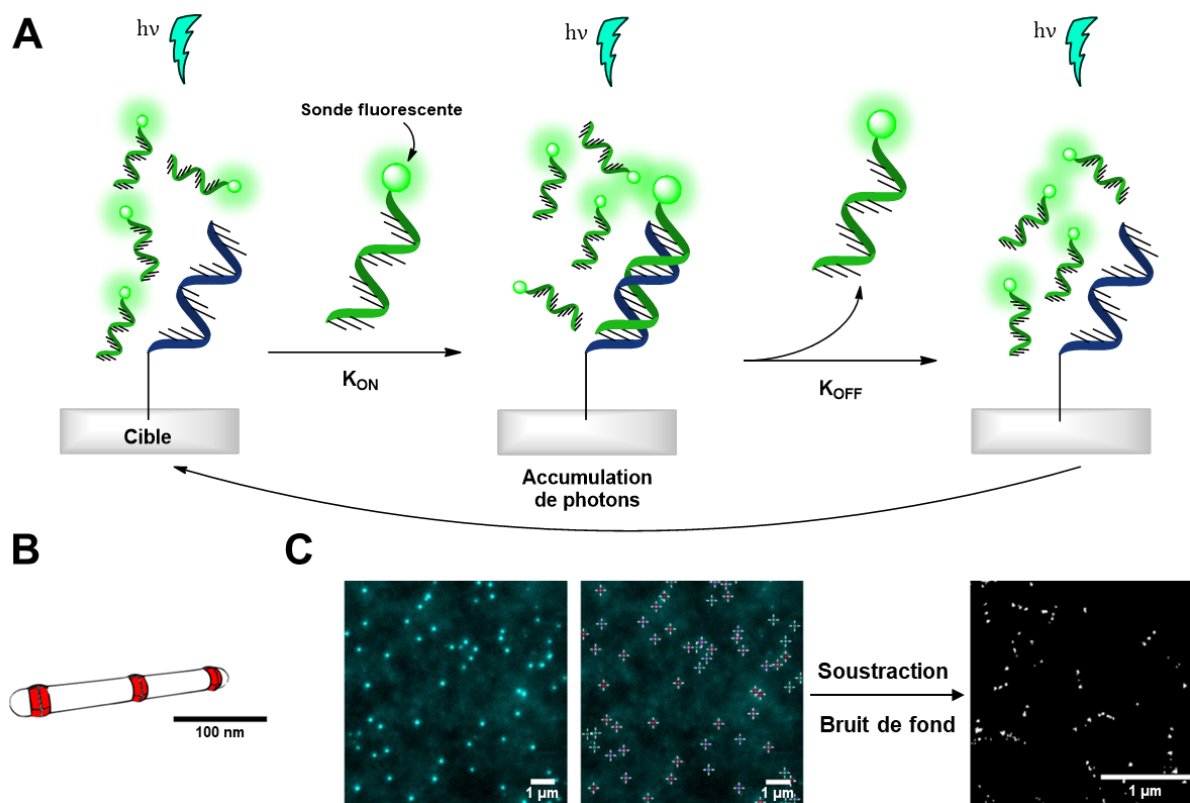


Figure 53. A) Principe du DNA-PAINT. B) Représentation schématique d'un origami d'ADN contenant trois sites de liaison (un brin d'ADN par zone rouge), séparés de 80 nm. C) Données expérimentales brutes suite à l'ajout du brin complémentaire de l'origami et localisation des zones d'accumulation. Après soustraction du bruit de fond, seules les zones d'accumulation sont visibles et correspondent aux origamis.

Ici, le rapport *on/off* est donc principalement contrôlé par la diffusion (définissant le temps *off*) et la constante de dissociation (k_D) ADN/ADN (définissant le temps *on*)¹⁵⁹ (**Figure 53A**). L'ajustement des séquences ODN imageurs (composition et longueur des bases) et de leur concentration est un moyen simple de fournir un temps de clignotement sélectif, prévisible et ajustable, et de découpler presque complètement ce paramètre des exigences photophysiques du fluorophore. Un autre avantage évident du DNA-PAINT est que les

brins de l'imageur hybridés à l'étiquette ADN sont continuellement échangés avec ceux en solution, ce qui permet un temps d'imagerie virtuellement infini (pas d'épuisement du fluorophore dans l'échantillon), d'où une accumulation de signaux plus importante et une meilleure sensibilité pour la détection de cibles peu abondantes.

Le potentiel du DNA-PAINT a été démontré dans diverses expériences. Il permet entre autres de détecter et quantifier des protéines et des ARNm (qPAINT)^{163,164}, et de réaliser du multiplexage (Exchange-PAINT) plus performant que les approches classiques¹⁶⁵. En effet l'Exchange-PAINT n'est limitée que par le nombre de séquences d'ADN orthogonales, contrairement aux expériences de multiplexage classiques qui sont limitées par le nombre de colorants spectralement distincts disponibles (typiquement 4).

Cependant, et malgré les résultats évidents obtenus avec le DNA-PAINT, cette méthode souffre d'un inconvénient majeur, son faible contraste. Le développement de cette technologie prometteuse est donc freiné par cet inconvénient majeur. La recherche actuelle vise à le corriger par une approche fluorogénique.(FRET DNA-PAINT¹⁶⁶, Fluorogenic DNA-PAINT¹⁴⁷).

Présentation du projet de recherche

L'objectif principal de cette thèse est le développement de nouvelles sondes fluorogéniques d'hybridation des AN, de type push-pull, utilisables dans le cadre de différentes techniques d'analyse par fluorescence (FRET, DRET, DNA-PAINT...). Nous désirons développer des sondes presque non fluorescentes lorsque l'AN qui les portent est simple brin, mais qui émettent de façon très brillante lorsque l'AN est en double brin. En éliminant du signal de fond toutes les contributions du plan focal et hors plan des espèces fluorescentes qui diffusent, le contraste de fluorescence devrait être considérablement amélioré (**Figure 54**). Par ailleurs, pour être compatibles avec l'étude dans les milieux biologiques, il faut que les longueurs d'onde d'absorption et d'émission de la sonde soient fortement décalées vers le rouge, afin de réduire le bruit de fond inhérent aux constituants cellulaires.

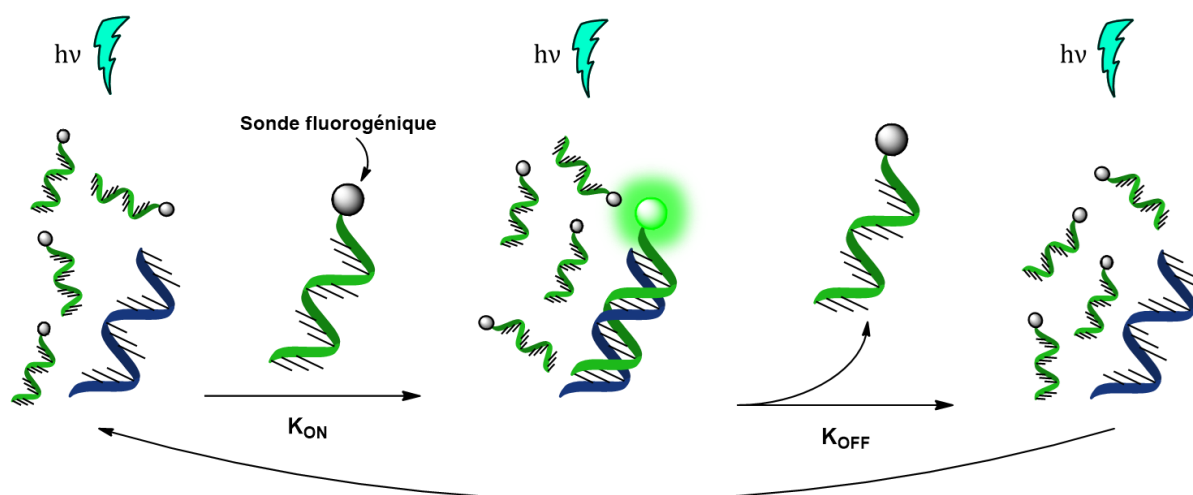


Figure 54 : Principe de fonctionnement d'une sonde fluorogénique d'hybridation de l'ADN. Le simple brin d'ADN en vert est le brin imageur (avec le fluorophore). Le simple brin d'ADN en bleu est la cible.

De plus, la sonde doit perturber le moins possible la stabilité et la structure du duplexe afin de ne pas compromettre l'échange dynamique des deux brins d'AN. Enfin, la structure de la sonde doit pouvoir être facilement modifiable, afin d'optimiser la réponse de fluorescence suivant le milieu d'études.

Dans ce cadre, nous nous sommes basés sur les travaux précédemment effectués au sein de l'équipe « Sondes Fluorescentes » pour développer, dans un premier temps, plusieurs sondes

fluorogéniques à l'hybridation, basées sur des noyaux « Chromone ». Ces travaux ont fait l'objet de deux publications qui seront présentées dans le chapitre suivant.

Dans un deuxième temps, nous nous sommes penchés sur le développement de nouvelles sondes de type *molecular rotor*. Ces dernières, basées sur l'effet stérique, ont déjà fait leur preuve dans l'hybridation fluorogénique (cf. **Chapitre 1 : III.2.2.** p.52). Deux sondes de type *molecular rotor*, dont l'une a déjà fait l'objet d'une publication, seront décrites dans un deuxième chapitre.

Enfin, dans un dernier chapitre, la synthèse et l'application de deux sondes interagissant soit par intercalation soit avec le petit sillon de l'ADN seront présentées.

Dans tous les cas, la synthèse des sondes fluorescentes ainsi que la caractérisation de leurs propriétés photophysiques seront décrites. Les méthodes d'incorporation (pré ou post-synthétique) dans les ODN ainsi que les propriétés photophysiques des simples brins marqués seront développées (**Figure 55**). Pour terminer, les études d'hybridation avec l'ADN ou l'ARN seront relatées.

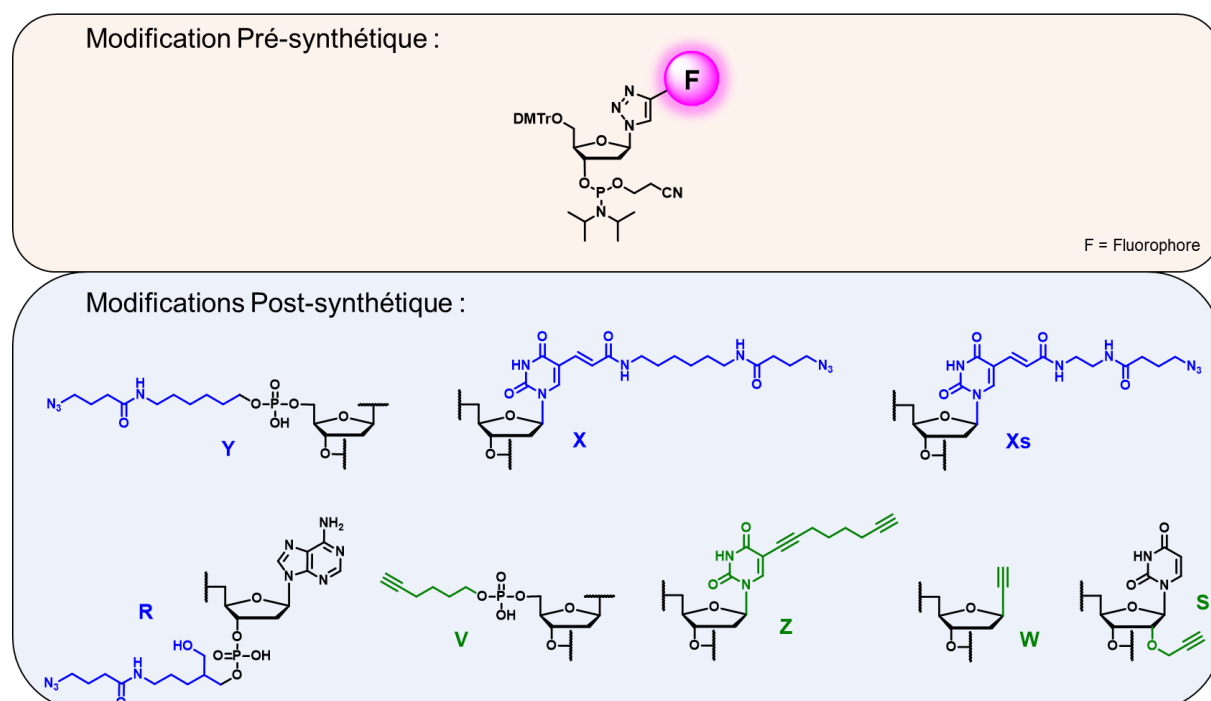


Figure 55. Types de modification utilisée dans ce projet de recherche pour les études d'hybridations fluorogéniques des ANs.

Chapitre 2 : Hybridation fluorogénique par sonde Push-Pull

I. Stratégie par FRET : Hydroxychromones

Publication 1

Les noyaux chromones sont des sondes push-pull connues principalement pour leur capacité à faire de l'ESIPT (c.f. **Chapitre 1 : II.1.2.** p. 30). Une étude sur des dérivés 3HC, entreprise par le passé au sein de notre équipe, a démontré les importantes capacités fluorogéniques de ce type de noyaux^{167,137}. De premier abord, celles-ci possèdent des propriétés photophysiques intéressante pour concevoir des sondes d'hybridation fluorogénique de l'ADN : forte sensibilité au taux d'hydratation, faible taille (équivalent à la taille d'une paire de bases), déplacement de Stokes très large (> 100nm), et émission dans le visible. Nous avons donc envisagé d'utiliser ce type de noyau chromone pour des études d'hybridation des AN potentiellement comme sonde éteinte avant hybridation puis allumée après hybridation, et comme donneur dans du FRET.

Dans ce cadre, nous nous sommes focalisés sur deux dérivés de 3HC, possédant des groupements donneurs méthoxy et diéthylamino en position para du phényle (**Figure 56**). L'introduction de ses groupements augmente le caractère « push-pull » de la 3-HC qui se caractérise par un décalage vers le rouge des bandes d'absorption et d'émission de fluorescence qui est d'autant plus important que le groupement donneur est fort (diéthylamino > méthoxy).

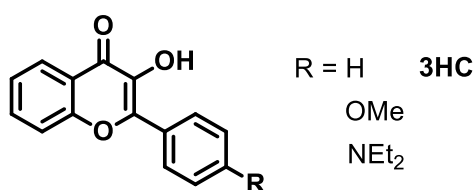


Figure 56. Dérivés de 3HC utilisés dans ce travail

Dans le but d'incorporer ces fluorophores dans l'ADN suivant l'approche pré-synthétique (cf. **Chapitre 1 : III.2.2.2.** p.55), nous avons dans un premier temps synthétisé les analogues nucléosidiques **M3HF** et **TdEAF**, contenant respectivement un groupement méthoxy et diéthylamino (**Figure 57**) et avons étudié leurs propriétés d'absorption et d'émission.

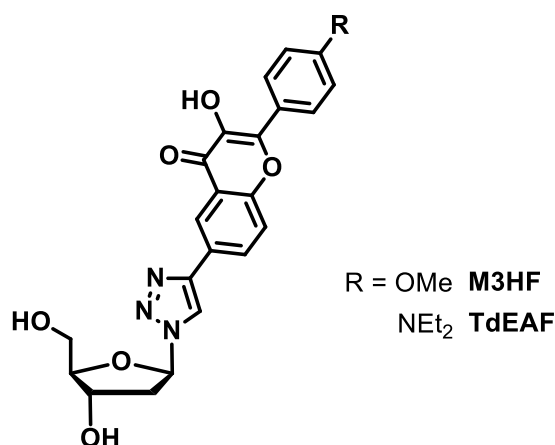


Figure 57. Structures des analogues nucléosidique **M3HF** et **TdEAF**.

Nous avons observé que les propriétés photophysiques de base des composés **M3HF** et **TdEAF** sont semblables à celles de la 3HC parente après couplage par click au désoxyribose. Ces composés absorbent dans l'UV/visible (ca. 370 nm et 440 nm, respectivement pour les dérivés méthoxy et diéthylamino), un domaine d'absorption compatible pour une excitation au laser violet, et présentent deux bandes N* et T* bien résolues dans leurs spectres d'émission, montrant que ces deux sondes fluorescent suivant un mécanisme de type ESIPT (cf. Chapitre 1 : II.1.2.). Comme attendu, certaines des propriétés photophysiques de **TMoC** et **TdEAF** sont améliorées comparativement à la 3-HC, avec un rendement quantique plus élevé (jusqu'à 60%), un décalage vers le rouge des bandes d'absorption et d'émission de fluorescence, un large déplacement de Stokes (~190 & 110 nm, respectivement).

Les deux sondes **M3HF** et **TdEAF** présentent néanmoins des différences. Ainsi, la variation du rapport N*/T* en fonction de la polarité et proticité du milieu diffère pour les deux sondes. Dans le cas de **M3HF** les deux bandes sont présentes dans le MeOH pur et le rapport N*/T* décroît lorsque le pourcentage de MeOH diminue dans le DMF. Comme la 3-HC parente le composé **M3HF** reste émissif dans l'eau pure. En revanche, **TdEAF** ne montre qu'une seule bande (N*) dans 100% de MeOH et la bande T* n'est observée que lorsque la proticité du milieu diminue de 80%. **TdEAF** est complètement éteint dans l'eau en accord avec le colorant parent. Ceci montre, que, comme on pouvait s'y attendre, l'effet push-pull est plus important dans le cas de **TdEAF** que dans celui de **M3HF**, du fait de la présence du groupement N, N-diéthylamine qui possède un effet (+M) plus fort que celui du OMe. Lors

de l'excitation électronique, la redistribution de la charge crée un moment dipolaire plus élevé de la forme normale dans l'état excité (N*) contrairement à son tautomère (T*). Cela se traduit par un déplacement vers le rouge de la bande N*, se mélangeant ainsi avec la bande T* pour conduire à une seule bande d'émission large, en particulier dans les milieux plus polaires et protiques.

La synthèse des phosphoramidites de **TM3HF** et **TdEAF** a ensuite été réalisée, puis ces derniers ont été incorporés au milieu de 16 séquences d'ODN simple-brins (15mères), présentant des différences au niveau de la nature des bases adjacentes au fluorophore incorporé. Une étude de dénaturation thermique a montré que l'incorporation des sondes dans un ODNss n'avait que peu d'influence sur la stabilité des duplexes formés avec des brins d'ODN complémentaires, quel que soit la nature du résidu (G, A, T, C ou site abasique) placé « en face » de la sonde. Cependant, la présence d'un résidu Cytosine semble préférentielle. De plus l'introduction de **TM3HF** et **TdEAF** dans l'ADN ne modifie pas la conformation canonique B de l'ADN double brin.

Des études concernant les propriétés photophysiques des ODN marqués par **M3HF** et **TdEAF** dans un tampon phosphate, ont révélées un déplacement vers le rouge du maximum d'absorption de la chromone soulignant un couplage excitonique probablement dû à l'empilement des nucléobases des résidus entourant le fluorophore dans l'ODN. Cette variation est caractéristique des fluorophores s'intercalant dans l'ADN. En ce qui concerne l'émission, tous les ODNss marqués par **M3HF** montrent deux bandes N* et T*, centrées à environ 440nm (N*) et 540 nm (T*), quelques soient les résidus environnant le fluorophore dans le simple-brin. Dans le cas des ODNss marqués par **TdEAF**, ils montrent tous une seule bande, centrée à environ 540 nm, quelques soient les résidus environnant le fluorophore dans le simple-brin. Les ODNss marqués par **TdEAF** sont tous très émissifs, ces résultats indiquent que dans un simple brin le fluorophore n'est plus dans de l'eau pure.

Des études d'hybridation ont ensuite été menées avec des séquences 15mères d'ODNss complémentaires, présentant des différences au niveau de la nature des bases adjacentes au fluorophore incorporé et au niveau de la nature du résidu (G, A, T, C ou site abasique) placé

« en face » de la sonde. Dans le cas des ODN marqués par **M3HF**, les résultats d'hybridation ont montré des spectres d'absorption et d'émission duale des ODNs différents de ceux des ODNs marqués avec une bande T* dominant l'émission plus intense et un pseudo déplacement de Stokes particulièrement large ($\Delta\lambda$ de l'ordre de 190 nm). Cependant, le rendement quantique est fortement impacté par la nature de la base adjacente. Il augmente lorsque la sonde est flanquée des bases Thymine ou Adénine et est quasiment nul lorsque des Guanines ou des Cytosines l'entourent. Dans le cas des ODNs et ODNs marqués par **TdEAF**, tous ne montrent qu'une bande unique centrée à environ 540 nm avec un rendement quantique important, quelques soient les résidus entourant le fluorophore dans l'ODN marqué. Ce résultat est remarquable car de nombreux fluorophores sont éteints par une ou plusieurs bases nucléiques (G étant souvent l'extincteur le plus efficace).

Par conséquent, **TdEAF** ne peut être utilisé comme sonde fluorogénique pour une approche « off/on ».

Compte tenu des déplacements de Stokes très importants obtenus lors de l'hybridation avec nos sondes, nous avons cherché à les valoriser pour du FRET fluorogénique avec **TdEAF** et **M3HF** comme donneurs et Cy5 comme accepteur (**Figure 58**).

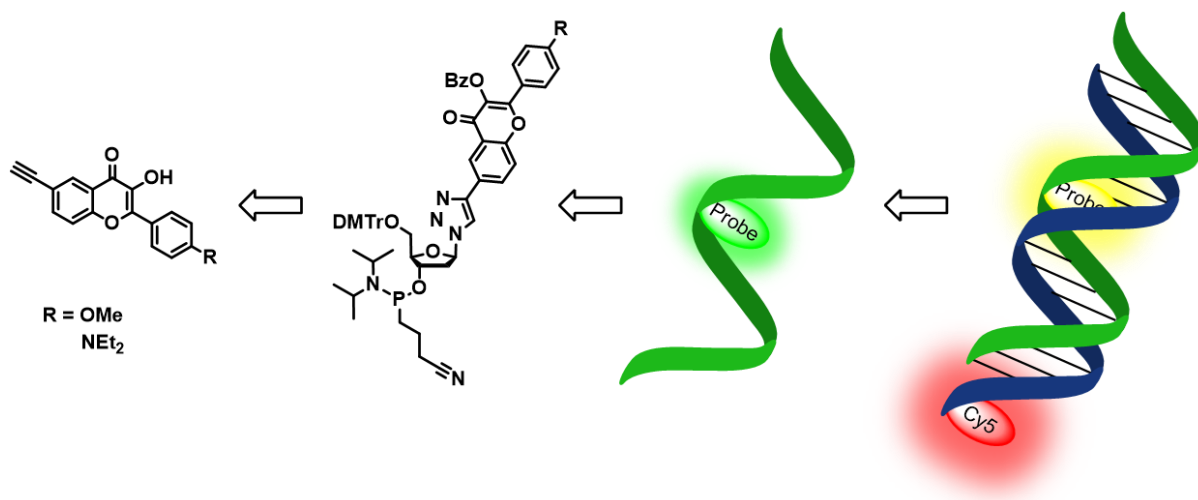


Figure 58. Développement de la méthode FRET des sondes à motif 3HC.

Les ODNs marqués par **M3HF** permettent de réaliser du FRET mais avec une sensibilité limitée (amplification du signal) du fait de l'excitation croisée et du donneur et de l'accepteur due au recouvrement des bandes d'absorption de **M3HF** et de Cy5. Par contre,

le couple FRET **TdEAF**/Cy5 ne présente pas cet inconvénient. Dans ce cas, le FRET est très efficace et sensible avec l'apparition de la bande d'émission de Cy5 lors le d'hybridation suite à l'excitation du donneur avec une contamination faible du signal due à l'excitation directe de l'accepteur.

L'ensemble de ces travaux est décrit dans la publication (1), présentée ci-après en cours de soumission au journal *International Journal of Molecular Science*.



Article

Design and synthesis of a fluorescent nucleoside incorporating a 3-hydroxychromone base substitute acting as a brightly emissive donor in a novel mega-Stokes shift FRET pair

Steve Vincent ^{†,1}, Nicolas P. F. Barthes ^{†,1}, Suman Mallick ^{1,2}, Guillaume Barnoin ¹, Pascal D. Giorgi ¹, Moses Moustakim ¹, Hoang-Ngoan Le ¹, Benoît Y. Michel ^{1,*} and Alain Burger ^{2,*}

¹ Institut de Chimie de Nice, CNRS UMR 7272, Université Côte d'Azur, Parc Valrose, 06108 Nice cedex 2, France ; steve.vincent@univ-cotedazur.fr (S.V.); suman22msc@gmail.com (S.M.); guillaume.barnoin@univ-cotedazur.fr (G.B.); lhngoan2109@gmail.com (H.-N.L.)

² Institut de Chimie de Nice, CNRS UMR 7272, Université Côte d'Azur, Parc Valrose, 06108 Nice cedex 2, France ; @gmail.com (S.M.)

[†] These authors have contributed equally to this work.

* Correspondence: benoit.michel@univ-cotedazur.fr (B.Y.M.); alain.burger@univ-cotedazur.fr (A.B.)

Abstract: Environment-sensitive and highly fluorescent nucleoside analogs (FNAs) incorporated into single-stranded sequences provide efficient and accurate probes for detecting nucleic acids (NA) and reporting their interactions. In this context, we report the design, synthesis, and photo-physical studies of two new solvatofluorochromic FNAs derived from push–pull 3-hydroxychromones (3HCs), followed by their successful incorporation into ODNs through the formation of their corresponding phosphoramidites. 3HC-based dyes are known to be multiparametric and environmentally sensitive fluorophores, exhibiting a ratiometric response due to the presence of two well-resolved bands in their emission spectra. Both synthesized FNAs embedding a 3HC base substitute retain or even improve these spectroscopic features by increasing the quantum yields and red-shifting the absorption and fluorescence emission. After easy conversion to amidite, the incorporation of these FNAs into ODN structures offers a major advantage of additional stability for the modified duplex. Furthermore, the observed large Stokes shifts were successfully leveraged to create a novel mega-Stokes shift FRET couple with reduced cross-excitation when paired with a red-emissive acceptor, typically indocarbocyanine Cy5. The fluorophores engineered thus represent a significant advance for 3HC-based dyes, which can be used as prospective markers for nucleic acids.

Citation: Vincent, S.; Barthes, N.P.F.; Mallick, S.; Barnoin, G.; Giorgi, P.D.; Moustakim, M.; Le, H.-N.; Michel, B.Y.; Burger, A. Design and synthesis of a fluorescent nucleoside incorporating a 3-hydroxychromone base substitute acting as a brightly emissive donor in a novel mega-Stokes shift FRET pair. *Int. J. Mol. Sci.* **2022**, *23*, x. <https://doi.org/10.3390/xxxxx>

Academic Editor: Firstname Last-name

Received: date

Accepted: date

Published: date

Publisher's Note: MDPI stays neutral with regard to jurisdictional claims in published maps and institutional affiliations.



Copyright: © 2022 by the authors. Submitted for possible open access publication under the terms and conditions of the Creative Commons Attribution (CC BY) license (<https://creativecommons.org/licenses/by/4.0/>).

1. Introduction

Hybridization probes based on organic fluorophores have gained popularity in recent years due to their broad applications in diagnostics, bioimaging, and medicinal chemistry. Fluorogenic dyes—i.e., those that "turn on" their fluorescence response or significantly increase their emission intensity upon interaction with their target—are the most sought after [1]. Indeed, markers that generate a novel fluorescent signal have a considerable advantage, such as the implementation of more convenient wash-free staining protocols, making them very attractive for diagnostic and imaging applications. Förster resonance energy transfer (FRET) provides access to a pseudo-fluorogenic effect due to the spectral shift in the fluorescence emission from the acceptor as a result of the probe binding to its target. FRET has become a valuable tool in biological research and diagnosis [2–5]. Because FRET is distance-dependent, FRET-based probes have found many applications in the detection and quantification of nucleic acids (NA, e.g. hybridization probes for genotyping or photonic imaging), in the study of NA conformational changes, and NA–NA/NA–protein and NA–small molecule interactions [2,3,6–8]. FRET refers to the

energy transfer from a donor in the excited state to an acceptor due to dipole–dipole interactions. It requires a spectral overlap of donor emission and acceptor absorption and a favorable orientation of the dipoles. It usually operates within a radius of 1 to 10 nm. This proximity leads to a decrease in the donor emission and a concomitant increase in the red-shifted acceptor emission. Thus, FRET probes constructed from an emissive donor/acceptor pair can capitalize on two sensing channels: *fluorogenicity* for the turn-on of the acceptor emission and *ratiometry* for the intensity ratio of donor and acceptor emissions. Nevertheless, due to the small Stokes shifts typically exhibited by donor dyes, cross-excitation remains a severe limiting factor in FRET. Therefore, large Stokes shifts are highly desirable to reduce the background signal by significantly improving the signal-to-noise ratio in experiments. Fluorophores with mega-Stokes shifts (>100 nm) are even more advantageous as they are immune to self-quenching. This photophysical property is also beneficial for reducing the background signal. However, the development of FRET pairs fulfilling this feature is hampered by the fact that the donors—which are typically push–pull dyes—are in general strongly quenched in aqueous media [9–11]. Other alternatives have been proposed. They mainly rely on pairs of a fluorescent donor and its quencher (e.g., molecular beacons — MB), but Stokes shifts generally remain modest [12–14]. More recently, combinations of a quenched donor presenting mega-Stokes shifts with a bright acceptor to perform fluorogenic FRET also known as DRET (Dark-Resonance Energy Transfer) have been introduced to target NAs with a contrasting ON/OFF response [15,16]. Additional desired properties of donor fluorophores for biological applications are absorption in the visible range, substantial absorptivity, good fluorescence quantum yields (on target) and high photostability to avoid photobleaching. In addition to these photophysical features, it is also essential to ensure ease of incorporation of these fluorochromes into oligonucleotide (ODN) structures without minimal disruption of its stability [17]. Thus, fulfilling all these conditions in an organic fluorophore is a real challenge.

Fluorophores based on a 3-hydroxychromone (3HC) unit belongs to the family of excited-state intramolecular proton transfer (ESIPT) dyes [18]. They display visible dual emission and are easily to incorporate into ODNs through a linker or by using their corresponding phosphoramidite. The 3-OH group, present in the core structure, plays a crucial role in the two resulting tautomeric forms. These tautomers emit separately from each other at two well-defined wavelengths (respectively, normal (N*) and tautomer (T*) emission bands, Scheme 1). The T* emission demonstrates particularly large apparent Stokes shifts (> 150 nm). ESIPT can be readily modulated by H-bonding and dipolar interactions as well as by the donating ability of the substituent at position 2. For example, in the case of 3HCs bearing a strongly mesomeric donating aryl group—typically, a *p*-diethylaminophenyl moiety (**dEAF**, Figure 2)—the dye shows high sensitivity to the aprotic environment, as reflected by the enhancement (in N* over T*) of the N* compared to the T* along with increasing solvent polarity. Noticeably, in polar protic solvents (e.g., MeOH), **dEAF** exhibits a single-band N* emission with significant Stokes shifts, but is strongly quenched in water [19–21]. Substitution of *p*-dimethylaminophenyl by a *p*-methoxyphenyl (**M3HE**, Figure 2), a medium electron-donating group, shifts the 3HC sensitivity to protic and hydrated media [22,23].

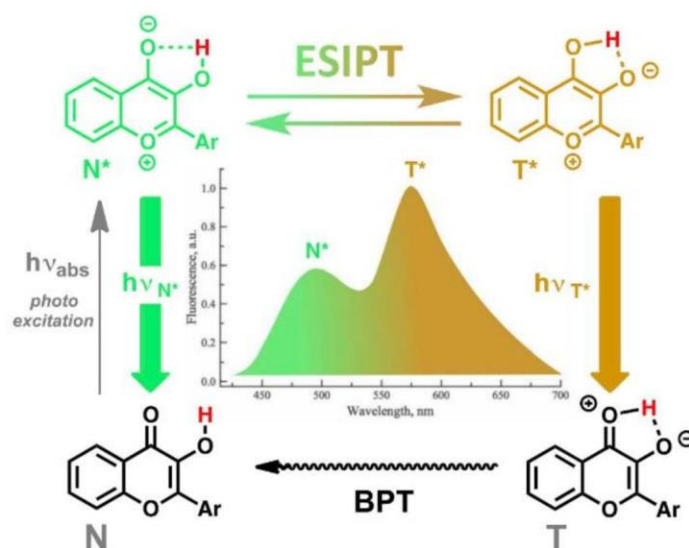


Figure 1. Principle of the ESIPT photoreaction for 3HC fluorophores. BPT stands for Back Proton Transfer.

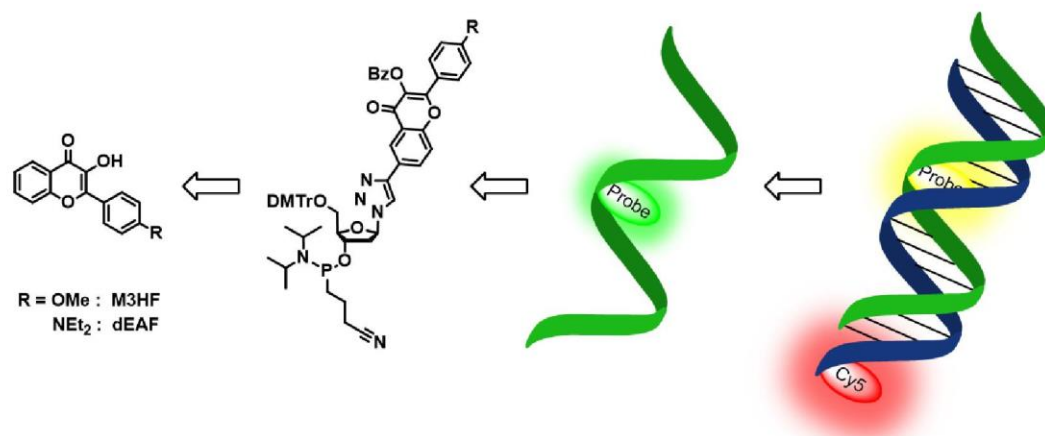


Figure 2. Schematic representation of the developed fluorogenic FRET approach based on a nucleoside analogue acting as a highly emissive donor upon hybridization.

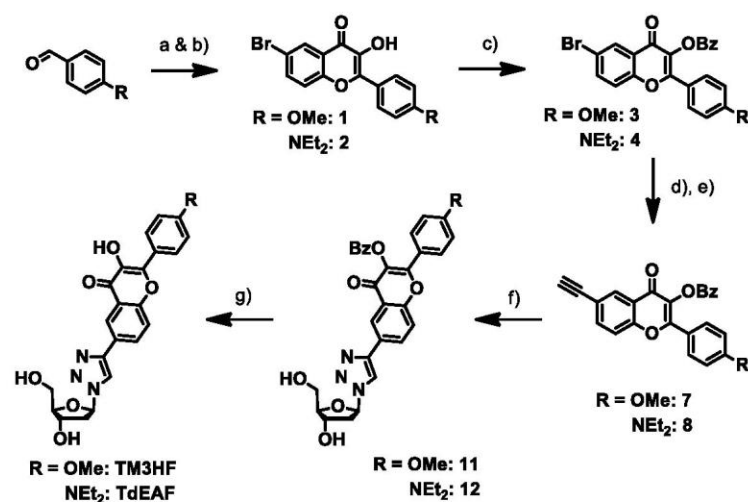
Our objective was to synthesize labeled ODNs with red-shifted turn-on emission after annealing with the complementary strand and thus create a novel mega-Stokes shift FRET pair in order to explore the full potential of this dye couple in detecting specific sequences. The characteristics of this fluorogenic emission must be both independent of the nature of neighboring base pairs but also capable of probing the local environment. The selected strategy was to first prepare the corresponding nucleoside amidites of both fluorophores (dEAF & M3HF) and to use these building blocks directly to obtain labeled single-stranded (ss) ODNs with a variety of composition (Figure 2). Position 6 of the benzene ring was preferred to produce the intended amidites, as chemical modification at this location should have minimal impact on the photophysics of the dye [24]. The 3-hydroxyl group was deprotected in order to benefit from the ESIPT mechanism. In ss-DNA, the dye will replace a natural base and be positioned centrally. After hybridization, it will be forced to interact with the duplex by intercalation (Figure 2). Herein, we report the synthesis and application of two new fluorescent nucleoside analogs (FNAs) based on 3HC scaffold with a mega-Stokes-shifted emission and an appreciable brightness. These FNAs were also modified into their corresponding phosphoramidites so that they could be site-specifically incorporated within a single-stranded structure using standard solid-phase

ODN synthesis protocol. Both dyes present exquisite environmental sensitivity with emissions exhibiting large Stokes shifts and show characteristic fluorogenic properties upon hybridization from ss- to ds-ODN with minimal impact on duplex stability. A novel mega-Stokes-shifted FRET couple was engineered when the **dEAF** donor was paired with a **Cy5** acceptor. Indeed, this indocarbocyanine was selected for its poor cross-excitation where our donor absorbs the most as well as for its convenient far-red emission.

2. Results and Discussion

2.1. Synthesis

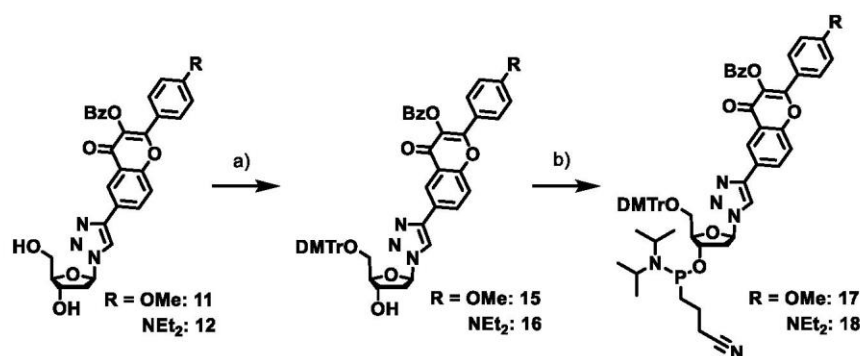
To generate the targeted 3HC-based fluorophores, keeping the photophysical properties of the parent 3HC intact, the strategy employed was to insert the sugar surrogate onto the 6-position of 3HC, as any modification at this location has minimal effect on the dye photophysics [24]. As for position 2, it is known to be the cornerstone for modulating the spectroscopic features due to its direct conjugation with the electron-withdrawing ketone. Therefore, it was decided to connect to the 2-position of the 3HC unit, two different electron-donating moieties (*p*-methoxy and *p*-*N,N*-diethylaminophenyl) that give the fluorochrome a reasonable size, viz. comparable to that of a natural base pair. The Algar-Flynn-Oyamada reaction [25] was first used to elaborate the flavonoid core, i.e., the basic structure of 3HC dyes (Scheme 1) [24]. This 2-step, one-pot process involves a smooth and efficient chalcone formation followed by oxidative cyclization. To this end, starting from 5'-bromo-2'-hydroxyacetophenone, a Claisen-Schmidt condensation with the corresponding carbaldehydes in the presence of sodium hydroxide in ethanol, followed by treatment with aqueous hydrogen peroxide, afforded the parent 3HCs **1** and **2** in appreciable yields (48% (OMe) & 77% (NEt₂)). Next, the 3-OH was masked with a benzoyl ester to provide **3** and **4**. Indeed, this protecting group prevents side reactions for all the downstream synthesis as well as improves hydrophobicity, which facilitates purification steps by silica gel column chromatography. TMS-acetylene was subsequently introduced onto the aryl bromide through a Sonogashira cross-coupling (Scheme 1). The silyl ether was removed to release the free alkyne, which was then clicked to the previously reported 1-azido-1,2-dideoxy- β -D-ribofuranose **10** [26–28] using the standard CuAAC assembly. Finally, removal of the benzoyl protection yielded the fluorophores **TM3HF** & **TdEAF** that closely resembles the related building block within the single-stranded structure. NMR, HRMS and HPLC attested the proper obtention of these model compounds (see SI and Figure S1). Before exploring their NA-related applications, the photophysical properties of these two FNAs were investigated to anticipate their behavior in a DNA environment (Table S1).



147

Scheme 1. Synthetic routes to **TM3HF** and **TdEAF**: a) KOH (25%), 5'-Bromo-2'-hydroxyacetophenone, EtOH, rt, 48 h. b) H₂O₂ (35%), EtOH, 0 °C, 24 h, [R = OMe: 48%, R = NEt₂: 77%]. c) Benzoyl chloride (3 eq.), Et₃N (6 eq.), Pyr, 0 °C, 24 h, [R = OMe: 70%, R = NEt₂: 95%]. d) TMS-acetylene (2 eq.), PdCl₂(PPh₃)₂ (11 mol%), CuI (7 mol%), Et₃N (6 eq.) THF, 65 °C, 24 h, [R = OMe: 74%, R = NEt₂: 73%]. e) Et₃NF (4 eq.), THF, rt, 2 h, [R = OMe: 65%, R = NEt₂: 78%]. f) 1-Azido-1,2-dideoxy-β-D-ribofuranose **10** (1.1 eq.), DIPEA (4.2 eq.), acetic acid (2.1 eq.), CuI (0.5 eq.), DCE, 40 °C, 1 h, [R = OMe: 94%, R = NEt₂: 99%]. g) NH₄OH (33%), MeOH/Pyr, rt, 6h, [R = OMe: 61%, R = NEt₂: 62%].

As for the corresponding fluorescent amidites, their synthesis was quite straightforward (Scheme 2). Restarting from intermediates **11** and **12**, their primary 5'-alcohol was then converted into the respective acid-labile dimethoxytrityl (DMTr) ethers **15** & **16**. Finally, classical phosphitylation was efficiently performed to afford the targeted amidites **17** and **18**. ODNs labeled with **TM3HF** or **TdEAF** were produced by site-selectively incorporating the requested amidites via solid-phase synthesis using conventional procedures (Supporting Information). The crude 15-mer sequences were treated with concentrated aqueous ammonia at room temperature for 12 h to remove all protecting groups and were then purified by reverse-phase HPLC using DMT-on strategy. The resulting tagged ODNs (5'-CGT TTT **YMY** TTT TGC) differ in their central context (**YMY** with **Y** = A, T, C or G and **M** = **TM3HF** or **TdEAF**). Complementary strands (5'-GCA AAA **YNY** AAA ACG-3' with **N** = A, T, G, C or *Ab* (abasic site) and **Y** = A, T, G or C), including those labeled with Cy5 where the acceptor is attached to the 5'-end, were purchased from Microsynth (Balgach, Switzerland). UV-Vis spectroscopic analyses, MS, and HPLC confirmed the integrity and purity of these modified ODNs (Figures S7–S12 and Table S2). For simplicity, a bold 3-letter code corresponding to the central codon of the sequence was employed to specify the single and double strands considered (e.g., respectively **AMA** and **AMA·TTT**).



Scheme 2. Synthesis of phosphoramidites **17** and **18** embedding a 3HC-based nucleobase mimic. a) DMTrCl (2.2 eq.), DBU (6.6 eq.), DMF/Pyr, 0 °C, 16 h, [R = OMe: 73%, R = NEt₂: 51%]. b) CEP-Cl (1.2 eq.), DIPEA (10 eq.), DCM, rt, 2.5 h, [R = OMe: 73%, R = NEt₂: 88%].

2.2. Photophysical features of model FNAs (**TM3HF** & **TdEAF**)

The 3HC-nucleobase mimics coupled with the deoxyribose surrogate i.e., **TM3HF** & **TdEAF**, were chosen as model compounds to characterize the photophysical properties of the fluorescent labels. Absorption and emission spectra of both dyes were recorded in different solvents of varying polarity and proticity (Table S1). The ground-state absorption properties are mainly due to the allowed $\pi-\pi^*$ transition, as inferred from their high molar extinction coefficient (21,000 & 40,000 L·mol⁻¹·cm⁻¹ for **TM3HF** and **TdEAF** respectively). The absorption maxima did not change significantly for **TM3HF** (348–359 nm) but in contrast varied ~35 nm for **TdEAF** along the increase in polarity (Figure 3). This indicates that the ground-state dipole moment is much higher for **TdEAF** than for **TM3HF**. Notably, the Stokes shift and emission maximum of both fluorochromes show a regular increment with increasing solvent polarity (Figures S4 and S5). Upon electronic excitation, the inherent charge redistribution creates a higher dipole moment in the excited state,

which allows for much better interaction with surrounding solvent molecules, resulting in remarkable solvatofluorochromism properties.

189
190

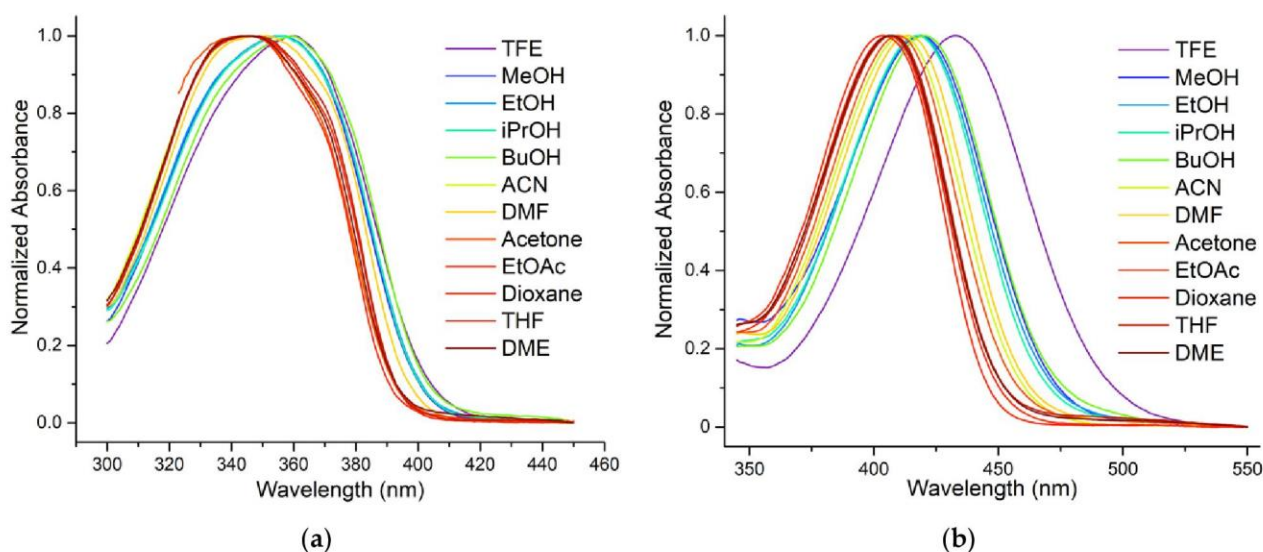


Figure 3. Absorbance observables of (a) **TM3HF** and (b) **TdEAF** in a set of solvents varying in polarity.

191
192

Originally, these synthesized dyes bearing a free 3-OH group were designed to function as an ESIPT fluorophore, viz. a dual emitter. Expectedly for both cases, ESIPT was observed but with notable differences between the two dyes. In the case of the moderate mesomeric donor **TM3HF**, both N^* and T^* bands are present in protic solvents and follow the classical effect, i.e., decreasing the N^*/T^* ratio alongside polarity drop-off. In contrast, the strongly positive mesomeric **TdEAF** shows only the emission band in polar protic solvents and unveil T^* when reaching aprotic ones. Due to the strong electron-donating ability of its *N,N*-diethylamino group and the higher dipole moment of the normal over the tautomer form in the excited state, the N^* band position exhibits strong solvent-dependent variation by contrast to T^* ; thus mixing them to lead to a single broad emission particularly in more polar protic solvents. This hypothesis was then confirmed by performing a titration of each FNA in an aprotic solvent with an incremental addition of methanol (Figure 4). During titration, we observed that two separate bands, clearly N^* and T^* , are present for **TM3HF** from the beginning until reaching 100%-methanol environment and decreasing the N^*/T^* ratio alongside polarity drop-off. While for the **TdEAF** titration, the two bands merged just after reaching 20%-methanol composition, resulting in one single-band emission. For both cases, methanol was used to probe the ESIPT mechanism instead of water, as **TdEAF** was not emissive in water.

193
194
195
196
197
198
199
200
201
202
203
204
205
206
207
208
209
210

Altogether, the data of **TM3HF** and **TdEAF** are like those of the parent chromones **M3HF** and **dEAF**. For instance in DMF, the maxima were 353 and 413 nm for absorption, 421 and 518 nm for the N^* emission band, and 544 and 590 nm for T^* , respectively for **TM3HF** and **TdEAF**. These results are significantly close to those of the parent dyes ($\lambda_{Abs} = 355$ and 407 nm, $\lambda_{N^*} = 421$ and 509 nm, $\lambda_{T^*} = 539$ and 585 nm). Our data are consistent with the fact that modifications introduced at position 6 have marginal impact on the spectroscopic properties.

211
212
213
214
215
216
217

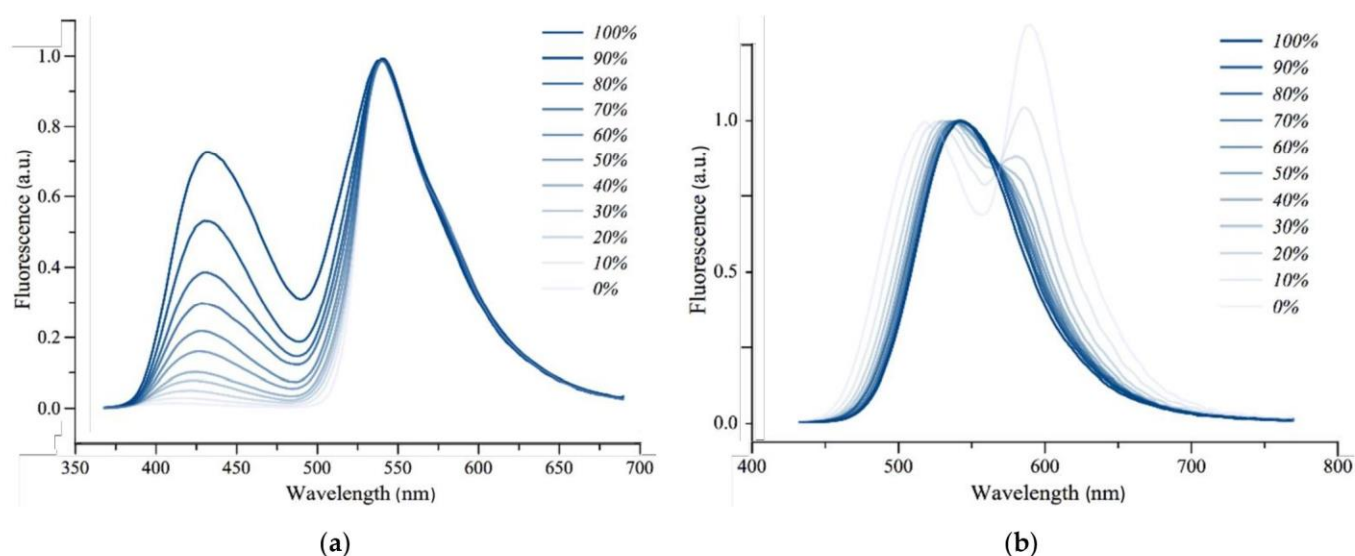


Figure 4. Fluorescence titrations of **TM3HF** (a) & **TdEAF** (b) in DMF by MeOH. Observables were normalized on T^* and N^* bands, respectively.

2.2. Photophysical properties of labeled ODNs

It was decided to incorporate each 3HC-based emitter on the central position of the ODN surrounded by 4 different base contexts such as **TMT**, **AMA**, **CMC** and **GMG**. The location of the marker in the middle of the sequence eliminates the potential situation of a sticky end association, thus ensuring an easier interpretation of the emission response. The goal of this screening was essentially to get large Stokes shifts upon hybridization. These 4 sequences, imposing 4 distinct environments around the fluorescence reporter, increase our scope of study to obtain a global overview rather than a specific situation.

To verify the impact of the fluorophores on the stability and structure of the duplexes, melting temperatures and circular dichroism studies of the labeled ds-ODNs were conducted and compared to that of corresponding wild-type sequences. Thermal denaturation and CD investigations (Tables S3, Figures S13-S15) revealed that the label **M** can replace any nucleobase leading stable duplexes with the B-conformation. Similar observations are commonly found in the literature when a natural nucleoside is replaced by a nucleoside analog labeled with a fluorophore [29–33].

Table 1. Spectroscopic properties of **TM3HF**- and **TdEAF**-labeled ODNs.

Sequences	λ_{Abs} (nm) ^a		λ_{N^*} (nm) ^b		λ_{T^*} (nm) ^c		I_{N^*}/I_{T^*} ^d		Φ (%) ^e	
	TM3F	TdEAF	TM3F	TdEAF	TM3F	TdEAF	TM3F	TdEAF	TM3F	TdEAF
TMT	367	440	442	551	540	—	0.20	—	8	34
TMT·ATA	372	431	442	549	545	—	0.09	—	29	45
TMT·AAA	375	436	445	551	546	—	0.10	—	27	35
TMT·ACA	372	430	446	553	545	—	0.12	—	30	43
TMT·AGA	359	433	441	551	545	—	0.13	—	11	34
TMT·AAbA	369	434	444	553	544	—	0.12	—	31	47
AMA	373	443	442	546	538	—	0.13	—	16	55
AMA·TTT	367	437	440	546	539	—	0.07	—	35	45
AMA·TAT	372	440	440	548	540	—	0.08	—	30	41
AMA·TCT	372	440	445	551	540	—	0.10	—	50	56
AMA·TGT	356	446	438	546	540	—	0.07	—	12	48
AMA·TAbT	365	439	438	549	540	—	0.07	—	28	56
CMC	363	440	446	546	542	—	0.13	—	2	54

CMC ·GTG	360	436	—	542	542	—	—	—	<< 1	48
CMC ·GAG	364	432	444	549	541	—	0.24	—	< 1	42
CMC ·GCG	362	435	446	543	548	—	0.30	—	< 1	60
CMC ·GGG	354	436	441	549	540	—	0.20	—	<< 1	38
CMC ·GAbG	361	432	446	548	539	—	0.57	—	< 1	52
GMG	366	439	445	548	542	—	0.09	—	1	32
GMG ·CTC	362	434	441	540	541	—	0.08	—	2	44
GMG ·CAC	373	434	442	546	542	—	0.12	—	5	38
GMG ·CCC	368	437	438	547	541	—	0.14	—	2	40
GMG ·CGC	358	433	436	547	542	—	0.09	—	1	41
GMG ·CAbC	363	435	437	544	543	—	0.10	—	2	49

a-c) Positions of the absorption, N*, and T* band maxima, respectively; d) ratio of the intensities at the two emission maxima; e) Fluorescence quantum yields were determined using both an excitation at the corresponding absorption maximum of **M** and 4'-(*N,N*-dimethylamino)-3-hydroxyflavone (**dMAF**) in EtOH ($\lambda_{\text{Ex}} = 407 \text{ nm}$, $\Phi = 27\%$) as a reference [34,35], $\pm 10\%$ mean standard deviation.

UV-Vis and fluorescence spectroscopy studies for labeled ss-ODNs of various compositions with the synthesized fluorophores were performed in phosphate-buffered saline at pH 7.4 (Figures S16–S19). **TM3HF**-tagged ss-ODNs, prepared from the corresponding amidite **17**, displayed an absorption maximum oscillating between 363–373 nm for the different neighboring base pairs investigated (Table 1, Figures 5 & S16). Upon hybridization with the complementary strands, a similar range for ds-ODNs was observed (354–375 nm). Compared to the absorption maximum of its respective FNA in various solvents, the absorption was red-shifted (e.g., $\lambda_{\text{Abs}} = 372 \text{ nm}$ for **AMA**·TCT in buffer and 357 nm for **TM3HF** in methanol); presumably due to stacking of the dye with the flanking bases in the duplex. As a matter of fact, bathochromic shift of the absorption is common with intercalating dyes (e.g., acridine, phenanthridinium, thienylchromone) [33,36,37]. Absorption spectra of **TdEAF**-labeled ss-ODNs—synthesized from its related amidite **18**—and the ds-ODNs also showed very similar profiles (e.g., $\lambda_{\text{Abs}} = 440 \text{ nm}$ for **AMA**·TCT in buffer and 420 nm for **TdEAF** in methanol).

The fluorescence emission maxima for the ds-DNAs derived from hybridization with the **TM3HF**-tagged ds-ODNs were located at 440 nm and 540 nm range for N* and T* bands independently of the adjacent bases, with a dominant T* emission likely in response to a less hydrated environment (Figure 5). After annealing, the N* and T* emission maxima of **TM3HF**-tagged ds-ODNs were located at 440 and 540 nm, respectively—independent of the adjacent bases—with a dominant T* emission likely in response to a less hydrated environment (Figure 5). Thanks to ESIPT reaction, this **TM3HF** marker demonstrated pseudo mega-Stokes shifts on its tautomer band when incorporated into DNA (~190 nm, Table 1 and Figure S18).

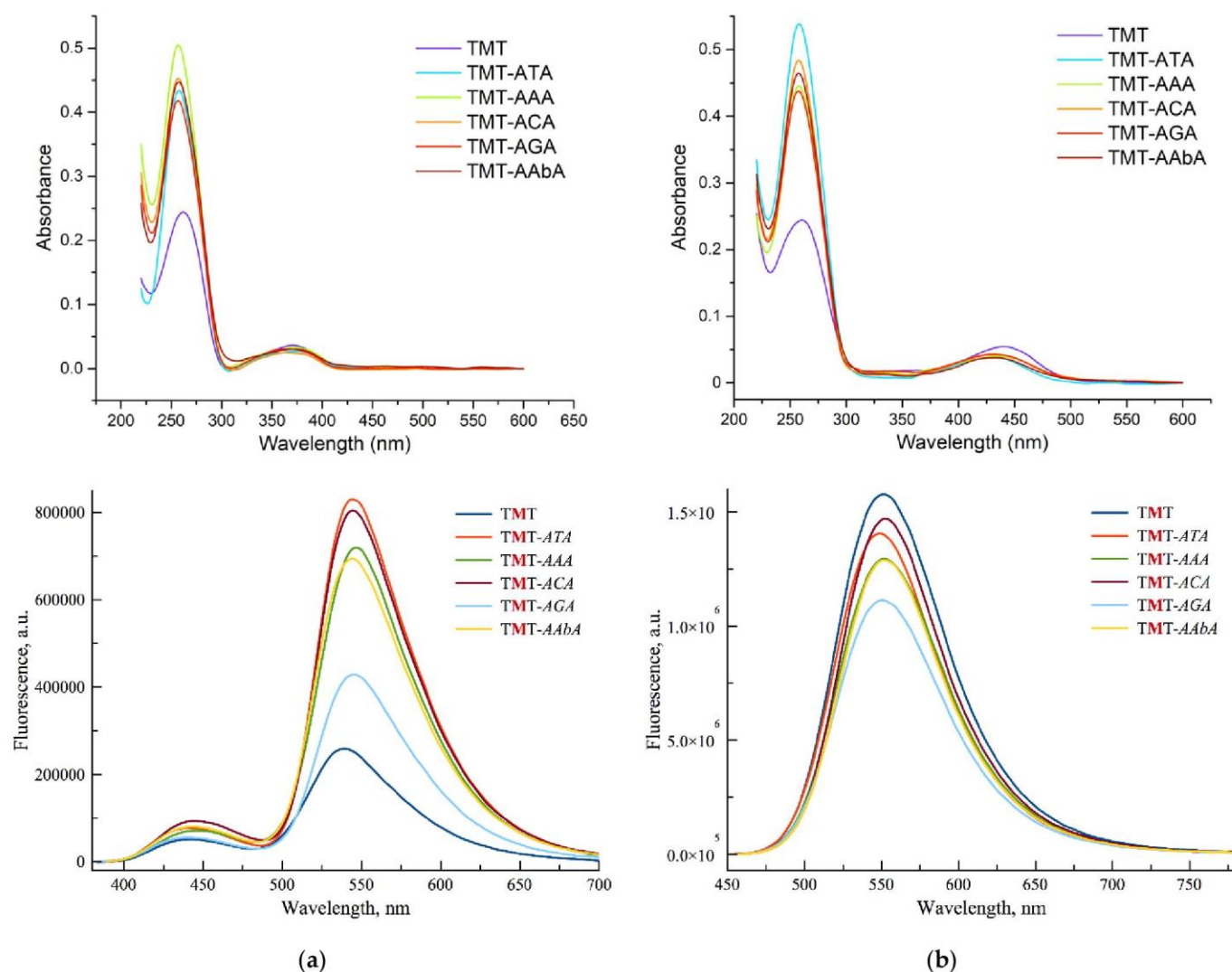


Figure 5. Absorption and fluorescence spectra in ss- and ds-contexts of the TMT sequence labeled with TM3HF (a) & TdEAF (b) in pH 7.4 phosphate-buffered saline. Excitation was performed at the absorption maximum.

Although TM3HF showed a fluorogenic response (3- to 4-fold increment in fluorescence emission intensity and brightness $B = \epsilon \times \Phi$, up to $10,000 \text{ M}^{-1}\cdot\text{cm}^{-1}$) and a characteristic dual emission upon duplex formation in the presence of neighboring bases such as thymines and adenines, this dye proved to be quenched by proximal G or C bases. This sensitivity to quenching by G and C flanking bases has previously been observed for DNA labeled with other 3HC dyes [33,38]. This fluorescence quenching phenomenon is commonly observed for nucleobase surrogates. It can be caused either by a photoinduced electron transfer (PET) mechanism resulting from the strong electron-donating capacity of G, or by the formation of non-emissive dark states [39–41]. Noticeably, ss- and ds-ODNs marked with TdEAF displayed very good quantum yields and brightness (viz. $\Phi \approx 30\text{--}60\%$, $B \sim 13\text{--}24,000 \text{ M}^{-1}\cdot\text{cm}^{-1}$) irrespective of the nature of adjacent base pairs (Table 1, Figures 4 & S18). These results are remarkable because this is the first example of a 3HC-based reporter whose fluorescence is shown to be totally independent of the reducing ability of surrounding nucleobases [33,38]. As predicted by photophysical studies of its related model nucleoside in a highly hydrated medium, TdEAF still exhibits mega-Stokes shifts ($\sim 110 \text{ nm}$) in a DNA environment, but as a single-band emission due to inhibition of the ESIP reaction. In a nutshell, the results of steady-state fluorescence spectroscopy studies for these two dyes are perfectly complementary; one presents a dual emission in

a specific context of base pairs, while the other exhibits a single emission band but once incorporated into DNA, it lights up permanently with high quantum yields. This sharp increase in quantum efficiency can be explained by the relocation of the fluorophore in a less hydrated environment—intercalated within adjacent nucleobases—but also by the reduction of both PET occurrence and dark species formation. Indeed, the substitution of *p*-methoxyl by the *p*-diethylamino group, a stronger mesomeric donor substituent, should logically rise the HOMO level and decrease the redox potential of the chromone dye. Consequently, electron transfer from guanine to **TdEAF** should be less favorable. This result is remarkable because many fluorophores are quenched by one or more nucleic bases; with G often being the most effective quencher [39]. Compared to the handful of FNAs insensitive to nucleobase quenching but retain Watson–Crick base-pairing ability [42,43], **TdEAF** is at least five times brighter. Moreover, it provides absorption in the blue range and emission in the red edge, as desired for a fluorophore replacing a natural base [39].

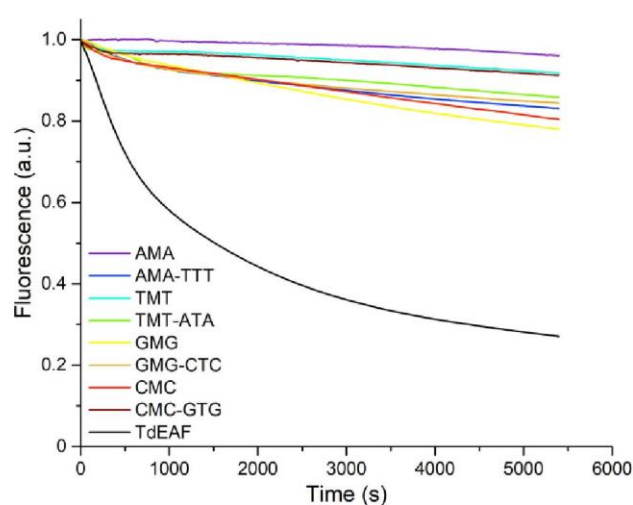


Figure 6. Photodegradation curves of **TdEAF**-labeled ss- and ds-ODNs in pH 7.4 phosphate-buffered saline as well as **TdEAF** in EtOH. Excitation was set at the absorption maximum.

Photostability of the fluorescent dyes remains a major prerequisite for bioimaging applications. As **TdEAF**-labeled sequences displayed attractive quantum yields and appeared as the most prospective, their photodegradation in ss- and ds-contexts was investigated under continuous sample illumination (Figure 6). The stability in ethanol of **TdEAF** was compared to that of Prodan, a reference push–pull fluorophore. The choice of this protic solvent is explained both by the fact that **TdEAF** is bright in EtOH and presents a single-band emission whose maximum is close to that observed in DNA (Table S1) but also that Prodan is stabilized there [44]. **TdEAF** exhibits a much higher photostability when the fluorescent tag is incorporated into DNA than as an unshielded FNA. Photobleaching decays showed that where **TdEAF**-labeled ODNs lost only 15–20% of their emission intensity over 1.5 hours of irradiation, the corresponding nucleoside analog exhibited an 80% loss. Similar conclusions were drawn from our thienyl 3-hydroxychromone; this natural base substitute proved to be much more photostable once introduced within DNA [33].

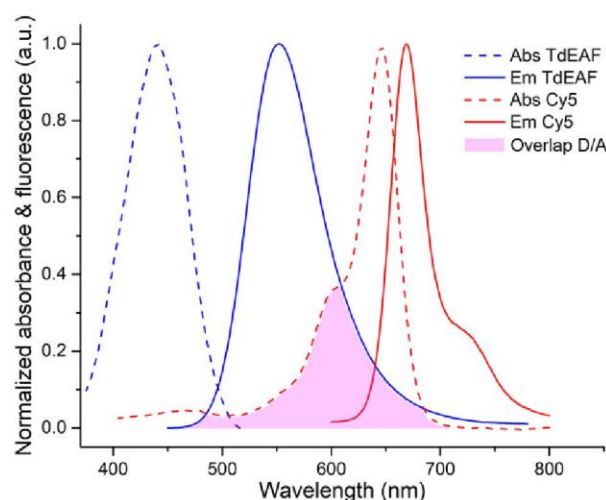


Figure 7. Normalized absorption and emission spectra of the **TdEAF** donor (D) and **Cy5** acceptor (A) emphasizing the spectral overlap of the two FRET partners.

Based on the experimental results, our data demonstrate that the dyes meet the requirements to act as a bright mega-Stokes shift FRET donor ($\lambda_{\text{Abs}} \approx 440$ nm, $\lambda_{\text{Em}} \approx 550$ nm, $B \sim 12\text{--}24,000$ $\text{M}^{-1}\cdot\text{cm}^{-1}$), with a view to developing a universal probe to sense interactions with DNA via fluorescence resonance energy transfer. For this purpose, **AMA** and **CMC** sequences were chosen since they gave rise to the brightest ds-DNA combinations (except for **CMC** with the **TM3HF** label, Table 1). **Cy5** was selected as the bright FRET acceptor because of the significant spectral overlap between its absorption and the red edge of donor emission as well as the almost complete absence of absorption where **TdEAF** absorbs the most, which considerably reduces cross-excitation (Figures 7, S20 & S21). For these reasons, **Cy5** was introduced on the complementary sequences at the 5'-terminal position.

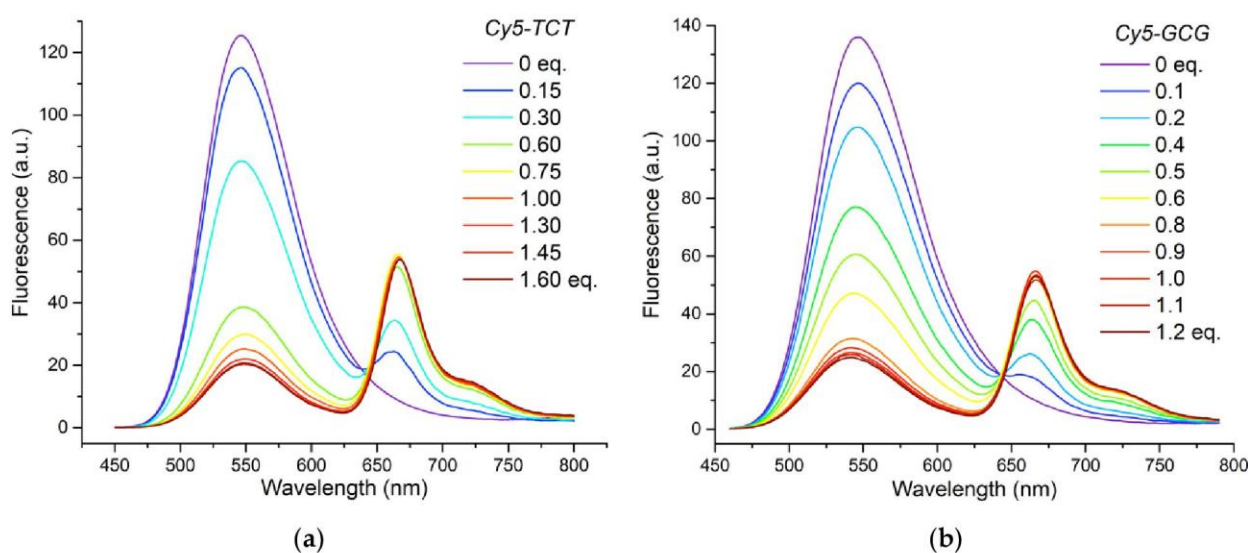


Figure 8. Fluorescence titration of **TdEAF**-labeled **AMA** (a) and **CMC** (b) ODNs by their complementary sequence tagged at the 5'-terminus with **Cy5**.

The Förster distance (distance where FRET is 50% efficient) was calculated for a randomly oriented donor-acceptor pair and was found to be ~ 56 Å (Equation S1 for $\kappa^2 = 2/3$). Furthermore, the emission band in the far-red region (675 nm) shows an appreciable quantum yield ($\Phi = 27\%$). Control and FRET experiments were performed with the single-labeled double strand **AMA-TCT** (or **CMC-GCG**) and doubly labeled ds **AMA-Cy5-TCT** (or **CMC-Cy5-GCG**). Considering a 3.4Å gap per base pair for B-DNA and assuming a

terminally stacked Cy5, the distance between **M** and Cy5 should be around 30 Å, which is favorable for FRET [45–49]. When Cy5-tagged DNAs were excited at 440 nm, no emission could be recorded, confirming that Cy5 does not absorb at this wavelength. Contrastingly, when the duplex was excited at the Cy5 absorption maximum (643 nm), the characteristic emission spectrum of this cyanine was confirmed. An efficient FRET was observed when the double-labeled ds **AMA**·Cy5-**TCT** (or **CMC**·Cy5-**GCG**) was excited at the donor absorption wavelength (440 nm). Indeed, comparison of the fluorescence spectra of **AMA**·Cy5-**TCT** and **CMC**·Cy5-**GCG** with their respective single-labeled **AMA**·**TCT** and **CMC**·**GCG** duplexes revealed a dramatic decrease in the donor emission intensity at 550 nm together with a 7-fold increase in Cy5 signal at 674 nm. As expected for the selected ds-DNAs, the energy transfer efficiency (Equation S2) was determined to be high (~81% for **AMA**·Cy5-**TCT** and **CMC**·Cy5-**GCG**). Further, the addition of 1 equivalent of Cy5-**TCT** was sufficient to almost reverse the intensity ratio at the emission maxima (Figure 8). Similar experiments were also conducted with **TM3HF**-labeled ODNs, but due to the absorption overlap of this dye with that of Cy5, the results were less satisfactory (Figures S22 & S23).

3. Conclusions

In summary, two promising fluorophores were synthesized from a 3HC scaffold on which two different electron-donating (donor) moieties were connected at position 2. The resulting push–pull dyes exhibit absorption in the UV and visible range (ca. 370 and 440 nm) compatible with violet and blue laser excitation, substantial extinction coefficient ($\epsilon_{\max} \approx 40,000 \text{ M}^{-1}\cdot\text{cm}^{-1}$ for **TdEAF**), large Stokes shifts (~110–190 nm), and high quantum yields (up to 60%). These two new 3HC-based emitters, with significantly improved photophysical properties, were also successfully converted to phosphoramidite derivatives. Position 6 of the chromone core was chosen as the anchor point for assembly with the deoxyribose surrogate, because any modification at this location has minimal impact on the photophysics of the dye. The corresponding amidites were then incorporated site-selectively into single-stranded sequences with a variety of adjacent base compositions. **TdEAF**-labeled ODNs retained all photophysical properties intact and showed improved photostability as well as high brightness (~ 13–24,000 $\text{M}^{-1}\cdot\text{cm}^{-1}$) regardless of the nature of the neighboring base pairs, which is remarkable. The dye can substitute any natural nucleobase to give stable duplexes in B conformation, making it a universal base. Compared to the brightest cyanine–styryl conjugate [16], which absorbs and fluoresces in comparable visible ranges, **TdEAF** is at least twice as bright and its quantum yield is less sensitive to the composition of surrounding bases. With respect to other established FNAs, **TdEAF** appears to be a promising fluorescent tag for single-molecule applications due to its superior brightness, improved photostability, and red-shifted absorption and emission [50]. To make the most of the key features offered by this fluorescent reporter, an efficient FRET system was developed in which the **TdEAF** label (tag) introduced within ss-ODNs acts as a donor and, in the complementary strand, Cy5 operates as an acceptor with reduced cross-excitation. Steady-state fluorescence studies demonstrated that the establishment of this FRET couple results in a clear visual change in emission color from yellow to far-red upon hybridization. To further increase the fluorogenic response, there are several possibilities such as reducing the donor–acceptor distance, using an acceptor either with a higher quantum yield or a more red-shifted fluorescence signal to limit cross-emission [16]. Hence, this novel mega-Stokes FRET donor should find applications in studying NA conformational changes in real time, developing diagnostic and screening tools, or imaging specific RNA and DNA sequences in the far-red.

References

1. Klymchenko, A.S. Solvatochromic and Fluorogenic Dyes as Environment-Sensitive Probes: Design and Biological Applications. *Acc. Chem. Res.* **2017**, *50*, 366–375. <http://doi.org/10.1021/acs.accounts.6b00517>
2. Medintz, I., Hildebrandt, N., Eds. *FRET – Förster Resonance Energy Transfer: From Theory to Applications*; Wiley-VCH: Weinheim, Germany; 2013, p. 791.
3. Rowland, C.E.; Brown, C.W.; Medintz, I.L.; Delehanty, J.B. Intracellular FRET-based probes: a review. *Methods Appl. Fluoresc.* **2015**, *3*, 042006. <http://doi.org/10.1088/2050-6120/3/4/042006>
4. Wu, L.; Huang, C.; Ben P. Emery; Sedgwick, A.C.; Bull, S. D.; He, X.-P.; Tian, H.; Yoon, J.; Sessler, J.L.; James, T.D. Förster resonance energy transfer (FRET)-based small-molecule sensors and imaging agents. *Chem. Soc. Rev.* **2020**, *49*, 5110–5139. <http://doi.org/10.1039/C9CS00318E>
5. Yuan, L.; Lin, W.; Zheng, K.; Zhu, S. FRET-Based Small-Molecule Fluorescent Probes: Rational Design and Bioimaging Applications. *Acc. Chem. Res.* **2013**, *46*, 1462–1473. <http://doi.org/10.1021/ar300273v>
6. Kwok, P.Y. Methods for genotyping single nucleotide polymorphisms. *Annu. Rev. Genomics Hum. Genet.* **2001**, *2*, 235–258. <http://doi.org/10.1146/annurev.genom.2.1.235>
7. Tomoike, F.; Abe, H. RNA imaging by chemical probes. *Adv. Drug Deliv. Rev.* **2019**, *147*, 44–58. <http://doi.org/10.1146/10.1016/j.addr.2019.08.001>
8. Wranne, M.S.; Füchtbauer, A.F.; Dumat, B.; Bood, M.; El-Sagheer, A.H.; Brown, T.; Gradén, H.; Grøtli, M.; Wilhelmsson, L.M. Toward Complete Sequence Flexibility of Nucleic Acid Base Analogue FRET. *J. Am. Chem. Soc.* **2017**, *139*, 9271–9280. <http://doi.org/10.1021/jacs.7b04517>
9. Eugenio Vazquez, M.; Rothman, D.M.; Imperiali, B. A new environment-sensitive fluorescent amino acid for Fmoc-based solid phase peptide synthesis. *Org. Biomol. Chem.* **2004**, *2*, 1965–1966. <http://doi.org/10.1039/b408001g>
10. Vázquez, M.E.; Blanco, J.B.; Imperiali, B. Photophysics and Biological Applications of the Environment-Sensitive Fluorophore 6- N, N-Dimethylamino-2,3-naphthalimide. *J. Am. Chem. Soc.* **2005**, *127*, 1300–1306. <http://doi.org/10.1021/ja0449168>
11. Loving, G.; Imperiali, B. A versatile amino acid analogue of the solvatochromic fluorophore 4-N,N-dimethylamino-1,8-naphthalimide: a powerful tool for the study of dynamic protein interactions. *J. Am. Chem. Soc.* **2008**, *130*, 13630–13638. <http://doi.org/10.1021/ja804754y>
12. Kuang, T.; Chang, L.; Peng, X.; Hu, X.; Gallego-Perez, D. Molecular Beacon Nano-Sensors for Probing Living Cancer Cells. *Trends Biotechnol.* **2017**, *35*, 347–359. <http://doi.org/10.1016/j.tibtech.2016.09.003>
13. Tyagi, S.; Marras, S.; Kramer, F.R. Wavelength-shifting molecular beacons. *Nat. Biotech.* **2000**, *18*, 1191–1196. <http://doi.org/10.1038/81192>
14. Li, Q.; Luan, G.; Guo, Q.; Liang, J. A new class of homogeneous nucleic acid probes based on specific displacement hybridization. *Nucleic Acids Res.* **2002**, *30*, E5–5. <http://doi.org/10.1093/nar/30.2.e5>
15. Barnoin, G.; Shaya, J.; Richert, L.; Le, H.-N.; Vincent, S.; Guérineau, V.; Mély, Y.; Michel, B.Y.; Burger, A. Intermolecular dark resonance energy transfer (DRET): upgrading fluorogenic DNA sensing. *Nucleic Acids Res.* **2021**, *49*, e72. <http://doi.org/10.1093/nar/gkab237>
16. Gebhard, J.; Hirsch, L.; Schwechheimer, C.; Wagenknecht, H.-A. Hybridization-Sensitive Fluorescent Probes for DNA and RNA by a Modular “Click” Approach. *Bioconjugate Chem.* **2022**. <http://doi.org/10.1021/acs.bioconjchem.2c00241>
17. Benson, S.; de Moliner, F.; Tipping, W.; Vendrell, M. Miniaturized Chemical Tags for Optical Imaging. *Angew. Chem. Int. Ed.* **2022**, *61*, e202204788. <http://doi.org/10.1002/anie.202204788>
18. Demchenko, A.P.; Tang, K.-C.; Chou, P.-T. Excited-state proton coupled charge transfer modulated by molecular structure and media polarization. *Chem. Soc. Rev.* **2013**, *42*, 1379–1408. <http://doi.org/10.1039/c2cs35195a>
19. Chou, P.-T.; Martinez, M.L.; Clements, J.H. The observation of solvent-dependent proton-transfer / charge-transfer lasers from 4'-diethylamino-3-hydroxyflavone. *Chem. Phys. Lett.* **1993**, *204*, 395–399. [http://doi.org/10.1016/0009-2614\(93\)89175-H](http://doi.org/10.1016/0009-2614(93)89175-H)
20. Klymchenko, A.S.; Ozturk, T.; Demchenko, A.P. Synthesis of furanochromones: a new step in improvement of fluorescence properties. **2002**, *43*, 7079–7082. [http://doi.org/10.1016/S0040-4039\(02\)01547-2](http://doi.org/10.1016/S0040-4039(02)01547-2)
21. Klymchenko, A.S.; Demchenko, A.P. Multiparametric probing of intermolecular interactions with fluorescent dye exhibiting excited state intramolecular proton transfer. *Phys. Chem. Chem. Phys.* **2003**, *5*, 461–468. <http://doi.org/10.1039/b210352d>
22. Sholokh, M.; Zamotaiev, O.M.; Das, R.; Postupalenko, V.Y.; Richert, L.; Dujardin, D.; Zaporozhets, O.A.; Pivovarenko, V.G.; Klymchenko, A.S.; Mély, Y. Fluorescent Amino Acid Undergoing Excited State Intramolecular Proton Transfer for Site-Specific Probing and Imaging of Peptide Interactions. *J. Phys. Chem. B* **2015**, *119*, 2585–2595. <http://doi.org/10.1021/jp508748e>
23. Zamotaiev, O.M.; Postupalenko, V.Y.; Shvachak, V.V.; Pivovarenko, V.G.; Klymchenko, A.S.; Mély, Y. Improved Hydration-Sensitive Dual-Fluorescence Labels For Monitoring Peptide–Nucleic Acid Interactions. *Bioconjugate Chem.* **2011**, *22*, 101–107. <http://doi.org/10.1021/bc100434d>
24. Vincent, S.; Mallick, S.; Barnoin, G.; Le, H.-N.; Michel, B.Y.; Burger, A. An Expeditious Approach towards the Synthesis and Application of Water-Soluble and Photostable Fluorogenic Chromones for DNA Detection. *Molecules* **2022**, *27*, 2267. <http://doi.org/10.3390/molecules27072267>
25. Dean, F.M.; Podimuang, V. 737. The course of the Algar–Flynn–Oyamada (A.F.O.) reaction. *J. Chem. Soc. Perkin Trans.* **1965**, 3978–3987. <http://doi.org/10.1039/JR9650003978>

26. Rolland, V.; Kotera, M.; Lhomme, J. Convenient Preparation of 2-Deoxy-3,5-di-O-*p*-toluoyl- α -D-erythro-pentofuranosyl Chloride. *Synth. Commun.* **1997**, *27*, 3505–3511. <http://doi.org/10.1080/00397919708007071>
27. Kolganova, N.A.; Florentiev, V.L.; Chudinov, A.V.; Zasedatelev, A.S.; Timofeev, E.N. Simple and stereoselective preparation of an 4-(aminomethyl)-1,2,3-triazolyl nucleoside phosphoramidite. *Chem. Biodivers.* **2011**, *8*, 568–576. <http://doi.org/10.1002/cbdv.201000047>
28. Štimac, A.; Kobe, J. Stereoselective synthesis of 1,2-*cis*- and 2-deoxyglycofuranosyl azides from glycosyl halides. *Carbohydr. Res.* **2000**, *329*, 317–324. [http://doi.org/10.1016/S0008-6215\(00\)00186-5](http://doi.org/10.1016/S0008-6215(00)00186-5)
29. Matray, T.J.; Kool, E.T. Selective and Stable DNA Base Pairing without Hydrogen Bonds. *J. Am. Chem. Soc.* **1998**, *120*, 6191–6192. <http://doi.org/10.1021/ja9803310>
30. Ogawa, A.K.; Abou-Zied, O.K.; Tsui, V.; Jimenez, R.; Case, D.A.; Romesberg, F.E. A Phototautomerizable Model DNA Base Pair. *J. Am. Chem. Soc.* **2000**, *122*, 9917–9920. <http://doi.org/10.1021/ja001778n>
31. Singh, I.; Hecker, W.; Prasad, A.K.; Parmar, V.S.; Seitz, O. Local disruption of DNA-base stacking by bulky base surrogates. *Chem. Commun.* **2002**, 500–501. <http://doi.org/10.1039/b110842e>
32. Brotschi, C.; Mathis, G.R.; Leumann, C.J. Bipyridyl- and Biphenyl-DNA: A Recognition Motif Based on Interstrand Aromatic Stacking. *Chem. Eur. J.* **2005**, *11*, 1911–1923. <http://doi.org/10.1002/chem.200400858>
33. Dziuba, D.; Postupalenko, V.Y.; Spadafora, M.; Klymchenko, A.S.; Guérineau, V.; Mély, Y.; Benhida, R.; Burger, A. A Universal Nucleoside with Strong Two-Band Switchable Fluorescence and Sensitivity to the Environment for Investigating DNA Interactions. *J. Am. Chem. Soc.* **2012**, *134*, 10209–10213. <http://doi.org/10.1021/ja3030388>
34. Ormson, S.M.; Brown, R.G.; Vollmer, F.; Rettig, W. Switching between charge- and proton-transfer emission in the excited state of a substituted 3-hydroxyflavone. *J. Photochem. Photobiol. A: Chem.* **1994**, *81*, 65–72. [http://doi.org/10.1016/1010-6030\(94\)03778-7](http://doi.org/10.1016/1010-6030(94)03778-7)
35. Melhuish, W.H. Quantum Efficiencies of Fluorescence of Organic Substances: Effect of Solvent and Concentration of the Fluorescent Solute. *J. Phys. Chem.* **1961**, *65*, 229–235. <http://doi.org/10.1021/j100820a009>
36. Asseline, U.; Delarue, M.; Lancelot, G.; Toulmé, F.; Thuong, N.T.; Montenay-Garestier, T.; Hélène, C. Nucleic acid-binding molecules with high affinity and base sequence specificity: intercalating agents covalently linked to oligodeoxynucleotides. *Proc. Natl. Acad. Sci. U. S. A.* **1984**, *81*, 3297–3301. <http://doi.org/10.1073/pnas.81.11.3297>
37. Amann, N.; Huber, R.; Wagenknecht, H.-A. Phenanthridinium as an artificial base and charge donor in DNA. *Angew. Chem. Int. Ed.* **2004**, *43*, 1845–1847. <http://doi.org/10.1002/anie.200353153>
38. Barthes, N.P.F.; Gavvala, K.; Dziuba, D.; Bonhomme, D.; Karpenko, I.A.; Dabert-Gay, A.S.; Debayle, D.; Demchenko, A.P.; Benhida, R.; Michel, B.Y.; Mély, Y.; Burger, A. Dual emissive analogue of deoxyuridine as a sensitive hydration-reporting probe for discriminating mismatched from matched DNA and DNA/DNA from DNA/RNA duplexes. *J. Mater. Chem. C* **2016**, *4*, 3010–3017. <http://doi.org/10.1039/C5TC03427B>
39. Michel, B.Y.; Dziuba, D.; Benhida, R.; Demchenko, A.P.; Burger, A. Probing of Nucleic Acid Structures, Dynamics, and Interactions With Environment-Sensitive Fluorescent Labels. *Front. Chem.* **2020**, *8*, 112. <http://doi.org/10.3389/fchem.2020.00112>
40. Sougnabé, A.; Lissouck, D.; Fontaine-Vive, F.; Nsangou, M.; Mély, Y.; Burger, A.; Kenfack, C.A. Electronic transitions and ESIPT kinetics of the thienyl-3-hydroxychromone nucleobase surrogate in DNA duplexes: a DFT/MD-TDDFT study. *RSC Adv.* **2020**, *10*, 7349–7359. <http://doi.org/10.1039/C9RA10419D>
41. Le, H.-N.; Brazard, J.; Barnoin, G.; Vincent, S.; Michel, B.Y.; Léonard, J.; Burger, A. Control of Intermolecular Photoinduced Electron Transfer in Deoxyadenosine-Based Fluorescent Probes. *Chem. Eur. J.* **2020**, *26*, 276–286. <http://doi.org/10.1002/chem.202003456>
42. Bood, M.; Fuchtbauer, A. F.; Wranne, M. S.; Ro, J. J.; Sarangamath, S.; El-Sagheer, A. H.; Rupert, D. L. M.; Fisher, R. S.; Magennis, S. W.; Jones, A. C.; Höök, F.; Brown, T.; Kim, B. H.; Dahlén, A.; Wilhelmsson, L. M.; Grøtli, M. Pentacyclic adenine: a versatile and exceptionally bright fluorescent DNA base analogue. *Chem. Sci.* **2018**, *9*, 1043–10. <http://doi.org/10.1039/C7SC05448C>
43. Del Nogal, A. W.; Fuchtbauer, A. F.; Bood, M.; Nilsson, J. R.; Wranne, M. S.; Sarangamath, S.; Pfeiffer, P.; Rajan, V. S.; El-Sagheer, A. H.; Dahlén, A.; Brown, T.; Grøtli, M.; Marcus Wilhelmsson, L. Getting DNA and RNA out of the dark with 2CNqA: A bright adenine analogue and interbase FRET donor. *Nucleic Acids Res.* **2020**, *48*, 7640–7652. <http://doi.org/10.1093/nar/gkaa525>
44. Niko, Y.; Didier, P.; Mély, Y.; Konishi, G.-I.; Klymchenko, A.S. Bright and photostable push-pull pyrene dye visualizes lipid order variation between plasma and intracellular membranes. *Sci. Rep.* **2016**, *6*, 18870. <http://doi.org/10.1038/srep18870>
45. Preus, S.; Kilsa, K.; Miannay, F.A.; Albinsson, B.; Wilhelmsson, L.M. FRETmatrix: a general methodology for the simulation and analysis of FRET in nucleic acids. *Nucleic Acids Res.* **2012**, *41*, e18–e18. <http://doi.org/10.1093/nar/gks856>
46. Preus, S.; Wilhelmsson, L.M. Advances in Quantitative FRET-Based Methods for Studying Nucleic Acids. *ChemBioChem* **2012**, *13*, 1990–2001. <http://doi.org/10.1002/cbic.201200400>
47. Börjesson, K.; Preus, S.; El-Sagheer, A.H.; Brown, T.; Albinsson, B.; Wilhelmsson, L.M. Nucleic Acid Base Analog FRET-Pair Facilitating Detailed Structural Measurements in Nucleic Acid Containing Systems. *J. Am. Chem. Soc.* **2009**, *131*, 4288–4293. <http://doi.org/10.1021/ja806944w>
48. Iqbal, A.; Arslan, S.; Okumus, B.; Wilson, T.J.; Giraud, G.; Norman, D.G.; Ha, T.; Lilley, D.M.J. Orientation dependence in fluorescent energy transfer between Cy3 and Cy5 terminally attached to double-stranded nucleic acids. *Proc. Natl. Acad. Sci. U. S. A.* **2008**, *105*, 11176–11181. <http://doi.org/10.1073/pnas.0801707105>
49. Cardullo, R.A.; Agrawal, S.; Flores, C.; Zamecnik, P.C.; Wolf, D.E. Detection of nucleic acid hybridization by nonradiative fluorescence resonance energy transfer. *Proc. Natl. Acad. Sci. U. S. A.* **1988**, *85*, 8790–8794. <http://doi.org/10.1073/pnas.85.23.8790>

-
50. Dziuba, D.; Didier, P.; Ciaco, S.; Barth, A.; Seidel, C. A. M.; Mély, Y. Fundamental photophysics of isomorphous and expanded fluorescent nucleoside analogues. *Chem. Soc. Rev.* **2021**, *50*, 7062–7107. <http://doi.org/10.1039/d1cs00194a> 505
506

II. Stratégie directe : Méthoxychromones

Publication 2

Les travaux précédemment décrits ont mis en évidence que **dEAF**, une fois incorporé dans l'ADN, produisait une seule bande d'émission très fortement décalée vers le rouge et qu'il était moins sensible à la photodégradation. Le potentiel du **dEAF** a été mis en évidence comme donneur pour du FRET. Cependant le type de marquage utilisé, liant cette chromone au plus proche du squelette phosphodésoxyribose, n'a pas permis d'exploiter le potentiel fluorogénique (off/on) du **dEAF** dû à la faible différence d'intensité du signal de la sonde avant et après hybridation avec l'ADN cible. Pour pallier ce problème, notre intérêt s'est porté alors sur une approche de marquage différente basée sur de la chimie click post-synthétique qui nous a permis d'explorer plus aisément différentes positions et liens de marquage. Par ailleurs pour renforcer la photostabilité du **dEAF** aux dégradations radicalaires, le groupement hydroxyle libre de la chromone a été remplacé par un groupement méthoxy (**Figure 59, 3-MC**). Cette substitution engendre potentiellement deux modifications physicochimiques de la sonde : la première est la disparition du mécanisme d'ESIPT, du fait de la disparition du proton labile, et la seconde est une différence de la solubilité de la sonde et donc, des propriétés solvatochromiques.

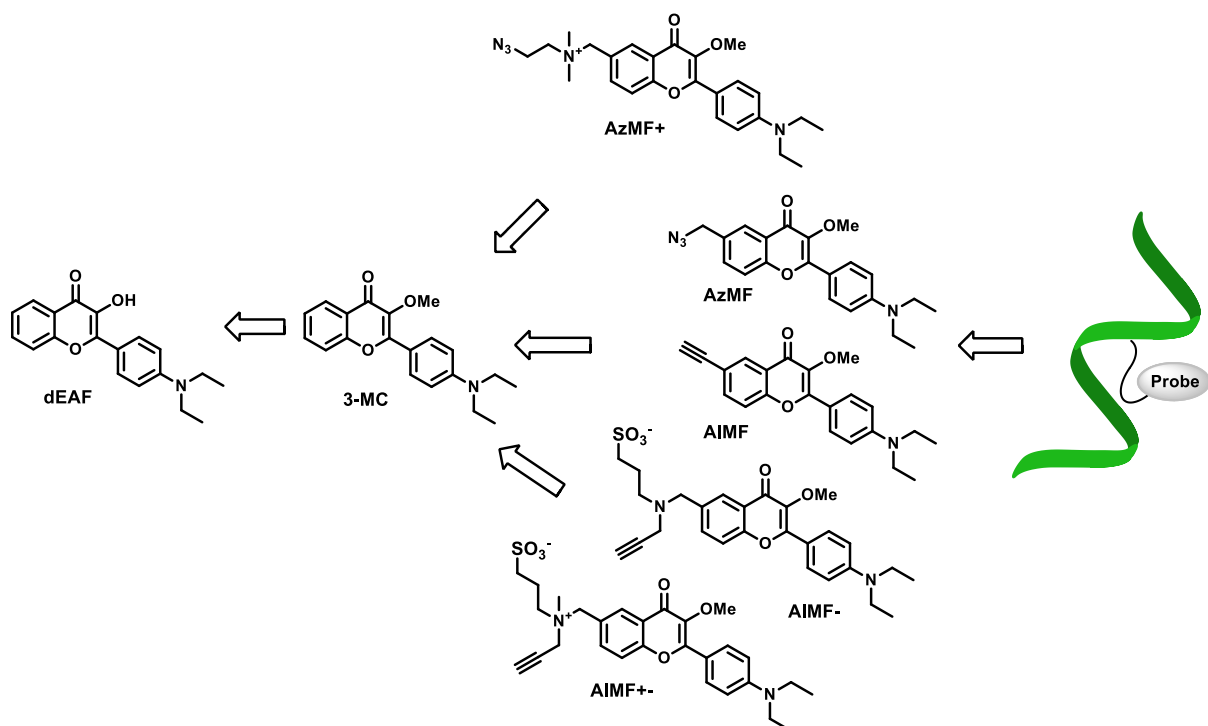


Figure 59. Développement des ODN marqué par des dérivés de méthoxychromone **3-MC** à partir de la référence **dEAF**.

Nous avons synthétisé plusieurs dérivés de **3-MC**, fonctionnalisés par un groupement azoture ou alcyne, en vue de préparer les ODN marqués *via* la stratégie de modification post-synthétique (CuAAC). Deux d'entre eux sont neutres (**AIMF**, **AzMF**) et les trois autres sont chargés (**AzMF+**, **AIMF-**, **AIMF+-**), en vue d'augmenter la solubilité dans des milieux aqueux et, éventuellement, d'accroître l'affinité du brin marqué pour sa cible AN complémentaire, par le biais d'interactions ioniques.

Dans un premier temps, nous avons « cliqué » le composé modèle (**AIMF**) avec un nucléoside « nu », fonctionnalisé par un groupement azoture en position 1', pour obtenir **AIMF-Nu** (**Figure 60**).

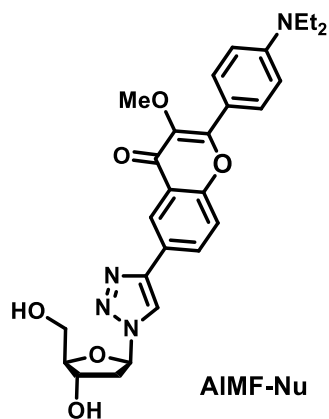


Figure 60. Structure du nucléoside marqué AIMF-Nu.

Les études photophysiques comparatives concernant AIMF-Nu, AIMF et AzMF n'ont pas révélé de différences notoires avec la sonde 3-MC de référence. Dans tous les cas on observe, suite à l'augmentation de la polarité du solvant, un très fort effet bathochrome au niveau des longueurs d'onde d'absorption et émission, ainsi qu'une baisse du rendement quantique, confirmant que les sondes dérivant de 3-MC sont de type *Push-Pull*. De plus, ces dernières montrent une très grande sensibilité à l'hydratation, permettant d'envisager leur utilisation dans le cadre d'expériences d'hybridation des AN. Enfin, elles sont plus photostables que la chromone de référence avec l'hydroxyle en position 2 libre et stables à des pH supérieurs à 5, ce qui est compatible à leur utilisation dans un environnement physiologique.

Les 5 dérivés de la sonde 3-MC (AIMF, AzMF, AzMF+, AIMF-, AIMF+-, Figure 59) ont ensuite été intégrés dans des séquences d'ADN simple-brins, fonctionnalisées par un groupement alcyne ou azoture, *via* des réactions de « click » CuAAC. Les sondes ont été introduites soit à l'extrémité 5' de l'ODN, soit au milieu de la séquence, et sont reliés à l'ODN par des liens de nature et de longueur différentes (Figure 61).

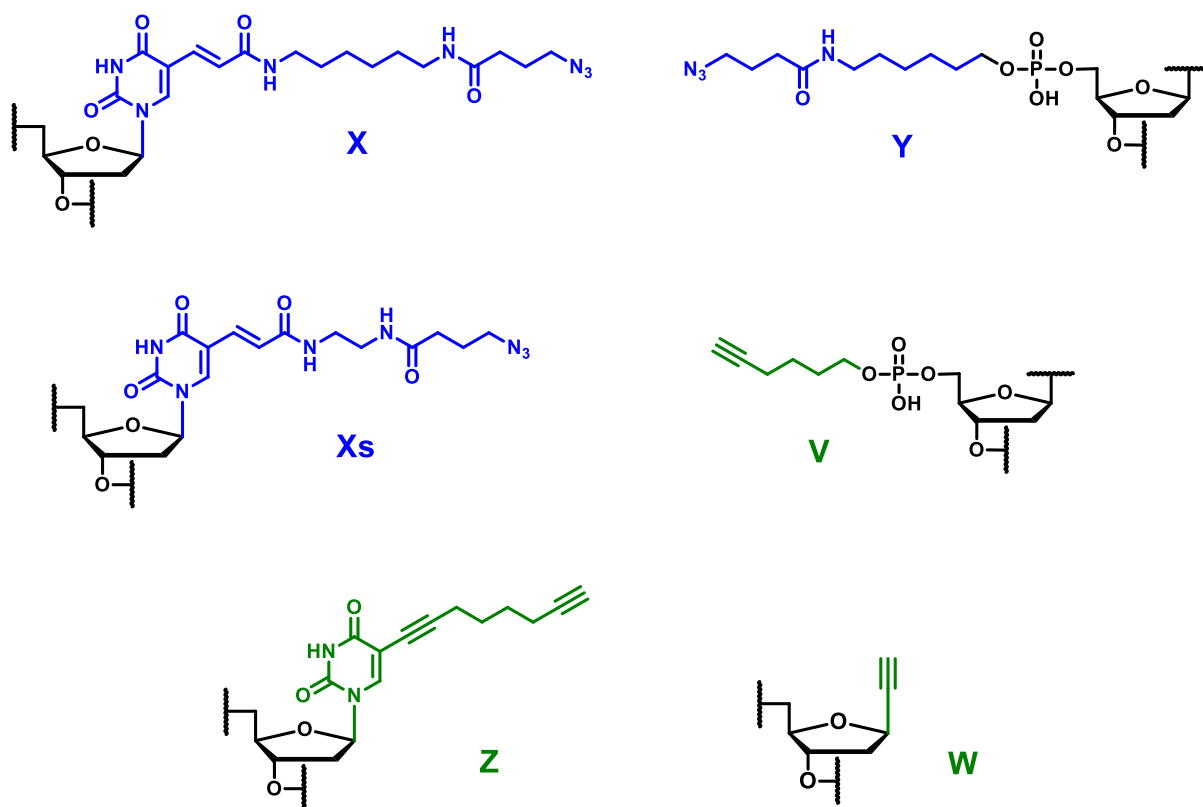


Figure 61. Structure des liens clicks sur l'ODN.

Les ODN fonctionnalisés devant être clickés, conceptualisés par nos soins, ont été synthétisés par l'entreprise Microsynth®.

En ce qui concerne la réaction « click », il faut noter que le protocole CuAAC est le fruit d'une optimisation précise des conditions expérimentales. En effet, la réaction de CuAAC entre les ODN et une molécule organique est très contraignante. Dans la majorité des cas, la solubilité des ODNs et celle des sondes sont opposées. L'ODN est soluble et stable dans l'eau ainsi que dans certains solvants polaires/protiques (MeOH), alors que la plupart des sondes organiques, apolaires, s'agrègent dans ces milieux. Il est donc nécessaire de trouver un mélange de solvants adéquat pour que la CuAAC fonctionne avec un ODN et une sonde soluble. Par ailleurs, comme décrit dans le chapitre 1 (p.59), la réaction de CuAAC dépend du nombre d'équivalents utilisé pour chaque réactif. Afin d'optimiser les rendements réactionnels des CuAAC, il a donc été nécessaire de :

1. Trouver un mélange de solvants adéquat pour que la CuAAC fonctionne avec un ODN et une sonde soluble. (Exemples de solvants utilisés : H₂O/MeOH, H₂O/DMSO, H₂O/DMF).
2. Trouver le ligand de CuAAC le mieux adapté à ce mélange de solvants, afin d'obtenir de meilleurs rendements. (Exemples de ligands utilisés : TBTA, THPTA, BTTEs).
3. Optimiser le nombre d'équivalents du mélange ligand/cuivre, de la sonde ainsi que du réducteur (ascorbate de sodium), pour que la réaction fonctionne avec de bon rendement.

L'optimisation de ces paramètres nous a permis d'obtenir dix séquences d'ODNss marquées, avec des taux de conversion compris entre 60 et 95%, suivant la sonde utilisée. Ces ODN ont ensuite été purifiés par HPLC semi-préparative (gradient de tampon TEAB (triéthylammonium bicarbonate)/acétonitrile ; (Méthode en SI).

Les analyses des propriétés photophysiques des 10 séquences d'ODNss marquées ont ensuite été effectuées et leur hybridation avec le brin ODN complémentaire a été étudiée.





Les résultats ont révélé que lorsque la sonde était en position 5' de l'ODN (**Y**, **V**), aucune augmentation de fluorescence lors de l'hybridation n'était observée. Au contraire, une diminution de la fluorescence avait lieu. Celle-ci pourrait s'expliquer par un éloignement de la sonde par rapport à l'ODN, suite à l'hybridation. Lorsque la sonde se situe au milieu de la séquence ODN, la longueur du lien semble jouer un rôle essentiel pour obtenir une amplification significative de fluorescence lors de l'hybridation, ainsi qu'un déplacement vers le rouge du maximum d'absorption à l'hybridation. Ainsi, les sondes de type **Z** et **Xs** ne sont que peu fluorogéniques lors de l'hybridation à l'ODN, alors que celle de type **X** conduit aux meilleurs résultats. Il se pourrait donc que seul dans ce dernier cas, le lien soit suffisamment long et flexible pour permettre un repliement de la sonde, propice à son intercalation ou à sa liaison au sillon de l'ADN. Dans le cas où la sonde est directement reliée en position 1' d'un sucre (**W**), les résultats semblent démontrer une intercalation dans le duplexe. Enfin, seules les sondes positionnées entre deux résidus Thymine ou Adénine dans les simple-brins conduisent à de bons résultats (amplification du signal de fluorescence d'un

facteur 13), celles situées entre deux résidus Cytosine ne conduisant qu'à de faibles variations de fluorescence lors de l'hybridation. Ceci pourrait s'expliquer par la capacité des bases Guanine, complémentaires des bases Cytosine dans le duplexe, d'éteindre les sondes fluorescentes voisines, par le biais du mécanisme PET (p.37).

Les études concernant ce travail et les résultats obtenus ont été publiés dans l'article suivant du journal *Molecules* (*cf vide infra*) dans la section *Medicinal chemistry* pour l'édition spéciale *Fluorescent Probes in Pharmaceutical and Drug Design Applications: Quantum Chemistry-Based Design, Synthesis, Photophysical and Chemical Properties, Biological Applications*.

Article

An Expeditious Approach towards the Synthesis and Application of Water-Soluble and Photostable Fluorogenic Chromones for DNA Detection

Steve Vincent , Suman Mallick, Guillaume Barnoin , Hoang-Ngoan Le, Benoît Y. Michel * 
and Alain Burger * 

Institut de Chimie de Nice, CNRS UMR 7272, Université Côte d'Azur, Parc Valrose, CEDEX 2, 06108 Nice, France; steve.vincent@univ-cotedazur.fr (S.V.); suman22msc@gmail.com (S.M.);

guillaume.barnoin@univ-cotedazur.fr (G.B.); lhngoan2109@gmail.com (H.-N.L.)

* Correspondence: benoit.michel@univ-cotedazur.fr (B.Y.M.); alain.burger@univ-cotedazur.fr (A.B.)

Abstract: The intensive research for hybridization probes based on organic molecules with fluorogenic properties is currently attracting particular attention due to their potential to efficiently recognize different DNA conformations and the local environment. However, most established organic chromophores do not meet the requirements of this task, as they do not exhibit good brightness in aqueous buffer media, develop aggregation and/or are not easily conjugated to oligodeoxynucleotides (ODNs) while keeping their photophysics intact. Herein, an important modification strategy was employed for a well-known fluorophore, 2-(4-(diethylamino)phenyl)-3-hydroxychromone (dEAF). Although this push-pull dye absorbs intensively in the visible range and shows emission with large Stokes shifts in all organic solvents, it is strongly quenched in water. This Achilles' heel prompted us to implement a new strategy to obtain a series of dyes that retain all the photophysical features of dEAF in water, conjugate readily with oligonucleotides, and furthermore demonstrate sensitivity to hydration, thus paving the way for a high-performance fluorogenic DNA hybridization probe.

Keywords: fluorescent dyes; chromones; post-synthetic ODN labeling; hybridization; fluorogenic sensing; multistep synthesis



Citation: Vincent, S.; Mallick, S.; Barnoin, G.; Le, H.-N.; Michel, B.Y.; Burger, A. An Expeditious Approach towards the Synthesis and Application of Water-Soluble and Photostable Fluorogenic Chromones for DNA Detection. *Molecules* **2022**, *27*, 2267. <https://doi.org/10.3390/molecules27072267>

Academic Editors: Ioannis Kostakis and Evagelos Gikas

Received: 2 March 2022

Accepted: 27 March 2022

Published: 31 March 2022

Publisher's Note: MDPI stays neutral with regard to jurisdictional claims in published maps and institutional affiliations.



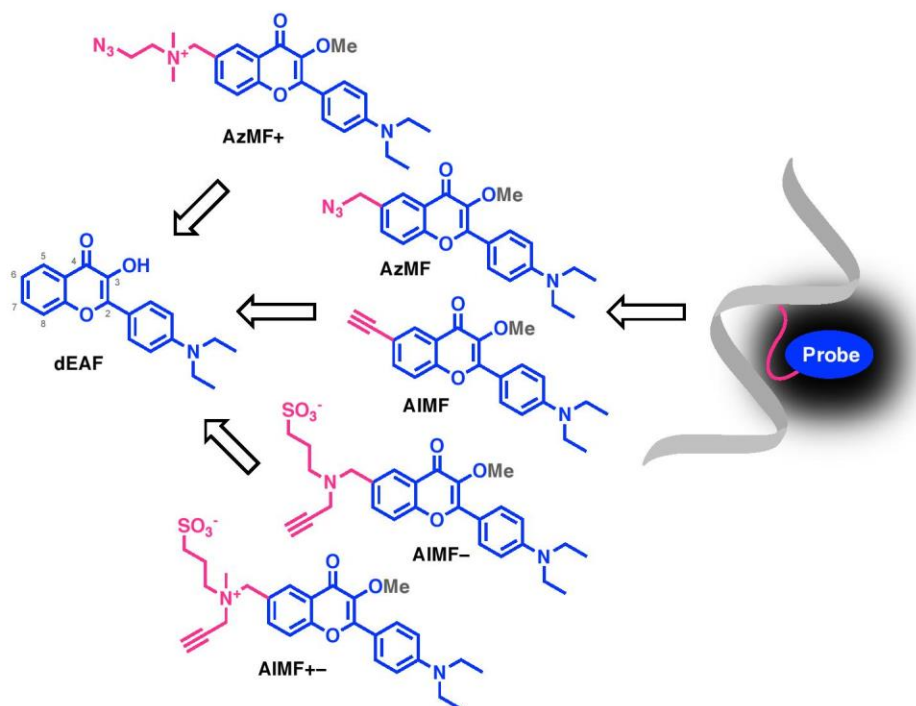
Copyright: © 2022 by the authors. Licensee MDPI, Basel, Switzerland. This article is an open access article distributed under the terms and conditions of the Creative Commons Attribution (CC BY) license (<https://creativecommons.org/licenses/by/4.0/>).

1. Introduction

The use of hybridization probes composed of organic fluorophores attached to single strands (ss) of nucleic acids has found broad applications in nanotechnology, diagnostics, biology, and medicinal chemistry [1–3]. Among organic labels, fluorescence reporters that “turn on” their emission (fluorogenic dyes) in response to interactions with their target are very attractive [4–6]. Ideally, this technique should exclude the double labeling required for quenching, energy transfer or excimer formation. This preference can be justified by the fact that the production of doubly labeled nucleic acid probes is associated with synthesis and purification issues, which also results in a higher production cost. For instance, the main source of error in detection methods based on Förster resonance energy transfer (FRET) is due to the absence of one of the partners of the FRET pair, which leads to false results [7]. The use of a unique marker should limit these complications and simplify the implementation of the technology. To this end, upon interactions with the target, the single fluorescent reporter should generate a novel fluorescence signal that can be recorded and interpreted (e.g., through a change in intensity, anisotropy, lifetime, or color). In addition, these tools should provide more convenient staining protocols as they should not require additional washing of excess reagents. This feature is particularly attractive for diagnostic and imaging applications. Although amplification of signal change is an important criterion for biological applications, other desired properties include absorption in the visible range, high brightness, large Stokes shifts, and significant photostability to limit photobleaching.

However, fulfilling all these requirements presents a challenge. Several groups have taken advantage of cyanine-derived dyes whose fluorescence emission is sensitive to viscosity [8,9]. The ability of these fluorophores to increase their signal intensity in rigid media has been used in the construction of forced-intercalation (FIT) probes [10]. FIT probes were first designed as PNA (peptide nucleic acid) or DNA containing a single cyanine (e.g., thiazole orange, TO). TO was covalently introduced as a nucleobase substitute. In their single-stranded form, probes incorporating TO exhibit low fluorescence. The formation of the probe–target duplex forces the intercalation of TO between the vicinal flat aromatic nucleobases and lights up its emission (10-fold increase in fluorescence). The performance of the probe can be further improved either by introducing modified nucleotides around it (gapmer) [11], by coupling a second partner for FRET or contact quenching [12,13].

In our project, we sought to exploit another option to turn on the fluorescence signal and for this, we propose to harness the peculiar properties of the known 2-(4-(diethylamino) phenyl)-3-hydroxychromone (**dEAF**, Scheme 1) [14,15]. This fluorophore belongs to the family of push–pull dyes demonstrating a Donor- π -Acceptor (D- π -A) relationship. The fluorophore **dEAF** incorporates in its structure a strong donor substituent—the diethylamino group—electronically coupled to the carbonyl acceptor group. It absorbs intensively in the visible range, exhibits large Stokes shifts in polar solvents, and is emissive in all screened solvents except water where it is strongly quenched. Consequently, shielding the dye from bulk water results in a turn-on of its emission (fluorogenicity), and thus a substantial increase of the signal-to-noise ratio (SNR). This fluorogenic behavior is expected when the labeled DNA single strand anneals to its target, as the environment of the formed duplex is hydrophobic on the inside and its grooves are less hydrated than the bulk water [16,17].



Scheme 1. Chemical structures of the parent chromone (**dEAF**) as well as the azido (**AzMF**) and alkynyl (**AIMF**) derivatives developed for click-type post-synthetic DNA labeling. Systematic flavonoid numbering was displayed on the original core.

Our objective was to synthesize labeled oligodeoxynucleotides (ODNs) with turn-on emission after annealing with their complementary strand. As a convenient and straightforward access, we selected an ODN labeling through a post-synthetic CuAAC coupling. For this purpose, we had to synthesize the corresponding azido and ethynyl derivatives of the reference 3-hydroxychromone **dEAF** (Scheme 1). Position 6 of the chromone scaffold

was preferred because chemical modification at this location should have minimal impact on the photophysics of the dye since it is not conjugated with the 4-ketone. The methoxy group was preferred over the hydroxyl group to radically improve the photostability of the chromone [18]. Three labeling methods were considered to allow for various modes of interaction of the dye with the double-stranded (ds) DNA (Figure 1). In **ss-DNA 1**, the fluorophore will substitute for a natural base and be positioned at the central position of the strand. After hybridization, it will be forced to intercalate (**ds-DNA 1**). For **ss-DNA 2–3**, the dye will be connected to a central or terminal position via a flexible tether. In the case of **ds-DNA 2–3**, the fluorescent reporter will be free to interact with the duplex either by intercalation/ π -stacking or by groove binding. For our research program, we considered all options (1,2 and 3).

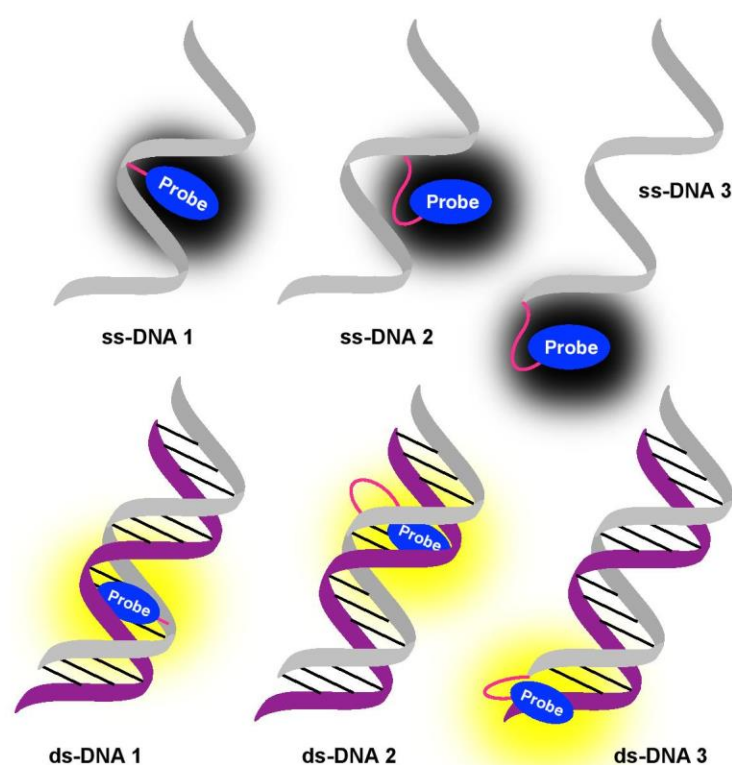


Figure 1. Schematic representation of the three ways to fluorescently label ODNs (**ss-DNA 1–3**) and turn on their emission upon hybridization (**ds-DNA 1–3**).

Herein, we report the synthesis and application of the critically modified **dEAF** derivatives with a significant increase in the water solubility and photostability while keeping intact, the rest of the photophysics. These modified dyes were also designed to be rapidly conjugated to ODNs using standard CuAAC click-chemistry protocol [19,20]. All synthesized probes are environment-sensitive and exhibit typical fluorogenic features upon hybridization. We investigated the solvent-dependent photophysical properties of the fluorophores using steady-state spectroscopic techniques before moving on to applications. Next, we adopted a post-synthetic approach to tag with them, a variety of ss-ODNs and explored their potential to sense the hybridization process upon interaction with the complementary sequence using UV-Vis and fluorescence spectroscopies.

2. Results and Discussion

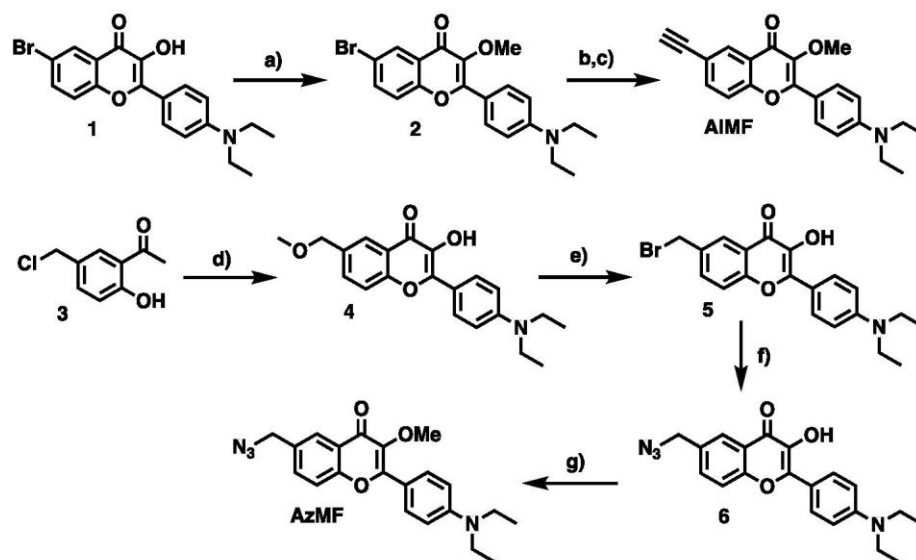
2.1. Synthesis

The 3-Hydroxychromones (3HCs) are very popular in the photophysics community for their unique ability to display environmentally sensitive excited-state intramolecular

proton transfer (ESIPT), their ease of preparation, and their relatively high brightness considering their modest size. This atypical photophysical signature arises from the presence of a hydroxyl group vicinal to the ketone. However, this OH group reacts rapidly by photochemistry when irradiated by a high intensity light source (usually the laser required for bioimaging related studies), which induces a low photostability. To counteract this problem, we decided to replace the hydroxyl with a methoxy group [16]. This simple modification significantly increases the photostability of the probe and, at the same time, simplifies the photophysics by preventing the ESIPT reaction from occurring.

We also introduced the diethylamino group into the conjugation, strategically positioned to act as a donor for these push–pull probes. This incorporation is known to shift the absorption and emission to longer wavelengths compared to the parent chromophore, making it more attractive for bioimaging applications. In our group, diethylaminohydroxyflavone has already been studied; it offers attractive photophysical properties such as large Stokes shifts, red-shifted emission wavelengths, and high quantum yields in non-aqueous media. On this basis, the methoxy version was therefore a logical next step in our research project on probe engineering for application in DNA sensing. Two molecules were developed with an alkyne (AIMF) and azide (AzMF) functional group, making them easy to conjugate with the target of interest through a Cu(I)-mediated click chemistry approach. It is noteworthy that these anchor points were located at position 6 (Scheme 1), as modifying this position of the benzo ring should not generate changes in photophysics. Indeed, this position is not mesomerically coupled to the acceptor carbonyl group and the inductive effects are negligible at four bonds away. Thus, this is an appropriate location to bind fluorescence reporters to DNA.

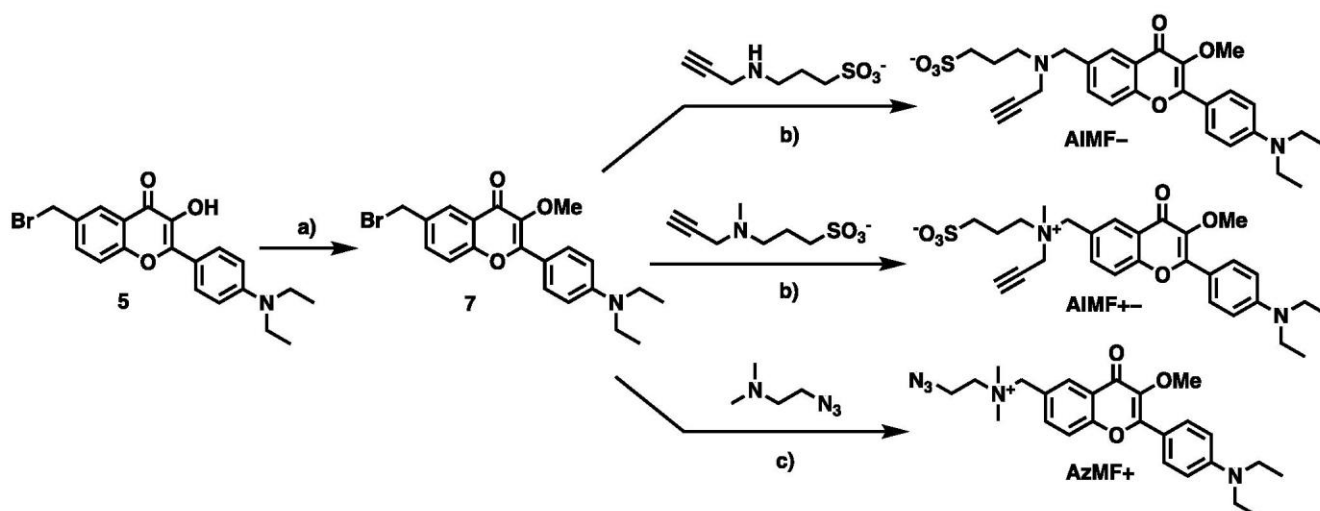
The chromone core for AIMF was synthesized according to our previously reported strategy [21]. As for the methylation of the 3-OH group, it was performed following an in-house protocol based on phase-transfer conditions (PTC) to afford the corresponding methyl ether 2 (Scheme 2) [22]. The ethynyl moiety was finally introduced using a standard Sonogashira coupling with TMS-acetylene. Subsequent cleavage of the silyl group provided AIMF, the first targeted fluorescent label.



Scheme 2. Synthetic routes to AIMF and AzMF: (a) Me₂SO₄ (4 eq.), 18-crown-6 (7 mol%), KOH, H₂O/DCM, rt, 88%. (b) TMS-acetylene (3 eq.), TEA (10 eq.), CuI (20 mol%), PdCl₂(PPh₃)₃ (20 mol%), DMF, 70 °C. (c) K₂CO₃, MeOH, rt, 64% over 2 steps. (d) *p*-Diethylaminobenzaldehyde (1.05 eq.), NaOH (1.05 eq.), H₂O₂, MeOH, rt, 97%. (e) HBr (47% in H₂O), reflux, quant. (f) NaN₃ (1.5 eq.), Acetone/DMF. (g) Me₂SO₄ (4 eq.), 18-crown-6 (7 mol%), KOH, H₂O/DCM, rt, 70% over 2 steps.

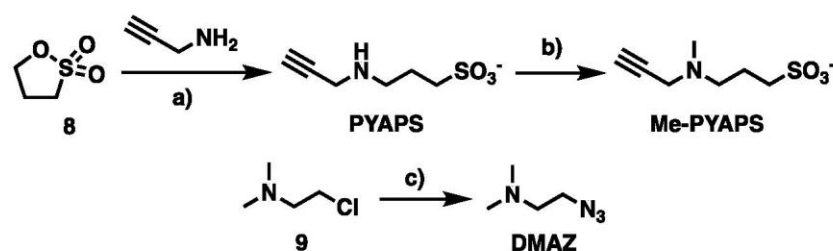
To avoid coupling the azide directly to the aromatic ring [23], an alternative synthetic route was considered for **AzMF**. The first step consists in the construction of the 3HC scaffold via an Algar-Flynn-Oyamada reaction [24] between *p*-diethylaminobenzaldehyde and **3** bearing a benzylic chloride, which was concomitantly displaced by a methoxide anion to yield **4**. Then, using harsh acidic conditions with conc. aqueous HBr solution, a bromide was incorporated in place of the methoxy group. A nucleophilic substitution on this benzyl position introduced the azide functionality required for post-synthetic labeling. Finally, to obtain **AzMF**, the 3-hydroxyl group was methylated using the same PTC procedure as **AIMF** (*vide supra*).

It is worth mentioning that the conversion of the 3-OH into the 3-OMe group induces a drop in the hydrophilicity of the chromophore. To counterbalance this effect, three linkers were designed to significantly improve the hydrophilic character of **AIMF** and **AzMF**. By introducing this type of tethers, we also wanted to study the influence of the charge on the photophysical and DNA interaction properties of the dye. The first one carries a negative charge (**AIMF**[−]), while the second a positive one (**AzMF**⁺) and the last is a zwitterionic label (**AIMF**^{+−}) (Scheme 3). The synthetic procedure of these three charged fluorophores is very similar to the **AIMF** and **AzMF** models.



Scheme 3. Synthetic routes to **AIMF**[−], **AIMF**^{+−}, and **AzMF**⁺: (a) Me₂SO₄ (4 eq.), 18-crown-6 (7 mol%), KOH, H₂O/DCM, 80%. (b) K₂CO₃ (2.5 eq.), H₂O/DMF, [**AIMF**[−], 95%], [**AIMF**^{+−}, 36%]. (c) THF, 63%.

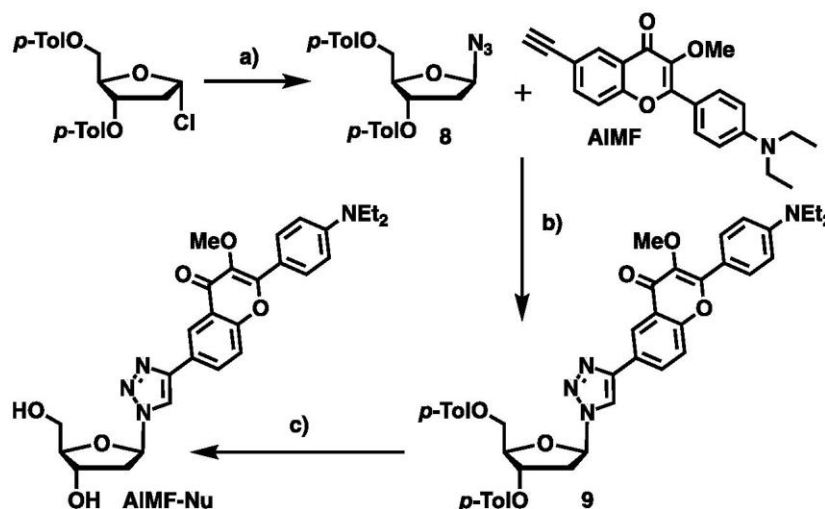
The first step, conversely to **AzMF**, is the establishment of the methoxy group leading to **7**. Since the introduction of a charge will complicate the purification process, it is wise to perform it in the last stage. The final step is the substitution of the benzyl bromide of **7** by three small amino molecules, two of them are described here for the first time (**PYAPS**, **Me-PYAPS**, Scheme 4). Note that owing to these clickable connectors, it is now possible to convert any fluorophore bearing a functional group which is prone to substitution on its main architecture, into its ionic conjugate with significantly increases water solubility. In this way, the possibility of modifying lipophilic probes for use in a polar solvent is opened.



Scheme 4. Synthetic pathways for the linkers **PYAPS**, **Me-PYAPS**, and **DMAZ**: (a) CH_3CN , 72%. (b) Formol, formic acid, quant. (c) NaN_3 (3 eq.), H_2O , quant.

2.2. Photophysics

To obtain an idea about the photophysical behavior of these fluorescent dyes in a DNA environment, a simple clicked model compound was designed, with the hope that this modified nucleoside could simulate the same photophysics. Thus, **AIMF-Nu** was synthesized using a standard CuAAC approach where **AIMF** was efficiently clicked with the 3',5'-bis-toluoyl azido sugar **8**, followed by cleavage of the esters of **9** by methanolysis (Scheme 5).



Scheme 5. Synthetic access to the **AIMF**-derived model nucleoside **AIMF-Nu**: (a) NaN_3 (5 eq.), Acetone, 0°C , 80%. (b) DIPEA (12 eq.), AcOH (6 eq.), CuI (2.8 eq.), DCE, 40°C , 98%. (c) K_2CO_3 , MeOH/DCM, 35°C , 56%.

Our photophysical characterization began by investigating the spectroscopic features of these three **dEAF**-based fluorophores in methoxy series (**AIMF**, **AzMF**, and **AIMF-Nu**) in several solvent environments with varying polarity and H-bonding ability. All of these three dyes follow the same trend in their absorption and emission properties, including quantum yields, in accordance with our expectations (Table S1, Supplementary Materials). Those values are comparable to those of the reference methoxychromone (**dEAMF**) [18], without significant differences. For example, in MeOH, the maxima of the absorption and emission spectra oscillate between 405–410 nm and 529–533 nm ($\Phi = 4.1$ –5%), respectively for **AIMF**, **AzMF**, and **AIMF-Nu**, significantly close to the **dEAMF** photophysical features ($\lambda_{\text{Abs}} = 405$ nm, $\lambda_{\text{Em}} = 501$ nm, $\Phi = 4.7\%$). These results confirmed that modifications introduced at position 6 have little influence on the photophysics compared to the parent chromone. Since **AIMF**, **AzMF**, and **AIMF-Nu** belong to a class of push-pull dyes, they show a progressive redshift in absorption and emission maxima when moving from a lower to a higher polarity solvent, as expected (positive solvatochromism, Figure 2 and Table S1, Supplementary Materials).

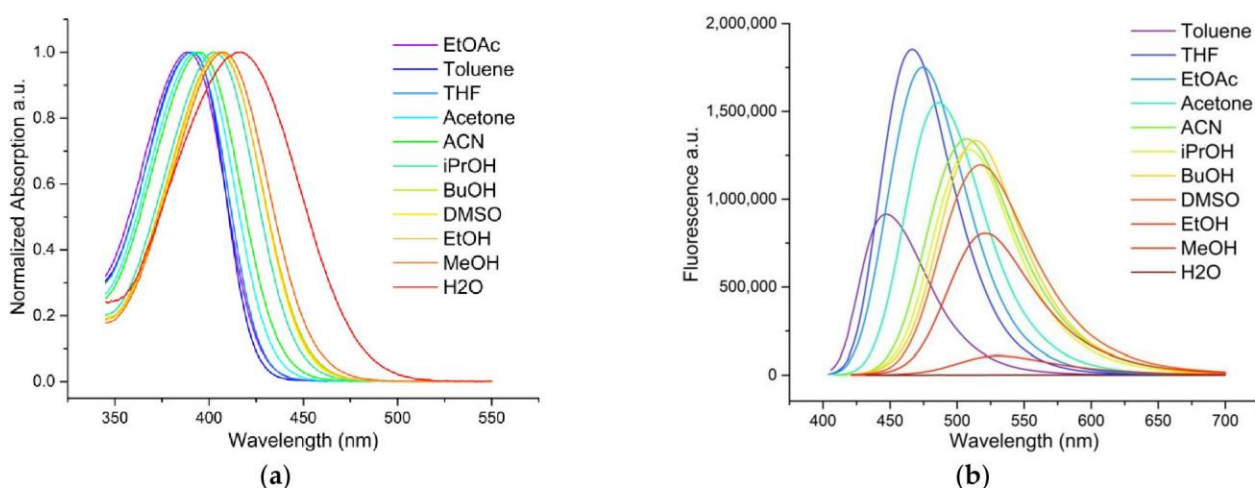


Figure 2. Absorption (a) and fluorescence (b) spectra of AIMF-Nu.

However, these bathochromic shifts are more pronounced in emission than in absorption (e.g., for AIMF-Nu, compare the wavelength range between toluene and MeOH in absorption 391–407 nm and emission 448–529 nm, $\Delta\lambda = 16$ vs. 81 nm). In line with dEAMF and other similar chromones conjugating strong electron-donating groups, this observation indicates that even though the dipole moments have parallel directions, the one in the excited state is larger than that in the ground state [25]. This means that the stabilization of the excited state by the solvent is therefore more important, and consequently the excited state has a greater sensitivity to polarity. As for the reference 3-methoxychromone dEAMF, low quantum yields were noticed in polar protic solvents, while high efficiencies were observed in apolar media. Such behavior is typical of push–pull dyes.

Interestingly, AIMF exhibits an exquisite sensitivity to the local hydration rate via three channels of information: a bathochromic λ -shift in absorption and emission as well as fluorescence intensity. Indeed, hydration studies revealed that increasing the water content to 10% results in a radical drop in quantum yield of ca. 50% (Figure 3 and Table S2, Supplementary Materials). This represents the most desirable feature for our developed dyes, as it opens the door to turn-on hybridization applications. Indeed, accommodation or base stacking of the reporter upon annealing should shield it from a water exposure and lead to a fluorescence signal enhancement.

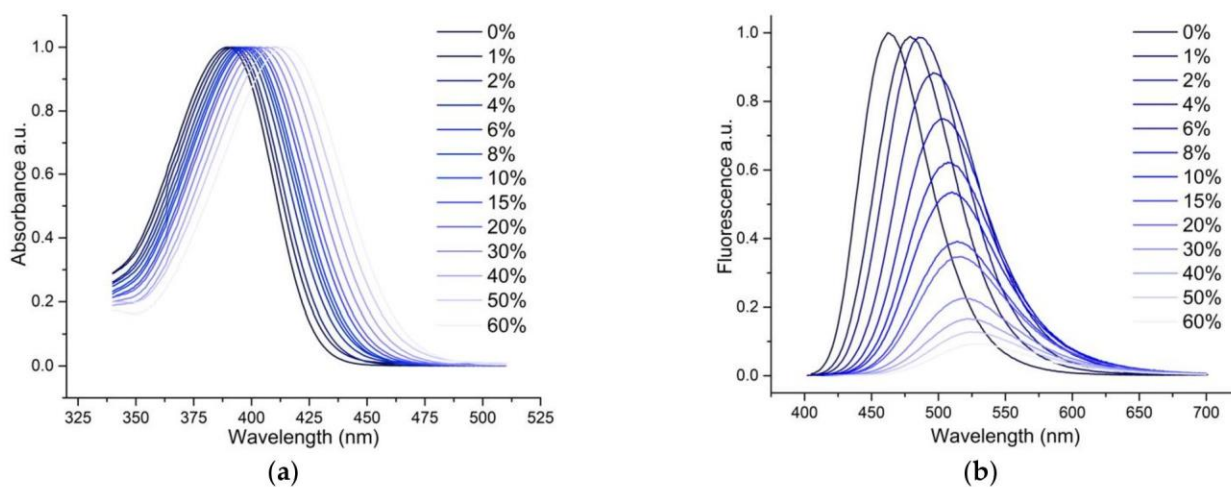


Figure 3. Absorption (a) and fluorescence (b) responses of AIMF to hydration. Data were recorded in gradual mixtures of water in THF.

To discover whether the advanced photophysics of the labels are compatible with a physiological environment, a pH titration was performed and provided a pK_A value of approx. 3.7 (Figures S1 and S2, Supplementary Materials). This result guarantees a stable fluorescence intensity over a comfortable working pH range of 5 to strongly basic media without risking a possible protonation of the tertiary aniline, the concomitant loss of the push–pull relationship and its associated photophysical properties. The photostability of the fluorescent markers was also checked to ensure that they are suitable for laser excitations, typical of bioimaging detection. To do so, the considered fluorophores were irradiated for 1 h with high-intensity xenon light at their absorption maximum, while monitoring their fluorescence intensity in protic and non-protic media. The decay in the number of photons collected by the detector means that a part of the dye population is photobleached. As a result, it is clear that methoxy derivatives (**AzMF** and **AIMF**) are considerably more photostable than their hydroxy counterparts (**AIHF** and the standard D- π -A 3HC **dEAF**), even more than the reference push–pull fluorophore, Prodan, which is an asset to be emphasized (Figure 4 and Figure S3, Supplementary Materials).

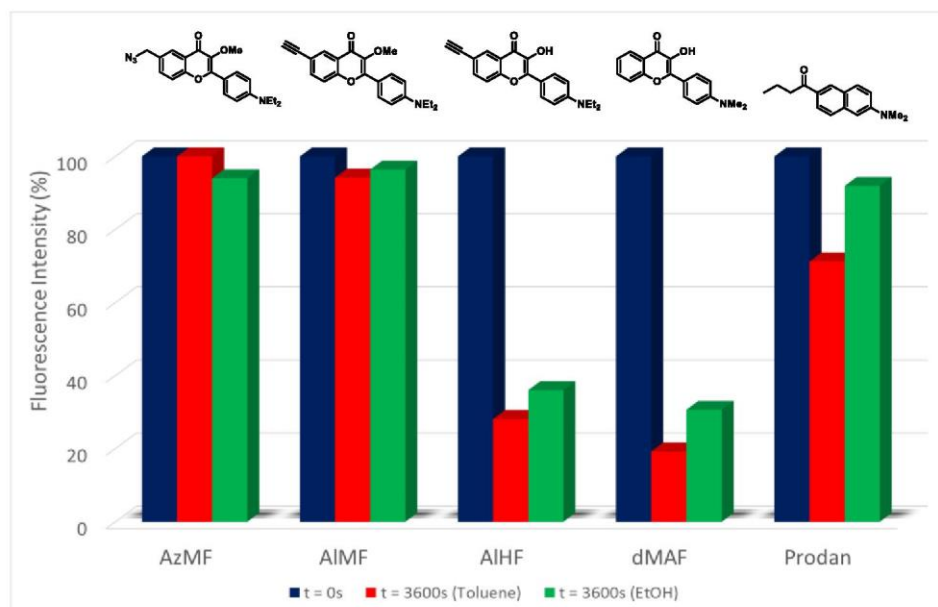


Figure 4. Photobleaching evolution of **AzMF**, **AIMF**, **AIHF**, and push–pull references **dMAF** and **Prodan** over the course of a one-hour experiment in toluene and EtOH.

As for the charged conjugates, the pK_A value and photostability were preserved since no modifications of the aniline moiety and the conjugation were made. In comparison with the reference compound **AIMF**, the main difference lies in the solvatochromic character. The positively charged and zwitterionic derivatives, respectively **AIMF+** and **AIMF+−**, displayed many differences from the neutral form (Table S3 and Figures S4–S9, Supplementary Materials), such as solvatochromism in absorption and emission; the solvatochromism being more exacerbated. These effects are less pronounced for the negatively charged **AIMF−**. One of the possible explanations is based on the distance and position of the charge with respect to the push–pull core (Scheme 3). The electric field produced by the proximal positive charge and the electron-rich carbonyl oxygen leads to an increase in the push–pull relationship between the donor and the acceptor. This results in a red-shifted absorption and emission of fluorophores [26], which is the consequence of what is known as the Stark effect, already reported for **dEAMF** (Figure 5 and Table S3, Supplementary Materials) [25].

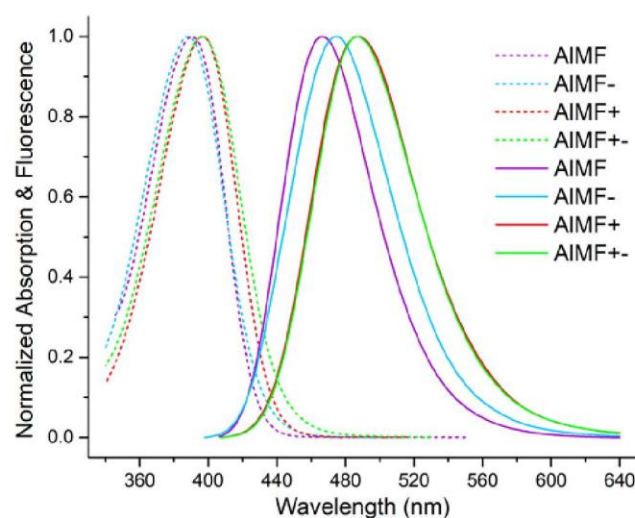


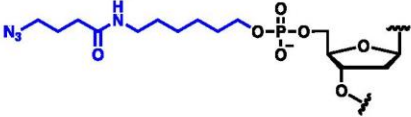
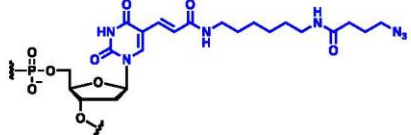
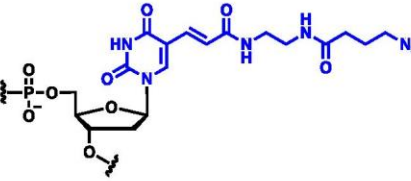
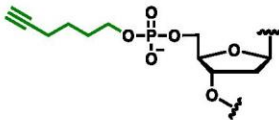
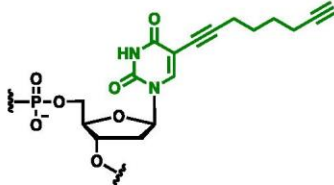
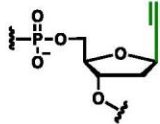
Figure 5. Photophysical comparison of neutral and charged dyes in THF. Dashed and solid lines refer to absorbance and fluorescence observables, respectively.

2.3. Spectroscopic Studies of Labeled ODNs

In this study, a post-synthetic CuAAC strategy was adopted with our synthesized push-pull dyes to tag single-stranded (ss) ODNs bearing varied azide and alkyne modifications. In order to optimize the fluorescence turn-on upon hybridization, sequences of diverse composition (AT- and GC-rich, polyA) with various linkers differing in size, flexibility, position onto the nucleotide, and location on the strand were selected (Table 1). Indeed, with a more or less short tether, three of them consist in a C5-modification of a central T base, and two others are positioned at the 5'-end. Finally, the last connector is ultra-short since it is directly attached to the anomeric position of the ribose unit, and thus allows the substitution of a nucleobase. By combining all these transformations, 10 sequences could be labeled and screened for their fluorogenic behavior upon hybridization (Table 1 and Table S4, Supplementary Materials).

A classical Cu(I)-mediated click protocol was employed to fluorescently label the listed ODNs. Once clicked onto the ODNs, since the charged conjugates demonstrated very similar photophysics to **AIMF** and **AzMF** (Tables S1–S3, Supplementary Materials) as well as to keep the work compact and concise, only **AIMF** and **AzMF** were described in the hybridization studies. As noticed in former works, post-synthetic click reaction is very sensitive to the type of fluorophores used. In fact, the main issue in ODN labeling is related to the solubility of the dye. Another important point is the concentration of each reagent; a slight modification can drastically affect the yields. The ligand employed proves to be the cornerstone for obtaining outstanding yields. Starting the screening with the first-generation copper ligand (**TBTA**), labeling yields limited to 20% were observed; this is probably due to its poor solubility in water. Next, the water-soluble **THPTA** ligand was tested, and a clear improvement in performance was noticed, as the yield was more than doubled (reaching about 50%). Finally, using one of the latest generation ligands, **BTTEs**, excellent yields were achieved (~90%) [27]. All labeled ODNs were analyzed and purified by RP-HPLC (Figures S10 and S11, Supplementary Materials). Their integrity and mass were confirmed by spectrophotometry and HRMS (Tables S5 and S6, Supplementary Materials). Indeed, labeled ODNs bear a typical signature in UV-Vis spectroscopy, corresponding to the absorption ratio between 260 nm (nucleobases) and 420–450 nm (clicked fluorophore), which should match with the ratio of their extinction coefficient (for dyes: $\epsilon_{\max} \simeq 41,000 \text{ M}^{-1} \cdot \text{cm}^{-1}$).

Table 1. Azide- and alkyne-functionalized ODNs used for post-synthetic fluorescent labeling with engineered dyes.

Sequence	Functionalization (Y, X, Xs, V, Z and W) *
5'- YCAG TCG CTC GCT GAC-3'	
5'- YGCA AAA TTT AAA ACG-3'	
5'-CAG TCG CXC GCT GAC-3'	
5'-GCA AAA TX T AAA ACG-3'	
5'-GCA AAA AAA AXA AAA AAA ACG-3'	
5'-GCA AAA TXs T AAA ACG-3'	
5'- VGCA AAA TTT AAA ACG-3'	
5'-GCA AAA TZ T AAA ACG-3'	
5'-GCA AAA TW T AAA ACG-3'	
5'-GCA AAA AAA AWA AAA AAA ACG-3'	

* Linkers ending in an azido group or a terminal alkyne are depicted in indigo or green, respectively.

First, the room temperature stability of the duplexes—formed from ss-ODNs modified with our dyes—was controlled by determining their melting temperature (Tables S7 and S8 and Figures S12–S14, Supplementary Materials). Then, the photophysical properties of the labeled ss-ODNs and their ds-constructs—obtained after hybridization of the complementary strand—were investigated (Table 2, charged probes in Table S9 and Figures S15–S17, Supplementary Materials). Interestingly, when the dyes were bound at the 5'-end, no increase in fluorescence intensity was noted and this observation was true for all sequence types with their respective linkers (Figures S18 and S19, Supplementary Materials). It is worth mentioning that the maximum fluorescent enhancement was obtained for the AT-rich context with the X-linker, while the most red-shifted absorption was remarked for the W-linker, i.e., the ethynyl-ribose located in the middle of the sequence.

Table 2. Photophysical features of the considered ODNs labeled with AIMF and AzMF.

Sequences	λ_{Abs} (nm) ^a		λ_{Em} (nm) ^b		Φ (%) ^c	
	AIMF	AzMF	AIMF	AzMF	AIMF	AzMF
YCAG	426	—	542	—	17	—
YCAG·GTC	427	—	543	—	7	—
YGCA	431	—	542	—	12	—
YGCA·CGT	429	—	544	—	5	—
CXC	424	—	542	—	21	—
CXC·GAG	427	—	542	—	15	—
TXT	432	—	542	—	16	—
TXT·AAA	449	—	546	—	41	—
AXA	432	—	550	—	11	—
AXA·TAT	441	—	547	—	34	—
TXsT	433	—	539	—	24	—
TXsT·AAA	430	—	542	—	22	—
VGCA	—	427	—	545	—	12
VGCA·CGT	—	421	—	545	—	5
TZT	—	430	—	545	—	16
TZT·AAA	—	431	—	545	—	28
TWT	—	431	—	547	—	15
TWT·AAA	—	437	—	542	—	30
AWA	—	428	—	552	—	8
AWA·TAT	—	429	—	531	—	34

^a Position of the absorption band maximum; ^b Position of the emission band maximum; ^c Quantum yield determined using *p*-dimethylaminoflavone (dMAF) in EtOH ($\lambda_{\text{Ex}} = 404$ nm, $\Phi = 27\%$) as a standard [28]. Linkers ending in an azido group or a terminal alkyne are depicted in indigo or green, respectively.

Note that those functionalized with the **Z**- and **Xs**-linkers showed only a small to almost no increment. These results clearly suggest that the chain length of the tether is crucial to obtain a turn-on emission upon hybridization. This would explain why **Z**- and **Xs**-linkers with medium-sized chain lengths do not allow a proper folding of the tag and thus, displayed almost no change in their fluorescence emission. Conversely, when the linker is long enough such as **X**, it provides sufficient flexibility for the fluorescent marker to interact with the grooves or force the intercalation during annealing. Thus, shielding its exposure to water allows the dye to recover its fluorescence potential and causes, in addition, redshifts in absorption by accommodation or stacking with adjacent nucleobases. Similarly, when the linker is short such as **W** and directly connected to the deoxyribose moiety, the clicked fluorophore is forced to intercalate inside the duplex with the neighboring base pairs, leading to the same photophysical conclusion as for **X**-tether ($\Phi \nearrow$, red-shifted λ_{Abs}).

In all the cases, the duplex formation was confirmed by an almost 2-fold increase in absorption at 260 nm. For the GC-rich sequence, almost no notable change in fluorescence intensity upon hybridization was detected. This can be explained by the reducing propensity of the guanine base, which is known to quench most of the fluorophores by photoinduced electron transfer (PET) process [1,29]. Alternatively, GC-rich duplexes being more stable are perhaps less prone to fluorophore intercalation.

It is worth noting that in all labeled sequences studied, absorption maxima of single- and double-stranded probes are identical to those of the hydrophilic charged dyes in bulk water ($\lambda_{\text{Abs}} \approx 430$ nm, Table 2, Tables S2 and S3, Supplementary Materials). This is therefore evidence of a highly hydrated environment around the fluorescent reporter, with the exception of the **TXT** vs. **TXT·AAA** and to a lesser extent **AXA** vs. **AXA·TAT** combinations for which a significant bathochromic shift is observed upon hybridization (10–20 nm). This result confirmed the ability of the aromatic fluorophore **AIMF** to stack with the neighboring base pairs [30].

To determine accordingly the highest fluorescence amplification from ss- to ds-ODNs labeled with **AIMF**, given that a 20-nm redshift occurred between the two contexts, the

entire absorption range was examined to define the most appropriate excitation wavelength (TXT vs. TXT·AAA, Table 3 and Figure 6 and Figure S20, Supplementary Materials). It was clear that excitation in the red edge of the ss absorption band should trigger a lower ss emission and thus, a higher contrast. Nevertheless, exciting too far from the absorption maximum should affect the brightness considerably. A good balance was found at the argon laser excitation (490-nm region), where a remarkable 13-fold fluorogenic turn-on was noticed, as attested by the bright green–yellow color of the cuvette inserts. With respect to the AXA sequence, almost a manifold fluorescence increase was recorded upon hybridization (AXA vs. AXA·TAT, Table S10 and Figure S21, Supplementary Materials).

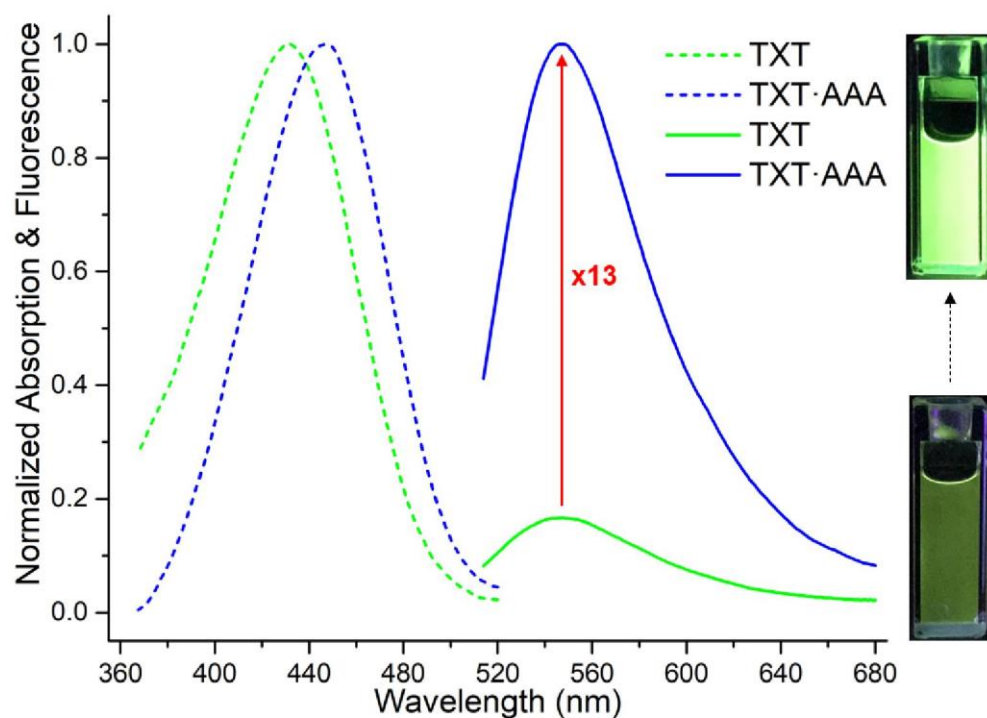


Figure 6. Absorbance (dashed) and fluorescence (solid) observables of TXT and TXT·AAA (488-nm excitation).

Table 3. Spectroscopic properties of TXT labeled with AIMF.

λ_{Ex} (nm) ^a	Brightness ($\text{L}\cdot\text{mol}^{-1}\cdot\text{cm}^{-1}$) ^b		Absorptivity Ratio ^c	Fluorescence Intensity Ratio ^d
	TXT	TXT·AAA		
430	6560	15,265	0.78	1.8
450	5350	16,810	1.11	3.7
480	1476	7572	1.84	10.4
490	764	4301	1.98	13.1
500	381	2054	1.96	13.4
510	212	760	1.90	12.9

^a Screening of the excitation wavelength; ^b Brightness calculation: absorptivity at the excitation wavelength \times Quantum Yield; ^c Absorbance of ds/Absorbance of ss; ^d Fluorescence intensity of ds/Fluorescence intensity of ss.

3. Materials and Methods

3.1. General Procedures

All reactions involving air- and water-sensitive conditions were performed in oven-dried glassware under argon by using Schlenk techniques employing a dual vacuum/argon manifold system and dry solvents. The synthetic intermediates were initially co-evaporated twice with toluene and dried in vacuo before use. All chemical reagents were purchased from commercial sources (Sigma-Aldrich (Saint-Louis, MO, USA), Acros (Geel, Belgium),

Alfa Aesar (Heysham, Lancashire, UK)) and were used as supplied. Anhydrous solvents were obtained according to standard procedures [31]. The reactions were monitored simultaneously by liquid chromatography-mass spectrometry (LC-MS) and thin-layer chromatography (TLC, silica gel 60 F254 plates). Compounds were visualized on TLC plates by both UV radiation (254 and 365 nm) and spraying with a staining agent (phosphomolybdic acid, KMnO_4 or ninhydrin) followed by subsequent warming with a heat gun. Column chromatography was performed with flash silica gel (40–63 μm) with the indicated solvent system using gradients of increasing polarity in most cases [32]. All NMR spectra (^1H , ^{13}C , and 2D) were recorded on 200 or 400 MHz Bruker advance spectrometers (Bruker, Billerica, MA, USA). The ^1H -NMR (200 and 400 MHz) and $^{13}\text{C}\{^1\text{H}\}$ -NMR (50 and 101 MHz, recorded with complete proton decoupling) spectra were obtained with samples dissolved in CDCl_3 , CD_2Cl_2 , CD_3OD or DMSO-d_6 with the residual solvent signals used as internal references: 7.26 ppm for CHCl_3 , 5.32 ppm for CDHCl_2 , 3.31 ppm for CD_2HOD , 2.50 ppm for $(\text{CD}_3)(\text{CD}_2\text{H})\text{S}(\text{O})$ regarding ^1H -NMR experiments, and 77.2 ppm for CDCl_3 , 53.8 ppm for CD_2Cl_2 , 49.0 ppm for CD_3OD , 39.4 ppm for $(\text{CD}_3)_2\text{S}(\text{O})$ concerning ^{13}C -NMR experiments [33]. Chemical shifts (δ) are given in ppm to the nearest 0.01 (^1H) or 0.1 ppm (^{13}C). The coupling constants (J) are given in hertz (Hz). The signals are reported as follows (s = singlet, d = doublet, t = triplet, m = multiplet, br = broad). Assignments of ^1H and ^{13}C -NMR signals were achieved with the help of D/H exchange, COSY, HMQC, HSQC, NOESY and HMBC experiments (Figures S22–S38). LC-MS spectra were recorded using an ion trap Esquire 3000 Plus mass spectrometer (Bruker, Billerica, MA, USA) equipped with an electrospray ionization (ESI) source in both positive and negative modes. High-resolution mass spectrometry (HRMS) was conducted with a hybrid ion trap-Orbitrap mass spectrometer (Thermo Fisher Scientific, Bremen, Germany)—combining quadrupole precursor selection with high-resolution and accurate-mass Orbitrap detection—using ESI techniques. Systematic flavone and nucleoside nomenclatures are used below for the spectral assignment of each synthesized derivative (Schemes S1–S4, Supplementary Materials). All solvents for absorption and fluorescence experiments were of spectroscopic grade. Absorbance spectra were recorded on a Cary 100 Bio UV-Vis spectrophotometer (Varian/Agilent, Palo Alto, CA, USA) using Suprasil[®] quartz 500- μL cuvettes (Heraeus, Hanau, Germany) with 1-cm path length. Stock solutions of the fluorescent nucleoside or ODNs were prepared using THF or Milli-Q[®] water (Merck Millipore, Burlington, MA, USA). The nucleoside sample used for spectroscopic measurements contained $\approx 0.2\%$ (v/v) of the stock solution solvent. Fluorescence measurements were conducted on a FluoroMax 4.0 spectrofluorometer (Jobin Yvon, Horiba, Kyoto, Japan) with a thermostatically controlled cell compartment at 20 ± 0.5 °C with slits open to 2 nm and were corrected for Raman scattering, lamp fluctuations and instrumental wavelength-dependent bias. Emission spectra were performed with an absorbance of about 0.05. The excitation wavelength corresponds to the absorption maximum of the considered sample, except when specified. Quantum yields were corrected according to the variation of the refractive index of the different solvents. They were determined by using *p*-DiMethylAminoFlavone (DMAF) in EtOH ($\lambda_{\text{Ex}} = 404$ nm, $\Phi = 27\%$) as a reference [28], with $\pm 10\%$ mean standard deviation. Fluorescent nucleoside AIMF-Nu was analyzed in duplicate at 10 and 2 μM , respectively for UV-Vis and fluorescence measurements. Labeled ODNs were analyzed in duplicate at 2 μM in phosphate-buffered saline pH 7.4 (50 mM sodium phosphate, 150 mM NaCl). In order to ensure reproducibility of hybridization and therefore of measurements, the double-stranded samples were first denatured and then cooled to room temperature.

3.2. Synthetic Procedures

6-Bromo-2-(4-diethylamino)phenyl-3-hydroxy-4H-chromen-4-one (1): 1-(5-Bromo-2-hydroxyphenyl)ethanone (1.7 g, 7.75 mmol, 1 eq.) and 4-(diethylamino)benzaldehyde (1.56 g, 8.52 mmol, 1.1 eq.) were solubilized in 1,2-dichloroethane (10 mL) and morpholine (10 mL). The reaction solution was irradiated by microwave (25 min, 100 °C, 200 W). The volatiles were removed in vacuo to give a reddish brown solid, which was solubilized in ethanol

(15 mL). To the stirred mixture cooled in an ice bath, were added sequentially an aq. 5 M NaOH solution (20 mL, 13 eq.) and H₂O₂ (30% *w/w* in H₂O, 7.65 mL, 10 eq.). After stirring overnight, the mixture was neutralized by an aq. 1 N HCl solution, and the resulting precipitate was filtered and washed with water and cyclohexane sequentially. Compound **1** was obtained as an orange solid. (2.24 g, 77%). *R_f* = 0.38 (Toluene/Acetone 4:1) or 0.58 (DCM/MeOH, 99.5:0.5). ¹H-NMR (CDCl₃, 200 MHz): δ 1.15 (t, ³*J* = 7.0 Hz, 6H, NCH₂-CH₃), 3.41 (q, ³*J* = 7.0 Hz, 4H, NCH₂-CH₃), 6.67 (d, ³*J* = 9.0 Hz, 2H, H_{meta}), 7.35 (d, ³*J* = 8.8 Hz, 1H, H8), 7.62 (dd, ³*J* = 8.8 Hz, ⁴*J* = 2.4 Hz, 1H, H7), 8.05 (d, ³*J* = 9.0 Hz, 2H, H_{ortho}), 8.26 (d, ⁴*J* = 2.4 Hz, 1H, H5), 9.37 (s, 1H, OH). ¹³C-NMR (CDCl₃, 50 MHz): δ 12.7 (N-CH₂-CH₃), 44.5 (N-CH₂-CH₃), 110.9 (C_m), 116.7 (C_p), 119.8 (C_i), 122.3 (C8), 127.6 (C6), 129.5 (C7), 135.5 (C_o), 136.9 (C5), 147.3 (C10), 149.1 (C2), 153.7 (C9), 171.0 (C4). HRMS (ESI⁺): *m/z* calcd for C₁₉H₁₈NO₃BrH⁺: 388.0543, 390.0522 [M + H]⁺; found: 388.0550, 390.0529 [M + H]⁺.

6-Bromo-2-(4-diethylamino)phenyl-3-methoxy-4H-chromen-4-one (2): To a stirred suspension of **1** (110 mg, 0.33 mmol, 1 eq.) in DCM (0.25 M, 6 mL), were sequentially added 18-crown-6 (25 mg, 7 mol%), an aq. KOH solution (25% *w/w*, 0.9 mL) and dimethyl sulfate (139 μL, 4 eq.). The reaction mixture was stirred 30 min at rt. After addition of H₂O (8 mL), the organic layer was extracted with DCM (3×), dried over mgSO₄, filtered and the volatiles were removed in vacuo. The residue was purified by flash chromatography on silica gel eluted with DCM/DCM-1% MeOH mixture (90:10 → 10:90, *v/v*) to provide the desired compound **2** as a yellow powder (101 mg, 0.4 mmol, 88%). *R_f* = 0.29 (DCM/MeOH 99.5:0.5). ¹H-NMR (CDCl₃, 400 MHz): δ 1.16 (t, ³*J* = 7.1 Hz, 6H, NCH₂-CH₃), 3.38 (d, ³*J* = 7.1 Hz, 4H, NCH₂-CH₃), 3.81 (s, 3H, OCH₃), 6.67 (d, ³*J* = 9.3 Hz, 2H, H_{meta}), 7.32 (d, ³*J* = 8.9 Hz, 1H, H8), 7.62 (dd, ³*J* = 8.9 Hz, ⁴*J* = 2.4 Hz, 1H, H7), 8.00 (d, ³*J* = 9.3 Hz, 2H, H_{ortho}), 8.30 (d, ⁴*J* = 2.4 Hz, 1H, H5). ¹³C-NMR (CDCl₃, 101 MHz): δ 12.6 (NCH₂-CH₃), 44.5 (NCH₂-CH₃), 56.7 (OCH₃), 110.8 (C_{meta}), 116.4 (C6), 117.6 (C_i), 119.6 (C8), 127.7 (C10), 128.2 (C5), 130.3 (C_{ortho}), 135.7 (C7), 140.0 (C3), 149.6 (C_{para}), 153.8 (C2), 157.0 (C9), 173.2 (C4). HRMS (ESI⁺): *m/z* calcd for C₂₀H₂₀BrNO₃H⁺: 402.0699, 404.0679 [M + H]⁺; found: 402.0698, 404.0679 [M + H]⁺.

2-(4-(Diethylamino)phenyl)-3-methoxy-6-((trimethylsilyl)ethynyl)-4H-chromen-4-one (AIMF-TMS): To a stirred solution of **2** (50 mg, 0.12 mmol) in dry DMF (3 mL) under argon, were sequentially added TMS-acetylene (53 μL, 0.37 mmol, 3 eq.), triethylamine (175 μL, 1.24 mmol, 10 eq.) and a mixture of CuI (5 mg, 20 mol%)/PdCl₂(PPh₃)₂ (18 mg, 20 mol%). The reaction mixture was warmed to 70 °C overnight. The volatiles were removed in vacuo and the residue was directly engaged in the next step.

2-(4-(Diethylamino)phenyl)-6-ethynyl-3-methoxy-4H-chromen-4-one (AIMF): To a 10-mL vial containing AIMF-TMS (20 mg, 45 μmol, 1 eq.), was added a minimum of MeOH (2 mL) to solubilize the compound. K₂CO₃ (63 mg, 0.45 mmol, 10 eq.) was then poured, and the resulting solution was stirred overnight at room temperature. The reaction mixture was quenched by acetic acid and reduced in vacuo to give the crude product. The residue was purified by preparative TLC (SiO₂) eluted with DCM/MeOH (99:1, *v/v*) to provide the desired product AIMF as a yellow powder (10 mg, 30 μmol, 64% over 2 steps). *R_f* = 0.24 (DCM/MeOH 99.5:0.5). ¹H-NMR (CDCl₃, 400 MHz): δ 1.16 (t, ³*J* = 7.2 Hz, 6H, NCH₂-CH₃), 3.04 (s, 1H, HC≡C), 3.38 (d, ³*J* = 7.2 Hz, 4H, NCH₂-CH₃), 3.82 (s, 3H, OCH₃), 6.67 (d, ³*J* = 9.2 Hz, 2H, H_{meta}), 7.38 (d, ³*J* = 8.7 Hz, 1H, H8), 7.62 (dd, ³*J* = 8.7, ⁴*J* = 2.0 Hz, 1H, H7), 8.00 (d, ³*J* = 9.2 Hz, 2H, H_{ortho}), 8.31 (d, ⁴*J* = 2.0 Hz, 1H, H5). ¹³C-NMR (CDCl₃, 101 MHz): δ 12.6 (NCH₂-CH₃), 44.5 (NCH₂-CH₃), 59.7 (OCH₃), 77.8 (HC≡C), 82.3 (HC≡C), 110.8 (C_{meta}), 116.5 (C6), 118.0 (C8), 118.4 (C_i), 124.2 (C10), 129.9 (C5), 130.2 (C_{ortho}), 136.0 (C7), 140.0 (C3), 149.5 (C_{para}), 154.7 (C2), 156.8 (C9), 173.7 (C4). HRMS (ESI⁺): *m/z* calcd for C₂₂H₂₁NO₃H⁺: 348.1594 [M + H]⁺; found: 348.1600.

1-(5-(Chloromethyl)-2-hydroxyphenyl)ethan-1-one (3): Adapted from the protocol described in [34]. To a solution of paraformaldehyde (2.4 g, 79.3 mmol, 1.08 eq.) in conc. HCl solution (45 mL), was added 2-hydroxyacetophenone (8.85 mL, 73.4 mmol, 1 eq.). Next, the reaction mixture was stirred at 35 °C for 5 h. A yellow precipitate was formed which was then filtered and washed with water (3×). The resulting solid was solubilized in DCM,

dried over mgSO_4 , filtered and the volatiles were removed in vacuo to obtain the product as a yellow powder (11.8 g, 63.9 mmol, 87%). $R_f = 0.52$ (Cyclohexane/EtOAc 4:1). $^1\text{H-NMR}$ (DMSO- d_6 , 400 MHz): δ 2.63 (s, 3H, H9), 4.76 (s, 2H, H8), 6.98 (d, $^3J = 8.5$ Hz, 1H, H4), 7.59 (dd, $^3J = 8.5$ Hz, $^4J = 2.2$ Hz, 1H, H5), 7.95 (d, $^4J = 2.2$ Hz, 1H, H7). $^{13}\text{C-NMR}$ (DMSO- d_6 , 101 MHz): δ 28.0 (C9), 45.9 (C8), 118.2 (C4), 120.5 (C2), 128.5 (C6), 131.8 (C7), 136.9 (C5), 160.6 (C3), 203.8 (C1).

2-(4-(Diethylamino)phenyl)-3-hydroxy-6-methoxymethyl-4H-chromen-4-one (4): To a stirred solution of **3** (2.5 g, 13.5 mmol, 1 eq.) in methanol (45 mL, 0.3 M) was added NaOH (1.66 g, 14.2 mmol, 1.05 eq.) and 4-(diethylamino)benzaldehyde (2.55 g, 14.2 mmol, 1.05 eq.). The reaction mixture was refluxed for 8 h. After cooling to 4 °C, H_2O_2 (30% w/w in H_2O , 5.5 mL) was added dropwise. Then, cold water (200 mL) was poured, and the reaction mixture was acidified with an aq. 2 N HCl solution to pH 6.5. MeOH was evaporated under reduced pressure. DCM (200 mL) was added, and the organic layer was extracted (3 \times). The combined organic phases were reduced in vacuo to give the crude compound **4** as a brown oil, which was pure enough to be taken to the next step without further purification (4.66 g, 13.2 mmol, 97%). $R_f = 0.44$ (Cyclohexane/EtOAc 4:1). $^1\text{H-NMR}$ (DMSO- d_6 , 400 MHz): δ 1.16 (t, $^3J = 7.0$ Hz, 6H, $\text{NCH}_2\text{-CH}_3$), 3.33 (s, 3H, OCH_3), 3.42 (q, $^3J = 7.0$ Hz, 4H, $\text{NCH}_2\text{-CH}_3$), 4.54 (s, 2H, OCH_2Ph), 6.80 (d, $^3J = 9.2$ Hz, 2H, H_{meta}), 7.68 (m, 2H, H7 and H8), 8.01 (d, $^4J = 2.0$ Hz, 1H, H5), 8.09 (d, $^3J = 9.2$ Hz, 2H, H_{ortho}). $^{13}\text{C-NMR}$ (CDCl_3 , 101 MHz): δ 12.0 ($\text{NCH}_2\text{-CH}_3$), 43.3 ($\text{NCH}_2\text{-CH}_3$), 57.2 (OCH_3), 72.3 (OCH_2), 110.3 (C_{meta}), 116.5 (C6), 117.7 (C8), 118.1 (C_i), 122.5 (C5), 124.2 (C10), 128.8 (C_{ortho}), 131.9 (C7), 142.6 (C3), 146.6 (C_{para}), 148.0 (C2), 153.1 (C9), 171.3 (C4).

6-(Bromomethyl)-2-(4-(diethylamino)phenyl)-3-hydroxy-4H-chromen-4-one (5): A mixture of **4** (610 mg, 1.7 mmol, 1 eq.) and 47% hydrobromic acid in H_2O (5 mL) was refluxed for 3 h. After cooling to room temperature, a saturated aq. solution of sodium carbonate was added slowly to neutralize the reaction until pH 7 was reached. Then, the solid was filtered to directly obtain the desired crude solid **5** as a khaki solid (960 mg, 2.4 mmol, quant.), which was directly committed to the next step without further purification. $R_f = 0.24$ (Cyclohexane/EtOAc 4:1). $^1\text{H-NMR}$ (CDCl_3 , 400 MHz): δ 1.23 (t, $^3J = 7.1$ Hz, 6H, $\text{NCH}_2\text{-CH}_3$), 3.45 (q, $^3J = 7.1$ Hz, 4H, $\text{NCH}_2\text{-CH}_3$), 4.60 (s, 2H, OCH_2Ph), 6.77 (d, $^3J = 9.1$ Hz, 2H, H_{meta}), 7.54 (d, $^3J = 8.7$ Hz, 1H, H8), 7.69 (dd, $^3J = 8.7$ Hz, $^4J = 2.1$ Hz, 1H, H7), 8.16 (d, $^3J = 9.1$ Hz, 2H, H_{ortho}), 8.22 (d, $^4J = 2.1$ Hz, 1H, H5).

6-(Azidomethyl)-2-(4-(diethylamino)phenyl)-3-hydroxy-4H-chromen-4-one (6): **5** (242 mg, 0.60 mmol, 1 eq.) was solubilized in a mixture of acetone (6 mL) and DMF (1.5 mL) to which was added NaN_3 (60 mg, 0.90 mmol, 1.5 eq.). The solution was stirred overnight at room temperature. Then, EtOAc (20 mL) was introduced, and acetone was evaporated under reduced pressure. A saturated aq. solution of NH_4Cl was added (10 mL) to quench the reaction. The organic layer was extracted with EtOAc ($\times 2$), dried over mgSO_4 , filtered, and concentrated in vacuo. The crude product was purified by flash chromatography on silica gel eluted with cyclohexane/ethyl acetate (9:1 \rightarrow 7:3, v/v) to give **6** as an orange powder, which was directly engaged in the next step.

6-Azidomethyl-2-(4-(diethylamino)phenyl)-3-methoxy-4H-chromen-4-one (AzMF): To a stirred solution of **6** (144 mg, 0.40 mmol, 1 eq.) in CH_2Cl_2 (2.6 mL), were sequentially added 18-crown-6 (30 mg, 7 mol%), an aq. KOH solution (25% w/w, 0.4 mL) and dimethyl sulfate (166 μL , 1.58 mmol, 4 eq.). The resulting mixture was stirred overnight at room temperature. After quenching the reaction by addition of H_2O (5 mL), the organic layer was extracted with CH_2Cl_2 (3 \times). The combined organic phases were dried over mgSO_4 , filtered and the volatiles were removed in vacuo. The residue was purified by flash chromatography on silica gel eluted with cyclohexane/ethyl acetate (9:1 \rightarrow 3:1, v/v) to give the desired compound as a yellow solid (146 mg, 0.38 mmol, 70% over 2 steps). $^1\text{H-NMR}$ (CDCl_3 , 400 MHz): δ 1.17 (t, $^3J = 7.1$ Hz, 6H, $\text{NCH}_2\text{-CH}_3$), 3.39 (q, $^3J = 7.1$ Hz, 4H, $\text{NCH}_2\text{-CH}_3$), 3.83 (s, 3H, OCH_3), 4.39 (s, 2H, $\text{N}_3\text{CH}_2\text{Ph}$), 6.68 (d, $^3J = 9.3$ Hz, 2H, H_{meta}), 7.46 (d, $^3J = 8.6$ Hz, 1H, H8), 7.54 (dd, $^3J = 8.6$ Hz, $^4J = 2.2$ Hz, 1H, H7), 8.02 (d, $^3J = 9.3$ Hz, 2H, H_{ortho}), 8.22 (d, $^4J = 2.2$ Hz, 1H, H5). $^{13}\text{C-NMR}$ (CDCl_3 , 101 MHz): δ 12.6 ($\text{NCH}_2\text{-CH}_3$), 44.5 ($\text{NCH}_2\text{-CH}_3$),

54.2 (N₃CH₂Ph), 59.7 (OCH₃), 110.8 (C_{meta}), 116.6 (C₆), 118.6 (C₈), 124.3 (C_i), 125.3 (C₅), 130.2 (C_{ortho}), 131.7 (C₁₀), 132.6 (C₇), 140.1 (C₃), 149.5 (C_{para}), 154.8 (C₂), 156.8 (C₉), 174.2 (C₄). HRMS (ESI⁺): *m/z* calcd for C₂₁H₂₂N₄O₃H⁺: 379.1765; [M + H]⁺; found: 379.1777.

6-(Bromomethyl)-2-(4-(diethylamino)phenyl)-3-methoxy-4H-chromen-4-one (7): To a stirred solution of **5** (240 mg, 0.60 mmol, 1 eq.) in DCM (12 mL), were sequentially added 18-crown-6 (79 mg, 0.30 mmol, 0.1 eq.), an aq. KOH solution (25% *w/w*, 1.7 mL, DCM/KOH 7:1) and dimethyl sulfate (282 μL, 2.98 mmol, 5 eq.). The reaction mixture was stirred for 30 min at room temperature. The organic layer was extracted with DCM (3×), dried over mgSO₄, filtered, and concentrated in vacuo. The residue was then purified by flash chromatography on silica gel eluted with cyclohexane/ethyl acetate (9:1 → 7:3, *v/v*) to give the desired compound **7** as a red oil (200 mg, 0.48 mmol, 80%). R_f = 0.58 (Cyclohexane/EtOAc 3:1). ¹H-NMR (CDCl₃, 400 MHz): δ 1.23 (t, ³J = 7.1 Hz, 6H, NCH₂-CH₃), 3.45 (q, ³J = 7.1 Hz, 4H, NCH₂-CH₃), 3.88 (s, 3H, OCH₃), 4.59 (s, 2H, BrCH₂Ph), 6.74 (d, ³J = 9.2 Hz, 2H, H_{meta}), 7.49 (d, ³J = 8.7 Hz, 1H, H₈), 7.67 (dd, ³J = 8.7 Hz, ⁴J = 2.2 Hz, 1H, H₇), 8.08 (d, ³J = 9.2 Hz, 2H, H_{ortho}), 8.24 (d, ⁴J = 2.2 Hz, 1H, H₅). ¹³C-NMR (CDCl₃, 101 MHz): δ 12.6 (NCH₂-CH₃), 32.4 (BrCH₂Ph), 44.5 (NCH₂-CH₃), 59.7 (OCH₃), 110.8 (C_{meta}), 116.6 (C₆), 118.6 (C₈), 124.2 (C_i), 125.8 (C₅), 130.2 (C_{ortho}), 133.7 (C₇), 134.1 (C₁₀), 140.1 (C₃), 149.5 (C_{para}), 154.7 (C₂), 156.8 (C₉), 174.1 (C₄). HRMS (ESI⁺): *m/z* calcd for C₂₁H₂₂BrNO₃H⁺: 416.0856, 418.0835 [M + H]⁺; found: 416.0870, 418.0848.

Acid 3-(prop-2-yn-1-ylamino)propane-1-sulfonic (PYAPS): To a solution of propargylamine (116 μL, 1.8 mmol, 1 eq.) in CH₃CN (5 mL) was added dropwise 1,3-propane sultone **8** (169 μL, 1.9 mmol, 1.05 eq.). The reaction mixture was stirred at room temperature for 2 d. The resulting precipitate was filtered and washed with CH₃CN to afford the desired compound **PYAPS** as a pinkish solid (230.5 mg, 1.31 mmol, 72%). R_f = 0.25 (DCM/MeOH 4:1). Green staining by ninhydrin. ¹H-NMR (DMSO-d₆, 400 MHz): δ 1.93 (p, ³J = 6.8 Hz, 2H, H₅), 2.60 (t, ³J = 6.8 Hz, 2H, H₄), 3.09 (t, ³J = 6.8 Hz, 2H, H₆), 3.68 (t, ⁴J = 2.5 Hz, 1H, H₁), 3.90 (d, ⁴J = 2.5 Hz, 2H, H₃). ¹³C-NMR (DMSO-d₆, 101 MHz): δ 21.7 (C₅), 35.6 (C₃), 46.0 (C₄), 48.8 (C₆), 75.1 (C₂), 79.4 (C₁). HRMS (ESI⁺): *m/z* calcd for C₆H₁₁NO₃SH⁺: 178.0532; [M + H]⁺; found: 178.0534.

Sodium 3-(methyl(prop-2-yn-1-yl)amino)propane-1-sulfonate (Me-PYAPS): **PYAPS** (150 mg, 0.85 mmol, 1 eq.), formol (37% formaldehyde in H₂O) (900 μL) and formic acid (903 μL) were heated overnight at 70 °C. Then, the solution was concentrated in vacuo until a paste was obtained. NaHCO₃ (1 g) was added to the solid until bubbling ceased to provide the sodium sulfonate salt **Me-PYAPS** as a white solid (375 mg, quant.). Bicarbonate salts contaminate the product due to the excess used. ¹H-NMR (DMSO-d₆, 400 MHz): δ 1.60–1.73 (m, 2H, H₅), 2.15 (s, 3H, H₇), 2.32–2.42 (m, 4H, H₄ and H₆), 3.07 (t, ⁴J = 2.4 Hz, 1H, H₁), 3.25 (d, ⁴J = 2.4 Hz, 2H, H₃). ¹³C-NMR (DMSO-d₆, 101 MHz): δ 22.7 (C₅), 40.7 (C₃), 44.3 (C₆), 48.9 (C₇), 53.7 (C₄), 75.1 (C₂), 81.5 (C₁). HRMS (ESI⁺): *m/z* calcd for C₇H₁₂NO₃SH⁺: 192.0689; [M + H]⁺; found: 192.0690.

2-Azido-N,N-dimethylethanamine (DMAZ): 3-Chloro-1,1-dimethylpropylamine **9** (800 mg, 5.6 mmol, 1 eq.) and NaN₃ (1.1 g, 16.7 mmol, 3 eq.) were sequentially dissolved in H₂O (18.5 mL, 0.3 M). The solution was stirred at 80 °C for 24 h. After cooling to room temperature, the reaction mixture was adjusted to pH 10 by addition of an aq. 0.5 M NaOH solution. The organic layer was then extracted with diethyl ether (3×). The combined extracts were dried over mgSO₄, filtered, and concentrated under vacuum to yield the product **DMAZ** as a yellowish liquid (970 mg, 9.03 mmol, quant.). ¹H-NMR (CDCl₃, 400 MHz): δ 2.24 (s, 6H, H₃ and H_{3'}), 2.47 (t, ³J = 6.2 Hz, 2H, H₂), 3.31 (t, ³J = 6.2 Hz, 2H, H₁). ¹³C-NMR (CDCl₃, 101 MHz): δ 45.5 (C₃ and C_{3'}), 49.1 (C₁), 58.0 (C₂). HRMS (ESI⁺): *m/z* calcd for C₄H₁₀N₄H⁺: 115.0978; [M + H]⁺; found: 115.0982.

Potassium N(3-(((2-(4-(diethylamino)phenyl)-3-methoxy-4H-chromen-6-yl)methyl), N(prop-2-yn-1-yl)amino)propane-1-sulfonate (AIMF-): To a solution of **7** (22 mg, 50 μmol, 1 eq.) in DMF (0.5 mL), were added **PYAPS** (19 mg, 0.11 mmol, 2 eq.), H₂O (0.4 mL), and K₂CO₃ (19 mg, 0.13 mmol, 2.5 eq.). The solution was stirred at room temperature for 24 h. Then, DMF and water were evaporated in vacuo and the crude (solubilized with DCM/MeOH)

was purified by flash chromatography on silica gel eluted with *i*-PrOH/NH₃/H₂O (12:2:1, *v/v*) to afford the desired product **AIMF**— as an orange solid (26 mg, 50 μmol, 95%). ¹H-NMR (MeOD, 400 MHz): δ 1.22 (t, ³J = 7.0 Hz, 6H, NCH₂-CH₃), 1.97–2.08 (m, 2H, H6'), 2.73 (t, ³J = 6.9 Hz, 2H, H5'), 2.90 (m, 2H, H7'), 3.49 (q, ³J = 7.0 Hz, 4H, NCH₂-CH₃), 3.78 (m, 2H, H2'), 3.79 (s, 3H, OCH₃), 3.94 (d, ³J = 2.6 Hz, 1H, H4'), 4.84 (s, 2H, H1'), 6.80 (d, ³J = 7.0 Hz, 2H, H_{meta}), 7.60 (d, ³J = 8.6 Hz, 1H, H8), 7.77 (dd, ³J = 8.6 Hz, ²J = 2.1 Hz 1H, H7), 8.07 (s, 1H, H5), 8.08 (m, ³J = 7.0 Hz, 2H, H_{ortho}). HRMS (ESI⁺): *m/z* calcd for C₂₇H₃₂N₂O₆SH⁺: 513.2054; [M – H]⁺; found: 513.2064.

3-(((2-(4-(diethylamino)phenyl)-3-methoxy-4-oxo-4H-chromen-6-yl)methyl)(methyl)(prop-2-yn-1-yl)ammonio)propane-1-sulfonate (**AIMF+**—): To a solution of **7** (80 mg, 0.19 mmol, 1 eq.) in DMF (4.5 mL), were added **Me-PYAPS** and water (2 mL). The reaction mixture was stirred at room temperature for 24 h before the volatiles were removed under vacuum. The residue (diluted with DCM/MeOH) was purified by flash chromatography on silica gel eluted with *i*-PrOH/NH₃/H₂O (12:2:1, *v/v*) to give the desired product **AIMF+**— as a yellow oil (36 mg, 68 μmol, 36%). ¹H-NMR (MeOD, 400 MHz): δ 1.23 (t, ³J = 7.1 Hz, 6H, NCH₂-CH₃), 2.07–2.17 (m, 2H, H6'), 2.86 (s, 3H, H8'), 2.88 (m, 2H, H5'), 3.07–3.14 (m, 2H, H7'), 3.50 (q, ³J = 7.1 Hz, 4H, NCH₂-CH₃), 3.68–3.69 (m, 5H, H2' and OCH₃), 4.30 (m, 1H, H4'), 4.79 (s, 2H, H1'), 6.81 (d, ³J = 9.0 Hz, 2H, H_{meta}), 7.72 (d, ³J = 8.6 Hz, 1H, H8), 7.96 (dd, ³J = 8.6 Hz, ²J = 2.0 Hz 1H, H7), 8.07 (d, ³J = 9.0 Hz, 2H, H_{ortho}), 8.35 (s, 1H, H5). ¹³C-NMR (MeOD, 101 MHz): δ 11.5, 21.0, 44.0, 44.7, 53.8, 58.7, 60.9, 64.4, 71.1, 77.6, 82.6, 110.7, 115.4, 119.2, 123.5, 123.9, 130.0, 130.2, 137.1, 139.5, 150.1, 156.0, 158.0, 173.9. HRMS (ESI⁺): *m/z* calcd for C₂₈H₃₄N₂O₆SH⁺: 527.2210; [M + H]⁺; found: 527.2215.

2-Azidoethyl-N-((2-(4-(diethylamino)phenyl)-3-methoxy-4-oxo-4H-chromen-6-yl)methyl)-N,N-dimethylethanammonium bromide (**AzMF+**): To a solution of **7** (12 mg, 29 μmol, 1 eq.) in anhydrous THF (0.4 mL, 80 mM), was added **DMAZ** (16 mg, 0.144 mmol, 5 eq.). The reaction mixture was stirred at room temperature for 6 h. The formed precipitate was centrifuged, and the upper layer was discarded. The compound was washed twice more after suspension in dry THF, centrifugation and removal of the supernatant. The recovered solid was dried under reduced pressure to provide **AzMF+** as a yellow powder (9.6 mg, 18 μmol, 63%). ¹H-NMR (MeOD, 400 MHz): δ 1.24 (t, ³J = 7.1 Hz, 6H, NCH₂-CH₃), 3.16 (s, 6H, H2' and H3'), 3.52 (q, ³J = 7.1 Hz, 4H, NCH₂-CH₃), 3.62 (t, ³J = 5.4 Hz, 2H, H5'), 3.83 (s, 3H, OCH₃), 4.08 (t, ³J = 5.4 Hz, 2H, H4'), 4.76 (s, 2H, H1'), 6.84 (d, ³J = 9.3 Hz, 2H, H_{meta}), 7.82 (d, ³J = 8.6 Hz, 1H, H8), 7.93 (d, ³J = 8.6 Hz, 1H, H7), 8.13 (d, ³J = 9.3 Hz, 2H, H_{ortho}), 8.35 (s, 1H, H5). ¹³C-NMR (MeOD, 101 MHz): δ 11.5 (NCH₂-CH₃), 44.0 (NCH₂-CH₃), 44.6 (C2', C3'), 49.5 (N₃CH₂), 54.2 (N⁺CH₂Ph), 58.7 (OCH₃), 62.6 (CH₂N⁺), 67.6 (N⁺CH₂Ph), 110.8 (C_{meta}), 115.4 (C6), 119.1 (C8), 123.8 (C_i), 123.9 (C10), 130.2 (C5), 130.2 (C_{ortho}), 137.2 (C7), 137.2 (C3), 139.6 (C_{para}), 150.2 (C2), 156.1 (C9), 174.1 (C4). HRMS (ESI⁺): *m/z* calcd for C₂₅H₃₂N₅O₃⁺: 450.2500 [M – H]⁺; found: 450.2500.

1-Azido-1,2-dideoxy-3,5-di-*O*-*p*-toluoyl-β-D-ribofuranose (**8**): Adapted from the procedure described in [35,36]. To a stirred solution of 1α-chloro-3,5-di-toluoyl-2-deoxy-L-ribose (1.4 g, 3.64 mmol, 1 eq.) in acetone (20 mL) at 0 °C, was slowly added NaN₃ (1.22 g, 18.2 mmol, 5.0 eq.). The reaction mixture was kept under vigorous stirring for 5 h. After completion, as evidenced by TLC monitoring, the reaction mixture was quenched with a saturated aq. NaHCO₃ solution (15 mL), and the organic layer was extracted with CH₂Cl₂ (3×). The combined extracts were dried over mgSO₄, filtered, and evaporated under reduced pressure. The crude oil obtained is a mixture of both anomers (β/α 9:1), which was subjected to flash chromatography on silica gel eluted with PE/Et₂O (19:1 → 4:1, *v/v*) to furnish the pure β anomer of **8** as a white crystalline compound (1.0 g, 80%). C₂₁H₂₃O₅N₃ (384.13). R_f = 0.67 (Toluene/Acetone 9:1). ¹H-NMR (CD₂Cl₂, 400 MHz): δ 2.43 (s, 3H, CH₃-Tol), 2.44 (s, 3H, CH₃-Tol), 2.46–2.49 (m, 2H, H2'), 4.55–4.67 (m, 3H, H4', H5'), 5.64 (ddd, ³J = 7.9 Hz, ³J = 4.4 Hz, ⁴J = 2.2 Hz, 1H, H3'), 5.77 (t, ³J = 5.1 Hz, 1H, H1'), 7.28–7.31 (m, 4H, H_{m-Tol}), 7.98 (d, ³J = 8.2 Hz, 2H, H_{o-Tol}), 8.05 (d, ³J = 8.2 Hz, 2H, H_{o-Tol}). ¹³C-NMR (CDCl₃, 50 MHz): δ 22.1 (CH₃), 22.1 (CH₃), 39.3 (C2'), 65.0 (C5'), 75.7 (C4'), 83.5 (C3'), 93.0 (C1'), 127.5 (C_i),

127.9 (C_i), 129.9 (C_m), 129.9 (C_m), 130.4 (C_o), 130.4 (C_o), 144.7 (C_p), 145.1 (C_p), 166.5 (CO), 166.8 (CO).

1,2-Dideoxy-1β-(4-(2-(4-(diethylamino)phenyl)-3-methoxy-4H-chromen-6-yl)-1H-1,2,3-triazol-1-yl)-3,5-di-O-p-toluoyl-β-D-ribofuranose (9): To a stirred solution of **AIMF** (10 mg, 30 μmol, 1 eq.) in DCE (2.5 mL) inside a 4-mL vial, were sequentially added **8** (18 mg, 50 μmol, 1.8 eq.), DIPEA (61 μL, 0.35 mmol, 12 eq.), acetic acid (10 μL, 0.17 mmol, 6 eq.) and CuI (16 mg, 80 μmol, 2.8 eq.). The reaction was heated at 40 °C for 1 h under an argon atmosphere to give a homogeneous blue solution. The mixture was concentrated under reduced pressure and the residue was purified by preparative TLC (SiO₂) eluted with DCM/MeOH (99:1, *v/v*) to give the desired product **9** as a yellow powder (21 mg, 30 μmol, 98%). ¹H-NMR (CDCl₃, 400 MHz): δ 1.14 (t, ³J = 7.0 Hz, 6H, NCH₂-CH₃), 2.28 and 2.37 (2s, 6H, H12 and H14), 2.84 (ddd, ²J = 14.2 Hz, ³J = 6.1 Hz, ³J = 3.3 Hz, 1H, H2'), 3.16–3.25 (m, 1H, H2'), 3.3–3.44 (m, 4H, NCH₂-CH₃), 3.84 (s, 3H, OCH₃), 4.49–4.54 (m, 1H, H5'), 4.58–4.66 (m, 2H, H5', H4'), 5.71–5.77 (m, 1H, H3'), 6.47 (t, ³J = 6.3 Hz, 1H, H1'), 6.69 (d, ³J = 9.2 Hz, 2H, H_m), 7.12 (d, ³J = 8.0 Hz, 2H, H_{m'}/H_{m''}), 7.21 (d, ³J = 8.2 Hz, 2H, H_{m'}/H_{m''}), 7.49 (d, ³J = 8.7 Hz, 1H, H8), 7.80 (d, ³J = 8.0 Hz, 2H, H_{o'}/H_{o''}), 7.90 (d, ³J = 8.2 Hz, 2H, H_{o'}/H_{o''}), 8.04 (m, 3H, Hα, H_o), 8.15 (dd, ³J = 8.7 Hz, ²J = 2.2 Hz, 1H, H7), 8.36 (d, ²J = 2.2 Hz, 1H, H5). ¹³C-NMR (CDCl₃, 101 MHz): δ 12.6 (NCH₂-CH₃), 15.3 (C12/C14), 21.7 (C12/C14), 38.2 (C2'), 44.5 (NCH₂-CH₃), 59.7 (OCH₃), 63.8 (C5'), 74.8 (C3'), 83.8 (C4'), 89.0 (C1'), 110.9 (C_m), 116.7 (C_i), 118.4 (C8), 118.9 (Cα), 122.3 (C5), 124.4 (C6), 126.4 (C_{i'}/C_{i''}), 126.6 (C_{i'}/C_{i''}), 126.8 (C10), 129.3 (C_{m'}/C_{m''}), 129.7 (C_{o'}/C_{o''}), 129.8 (C_{o'}/C_{o''}), 130.2 (C_o), 130.5 (C7), 140.3 (C3), 144.1 (C_{p'}/C_{p''}), 144.5 (C_{p'}/C_{p''}), 147.0 (Cβ), 149.5 (C_p), 154.8 (C9), 156.7 (C2), 165.9 (C11/C13), 166.2 (C11/C13), 172.7 (C4).

1,2-Dideoxy-1-(4-(2-(4-(diethylamino)phenyl)-3-methoxy-4-oxo-4H-chromen-6-yl)-1H-1,2,3-triazol-1-yl)-β-D-ribofuranose (AIMF-Nu): In a 4-mL vial, **9** (21 mg, 30 μmol, 1 eq.) was solubilized in MeOH (0.6 mL) and few drops of DCM. Then, K₂CO₃ (20 mg, 0.14 mmol, 5 eq.) was added and the reaction mixture was stirred overnight at 35 °C. The mixture was then quenched by a minimum of acetic acid and the solvents were removed in vacuo. The crude was purified by preparative RP-TLC (C18) eluted with H₂O/acetonitrile (50:50, *v/v*) to give the desired product **AIMF-Nu** as a yellow solid (8 mg, 20 μmol, 56%). R_f = 0.11 (DCM/MeOH, 99.8:0.2). ¹H-NMR (CDCl₃, 400 MHz): δ 1.13 (t, ³J = 7.0 Hz, 6H, NCH₂-CH₃), 2.47 (ddd, ³J = 13.6 Hz, ³J = 6.0 Hz, ³J = 4.7 Hz, 1H, H2'), 2.70–2.79 (m, 1H, H2'), 3.35–3.44 (m, 4H, NCH₂-CH₃), 3.58 (dd, ³J = 12.0 Hz, ³J = 5.0 Hz, 1H, H5'), 3.68 (dd, ³J = 12.0 Hz, ³J = 3.9 Hz, 1H, H5'), 3.72 (s, 3H, OCH₃), 3.97 (m, 1H, H4'), 4.50 (m, 1H, H3'), 6.38 (t, ³J = 6.0 Hz, 1H, H1'), 6.71 (d, ³J = 9.3 Hz, 2H, H_{meta}), 7.62 (d, ³J = 8.8 Hz, 1H, H8), 8.00 (d, ³J = 9.2 Hz, 2H, H_{ortho}), 8.12 (dd, ³J = 8.8 Hz, ³J = 2.1 Hz, 1H, H7), 8.44 (d, ³J = 2.1 Hz, 1H, H5), 8.56 (s, 1H, Hα). ¹³C-NMR (CDCl₃, 101 MHz): δ 11.5 (NCH₂-CH₃), 40.4 (C2'), 44.0 (NCH₂-CH₃), 58.7 (OCH₃), 61.9 (C5'), 70.8 (C3'), 88.4 (C4'), 89.0 (C1'), 110.7 (C_{meta}), 115.8 (C_i), 118.5 (C8), 119.9 (Cα), 121.3 (C5), 123.9 (C10), 127.3 (C6), 130.1 (C_{ortho}), 130.6 (C7), 139.5 (C3), 146.2 (Cβ), 150.0 (C_{para}), 154.8 (C9), 158.0 (C2), 174.6 (C4). HRMS (ESI⁺): *m/z* calcd for C₂₇H₃₀N₄O₆H⁺: 507.2238 [M + H]⁺; found: 507.2240.

4. Conclusions

In summary, novel fluorogenic derivatives of **dEAF** were synthesized with different kinds of linkers (from neutral to ionic) bearing appropriate functional groups, allowing the development of a toolbox of dyes, easy to conjugate with biomolecules. Compared to the parent chromone, these original fluorophores retained all photophysical properties intact, while improving solubility and photostability in aqueous media. They were then used to post-synthetically label ODNs of different compositions via Cu(I)-mediated click chemistry. The resulting ODN probes showed bright turn-on emission after annealing with the complementary strand. Position 6 of the chromone scaffold was chosen as the site of chemical modification because at this location, the impact on the photophysics of the dye is minimal. The methoxy group was preferred over the hydroxyl group to drastically enhance the photostability of the 3-OH chromone. A variety of tethers in terms of length

and functionality were engineered and connected to different sites on the ODN (5'-end, internal C5-dT base, anomeric position). Conjugation of the dye at the 5'-terminus of the single strand generally demonstrated no change in its fluorescence emission upon hybridization due to its constant exposure to bulk water. However, when the dye was placed in the middle of the ODN, the quantum yield increased 13-fold compared to the single-stranded context. More importantly, this result—obtained after selective excitation at 488 nm (matching with the argon laser commonly used on all fluorescence microscopes)—still revealed a prospective Stokes shift of 56 nm. In this regard, our fluorogenic AIMF conjugate compares favorably with the TO/JO FIT-probes, which were synthesized to generate a FRET pair and a larger Stokes shift for easier and more sensitive detection [37]. We believe that these dyes will prove very helpful for diagnostic and bioimaging purposes by targeting specific nucleic acid sequences.

Supplementary Materials: The following supporting information can be downloaded at: <https://www.mdpi.com/article/10.3390/molecules27072267/s1>. Schemes S1–S4: Overview of the synthesis schemes; Tables S1–S3 and Figures S1–S9: Photophysical characterization; Tables S4–S10 and Figures S10–S21: Spectroscopic studies of model odns; Figures S22–S38: NMR spectra. Reference [38] are cited in the supplementary materials.

Author Contributions: Conceptualization, B.Y.M. and A.B.; formal analysis, S.V., G.B. and H.-N.L.; funding acquisition, B.Y.M. and A.B.; investigation, S.V., G.B. and S.M.; methodology, S.V.; supervision, B.Y.M. and A.B.; writing—review and editing, S.V., S.M., A.B. and B.Y.M. All authors have read and agreed to the published version of the manuscript.

Funding: This research work was funded by the Agence Nationale de la Recherche (PFPIImaging—18-CE09-0020-01, UCA JEDI project: ANR-15-IDEX-01) and the LIFE graduate school (UCA). We thank the French Government for the PhD grants of S.V., H.-N.L. and G.B., respectively. We are grateful to the CNRS Emergence@INC2020 program for both the financial support and the postdoctoral fellowship of S.M.

Institutional Review Board Statement: Not applicable.

Informed Consent Statement: Not applicable.

Data Availability Statement: Experimental data are available within this research article and in the related Supplementary Materials.

Acknowledgments: Thanks to N.P.F. Barthes for his seminal work on the project.

Conflicts of Interest: The authors declare no conflict of interest.

Sample Availability: Samples of the compounds are not available from the authors.

References

1. Michel, B.Y.; Dziuba, D.; Benhida, R.; Demchenko, A.P.; Burger, A. Probing of Nucleic Acid Structures, Dynamics, and Interactions With Environment-Sensitive Fluorescent Labels. *Front. Chem.* **2020**, *8*, 112. [CrossRef]
2. Braselmann, E.; Rathbun, C.; Richards, E.M.; Palmer, A.E. Illuminating RNA Biology: Tools for Imaging RNA in Live Mammalian Cells. *Cell Chem. Biol.* **2020**, *27*, 891–903. [CrossRef]
3. Tomoike, F.; Abe, H. RNA imaging by chemical probes. *Adv. Drug Deliv. Rev.* **2019**, *147*, 44–58. [CrossRef]
4. Jullien, L.; Gautier, A. Fluorogen-based reporters for fluorescence imaging: A review. *Methods Appl. Fluoresc.* **2015**, *3*, 042007. [CrossRef] [PubMed]
5. Klymchenko, A.S. Solvatochromic and Fluorogenic Dyes as Environment-Sensitive Probes: Design and Biological Applications. *Acc. Chem. Res.* **2017**, *50*, 366–375. [CrossRef]
6. Suseela, Y.V.; Narayanaswamy, N.; Pratihari, S.; Govindaraju, T. Far-red fluorescent probes for canonical and non-canonical nucleic acid structures: Current progress and future implications. *Chem. Soc. Rev.* **2018**, *47*, 1098–1131. [CrossRef] [PubMed]
7. Lakowicz, J.R. *Principles of Fluorescence Spectroscopy*, 3rd ed.; Springer: New York, NY, USA, 2006; p. 954. [CrossRef]
8. Wang, Y.-N.; Xu, B.; Qiu, L.-H.; Sun, R.; Xu, Y.-J.; Ge, J.-F. Viscosity sensitive fluorescent dyes with excellent photostability based on hemicyanine dyes for targeting cell membrane. *Sens. Actuators B* **2021**, *337*, 129787. [CrossRef]
9. Cao, J.; Hu, C.; Liu, F.; Sun, W.; Fan, J.; Song, F.; Sun, S.; Peng, X. Mechanism and Nature of the Different Viscosity Sensitivities of Hemicyanine Dyes with Various Heterocycles. *ChemPhysChem* **2013**, *14*, 1601–1608. [CrossRef]

10. Köhler, O.; Jarikote, D.V.; Singh, I.; Parmar, V.S.; Weinhold, E.; Seitz, O. Forced intercalation as a tool in gene diagnostics and in studying DNA–protein interactions. *Pure Appl. Chem.* **2005**, *77*, 327–338. [[CrossRef](#)]
11. Hövelmann, F.; Gaspar, I.; Chamiolo, J.; Kasper, M.; Steffen, J.; Ephrussi, A.; Seitz, O. LNA-enhanced DNA FIT-probes for multicolour RNA imaging. *Chem. Sci.* **2016**, *7*, 128–135. [[CrossRef](#)]
12. Hövelmann, F.; Seitz, O. DNA Stains as Surrogate Nucleobases in Fluorogenic Hybridization Probes. *Acc. Chem. Res.* **2016**, *49*, 714–723. [[CrossRef](#)]
13. Okamoto, A. ECHO probes: A concept of fluorescence control for practical nucleic acid sensing. *Chem. Soc. Rev.* **2011**, *40*, 5815–5828. [[CrossRef](#)] [[PubMed](#)]
14. Chou, P.-T.; Martinez, M.L.; Clements, J.H. The observation of solvent-dependent proton-transfer/charge-transfer lasers from 4'-diethylamino-3-hydroxyflavone. *Chem. Phys. Lett.* **1993**, *204*, 395–399. [[CrossRef](#)]
15. Klymchenko, A.S.; Ozturk, T.; Demchenko, A.P. Synthesis of furanochromones: A new step in improvement of fluorescence properties. *Tetrahedron Lett.* **2002**, *43*, 7079–7082. [[CrossRef](#)]
16. Howard, J.J.; Lynch, G.C.; Pettitt, B.M. Ion and solvent density distributions around canonical B-DNA from integral equations. *J. Phys. Chem. B* **2011**, *115*, 547–556. [[CrossRef](#)]
17. Barthes, N.P.F.; Gavvala, K.; Dziuba, D.; Bonhomme, D.; Karpenko, I.A.; Dabert-Gay, A.S.; Debayle, D.; Demchenko, A.P.; Benhida, R.; Michel, B.Y.; et al. Dual emissive analogue of deoxyuridine as a sensitive hydration-reporting probe for discriminating mismatched from matched DNA and DNA/DNA from DNA/RNA duplexes. *J. Mater. Chem. C* **2016**, *4*, 3010–3017. [[CrossRef](#)]
18. Kucherak, O.A.; Richert, L.; Mély, Y.; Klymchenko, A.S. Dipolar 3-methoxychromones as bright and highly solvatochromic fluorescent dyes. *Phys. Chem. Chem. Phys.* **2012**, *14*, 2292–2300. [[CrossRef](#)] [[PubMed](#)]
19. Fantoni, N.Z.; El-Sagheer, A.H.; Brown, T. A Hitchhiker's Guide to Click-Chemistry with Nucleic Acids. *Chem. Rev.* **2021**, *121*, 7122–7154. [[CrossRef](#)] [[PubMed](#)]
20. Amblard, F.; Cho, J.H.; Schinazi, R.F. Cu(I)-catalyzed Huisgen azide-alkyne 1,3-dipolar cycloaddition reaction in nucleoside, nucleotide, and oligonucleotide chemistry. *Chem. Rev.* **2009**, *109*, 4207–4220. [[CrossRef](#)]
21. Le, H.-N.; Zilio, C.; Barnoin, G.; Barthes, N.P.F.; Guignon, J.-M.; Martinet, N.; Michel, B.Y.; Burger, A. Rational design, synthesis, and photophysics of dual-emissive deoxyadenosine analogs. *Dyes Pigments* **2019**, *170*, 107553. [[CrossRef](#)]
22. Dziuba, D.; Benhida, R.; Burger, A. A Mild and Efficient Protocol for the Protection of 3-Hydroxychromones Under Phase-Transfer Catalysis. *Synthesis* **2011**, *47*, 2159–2164. [[CrossRef](#)]
23. Kolb, H.C.; Finn, M.G.; Sharpless, K.B. Click Chemistry: Diverse Chemical Function from a Few Good Reactions. *Angew. Chem. Int. Ed.* **2001**, *40*, 2004–2021. [[CrossRef](#)]
24. Dean, F.M.; Podimuang, V. 737. The course of the Algar–Flynn–Oyamada (A.F.O.) reaction. *J. Chem. Soc.* **1965**, 3978–3987. [[CrossRef](#)]
25. Nemkovich, N.A.; Baumann, W.; Pivovarenko, V.G. Dipole moments of 4'-aminoflavonols determined using electro-optical absorption measurements of molecular Stark-effect spectroscopy. *J. Photochem. Photobiol. A* **2002**, *153*, 19–24. [[CrossRef](#)]
26. Klymchenko, A.S.; Demchenko, A.P. Electrochromic Modulation of Excited-State Intramolecular Proton Transfer: The New Principle in Design of Fluorescence Sensors. *J. Am. Chem. Soc.* **2002**, *124*, 12372–12379. [[CrossRef](#)]
27. Ivancová, I.; Leone, D.-L.; Hocek, M. Reactive modifications of DNA nucleobases for labelling, bioconjugations, and cross-linking. *Curr. Opin. Chem. Biol.* **2019**, *52*, 136–144. [[CrossRef](#)] [[PubMed](#)]
28. Ormson, S.M.; Brown, R.G.; Vollmer, F.; Rettig, W. Switching between charge- and proton-transfer emission in the excited state of a substituted 3-hydroxyflavone. *J. Photochem. Photobiol. A* **1994**, *81*, 65–72. [[CrossRef](#)]
29. Dziuba, D.; Didier, P.; Ciaco, S.; Barth, A.; Seidel, C.A.M.; Mély, Y. Fundamental photophysics of isomorphous and expanded fluorescent nucleoside analogues. *Chem. Soc. Rev.* **2021**, *50*, 7062–7107. [[CrossRef](#)]
30. Hainke, S.; Seitz, O. Binaphthyl-DNA: Stacking and Fluorescence of a Nonplanar Aromatic Base Surrogate in DNA. *Angew. Chem. Int. Ed.* **2009**, *48*, 8250–8253. [[CrossRef](#)]
31. Armarego, W.L.F.; Chai, C.L.L. *Purification of Laboratory Chemicals*, 8th ed.; Butterworth-Heinemann: Oxford, UK, 2017; p. 1024. [[CrossRef](#)]
32. Still, W.C.; Kahn, M.; Mitra, A. Rapid chromatographic technique for preparative separations with moderate resolution. *J. Org. Chem.* **1978**, *43*, 2923–2925. [[CrossRef](#)]
33. Fulmer, G.R.; Miller, A.J.M.; Sherden, N.H.; Gottlieb, H.E.; Nudelman, A.; Stoltz, B.M.; Bercaw, J.E.; Goldberg, K.I. NMR Chemical Shifts of Trace Impurities: Common Laboratory Solvents, Organics, and Gases in Deuterated Solvents Relevant to the Organometallic Chemist. *Organometallics* **2010**, *29*, 2176–2179. [[CrossRef](#)]
34. Wulff, G.; Akelah, A. Enzyme-analogue built polymers, 6. Synthesis of 5-vinylsalicylaldehyde and a simplified synthesis of some divinyl derivatives. *Die Makromol. Chem.* **1978**, *179*, 2647–2651. [[CrossRef](#)]
35. Kolganova, N.A.; Florentiev, V.L.; Chudinov, A.V.; Zasedatelev, A.S.; Timofeev, E.N. Simple and stereoselective preparation of an 4-(aminomethyl)-1,2,3-triazolyl nucleoside phosphoramidite. *Chem. Biodivers.* **2011**, *8*, 568–576. [[CrossRef](#)] [[PubMed](#)]
36. Štimac, A.; Kobe, J. Stereoselective synthesis of 1,2-cis- and 2-deoxyglycofuranosyl azides from glycosyl halides. *Carbohydr. Res.* **2000**, *329*, 317–324. [[CrossRef](#)]
37. Hövelmann, F.; Gaspar, I.; Ephrussi, A.; Seitz, O. Brightness Enhanced DNA FIT-Probes for Wash-Free RNA Imaging in Tissue. *J. Am. Chem. Soc.* **2013**, *135*, 19025–19032. [[CrossRef](#)] [[PubMed](#)]
38. Reichardt, C. Solvatochromic dyes as solvent polarity indicators. *Chem. Rev.* **1994**, *94*, 2319–2358. [[CrossRef](#)]

Conclusion

L'ensemble des études, par hybridation directe, de brins marqués par des chromones méthoxylées (**AzMF**, **AIMF**, **AzMF+**, **AIMF-**, **AIMF+-**) ont montré que dans tous les cas, l'hybridation à l'AN complémentaire conduit à un effet fluorogénique, passant d'un système éteint pour le simple brin (pas ou peu de fluorescence) à un système allumé (fluorescence) après hybridation. Cet effet repose sur le fait que la sonde est sensible à la variation de la polarité du milieu qui l'entoure. Dans le cas d'un environnement aqueux, le système est éteint (simple brin) puis, lors de l'hybridation, le marqueur se retrouve dans un milieu plus hydrophobe, ce qui induit sa fluorescence. Grâce à cette méthode, une augmentation d'un facteur 13 du signal de fluorescence est obtenue.

Au contraire, nous avons observé que dans le cas du dérivé hydroxychromone **TdEAF**, le rendement quantique est élevé dans le simple brin, indépendamment des bases qui l'entourent et, de surcroît, reste inchangé lors de l'hybridation. C'est une propriété rarement observée pour les sondes fluorescentes couplées à l'ADN. Cette propriété nous a permis de construire un système FRET fiable, qu'importe la séquence de l'oligonucléotide utilisée. Ce comportement n'est pas observé avec les sondes méthoxychromones.

Par exemple, lorsque le fluorophore est couplé sur une position terminale, le rendement quantique chute systématiquement après hybridation du simple brin avec sa séquence complémentaire (**Y** ou **V**). Par ailleurs, notre étude a également montré que lorsque le résidu marqué est positionné en milieu de séquence, et que le lien entre le fluorophore et l'ODN est soit très court (**W**), soit plus long (**X**), le signal de fluorescence est accru après hybridation. Lorsque le lien reliant l'ODN et le fluorophore est de longueur intermédiaire (**Xs**, **Z**), il n'est pas assez flexible pour permettre la bonne interaction avec le double brin. Ces résultats montrent l'importance de la nature du lien et de la position de marquage sur les propriétés de photo-physique de la sonde. Grâce à ces précieux résultats, nous avons été en mesure de mieux conduire les projets suivants, concernant l'élaboration de nouveaux fluorophores.

Chapitre 3 : Hybridation
fluorogénique par *molecular*
rotor

I. Chromone rotor

Publication 3

Au cours des études concernant les sondes de type « méthoxychromone » décrites dans la publication 2, j'ai eu l'occasion de développer une sonde comportant un groupement donneur thiophène (6-EMT, **Figure 62A**). Les études photophysiques ont révélé qu'à l'opposé de ses semblables, cette sonde possédait un rendement quantique très faible dans tous les solvants, même les plus apolaires (<1% dans le THF), tout en conservant un déplacement de Stokes conséquent de 140nm. Cependant, nous avons noté que dans les solvants les plus visqueux (Butanol *e.g.*), les rendements quantiques sont légèrement supérieurs (3,7% dans le BuOH). Après une titration méthanol/glycérol, il s'est révélé que le rendement quantique augmentait fortement avec la hausse croissante de glycérol. Cette propriété est le propre des sondes de type *molecular rotor* (cf. **Chapitre 1 : II.1.3.** p.32).

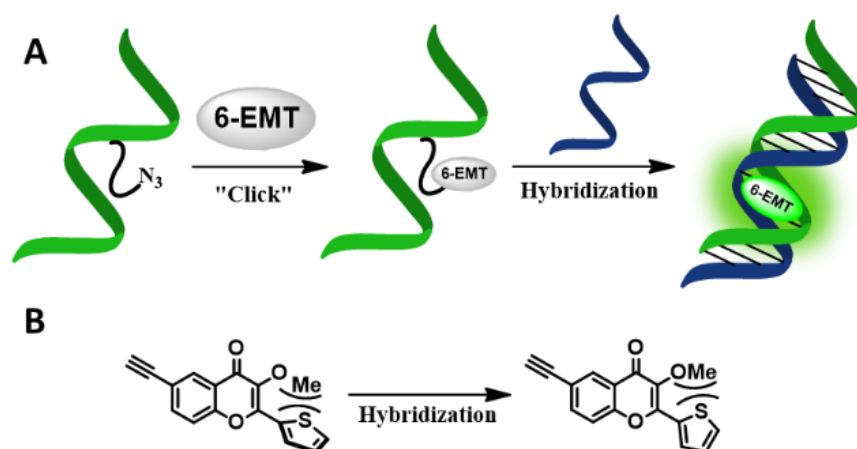


Figure 62. A) Représentation schématique de l'hybridation fluorogénique de l'ODN. B) Effet de rotation du groupement thiophène suite à l'intercalation pour retrouver une planéité et ainsi de la fluorescence.

Cette propriété nous a poussés à incorporer cette sonde dans différentes séquences d'ODNss, suivant la stratégie post-synthétique (**Figure 62A**). Pour ce faire, nous avons synthétisé la sonde fonctionnalisée par un groupement alcyne, que nous avons ensuite « clickée » sur des séquences d'ODN commerciales fonctionnalisées par un groupement azoture, en position 5'-terminale (**Figure 63**, type **Y**) ou en milieu de séquence de l'ODN (**Figure 63**, types **X** et **Xs**).

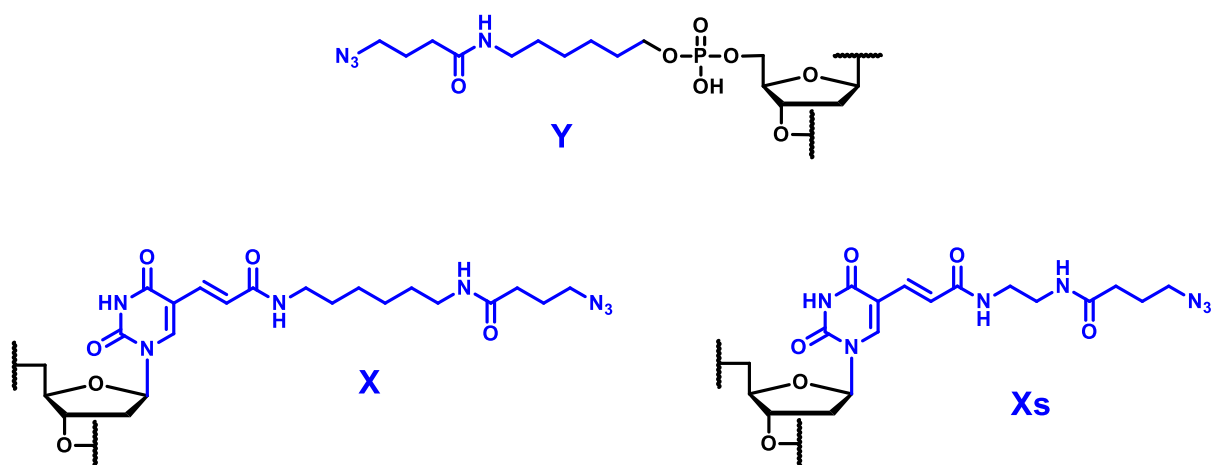


Figure 63. Structure des liens click sur l'ODN.

Nous avons ensuite étudié photophysiquement l'hybridation des séquences marquées par **6-EMT** avec leur cible complémentaire (Figure 62B) : une amplification du signal de fluorescence pourrait alors signifier que la sonde **6-EMT** s'intercale entre deux plateaux de bases des duplexes.

De façon identique aux sondes dérivées de **3-MC**, précédemment décrites, seul le marquage de type **X** produit une amplification du signal de fluorescence d'un facteur 10, que nous attribuons à un aplanissement de la sonde à la suite de l'intercalation dans le duplexe. Comme les résultats des dérivés de **3-MC** le laissaient prévoir, les marquages de type **Y** et **Xs** n'ont pas permis une amplification significative du signal de fluorescence.

Le marquage, au milieu d'une séquence d'ODN, via un lien de type **X** pourrait donc être généralisé à tout type de sondes intercalantes et à tout type de séquences d'ODN, la sonde devant être positionnée entre deux résidus Thymine pour obtenir la meilleure réponse fluorogénique lors de l'hybridation.

Les résultats de ce travail sont décrits en détail dans l'article suivant, actuellement en soumission au journal ChemPlusChem.

A Fluorogenic Covalent Chromone-Based Intercalator with a mega-Stokes Shift for Sensing DNA Hybridization

Steve Vincent, Suman Mallick, Guillaume Barnoin, Hoang-Ngoan Le, Alain Burger,* and Benoît Y. Michel*[a]

Dedicated to Prof. Dr. Jean-François Gal on the occasion of his 77th birthday

[a] S. Vincent, Dr. S. Mallick, Dr. G. Barnoin, Dr. H.-N. Le, Prof. Dr. A. Burger, and Dr. B. Y. MICHEL
 Institut de Chimie de Nice, CNRS UMR 7272
 Université Côte d'Azur
 Parc Valrose, 06108 Nice cedex 2, France
 E-mails: burger@univ-cotedazur.fr; benoit.michel@univ-cotedazur.fr

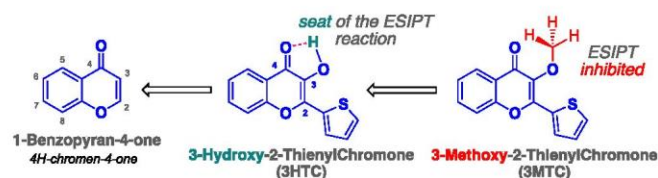
Part of a Special Collection "Institute Feature" commemorating the 10th anniversary of the Institut de Chimie de Nice (ICN)
 Supporting information for this article and the ORCID identification numbers of authors are available on the WWW under

Abstract: Forced intercalation (FIT) probes have proven to be reliable, rapid, inexpensive and accurate method for the detection and visualization of specific nucleic acid sequences. Accommodation of a rationally designed chromone-based fluorogen within a double-stranded DNA structure was investigated by UV-Vis spectrophotometry and steady-state fluorescence spectroscopy under physiological pH conditions. After selective excitation matching with the 350-nm laser, the intrinsically negligible fluorescence of the tethered electroneutral label in a single-stranded context was 10-fold increased upon duplex formation. This fluorescence enhancement is also accompanied by a mega-Stokes shift (~100 nm) placing the emission in the cyan color range; both features being appreciable for bio-imaging purposes. In a nutshell, its fluorogenic behavior and its marginal impact on the double helix make this dye a prospective tool for selectively sensing sequences of interest with a remarkable ON/OFF contrast.

Introduction

Chromone dyes belong to the family of flavonoids—which are a group of plant secondary metabolites—found in vascular plants such as ferns and flowering plants.^[1] 1-Benzopyran-4-one is the core fragment common to all flavones, which are considered a class of natural dyes (Scheme 1).^[2] Flavone derivatives with a hydroxyl group at the 3-position of the heterocycle are called 3-hydroxychromones (3HCs).^[3] These have been widely studied in the last decades because of their atypical photophysical properties.^[4] Indeed, 3HCs are ratiometric fluorescent dyes presenting a well-resolved dual emission resulting from two excited species—the normal form (N*) and its tautomer (T*)—obtained after an excited-state intramolecular proton transfer (ESIPT) reaction.^[5] It is noteworthy that the intensity ratio of these two-color fluorophores is extremely sensitive to environmental changes and their N* band exhibits remarkable solvatochromism over a wide range of polarity.^[6] In our group, we have synthesized a library of 3HC derivatives over the past few years, extensively investigated their photophysics, and explored a variety of nucleic acid (NA)-related applications.^[7] These advanced probes allowed us to overcome several bottlenecks encountered with currently used biosensors for NA labeling.^[8] After a proof of concept of the 3HC efficiency for

internal DNA labeling,^[9] this nucleobase replacement strategy was applied to preliminary mechanistic studies of DNA repair involving base excision.^[10] The mechanism of DNA methylation involving as a key step, the 5mC eversion by a chaperone protein UHRF1 was also studied with this two-color reporter.^[11] Both examples of this two-band fluorescence-based approach attested to the outstanding sensitivity of this nucleobase surrogate to small structural changes accompanying base flipping, while the structure of the duplex and its protein affinity were marginally affected, as subsequently confirmed.^[12] Recently, we engineered an efficient synthetic access to DNA major groove labeling by electronically compiling a 3HC fluorochrome onto deoxyadenosine and uridine moieties.^[13]



Scheme 1. Numbering and general structures of the chromone scaffold involved in the present study.

Labeling a NA by means of emissive dyes to establish a fluorescent probe has been an active area of research in modern chemical biology for accurately sensing and localizing sequences of interest within cells.^[14] Fluorescence is the technique of choice due to its non-invasive nature, exquisite sensitivity and simplicity of implementation.^[15] To advance this research field, a variety of probes have been developed such as FRET-based binary probes and molecular beacons,^[16] reactive probes,^[17] ECHO probes,^[18] molecular rotors,^[19] and forced intercalation (FIT) probes.^[20] Of these, fluorogenic FIT-probes shows a marked enhancement of fluorescence upon sequence-specific hybridization.^[21] This turn-on is mainly due to steric changes in the vicinity of the reporter which will prevent the free rotation of the scaffold around a strategic single bond and thus force the system to adopt a planar conformation capable of fluorescing.^[20a] Note that fluorogenic hybridization probes are also very useful for imaging NA in living cells, where distinguishing unbound and bound probes is almost impossible.^[22]

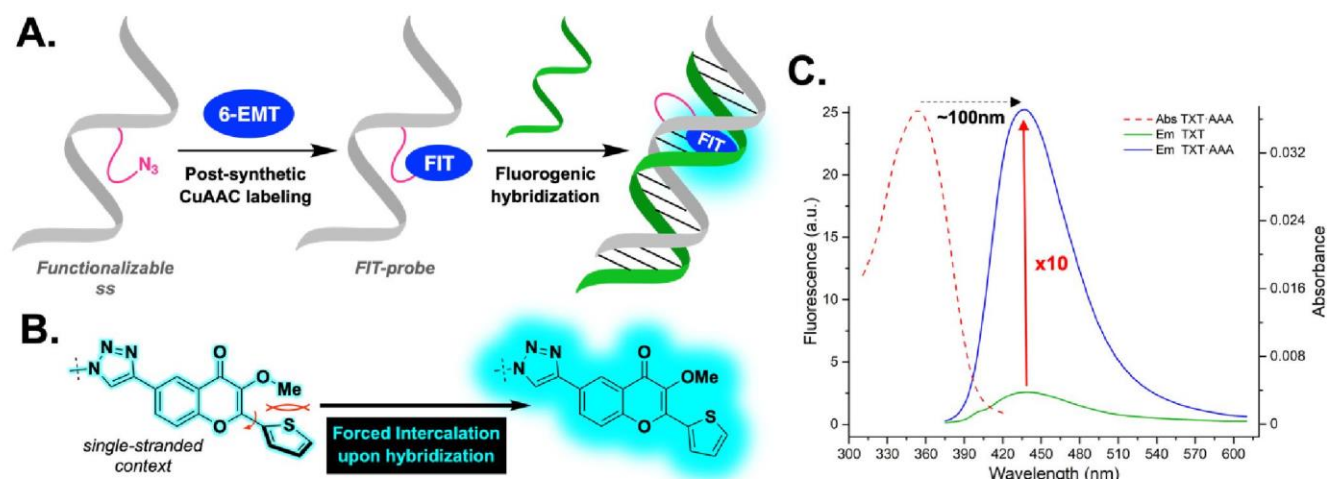


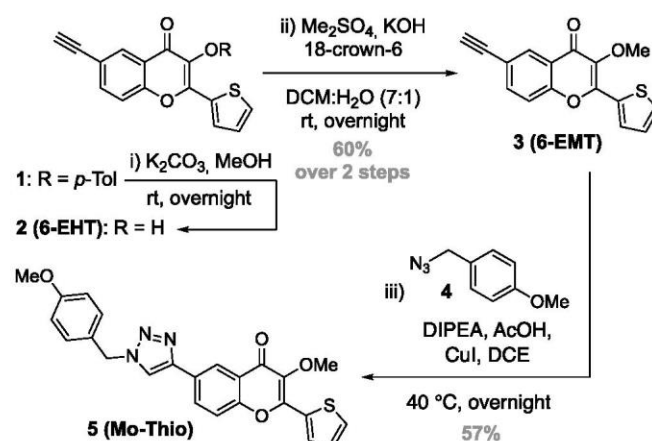
Figure 1. (A) Schematic representation of the operating principle of the developed FIT-probe to specifically sense a sequence by hybridization. (B) Zoomed in on the 6-EMT reporter clicked on a single strand to shed light on the forced intercalation at the molecular level. (C) Photophysical channels of information through which fluorogenic detection occurs.

Literature data show that a planar aromatic moiety, associated with a cationic group, is required for efficient intercalation into the polyanion that is DNA.^[23] Several classes of dyes, such as phenanthridine derivatives, thiazole orange (TO) analogs and cyanines have been developed on the basis of the above prerequisites and successfully applied to detect NA in the cells, as well as in real-time polymerase chain reaction (PCR).^[24] Much less attention has been paid to the development of fluorescent covalent intercalators that are electrically neutral, sensitive to the local environment, and derived from natural small dyes.^[25] In addition to the ability to substantially increase their fluorescence intensity upon intercalation, such size-controlled emitters could minimize duplex destabilization.^[26] Herein, we report the synthesis and spectroscopic features of a novel 3HC-based FIT-probe, which is small,^[27] electroneutral, easy to chemically conjugate with functionalized ODNs. After screening different parameters such as the nature of the linker and its location, a single-stranded FIT-probe was eventually identified as promising upon hybridization, since it demonstrated a 10-fold fluorescence enhancement accompanied by a mega-Stokes shift placing the emission in the cyan region (Figure 1).

Results and Discussion

Molecular design and synthesis. Engineering a new fluorogenic probe with robust photophysical properties in aqueous media is a great challenge.^[28] The most common approach—which has proven particularly successful so far—is to modify the structure of well-known dye families.^[29] To produce a novel fluorescence turn-on FIT dye based on a 3HC platform to be used for labeling NA, the fluorochrome must be able to be easily connected to ODNs through a linker of variable size and flexibility that can ultimately allow its adequate incorporation into the duplex. Moreover, the fluorophore must exhibit a strong change in emission intensity during hybridization.

Keeping these requirements in mind, the 6-EMT label was proposed, which is composed of a 3-methoxychromone (3MC) core unit branched by two moieties, namely an ethynyl group at position 6 and a 5-membered ring (thiophene) on the 2-position (Figures 1B & Scheme 2). Besides blocking the ESIPT reaction,^[30] the presence of the methyl group was previously shown to affect the planarity of the fluorochrome, and thus quenches the fluorescence of 2-thienyl-3MC.^[13] As the terminal alkyne has little impact on photophysics—because it is not electronically coupled with the acceptor group (4-ketone)—its role is exclusively related to the subsequent labelling of NA by post-synthetic click reaction.



Scheme 2. Synthetic pathway of the fluorogenic tag 6-EMT and the derived model compound Mo-Thio.

Typically, 3HCs are dual emitters that fluoresce only when the aromatic ring at the 2-position is remains coplanar with the rest of the core. The coplanarity of the entire conjugated π -system is therefore essential to achieve a light-on effect. In our case, we used this phenomenon in a reverse manner. We intentionally converted the 3-OH to a methoxy group in order

to increase steric hindrance and push the conjugated thiophene out of the plane, thus becoming a poor fluorophore. The idea behind this being, once clicked to a single-stranded ODN, selective hybridization with a complementary sequence should force the fluorogen to flatten to allow for accommodation; in other words, the thienyl unit would become coplanar with the chromone part, which should result in a dramatic increase in fluorescence intensity (Figures 1A&B).

The synthesis strategy of **3** (**6-EMT**) was similar to that commonly used for our developed 3HC derivatives.^[13b] Namely, a Claisen-Schmidt condensation in alkaline medium providing the corresponding chalcone which undergoes, in the same reaction pot, an oxidative cyclization according to an Algar-Flynn-Oyamada mechanism,^[31] affording the 3HC scaffold. For subsequent click-type post-functionalizations,^[32] the incorporation of an alkyne moiety, with no significant effect on photophysics, was paramount.^[30a] The ethynyl unit was introduced at position 6 by a classical sequence composed of a Sonogashira coupling in the presence of TMS-acetylene, followed by a cleavage of the silyl group with a fluoride source, leading to our starting point **1**, the 3-protected chromone.^[13b] Ester removal under transesterification conditions yielded **2** (**6-EHT**).

The synthetic route to the **6-EMT** label—consisting of the protection of the 3-OH group via an in-house methylation procedure using phase transfer conditions^[33]—is depicted in Scheme 2. The derived model compound **5** (**Mo-Thio**), on the other hand, is prepared by a standard Cu(I)-catalyzed azide-alkyne cycloaddition (CuAAC) protocol from **4**.^[30a] Since this conjugate closely resembles the final fluorescent system once clicked onto the ODN, the study of its photophysics should allow to mimic that of the single-stranded probe, thus providing essential information.

Photophysical properties of Mo-Thio. Our spectroscopic investigations first started with the clickable **6-EMT** tag. The extinction coefficient, which is required to estimate the brightness of the marker, was determined in THF ($\epsilon = 23,200 \text{ L}\cdot\text{mol}^{-1}\cdot\text{cm}^{-1}$) and is in line with our expectations considering similar reported 3HC derivatives.^[34]

Once covalently bound to the ODN, the clicked label will be in a more or less hydrated environment.^[35] In order to better understand its optical behavior in water, a titration of **Mo-Thio**—the derived clicked tag—was performed by adding an incremental amount of water to a THF solution (Figure S1 in the Supporting Information). This experiment revealed a 20-nm bathochromic shift on the emission, which is typical of a dye with a moderate push-pull relationship (confers the electronic conjugation between the endocyclic oxygen and the 4-ketone, respectively donor and acceptor). As attested by the observed hypochromism and midband broadening, solubility issues occurred beyond 60% and led to the formation of H-aggregates^[36] that do not reflect the reality in an oligonucleotide context. The photostability of **Mo-Thio** was also checked before proceeding with the solvent spectroscopic study.^[37] Due to the inhibition of its ESIPT reaction, the dye retains almost 95% of its initial emission intensity after one hour of continuous irradiation. This result is similar to those already reported for the 3-methoxychromones^[30a,b] and compares favorably with Prodan^[38]—the reference push-pull chromophore—and very

clearly with **dMAF**, the methyl group-free 3HC (Figure S2 in the Supporting Information).

Next, the photophysical properties (UV-Vis absorption and fluorescence) of **Mo-Thio** were investigated in detail in a set of eleven solvents varying in polarity. Four protic (hexafluoroisopropanol, methanol, ethanol, *n*-butanol) and six aprotic (acetonitrile, DMF, dichloromethane, ethyl acetate, THF, toluene) solvents were selected (Table 1) and ranked using the empirical Reichardt scale; this polarity index taking into account the H-bonding solvent ability.

Table 1. Spectroscopic features of **Mo-Thio**.

Solvent ^[a]	$E_T^N(30)^{[b]}$	$\lambda_{\text{Abs}}^{[c]}$	$\lambda_{\text{Em}}^{[c]}$	Φ (%) ^[e]
HFIP	1.07	352	435	4.1
MeOH	0.76	342	442	2.1
EtOH	0.65	342	437	2.4
BuOH	0.59	343	432	3.7
CH ₃ CN	0.46	335	456	0.7
DMF	0.39	339	457	1.6
CH ₂ Cl ₂	0.31	339	454	1.1
EtOAc	0.23	333	448	0.4
THF	0.21	335	449	0.8
Toluene	0.10	338	453	0.9

[a] Due to the lack of solubility of the considered fluorophore, water was not considered in this study. [b] Normalized Reichardt's empirical solvent polarity index.^[39] [c,d] Positions of the absorption and emission band maxima, respectively. [e] Quantum yields were determined using 4'-(*N,N*-dimethylamino)-3-hydroxyflavone (**dMAF**) in EtOH ($\lambda_{\text{Ex}} = 407 \text{ nm}$, $\Phi = 27\%$) as a standard.^[40]

The **Mo-Thio** conjugate shows a single absorption band centered at 338–365 nm (Figure 2). The position of the absorption maxima does not correlate properly with the solvent polarity, but nevertheless exhibits slightly positive solvatochromism. Since this fluorophore is not a prominent push-pull dye with significant charge transfer, the solvatofluorochromism is expected to be weak. The absorptivity was found to be similar to that of the parent compound, as the new triazole connecting linker is not directly in conjugation with the push-pull relationship operating within the chromophore.

As for the emission maxima, they oscillate in the range 432–453 nm (Figure 2), without displaying any notable solvatochromism, which attests to the poor push-pull character of this clicked dye. In protic media, the single emission band appears rather broad and quantum yields are admittedly low (2.1–4.1 %) but remain higher than in aprotic solvents (0.4–1.6 %). Note that in non-protogenic medium, two emission bands seem to emerge from the background noise, this could be due to the emission of different twisted excited forms.

Interestingly, the emission signal is strongest ($\Phi = 4.1 \%$) in HFIP, which is the most viscous solvent, thus restraining molecular rotation. This hypothesis was further supported by

carrying out a titration experiment with an increasing concentration of glycerol in a methanolic solution of the dye. When the amount of glycerol in the medium was increased from 10 to 50%, the quantum yield more than doubled (8 to 17%, Figure S3 in the Supporting Information). Additionally, as HFIP is an organic solvent which is more polar than water, it has the crucial advantage of perfectly solubilizing the fluorochrome avoiding that it aggregates and therefore constitutes an excellent observation model.

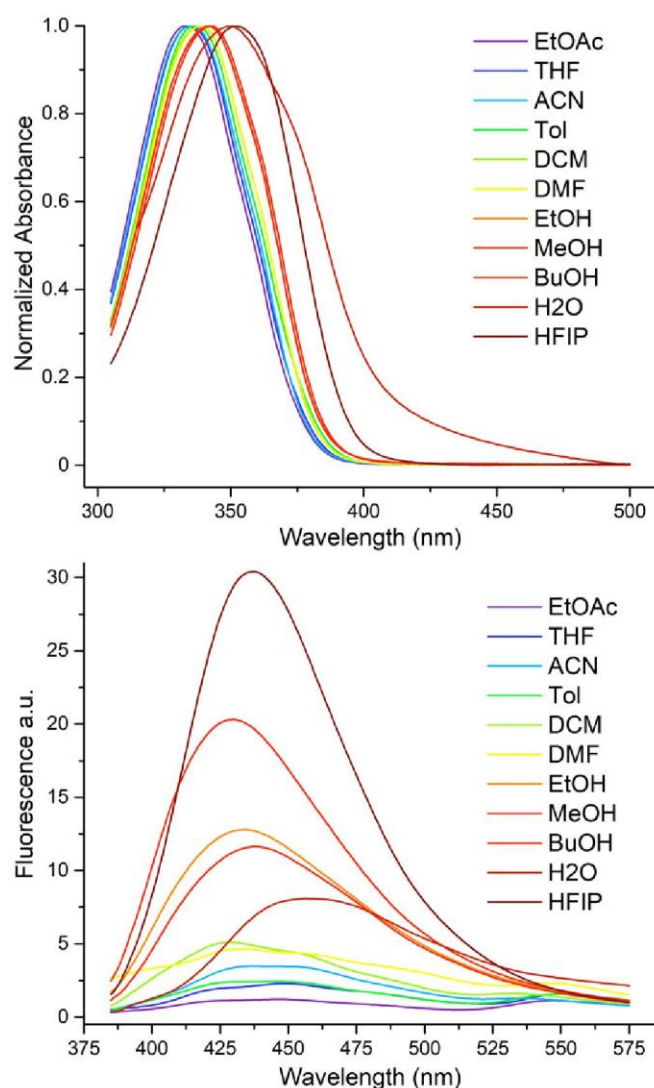


Figure 2. Absorbance (*top*) and fluorescence (*bottom*) observables of Mo-Thio in a set of solvents varying in polarity.

In summary, the fluorescence signal both in form and intensity is markedly different between protogenic and aprotic solvents. It seems that for protic media, H-bonds play a crucial role in stabilizing the excited state, which after charge redistribution is usually more polar than the ground state. This trend is less pronounced for HFIP, where its steric hindrance may affect H-bonding. Hydration studies were also performed, and their results are substantially similar to those of the parent core (Figure S1 in the Supporting Information). This is practically a tailor-made situation for our research project, as

this dye exhibits the strongest emission in an environment that is somewhat different from bulk water, precisely more viscous i.e., with restricted rotational movements; an environment typical of what FIT probes encounter when accommodated in a double-stranded DNA. Although this fluorophore does not display a large charge transfer, Stokes shifts vary over the range 83–100 nm in the presence of protic solvents and become “mega” (viz. >100 nm) in aprotic media. Since the emission is centered in the turquoise region (ca. 450 nm), this allows filtering out the residual autofluorescence signal from biomolecules, while using this reporter to detect NA.

Spectroscopic features of labeled ODNs. For the preparation of the single-stranded probes, 15-mer ODNs modified with azide-functionalized linkers (more or less long) were selected. The **6-EMT** tag was then efficiently conjugated via a CuAAC post-synthetic labeling procedure described previously (Tables S1 and S2 in the Supporting Information).^[30a] The composition of the sequences employed and the structure of the linkers are depicted in Table 2. The code is as follows: **X** and **Xs** represent the dye clicked onto a central uridine with a long and shorter linker, respectively; **Y** is a flexible spacer for 5'-conjugation. Thus, different locations (middle vs. terminal positions) were explored to evaluate the ability of the label to accommodate, intercalate or stack with the neighboring base pairs in a ds-context. For that purpose, the 3 labeled sequences (**TXT**, **TXsT** & **YGCA**) were selectively hybridized with their complementary strand and the corresponding photophysics was reported in Table 3.

Table 2. Azide-functionalized ODNs used for post-synthetic fluorescent labeling with the **6-EMT** tag.

Sequence ^[a]	Functionalization (Y , X , & Xs)
5'- YGCA AAA TTT AAA ACG-3'	
5'-GCA AAA TXT AAA ACG-3'	
5'-GCA AAA TXsT AAA ACG-3'	

[a] Regarding the sequence editing, only the codon—on which the modification allowing labeling is located—was bolded and will be used further to name the strand.

The first observation that can be made, is at the level of the absorption domain (Figure S5 in the Supporting Information). It appears clearly that in two of the three cases (**TXT** & **YGCA**), the absorption maximum remains unchanged after hybridization ($\Delta\lambda = 0\text{--}4$ nm). It seems that the marker is in a very hydrated environment in a ss-context ($\lambda_{\text{Abs}} \approx 350$ nm similar to that of HFIP and water). Only the short linker seems to have the appropriate size to allow the electroneutral and hydrophobic dye to shield from water ($\lambda_{\text{Abs}} \approx$ that of EtOH). Thus, after hybridization, the fluorescent tag will intercalate in

the double strand and will undergo a 10-nm bathochromic shift, which is commonly reported for flat intercalating dyes.^[41] This is also confirmed by the position of the emission maxima which are around 436 nm, typical of a less hydrated environment (Figure S1).

Table 3. Photophysical features of labeled ss- and ds-ODNs.

ODN	$\lambda_{\text{Abs}}^{[a]}$	$\lambda_{\text{Em}}^{[b]}$	Φ (%) ^[c]
YGCA	352	437	1.2
YGCA·CGT	352	434	0.9
TXT	352	439	1.1
TXT·AAA	356	437	10.9
TXsT	343	435	1.9
TXsT·AAA	354	435	6.6

[a-c] As in Table 1.

The single-stranded sequences were poorly emissive, with quantum yields ranging from only 1.1 to 1.9%. After duplex formation with the complementary sequence, QY increased significantly to ~11% for **TXT** (embedding the longer linker) and ~7% for **TXsT** (the shorter one), while Φ remained almost unchanged for the **YGCA** sequence where the reporter is attached to the 5'-terminus (Figure 3). These differences can be rationally explained because when the linker is longer, the label has more flexibility to fold and thus properly intercalate into the DNA double helix. For the shorter linker, the intercalation was less efficient because of the degree of freedom of the side chain which is less important. As for the 5'-labeling, it seems that there is no intercalation. π -stacking with the last base plate cannot be ruled out; however, if so, it would not be sufficient to constrain the fluorogen and cause a turn-on of its emission.

To sum up, the duplex intercalation in the **TXT** context effectively screens the dye from bulk water and provides a much more constrained environment where rotational motions are limited. Hence, it explains the observed fluorogenic character, viz. a 10-fold fluorescence enhancement in emission intensity, as evidenced by the bright cyan light-on of the cuvette inserts (Figure 3).

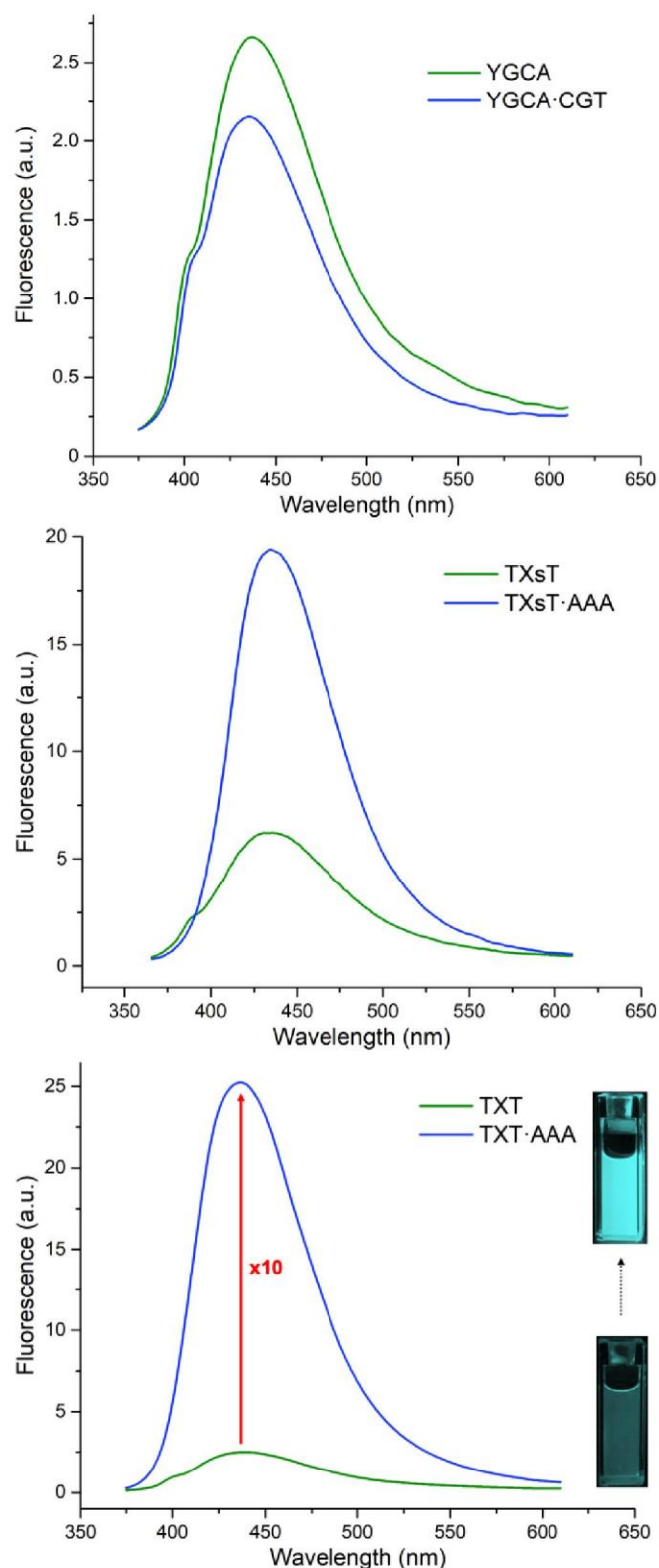


Figure 3. Emission spectra of the 3 ss-probes and their corresponding ds-constructs.

It is well known in the literature that a nucleobase modification based on a flexible spacer arm will affect the stability of the duplex.^[7] Thermal denaturation studies were then performed to evaluate the impact of the clicked fluorogen

on duplex integrity. To this end, the labeled sequences were annealed with their complementary strand and the duplex melting temperatures were compared to that of the corresponding wild-type duplex (Table 4 and Figure S6). It is clear that the azido spacer itself has a 2–4 °C impact on the stability of the double strand.^[30a] Nevertheless, once the dye is conjugated to it, the influence is not the same depending on the positioning of the reporter on the strand. When the probe is in the middle of the sequence, a moderate impact is observed ($\Delta T_m = 5\text{--}7$ °C), but when the aromatic sensor is at the 5'-end, a stabilization takes place (+1 °C). This supports the idea that a π -stacking occurs and as reported for cyanines,^[42] its hydrophobic interaction with the terminal base pair stabilizes the system.

Another proof, admittedly by the absurd, but which correlates our previous statement on the capacity of the spacer arm to allow accommodation. Indeed, it is noteworthy that when the flexible tether is longer, the destabilization is less. This corroborates in an indirect way that the folding and consequently the intercalation is better and destabilizes the system less when the flexibility of the linker is greater.

Overall, we can conclude that the labeling effect is rather reasonable. Our DNA study systems are therefore perfectly matched at room temperature.

Table 4. Thermal denaturation analyses of the ds-constructs (ds-ODNs) labeled with **6-EMT**.

Sequence	T_m (°C)		
	6-EMT	Wild-Type ^[b]	ΔT_m ^[a]
YGCA ·CGT	46.7	45.9	+ 0.8
TXT ·AAA	40.7	45.9	– 5.2
TXsT ·AAA	39.1	45.9	– 6.8

[a] T_m of the corresponding duplex formed from unmodified ODNs. [b] ΔT_m refers to the difference of T_m between the labeled and canonical ds-ODNs.

Maintenance of the B conformation of the resulting labeled duplexes was confirmed by circular dichroism. A spectral signature clearly overlaps with that of the wild-type ds-structure, evidencing that there is no disruption of the helical conformation by fluorogen accommodation and thus attesting to the integrity of the double helix (Figure S7 in the Supporting Information).

Conclusion

In a nutshell, a novel chromone-based fluorogenic probe was engineered to detect DNA hybridization. Detailed spectroscopic studies were conducted on a model substrate to define and better understand the sensor photophysics using UV–Vis absorption and fluorescence spectroscopies. The poorly fluorescent **6-EMT** tag was then employed to label ODNs functionalized with different azido-tethers using a post-synthetic click-type strategy. After screening, a single-stranded probe demonstrated a 10-fold increase in fluorescence intensity upon hybridization with its complementary sequence. The forced intercalation of this fluorogen, within the DNA duplex, is the trigger for this

remarkable turn-on emission. Although not a traditional push–pull type fluorophore, this dye still exhibits a mega-Stokes shift, making it useful for bio-imaging purposes. This fluorochrome is also highly photostable and showed only marginal destabilization on the double helix. In sum, this chromone-based reporter allows fluorogenic sensing of the double-stranded DNA structure and pave the way for the development of new diagnostic tools based on FIT probes.

Experimental Section

General methods and instruments. All reactions involving air- and water-sensitive conditions were carried out in oven-dried glassware with anhydrous solvents, as well as under argon by using Schlenk techniques employing a dual vacuum/argon manifold system. The synthesis intermediates were initially co-evaporated twice with toluene and dried *in vacuo* before use. All chemical reagents were purchased from commercial sources (Sigma-Aldrich (Saint-Louis, MO, USA), Acros (Geel, Belgium), Alfa Aesar (Heysham, Lancashire, UK)) and were used as supplied. Anhydrous solvents were obtained according to standard procedures.^[43] The reactions were monitored simultaneously by liquid chromatography-mass spectrometry (LC-MS) and thin-layer chromatography (TLC, silica gel 60 F254 plates). Compounds were visualized on TLC plates by both UV radiation (254 and 365 nm) and spraying with a staining agent (phosphomolybdic acid, KMnO_4 or ninhydrin) followed by subsequent warming with a heat gun.^[44] Column chromatography was performed with flash silica gel (40–63 μm) with the indicated solvent system using gradients of increasing polarity in most cases.^[45] All NMR spectra (^1H , ^{13}C and 2D) were recorded on Avance™ 200 or 400 MHz NMR spectrometers (Bruker, Billerica, MA, USA). The ^1H -NMR (200 and 400 MHz) and $^{13}\text{C}\{^1\text{H}\}$ -NMR spectra (50 and 101 MHz, recorded with complete proton decoupling) were obtained with samples dissolved in CDCl_3 with the residual solvent signal used as internal references: 7.26 ppm for CHCl_3 regarding ^1H -NMR experiments and 77.1 ppm for CDCl_3 concerning ^{13}C -NMR experiments.^[46] Chemical shifts (δ) are given in ppm to the nearest 0.01 (^1H) or 0.1 ppm (^{13}C). The coupling constants (J) are given in hertz (Hz). The signals are reported as follows (s = singlet, d = doublet, t = triplet, m = multiplet, br = broad). Assignments of ^1H - and ^{13}C -NMR signals were achieved with the help of D/H exchange, COSY, HMQC, HSQC, NOESY and HMBC experiments (Figures S8–10 in the Supporting Information). LC-MS spectra were recorded using an Esquire™ 3000 Plus ion trap mass spectrometer (Bruker Daltonics, Billerica, MA, USA) equipped with an electrospray ionization (ESI) source in both positive and negative modes (ESI-ITMS). High-resolution mass spectrometry (HRMS) was conducted with a hybrid ion trap-Orbitrap mass spectrometer (Thermo Fisher Scientific, Bremen, Germany)—combining quadrupole precursor selection with high-resolution and accurate-mass Orbitrap detection—using ESI techniques. The systematic flavone nomenclature is used below for the spectral assignment of each synthesized derivative. Wild-type and clickable ODNs were ordered purified and ready-to-use (Microsynth AG, Balgach, Switzerland). Labeled ODNs were analyzed (0.5 mL/min) and purified (2.0 mL/min) by RP-HPLC—including the following apparatus: Waters™ 600 Controller with Waters™ 996 Photodiode Array Detector (Waters, Milford, MA, USA)—using analytical and semi-preparative Clarity® Oligo-RP™ C18 columns with the respective dimensions: 300 × 4.60 mm and 250 × 10 mm, 5- μm particle size, 100 Å (Phenomenex, Torrance, CA, USA). The corresponding gradient system was employed: 100% A (kept 2 min) — (10 min) → 40% A/60% B (kept 2 min) — (2 min) → 10% A/90% B (kept 6 min) — (5 min) → 100% A with A = 0.9 TEAB buffer 100 mM pH 7.8: 0.1 CH_3CN and B = 0.9 CH_3CN : 0.1 TEAB (Figure S4 in the Supporting Information). To prepare a 100mM triethylamine bicarbonate (TEAB) buffer $[(\text{Et}_3\text{NH})\text{HCO}_3]$: pass CO_2 into a 0.1M Et_3N deionized aq. solution until the pH reaches about 7.8 and store at

4 °C. All solvents for absorption and fluorescence experiments were of spectroscopic grade. Absorbance spectra were recorded on a Cary 100 Bio UV–Vis spectrophotometer (Varian/Agilent, Palo Alto, CA, USA) using 500- μ L cuvettes (Hellma, Müllheim, Germany) in Suprasil® quartz (Heraeus, Hanau, Germany) with 1-cm path length. The fluorophore or ODN stock solutions were prepared using dimethylformamide or Milli-Q® water (Merck Millipore, Burlington, MA, USA). The dye sample used for spectroscopic measurements contained $\approx 0.2\%$ (v/v) of the stock solution solvent. Fluorescence measurements were conducted on a FluoroMax 4.0 spectrofluorometer (Jobin Yvon, Horiba, Kyoto, Japan) in a thermostatically controlled cell compartment at 20 ± 0.5 °C with slits open to 2 nm and were corrected for Raman scattering, lamp fluctuations, and instrumental wavelength-dependent bias. Emission spectra were performed with an absorbance of approximately 0.05 at the excitation wavelength corresponding to the absorption maximum of the considered sample, except when specified. Quantum yields were corrected according to the variation of the refractive index of the different solvents. They were determined by comparing the integrated area of the corrected emission spectrum of the sample with that of 4'-(*N,N*-dimethylamino)-3-hydroxyflavone (dMAF, $\lambda_{\text{ex}} = 407$ nm, $\Phi = 27\%$) used as a reference,^[40] with $\pm 10\%$ mean standard deviation. The fluorochromes **6-EMT** and **Mo-Thio** were characterized in duplicate at 10 and 2 μ M, respectively, for UV–Vis and fluorescence measurements. Labeled ss- and ds-ODNs were analyzed in duplicate at 2 μ M in phosphate-buffered saline, pH 7.4 ([P] = 12 mM and [Na] = 170 mM). Preparation of a 2 μ M ODN duplex solution: In a 500- μ L quartz cuvette, sample was prepared by mixing the solutions of the modified ss-ODN (8 μ M, 125 μ L) and its complementary wild-type sequence (8 μ M, 125 μ L) with a PBS solution (250 μ L containing 24 mM sodium phosphate and 300 mM NaCl). To ensure reproducibility of hybridization and therefore measurements, the double-stranded samples were first denatured and then cooled to room temperature. Melting curves were recorded in duplicate in a Peltier-thermostatted cell holder by following the temperature-dependence of absorbance changes at 260 nm of the sample (2 μ M concentration of each strand). The temperature range for the denaturation measurement was 5–80 °C. Speed of heating was 0.3 °C/min. Melting observables were converted to a plot of α versus temperature, where α represents the fraction of single strands in the duplex state. Melting temperatures (T_m) were extracted from these curves after differentiation as reported.^[47] Photostability studies were conducted in a 100- μ L fluorescence cell; excitation and emission slits were set at 8 nm and sample concentrations were 2 μ M. Circular dichroism (CD) experiments were performed at 20 °C on a J-810 spectropolarimeter (JASCO, Tokyo, Japan). The wavelength range for CD measurements was 230–320 nm. Spectra were recorded from samples with a concentration of 2 μ M for each strand. Reported values for the whole photophysical characterization are the average of two or more independent and reproducible measurements; ± 1 nm for wavelengths and ± 0.5 °C for T_m .

Synthesis. 6-Ethynyl-3-hydroxy-2-(thiophen-2-yl)-4H-chromen-4-one (2, 6-EHT): To a stirred solution of **1** (252 mg, 0.65 mmol)^[13b] in CH_2Cl_2 (3.2 mL), a saturated solution of K_2CO_3 in MeOH (3.2 mL) was added. The reaction mixture was stirred at room temperature overnight before being quenched by the addition of a few drops of glacial acetic acid and volatiles were concentrated under reduced pressure. The resulting residue was washed twice with cyclohexane to remove some impurities and then dried to give the crude product **2** (**6-EHT**) as a yellow solid (174 mg, 0.65 mmol, quant.), which was directly engaged in the next step. HRMS (ESI⁺): *m/z* calcd for $\text{C}_{15}\text{H}_9\text{O}_3\text{S}^+$: 269.0267 [M + H]⁺; found: 269.0251.

6-Ethynyl-3-methoxy-2-(thiophen-2-yl)-4H-chromen-4-one (3, 6-EMT): To a stirred solution of **6-EHT** (174 mg, 0.65 mmol, 1 eq.) in CH_2Cl_2 (6.5 mL), were sequentially added 18-crown-6 (85 mg, 10 mol%), a KOH aq. solution (25% w/v, 0.9 mL, DCM/KOH 7:1), and dimethyl sulfate (323 μ L, 3.25 mmol, 5 eq.). The resulting mixture was stirred

overnight at room temperature. After quenching the reaction by addition of H_2O (13 mL), the organic layer was extracted with CH_2Cl_2 (3 \times). The combined organic phases were dried over MgSO_4 , filtered and the volatiles were removed *in vacuo*. The residue was purified by flash chromatography on silica gel eluted with cyclohexane/ethyl acetate (9:1 \rightarrow 1:1, v/v) to afford the desired compound **3** (**6-EMT**) as a yellowish solid (111 mg, 0.39 mmol, 60% over 2 steps). *Rf* = 0.52 (Cyclohexane/EtOAc 3:1). ¹H-NMR (CDCl_3 , 400 MHz): δ 3.07 (s, 1H, HC \equiv C), 4.00 (s, 3H, OCH $_3$), 7.15 (dd, ³*J* = 5.0 Hz, ³*J* = 3.9 Hz, 1H, H β), 7.42 (d, ³*J* = 8.7 Hz, 1H, H8), 7.57 (dd, ³*J* = 5.0 Hz, ⁴*J* = 1.1 Hz, 1H, H γ), 7.67 (dd, ³*J* = 8.7 Hz, ⁴*J* = 2.0 Hz, 1H, H7), 7.88 (dd, ³*J* = 3.9 Hz, ⁴*J* = 1.1 Hz, 1H, H α), 8.30 (d, ⁴*J* = 2.0 Hz, 1H, H5). ¹³C-NMR (CDCl_3 , 101 MHz): δ 59.7 (OCH $_3$), 78.2 (HC \equiv C), 82.0 (HC \equiv C), 118.2 (C8), 119.0 (C6), 124.2 (C10), 127.6 (C β), 129.8 (C α), 129.9 (C5), 131.5 (C3), 131.9 (C γ), 136.6 (C7), 138.7 (C11), 151.8 (C2), 154.5 (C9), 173.2 (C4). HRMS (ESI⁺): *m/z* calcd for $\text{C}_{16}\text{H}_{11}\text{O}_3\text{S}^+$: 283.0423 [M + H]⁺; found: 283.0442.

1-(Azidomethyl)-4-methoxybenzene (4): To a stirred solution of NaN_3 (1.05 g, 16.15 mmol, 2.5 eq.) in DMSO, was added PMBCl (1.0 g, 6.39 mmol, 1 eq.). The solution was stirred at 45 °C overnight until the starting material was consumed (monitored by GC-MS). The reaction mixture was cooled to room temperature and then quenched with H_2O (30 mL). The organic layer was extracted with Et_2O (3 \times 20 mL). The combined organic phases were washed with H_2O (2 \times 30 mL) and brine (30 mL), dried over MgSO_4 , filtered and the volatiles were removed *in vacuo* to yield the desired product **4** as yellowish oil (1.04 g, 6.39 mmol, quant.). *Rf* = 0.70 (Cyclohexane/EtOAc 3:1). ¹H-NMR (CDCl_3 , 400 MHz): δ 3.84 (s, 3H, 2H), 4.30 (s, 2H), 6.95 (d, *J* = 8.7 Hz, 2H), 7.28 (d, *J* = 8.7 Hz, 2H). ¹³C-NMR (CDCl_3 , 101 MHz): δ 54.4 (N $_3$ CH $_2$), 55.3 (OCH $_3$), 114.2 (C $_{ortho}$), 127.5 (C $_{para}$), 129.8 (C $_{meta}$), 159.7 (C $_i$). HRMS (ESI⁺): *m/z* calcd for $\text{C}_8\text{H}_{10}\text{N}_3\text{O}^+$: 164.0818 [M + H]⁺; found: 164.0833.

3-Methoxy-6-(1-(4-methoxybenzyl)-1H-1,2,3-triazol-4-yl)-2-(thiophen-2-yl)-4H-chromen-4-one (5, Mo-Thio): To a stirred solution of **6-EMT** (41 mg, 0.15 mmol, 1 eq.) in DCE, were sequentially added **4** (43 mg, 0.26 mmol, 1.8 eq.), DIPEA (306 μ L, 1.74 mmol, 12 eq.), acetic acid (50 μ L, 0.87 mmol, 6 eq.), and CuI (78 mg, 0.41 mmol, 2.8 eq.). The resulting solution was heated at 40 °C overnight under an argon atmosphere to give a homogeneous blue liquid. The reaction mixture was cooled to room temperature and then concentrated under reduced pressure. The crude was purified by flash chromatography on silica gel eluted with cyclohexane/ethyl acetate (9:1 \rightarrow 3:2, v/v) to provide the desired product **5** (**Mo-Thio**) as a yellowish powder (37 mg, 0.08 mmol, 57%). *Rf* = 0.14 (Cyclohexane/EtOAc 3:1). ¹H-NMR (CDCl_3 , 400 MHz): δ 3.77 (s, 3H, PhOCH $_3$), 3.99 (s, 3H, OCH $_3$), 5.46 (s, 2H, H12), 6.87 (d, ³*J* = 8.7 Hz, 2H, H $_{meta}$), 7.16 (dd, ³*J* = 5.0 Hz, ³*J* = 3.9 Hz, 1H, H β), 7.24 (d, ³*J* = 8.7 Hz, 2H, H $_{ortho}$), 7.54 (d, ³*J* = 8.8 Hz, 1H, H8), 7.57 (dd, ³*J* = 5.0 Hz, ⁴*J* = 1.2 Hz, 1H, H γ), 7.69 (s, 1H, H α'), 7.91 (dd, ³*J* = 3.9 Hz, ⁴*J* = 1.2 Hz, 1H, H α), 8.28 (d, ⁴*J* = 2.2 Hz, 1H, H5), 8.33 (dd, ³*J* = 8.8 Hz, ⁴*J* = 2.2 Hz, 1H, H7). ¹³C-NMR (CDCl_3 , 400 MHz): δ 54.0 (C12), 55.4 (PhOCH $_3$), 59.7 (OCH $_3$), 114.7 (C $_{meta}$), 118.6 (C8), 119.9 (C α'), 122.0 (C5), 124.3 (C10), 126.2 (C $_i$), 127.6 (C β), 127.7 (C6), 129.8 (C α), 129.9 (C $_{ortho}$), 131.0 (C7), 131.7 (C3), 131.8 (C γ), 138.7 (C11), 146.6 (C β'), 151.9 (C2), 154.8 (C9), 160.2 (C $_{para}$), 173.9 (C4). HRMS (ESI⁺): *m/z* calcd for $\text{C}_{24}\text{H}_{20}\text{N}_3\text{O}_4\text{S}^+$: 446.1169 [M + H]⁺; found: 446.1166.

Typical conjugation procedure for labeling ODNs with the 6-EMT dye. First, a 5 mM aq. solution of $\text{CuSO}_4 \cdot 5\text{H}_2\text{O}$ and the BTES ligand^[48] was freshly prepared. In a 200- μ L vial, were sequentially added the ODN sequence to be labeled (0.2 mM aq. solution, 50 μ L, 10 nmol, 1 eq.), DMSO (20 μ L), **6-EMT** label (5 mM in DMSO, 10 μ L, 50 nmol, 5 eq.), sodium ascorbate (5 mM aq. solution, 10 μ L, 50 nmol, 5 eq.), and finally the 5 mM CuSO_4 /BTES aq. solution (10 μ L, 50 nmol, 5 eq.). The reaction mixture was vortexed overnight at room temperature. The resulting solution was removed from the vial, which was then

rinsed with minimal H₂O and DMSO. The combined solution was passed through a 0.22- μ m H-PTFE syringe filter before being purified by RP-HPLC (for conditions, *vide supra* and Figure S4 in the Supporting Information).

Acknowledgements

This research work was funded by the Agence Nationale de la Recherche (PFPIImaging – 18-CE09-0020-01, UCA JEDI project: ANR-15-IDEX-01) and the LIFE and SPECTRUM graduate schools (UCA). We thank the French Government for the PhD grants of S.V., H.-N.L. and G.B., respectively. We are grateful to the CNRS Emergence@INC2020 program for both the financial support and the postdoctoral fellowship of S.M.

Keywords: DNA hybridization probe • Fluorogenic dye • Forced intercalation • Chromone • Fluorescent labeling

- [1] S. Khadem, R. J. Marles, *Molecules* **2012**, *17*, 191–206.
- [2] C. F. M. Silva, D. C. G. A. Pinto, A. M. S. Silva, *ChemMedChem* **2016**, *11*, 2252–2260.
- [3] A. Gaspar, M. J. Matos, J. Garrido, E. Uriarte, F. Borges, *Chem. Rev.* **2014**, *114*, 4960–4992.
- [4] a) A. S. Klymchenko, Y. Mély, in *Progress in Molecular Biology and Translational Science*, Vol. 113 (Ed.: M. C. Morris), Academic Press, Burlington, VT, USA **2013**, Ch. 2, pp. 35–58; b) A. P. Demchenko, A. S. Klymchenko, V. G. Pivovarenko, S. Ercelen, in *Fluorescence Spectroscopy, Imaging and Probes*, Springer Series on Fluorescence, Vol. 2 (Eds: R. Kraayenhof, A. J. W. G. Visser, H. C. Gerritsen), Springer, Berlin, Heidelberg, Germany **2002**, Ch. 5, pp. 101–110.
- [5] a) T. Kumpulainen, B. Lang, A. Rosspeintner, E. Vauthey, *Chem. Rev.* **2017**, *117*, 10826–10939; b) V. I. Tomin, A. P. Demchenko, P.-T. Chou, *J. Photochem. Photobiol. C: Photochem. Rev.* **2015**, *22*, 1–18.
- [6] A. C. Sedgwick, L. Wu, H.-H. Han, S. D. Bull, X.-P. He, T. D. James, J. L. Sessler, B. Z. Tang, H. Tian, J. Yoon, *Chem. Soc. Rev.* **2018**, *46*, 7105–39.
- [7] B. Y. Michel, D. Dziuba, R. Benhida, A. P. Demchenko, A. Burger, *Front. Chem.* **2020**, *8*, 112.
- [8] a) D. Dziuba, P. Didier, S. Ciaco, A. Barth, C. A. M. Seidel, Y. Mély, *Chem. Soc. Rev.* **2021**, *50*, 7062–7107; b) K. Nakatani, Y. Tor, (Eds) in *Modified Nucleic Acids*, Nucleic Acids and Molecular Biology Series, Vol. 31, Springer, Cham, Switzerland **2016**, p. 276; c) A. P. Demchenko, in *Introduction to Fluorescence Sensing*, third ed., Vol. 1: Materials and Devices, Springer, Cham, Switzerland **2020**, p. 657.
- [9] a) D. Dziuba, V. Y. Postupalenko, M. Spadafora, A. S. Klymchenko, V. Guérineau, Y. Mély, R. Benhida, A. Burger, *J. Am. Chem. Soc.* **2012**, *134*, 10209–10213; b) M. Spadafora, V. Y. Postupalenko, V. V. Shvadchak, A. S. Klymchenko, Y. Mély, A. Burger, R. Benhida, *Tetrahedron* **2009**, *65*, 7809–7816.
- [10] a) A. A. Kuznetsova, N. A. Kuznetsov, Y. N. Vorobjev, N. P. F. Barthes, B. Y. Michel, A. Burger, O. S. Fedorova, *PLoS One* **2014**, *9*, e100007; b) A. A. Kuznetsova, O. A. Kladova, N. P. F. Barthes, B. Y. Michel, A. Burger, O. S. Fedorova, N. A. Kuznetsov, *Russ. J. Bioorg. Chem.* **2019**, *45*, 591–598.
- [11] V. Kilin, K. Gavvala, N. P. F. Barthes, B. Y. Michel, D. Shin, C. Boudier, O. Mauffret, V. Yashchuk, M. Mousli, M. Ruff, et al., *J. Am. Chem. Soc.* **2017**, *139*, 2520–2528.
- [12] a) M. Sholokh, R. Sharma, N. Grytsyk, L. Zaghzi, V. Y. Postupalenko, D. Dziuba, N. P. F. Barthes, B. Y. Michel, C. Boudier, O. A. Zaporozhets, et al., *Chem. Eur. J.* **2018**, *24*, 388–13; b) L. Zargarian, A. Ben Imeddourène, K. Gavvala, N. P. F. Barthes, B. Y. Michel, C. A. Kenfack, N. Morellet, B. René, P. Fossé, A. Burger, et al., *J. Phys. Chem. B* **2017**, *121*, 11249–11261.
- [13] a) H.-N. Le, J. Brazard, G. Barnoin, S. Vincent, B. Y. Michel, J. Léonard, A. Burger, *Chem. Eur. J.* **2020**, *26*, 276–286; b) H.-N. Le, C. Zilio, G. Barnoin, N. P. F. Barthes, J.-M. Guignonis, N. Martinet, B. Y. Michel, A. Burger, *Dyes Pigments* **2019**, *170*, 107553; c) N. P. F. Barthes, K. Gavvala, D. Dziuba, D. Bonhomme, I. A. Karpenko, A. S. Dabert-Gay, D. Debayle, A. P. Demchenko, R. Benhida, B. Y. Michel, et al., *J. Mater. Chem. C* **2016**, *4*, 3010–3017; d) K. Gavvala, N. P. F. Barthes, D. Bonhomme, A. S. Dabert-Gay, D. Debayle, B. Y. Michel, A. Burger, Y. Mély, *RSC Adv.* **2016**, *6*, 87142–87146; e) O. A. Kladova, A. A. Kuznetsova, N. P. F. Barthes, B. Y. Michel, A. Burger, O. S. Fedorova, N. A. Kuznetsov, *Russ. J. Bioorg. Chem.* **2019**, *45*, 599–607; f) D. Dziuba, I. A. Karpenko, N. P. F. Barthes, B. Y. Michel, A. S. Klymchenko, R. Benhida, A. P. Demchenko, Y. Mély, A. Burger, *Chem. Eur. J.* **2014**, *20*, 1998–2009.
- [14] a) L. M. Wilhelmsson, Y. Tor, (Eds) in *Fluorescent Analogues of Biomolecular Building Blocks: Design and Applications*, Wiley-VCH, Hoboken, NJ, USA **2016**, p. 448; b) P. Herdewijn, (Ed.) in *Modified Nucleosides: in Biochemistry, Biotechnology and Medicine*, Wiley-VCH, Weinheim, Germany **2008**, p. 658.
- [15] J. R. Lakowicz, in *Principles of Fluorescence Spectroscopy*, third ed.; Springer, New York, NY, USA **2006**, p. 954.
- [16] I. Medintz, N. Hildebrandt, (Eds) in *FRET – Förster Resonance Energy Transfer: From Theory to Applications*, Wiley-VCH, Weinheim, Germany **2013**, p. 791.
- [17] W. Shi, H. Ma, *Chem. Commun.* **2012**, *48*, 8732–13.
- [18] a) A. Okamoto, *Appl. Microsc.* **2019**, *49*, 14; b) G. Hayashi, A. Okamoto, *Chem. Rec.* **2013**, *13*, 209–217; c) A. Okamoto, *Chem. Soc. Rev.* **2011**, *40*, 5815–5828.
- [19] a) S.-C. Lee, J. Heo, H. C. Woo, J.-A. Lee, Y. H. Seo, C.-L. Lee, S. Kim, O.-P. Kwon, *Chem. Eur. J.* **2018**, *24*, 13706–13718; b) D. Su, C. L. Teoh, L. Wang, X. Liu, Y.-T. Chang, *Chem. Soc. Rev.* **2017**, *46*, 4833–4844; c) M. Dal Molin, Q. Verolet, S. Soleimanpour, S. Matile, *Chem. Eur. J.* **2015**, *21*, 6012–6021.
- [20] a) F. Hövelmann, O. Seitz, *Acc. Chem. Res.* **2016**, *49*, 714–723. b) O. Köhler, D. V. Jarikote, I. Singh, V. S. Parmar, E. Weinhold, O. Seitz, *Pure Appl. Chem.* **2005**, *77*, 327–338.
- [21] a) J. Gebhard, L. Hirsch, C. Schwechheimer, H.-A. Wagenknecht, *Bioconjugate Chem.* **2022**, DOI 10.1021/acs.bioconjchem.2c00241; b) J. Chamiolo, G.-M. Fang, F. Hövelmann, D. Friedrich, A. Knoll, A. Loewer, O. Seitz, *ChemBioChem* **2019**, *20*, 595–604; c) I. Gaspar, F. Hövelmann, J. Chamiolo, A. Ephrussi, O. Seitz, *ACS Chem. Biol.* **2018**, *13*, 742–749; d) F. Hövelmann, I. Gaspar, J. Chamiolo, M. Kasper, J. Steffen, A. Ephrussi, O. Seitz, *Chem. Sci.* **2016**, *7*, 128–135; e) F. Hövelmann, I. Gaspar, S. Loibl, E. A. Ermilov, B. Röder, J. Wengel, A. Ephrussi, O. Seitz, *Angew. Chem. Int. Ed.* **2014**, *53*, 11370–11375; f) F. Hövelmann, I. Gaspar, A. Ephrussi, O. Seitz, *J. Am. Chem. Soc.* **2013**, *135*, 19025–19032; g) F. Hövelmann, L. Bethge, O. Seitz, *ChemBioChem* **2012**, *13*, 2072–2081; h) Kummer, A. Knoll, E. Socher, L. Bethge, A. Herrmann, O. Seitz, *Angew. Chem. Int. Ed.* **2011**, *50*, 1931–1934. i) E. Socher, L. Bethge, A. Knoll, N. Jungnick, A. Herrmann, O. Seitz, *Angew. Chem. Int. Ed.* **2008**, *47*, 9555–9559; j) E. Socher, D. V. Jarikote, A. Knoll, L. Röglin, J. Burmeister, O. Seitz, *Anal. Biochem.* **2008**, *375*, 318–330.
- [22] A. S. Klymchenko, *Acc. Chem. Res.* **2017**, *50*, 366–375.
- [23] R. R. Sinden, C. E. Pearson, V. N. Potaman, D. W. Ussery, in *Genes and Genomes*, Advances in Genome Biology, Vol. 5 (Ed.: R. S. Verma), Elsevier, Stamford, CT, USA **1998**, pp. 1–141.
- [24] a) E. Braselmann, C. Rathbun, E. M. Richards, A. E. Palmer, *Cell Chem. Biol.* **2020**, *27*, 891–903; b) F. Tomoike, H. Abe, *Adv. Drug Deliv. Rev.* **2019**, *147*, 44–58; c) E. Socher, O. Seitz, in *Molecular Beacons: Signalling Nucleic Acid Probes, Methods and Protocols*, Methods in Molecular Biology, Vol. 429 (Eds: A. Marx, O. Seitz), Humana Press, Totowa, NJ, USA **2008**, Ch. 13, pp. 187–197.
- [25] Y. V. Suseela, N. Narayanaswamy, S. Pratihari, T. Govindaraju, *Chem. Soc. Rev.* **2018**, *47*, 1098–1131.
- [26] a) Y. Wang, Y. Hu, T. Wu, X. Zhou, Y. Shao, *Anal. Chem.* **2015**, *87*, 11620–11624; b) N. K. Janjua, A. Shaheen, A. Yaqub, F. Perveen,

- S. Sabahat, M. Mumtaz, C. Jacob, L. A. Ba, H. A. Mohammed, *Spectrochim. Acta A* **2011**, *79*, 1600–1604.; c) P. A. Ragazzon, T. Bradshaw, C. Matthews, J. Iley, S. Missailidis, *Anticancer Res.* **2009**, *29*, 2273–2283.
- [27] S. Benson, F. de Moliner, W. Tipping, M. Vendrell, *Angew Chem Int Ed Engl* **2022**, *61*, e202204788.
- [28] E. Kozma, P. Kele, *Org. Biomol. Chem.* **2019**, *17*, 215–233.
- [29] L. Jullien, A. Gautier, *Methods Appl. Fluoresc.* **2015**, *3*, 042007.
- [30] a) S. Vincent, S. Mallick, G. Barnoin, H.-N. Le, B. Y. Michel, A. Burger, *Molecules* **2022**, *27*, 2267; b) N. P. F. Barthes, K. Gavvala, D. Bonhomme, A. S. Dabert-Gay, D. Debayle, Y. Mély, B. Y. Michel, A. Burger, *J. Org. Chem.* **2016**, *81*, 10733–10741; c) R. Kreder, S. Oncul, O. A. Kucherak, K. A. Pyrshev, E. Real, Y. Mély, A. S. Klymchenko, *RSC Adv.* **2015**, *5*, 22899–22905; d) O. A. Kucherak, L. Richert, Y. Mély, A. S. Klymchenko, *Phys. Chem. Chem. Phys.* **2012**, *14*, 2292–2300.
- [31] a) Z. Wang, in *Comprehensive Organic Name Reactions and Reagents*, Wiley-VCH, Weinheim, Germany **2010**, Ch. 13, pp. 52–56; b) A. Sharma, H. Singh Tuli, A. K. Sharma, in *Current Aspects of Flavonoids: Their Role in Cancer Treatment*, (Ed.: H. Singh Tuli), Springer, Singapore **2019**, pp. 23–38; c) F. M. Dean, V. Podimuang, *J. Chem. Soc. Perkin Trans.* **1965**, 3978–3987.
- [32] a) N. Z. Fantoni, A. H. El-Sagheer, T. Brown, *Chem. Rev.* **2021**, *121*, 7122–7154; b) F. Amblard, J. H. Cho, R. F. Schinazi, *Chem. Rev.* **2009**, *109*, 4207–4220; c) H. C. Kolb, M. G. Finn, K. B. Sharpless, *Angew. Chem. Int. Ed.* **2001**, *40*, 2004–2021.
- [33] D. Dziuba, R. Benhida, A. Burger, *Synthesis* **2011**, *47*, 2159–2164.
- [34] A. S. Klymchenko, V. G. Pivovarenko, A. P. Demchenko, *Spectrochim. Acta A* **2003**, *59*, 787–792.
- [35] J. J. Howard, G. C. Lynch, B. M. Pettitt, *J. Phys. Chem. B* **2011**, *115*, 547–556.
- [36] Y. Deng, W. Yuan, Z. Jia, G. Liu, *J. Phys. Chem. B* **2014**, *118*, 14536–14545.
- [37] A. P. Demchenko, *Methods Appl. Fluoresc.* **2020**, *8*, 022001.
- [38] Y. Niko, P. Didier, Y. Mély, G.-I. Konishi, A. S. Klymchenko, *Sci. Rep.* **2016**, *6*, 18870.
- [39] C. Reichardt, *Chem. Rev.* **1994**, *94*, 2319–2358.
- [40] S. M. Ormson, R. G. Brown, F. Vollmer, W. Rettig, *J. Photochem. Photobiol. A: Chem.* **1994**, *81*, 65–72.
- [41] a) S. Hainke, O. Seitz, *Angew. Chem. Int. Ed.* **2009**, *48*, 8250–8253; b) I. Singh, W. Hecker, A. K. Prasad, V. S. Parmar, O. Seitz, *Chem. Commun.* **2002**, 500–501.
- [42] B. G. Moreira, Y. You, R. Owczarzy, *Biophys. Chem.* **2015**, *198*, 36–44.
- [43] W. L. F. Armarego, C. L. L. Chai, in *Purification of Laboratory Chemicals*, eighth ed., Butterworth-Heinemann, Oxford, UK **2017**, p. 1024.
- [44] H. Jork, W. Funk, W. R. Fischer, H. Wimmer, in *Thin-Layer Chromatography: Reagents and Detection Methods*, Vol. 1a, Physical and Chemical Detection Methods: Fundamentals, Reagents I, VCH, Weinheim, Germany **1990**, p. 464.
- [45] W. C. Still, M. Kahn, A. Mitra, *J. Org. Chem.* **1978**, *43*, 2923–2925.
- [46] N. R. Babji, E. O. McCusker, G. T. Whiteker, B. Canturk, N. Choy, L. C. Creemer, C. V. D. Amicis, N. M. Hewlett, P. L. Johnson, J. A. Knobelsdorf, et al., *Org. Process Res. Dev.* **2016**, *20*, 661–667.
- [47] K. J. Breslauer, in *Energetics of Biological Macromolecules*, Methods in Enzymology, Vol. 259 (Eds: M. L. Johnson, G. K. Ackers), Academic Press, San Diego, CA, USA **1995**, pp. 221–242.
- [48] I. Ivancová, D.-L. Leone, M. Hocek, *Curr. Opin. Chem. Biol.* **2019**, *52*, 136–144.

II. Malachite Green

II.1. Introduction

Afin d'obtenir un système de *molecular rotor* avec une meilleure amplification de fluorescence que celui précédemment décrit avec le **6-EMT**, nous nous sommes intéressés à la Malachite Green (MG), qui possède un très faible rendement quantique en solution.

La Malachite Green fait partie de la famille des triarylméthanés. Dans celle-ci, on retrouve également les sondes méthyl violet, Victoria bleu ou phénolphtaleine (**Figure 64**).

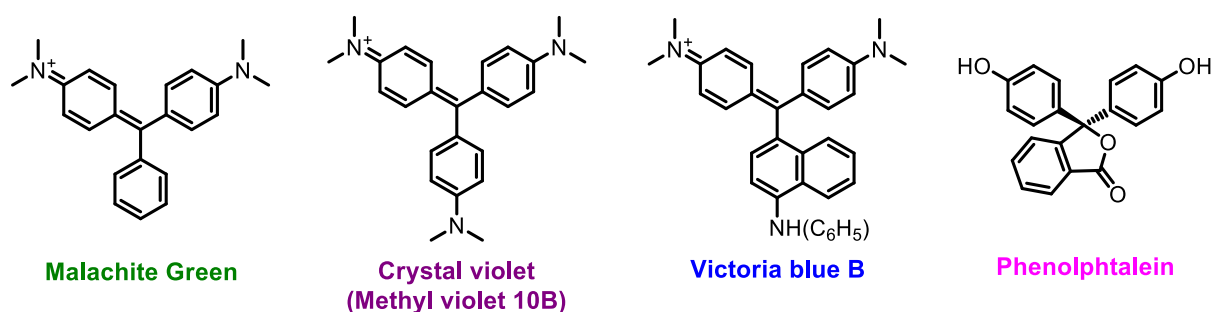


Figure 64. Exemples de triarylméthane.

Les applications de la **MG** sont retrainées. Celle-ci fait partie des molécules utilisées dans la technologie FAP (*Fluorogen Activating Proteins*), tout comme le Thiazole Orange (TO). La technologie FAP, introduite en 2008 par Szent-Gyorgyi *et al.*¹⁶⁸ est un système fluorogénique basé sur la reconnaissance du site actif d'une protéine (FAP) par une petite sonde organique, ce qui active la fluorescence de cette dernière (**Figure 65**).

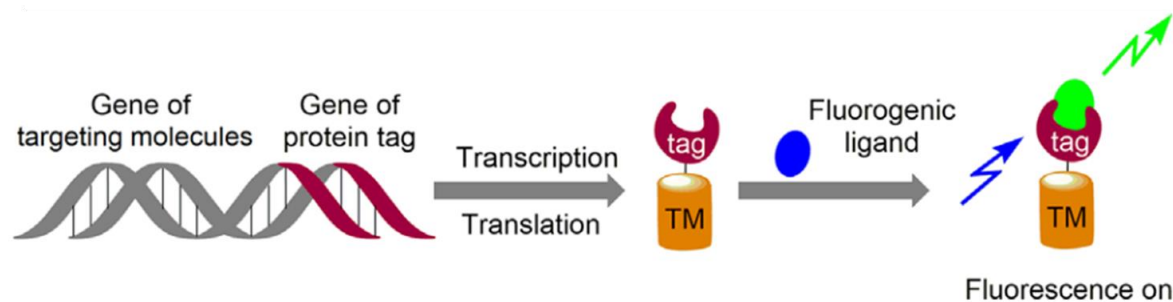


Figure 65. Méthode d'utilisation des molécules FAP spécifiques d'une protéine (*tag protein*) pour l'imagerie d'une cible (TM : *Targeting molecules*).¹⁶⁹

Le **TO** et la **MG** sont capables, sur certaines FAP, d'interagir avec une affinité nanomolaire, à l'instar de certains ligands vis-à-vis de leurs récepteurs, via des interactions de Van der Waals, de π -stacking et des liaisons Hydrogène. Contrairement au **TO**, la **MG** possède un nombre de degrés de liberté supérieure (**Figure 66**).

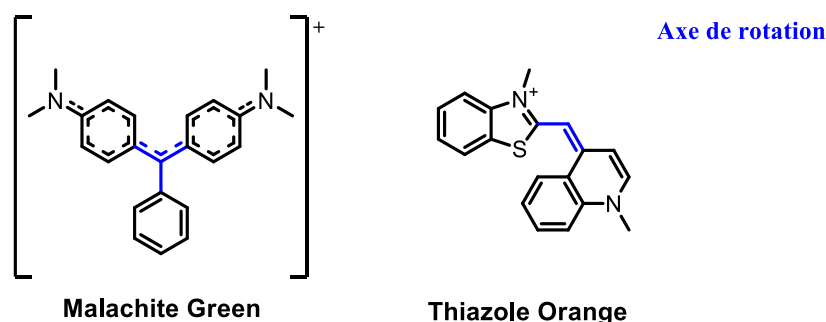


Figure 66. Différence de degrés de liberté entre les FAP Malachite Green et Thiazole Orange.

Cette différence induit une plus grande difficulté pour atteindre un système plan, mais conduit à une amplification bien supérieure lorsque la planéité est obtenue. Dans certains systèmes FAP utilisant la **MG**, une amplification de fluorescence d'un facteur 18 000 a été observée¹⁶⁹. Ceci a mené les chercheurs à utiliser ces sondes FAP dans des techniques de microscopie à molécule unique¹⁷⁰. Dans ces systèmes, la **MG** a également été utilisée comme accepteur FRET, par couplage avec plusieurs donneurs Cy3^{169,171}.

D'autres études prouvent qu'il est également possible d'utiliser la **MG** comme senseur de doubles brins d'ADN^{172,173,174}, d'aptamères^{175,176} ou de G-quadruplexes¹⁷⁷. Néanmoins, ce senseur a été étudié comme ligand labile sur des cibles d'acides nucléiques de structures différentes. Dans le cadre de mon travail de thèse, j'ai intégré la sonde **MG** dans des séquences d'ADN afin d'étudier leur hybridation avec leur brin complémentaire.

II.2. Résultats et discussion

Comme pour les précédents marqueurs, la sonde **MG** a été introduite dans des ODNs de façon post-synthétique, à partir de précurseurs **2** et **5** possédant respectivement une fonction alcyne ou azoture sur un des cycles aromatiques. (**Schéma 4**).

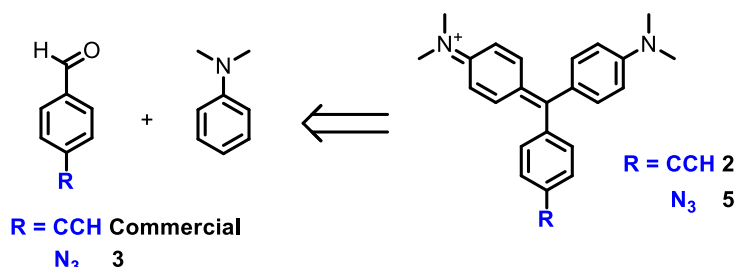


Schéma 4. Retrosynthèse de la malachite green clickable.

II.2.1. Synthèse

Nous avons choisi de positionner la fonction à « clicker » en para sur le cycle aromatique phényle, cette position n'interférant que peu avec le noyau du fluorophore. Puisque la **MG** est symétrique, cette position est également la plus simple à fonctionnaliser (**Schéma 4**).

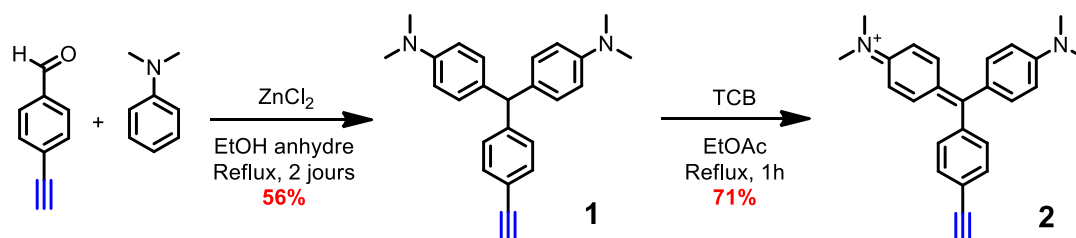


Schéma 5. Synthèse de la malachite green alcyne.

La synthèse du dérivé alcyne (**2**) est très simple et s'effectue en seulement deux étapes. La première est la formation de la leuco malachite green (LMG : **1**), par condensation du 4-éthynylbenzaldéhyde avec la diméthylaniline, en présence de chlorure de zinc. L'étape d'oxydation pour obtenir la **MG** est très favorable et s'effectue même au simple contact de l'air. Elle s'accompagne d'un changement de couleur (du jaune (**LMG**) au vert (**MG**)). Pour accélérer ce processus, un simple ajout de tétrachloro-p-benzoquinone (TCB) permet d'obtenir la **MG** après 1h (**Schéma 5**).

Le dérivé **MG** azoture **5**, quant à lui, est obtenu en trois étapes (**Schéma 6**).

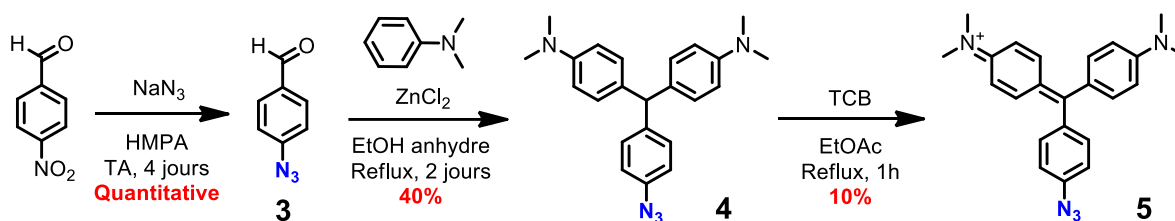
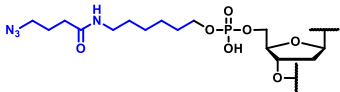
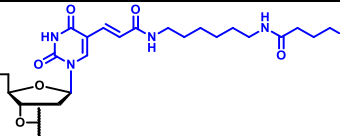
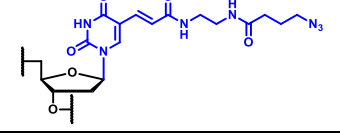
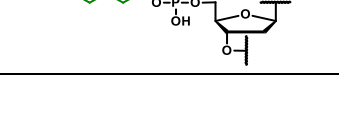



Schéma 6. Synthèse de la malachite green azoture.

Le 4-azidobenzaldéhyde n'étant pas distribué commercialement, sa synthèse a été réalisée à partir du 4-nitrobenzaldéhyde et d'azoture de sodium, suivant le protocole décrit par A. Herner et al.¹⁷⁸. Cette réaction est une substitution nucléophile aromatique, dont la cinétique est lente. Le dérivé **3** est ainsi obtenu avec un rendement quantitatif. Les deux étapes suivantes sont similaires à la synthèse du dérivé alcyne **2** : après formation de la **LMG-N₃** **4** avec un rendement de 40%, l'oxydation au TCB conduit au **MG-N₃** **5** avec un faible rendement de 10% malgré une conversion totale vers le produit désiré **5** (Schéma 6). Ceci est dû aux difficultés de purification par gel de silice (molécule chargée).

Les deux sondes **MG** ont ensuite été incorporées dans différents brins d'ODN présentant un lien azoture ou lien alcyne (Tableau 3), par le biais d'une réaction de CuAAC. Les conditions utilisées sont les mêmes que lors des projets précédents, de même que les séquences ODN utilisées (Tableau 3).

Tableau 3. Descriptif des séquences pour les réactions « click » post-synthétiques.

Séquences et positionnement de la modification	Acronymes	Structure du lien
5'- YCAG TCG CTC GCT GAC-3'	YCAG	
5'- YGCA AAA TTT AAA ACG-3'	YGCA	
5'-CAG TCG CXC GCT GAC-3'	CXC	
5'-GCA AAA TXt AAA ACG-3'	TXt	
5'- VGCA AAA TTT AAA ACG-3'	VGCA	



II.2.2. Hybridation fluorogénique

Nous avons tout d'abord étudié l'hybridation des séquences d'ODNss marquées par la MG avec leur cible complémentaire, par hybridation directe.

Malheureusement, pour toutes les séquences marquées, quel que soit le brin d'ODN complémentaire, les résultats n'ont été que très peu concluants (Les résultats sont exposés dans la partie expérimentale : Tableau S2-S3, figure S3-S4). La **MG**, très éteinte dans le simple brin ($\Phi < 0,2\%$), le reste après hybridation. Cela signifie probablement que lors de l'hybridation en double brin l'environnement de l'ADN ne permet pas de rendre plane la **MG** et de restreindre l'agitation moléculaire autour des liaisons simples du colorant (**Figure 67**).

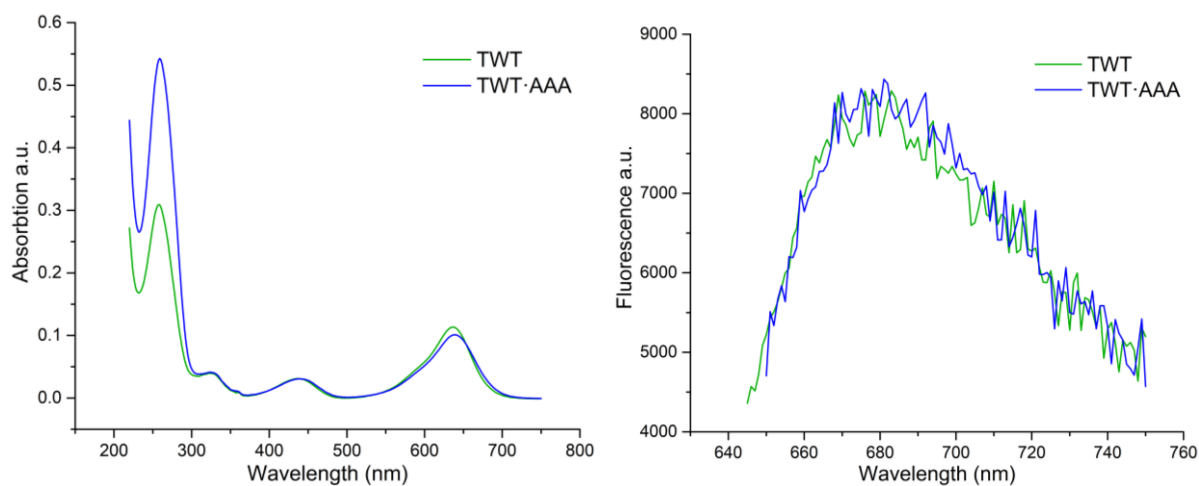


Figure 67. Un exemple de l'effet non-fluorogénique de la MG entre un simple et double brin d'ODN.

II.2.3. DRET

Puisque la sonde **MG** est éteinte aussi bien en simple qu'en double-brin, la technique de l'hybridation directe n'est donc pas adaptée. Nous avons donc voulu tester le DRET (**Chapitre 1 : II.2.4.**, p.41), qui est du FRET applicable dans le cas d'un donneur éteint. Pour

ce faire, nous avons réalisé des expériences d'hybridation entre les ODNs incorporant la sonde **MG** et leurs brins complémentaires, marqués par l'accepteur Cy5. Le choix de Cy5 se justifie car le spectre d'émission de la **MG** se recouvre en partie avec le spectre d'absorption de Cy5 (**Figure 68**). Cependant, une excitation de la S_1 ($\epsilon \approx 55\,000\text{ L}\cdot\text{mol}^{-1}\cdot\text{cm}^{-1}$) de la **MG** conduirait à de l'excitation croisée trop grande du fait de son faible déplacement de Stokes ($\approx 20\text{ nm}$). Par contre, si l'on compare les spectres d'absorption de la **MG** et de Cy5, on s'aperçoit que la S_2 ($\epsilon \approx 27\,000\text{ L}\cdot\text{mol}^{-1}\cdot\text{cm}^{-1}$) de la **MG** se trouve dans une zone où Cy5 absorbe très faiblement ($430 < \lambda < 460\text{ nm}$) (**Figure 68**).

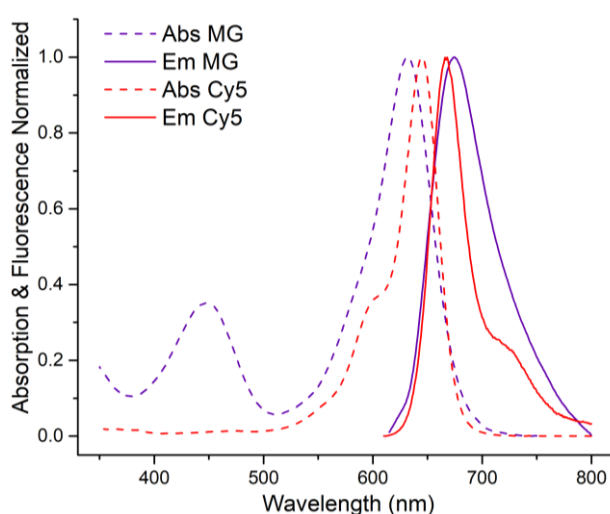


Figure 68. Spectre d'absorption et d'émission de Cy5 et de la MG dans le PBS.

Des expériences de DRET intermoléculaire ont alors été réalisées, en excitant **MG** à 440 nm, avec 2 séquences d'ODNs marquées, différentes de par la nature du lien « click ».

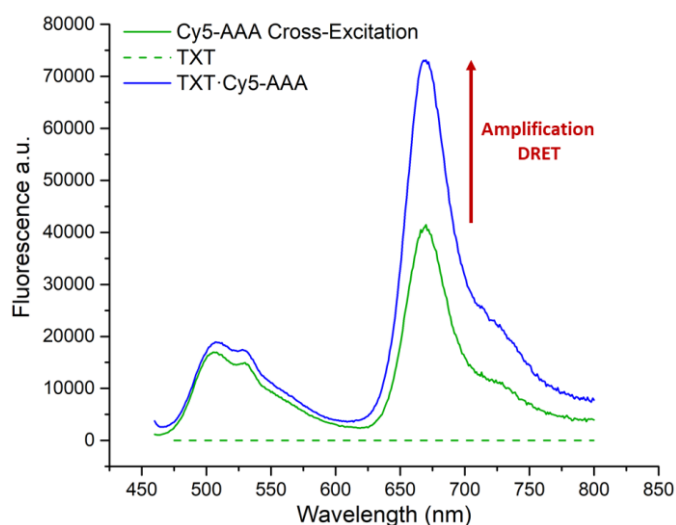


Figure 69. Exemple d'un spectre de DRET fluorogénique avec la séquence marqué TXT couplé au brin complémentaire Cy5 comparé au spectre de Cy5 seule obtenu par excitation directe à 440 nm.

Les résultats n'ont pas été concluants (**Figure 69**, Figure S5). Une composante DRET est tout de même observée lors de l'utilisation de la séquence T~~X~~T, mais l'émission de fluorescence est principalement due à l'excitation directe de Cy5, qui pourtant est faible à cette longueur d'onde d'excitation.

Malgré les propriétés photophysiques qui semblaient adéquates (éteint, large Stokes shift (S2)), la Malachite Green ne semble pas un bon donneur pour du DRET dans un duplexe d'ADN dû à sa faible capacité à transférer son énergie par résonance à l'accepteur. Nous n'avons pas poursuivi dans cette voie.

II.2.4. G-quadruplexes

La **MG** est connue pour interagir de façon non covalente avec les motifs G-quadruplexes, *via* des interactions π -stacking¹⁷⁷ (**Figure 70**). Ceci se traduit par une augmentation de la fluorescence de la **MG** d'environ 100 fois, ce qui fournit ainsi une méthode pratique pour la détection d'un motif G-quadruplexe. Ces résultats indiquent que la rotation autour des liaisons simples est fortement réduite lors de l'interaction avec le G-quadruplexe et que la planéité est atteinte.

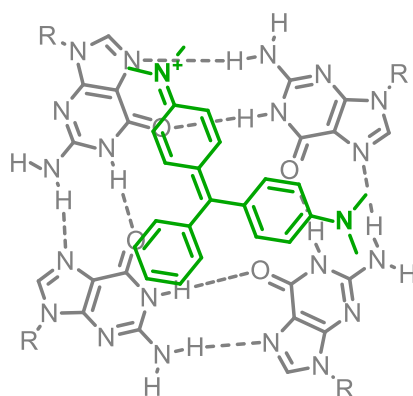


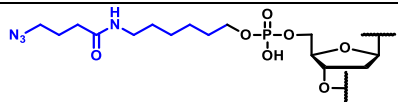
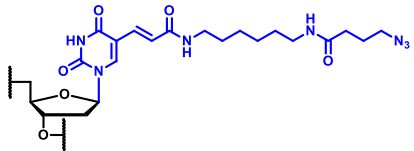
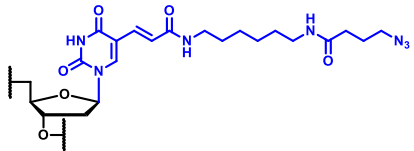
Figure 70. Complexe formé entre la MG (en vert) et une structure G-quadruplexe (représentée en gris)

Nous nous sommes alors attachés à incorporer la **MG** dans la même séquence d'ADN (d(G₂T)₁₃G), riche en résidus Guanine, afin d'étudier son potentiel fluorogénique dans le cadre d'un changement conformationnel d'un ADNss linéaire à un ADN structuré en G-quadruplexe. En effet, lorsqu'elle est incorporée dans un simple brin d'ADN, la **MG** ne devrait être que très peu fluorescente mais son intercalation dans le G-quadruplexe pourrait se traduire par un fort gain en rendement quantique.

Les G-quadruplexes peuvent exister sous différentes conformations (cf **Chapitre 1 : II.1.2.**, **Figure 31**, p.49). Or, l'intercalation de la **MG** lors de la formation du G-quadruplexe peut dépendre de la position de la sonde dans le brin d'ADN. C'est pourquoi nous avons décidé d'incorporer la **MG** à trois positions différentes du simple brin d'ADN (en position 5' terminale et interne, en début et milieu de séquence).

Les ODNs marqués par la **MG** ont été préparés *via* la stratégie post-synthétique, impliquant le dérivé alcyne de la **MG** (**2**, **Schéma 5**) et trois précurseurs de l'AN, fonctionnalisés par un groupement azoture, soit au niveau du groupement phosphodiester, en position terminale 5', soit au niveau de bases thymine de nucléosides positionnés à deux endroits différents de l'ADN (**Tableau 4**). Après couplage, les séquences d'ADN ont été purifiées par HPLC semi-préparative.

Tableau 4. Descriptif des séquences G-quadruplex pour les réactions de post-synthétique.

Séquences	Acronymes	Lien Azoture
X GGG TGG TGG TGG TGG TGG TGG TGG TGG TGG TGG TGG TGG TG	5' X	
GGG XGG TGG TGG TGG TGG TGG TGG TGG TGG TGG TGG TGG TG	5' XGG	
GGG TGG TGG TGG TGG TGG TGG XGG TGG TGG TGG TGG TGG TG	XGG	

Les G-quadruplexes ont été formés en présence d'un sel de potassium ou de sodium. Sans la présence de ce métal alcalin, la séquence reste en simple-brin¹⁷⁹. Il est alors possible de suivre la formation d'un G-quadruplexe par une simple titration en sel par spectroscopie d'absorption UV/visible et par CD¹⁷⁷.

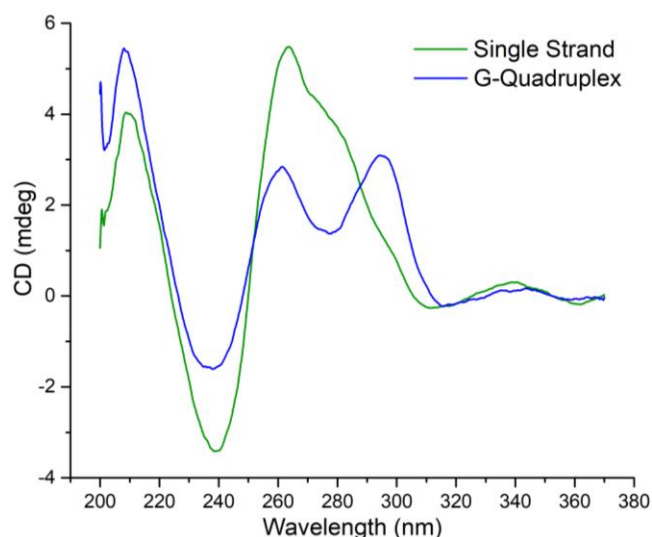


Figure 71. Spectres de dichroïsme circulaire de la séquence XGG avant (vert) et après ajout de sel, Na⁺ (bleu).

Nous avons donc examiné les spectres d'absorption et d'émission des trois ODNs marqués, en présence de quantités croissantes de KCl ou NaCl. En CD nous avons observé la diminution de la bande d'absorption positive à 260 nm et l'augmentation de celle à 300 nm (**Figure 71**) qui laisse supposer la formation d'un G-Quadruplexe antiparallèle¹⁸⁰. En effet, les spectres CD obtenus sont similaires à ceux décrits dans la littérature pour la séquence que nous avons utilisée pour nos travaux¹⁷⁷ (voir SI). Cependant, les spectres d'absorption et d'émission des 3 séquences marquées ne montrent aucun déplacement bathochrome des maxima d'absorption et d'émission de MG ni d'amplification du signal de fluorescence à l'inverse de ce qui avait été observée pour la MG en interaction avec la séquence d(G₂T)₁₃G (**Figure 72**, Figure S6). Au contraire, on observe une diminution de la fluorescence avec l'augmentation de la concentration en sel.

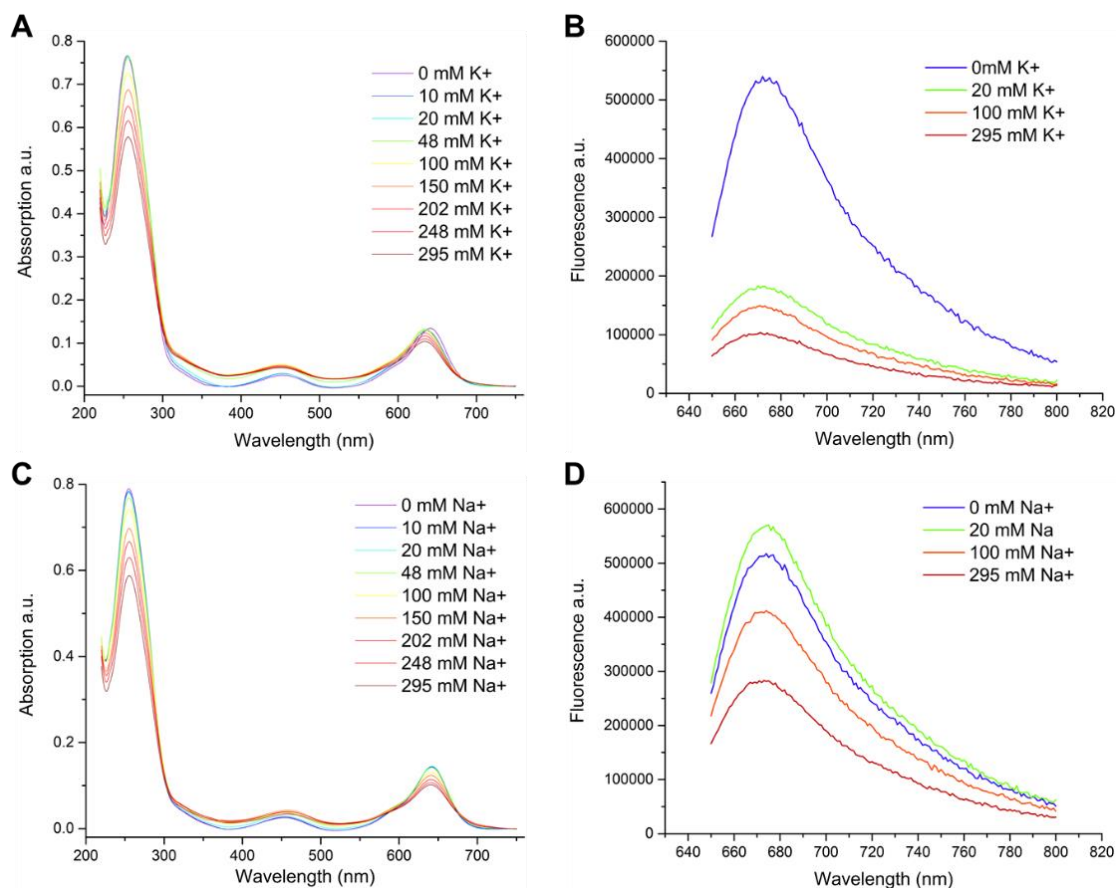


Figure 72. Exemple de la titration de la séquence 5'XGG : A) Spectres d'absorption de la titration en potassium. B) Spectres d'émission de la titration en potassium. C) Spectres d'absorption de la titration en sodium. D) Spectres d'émission de la titration en sodium.

De ce fait, nous supposons que la structure simple-brin interagit légèrement avec la sonde et que lors de la formation du G-quadruplexe, la **MG** ne s'intercale pas mais est éjectée hors de la structure secondaire et ainsi exposée au milieu aqueux. On peut en conclure que la Malachite Green et la façon dont elle est liée à l'ODN ne sont pas adaptées pour ce type d'étude.

II.2.5. Interaction avec des protéines

De nombreuses protéines interagissent avec les structures primaires ou secondaires des acides nucléiques pour effectuer divers mécanismes biologiques^{181,182,183}. Il est parfois nécessaire de pouvoir les identifier. Nous sommes donc attachés à étudier l'interaction de plusieurs protéines, prises comme modèles d'étude, avec des ODNs marqués avec la **MG** puis avec les duplexes complémentaires.

Dans un 1^{er} temps, nous avons choisi 3 types de protéines connues pour interagir soit avec des ODNs, soit avec des ODNs. Par ailleurs, nous avons aussi testé la capacité des ODNs marqués à interagir avec la BSA, l'albumine de sérum bovin, connue pour interagir avec des composés hydrophobes.

Les protéines ont été ajoutées en excès dans une solution contenant les séquences ODN marquées (simple ou double-brin), puis les spectres d'absorption et émission du mélange ont été réalisés. Malheureusement, les résultats ne montrent aucun effet fluorogénique notable (**Figure 73**), quelle que soit la protéine utilisée. Les résultats de tous ces essais sont décrits dans la partie expérimentale (Figure S7-S9).

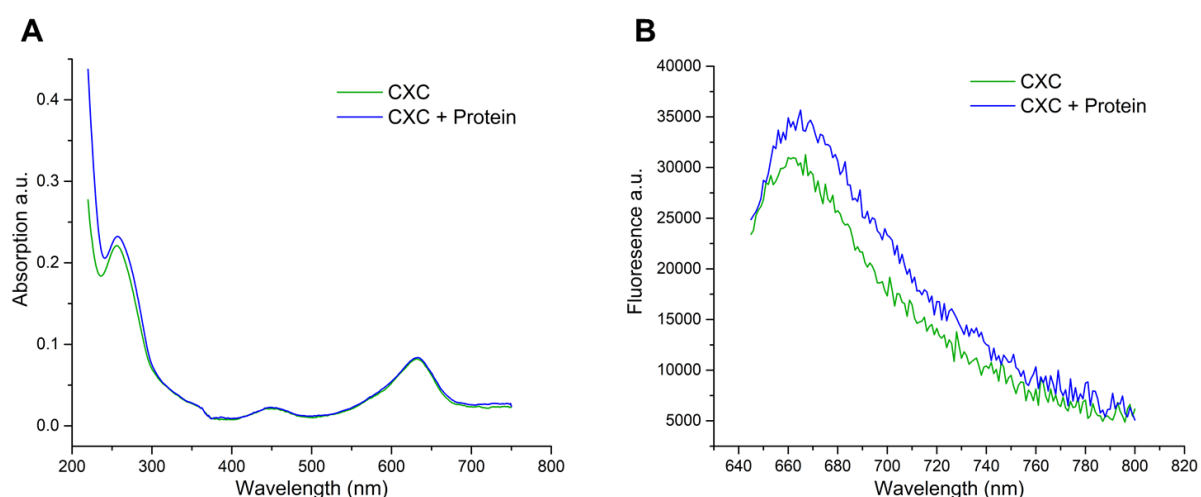


Figure 73. Exemple d'interaction du simple brin CXC avec la protéine ligand des ADNss. A) en absorption. B) en émission.

Conclusion

Dans ce chapitre, nous avons étudié le potentiel de deux nouvelles structures de type « *molecular rotor* », en tant que sondes d'hybridation fluorogéniques. Dans le cas de la chromone thiophène **6-EMT**, une amplification de fluorescence d'un facteur 10 a été obtenue lors de l'hybridation. Dans le cas de la sonde Malachite Green (MG) modifiée, aucune amplification n'a été détectée. Une hypothèse plausible est basée sur le nombre de degrés de liberté. Dans le cas de la **6-EMT**, la perte de planéité de la molécule provient de la rotation d'une seule liaison σ entre la chromone et son groupement donneur thiophène, alors que dans le cas de la MG, il existe 3 liaisons σ , ce qui rend l'aplanissement total de la molécule bien plus contraignant.

Chapitre 4 : Sondes Miami – Ligand et intercalant

I. Introduction

Dans ce chapitre, nous allons nous intéresser à une famille de sondes particulières, appelées « Miami ». Comme un grand nombre de molécules fluorescentes, elles tirent leur nom de la ville dans lesquelles elles ont été développées. En 2013, les équipes du Dr. Wilson et du Pr. Westerlund développent deux nouvelles sondes, la « Miami Green » et « Miami Yellow » (**Figure 74A**), possédant un comportement de On/Off, à la suite d'une interaction avec un système biologique. Leurs propriétés photophysiques ainsi que leurs interactions avec l'ADN ont été décrites dans un article publié dans *J. Phys. Chem. B*¹⁸⁴. La même année, les Dr. Wilson et Pr. Westerlund publient, dans *Organic letters*¹⁸⁵, un article dans lesquels les auteurs proposent les modes d'interaction des deux sondes avec l'ADNs. Leurs analyses s'appuient sur des études d'absorption dichroïque en lumière polarisée circulaire et linéaire. Les résultats obtenus ont été comparés avec ceux obtenus dans le cas des sondes de référence « DAPI » et « Hoechst ». De cette publication, les auteurs ont proposé que la sonde Miami Green se lierait préférentiellement dans le petit sillon de l'hélice ADNs, tandis que la Miami Yellow jouerait le rôle d'intercalant (**Figure 74B**).

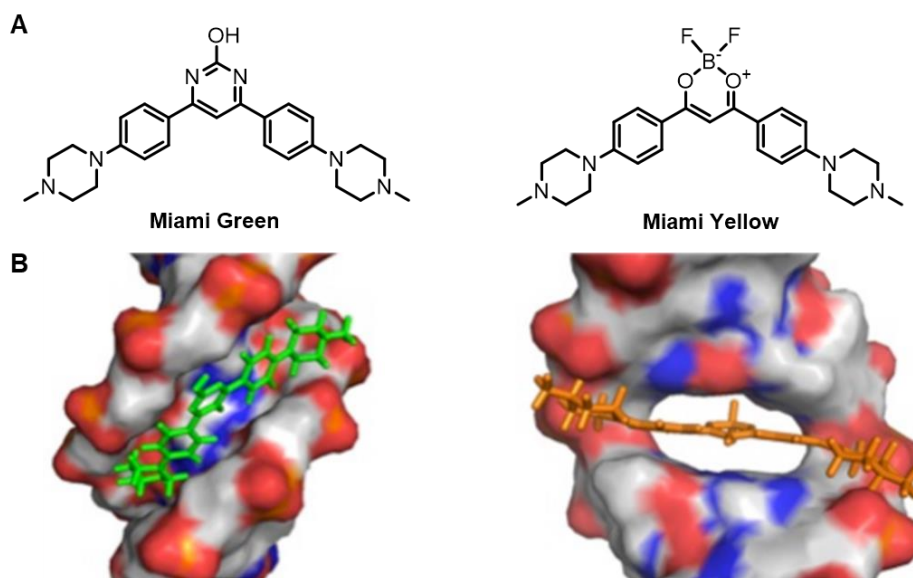


Figure 74. A) Structure des sondes Miami Green et Miami Yellow. B) Méthode d'interaction des sondes avec l'ADNs, par interaction avec le petit sillon (gauche) ou par intercalation (droite)¹⁸⁵.

Par la suite, les mêmes équipes ont développé quatre dérivés des sondes Miami Green et Yellow, possédant des systèmes de conjugaison plus étendus¹⁸⁶. Pour ces quatre dérivés, une

ou deux doubles liaisons ont été intégrées de part et d'autre du cycle central. Deux molécules asymétriques (**Figure 75A et B**) et deux molécules symétriques (**Figure 75C et D**), ont ainsi été évaluées en tant que sondes fluorogéniques, lors de l'hybridation d'ADN.

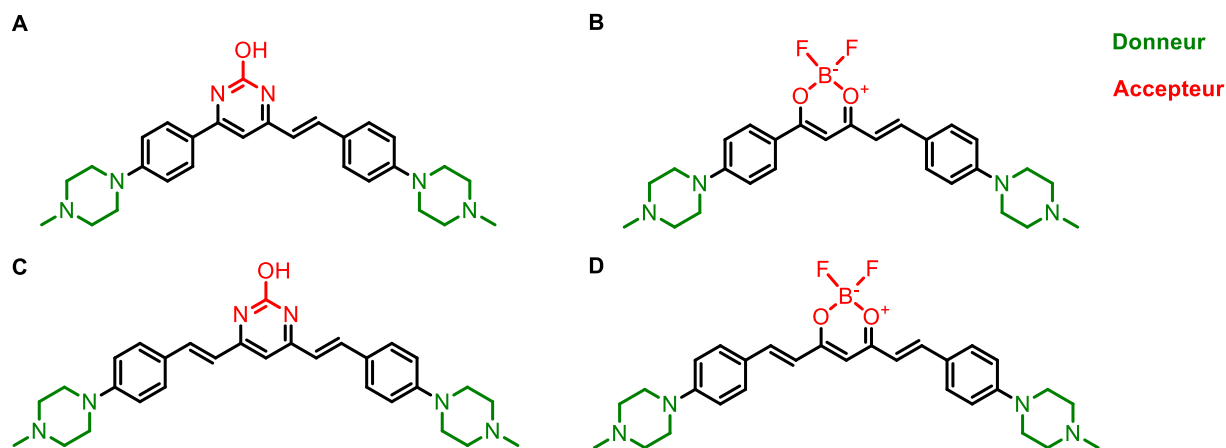


Figure 75. Structures asymétriques contenant une seule double liaison A) dérivés de Miami Green, B) dérivés de Miami Yellow. Structures symétriques contenant deux doubles liaisons C) dérivés de Miami Green, D) dérivés de Miami Yellow.

Les résultats ont montré un décalage, vers le rouge, des bandes d'absorption et d'émission de ces dérivés, d'autant plus grand que le système conjugué est étendu. Par ailleurs, la présence des doubles liaisons dans ces structures conduit à une plus grande flexibilité, ce qui réduit le rendement quantique de ces dérivés lorsqu'ils sont en solution (*molecular rotor*). Lors des expériences d'hybridation, les deux sondes asymétriques (**Figure 75A et B**) conduisent à des facteurs d'amplification de fluorescence allant jusqu'à 92, tandis que pour les structures plus étendues (**Figure 75C et D**), ce facteur est seulement de 10.

Vu le potentiel fluorogénique des deux noyaux Miami asymétriques, contenant une seule double liaison, nous avons décidé de les étudier en les couplant à des ODN.

II. Résultats et discussion

II.1. Synthèse

Nous nous sommes tout d'abord attachés à élaborer deux sondes contenant une seule double liaison, fonctionnalisées soit par un groupement azoture (**Schéma 7**, composés **8** et **12**) soit par un groupement alcynyle au niveau de l'azote d'un des motifs piperazine (**Schéma 7**, composés **9** et **13**). La rétrosynthèse de ces composés est présentée dans le **Schéma 7**. Ils proviennent respectivement de deux intermédiaires azoture **3** et alcynyle **5**, eux-mêmes préparés à partir de la 4'-piperazinoacétophénone commerciale.

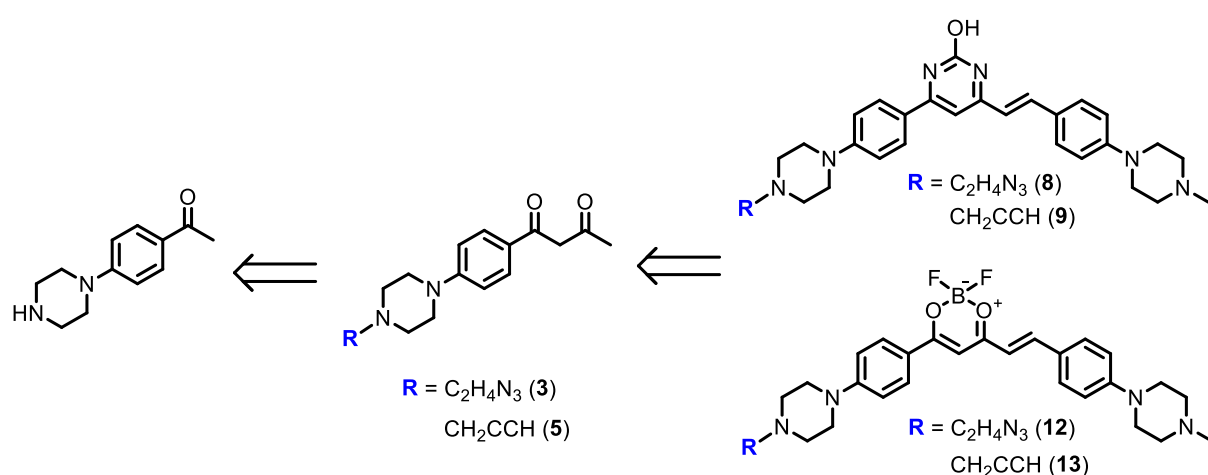


Schéma 7. Rétrosynthèse des dérivés click de Miami.

II.1.1. Synthèse des intermédiaires communs azoture **3** & alcynyle **5**

i. Intermédiaire azoture

La synthèse de ces 2 intermédiaires a été effectuée à partir de la 4'-piperazinoacétophénone commerciale (**Schéma 8**). L'alkylation de la fonction amine secondaire a été réalisée au moyen du 1-bromo-2-chloroéthane, à T° ambiante. Le composé **1** a ainsi été obtenu avec un rendement de 52%, après purification, le dimère étant un produit secondaire de la réaction. Le chlore a ensuite été substitué par un groupement azoture, au moyen d'azoture de sodium. Le composé **2** a été obtenu avec 89% de rendement après purification. La dicétone **3** a été formée par la suite *via* une condensation de Claisen croisée avec l'acétate d'éthyle, puis purifiée sur colonne de gel de silice (Rendement = 56%)

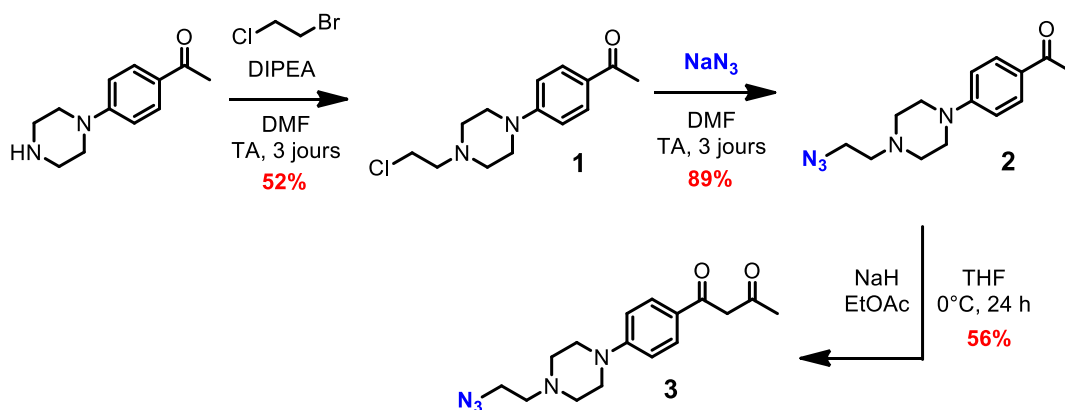


Schéma 8. Synthèse de l'intermédiaire azoture 3.

ii. Intermédiaire alcyne

Tout comme pour l'intermédiaire azoture 3, la synthèse de l'intermédiaire alcyne 5 a été effectuée à partir de la 4'-piperazinoacétophénone, en deux étapes (Schéma 9). La première est l'alkylation de l'amine secondaire du motif pipérazine par le bromure de propargyle, qui conduit au produit 4 avec 22% de rendement après purification. La seconde étape est la même que pour l'intermédiaire azoture 3, *i.e.* la condensation de l'acétate d'éthyle pour conduire quantitativement au dérivé dicétone 5.

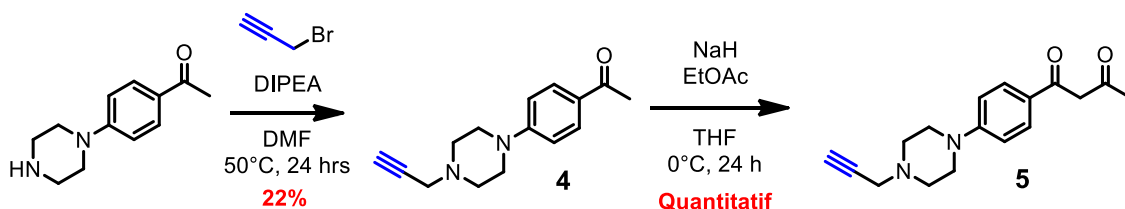


Schéma 9. Synthèse de l'intermédiaire alcyne 5.

II.1.2. Synthèse des sondes click

i. Dérivés Pyrimidine

La synthèse des sondes fonctionnalisées est décrite dans le Schéma 10. Les précurseurs 6 et 7 ont tout d'abord été préparés *via* une condensation de l'urée avec les composés dicarbonylés précédemment synthétisés (3 ou 5), avec des rendements respectifs de 31% et 100%. Puis les composés 8 et 9 ont été obtenus par condensation des produits 6 et 7 avec la 4-(4-méthyl-1-pipérazinyl)-benzaldéhyde, en présence de Me₃SiCl (TMSCl), dans le DMF et à 90°C (Schéma 10), avec des rendements de 79% et 100%, respectivement.

Le TMSCl a été plusieurs fois décrit comme étant promoteur de nombreuses réactions de condensation, par augmentation de la réactivité de l'aldéhyde aromatique^{187,188}.

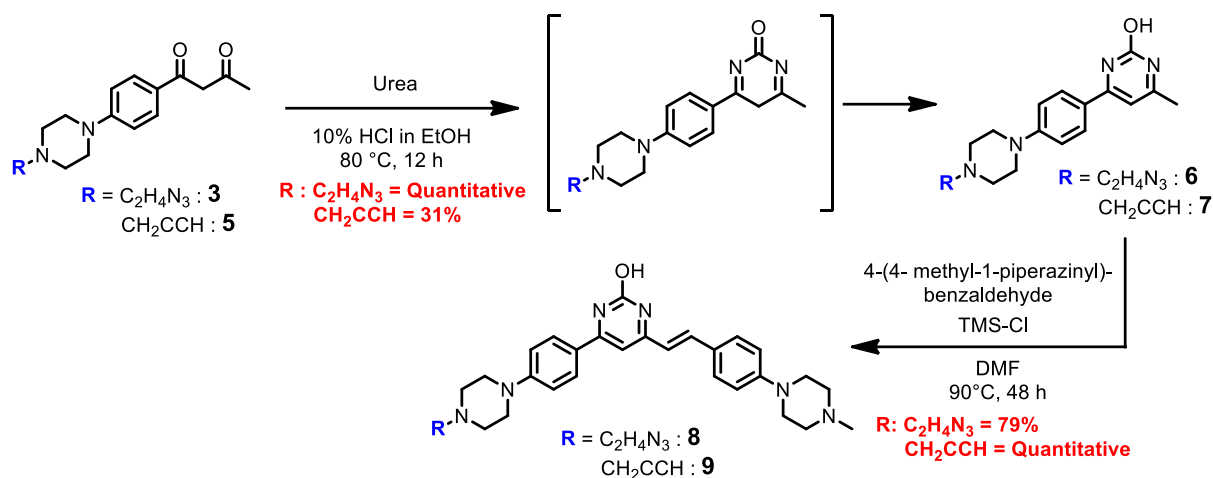


Schéma 10. Préparation des produits finaux pyrimidiques **8** et **9**.

ii. Dérivés organoborés

Tout comme les dérivés pyrimidiques, la synthèse des composés organoborés **12** et **13** se déroule en deux étapes (Schéma 11). La première génère les cycles organoborés **10** et **11**. Cette réaction implique la rupture de la liaison B-F (dont l'enthalpie de liaison est la plus forte connue : 646 kJ/mol), et la formation d'un cycle à 6 chaînons aromatique. Les composés **10** et **11** sont ensuite condensés avec la 4-(4-méthyl-1-pipérazinyl)-benzaldéhyde, en présence d'un acide de Lewis faible et d'une amine primaire, pour conduire aux sondes **12** et **13** avec des rendements respectifs de 53% et 74%.

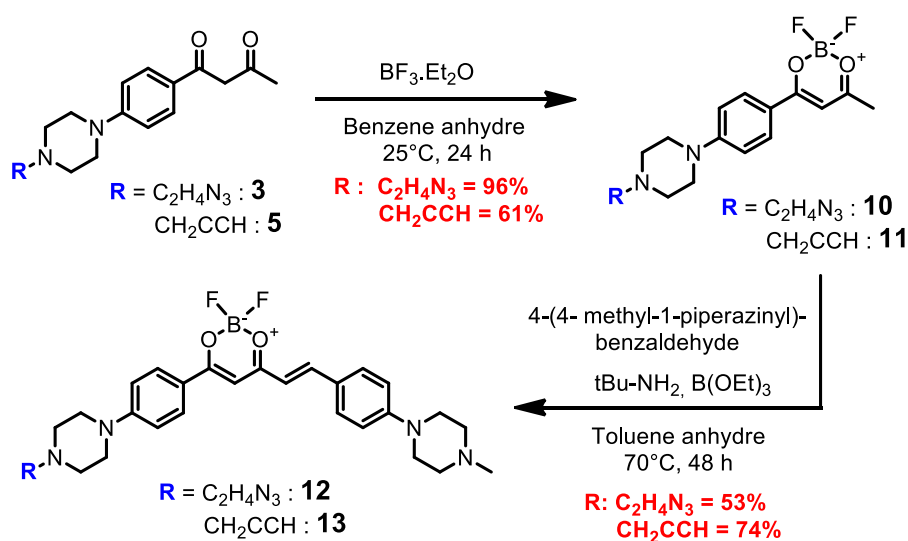


Schéma 11. Préparation des produits finaux organoborés **12** et **13**.

II.2. Caractérisations photophysiques des sondes dérivées de MG et MY

Les nouveaux composés synthétisés (**8**, **9** et **12**, **13**), dérivés des structures des sondes Miami Green et Yellow, peuvent se comporter comme des sondes push-pull (D- π -A- π -D). Au vu de leur structure, ils pourraient de plus avoir des propriétés de *molecular rotor*. Pour étudier ces différentes propriétés, nous avons mesuré les longueurs d'onde absorbées et émises par ces sondes, dans des milieux de différentes polarités. Comme on pouvait s'y attendre dans le cas de sondes « push-pull l'augmentation de la polarité du solvant induit globalement un effet bathochrome en absorption/émission, (Tableau 5, figure S3). Le coefficient d'extinction molaire (ϵ) a été déterminé pour les quatre dérivés. Celui-ci est de 30 000 cm⁻¹.M⁻¹ pour les dérivés pyrimidiques (**8** et **9**) et de 78 000 cm⁻¹.M⁻¹ pour les organoborés (**12** et **13**). Les rendements quantiques sont faibles à modestes pour les composés **8** et **9**. Les composés **12** et **13** se comportent différemment, ils sont très émissifs dans les solvants apolaires mais le rendement quantique baisse graduellement avec l'augmentation de la polarité du solvant. L'ensemble de nos données ne sont pas favorables à un effet « molecular rotor » très marqué puisque les rendements quantiques les plus élevés ont été obtenus dans des solvants non visqueux à l'exception de BuOH. Une donnée est également remarquable dans le Tableau 5, c'est le déplacement de Stokes ($\Delta\lambda$). Dans le cas des deux sondes, ces valeurs sont très élevées, notamment pour le composé pyrimidique **8** (121nm < $\Delta\lambda$ < 172 nm).

Tableau 5. Effet des solvants sur les caractéristiques photophysiques des sondes pyrimidique **8** et organoborée **12**.

Solvent	$E_T(30)$	λ_{abs}^a		λ_{em}^b		$\Delta\lambda^c$		Φ (%) ^d	
		8	12	8	12	8	12	8	12
MeOH	55.4	426	514	598	638	172	124	7	8
BuOH	49.7	424	513	580	627	156	114	28	43
CH₃CN	45.6	410	528	575	644	165	116	8	4
DMSO	45.1	426	548	573	656	147	108	22	9
Acetone	42.2	-	523	-	627	-	104	-	12
CH₂Cl₂	40.7	418	528	555	625	137	97	17	40
EtOAc	38.1	410	511	543	601	133	90	17	55
THF	36.2	404	516	525	601	121	85	28	85
Toluene	33.9	-	515	-	569	-	54	-	100

^a Longueur d'onde du maximum d'absorption. ^b Longueur d'onde du maximum d'émission. ^c Déplacement de Stokes ($\lambda_{em} - \lambda_{abs}$). ^d Φ est le rendement quantique de fluorescence.

Par ailleurs, lors de toutes les études photophysiques, nous avons observé que les sondes **8** et **9** avaient un comportement similaire. Il en est de même que pour les sondes **12** et **13**. Ceci confirme que les groupements azoture et alcyne sont bien positionnés, et ne modifient pas les propriétés photophysiques des sondes. Seules les propriétés photophysiques des sondes **8** et **12** seront ici commentées.

Dans un deuxième temps, nous avons examiné l'effet du taux d'hydratation sur les longueurs d'onde absorbées et émises par les sondes **8** et **12**, en fonction de différents mélanges THF/eau (Tableau S1). Lorsque le pourcentage d'eau augmente, la sonde pyrimidique **8** subit un effet bathochrome très prononcé, tant en absorption qu'en émission, ainsi qu'une diminution de son rendement quantique (Figure 76A). Dans le cas de la sonde organoborée **12**, on ne remarque qu'un très faible effet bathochrome mais une diminution bien plus marquée du rendement quantique (Figure 76B).

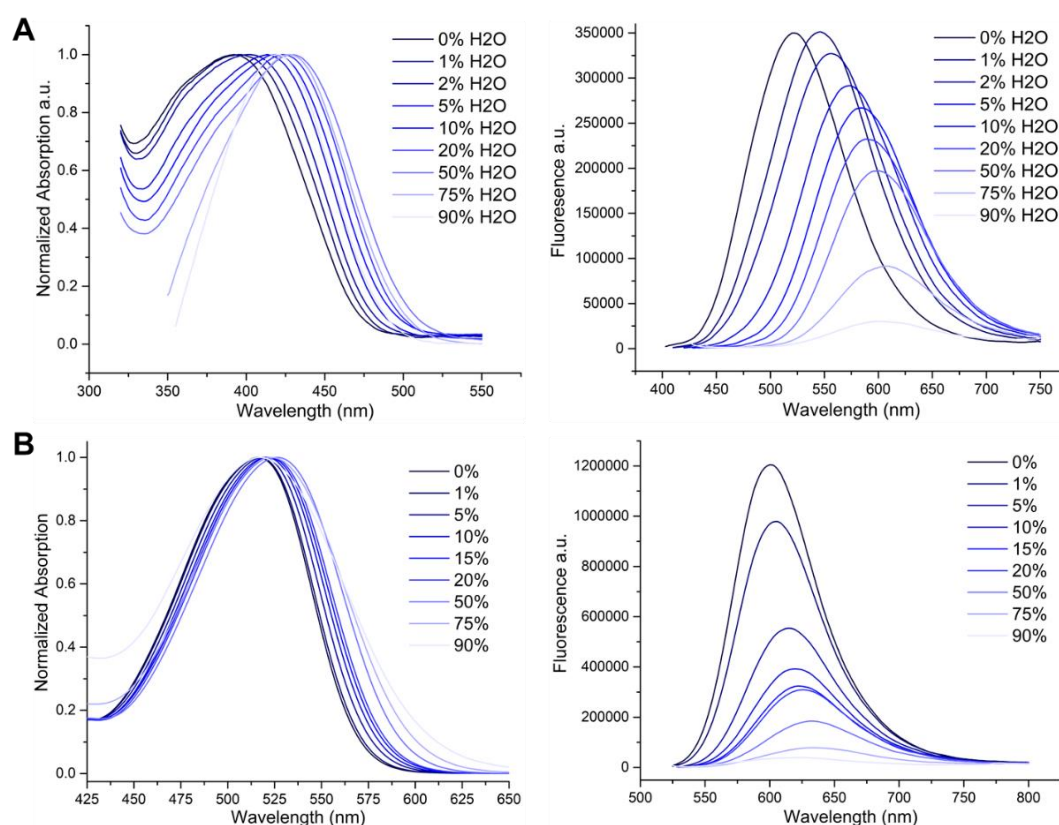


Figure 76. A) Spectres d'absorption (gauche) et d'émission (droite) de la sonde pyrimidique **8**, suite à l'augmentation du pourcentage d'eau dans le THF. B) Spectres d'absorption (gauche) et d'émission (droite) de la sonde organoborée **12** suite à l'augmentation du pourcentage d'eau dans le THF.

Nous avons ensuite étudié les propriétés physicochimiques de ces sondes, qui possèdent différentes fonctions acide et amine, en fonction du pH, dans le PBS, par addition de NaOH (1M) ou HCl (1M). Certaines d'entre elles n'entrent pas en jeu dans la conjugaison de la molécule. C'est ainsi le cas des deux amines tertiaires des motifs piperazine. Nous supposons alors qu'au moins une de ces deux amines est protonée ($pK_a = 8,3$) à pH physiologique, quel que soit la sonde. Dans le cas de la sonde **8** (et **9**), il existe deux valeurs de pK_a : l'une à 4,2 et l'autre à 9,9 (Figure S1). Le pK_a à 4,2 pourrait correspondre à celui d'une amine sp^2 du cycle pyrimidique qui, en se protonant, deviendrait fortement électro attracteur. Ceci générerait une bande déplacée vers le rouge (Figure 77A). Le pK_a à 9,9, lui, serait associé au proton de l'hydroxypyrimidine ou plutôt de celui du NH de la forme tautomère pyrimidinone (voir la cytosine^{189,190,191}). Les deux points isobestiques observés dans la Figure 77A sont accord avec cette interprétation pour deux équilibres acido-basiques. Quant aux sondes organoborées (**12** et **13**), elles ne présentent pas de fonctions acide ou basique de ce type et donc les variations de maxima d'absorption observées par spectrométrie UV sont plus modestes (Figure 77B).

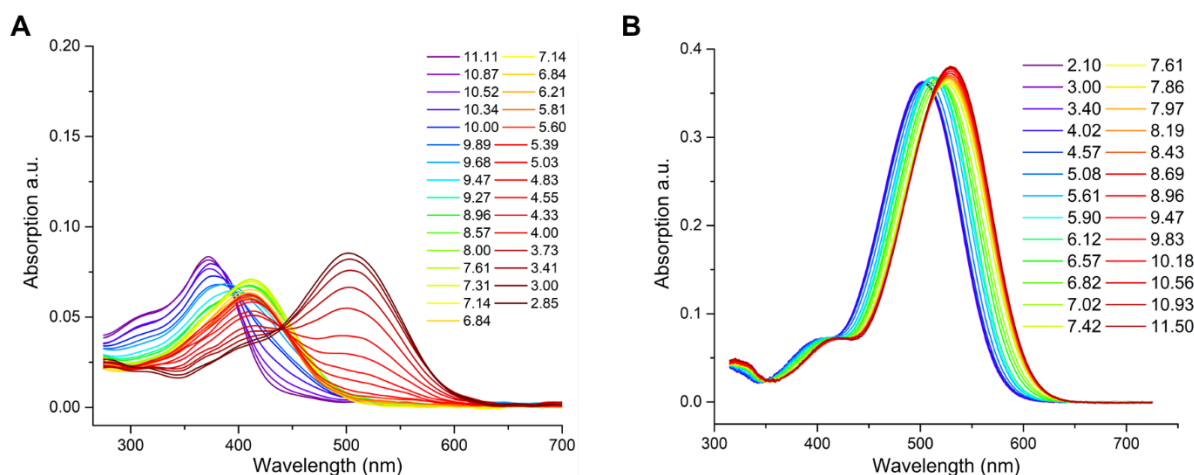


Figure 77. Titration pH, dans le PBS, par addition de NaOH (1M) ou HCl (1M). A) de la sonde pyrimidique **8** B) de la sonde organoborée **12**.

Finalement, nous avons examiné la photostabilité de ces quatre sondes. Après plus de 30 min d'irradiation au maximum d'absorption, avec une ouverture de fente 8x8, les sondes ne se sont que très peu dégradées (Figure S4-S5), ce qui est important dans le cadre d'une application en imagerie.

II.3. Caractérisations Photophysiques des ODNs marqués

II.3.1. Etude de l'hybridation d'ODNs

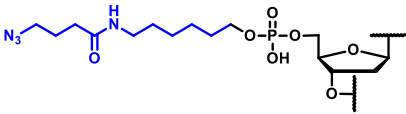
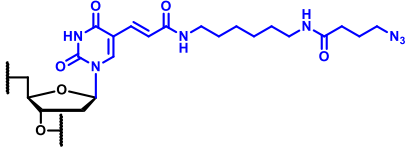
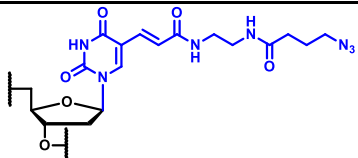
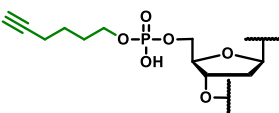
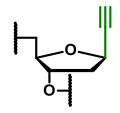
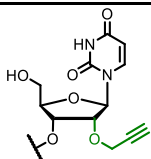
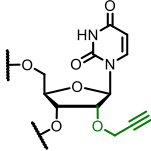
Nous avons incorporé les sondes **8/9** et **12/13** dans neuf séquences d'ODN fonctionnalisées par des groupements azoture ou alcyne, *via* des réactions click CuAAC. Le **Tableau 6** résume ces neuf séquences porteuses d'une fonction alcyne ou azoture. Sept d'entre elles sont identiques à celles utilisées précédemment (cf. Publication 2, p.111) et deux sont nouvelles. Elles ont été ajoutées à notre bibliothèque d'ODNs.

Les études faites auparavant sur la sonde Miami Green indiquent que celle-ci devrait se localiser dans le petit sillon de l'ADN. Deux autres séquences « click » ont alors été choisies pour orienter la sonde vers ce sillon : la **SGCA** et la **TST**. Dans celles-ci, un court lien alcyne se situe en position 2' du sucre d'un nucléoside U. Dans ces deux séquences, ce nucléoside est positionné soit à l'extrémité 5', soit au milieu de l'ODN.

Les réactions « click » de ces 9 séquences avec nos dérivés de Miami (**8, 9, 12, 13**) a conduit à 18 simples brins d'ODNs marqués (**Tableau 6**).

Les séquences ODN « azoture » ont été couplées avec les sondes alcyne **9** et **13** et les séquences ODN « alcyne » avec les sondes azoture **8** et **12**. La purification ainsi que les caractérisations structurales des 18 ODNs marqués ont été réalisées suivant les mêmes protocoles que décrit précédemment (Tableau S3-S5, Figure S7-S8).

Tableau 6. Description des séquences d'ODNs fonctionnalisés utilisées pour les réactions CuAAC avec les dérivés de Miami.

Séquences	Noms	Lien de CuAAC
5'- YGCA AAA TTT AAA ACG-3'	YGCA	
5'-GCA AAA TX T AAA ACG-3'	TX T	
5'-GCA AAA AAA AX A AAA AAA ACG-3'	AX A	
5'-GCA AAA TXs T AAA ACG-3'	TXs T	
5'- VGCA AAA TTT AAA ACG-3'	VGCA	
5'-GCA AAA TW T AAA ACG-3'	TW T	
5'-GCA AAA AAA AW A AAA AAA ACG-3'	AW A	
5'- SGCA AAA TTT AAA ACG-3'	SGCA	
5'-GCA AAA TST AAA ACG-3'	TST	

Les 18 ODNs marqués ont tout d'abord été caractérisés photophysiquement, puis sur les duplexes obtenus après hybridation avec des ODN complémentaires.

Tous les spectres d'absorption et d'émission des simples et doubles brins sont disponibles dans la partie expérimentale (Figure S9-S12, **Figure 78**).

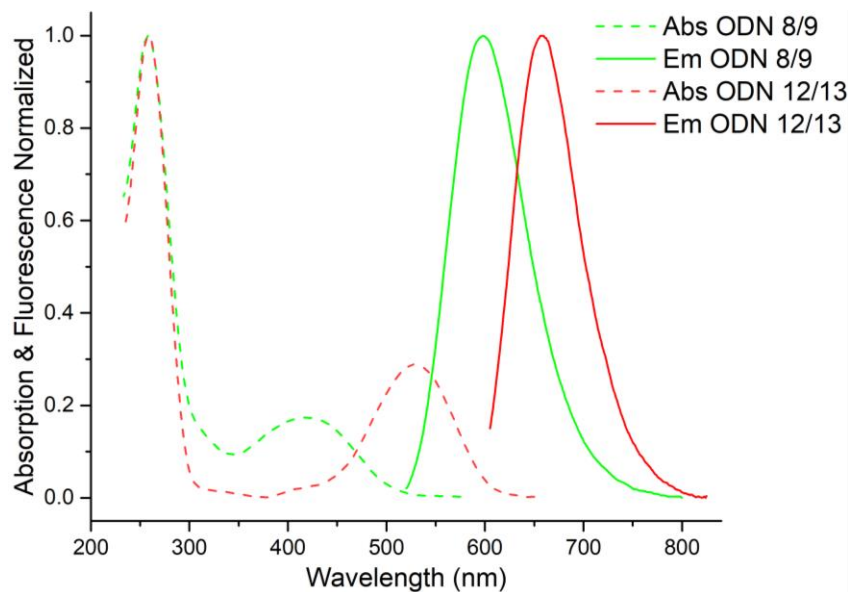


Figure 78. Représentation des spectres d'absorption et d'émission des ODN marqués par la sonde 8/9 ou 12/13.

Les **tableaux 7 et 8** rassemblent les données relatives à certaines séquences simple-brins marquées, contenant un lien azoture (**Tableau 7**) ou alcyne (**Tableau 8**).

Tableau 7. Etude spectroscopique, dans le PBS, des ODNs marqués par un lien azoture et des duplexes après hybridation avec le brin complémentaire dans le PBS.

Séquences	$\lambda_{\text{abs}} \text{ (nm)}^a$		$\lambda_{\text{em}} \text{ (nm)}^b$		$\Phi \text{ (\%)}^c$		Brillance ($\text{L}\cdot\text{mol}^{-1}\cdot\text{cm}^{-1}$) ^d	
	9	13	9	13	9	13	9	13
YGCA	431	527	589	646	8	7	2,400	5,460
YGCA·CGT	458	542	597	650	35	14	10,500	11,000
TXT	420	529	591	642	7	11	2,100	5,500
TXT·AAA	447	544	602	652	31	16	9,300	12,500
AXA	424	528	594	652	6	7	1,800	4,700
AXA·TTT	445	539	596	651	30	15	9,000	11,700
TXsT	/	530	/	640	/	12	/	9,400
TXsT·AAA	/	538	/	647	/	14	/	11,000

^a Longueur d'onde du maximum d'absorption. ^b Longueur d'onde du maximum d'émission. ^c Rendement quantique déterminé en utilisant le Nile Blue dans EtOH ($\Phi = 0,27$) comme référence. ^d Brillance calculée au maximum d'absorption selon la relation : $\epsilon \times \Phi$.

Tableau 8. Etude spectroscopique, dans le PBS, des ODNs marqués par un lien alcyne et des duplexes après hybridation avec le brin complémentaire dans le PBS.

Séquences	$\lambda_{\text{abs}}(\text{nm})^a$		$\lambda_{\text{em}}(\text{nm})^b$		$\Phi(\%)^c$		Brillance ($\text{L}\cdot\text{mol}^{-1}\cdot\text{cm}^{-1}$) ^d	
	8	12	8	12	8	12	8	12
VGCA	425	530	591	646	5	5	1,500	3,900
VGCA·CGT	437	542	595	653	11	8	3,300	6,200
TWT	421	528	593	650	4	5	1,200	3,900
TWT·AAA	450	543	596	652	13	9	3,900	7,000
AWA	422	524	597	651	4	4	1,200	3,100
AWA·TTT	455	544	600	656	22	13	6,600	10,100
SGCA	422	530	589	646	5	5	1,500	3,900
SGCA·CGT	418	540	596	652	8	5.5	2,400	4,300
TST	416	530	594	651	4	4	1,200	3,100
TST·AAA	464	551	595	656	7	6	2,100	4,700

^a Longueur d'onde du maximum d'absorption. ^b Longueur d'onde du maximum d'émission. ^c Rendement quantique déterminé en utilisant le Nile Blue dans EtOH ($\Phi = 0,27$) comme référence. ^d Brillance calculée au maximum d'absorption selon la relation : $\epsilon \times \Phi$.

Au travers de ces deux tableaux, on remarque que les sondes pyrimidiques (**8** et **9**) interagissent très fortement avec l'ODN complémentaire lors de son hybridation. En effet, pour la quasi-totalité des séquences, on observe une augmentation significative du rendement quantique et du déplacement bathochrome en absorption ($12 < \Delta\lambda_{\text{abs}} < 48$ nm) et en émission ($1 < \Delta\lambda_{\text{em}} < 11$ nm). Le $\Delta\lambda_{\text{abs}}$ le plus large a été obtenu avec TST après hybridation. Cette différence est particulièrement importante. Le déplacement vers le rouge du maximum d'absorption a également été observé pour les sondes organoborées (**12** et **13**), mais dans une moindre mesure.

Grâce à ces mesures, nous avons pu déterminer le facteur d'amplification de fluorescence observée lors de l'hybridation, ce facteur étant défini comme le rapport de l'intensité de fluorescence du double brin sur celle du simple brin. L'intensité de fluorescence est dépendante de la longueur d'onde d'excitation du fluorophore. Plus cette longueur d'onde est proche du maximum d'absorption, plus cette intensité sera élevée. Dans notre cas, la longueur d'onde du maximum d'absorption du simple-brin est différente de celle du double brin. Il est alors possible de faire varier le rapport d'intensité de fluorescence grâce à un

changement de la longueur d'onde d'excitation. De la même manière, il est possible de faire varier le rapport de brillance. En effet, le coefficient d'extinction molaire d'une sonde est dépendant de la longueur d'onde, contrairement à son rendement quantique.

En conséquence, nous avons effectué un screening des longueurs d'ondes d'excitation pour chaque simple et double brin. Ceci nous a permis de déterminer le meilleur facteur d'amplification de fluorescence et de brillance (**Tableau 9**). Dans le cas des sondes pyrimidiques **8** et **9**, la longueur d'excitation optimale est de 510 nm. Dans le cas des sondes organoborées **12** et **13**, cette longueur d'onde est de 590 nm.

Tableau 9. Effet de l'hybridation sur la brillance, le rapport d'absorption et l'amplification de fluorescence pour deux longueurs d'onde d'excitation.

Sonde sur la séquence	λ_{Ex} (nm) ^a	YGCA	YGCA·CGT	Rapport d'absorbance ^c	Amplification de Fluorescence ^d
		Brillance (L.mol ⁻¹ .cm ⁻¹) ^b			
9	430	1 934	5 099	0,8	5,4
	510	39	1 275	13,5	15
13	540	4 958	10 830	1,1	3,4
	590	1 329	5 252	1,9	6

Sonde sur la séquence	λ_{Ex} (nm) ^a	TXT	TXT·AAA	Rapport d'absorbance ^c	Amplification de Fluorescence ^d
		Brillance (L.mol ⁻¹ .cm ⁻¹) ^b			
9	420	1 517	7 000	0,8	6
	510	152	3080	4,3	12
13	540	7 605	12 699	1,1	2,4
	590	1 960	6 603	2,2	4

Sonde sur la séquence	λ_{Ex} (nm) ^a	AXA	AXA·TTT	Rapport d'absorbance ^c	Amplification de Fluorescence ^d
		Brillance (L.mol ⁻¹ .cm ⁻¹) ^b			
9	430	1417	7529	1	7
	510	64	1506	4,4	15
13	540	4676	12869	1,1	3
	590	1182	5315	1,6	5

Sonde sur la séquence	λ_{Ex} (nm) ^a	TXsT	TXsT·AAA	Rapport d'absorbance ^c	Amplification de Fluorescence ^d
		Brillance (L.mol ⁻¹ .cm ⁻¹) ^b			
13	540	8 704	10 817	1	1,2
	590	2 423	4 435	1,4	2

Sonde sur la séquence	λ_{Ex} (nm) ^a	VGCA	VGCA·CGT	Rapport d'absorbance ^c	Amplification de Fluorescence ^d
		Brillance (L.mol ⁻¹ .cm ⁻¹) ^b			
8	430	1 168	2 555	0,9	3,3
	510	117	613	2,2	8
12	540	3 278	5 734	1	2,4
	590	946	2 752	1,7	4

Sonde sur la séquence	λ_{Ex} (nm) ^a	TWT	TWT·AAA	Rapport d'absorbance ^c	Amplification de Fluorescence ^d
		Brillance (L.mol ⁻¹ .cm ⁻¹) ^b			
8	420	902	2 637	0,75	4,4
	510	72	745	2,8	13
12	530	3 471	6 383	1	2
	590	902	3 258	1,9	3

Sonde sur la séquence	λ_{Ex} (nm) ^a	AWA	AWA·TTT	Rapport d'absorbance ^c	Amplification de Fluorescence ^d
		Brillance (L.mol ⁻¹ .cm ⁻¹) ^b			
8	420	745	4 456	0,9	12
	510	30	1 671	8	30
12	520	2 802	9 292	1	5
	610	196	2 121	3,3	10

Sonde sur la séquence	λ_{Ex} (nm) ^a	SGCA	SGCA·CGT	Rapport d'absorbance ^c	Amplification de Fluorescence ^d
		Brillance (L.mol ⁻¹ .cm ⁻¹) ^b			
8	420	1 200	5 570	1	1,6
	510	228	1 671	1	4
12	530	3 779	4 079	1	1,2
	590	1 096	1 665	1,4	2

Sonde sur la séquence	λ_{Ex} (nm) ^a	TST	TST·AAA	Rapport d'absorbance ^c	Amplification de Fluorescence ^d
		Brillance (L.mol ⁻¹ .cm ⁻¹) ^b			
8	420	923	2 607	0,8	3
	510	52	1 932	11	9,5
12	530	2 894	3 921	0,8	2,4
	590	897	2 483	1,8	5

^a Détermination de la longueur d'onde optimale. ^b Calcul de la brillance : absorptivité à la longueur d'onde d'excitation * Rendement Quantique. ^c Calculée par : Absorbance du double brin / Absorbance du simple brin. ^d Calculée par : Intensité du double brin / Intensité du simple brin

Grâce à l'effet bathochrome observé en absorption lors de l'hybridation, des amplifications remarquables ont été obtenues. Le meilleur résultat se retrouve pour la séquence AWA, marquée par la sonde pyrimidique **8**. Avec un déplacement vers le rouge de 33 nm en absorption, un facteur allant jusqu'à 30 est obtenu en fluorescence (**Figure 79A**). Mais l'effet bathochrome le plus spectaculaire est celui observé avec la séquence TST (**Tableau 8**), marquée par la sonde **8**. Dans ce cas-ci, une valeur de 48 nm permet, à elle seule, l'amplification du signal de fluorescence de presque 10 (**Figure 79B**).

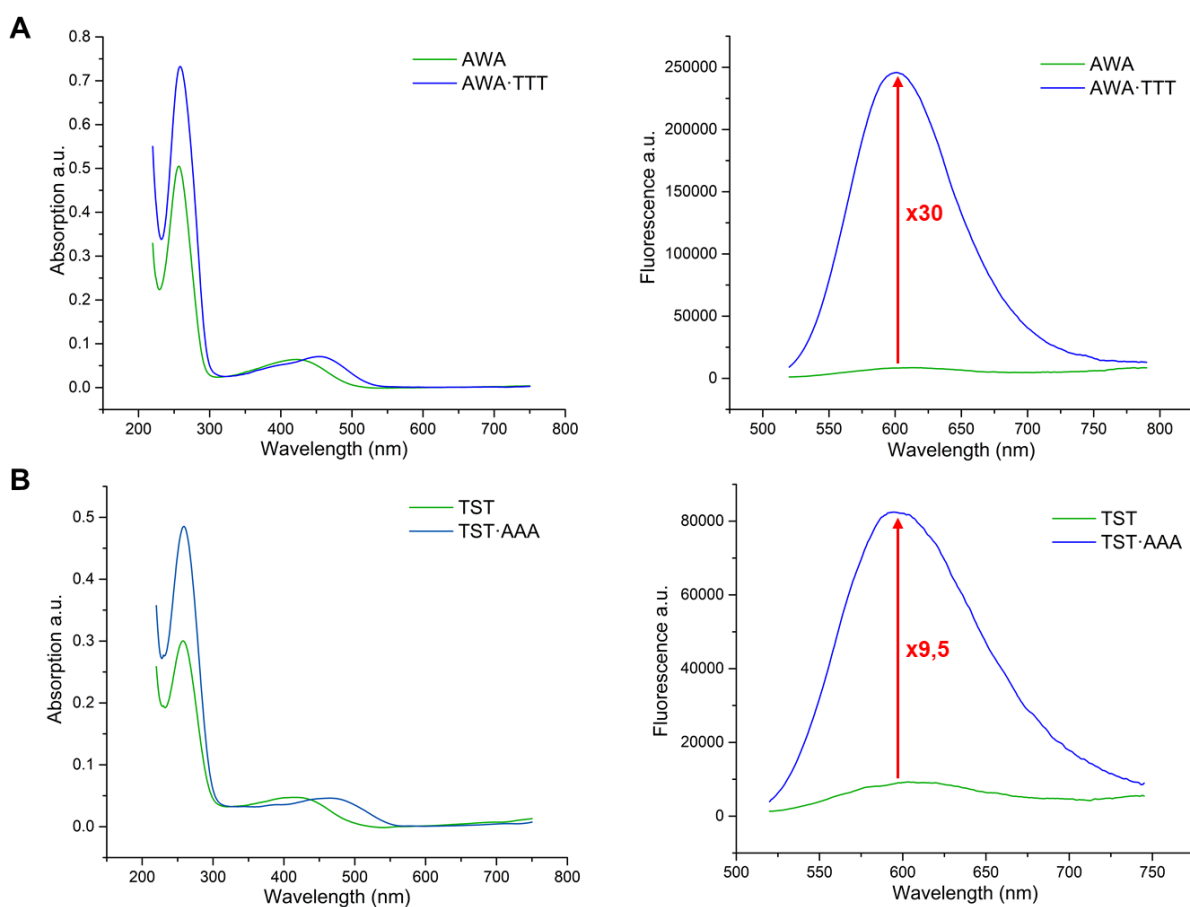


Figure 79. Spectres d'absorption (gauche) et d'émission (droite) du simple et double brin marqué par **8** sur la séquence A) AWA B) TST, avec λ_{Ex} = 510nm.

Dans le cas des sondes organoborées, c'est également la séquence AWA qui permet d'obtenir la plus grande amplification, d'un facteur 10. Ce facteur, plus faible que dans le cas des sondes pyrimidiques, reste néanmoins satisfaisant pour une sonde présentant ce déplacement de Stokes et émettant dans ces longueurs d'ondes (**Figure 80**). Dans la littérature, les sondes fluorogéniques utilisées pour le marquage covalent des AN possèdent des longueurs d'onde d'émission maximum d'environ 550 nm³⁷.

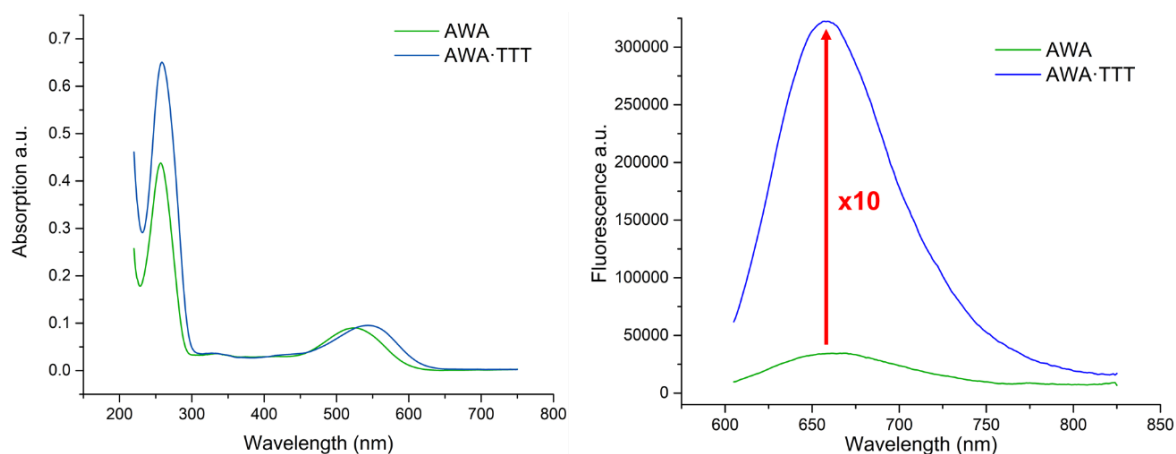


Figure 80. Spectres d'absorption (gauche) et d'émission (droite) du simple et double brin marqué par 12 sur la séquence AWA, avec $\lambda_{\text{ex}} = 610\text{nm}$.

Au vu de tous ces résultats, on constate que le facteur d'amplification est augmenté lorsque la séquence marquée est composée d'Adénine ou lorsque la sonde a la possibilité d'être proche de ces dernières. Au sein de notre équipe, des observations similaires avaient déjà été faites lors d'études précédentes réalisées avec d'autres fluorophores. Pourquoi cette particularité ? Il est connu que les simples brins poly A ont tendance à se structurer en hélice dû à l'empilement des bases puriques A. Cette structuration particulière pourrait favoriser l'expulsion de la sonde du simple brin structuré et l'exposer plus au solvant^{46,50}. A l'inverse la formation du duplexe riche en paires AT serait plus accommodant qu'un duplexe comportant des paires GC, qui est plus stable, et serait ainsi plus favorable à l'intercalation de la sonde. Ceci aurait pour conséquence d'éteindre la fluorescence du simple brin et produire une amplification accrue du signal de fluorescence lors de l'hybridation. Cette interprétation pourrait s'appliquer au dérivé de la Miami Yellow (noyau organoboré) pour lequel l'intercalation dans le duplexe est privilégié. Une autre possibilité pourrait être le résultat d'une liaison plus favorable au petit sillon du fluorophore dérivé de la Miami green comme c'est le cas des colorants DAPI et Hoechst pour les duplexes riches en paires AT^{174,69}.

Cette dernière explication est cependant difficilement envisageable pour **W** pour lequel le fluorophore substitue une base nucléique et donc est forcé à s'intercaler. Elle est également peu probable pour les séquences avec la sonde liée à un bras espaceur court comme **S** sensibles à l'hybridation. Par analogie avec le pyrène¹⁹² couplé par un bras court (un méthylène) à de l'uridine ou de l'adénosine, l'intercalation dans de l'ADNs du dérivé de la Miami Green nous semble le mode de liaison privilégié.

II.3.2. Etude sur une cible ARN

i. L'ARNm Oskar

Décrite de nombreuses fois dans la littérature, l'imagerie de l'ARNm Oskar, dans un contexte cellulaire (cellule œuf de la drosophile), a été utilisée comme preuve de concept lors de l'élaboration de nouveaux systèmes fluorescents. Ainsi, en 2003, Bratu *et al.* ont utilisé ce système pour valider l'utilisation d'un double *molecular beacon*, composé de deux sondes doublement marquées¹⁹³. Le groupe d'Oliver Seitz a également plusieurs fois ciblé cet ARN, pour valider ses travaux sur les sondes d'hybridation fluorogéniques (sondes FIT)¹¹⁸.

Au cours des précédents travaux réalisés dans l'équipe, une collaboration a été établie avec l'équipe dirigée par le Dr. Florence Besse, de l'Institut de Biologie Valrose à Nice. Cette collaboration a permis de valider le principe du DRET pour imager l'ARNm *oskar*^{194,46} (**Figure 81**).

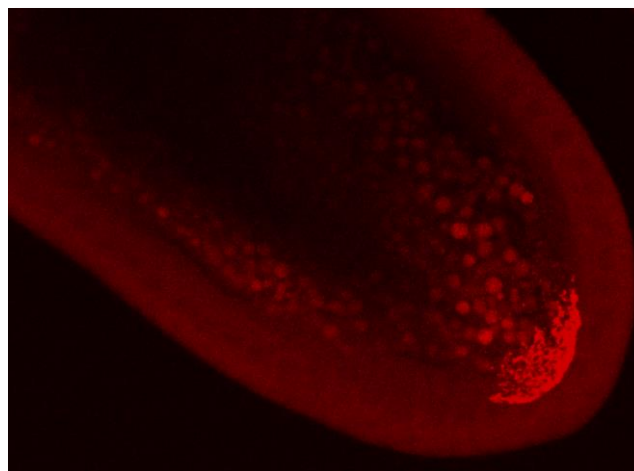


Figure 81. Image de la cible ARNm *oskar* dans la cellule œuf de la drosophile résultant de l'empilement de coupes confocales en utilisant des sondes binaires d'hybridation reposant sur un système DRET.

Nous avons donc entrepris de tester ce système pour évaluer nos sondes Miami *via* l'étude de l'hybridation de l'ARNm *oskar* avec des séquences complémentaires marquées, d'abord *in vitro* puis dans un contexte cellulaire.

ii. Etudes in-vitro

La séquence cible ARNm *oskar* est composée de 2916 nucléotides. Pour les études *in-vitro*, il est donc nécessaire de choisir une portion plus courte de cette séquence. Dans notre cas, nous avons utilisé comme cible la séquence d'ARN appelée **Oskar**, constituée de 53 nucléotides (**Tableau 10**), déjà choisie lors de l'étude faite précédemment dans l'équipe.

D'un autre côté, nous avons élaboré quatre séquences d'ADN, fonctionnalisées par un groupement azoture ou alcyne, contenant 24 résidus, complémentaires de l'extrémité 3'-de l'ARN **Oskar**. Ces séquences sont plus courtes que la cible, mimant ainsi l'interaction recherchée *in-vivo*. Nous avons choisi d'utiliser de l'ADN et non pas de l'ARN, du fait de la plus grande simplicité d'obtenir des ADN modifiés. Les duplexes formés seront donc de type ADN:ARN¹⁹⁵. Ceux-ci sont majoritairement de conformation A, mais possèdent tout de même des paramètres structuraux différents d'un duplexe ARN:ARN.

Les positions de marquage sur l'ODN différent suivant les cas (**Tableau 10** et **Figure 82**). Compte tenu des résultats précédents (cf. p.170-171), nous avons placé les résidus « click » dans les zones les plus riches en A de la séquence devant être « clickée ».

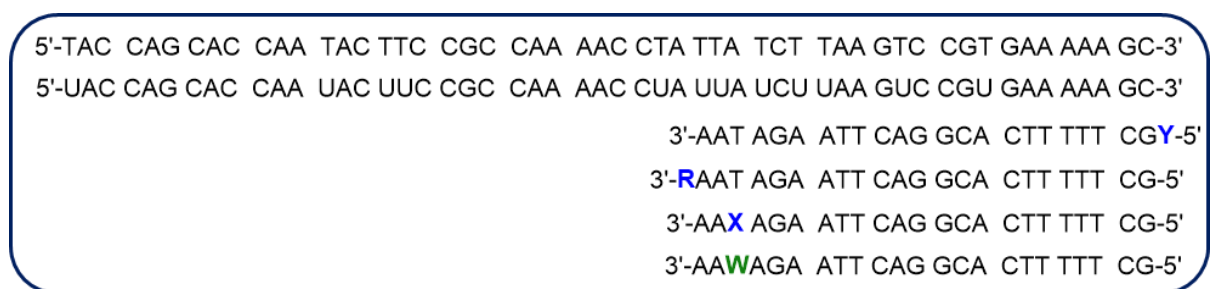
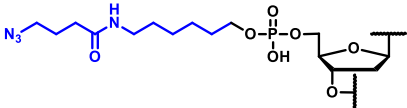
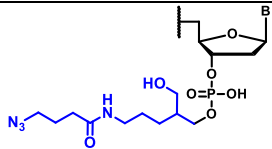
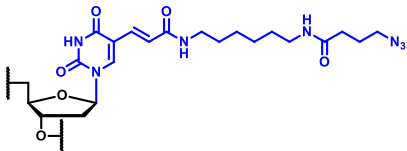
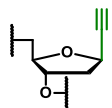


Figure 82. Séquences ARN Oskar, cADN Oskar et brins complémentaires marquées avec la sonde de la section visée de Oskar.

Afin d'évaluer si les dérivés de Miami sont des sondes préférentielles à une hybridation en conformation B (ADN:ADN) ou A (ARN:ARN, ARN:ADN), la séquence ARN Oskar (**Oskar**) a été commandée dans sa version ADN complémentaire (cDNA Oskar : **OskarDNA**). Pour rappel les sondes Miami pourraient interagir soit par liaison au petit sillon de l'ADN-B soit par intercalation¹⁸⁵.

Tableau 10. Description des séquences utilisés pour l'analyse *in-vitro*.

Séquences	Noms	Lien de CuAAC
5'-UAC CAG CAC CAA UAC UUC CGC CAA AAC CUA UUA UCU UAA GUC CGU GAA AAA GC-3'	Oskar	Aucun
5'-TAC CAG CAC CAA TAC TTC CGC CAA AAC CTA TTA TCT TAA GTC CGT GAA AAA GC-3'	OskarDNA	Aucun
5'- YGCT TTT TCA CGG ACT TAA GAT AA-3'	YGCT	
5'-GCT TTT TCA CGG ACT TAA GAT AAR-3'	AAR	
5'-GCT TTT TCA CGG ACT TAA GAX AA-3'	GAX	
5'-GCT TTT TCA CGG ACT TAA WAT AA-3'	WAT	

Les résultats de l'analyse photophysique des simples et doubles brins, sont résumés dans les deux tableaux suivants (**Tableau 11**, **Tableau 12**). Dans le premier, on retrouve les résultats obtenus avec les sondes pyrimidiques et dans le second, avec les sondes organoborées.

Tableau 11. Comparaison des études spectroscopiques concernant les simples-brins et les duplexes ARN:ADN et ADN:ADN, marqués par les sondes **8** et **9**.

Séquences	λ_{Abs}^a		λ_{Em}^b		Φ (%) ^c		Amplification de fluorescence ^d	
	ARN	ADN	ARN	ADN	ARN	ADN	ARN	ADN
YGCT	433	435	585	585	18	17	1.3	3.0 ↑
YGCT·CGA	431	443 ↑	582	600 ↑	23	37 ↑		
AAR	433	433	585	585	25	20	1.2	3.7 ↑
AAR·TT	431	442 ↑	585	590 ↑	23	59 ↑		
GAX	431	431	581	583	22	19	1.5	1.7
GAX·CTA	431	432	585	587	26	25		
WAT	434	436	585	583	10	7	0.9	3.8 ↑
WAT·CTA	432	444 ↑	585	596 ↑	9	20 ↑		

^a Longueur d'onde du maximum d'absorption. ^b Longueur d'onde du maximum d'émission. ^c Rendement quantique déterminé en utilisant le Nile Blue dans EtOH ($\Phi = 0,27$) comme référence^{196,197}. ^d Calculée par : Intensité du double-brin / Intensité du simple-brin. Les flèches montrent une augmentation ou diminution des valeurs en comparaison à la cible en ARN.

Tableau 12. Comparaison des études spectroscopiques concernant les simples-brins et les duplexes ARN:ADN et ADN:ADN marqués par les sondes **12** et **13**.

Séquences	λ_{abs}^a		λ_{em}^b		Φ (%) ^c		Amplification de fluorescence ^d	
	ARN	ADN	ARN	ADN	ARN	ADN	ARN	ADN
YGCT	528	530	640	640	16	15	0.9	1.7 ↑
YGCT·CGA	523	542 ↑	638	653 ↑	14	21 ↑		
AAR	527	527	642	642	20	18	1.3	2.0 ↑
AAR·TT	525	536 ↑	642	652 ↑	19	29 ↑		
GAX	530	530	639	639	26	24	1.1	1.2
GAX·CTA	528	531	640	644	25	28		
WAT	530	532	641	639	15	12	0.8	1.4 ↑
WAT·CTA	526	540 ↑	642	655 ↑	12	14 ↑		

^a Longueur d'onde du maximum d'absorption. ^b Longueur d'onde du maximum d'émission. ^c Rendement quantique déterminé en utilisant le Nile Blue dans EtOH ($\Phi = 0,27$) comme référence^{196,197}. ^d Calculée par : Intensité du double-brin / Intensité du simple-brin. Les flèches montrent une augmentation ou diminution des valeurs en comparaison à la cible en ARN.

Les résultats obtenus avec l'ARN **Oskar** ne démontrent qu'une très faible modification des propriétés photophysiques lors de l'hybridation, et aucune amplification de fluorescence significative n'est observée (Figure S14-S17).

A contrario, l'hybridation à la version cADN d'Oskar (**OskarDNA**) conduit à une modification des propriétés photophysiques (effet bathochrome) ainsi qu'une amplification du signal de fluorescence. La conformation adoptée par le double brin semble donc avoir un rôle significatif au niveau de l'interaction de la sonde avec l'acide nucléique.

De plus, si l'on compare les résultats obtenus lors de l'étude d'hybridation précédente (cf. p.164) avec ceux-ci, on remarque que les facteurs d'amplification sont moindres lorsque la cible est l'ARN-oskar ou l'ADN-oskar. L'hypothèse la plus probable est reliée à la constitution des séquences ODNs. Dans la partie précédente, le choix des séquences d'ODNs a été guidé pour optimiser la réponse spectrale lors de l'hybridation. On sait par exemple que les marqueurs (**8, 9, 12, 13**) sont préférentiellement fluorescents lors de l'hybridation de séquences riches en bases AT (ex : séquence **TXT**). De même, la proximité de multiples bases A autour de la sonde permet d'obtenir un signal faible du simple brin et un effet bathochrome important (ex : séquence **AWA**). Ces critères ne sont pas tous présents dans les séquences de l'ARNm et ADN-oskar que nous avons choisies pour cibles. Il pourrait donc être possible, en considérant la totalité de l'ARNm Oskar (2916 résidus), de trouver une autre séquence cible plus adaptée à une étude d'hybridation fluorogénique.

Conclusion & Perspective

Mes travaux de thèse se sont articulés autour de la synthèse et de la caractérisation de nouveaux fluorophores pour le marquage spécifique des acides nucléiques. D'un point de vue global, la stratégie consistait à greffer sur le simple brin d'ADN des colorants peu fluorescents capables d'accroître drastiquement leur fluorescence en réponse à un changement environnemental induit par l'hybridation de la sonde sur son brin complémentaire. En jouant sur divers paramètres physico-chimiques tels que la viscosité, le taux d'hydratation ou l'encombrement stérique, plusieurs sondes, aptes à signaler la reconnaissance de leur brin complémentaire par une réponse fluorogénique, ont été développées.

Pour conclure ce manuscrit, je vous propose un bref historique de mes 3 années de thèse afin de reprendre chronologiquement les étapes clés qui ont permis d'aboutir à la conception de sondes fluorogéniques performantes.

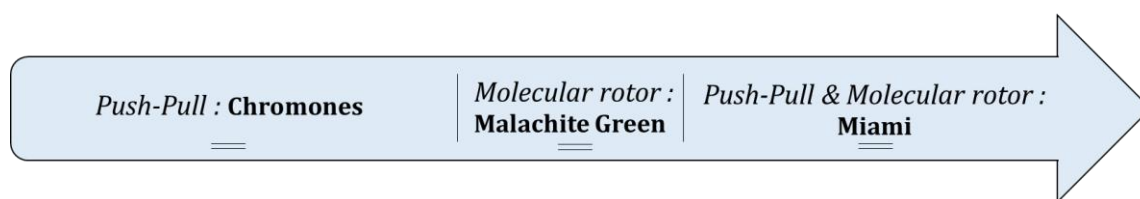


Figure 83 : Chronologie du développement des sondes au cours de la thèse.

A partir des dérivés de méthoxychromones alcyne **AIMF**, **AIMF-**, **AIMF+-** et azoture **AzMF** et **AzMF+**, un travail de méthodologie de synthèse a permis de concevoir un procédé post-synthétique universel de greffage covalent d'un colorant sur un oligonucléotide. La réaction de CuAAC réalisée dans des conditions permettant la solubilité de l'ODN ainsi que celle de la sonde (mélange eau/DMSO) en présence d'ascorbate de sodium (réducteur) avec le BTTES pour ligand du cuivre a été développée pour concevoir les premières sondes oligonucléotides. En bénéficiant des avantages intrinsèques à un procédé de synthèse post-synthétique des sondes oligonucléotides comme la réduction du nombre d'étapes de synthèse des fluorophores, la possibilité de lier ces derniers sur des liens de nature chimique et de taille différente, les dérivés méthoxychromones ont été incorporés au sein de nombreuses sondes oligonucléotides. Ces dernières se sont avérées intéressantes notamment en raison de leurs bonnes photostabilités et de leurs capacités à détecter des séquences d'ADN riches en paires AT avec des facteurs d'amplification supérieurs à la dizaine aux

alentours de 540 nm, lorsque le fluorophore était incorporé en position interne. Ces études ont d'ailleurs également permis de discriminer les positions de marquage post-synthétique puisque l'introduction de ces colorants en position 5' a abouti, à la suite de l'hybridation sur les mêmes cibles, à des amplifications de fluorescence par un facteur 2. Cette différence s'explique principalement par la capacité de ces fluorophores, sensibles au taux d'hydratation, à se réfugier dans un environnement moins hydraté à la suite de l'hybridation plus facilement en position interne qu'en position externe. Aucune généralité n'a pu être conclue au regard de la longueur du lien utilisé. Par exemple, l'utilisation d'un lien court (Alcyne directement sur le nucléoside) s'est révélé adéquat pour la **AzMF** (Facteur ≈ 5 avec la séquence AWA) alors qu'un lien long a été nécessaire pour révéler le potentiel de **AIMF** (Facteur 13 avec la séquence TXT).

Le point important de cette première partie concerne la simplicité et de la robustesse de cette réaction « click », dont les rendements de couplage sont élevés (conversion comprise entre 60 et 95%), qui a ainsi permis d'envisager sereinement la synthèse des futures sondes oligonucléotides. Malencontreusement, le contraste entre les états hybridés et non hybridés des méthoxychromones a été globalement faible, notamment en raison de rendements quantiques trop importants dans le simple brin. Les objectifs se sont alors recentrés sur le développement de colorants présentant une grande sensibilité à la contrainte stérique (*molecular rotor*). En utilisant ce type de fluorophore, une fluorescence très faible était attendue lorsque la sonde n'est pas restreinte, comme cela peut-être le cas dans un ADN simple brin. La sonde **6-EMT** a permis d'engendrer des facteurs d'amplification similaires aux sondes de première génération (≈ 10). Cette amplification étant vraisemblablement due à la rotation du groupement donneur thiophène instaurant la planéité du système π . D'autres sondes, dérivées de Malachite green, possédant des domaines d'émission plus décalées vers le rouge ont également été synthétisées. Les résultats des expériences d'hybridation se sont révélés moins bon. En effet, la fluorescence infime observée sous la forme simple brin a été impossible à exacerber. Il a alors été envisagé de réaliser des expériences de DRET en présence de l'accepteur Cy5 afin de raviver la fluorescence de ce *molecular rotor*. On remarque que le DRET fonctionne mais seulement dans une moindre

mesure et ne permet pas de palier à la fluorescence résiduelle provenant de la cross-excitation de Cy5. Des méthodes annexes telles que l'utilisation de G-quadruplex ou de protéines n'ont également pas permis d'obtenir des amplifications de fluorescence convenables.

En réalisant un bilan de ces expériences, il est possible d'entrevoir un fort potentiel pour un fluorophore combinant de façon synergique le caractère *molecular rotor* afin de neutraliser la fluorescence du simple brin et le caractère *push-pull* afin de faciliter le *turn-on* sur la cible.

Le développement des dérivés « push-pull molecular rotor » de la Miami Green a alors été entrepris. Un premier dérivé au noyau pyrimidique et le second organoboré. Au regard de leurs structures, il est possible d'apercevoir la présence d'un système *Push-Pull* formé entre le groupement donneur pipérazine (commun aux deux) et le groupement électro-attracteur pyrimidique / organoboré ainsi que de nombreux axes de rotations autour des liaisons sigma. L'étude de leurs propriétés photophysiques montre leurs parfaites adéquations avec le projet de recherche grâce à des longueurs d'ondes d'absorption ($\lambda_{\text{abs}(8/9)} \approx 450 \text{ nm}$, $\lambda_{\text{abs}(12/13)} \approx 530 \text{ nm}$) et d'émission ($\lambda_{\text{em}(8/9)} \approx 600 \text{ nm}$, $\lambda_{\text{em}(12/13)} \approx 660 \text{ nm}$) nettement dans le rouge, des déplacements de Stokes bien supérieurs à 100 nm et des possibilités d'incrémentations de fluorescence remarquables. Comme énoncé dans la littérature, il a été observé que ces deux sondes interagissent avec l'ADN par des mécanismes différents en fonction de leur noyau, expliquant ainsi les résultats singuliers entre les multiples séquences marquées. Les dérivés pyrimidiques **8** & **9** ont interagit préférentiellement avec le petit sillon de l'ADN et les composés organoboré **12** & **13** comme intercalants entre les plateaux de bases du duplexe. Les études d'hybridation ont fait éclore des résultats très intéressants avec des amplifications de fluorescence supérieures à 30.

Au bénéfice de propriétés spectrales d'absorption et d'émission de fluorescence déplacées vers le rouge, la pertinence des colorants (Miami) incorporés a été accentuée en réduisant considérablement leurs interférences avec les propriétés spectrales du matériel biologique présent au sein de la cellule. Tout en conservant des brillances considérables, un filtre supplémentaire a été apporté en leur conférant des déplacements de Stokes importants. Il

devient alors envisageable de prochainement franchir une étape supplémentaire en réalisant des expériences de DNA PAINT afin d'évaluer leur potentiel pour de la microscopie super-résolutive. Il est à noter qu'un contexte propice, dans lequel le colorant est entouré de sandwiches d'adénosines, a permis de révéler le potentiel de la majorité des fluorophores synthétisés. Il sera alors judicieux d'utiliser ces constructions afin d'évaluer les performances des sondes à l'échelle de la molécule unique.

D'autre part, tout au long des études menées, la structure des acides nucléiques a été modifiée afin de réaliser les réactions de CuAAC. En fonction des modifications effectuées i.e. nucléoside 2' alcyne, Thymine azoture, etc... des résultats très différents ont pu être observés. Il serait donc pertinent à l'avenir d'engager de nouvelles modifications du squelette afin d'améliorer la performance des sondes. Le chapitre introductif faisait mention des structures à chaîne ouverte de type PNA sérinol et des sucres contraints (LNA) en évoquant leurs impacts respectifs sur les propriétés des sondes. Au regard des travaux effectués par l'équipe d'O. Seitz, l'utilisation de ces structures a permis d'amplifier considérablement la fluorescence à l'hybridation de ses sondes lors de la formation du duplexe. Pour compléter ce projet, il serait donc très intéressant de réaliser la synthèse de ces structures (LNA et PNA) marquées par nos différents colorants afin d'étudier les propriétés photophysiques de ces nouvelles sondes et espérer démultiplier leurs capacités de détection des acides nucléiques.

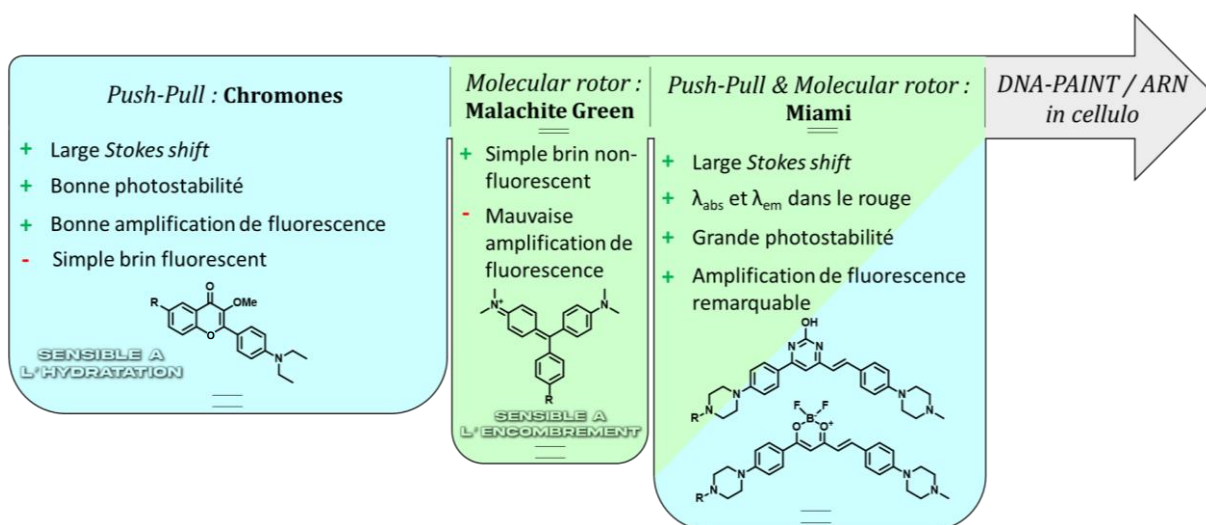


Figure 84 : Résumé des propriétés principales des sondes envers les objectifs du projet pour des applications futures.

Chapitre 5 : Partie expérimentale

I. Publication 1

Supporting Information To:

Design and synthesis of a fluorescent nucleoside incorporating a 3-hydroxychromone nucleobase substitute acting as a highly emissive donor in a novel FRET pair with a mega-Stokes shift

Steve Vincent ¹, Nicolas P. F. Barthes ², Suman Mallick ¹, Guillaume Barnoin, Pascal D. Giorgi, Moses Moustakim, Benoît Y. Michel ^{2,*} and Alain Burger ^{2,*}

¹ *Institut de Chimie de Nice, CNRS UMR 7272, Université Côte d'Azur, Parc Valrose, 06108 Nice cedex 2, France ; steve.vincent@univ-cotedazur.fr (S.V.); suman22msc@gmail.com (S.M.); guillaume.barnoin@univ-cotedazur.fr (G.B.); lhngoan2109@gmail.com (H.-N.L.)*

* *Correspondence: benoit.michel@univ-cotedazur.fr (B.Y.M.); alain.burger@univ-cotedazur.fr (A.B.)*

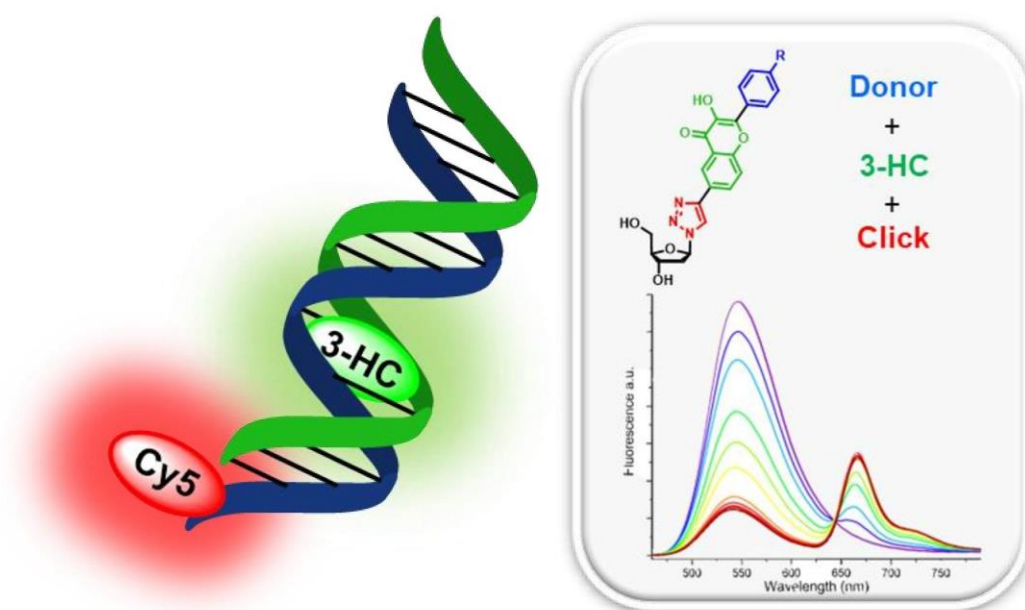


Table of contents

EXPERIMENTAL SECTION	3
GENERAL METHODS:	3
SUPPORTING INFORMATION	4
1. SYNTHETIC PROCEDURES.....	4
Preparation of the 3-HC fluorophores	4
Preparation of the azido- β -D-ribofuranose.....	7
Preparation of the fluorescent emissive nucleosides	7
Preparation of the fluorescent amidites	10
2. PHOTOPHYSICAL CHARACTERIZATION OF THE NUCLEOSIDES	11
2.2. Steady-state fluorescence measurements	12
2.3. ESIPT Study.....	12
2.4. Emission Fluorescence Spectra	13
3. MODEL ODNs SPECTROSCOPIC STUDIES	14
3.1. ODNs synthesis and purification.....	14
3.2. MALDI TOF/TOF analysis of ODNs	15
3.3. Temperature-induced denaturation studies.....	17
3.4. Circular Dichroism	19
3.5. Steady-state fluorescence measurements	19
3.6. UV/visible & Fluorescence spectra.....	19
4. FRET STUDY	22
4.1. UV/visible & Fluorescence spectra.....	23
NMR SPECTRA	25

Experimental section

General methods:

All non-aqueous reactions involving water-sensitive reagents were performed in oven dried glassware under argon using dry solvents. The synthetic intermediates were coevaporated twice with toluene beforehand and dried in vacuo before use. All chemical reagents were obtained from commercial sources and were used as supplied. Anhydrous solvents were obtained according to standard procedures.¹ The reactions were monitored by thin-layer chromatography (TLC, Merck silica gel 60 F254 plates) and visualized both by UV radiation (254 & 365 nm) and by spraying with phosphomolybdic acid in ethanol followed by a subsequent warming with a heat gun. Column chromatography² was performed with flash silica gel (40–63 mm). All NMR spectra (¹H, ¹³C, ²D) were recorded on 200 or 500 Bruker Advance Spectrometers (200 or 500 MHz). ¹H NMR (200 and 500 MHz), ¹³C NMR (50 and 125 MHz, recorded with complete proton decoupling) spectra were obtained with samples dissolved in CDCl₃, CD₂Cl₂, CD₃OD, [D₆]DMSO, [D₆]acetone, CD₃CN or C₅D₅N with the residual solvent signals used as internal references: 7.26 ppm for CHCl₃, 5.32 ppm for CDHCl₂, 3.31 ppm for CD₂HOD, 2.50 ppm for (CD₃)(CD₂H)S(O), 2.05 ppm for (CD₃)(CD₂H)C(O), 1.94 ppm for CD₂H₂CN, 8.74 ppm for C₅D₄HN regarding ¹H NMR experiments, and 77.2 ppm for CDCl₃, 53.8 ppm for CD₂Cl₂, 49.0 ppm for CD₃OD, 39.4 ppm for (CD₃)₂S(O), 30.8 ppm for (CD₃)₂C(O), 118.7 ppm for CD₃CN, 150.3 ppm for C₅D₅N concerning ¹³C NMR experiments.³ Chemical shifts (δ) are given in ppm to the nearest 0.01 (1H) or 0.1 ppm (¹³C). The coupling constants (J) are given in Hertz (Hz). The signals are reported as follows: (s=singlet, d=doublet, t=triplet, m=multiplet, br=broad). Assignments of ¹H and ¹³C NMR signals were achieved with the help of D/H exchange, COSY, DEPT, APT, HMQC, HSQC, HMBC experiments. Regular mass spectra (MS) were recorded on an Esquire 3000 Plus apparatus with ESI in both positive and negative mode. High-resolution mass spectrometry was conducted with a FINIGAN MAT 95 spectrometer with EI or ESI ionization techniques. Supplementary data associated with this article (the experimental protocols for the synthesis of intermediates **1** through **18**, the ¹H NMR, ¹³C NMR and (in part) ¹H–¹³C COSY, ¹H–¹³C HMQC and ¹H–¹³C HMBC spectra of all compounds) can be consulted in the Supporting Information. Systematic flavone and nucleobase nomenclatures are used below for the assignments of each spectrum. All solvents for absorption and fluorescence experiments were of spectroscopic grade. Absorption spectra were recorded on a Cary 4 spectrophotometer (Varian) using 1cm quartz cells. Stock solutions were prepared using dioxane. The samples used for spectroscopic measurements contained \approx 0.1% v/v of the stock solvent. Fluorescence spectra were recorded on FluoroMax 4.0 spectrofluorometer (Jobin Yvon, Horiba). Excitation wavelength was used as mentioned in the corresponding experiments.

¹ W. L. F. Armarego and C. L. L. Chai, *Purification of Laboratory Chemicals*, 7th ed.; Butterworth-Heinemann: Oxford, 2013.

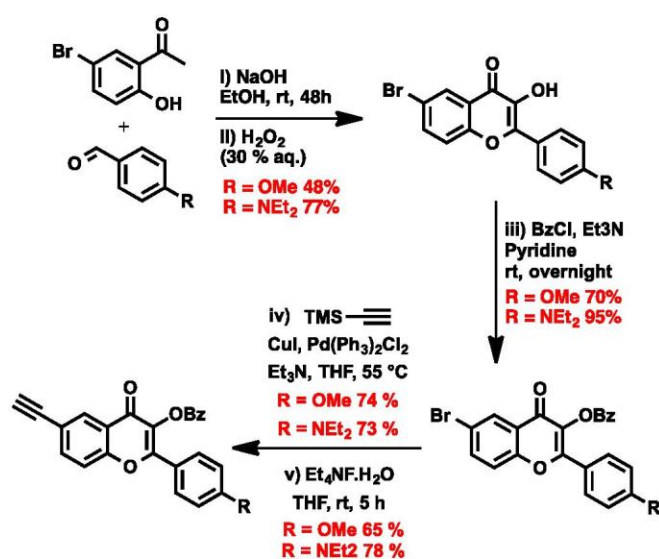
² W. C. Still, M. Kahn and A. Mitra, *J. Org. Chem.* **1978**, *43*, 2923–2925.

³ H. E. Gottlieb, V. Kotlyar and A. Nudelman, *J. Org. Chem.* **1997**, *62*, 7512–7515.

Supporting Information

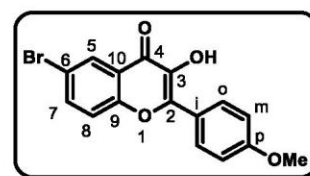
1. Synthetic Procedures

Preparation of the 3-HC fluorophores



6-bromo-2-(4-(methoxy)phenyl)-3-hydroxy-4H-chromen-4-one **1**

Initially 1-(5-bromo-2-hydroxyphenyl)ethanone (2 g, 9.3 mmol) and 4-(methoxy)benzaldehyde (1.28 g, 9.3 mmol) were solubilized in ethanol (47 mL). The reaction mixture was stirred at rt for 48 hours protected from light. The mixture turned to a bright yellow aspect. Then, 35 % H₂O₂ solution (2 mL) was added sequentially at 0°C. After stirring overnight, the mixture was neutralised by addition of water (300 mL) and AcOH until reaching pH 3 to allow precipitation of the desired compound. 6-bromo-2-(4-(methoxy)phenyl)-3-hydroxy-4H-chromen-4-one was obtained after filtration and washes with water and cyclohexane sequentially, as a orange solid **1** (1.55 g, 50%). C₁₆H₁₁O₄Br (347.16).



R_f = 0.21 (Toluene/Acetone: 50/50).

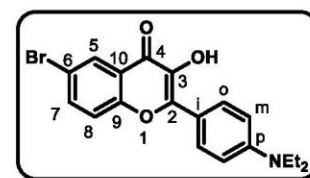
¹H NMR (CDCl₃, 200 MHz): δ (ppm): 3.90 (s, 3H, O—CH₃), 7.06 (d, ³J = 8.8 Hz, 2H, H_{meta}), 7.48 (d, ³J = 8.8 Hz, 2H, H₈), 7.77 (d, ³J = 8.8 Hz, 1H, H₇), 8.23 (d, ³J = 8.8 Hz, 2H, H_{ortho}), 8.38 (s, 1H, H₅).

¹³C NMR (50 MHz, C₅D₅N): δ (ppm): 57.2 (O—CH₃), 116.3 (C_m), 119.3 (C_p), 122.7 (C_i), 126.0 (C₈), 132.2 (C₆), 137.0 (C₇), 137.5 (C_o), 138.0 (C₅), 148.7 (C₁₀), 151.2 (C₂), 163.3 (C₉), 174.5 (C₄).

HRMS (ESI⁺): *m/z* calcd for C₁₆H₁₁O₄Br: 346.99135 [M-H]⁺; found: 346.99182.

6-bromo-2-(4-(diethylamino)phenyl)-3-hydroxy-4H-chromen-4-one **2**

Initially 1-(5-bromo-2-hydroxyphenyl)ethanone (1.7 g, 7.75 mmol) and 4-(diethylamino)benzaldehyde (1.557 g, 8.52 mmol) were solubilized in 1,2-dichloroethane (10 mL) and Morpholine (10 mL). The reaction mixture was irradiated by microwave (25min, 100 °C, 200W). The mixture turned to a dark red-brown aspect, and the volatile may be removed under *vacuo*. Then to a stirring solution of the previous residue, solubilized in ethanol (15 mL), aqueous NaOH solution (5M, 13 eq.) and 35 % H₂O₂ solution (7.65 mL, 23.24 mmol) were added sequentially at 0°C. After stirring overnight, the mixture was neutralised by 1N aqueous HCl solution, and the resulting precipitate was filtered and washed with water and cyclohexane sequentially. 6-bromo-2-(4-(diethylamino) phenyl)-3-hydroxy-4H-chromen-4-one was obtained as a orange solid **2** (2.235 g, 77%). C₁₉H₁₈NO₃Br (388.26).



R_f = 0.38 (Toluene/Acetone: 80/20).

¹H NMR (Acetone-*d*₆, 200 MHz): δ (ppm): 1.21 (t, ³J = 7.0 Hz, 6H, NCH₂—CH₃), 3.51 (q, ³J = 7.0 Hz, 4H, NCH₂—CH₃), 6.86 (d, ³J = 8.4 Hz, 2H, H_{meta}), 7.70 (d, ³J = 9.0 Hz, 1H, H₈), 7.87 (dd, ³J = 9.0 Hz, ⁴J = 2.3 Hz, 1H, H₇), 8.30 – 8.12 (m, 3H).

¹³C-NMR (DMSO-*d*₆, 50 MHz): δ (ppm): 12.4 (N-CH₂—CH₃), 43.6 (N—CH₂—CH₃), 110.9 (C_m), 116.5 (C_p), 120.7 (C_i), 123.0 (C₈), 126.4 (C₆), 129.5 (C₇), 135.4 (C_o), 137.2 (C₅), 147.5 (C₁₀), 148.5 (C₂), 153.0 (C₉), 170.4 (C₄).

HRMS (ESI⁺): *m/z* calcd for C₁₉H₁₉NO₃Br: 388.05428 [M-H]⁺; found: 388.05496.

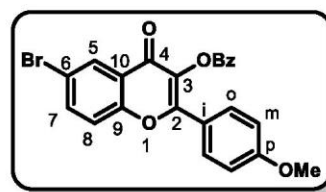
6-bromo-2-(4-(methoxy)phenyl)-4-oxo-4H-chromen-3-yl benzoate 3

Initially **1** (1.5 g, 4.3 mmol) was solubilized in Pyridine (29 mL). Et₃N (3.65 mL, 26.5 mmol, 6 eq.) and BzCl (1.5 mL, 12.9 mmol, 3 eq.) were added at 0°C. The reaction was kept under intense stirring at room temperature overnight before the reaction was complete. Upon completion the volatiles were removed *in vacuo* and the residue was washed with a sat. NH₄Cl solution and extracted by DCM (3 times). The organic layers were then combined and washed with saturated NaHCO₃ (2 times) and brine. The resulting organic layer was dried over MgSO₄, concentrated and purified by flash chromatography (Toluene/Et₂O: 100/0 to 70/30) to provide yellow crystal as the desired compound **3** (1.36 g, 70%). C₂₃H₁₅O₅Br (451.27).

R_f = 0.54 (Toluene/Acetone: 95/5).

¹H NMR (CDCl₃, 200 MHz): δ (ppm): 3.83 (s, 3H, O-CH₃), 7.05 (d, ³J = 9.1 Hz, 2H, H_{meta}), 7.46–7.57 (m, 1H, H₈), 7.62 (d, ³J = 8.5 Hz, 2H, H_{meta}Ph), 7.74 (d, ³J = 7.6 Hz, 1H, H_{para}Ph), 7.93–8.05 (m, 3H, H₇ & H_{ortho}), 8.18 (dd, ³J = 8.5 Hz, ⁴J = 1.3 Hz, 2H, H_{ortho}Ph), 8.27 (d, ⁴J = 2.5 Hz, 1H, H₅).

HRMS (ESI⁺): *m/z* calcd for C₂₃H₁₆O₅Br: 451.01756 [M-H]⁺; found: 451.01791.



6-bromo-2-(4-(diethylamino)phenyl)-4-oxo-4H-chromen-3-yl benzoate 4

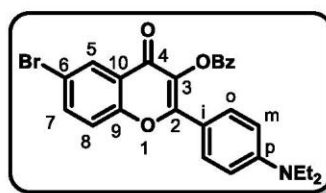
Initially **2** (1.1 g, 2.83 mmol) was solubilized in Pyridine (19 mL). Et₃N (3.3 mL, 17 mmol, 6 eq.) and BzCl (2.7 mL, 8.5 mmol, 3 eq.) were added at 0°C. The reaction was kept under intense stirring at room temperature overnight before the reaction was complete. Upon completion the volatiles were removed *in vacuo* and the residue was washed with a sat. NH₄Cl solution and extracted by DCM (3 times). The organic layers were then combined and washed with saturated NaHCO₃ (2 times) and brine. The resulting organic layer was dried over MgSO₄, concentrated and purified by flash chromatography (Toluene/Acetone: 100/0 to 70/30) to provide yellow crystal as the desired compound **4**. (1.33 g, 95%). C₂₆H₂₂NO₄Br (492.37).

R_f = 0.45 (Toluene/Acetone: 80/20).

¹H NMR (CDCl₃, 200 MHz): δ (ppm): 1.17 (t, ³J = 7.2 Hz, 6H, NCH₂-CH₃), 3.37 (q, ³J = 7.0 Hz, 4H, NCH₂-CH₃), 6.64 (d, ³J = 9.2 Hz, 2H, H_{meta}), 7.43 (d, ³J = 9.0 Hz, 1H, H₈), 7.48–7.55 (m, 2H, H_{meta}Ph), 7.63 (m, 1H, H_{para}Ph), 7.74 (dd, ³J = 9.0 Hz, ⁴J = 2.4 Hz, 1H, H₇), 7.86 (d, ³J = 9.2 Hz, 2H, H_{ortho}), 8.26 (d, ³J = 7.0 Hz, 2H, H_{ortho}Ph), 8.35 (d, ⁴J = 2.4 Hz, 1H, H₅).

¹³C-NMR (CDCl₃, 50 MHz): δ (ppm): 12.5 (N-CH₂-CH₃), 44.4 (N-CH₂-CH₃), 110.8 (C_{meta}), 115.2 (C_i), 118.0 (C₁₀), 119.7 (C₈), 125.1 (C₆), 128.5 (C₅), 128.6 (C_{meta}Ph), 128.9 (C_iPh), 130.0 (C_{ortho}), 130.6 (C_{ortho}Ph), 132.1 (C₃), 133.6 (C_pPh), 136.2 (C₇), 149.8 (C_{para}), 154.1 (C₂), 157.1 (C₉), 163.7 (CO), 170.4 (C₄).

HRMS (ESI⁺): *m/z* calcd for C₂₆H₂₃NO₄Br: 492.08050 [M-H]⁺; found: 492.08096.



2-(4-(methoxy)phenyl)-4-oxo-6-((trimethylsilyl)ethynyl)-4H-chromen-3-yl benzoate 5

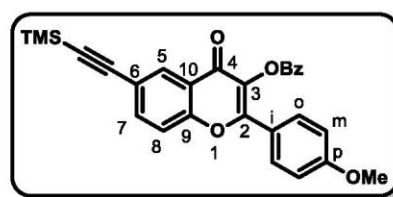
To a stirring solution of **3** (1.33 g, 2.88 mmol) was solubilized in dry THF (19 mL). TMS-acetylene (822 μL, 5.76 mmol, 2 eq.), PdCl₂(PPh₃)₂ (370 mg, 0.32 mmol, 11 mol. %) and CuI (39 mg, 0.202 mmol, 7 mol. %) and Et₃N (2.4 mL, 17.28 mmol, 6 eq.) were then added sequentially, and the mixture was stirred at 65°C overnight. After completion, the reaction mixture was then filtered through a Dicalite® pad and concentrated under vacuum prior to a chromatography on silica gel being carried out (Toluene/Et₂O: 100/0 to 70/30) to give a pale yellow-orange solid **5** (1.0 g, 74%). C₂₈H₂₄O₅Si (468.58).

R_f = 0.65 (Toluene/Acetone: 95/5).

¹H NMR (CDCl₃, 200 MHz): δ (ppm): 0.04 (s, 9H, Si-CH₃), 3.55 (s, 3H, OCH₃), 6.68 (d, ³J = 8.9 Hz, 2H, H_{meta}), 7.19–7.32 (m, 3H, H_{meta}Ph & H₈), 7.35–7.73 (m, 1H, H_{para}Ph), 7.49 (dd, ³J = 8.7 Hz, ⁴J = 2.0 Hz, 1H, H₇), 7.64 (d, ³J = 8.9 Hz, 2H, H_{ortho}), 7.92–8.03 (m, 2H, H_{ortho}Ph), 8.11 (d, ⁴J = 2.0 Hz, 1H, H₅).

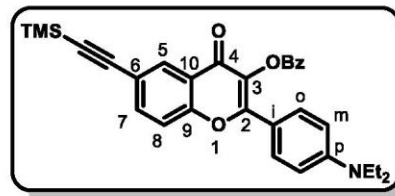
¹³C-NMR (CDCl₃, 50 MHz): δ (ppm): 0.1 (Si-CH₃), 55.4 (OCH₃), 95.9 (C_{alkyne}), 103.3 (C_{alkyne}), 114.3 (C_m), 118.3 (C₈), 120.5 (C₆), 122.0 (C_i), 123.5 (C₁₀), 128.7 (C_iPh), 128.7 (C_mPh), 129.8 (C₅), 130.1 (C_{ortho}), 130.6 (C_oPh), 133.3 (C₃), 134.0 (C_pPh), 136.9 (C₇), 155.0 (C_{para}), 156.3 (C₉), 162.1 (C₂), 163.8 (CO), 171.3 (C₄).

HRMS (ESI⁺): *m/z* calcd for C₂₈H₂₅O₅Si: 469.14658 [M-H]⁺; found: 469.14691.



2-(4-(diethylamino)phenyl)-4-oxo-6-((trimethylsilyl)ethynyl)-4H-chromen-3-yl benzoate 6

To a stirring solution of **4** (1.4 g, 2.84 mmol) was solubilized in dry THF (19 mL). TMS-acetylene (812 μ L, 5.687 mmol, 2 eq.), PdCl₂(PPh₃)₂ (222 mg, 0.3 mmol, 11 mol. %), CuI (38 mg, 0.199 mmol, 7 mol. %) and Et₃N (2.4 mL, 17.06 mmol, 6 eq) were then added sequentially, and the mixture was stirred at 65°C overnight. After completion, the reaction mixture was then filtered through a Dicalite® pad and concentrated under vacuum prior to a chromatography on silica gel being carried out (Toluene/Acetone: 100/0 to 70/30) to give a pale yellow-orange solid **6** (1.06 g, 73%). C₃₁H₃₁NO₄Si (509.68).



R_f=0.75 (Toluene/Acetone: 80/20).

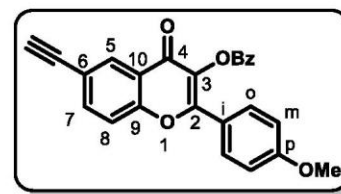
¹H NMR (CDCl₃, 200 MHz): δ (ppm): 0.28 (s, 9H, Si-CH₃), 1.17 (t, ³J = 7.0 Hz, 6H, N-CH₂-CH₃), 3.37 (q, ³J = 6.4 Hz, 4H, N-CH₂-CH₃), 6.63 (d, ³J = 8.0 Hz, 2H, H_{meta}), 7.45-7.52 (m, 2H, H_{meta}Ph & H8), 7.64 (m, 2H, H_{para}Ph), 7.71 (dd, ³J = 8.7 Hz, ⁴J = 2.0 Hz, 1H, H7), 7.86 (d, ³J = 8.0 Hz, 2H, H_{ortho}), 8.27 (d, ³J = 7.4 Hz, 2H, H_{ortho}Ph), 8.33 (d, ⁴J = 2.0 Hz, 1H, H5).

¹³C-NMR (CDCl₃, 50 MHz): δ (ppm): 0.0 (Si-CH₃), 12.6 (N-CH₂-CH₃), 44.5 (N-CH₂-CH₃), 77.2 (C_{alkyne}), 95.3 (C_{alkyne}), 110.8 (C_m), 115.5 (C_i), 118.1 (C8), 120.1 (C6), 123.7 (C10), 128.7 (C_mPh), 129.1 (C_pPh), 129.9 (C5), 130.1 (C_{ortho}), 130.7 (C_oPh), 132.2 (C3), 133.8 (C_pPh), 136.5 (C7), 149.9 (C_{para}), 155.0 (C2), 157.0 (C9), 163.9 (CO), 171.0 (C4).

HRMS (ESI⁺): *m/z* calcd for C₃₁H₃₂NO₄Si: 510.20992 [M-H]⁺; found: 510.20993.

2-(4-(methoxy)phenyl)-6-ethynyl-4-oxo-4H-chromen-3-yl benzoate 7

To a stirred solution of **5** (1 g, 2.13 mmol) solubilized in THF (14 mL) was added Et₃NF (1.28 g, 8.54 mmol, 4 eq.). The reaction was stirred for 2 hours. Upon completion the reaction was quenched by the addition of NH₄Cl and extracted with DCM (3 times). The combined organic layers were dried over MgSO₄, filtered and evaporated under *vacuo*. The resulting residue was purified via flash chromatography (Toluene/Et₂O: 100/0 to 70/30) to yield a pure orange solid **7** (546.6 mg, 65%). C₂₅H₁₆O₅ (396.39).



R_f = 0.34 (Toluene/Acetone: 95/5).

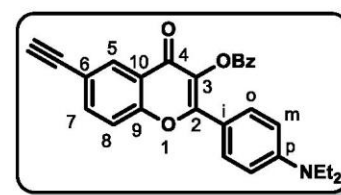
¹H NMR (CDCl₃, 200 MHz): δ (ppm): 3.15 (s, 1H, H_{alkyne}), 3.84 (s, 3H, OCH₃), 6.97 (d, ³J = 9.1 Hz, 2H, H_{meta}), 7.45 – 7.59 (m, 3H, H8 & H_{meta}Ph), 7.60 – 7.72 (m, 1H, H_{para}Ph), 7.79 (dd, ³J = 8.7 Hz, ⁴J = 2.0 Hz, 1H, H7), 7.92 (d, ³J = 9.1 Hz, 2H, H_{ortho}), 8.22 (dd, ³J = 8.4 Hz, ⁴J = 1.3 Hz, 2H, H_{ortho}Ph), 8.39 (d, ⁴J = 2.0 Hz, 1H, H5).

¹³C-NMR (CDCl₃, 50 MHz): δ (ppm): 55.7 (OCH₃), 78.7 (C_{alkyne}), 82.2 (CH_{alkyne}), 114.5 (C_m), 118.6 (C8), 119.6 (C_i), 122.2 (C6), 123.8 (C10), 128.4 (C_pPh), 128.9 (C_mPh), 129.3 (C5), 130.3 (C_{ortho}), 130.4 (C3), 130.8 (C_oPh), 134.1 (C_pPh), 137.2 (C7), 155.5 (C_{para}), 156.6 (C2), 162.3 (C9), 164.0 (CO), 168.2 (C4).

HRMS (ESI⁺): *m/z* calcd for C₂₅H₁₇O₅: 397.10705 [M-H]⁺; found: 397.10678.

2-(4-(diethylamino)phenyl)-6-ethynyl-4-oxo-4H-chromen-3-yl benzoate 8

To a stirred solution of **6** (1 g, 1.96 mmol) solubilized in THF (13 mL) was added Et₃NF (1.18 g, 7.85 mmol, 4 eq.). The reaction was stirred for 2 hours. Upon completion the reaction was quenched by the addition of NH₄Cl and extracted with DCM (3 times). The combined organic layers were dried over MgSO₄, filtered and evaporated under *vacuo*. The resulting residue was purified via flash chromatography (Toluene/Acetone: 100/0 to 70/30) to yield a pure orange solid **8** (665.4 mg, 78%). C₂₈H₂₃NO₄ (437.50).



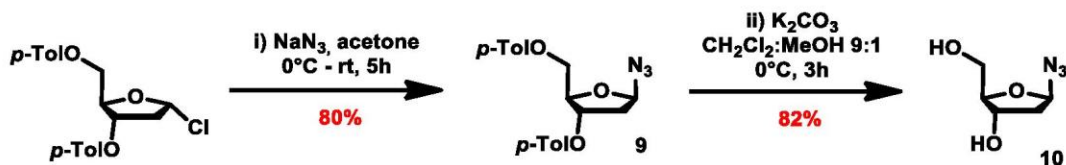
R_f = 0.75 (Toluene/Acetone: 80/20).

¹H NMR (CDCl₃, 200 MHz): δ (ppm): 1.08 (t, ³J = 7.1 Hz, 6H, N-CH₂-CH₃), 3.04 (s, 1H, H_{alkyne}), 3.29 (q, ³J = 7.1 Hz, 4H, NCH₂-CH₃), 6.55 (d, ³J = 9.2 Hz, 2H, H_{meta}), 7.36 – 7.50 (m, 3H, H8 & H_{meta}Ph), 7.51 – 7.59 (m, H_{para}Ph), 7.65 (dd, ³J = 8.7 Hz, ⁴J = 2.0 Hz, 1H, H7), 7.78 (d, ³J = 9.2 Hz, 2H, H_{ortho}), 8.13 – 8.24 (m, 2H, H_{ortho}Ph), 8.28 (d, ⁴J = 2.0 Hz, 1H, H5).

¹³C-NMR (CDCl₃, 50 MHz): δ (ppm): 12.5 (N-CH₂-CH₃), 44.4 (N-CH₂-CH₃), 78.1 (C_{alkyne}), 82.2 (CH_{alkyne}), 110.9 (C_m), 115.3 (C_i), 118.2 (C8), 118.9 (C6), 123.6 (C10), 128.6 (C_mPh), 129.0 (C_pPh), 130.0 (C5 & C_{ortho}), 130.6 (C_oPh), 132.2 (C3), 133.7 (C_pPh), 136.5 (C7), 149.8 (C_{para}), 155.1 (C2), 157.0 (C9), 163.8 (CO), 170.8 (C4).

HRMS (ESI⁺): *m/z* calcd for C₂₈H₂₄NO₄: 438.16998 [M-H]⁺; found: 438.17041.

Preparation of the azido- β -D-ribofuranose



The starting 1'- α -chloro-3',5'-di-*O*-toluoyl-2'-deoxy-*L*-ribose was synthesized as described by Hoffer and co-workers.⁴

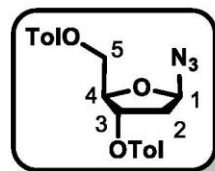
1-Azido-1,2-dideoxy-3,5-di-*O*-toluoyl- β -D-ribofuranose 9

To a stirred solution of 1'- α -Chloro-3',5'-di-toluoyl-2'-deoxy-*L*-ribose (1.4 g, 3.64 mmol) in solution of acetone (20 mL) at 0°C, was slowly added NaN₃ powder (1.22 g, 18.2 mmol, 5.0 eq.). The reaction mixture was kept under vigorous stirring for 5 hours. After completion as evidence by TLC's monitoring, the reaction mixture was quenched with saturated aqueous solution of NaHCO₃ (15 mL). After three times extraction with CH₂Cl₂, the combined organic layer was washed with MgSO₄, filtered and evaporated under reduced pressure. The crude oil obtained made of the mixture of the both anomers ($\beta/\alpha = 90/10$) were subjected to flash chromatography on silica gel (PE/Et₂O: 95/5 to PE/Et₂O: 4/1) to furnished a pure white crystal, as the desired compound 9 (1.0 g, 80%). C₂₁H₂₃O₅N₃ (384.13).

R_f = 0.67 (Toluene/Acetone: 90/10).

¹H-NMR (CD₂Cl₂, 400 MHz): δ = 2.43 (s, 3H, CH₃-Tol), 2.44 (s, 3H, CH₃-Tol), 2.46 – 2.49 (m, 2H, H_{2'}), 4.55–4.67 (m, 3H, H_{4'}, H_{5'}), 5.64 (ddd, ³J = 7.9 Hz, ³J = 4.4 Hz, ⁴J = 2.2 Hz, 1H, H_{3'}), 5.77 (t, ³J = 5.1 Hz, 1H, H_{1'}), 7.28–7.31 (m, 4H, H_{m-Tol}), 7.98 (d, ³J = 8.2 Hz, 2H, H_{o-Tol}), 8.05 (d, ³J = 8.2 Hz, 2H, H_{o-Tol}).

¹³C-NMR (CD₂Cl₂, 101 MHz): δ = 22.1 (CH₃), 22.1 (CH₃), 39.3 (C₂), 65.0 (C₅), 75.7 (C₄), 83.5 (C₃), 93.0 (C₁), 127.5 (C_i), 127.9 (C_i), 129.9 (C_m), 129.9 (C_m), 130.4 (C_o), 130.4 (C_o), 144.7 (C_p), 145.1 (C_p), 166.5 (CO), 166.8 (CO).



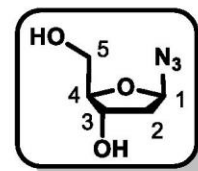
1-Azido-1,2-dideoxy- β -D-ribofuranose 10

To a stirred solution of 9 (3 g, 7.59 mmol) in mixture of DCM/MeOH (9/1, 41 mL), K₂CO₃ powder (2.36 g, 17.07 mmol, 2.25 eq.) was slowly added at 0°C. After completion, the reaction mixture was filtered through a celite pad, washed with a DCM/MeOH solution. The volatiles were removed in vacuo prior a flash chromatography purification on silica gel being carried out (DCM/MeOH: 100/0 to 90/10), to provide white crystals as the desired compound 10 (985.3 mg, 82%). C₅H₁₀O₃N₃ (156.14).

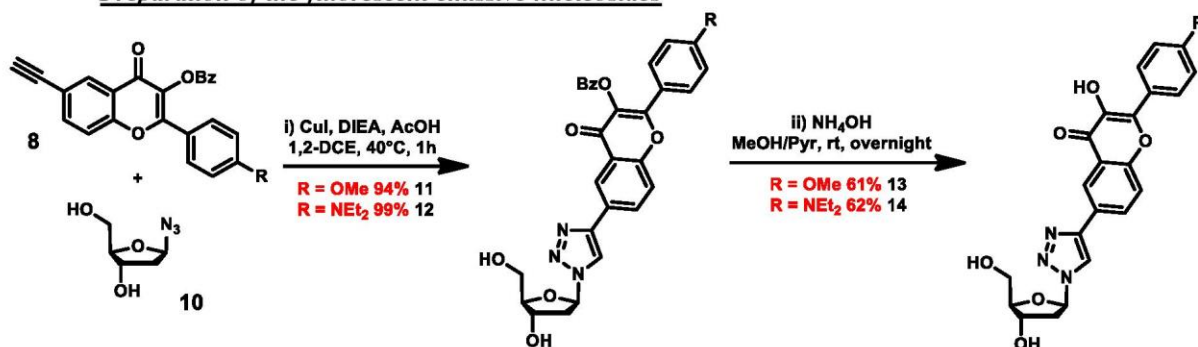
R_f = 0.10 (Toluene/Acetone: 60/40).

¹H NMR (CD₃OD-*d*⁴, 200 MHz): δ (ppm): 1.93 – 2.20 (m, 2H, H₂), 3.59–3.61 (m, 2H, H₅), 3.89 (dd, ³J = 9.2 Hz, ³J = 5.0 Hz, 1H, H₄), 4.34 (q, ³J = 5.7 Hz, 1H, H₃), 5.54 (dd, ³J = 5.6 Hz, ³J = 4.2 Hz, 1H, H₁).

¹³C-NMR (CD₃OD-*d*⁴, 50 MHz): δ (ppm): 42.6 (C₂), 64.5 (C₅), 72.9 (C₃), 89.6 (C₁), 93.6 (C₄).



Preparation of the fluorescent emissive nucleosides



⁴ M. Hoffer, *Eur. J. Inorg. Chem.*, **1960**, 93, 2777–2781.

1,2-dideoxy-1-(4-(2-(4-methoxyphenyl)-3-benzoyloxy-4-oxo-4H-chromen-6-yl)-1H-1,2,3-triazol-1-yl)- β -D-ribofuranose **11**

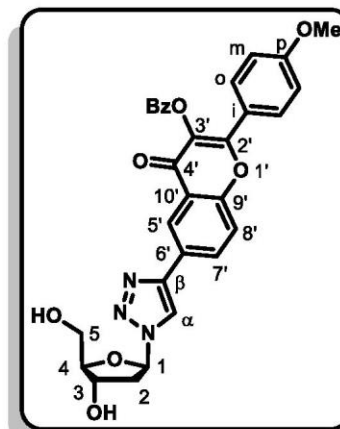
Initially **7** (140 mg, 0.88 mmol) was solubilized in the littlest amount of DMF (about 100 μ L). Then, DCE (23 mL) and **7** (384 mg, 0.97 mmol, 1.1 eq.) were sequentially added prior to the addition of DIEA (644 μ L, 3.695 mmol, 4.2 eq.), Acetic acid (106 μ L, 1.847 mmol, 2.1 eq.) and CuI (88 mg, 0.44 mmol, 0.5 eq.). The reaction was heated at 40 $^{\circ}$ C for 1 hr under an Argon atmosphere. Upon completion of the reaction, the reaction mixture was centrifuged for settling solid particles and the supernatant was carefully taken out with a syringe with a fine needle. The solid was then dried under high vacuum to give an anise-colored solid, as the desired compound **11** (461.4 mg, 94%). $C_{30}H_{25}N_3O_8$ (555.54).

R_f = 0.43 (DCM/MeOH: 90/10).

1H -NMR (Pyridine- d^5 , 500 MHz): δ = 2.91 (ddd, 2J = 13.2 Hz, 3J = 6.5 Hz, 3J = 5.0 Hz, 1H, H2), 3.19 (dt, 2J = 13.2 Hz, 3J = 5.8 Hz, 1H, H2), 3.69 (s, 3H, OCH₃), 4.17 (dt, 3J = 8.9 Hz, ^{2-3}J = 4.1 Hz, 1H, H5), 4.24 (dt, 3J = 11.6 Hz, ^{2-3}J = 4.1 Hz, 1H, H5), 4.67 (q, 3J = 4.1 Hz, 1H, H4), 5.22 – 5.27 (m, 1H, H3), 6.93 – 7.01 (m, 1H, H1), 7.08 (d, 3J = 9.0 Hz, 2H, H_{meta}), 7.48 (t, 3J = 7.8 Hz, 2H, H_{meta}Ph), 7.66 (d, 3J = 8.8 Hz, 1H, H8'), 8.13 (d, 3J = 9.0 Hz, 2H, H_{ortho}), 8.43 (dd, 3J = 8.3 Hz, 3J = 1.3 Hz, 1H, H_{ortho}Ph), 8.47 (dd, 3J = 8.8 Hz, 3J = 2.1 Hz, 1H, H7'), 8.96 (d, 3J = 2.1 Hz, 1H, H5'), 9.02 (s, 1H, H α).

^{13}C -NMR (Pyridine- d^5 , 125 MHz): δ = 42.4 (C2), 55.9 (OCH₃), 63.0 (C5), 71.8 (C3), 90.3 (C1), 90.5 (C4), 115.3 (C_{meta}), 119.9 (C8'), 121.0 (C α), 122.8 (C5'), 122.9 (C_i), 124.8 (C10'), 129.5 (C6'), 129.7 (C_mPh), 131.0 (C_{ortho}), 131.3 (C_oPh), 132.1 (C7'), 134.3 (C3'), 134.8 (C_iPh), 146.9 (C β), 155.8 (C_{para}), 156.9 (C9'), 163.0 (C2'), 164.8 (CO), 172.3 (C4').

HRMS (ESI⁺): m/z calcd for $C_{30}H_{26}N_2O_8$: 556.17144 [M-H]⁺; found: 556.17181.



1,2-dideoxy-1-(4-(2-(4-(diethylamino)phenyl)-3-benzoyloxy-4-oxo-4H-chromen-6-yl)-1H-1,2,3-triazol-1-yl)- β -D-ribofuranose **12**

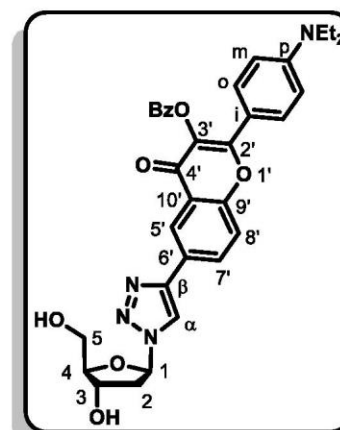
Initially **8** (150 mg, 0.94 mmol) was solubilized in the littlest amount of DMF (about 100 μ L). Then, DCE (24 mL) and **X** (454 mg, 1.04 mmol, 1.1 eq.) were sequentially added prior to the addition of DIEA (690 μ L, 3.96 mmol, 4.2 eq.), Acetic acid (113 μ L, 1.98 mmol, 2.1 eq.) and CuI (94 mg, 0.47 mmol, 0.5 eq.). The reaction was heated at 40 $^{\circ}$ C for 1 hr under an Argon atmosphere. Upon completion of the reaction, the reaction mixture was centrifuged for settling solid particles and the supernatant was carefully taken out with a syringe with a fine needle. The solid was then dried under high vacuum to give an anise-colored solid, as the desired compound **12** (556 mg, 99%). $C_{33}H_{32}N_4O_7$ (596.64).

R_f = 0.43 (DCM/MeOH: 90/10).

1H -NMR (Pyridine- d^5 , 500 MHz): δ = 0.98 (t, 3J = 7.0 Hz, 6H, NCH₂-CH₃), 2.89 (ddd, 3J = 13.2 Hz, 3J = 6.5 Hz, 3J = 5.0 Hz, 1H, H2), 3.15 – 3.22 (m, 1H, H2), 3.20 (q, 3J = 7.0 Hz, 4H, NCH₂-CH₃), 4.16 (dd, 3J = 11.9 Hz, 3J = 4.1 Hz, 1H, H5), 4.23 (dd, 3J = 11.9 Hz, 3J = 3.8 Hz, 1H, H5), 4.65 (m, 1H, H4), 5.24 (m, 1H, H3), 6.74 (d, 3J = 9.2 Hz, 2H, H_{meta}), 6.95 (t, 3J = 6.0 Hz, 1H, H1), 7.48 (m, 2H, H_{meta}Ph), 7.63 (d, 3J = 8.7 Hz, 1H, H8'), 8.14 (d, 3J = 9.2 Hz, 2H, H_{ortho}), 8.43 (dd, 3J = 8.7 Hz, 3J = 2.1 Hz, 1H, H7'), 8.48 (d, 3J = 7.2 Hz, 2H, H_{ortho}Ph), 8.96 (d, 3J = 2.1 Hz, 1H, H5'), 8.98 (s, 1H, H α).

^{13}C -NMR (Pyridine- d^5 , 125 MHz): δ = 13.0 (NCH₂-CH₃), 42.3 (C2), 44.8 (NCH₂-CH₃), 63.0 (C5), 71.8 (C3), 90.3 (C1), 90.5 (C4), 111.9 (C_{meta}), 116.3 (C_i), 119.7 (C8'), 120.9 (C α), 122.9 (C5'), 124.9 (C10'), 129.2 (C6'), 129.7 (C_mPh), 130.9 (C_{ortho}), 131.3 (C_oPh), 131.7 (C7'), 133.2 (C3'), 134.7 (C_iPh), 147.1 (C β), 150.0 – 152.0 (C_{para}), 155.8 (C9'), 157.6 (C2'), 164.9 (CO), 171.9 (C4').

HRMS (ESI⁺): m/z calcd for $C_{33}H_{33}N_4O_7$: 597.23248 [M-H]⁺; found: 597.23456.



1,2-dideoxy-1-(4-(2-(4-methoxyphenyl)-3-hydroxy-4-oxo-4H-chromen-6-yl)-1H-1,2,3-triazol-1-yl)-b-D-ribofuranose 13 (TM3HF)

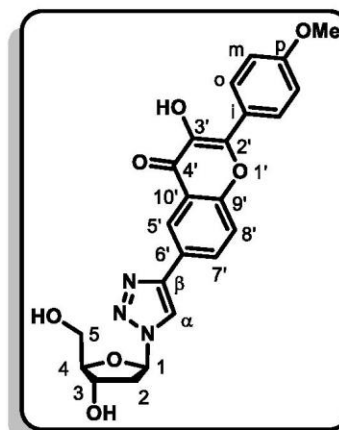
To a stirred suspension of **11** (30 mg, 0.054 mmol) in MeOH (3 mL)/Pyridine (1 mL) was dropwise added a 33 % ammonium hydroxide aq. solution (2.2 mL). Protected from light, the reaction mixture was stirred at rt for 6 h and then the volatiles were evaporated and the residue acidified with aq. AcOH (1.9 mL in 14 mL of water). The resulting solution was stored 12 h at 0 °C. The heterogeneous mixture was centrifuged for settling solid particles and the supernatant was carefully taken out with a syringe with a fine needle. The precipitate was triturated with acetonitrile and MeOH, and after centrifugation the supernatant was removed by suction. The final product was partially solubilized in water (300 μ L). The resulting solution was frozen and lyophilized to provide the desired compound **13** as a yellow solid (14.9 mg, 61%). C₂₃H₂₁N₃O₇ (451.44).

R_f = 0.23 (DCM/MeOH: 90/10).

¹H-NMR (DMSO-*d*⁶, 500 MHz): δ = 2.44 (ddd, ²*J* = 13.3 Hz, ³*J* = 6.0 Hz, ³*J* = 4.6 Hz, 1H, H₂), 2.70 (dt, ²*J* = 13.3 Hz, ³*J* = 6.0 Hz, 1H, H₂), 3.45 – 3.51 (m, 1H, H₅), 3.58 (dd, ²*J* = 10.7 Hz, ³*J* = 5.2 Hz, 1H, H₅), 3.86 (s, 3H, OCH₃), 3.91 (dd, ³*J* = 8.7 Hz, ³*J* = 5.2 Hz, 1H, H₄), 4.41 – 4.47 (m, 1H, H₃), 4.93 (t, ³*J* = 5.6 Hz, 1H, OH), 5.39 (d, ³*J* = 4.4 Hz, 1H, OH), 6.42 (t, ³*J* = 6.2 Hz, 1H, H₁), 7.15 (d, ³*J* = 9.1 Hz, 2H, H_{meta}), 7.88 (d, ³*J* = 8.8 Hz, 1H, H_{8'}), 8.23 (d, ³*J* = 9.1 Hz, 2H, H_{ortho}), 8.29 (dd, ³*J* = 8.8 Hz, ³*J* = 2.2 Hz, 1H, H_{7'}), 8.55 (d, ³*J* = 2.2 Hz, 1H, H_{5'}), 8.97 (s, 1H, H _{α}), 9.58 (s, 1H, OH).

¹³C-NMR (DMSO-*d*⁶, 125 MHz): δ = 40.0 (C₂), 55.3 (OCH₃), 61.5 (C₅), 70.3 (C₃), 88.2 (C₄), 88.3 (C₁), 114.0 (C_{meta}), 119.2 (C_i), 120.3 (C_{8'}), 120.5 (C _{α}), 120.6 (C_{5'}), 123.4 (C_{10'}), 126.9 (C_{6'}), 129.4 (C_{ortho}), 130.4 (C_{7'}), 138.2 (C_{3'}), 145.4 (C _{β}), 145.7 (C_{9'}), 153.9 (C_{para}), 160.4 (C_{2'}), 172.5 (C_{4'}).

HRMS (ESI⁺): *m/z* calcd for C₂₃H₂₂N₃O₇: 452.14523 [M-H]⁺; found: 452.14536.



1,2-dideoxy-1-(4-(2-(4-(diethylamino)phenyl)-3-hydroxy-4-oxo-4H-chromen-6-yl)-1H-1,2,3-triazol-1-yl)-b-D-ribofuranose 14 (TdEAF)

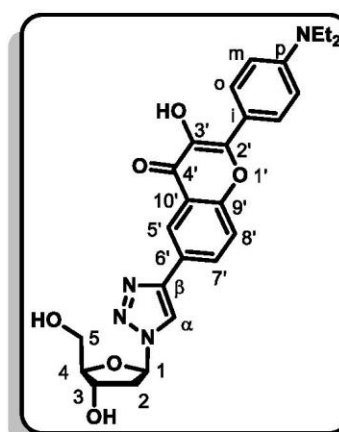
To a stirred suspension of **12** (30 mg, 0.05 mmol) in MeOH (3 mL)/Pyridine (2 mL) was dropwise added a 33 % ammonium hydroxide aq. solution (3.2 mL). Protected from light, the reaction mixture was stirred at rt for 10 h and then the volatiles were evaporated and the residue acidified with aq. AcOH (1.8 mL in 13 mL of water). The resulting solution was stored 12 h at 0 °C. The heterogeneous mixture was centrifuged for settling solid particles and the supernatant was carefully taken out with a syringe with a fine needle. The precipitate was triturated with acetonitrile and MeOH, and after centrifugation the supernatant was removed by suction. The final product was partially solubilized in water (300 μ L). The resulting solution was frozen and lyophilized to provide the desired compound **14** as an orange solid (15.3 mg, 62%). C₂₆H₂₈N₄O₆ (492.53).

R_f = 0.28 (DCM/MeOH: 90/10).

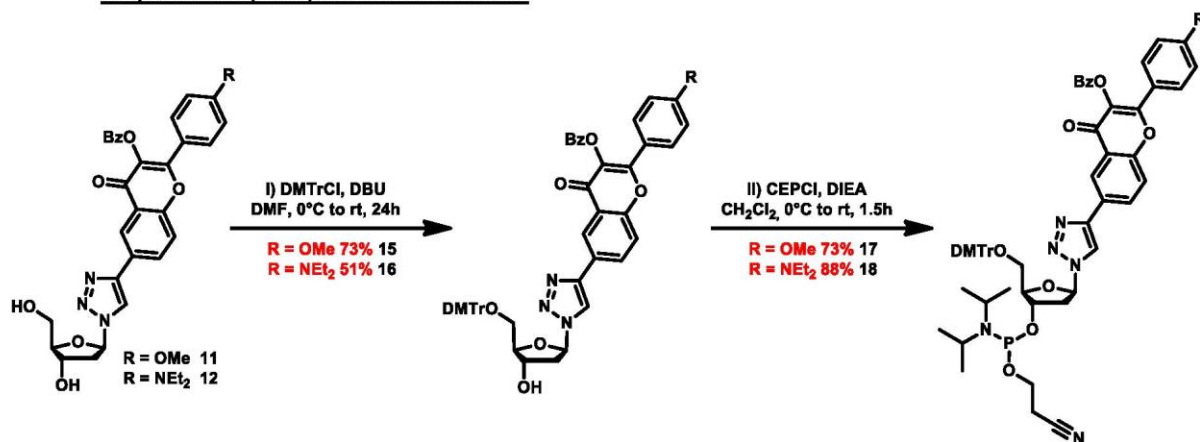
¹H NMR (CDCl₃, MeOD-*d*₄, 500 MHz): δ (ppm): 1.16 (t, ³*J* = 7.0 Hz, 6H, NCH₂-CH₃), 2.48 – 2.56 (m, 1H, H₂), 2.69 – 2.79 (m, 1H, H₂), 3.40 (q, ³*J* = 7.0 Hz, 4H, NCH₂-CH₃), 3.65 (dd, ³*J* = 12.1 Hz, ³*J* = 4.4 Hz, 1H, H₅), 3.75 (dd, ³*J* = 12.1 Hz, ³*J* = 3.7 Hz, 1H, H₅), 4.04 (m, 1H, H₄), 4.52 (m, 1H, H₃), 6.40 (t, ³*J* = 6.0 Hz, 1H, H₁), 6.72 (d, ³*J* = 9.3 Hz, 2H, H_{meta}), 7.61 (d, ³*J* = 8.8 Hz, 1H, H_{8'}), 8.13 (d, ³*J* = 9.1 Hz, 2H, H_{ortho}), 8.18 (dd, ³*J* = 8.8 Hz, ³*J* = 2.1 Hz, 1H, H_{7'}), 8.39 (d, ³*J* = 2.1 Hz, 1H, H_{5'}), 8.45 (s, 1H, H _{α}).

¹³C NMR (CDCl₃, MeOD-*d*₄, 126 MHz): δ (ppm): 11.5 (NCH₂-CH₃), 40.4 (C₂), 43.6 (NCH₂-CH₃), 61.2 (C₅), 70.0 (C₃), 87.6 (C₄), 88.4 (C₁), 110.1 (C_{meta}), 117.7 (C_i), 118.1 (C_{8'}), 118.9 (C _{α}), 120.7 (C_{5'}), 124.6 (C_{10'}), 127.4 (C_{6'}), 129.0 (C_{ortho}), 129.5 (C_{7'}), 136.3 (C_{3'}), 147.8 (C _{β}), 148.5 (C_{9'}), 150.6 (C_{para}), 156.6 (C_{2'}), 174.3 (C_{4'}).

HRMS (ESI⁺): *m/z* calcd for C₂₆H₂₉N₄O₆: 493.20816 [M-H]⁺; found: 493.20837.



Preparation of the fluorescent amidites



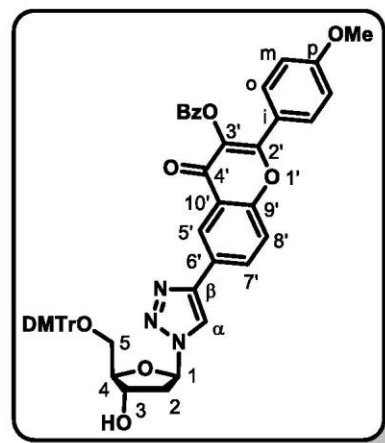
1,2-dideoxy-1-(4-(2-(4-methoxyphenyl)-3-hydroxy-4-oxo-4H-chromen-6-yl)-1H-1,2,3-triazol-1-yl)-5-O-(bis-(4-methoxyphenyl)(phenyl)methyl)-b-D-ribofuranose 15

To a stirred solution of **11** (803 mg, 1.45 mmol) in dry pyridine (15 mL) was added DIEA (636 μ L, 2.4 eq, 3.47 mmol) at 0 °C, followed by a portionwise addition of DMTrCl (606 mg, 1.2 eq, 1.74 mmol). The reaction mixture was stirred at rt for 16 h. Upon completion of the reaction, the volatiles were evaporated and the residue purified by flash chromatography (Toluene/Acetone: 95/5 to 25/75) to provide the desired compound **15** as a yellow foam (903 mg, 73 %). C₅₁H₄₃N₃O₁₀ (857.92).

R_f = 0.55 (Toluene/Acetone = 1:1).

¹H NMR (CDCl₃, CD₂Cl₂, 500 MHz): δ (ppm): 2.52 – 2.69 (m, 1H), 2.86 – 3.03 (m, 1H), 3.20 – 3.41 (m, 2H), 3.71 (s, 6H), 3.84 (s, 3H), 4.15 (q, ³J = 4.6 Hz, 1H), 4.63 – 4.78 (m, 1H), 6.41 (dd, ³J = 6.5 Hz, ³J = 4.9 Hz, 1H), 6.78 (d, ³J = 8.8 Hz, 4H), 6.95 – 7.05 (m, 2H), 7.12 – 7.32 (m, 7H), 7.37 (dd, ³J = 8.2 Hz, ²J = 1.7 Hz, 2H), 7.56 (t, ³J = 7.4 Hz, 2H), 7.63 (d, ³J = 8.8 Hz, 1H), 7.66 – 7.75 (m, 1H), 7.96 (d, ³J = 9.0 Hz, 2H), 8.09 (dd, ³J = 8.9 Hz, ²J = 2.2 Hz, 1H), 8.12 (s, 1H), 8.16 – 8.26 (m, 2H), 8.48 (d, ³J = 2.1 Hz, 1H).

¹³C NMR (CDCl₃, CD₂Cl₂, 126 MHz): δ (ppm): 21.5, 41.1, 55.5, 55.8, 64.2, 72.0, 86.8, 87.2, 98.3, 113.5, 114.6, 119.3, 119.8, 122.4, 122.4, 124.1, 125.6, 127.2, 128.3, 128.5, 128.5, 129.1, 129.2, 129.3, 130.3, 130.4, 130.7, 131.7, 135.9, 136.2, 138.3, 145.1, 146.4, 155.5, 156.7, 159.0, 162.5, 164.1, 172.0.



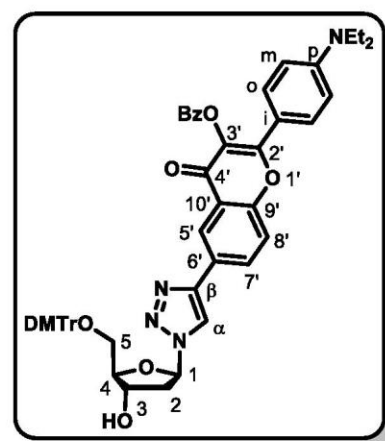
1,2-dideoxy-1-(4-(2-(4-(diethylamino)phenyl)-3-hydroxy-4-oxo-4H-chromen-6-yl)-1H-1,2,3-triazol-1-yl)-5-O-(bis-(4-methoxyphenyl)(phenyl)methyl)-b-D-ribofuranose 16

To a stirred solution of **12** (540 mg, 0.91 mmol) in DMF (18 mL)/Pyridine (8 mL) was added DBU (1.03 mL, 7.2 eq, 6.52 mmol) at 0 °C, followed by a portionwise addition of DMTrCl (759 mg, 2.4 eq, 2.17 mmol). The reaction mixture was stirred at rt for 16 h. Upon completion of the reaction, MeOH was added to quench the reaction and the volatiles were evaporated. The residue was purified by flash chromatography (Toluene/Acetone: 95/5 to 25/75) to provide the desired compound **16** as an orange foam (412 mg, 51 %). C₅₄H₅₀N₄O₉ (899.01).

R_f = 0.66 (Toluene/Acetone = 1:1).

¹H NMR (ACN-d₆, 200 MHz): δ (ppm): 1.06 (t, ³J = 7.0 Hz, 6H), 2.44 – 2.47 (m, 1H), 2.78 – 2.96 (m, 1H), 3.18 (m, ²J = 4.2 Hz, 1H), 3.32 (q, ³J = 7.0 Hz, 4H), 3.63 (m, 7H), 4.07 (m, 1H), 4.54 – 4.75 (m, 1H), 6.36 (dd, ³J = 6.6 Hz, ³J = 4.3 Hz, 1H), 6.65 (d, ³J = 9.3 Hz, 2H), 6.74 (d, ³J = 8.7 Hz, 4H), 7.21 (m, 7H), 7.32 (m, 2H), 7.57 (m, 2H), 7.70 (m, 1H), 7.83 (d, ³J = 9.1 Hz, 2H), 7.98 (dd, ³J = 8.8 Hz, ⁴J = 2.1 Hz, 1H), 8.19 (m, 2H), 8.29 (s, 1H), 8.42 (d, ⁴J = 2.1 Hz, 1H).

¹³C-NMR (ACN-d₆, 50 MHz): δ (ppm): 12.8 (2C), 21.5 (1C), 40.8 (1C), 45.1 (2C), 55.8 (2C), 64.6 (1C), 71.8 (1C), 87.8 (1C), 89.6 (1C), 111.9 (2C), 114.0 (2C), 115.8 (1C), 119.9 (1C), 121.0 (1C), 122.3 (1C), 124.6 (1C), 126.3 (1C), 127.8 (1C), 128.8 (2C), 129.0 (2C), 129.2 (2C), 129.8 (1C), 129.9 (2C), 130.0 (2C), 130.8 (2C), 130.9 (2C), 131.1 (2C), 131.8 (1C), 132.7 (1C), 135.1 (1C), 136.8 (1C), 136.9 (1C), 145.9 (1C), 146.9 (1C), 151.0 (1C), 155.9 (1C), 157.8 (1C), 159.5 (2C), 164.8 (1C), 171.8 (1C).



1,2-dideoxy-1-(4-(2-(4-methoxyphenyl)-3-hydroxy-4-oxo-4H-chromen-6-yl)-1H-1,2,3-triazol-1-yl)-5-O-(bis-(4-methoxyphenyl)(phenyl)methyl)-b-D-ribofuranose cyanoethyl diisopropylphosphoramidite 17

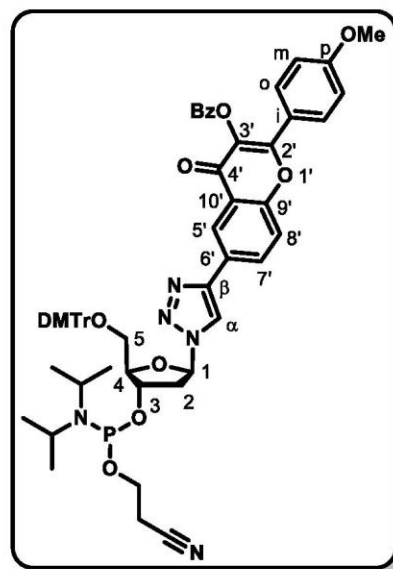
To a solution of **15** (300 mg, 0.350 mmol, 1 eq.) in freshly distilled DCM (2.5 mL) under argon, DIPEA (616 μ L, 3.5 mmol, 10 eq.) and 2-cyanoethyl diisopropylchlorophosphoramidite (95 μ L, 0.420 mmol, 1.2 eq.) were added and the reaction mixture was stirred at r.t. for 2.5 hours. The resulting mixture was purified by flash chromatography eluted with $\text{CH}_2\text{Cl}_2/\text{Acetone}$ (100/0 \rightarrow 80/20, v/v) to give the desired compound **17** (271 mg, 0.256 mmol, 73%). $\text{C}_{60}\text{H}_{60}\text{N}_5\text{O}_{11}\text{P}$ (1058.14).

$R_f = 0.50$ (Tol/Acetone = 9/1).

$^1\text{H NMR}$ (CD_2Cl_2 , 200 MHz): δ (ppm): 1.18 (m, 12H), 2.30 (m 2H), 2.49 (t, $^3J = 6.2$ Hz, 1H), 2.64 (t, $^3J = 6.2$ Hz, 1H), 2.70 – 2.83 (m, 1H), 2.90 – 3.04 (m, 1H), 3.28 – 3.34 (m, 2H), 3.71 (m, 10H), 3.85 (s, 3H), 4.26 – 4.37 (m, 1H), 4.73 – 4.89 (m, 1H),

6.45 (m, 1H), 6.78 (m, 4H), 7.01 (d, $^3J = 8.9$ Hz, 2H), 7.13 – 7.32 (m, 9H), 7.37 (d, $^3J = 7.2$ Hz, 2H), 7.64 (m, 3H), 7.97 (d, $^3J = 8.9$ Hz, 2H), 8.02 – 8.09 (m, 1H), 8.16 – 8.24 (m, 3H), 8.50 (s, 1H).

$^{31}\text{P-NMR}$ (CD_2Cl_2 , 162 MHz): δ (ppm): 148.93, 148.97.



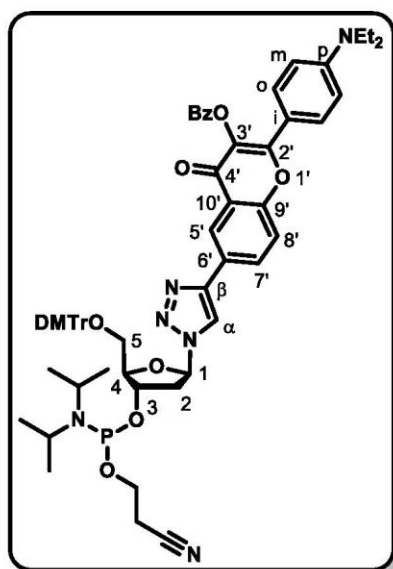
1,2-dideoxy-1-(4-(2-(4-(diethylamino)phenyl)-3-hydroxy-4-oxo-4H-chromen-6-yl)-1H-1,2,3-triazol-1-yl)-5-O-(bis-(4-methoxyphenyl)(phenyl)methyl)-b-D-ribofuranose cyanoethyl diisopropylphosphoramidite 18

To a solution of **16** (250 mg, 0.278 mmol, 1 eq.) in freshly distilled DCM (2.5 mL) under argon, DIPEA (489 μ L, 2.78 mmol, 10 eq.) and 2-cyanoethyl diisopropylchlorophosphoramidite (75 μ L, 0.334 mmol, 1.2 eq.) were added and the reaction mixture was stirred at r.t. for 2.5 hours. The resulting mixture was purified by flash chromatography eluted with $\text{CH}_2\text{Cl}_2/\text{Acetone}$ (100/0 \rightarrow 80/20, v/v) to give the desired compound **18** (268 mg, 0.244 mmol, 88%). $\text{C}_{63}\text{H}_{67}\text{N}_6\text{O}_{10}\text{P}$ (1099.23).

$R_f = 0.50$ (Tol/Acetone = 9/1).

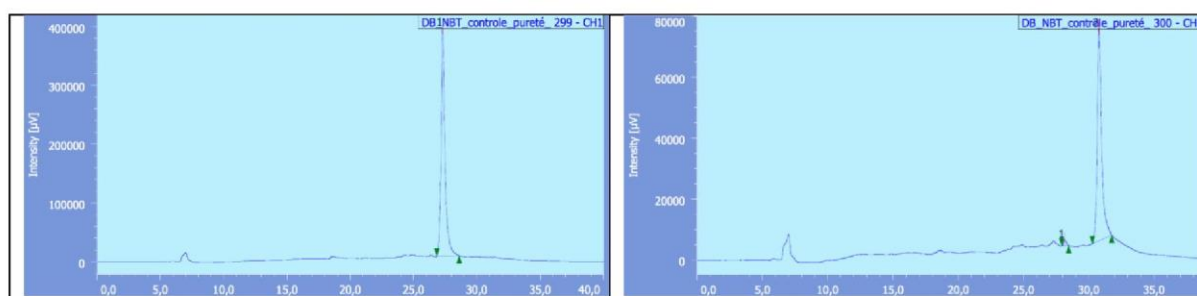
$^1\text{H NMR}$ (CDCl_3 , 200 MHz): δ (ppm): 1.18 (m, 18H), 2.48 (t, $^3J = 6.2$ Hz, 1H), 2.64 (t, $^3J = 6.2$ Hz, 1H), 2.68 – 2.82 (m, 1H), 2.89 – 3.04 (m, 1H), 3.27 – 3.45 (m, 5H), 3.54 – 3.90 (s, 10H), 4.26 – 4.36 (m, 1H), 4.72 – 4.87 (m, 1H), 6.44 (m, 1H), 6.68 – 6.81 (m, 6H), 7.13 – 7.30 (m, 9H), 7.38 (d, $^3J = 6.8$ Hz, 2H), 7.53 – 7.75 (m, 3H), 7.91 (d, $^3J = 9.2$ Hz, 2H), 8.00 – 8.07 (m, 1H), 7.14 (d, $^4J = 2.3$ Hz, 1H), 8.23 – 8.27 (m, 2H), 8.47 (d, $^4J = 2.3$ Hz, 1H).

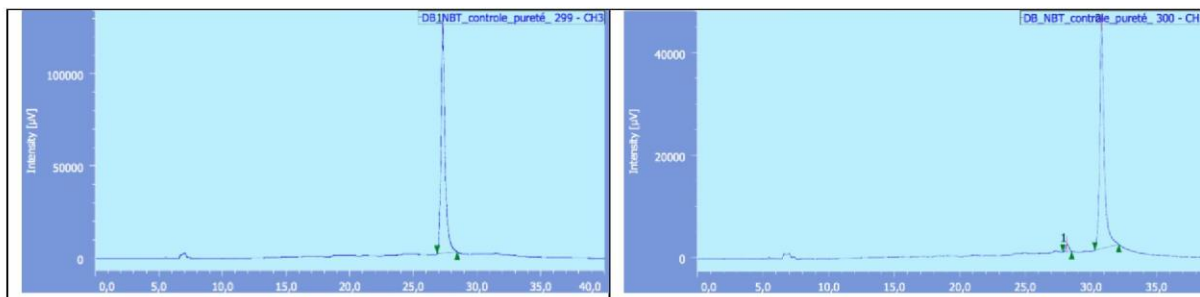
$^{31}\text{P-NMR}$ (CD_2Cl_2 , 162 MHz): δ (ppm): 148.93, 148.99.



2. Photophysical characterization of the nucleosides

Figure 1: HPLC analysis of both nucleosides (TM3HF: left and TdEAF: right) at 260 nm (Top) and 390 nm (Bottom).





2.2. Steady-state fluorescence measurements

Table 1: Spectroscopic properties of 3-HC nucleoside analogs TM3HF and TdEAF.

Solvent	$E_T(30)^a$	λ_{abs}^a		$\lambda_{N^*}^b$		$\lambda_{T^*}^c$		$I_{N^*}/I_{T^*}^d$		Φ (%) ^e	
		TM3HF	TdEAF	TM3HF	TdEAF	TM3HF	TdEAF	TM3HF	TdEAF	TM3HF	TdEAF
HFIP	65.3	357	442	453	559	-	-	-	-	21	1
TFE	59.8	359	433	445	556	-	-	-	-	12	4
MeOH	55.4	357	420	436	542	538	-	0,77	-	6	18
EtOH	51.9	358	419	429	534	542	-	0,26	-	6	34
iPrOH	48.4	358	417	424	525	540	555	0,15	1,19	6	36
CH ₃ CN	45.6	348	410	424	522	535	578	0,022	0,95	4	15
DMF	43.2	353	413	421	518	544	590	0,078	0,80	7	9
DMSO	45.1	343	418	425	526	545	592	0,137	0,76	7	15
Acetone	42.2	348	408	421	502	541	582	0,026	0,97	6	10
DCE	41.3	351	416	425	492	533	581	0,045	0,74	13	27
CH ₂ Cl ₂	40.7	354	417	467	490	531	578	0,098	0,85	4	26
CHCl ₃	39.1	357	421	425	491	531	569	0,013	0,85	12	28
EtOAc	38.1	350	405	408	469	538	576	0,0086	0,78	10	16
Dioxane	36.0	352	406	433	446	539	576	0,018	0,64	15	15
THF	36.2	353	407	428	469	542	581	0,02	0,96	13	14
DME	38.2	351	406	420	475	540	581	0,021	1,13	9	11

Footnotes: a) position of the absorption band maximum; b) position of the N* band maximum; c) position of the T* band maximum; d) the ratio of two intensity maxima; e) Φ is the fluorescence quantum yield.

2.3. ESIPT Study

Figure 2: emission spectra TM3HF in CH₃CN/MeOH solutions

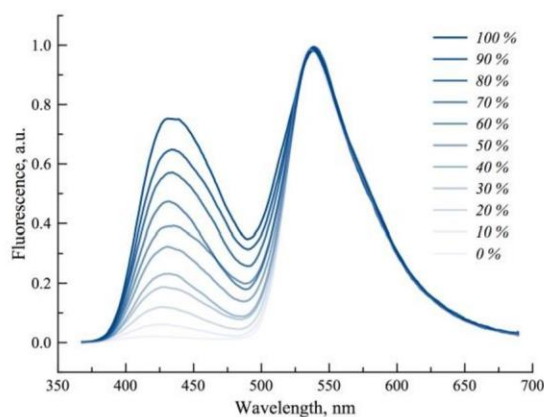
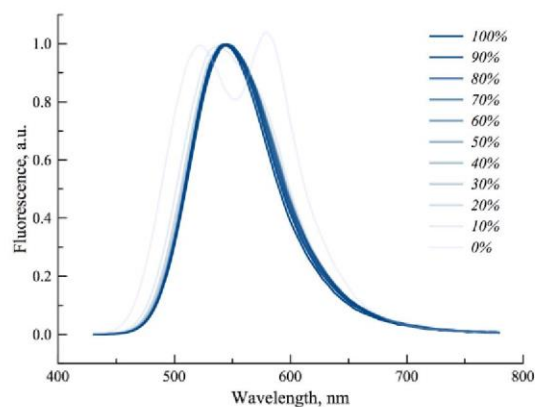


Figure 3: emission spectra of TdEAF in CH₃CN/MeOH solutions



2.4. Emission Fluorescence Spectra

Figure 4: Fluorescence emission spectra of TM3HF in apolar versus polar solvents

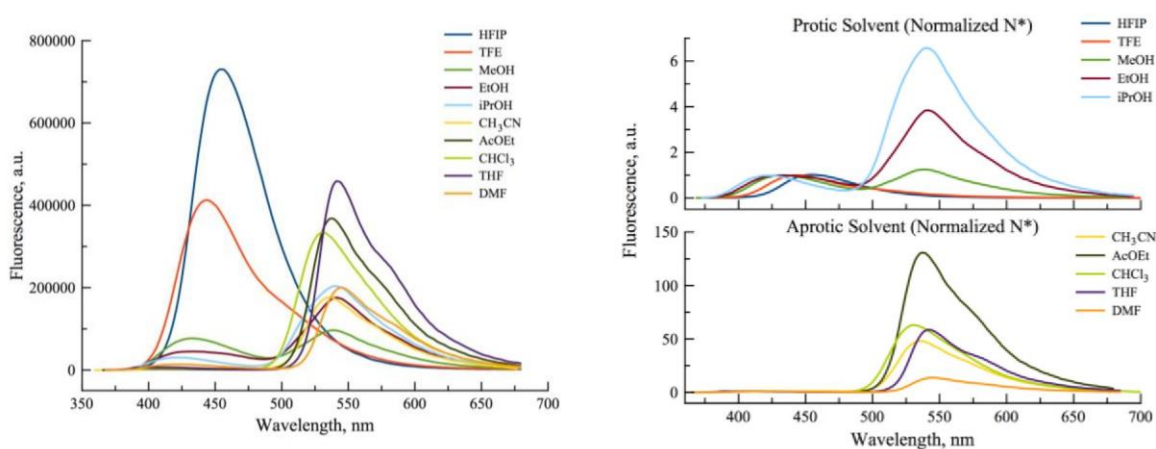


Figure 5: Fluorescence emission spectra of TdEAF in apolar versus polar solvents.

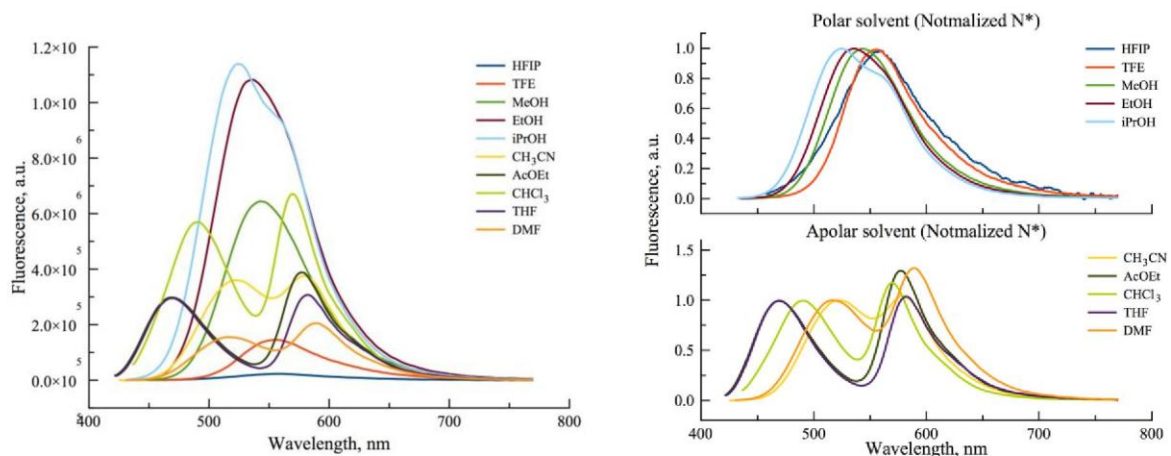
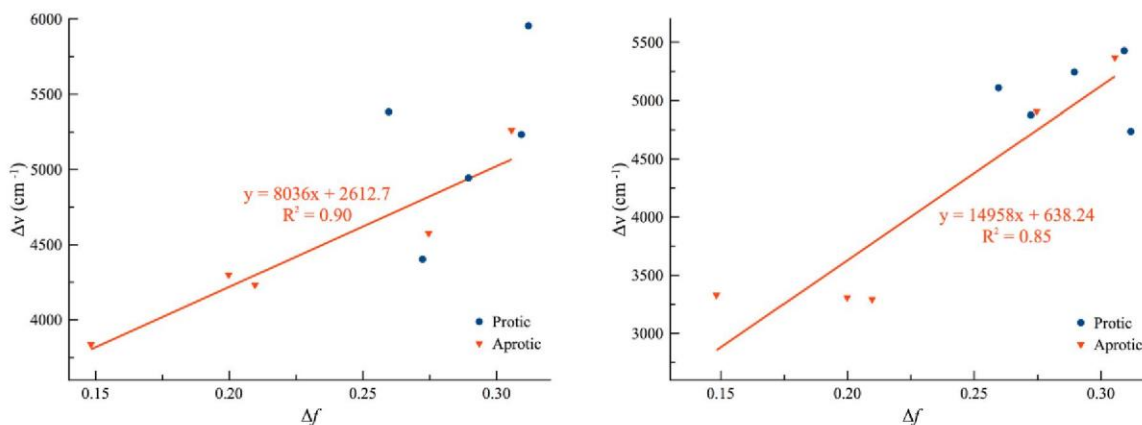


Figure 6: Lippert-Mataga Plots for TM3HF (left) and TdEAF (right)



3. Model ODNs spectroscopic studies

3.1. ODNs synthesis and purification

The ODN synthesis was performed on an Expedite 8900 DNA synthesizer (Applied Biosystem) using the “trityl off” mode and mild phosphoramidite chemistry on a 0.2 μmol scale. Reagents and solvents, as well as dT, Ac-dC, Pac-dA, and dmf-dG phosphoramidites were purchased from Link Technologies. The standard DNA assembly protocol “DMT-off” was used except for the following modifications: 5-Ethylthio-1H-tetrazole (ETT) was used as activating agent; Pac-anhydride was used for capping; a longer coupling time (1200 s) was applied to the 3HC phosphoramidite. Non-labelled ODNs were purchased from Microsynth AG. The ODNs were cleaved from the solid support and deprotected with concentrated aqueous ammonia at room temperature for 12 h. The ODNs were analyzed (0.5 mL/min) and purified (2.5 mL/min) by RP HPLC (HPLC apparatus: Waters™ 600 Controller with Waters™ 996 Photodiode Array Detector and Jasco LC-Net II / ADC apparatus. Columns: analytical, 300 × 4.60 mm, 5 μm particle size, Clarity® 100Å, Phenomenex®; semi-preparative, Clarity® 5u Oligo-RP column 250 x 10 mm Phenomenex®). The following gradient system was used: 100 % A –(30 min)→ 60 % A / 40 % B –(5 min)→ 100 % B –(5 min)→ 100 % A with A=Buffer pH 7.0 (1.9 L of MilliQ® water, 160 mL acetonitrile, 28 mL triethylamine, 12 mL of acetic acid) and B=0.2 CH₃CN:0.8 Buffer.

Figure 7: HPLC profile of TMT single strand ODN (390 nm) labelled with TM3HF (left) or TdEAF (right)

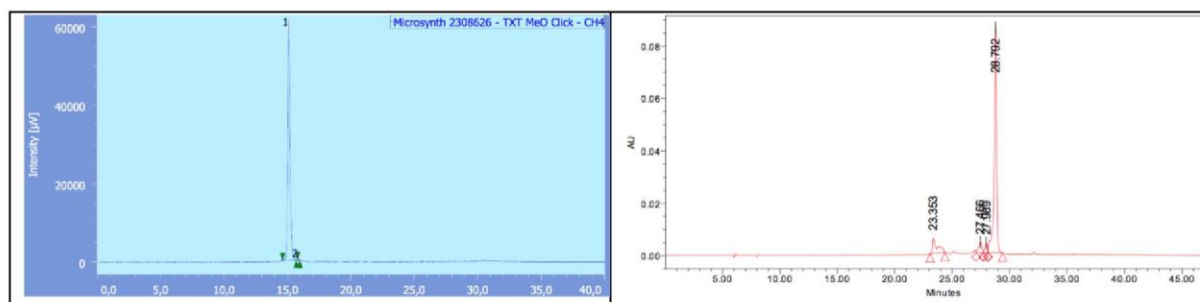


Figure 8: HPLC profile of AMA single strand ODN (390 nm) labelled with TM3HF (left) or TdEAF (right)

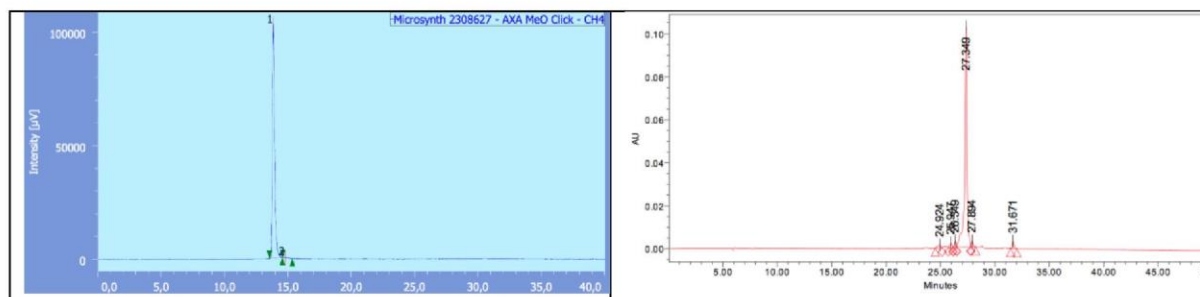


Figure 9: HPLC profile of CMC single strand ODN (390 nm) labelled with TM3HF (left) or TdEAF (right)

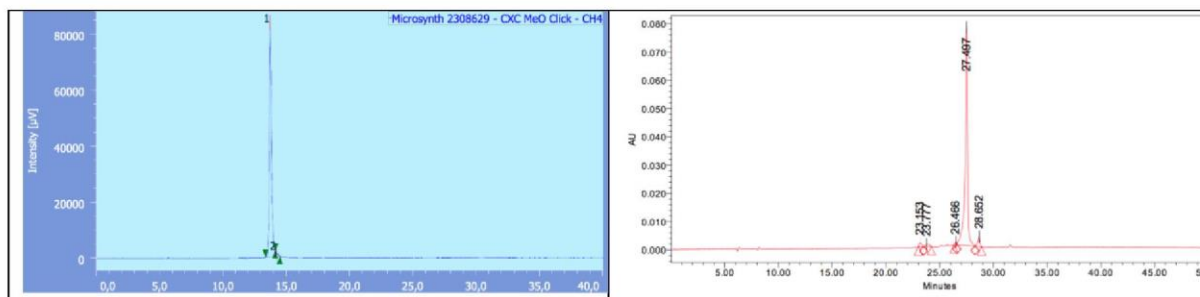
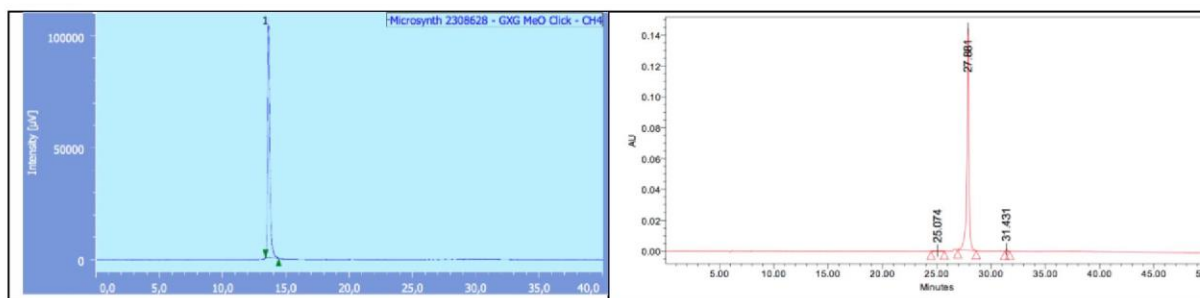


Figure 10: HPLC profile of GMG single strand ODN (390 nm) labelled with TM3HF (left) or TdEAF (right)



3.2. MALDI TOF/TOF analysis of ODNs

Dibasic Ammonium Citrate (DAC) (98% capillary GC) was obtained from Sigma. Acetonitrile of HPLC grade was purchased from VWR chemical. Ultrapure 3-Hydroxypicolinic Acid (3-HPA) MALDI matrix was purchase to Protea Biosciences. C4 pipette tips (Zip-Tip) were from Millipore.

The samples (500 pmol) were diluted to 10 μ L of water and were desalted with a C4 pipette Tips (Zip-tip). The Zip-tip was activated before use with 2 x 5 μ L of water: CH₃CN (50:50) and 2 x 5 μ L of DAC (50 mg/ml diluted in water). The 10 μ L of the ODN solution was loaded on Zip-tip by drawing and expelling ten times. Next the zip-tip was washed with 3 x 5 μ L of DAC (50 mg/mL) and 3 x 5 μ L of water. Elution was performed with 1.5 μ L of 3-HPA matrix (80 mg/mL, 50:50 CH₃CN:DAC) directly on MALDI plate. The ODN profile obtained in a ABSciex MALDI-TOF/TOF mass spectrometer in reflector mode with external calibration mixture (cal Mix 1+2 distributed by ABSciex). MALDI-TOF/TOF-MS analysis: MS spectra were recorded manually in a mass range of 500-6000 Da resulting from 400 laser shots of constant intensity fixed at 6200. Data were collected using 4000 series Explorer (AB SCIEX) experiments.

Table 2: Mass of the single strand DNA.

ODN	Sequence	MALDI-TOF found (calcd) [M ⁺]	
		TM3HF	TdEAF
TMT	5'-d-CGTTTTT M TTTTTGC-3'	4728.7 (4730.4)	4788.6 (4773.4)
AMA	5'-d-CGTTTTT A TTTTTGC-3'	4749.0 (4748.2)	4790.1 (4790.2)
CMC	5'-d-CGTTTTT C MTTTTTGC-3'	4701.7 (4700.2)	4743.2 (4743.2)
GMG	5'-d-CGTTTTT G MTTTTTGC-3'	4789.3 (4780.2)	4823.6 (4822.2)

Figure 11: Mass spectra of TM3HF single strand

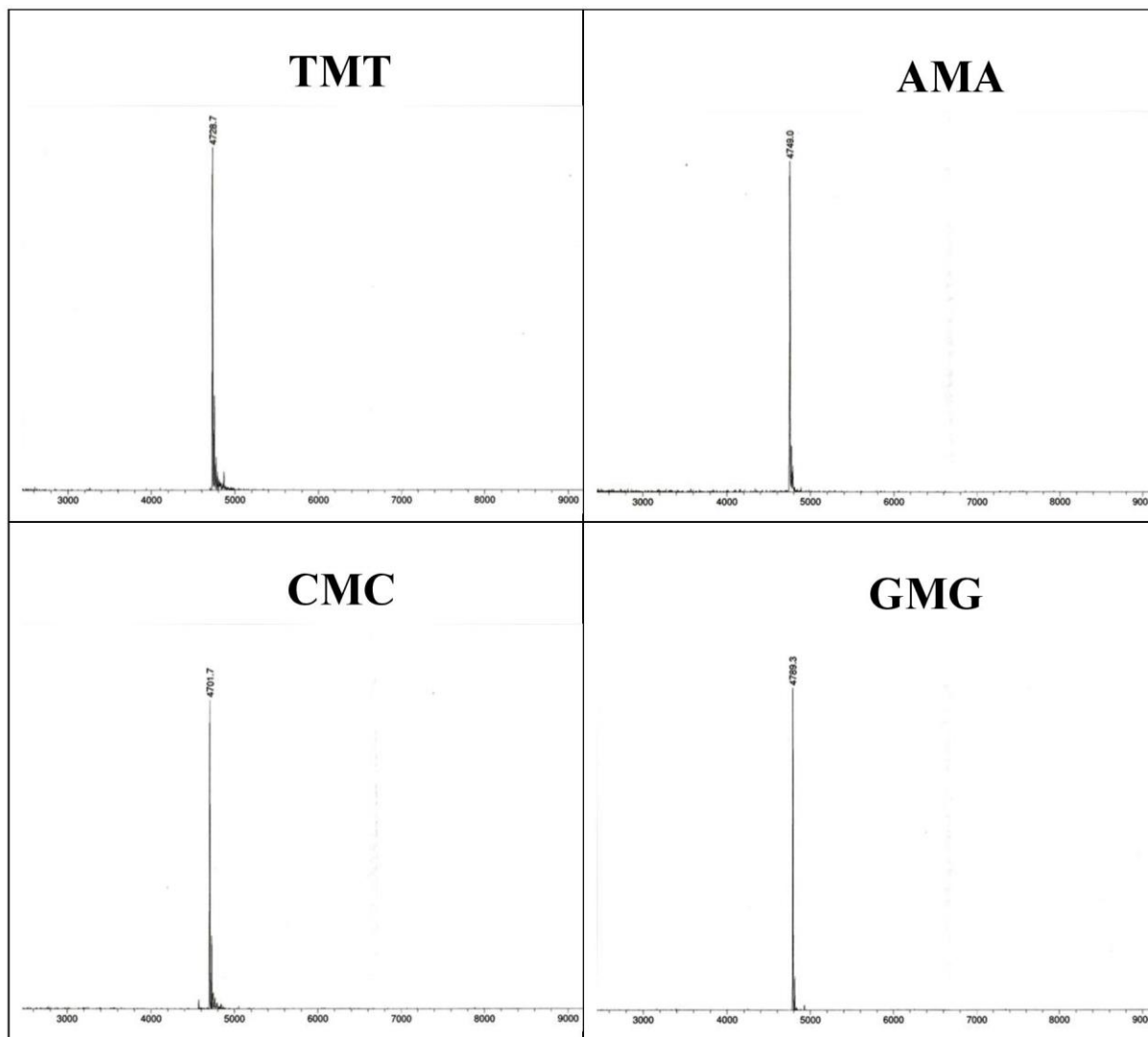
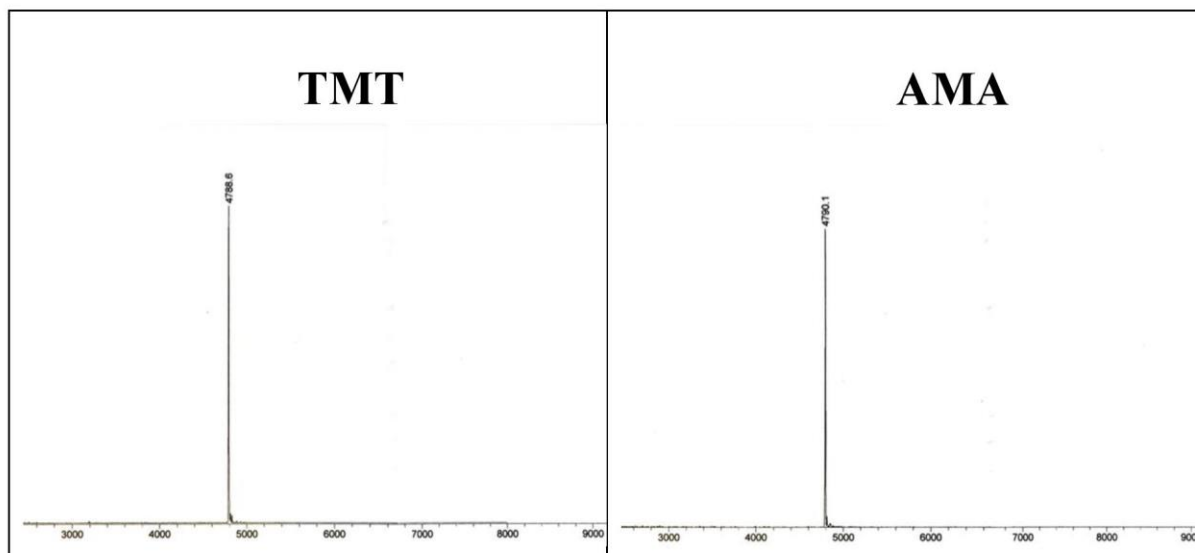
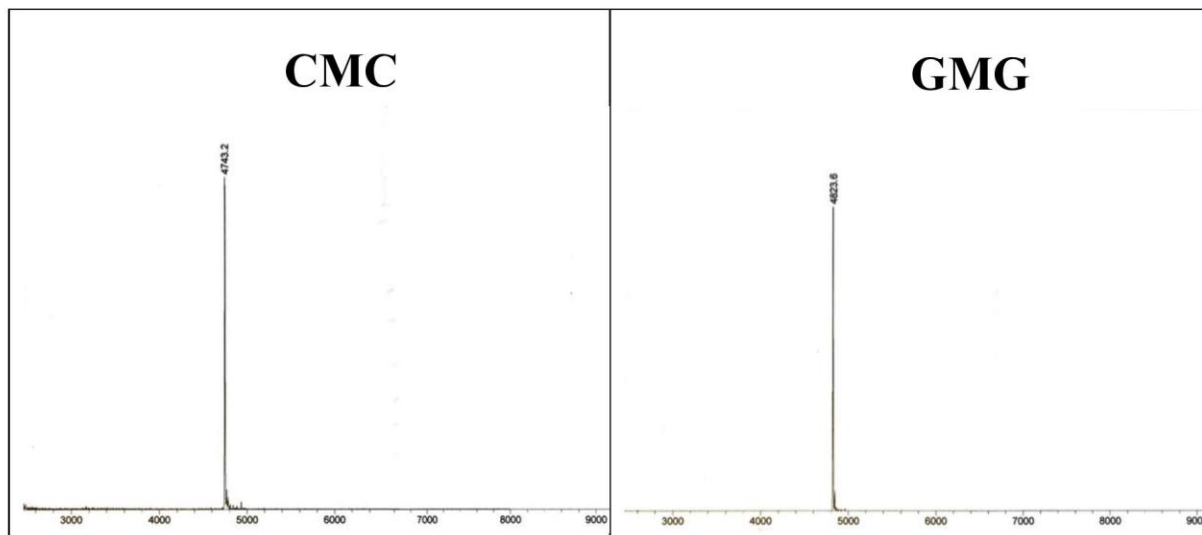


Figure 12: Mass spectra of TdEAF single strand





3.3. Temperature-induced denaturation studies

The ODNs were analyzed by UV/visible spectroscopy in duplicate in cacodylate buffer pH 7.0 (10 mM cacodylate, 150 mM NaCl, 1 mM EDTA).

Preparation of the single strand solution: the solution of the sample was prepared by mixing 400 μ L of a stock solution of 20 mM Cacodylate buffer solution pH 7.0, 80 μ L of 1.5 M NaCl solution, 10 μ L of 80 mM EDTA solution, 25 μ L of 64 μ M ssODN and 285 μ L of MilliQ[®] water.

Preparation of the double strand solution: 400 μ L of a stock solution of 20 mM Cacodylate buffer solution pH 7.0, 80 μ L of 1.5 M NaCl solution, 10 μ L of 80 mM EDTA solution, 25 μ L of 64 μ M ODN 1, 25 μ L of 64 μ M ODN 2 and 260 μ L of MilliQ[®] water.

Melting curves were recorded by following the temperature-dependence of the absorbance changes at 260 nm of the sample (2 μ M concentration of each strand). Absorption spectra were recorded in a Peltier thermostated cell holder on a Cary 4 spectrophotometer (Varian). The pathlength of cell was 1 cm. The temperature range for denaturation measurement was 5 – 80 $^{\circ}$ C. Speed of heating was 0.3 $^{\circ}$ C/min. The melting curves were converted into a plot of α versus temperature, where α represents the fraction of single-strands in the duplex state. The melting temperatures were extracted from these curves after differentiation as described elsewhere.

Table 3: Melting temperatures of the duplexes.

Duplexes	T_m ($^{\circ}$ C)					
	TM3HF	TdEAF	Wild Type ^a	ΔT_m	TM3HF ($^{\circ}$ C) ^b	ΔT_m TdEAF ($^{\circ}$ C) ^b
TMT·ATA	44.5	44.0	50.8 [48.4]	- 6.3		- 6.8
TMT·AAA	41.0	41.0	42.1 [42.8]	+ 2.1		- 1.1
TMT·ACA	45.0	44.9	40.9 [42.1]	+ 4.1		+ 4.0
TMT·AGA	42.5	42.0	42.8 [44.8]	- 0.3		- 0.8
TMT·AAbA	46.5	45.0	33.1	+ 13.4		+ 11.9
AMA·TTT	43.0	41.9	50.6 [48.4]	- 7.6		- 8.7
AMA·TAT	40.5	40.4	39.2 [41.0]	+ 1.3		+ 1.2
AMA·TCT	44.5	45.9	39.8 [38.6]	+ 4.7		+ 6.1
AMA·TGT	41.5	41.4	40.7 [42.4]	+ 0.8		+ 0.7
AMA·TAbT	42.0	41.9	33.7	+ 8.3		+ 8.2
CMC·GTG	45.6	44.4	55.1 [54.0]	- 9.5		- 10.7
CMC·GAG	43.6	42.9	45.8 [46.1]	- 2.2		- 2.9
CMC·GCG	48.6	47.4	47.2 [44.7]	+ 1.4		+ 0.2

CMC·GGG	45.1	44.4	50.3 [50.1]	- 5.2	- 5.9
CMC·GAbG	48.6	47.9	40.5	+ 8.1	+ 7.4
GMG·CTC	50.1	48.5	55.2 [54.0]	- 5.1	- 6.7
GMG·CAC	48.0	48.0	46.0 [46.9]	+ 2.0	+2.0
GMG·CCC	51.1	50.5	45.9 [45.2]	+ 5.2	+ 4.6
GMG·CGC	48.6	48.0	49.6 [49.1]	- 1.0	- 1.6
GMG·CAbC	49.6	49.0	40.5	+ 9.1	+ 8.5

^a T_m of the corresponding duplexe formed from unmodified ODNs and its theoretical values given in square brackets. ^b ΔT_m refers to the difference of T_m between the labelled and wild type ODNs.

Figure 13: Melting Temperature curves of TM3HF duplexes

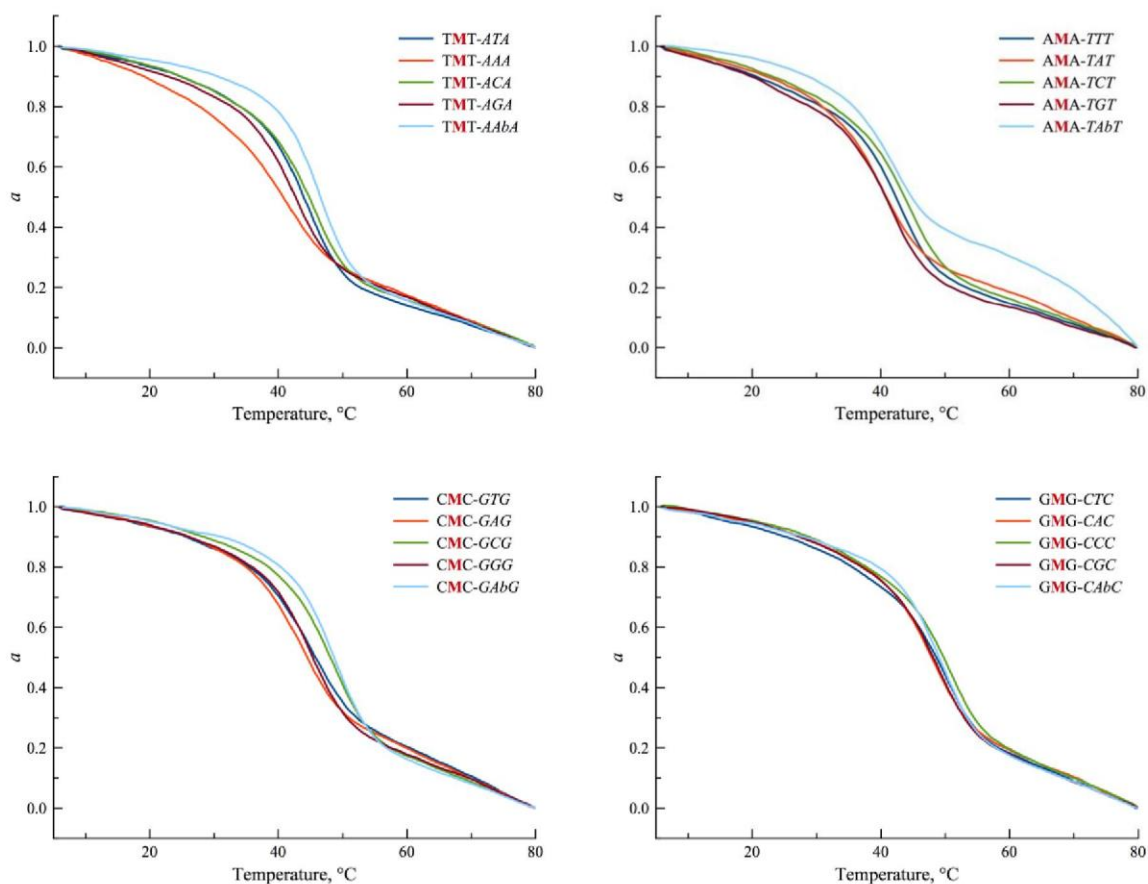
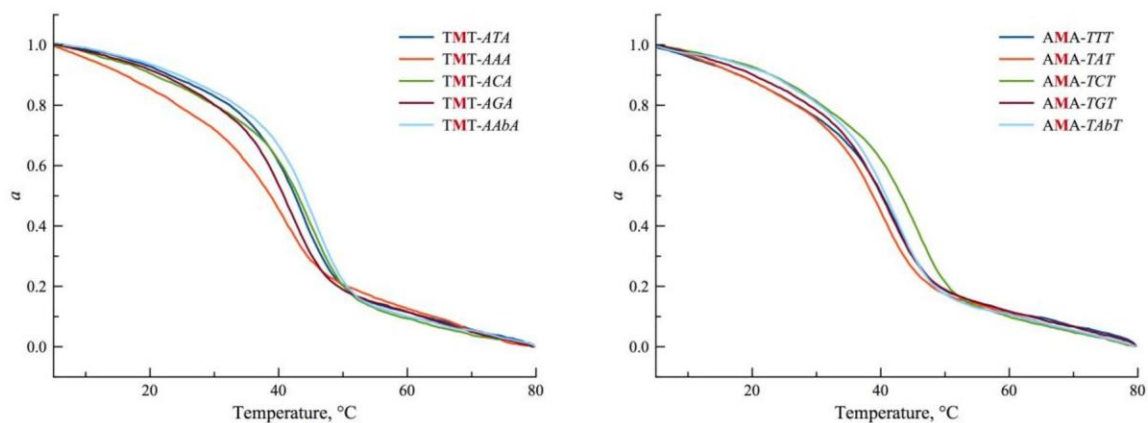
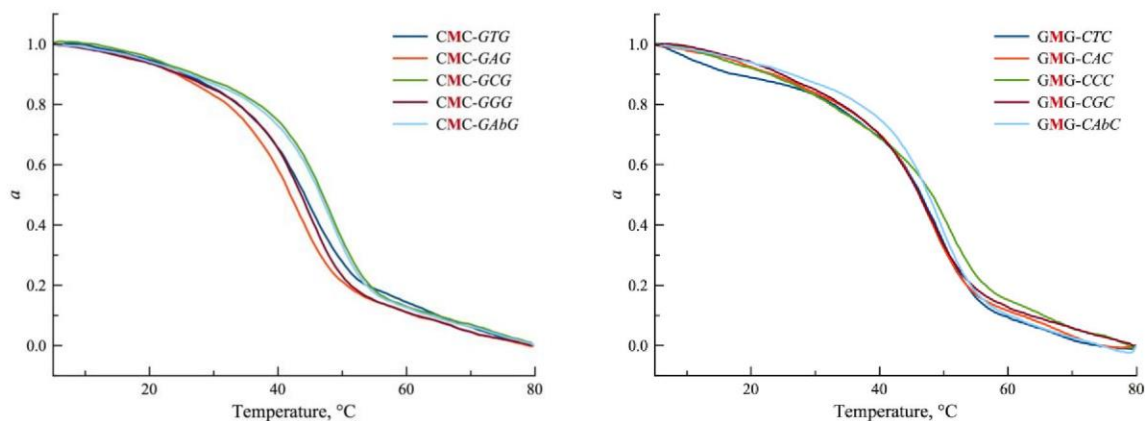


Figure 14: Melting Temperature curves of TdEAF duplexes

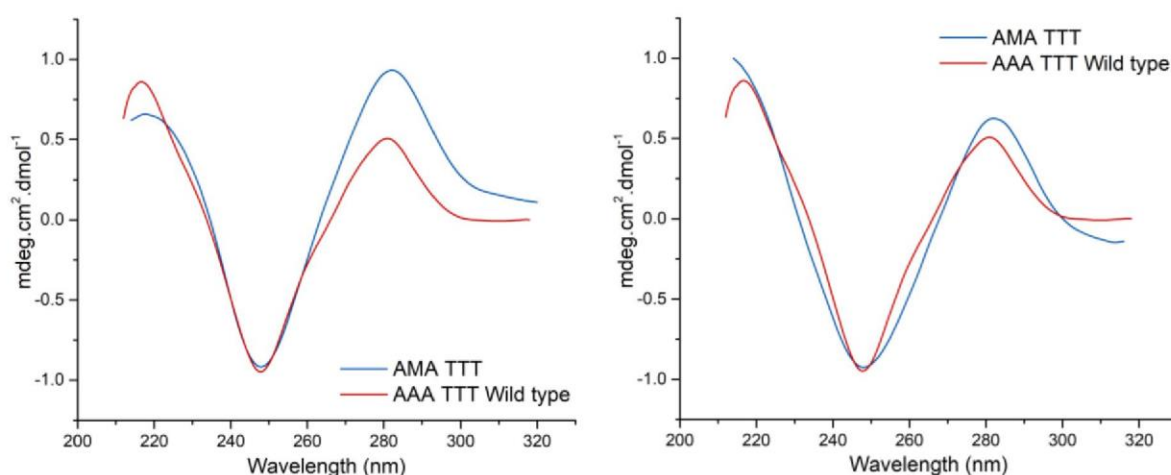




3.4. Circular Dichroism

Circular dichroism spectra were recorded in duplicate with 2 μM solution of the canonical dsDNA and labelled dsDNA (3HC (**M**) opposite **A**, **T** or **Ab**) in buffer pH 7.0 (10 mM cacodylate buffer, 150 mM NaCl, 1 mM EDTA) at 20 °C on a Jasco J-810 spectropolarimeter. Two maxima, typical for B-DNA duplexes, were observed in CD spectra: one negative at 249 nm and the other positive at 282 nm.

Figure 15: Representative CD spectra of TM3HF (left) and TdEAF (right) duplexes in comparison to wild type canonical duplexes



3.5. Steady-state fluorescence measurements

The absorption and fluorescence experiments were realized in triplicate in pH 7.0 phosphate buffer (10 mM cacodylate buffer, 150 mM NaCl, 1 mM EDTA). The absorption spectra were recorded on a Cary 300 Scan spectrophotometer (Varian) using 1cm quartz cells at 20 °C. The fluorescence spectra were recorded on a FluoroMax 4.0 spectrofluorometer (Jobin Yvon, Horiba) by using excitation and emission slits of 2 nm and were corrected at excitation and emission. They were taken with absorbance of about 0.05 at 20 °C at the excitation wavelength mentioned in the corresponding experiments. The quantum yields were corrected according to the variation of the refractive index of the different solvents. Quantum yields were determined by using *p*-dimethylaminoflavone (dMAF) in EtOH ($\lambda_{\text{ex}} = 404 \text{ nm}$, $\Phi = 0.27$) as the standard reference.^{5, 6}

3.6. UV/visible & Fluorescence spectra

⁵ S. M. Ormson, R. G. Brown, F. Vollmer, W. Rettig, *J. Photochem. Photobiol. A* **1994**, *81*, 65-72.

⁶ W. H. Melhuish, *J. Phys. Chem.* **1961**, *65*, 229-235.

Figure 15: UV/visible spectra of TM3HF labeled ODNs.

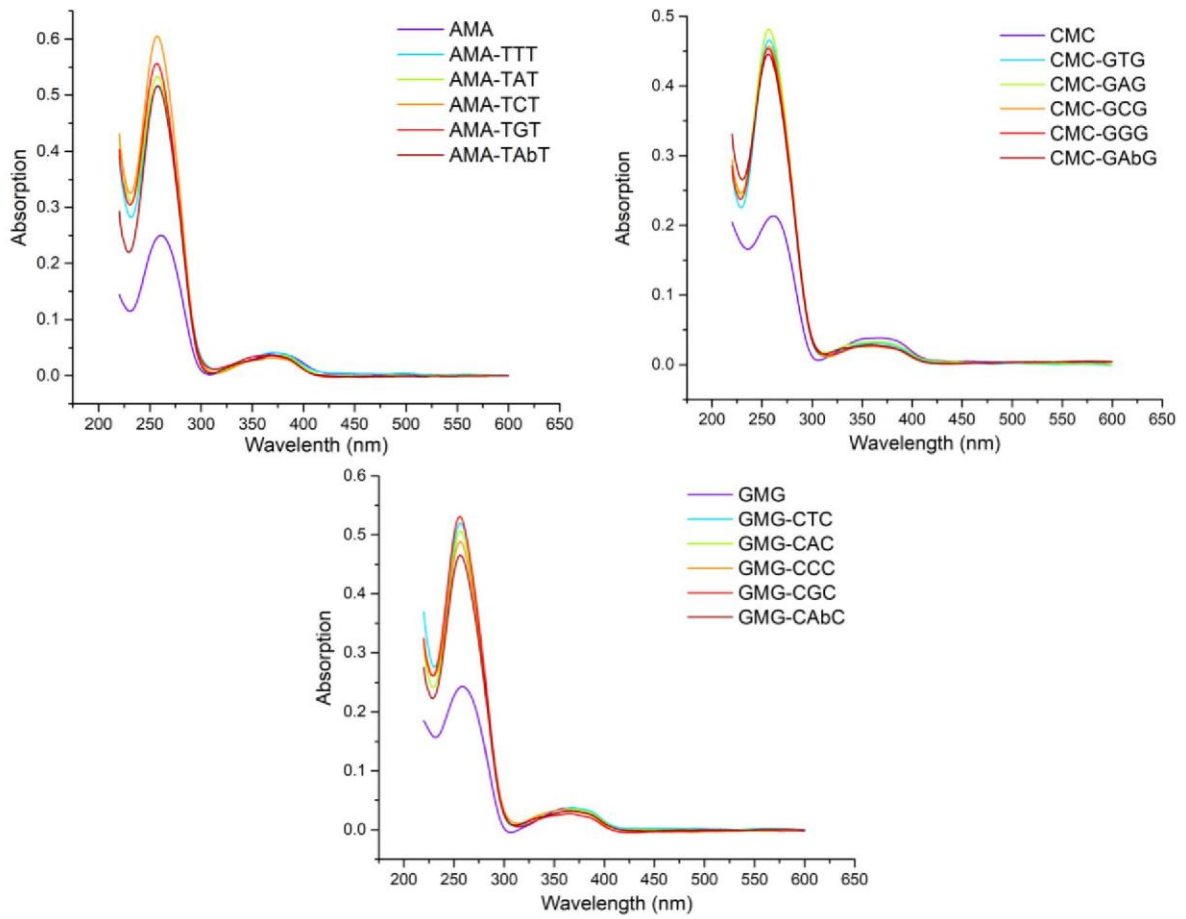
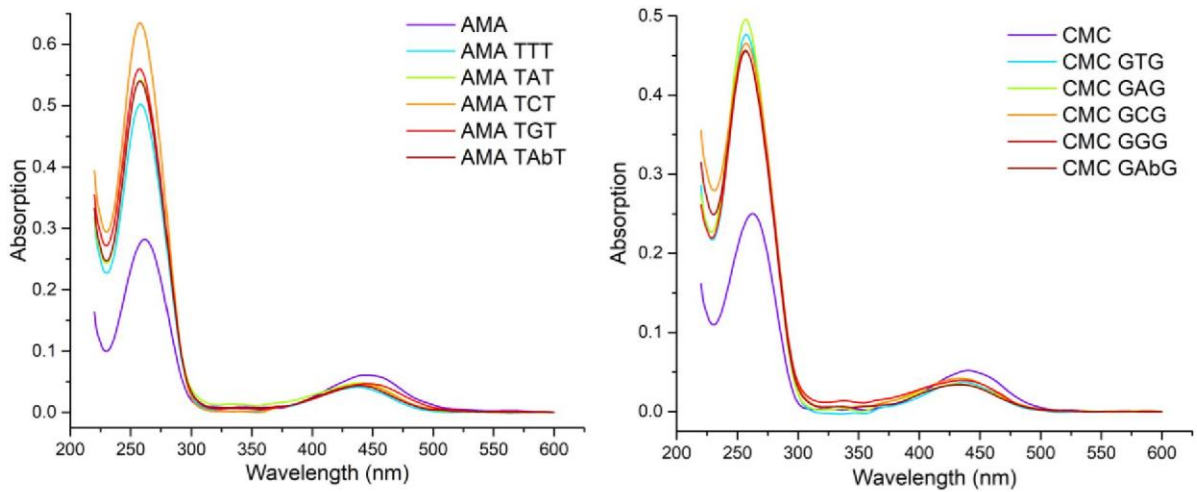


Figure 17: UV/visible spectra of TdEAF labeled ODNs.



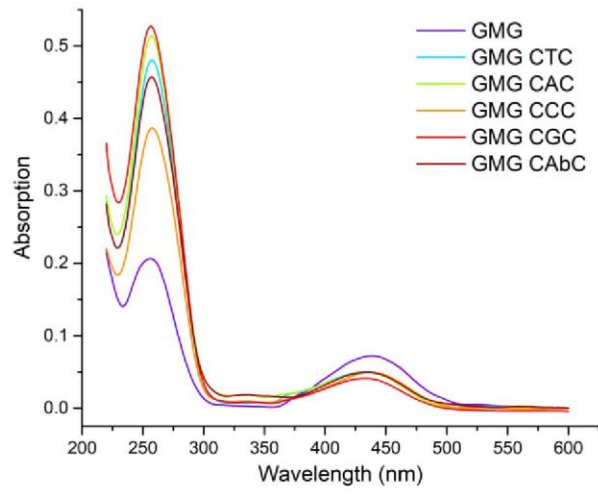


Figure 18: Fluorescence emission spectra of TM3HF labeled ODNs.

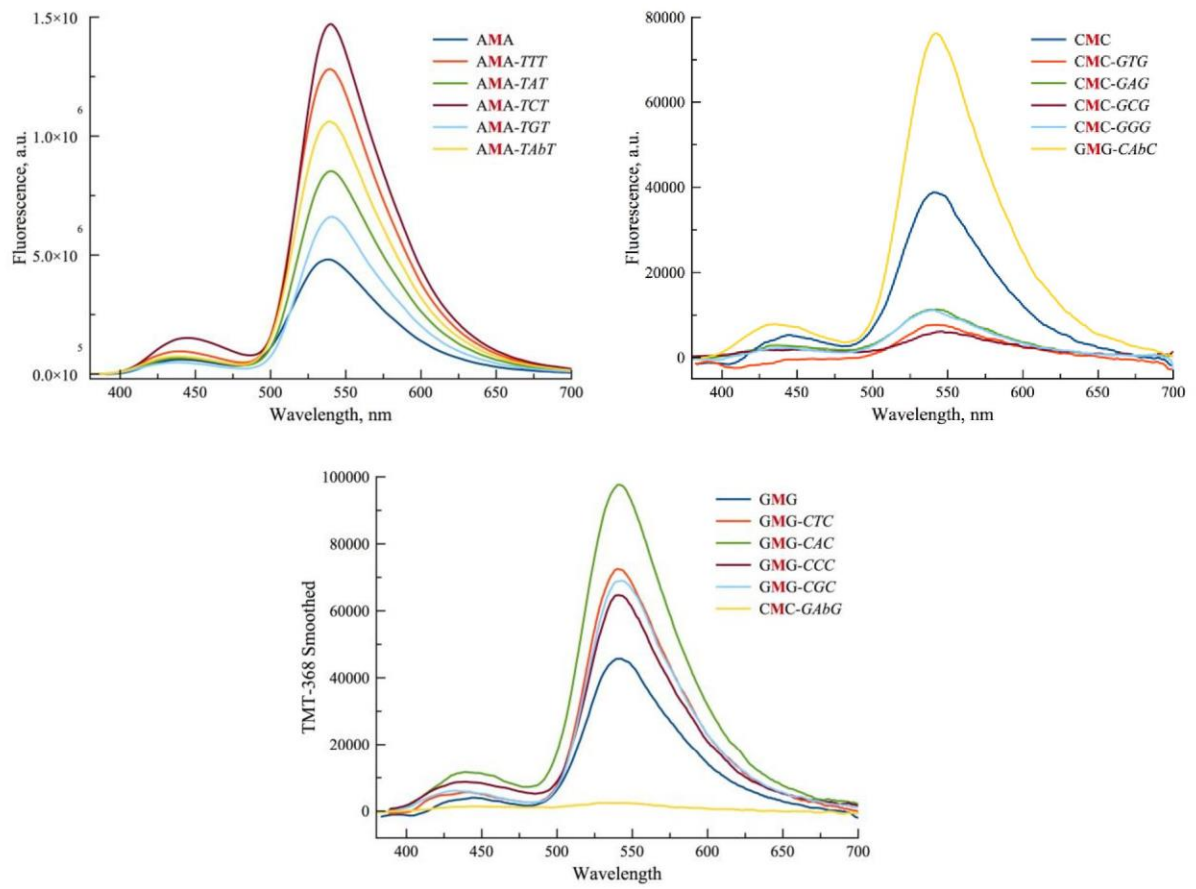
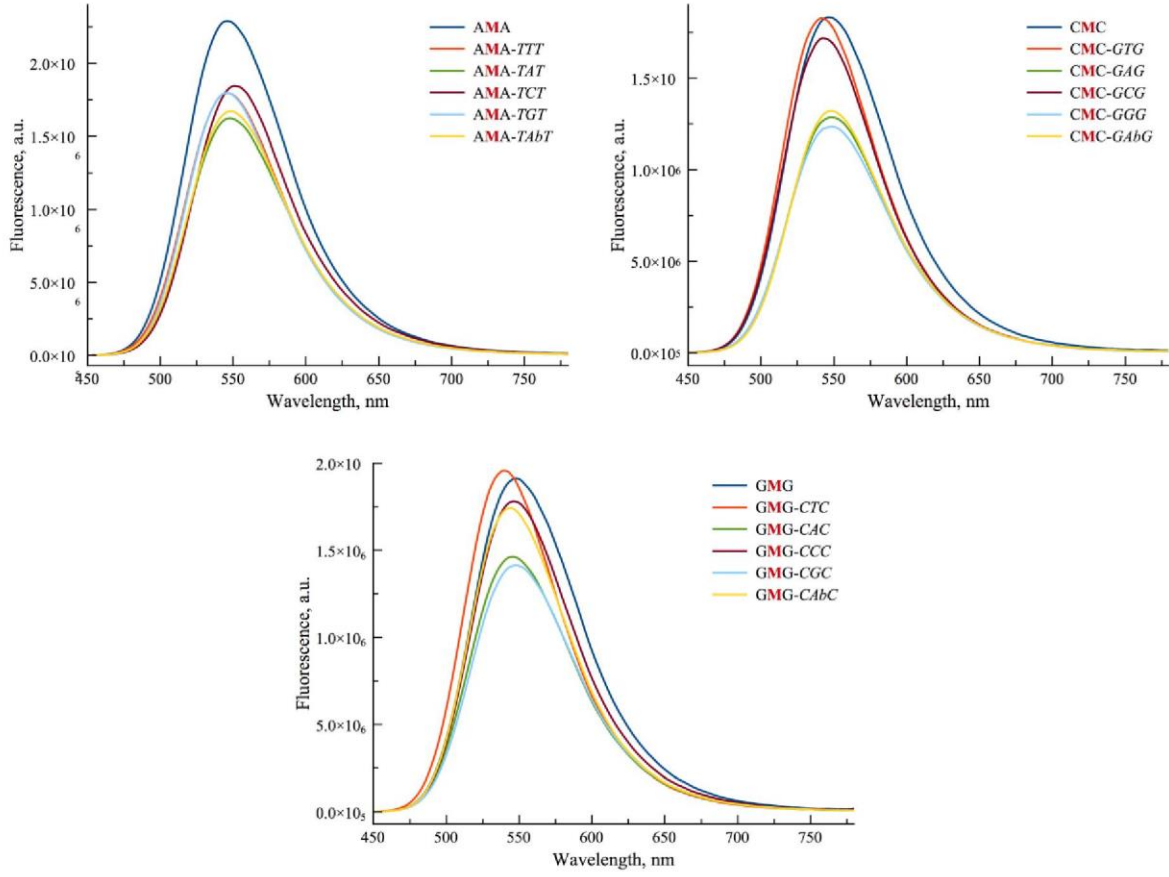


Figure 19: Fluorescence emission spectra of TdEAF labeled ODNs.



4. FRET study

Equation 1: Forster distance

$$R_0 = 0.211 \sqrt[6]{(\kappa^2 n^{-4} Q_D J(\lambda))}$$

where κ^2 describes the relative orientation in space of the transition dipoles of the donor and acceptor (usually assumed to be equal to $2/3$, which is appropriate for dynamic random averaging of the donor and acceptor); n is the refractive index of the medium (1.4 for biomolecules in aqueous solution) and Q_D is the quantum yield of the donor in the absence of acceptor; $J(\lambda)$ ($M^{-1} \cdot cm^{-1} \cdot nm^{-4}$) the spectral overlap integral of the donor emission and the acceptor absorption.

Equation 2 : Energy transfer efficiency

$$E = \left(1 - \frac{F_{DA}}{F_D}\right) \times 100$$

where F_D and F_{DA} are respectively, the relative fluorescence intensities in the absence and presence of the acceptor.

Table 4: Spectroscopic properties of TM3HF labeled ODNs and FRET study with Cy5.

Sequence	λ_{abs}^a	λ_{N*}^b	λ_{T*}^c	I_{N*}/I_{T*}^d	Φ (%) ^e	FRET amplification ^f
AMA	369	337	538	0.14	16	-
AMA-TCT	369	444	540	0.11	50	-
AMA-Cy5TCT	-	-	-	-	-	2.0
CMC	367	439	536	0.22	2	-
CMC-GCG	367	-	541	-	0.5	-
CMC-Cy5GCG	-	-	-	-	-	1.2

Footnotes: a) position of the absorption band maximum; b) position of the N* band maximum; c) position of the T* band maximum; d) the ratio of two intensity maxima; e) Φ is the fluorescence quantum yield; f) Fluorescence amplification at the emission maximum of Cy5 (667nm) between the ODNs and the ODNs bearing Cy5.

Table 5: Spectroscopic properties of TdEAF labeled ODNs and FRET study with Cy5.

Sequence	λ_{abs}^a	$\lambda_{\text{N}^*}^b$	$\lambda_{\text{T}^*}^c$	$I_{\text{N}^*}/I_{\text{T}^*}^d$	Φ (%) ^e	FRET amplification
AMA	447	-	546	-	55.5	-
AMA-TCT	440	-	552	-	56.1	-
AMA-Cy5TCT	-	-	-	-	-	7.2
CMC	451	-	552	-	53.5	-
CMC-GCG	447	-	550	-	60.3	-
CMC-Cy5GCG	-	-	-	-	-	5.6

Footnotes: a) position of the absorption band maximum; b) position of the N* band maximum; c) position of the T* band maximum; d) the ratio of two intensity maxima; e) Φ is the fluorescence quantum yield; f) Fluorescence amplification at 667nm between the ODNs and the ODNs bearing Cy5.

4.1. UV/visible & Fluorescence spectra

Figure 20: UV/visible spectra of TdEAF (AMA) labeled ODN titrate by Cy5.

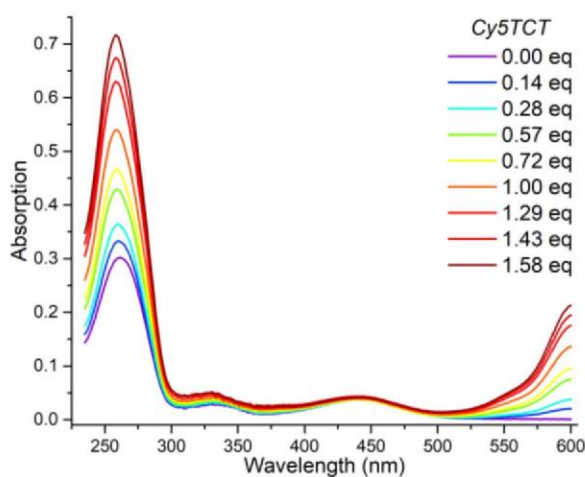


Figure 21: UV/visible spectra of TdEAF (CMC) labeled ODN titrate by Cy5.

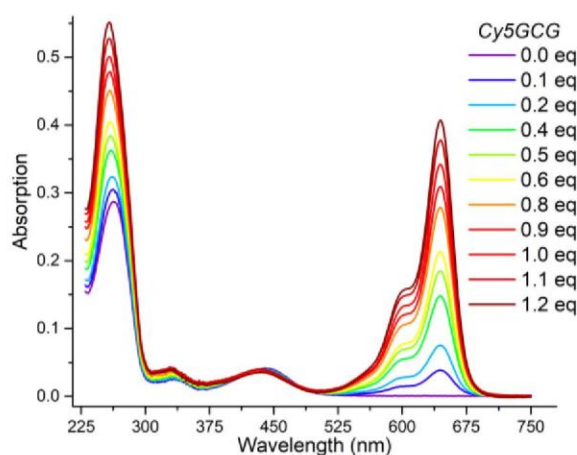


Figure 22: UV/visible and Fluorescence spectra of TM3HF (AMA) labeled ODN.

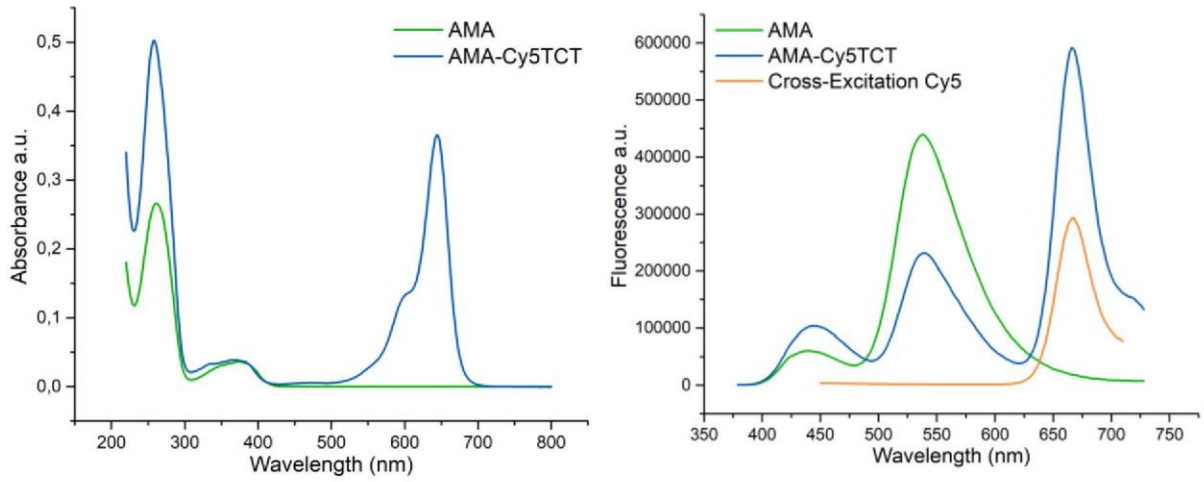
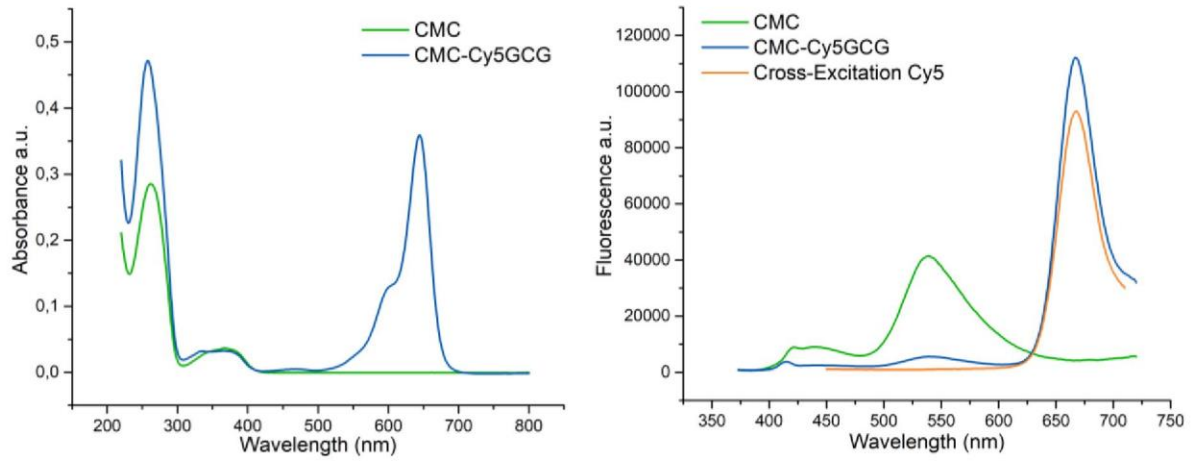


Figure 23: UV/visible and Fluorescence spectra of TM3HF (CMC) labeled ODN.



II. Publication 2

Supporting Information to:

An expeditious approach towards the synthesis and application of water-soluble and photostable fluorogenic chromones for DNA detection

Steve Vincent, Suman Mallick, Guillaume Barnoin, Hoang-Ngoan Le, Benoît Y. Michel* and Alain Burger*

Université Côte d'Azur (UCA), Institut de Chimie de Nice, UMR 7272, CNRS, Parc Valrose, 06108 Nice cedex 2 (France)

*Correspondence:

benoit.michel@univ-cotedazur.fr, alain.burger@univ-cotedazur.fr

Table of contents

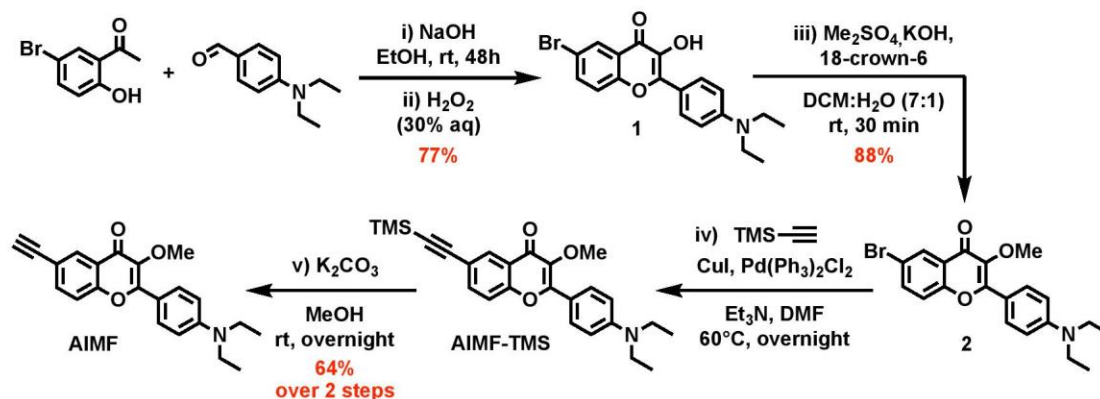
EXPERIMENTAL SECTION	3
1. OVERVIEW OF THE SYNTHESIS SCHEMES.....	3
1.1 Preparation of the 3-OMe chromone labels	3
1.2 Preparation of the <i>AIMF</i> -based model nucleoside	4
2. PHOTOPHYSICAL CHARACTERIZATION.....	4
2.1 Absorptivity determination	4
2.2 Steady-state fluorescence measurements of neutral labels	4
2.3 pK_A study	5
2.4 Photobleaching studies	5
2.5 Hydration study.....	6
2.6 Steady-state fluorescence measurements of charged labels	7
2.7 Absorption & emission spectra of charged labels	8
3. SPECTROSCOPIC STUDIES OF MODEL ODNs	9
3.1 ODN synthesis and purification	9
3.2 HRMS analysis of labeled ODNs	11
3.3 Temperature-induced denaturation studies	11
3.4 Steady-state fluorescence measurements	13
3.5 Absorbance & fluorescence spectra.....	14
NMR SPECTRA	20

Experimental Section

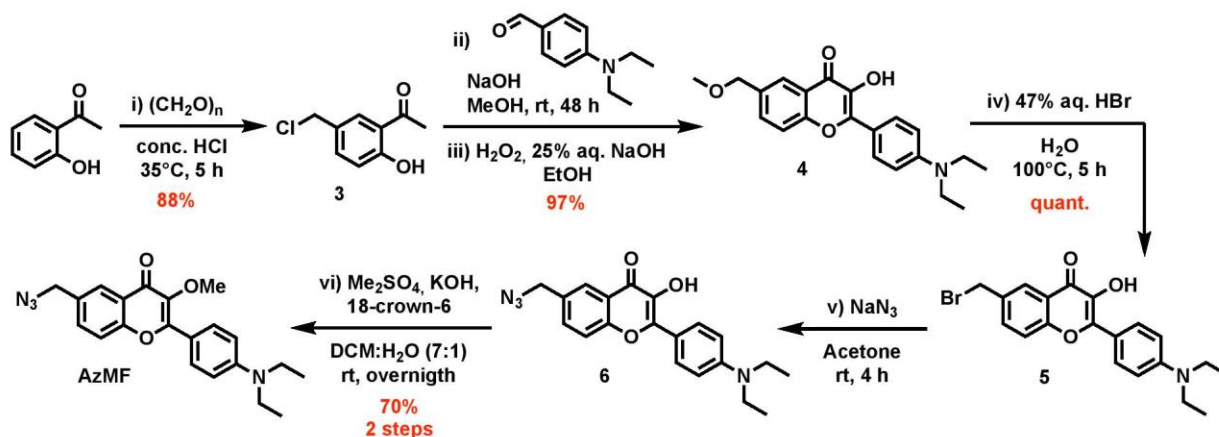
1. OVERVIEW OF THE SYNTHESIS SCHEMES

1.1 Preparation of the 3-OMe chromone labels

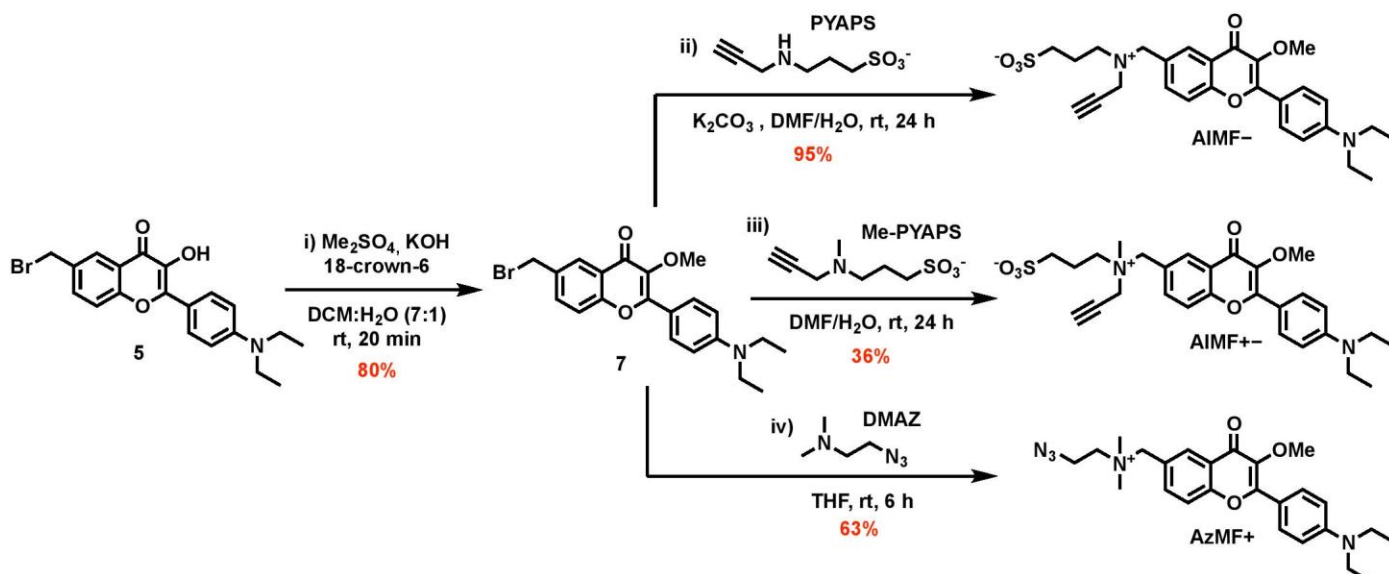
Scheme S1. Synthetic access to the alkyne derivative AIMF.



Scheme S2. Synthetic access to the azide derivative AzMF.

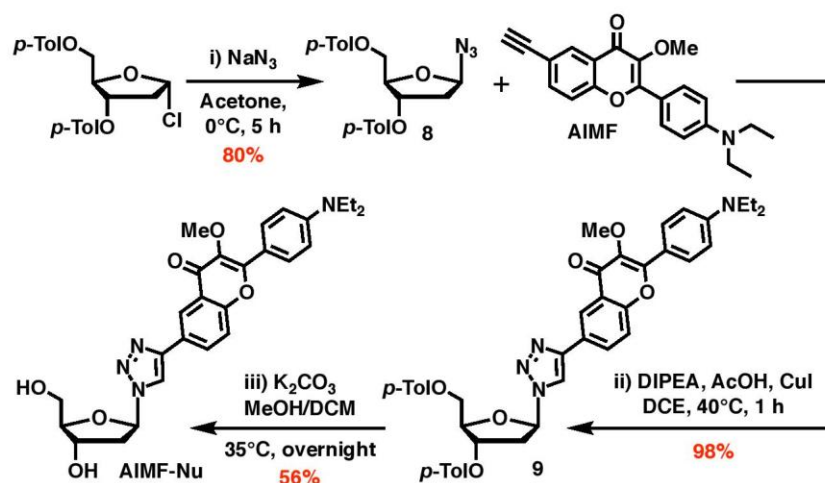


Scheme S3. Synthetic access to the charged dyes AIMF⁻, AIMF^{+,-}, and AzMF⁺.



1.2 Preparation of the AIMF-based model nucleoside

Scheme S4. Synthetic access to AIMF-Nu.



2. PHOTOPHYSICAL CHARACTERIZATION

2.1 Absorptivity determination

Due to a small amount of the reference AIMF-Nu, its molar extinction coefficient was not determined by the conventional weighting method, but by the NMR method, which is known to be more accurate. Thus, using vanillin as a reference, the concentration of the stock solution was accurately defined from the median area of several clearly resolved peaks. A series of dilutions in cascade allowed to calculate the corresponding absorptivity by UV-Vis spectroscopy (for all the considered dyes: $\epsilon_{\max} \approx 41,000 \text{ M}^{-1} \cdot \text{cm}^{-1}$).

2.2 Steady-state fluorescence measurements of neutral labels

Table S1. Spectroscopic properties of AzMF, AIMF and its derived nucleoside analog (AIMF-Nu).

Solvent	$E_T(30)^a$	λ_{abs}^b			λ_{em}^c			$\Phi (\%)^d$		
		AIMF-Nu	AIMF	AzMF	AIMF-Nu	AIMF	AzMF	AIMF-Nu	AIMF	AzMF
H ₂ O ^e	63.1	417	410	413	550	550	550	0.4	0.4	0.3
MeOH	55.4	407	410	405	529	533	530	5	4.1	5
EtOH	51.9	406	408	404	522	524	520	38	30	38
BuOH	49.7	406	408	403	514	517	514	64	64	77
CH ₃ CN	45.6	395	397	394	504	509	509	68	62	64
DMF	43.2	nc.	402	397	nc.	505	501	nc.	73	86
DMSO	45.1	406	408	nc.	516	517	nc.	72	80	nc.
CH ₂ Cl ₂	40.7	nc.	402	398	nc.	485	480	nc.	55	69
EtOAc	38.1	389	392	388	474	474	469	68	60	70
THF	36.2	391	395	390	466	479	471	75	81	86
Toluene	33.9	391	393	390	448	448	447	40	56	61
Cyclohexane	30.9	ns.	386	383	ns.	422	423	ns.	24	32

Footnotes: a) Normalized Reichardt's empirical solvent polarity index;¹ b) position of the absorption band maximum; c) position of the emission band maximum; d) quantum yield determined using *p*-dimethylaminoflavone (dMAF) in EtOH ($\Phi = 0.27$) as a reference²; e) due to the lack of solubility of the considered fluorophores, potential H-aggregates are likely to have formed in water.

¹ C. Reichardt, *Chem. Rev.* **1994**, 94, 2319–2358.

² S. M. Ormson, R. G. Brown, F. Vollmer and W. Rettig, *J. Photochem. Photobiol. A* **1994**, 81, 65–72.

2.3 pK_A study

Figure S1. pK_A study of AIMF.

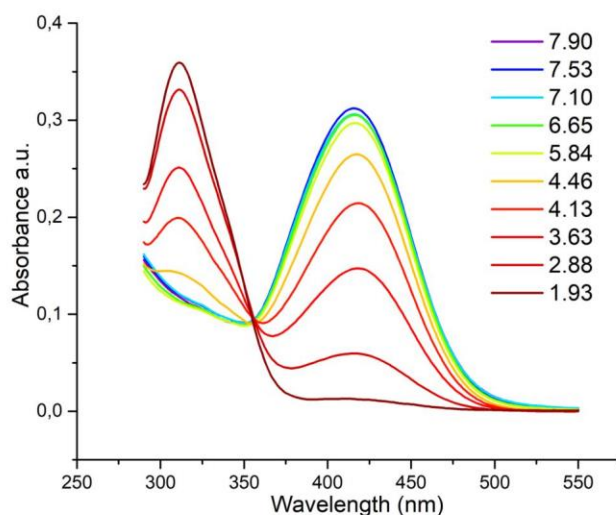
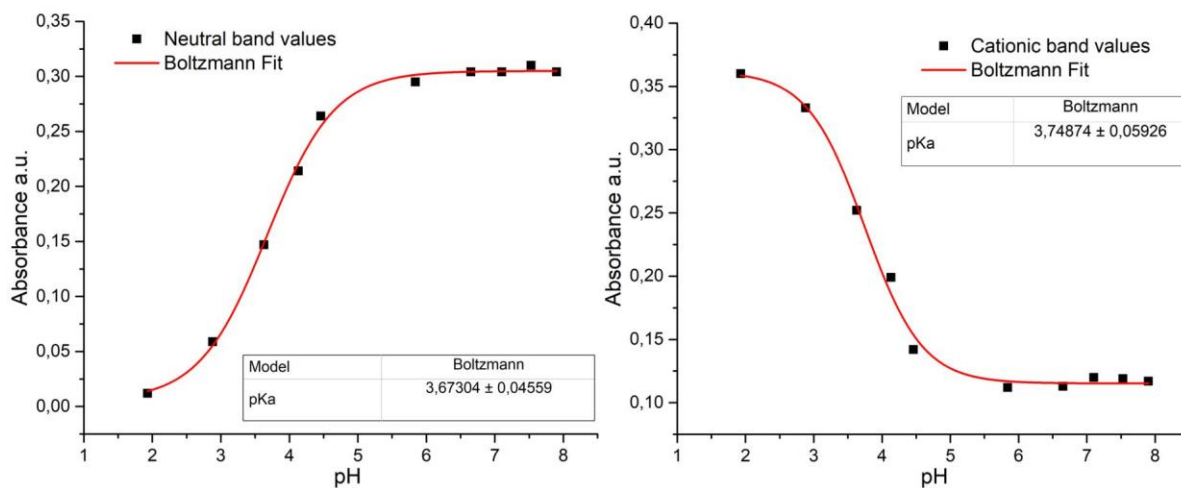
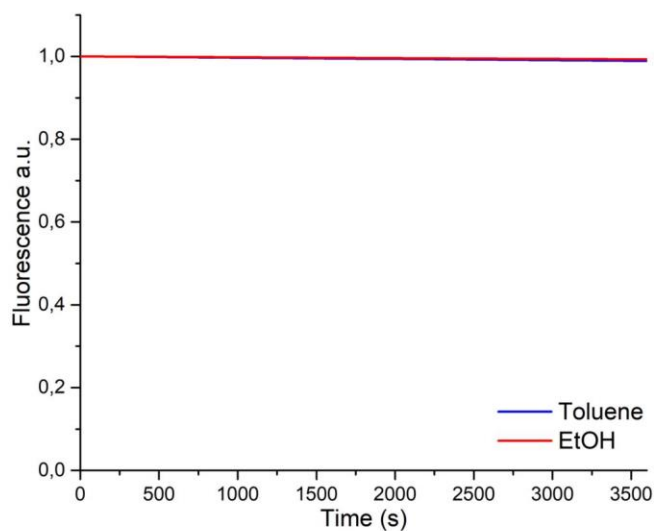


Figure S2. pK_A titration curves of AIMF.



2.4 Photobleaching studies

Figure S3. Photobleaching decays of AIMF.



Footnotes: To a 2 μ M solution of dye in a cuvette, with an 8x8 aperture slit, the evolution of fluorescence intensity was monitored over 1 hour. The fluorescence is recorded at its maximum intensity (448 nm in toluene, 522 nm in EtOH) with an excitation wavelength corresponding to the absorption maximum in the considered solvent (391 nm in toluene, 406 nm in EtOH).

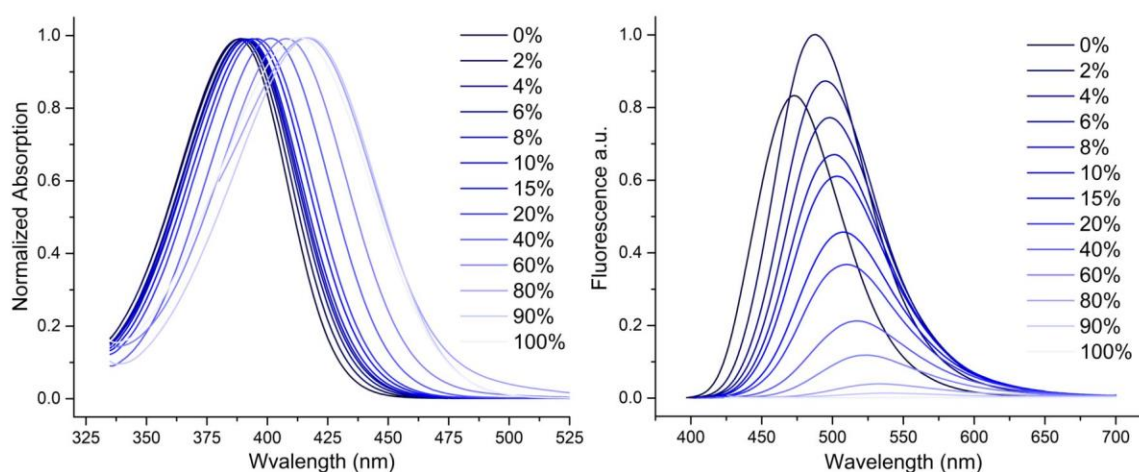
2.5 Hydration study

Table S2. Hydration study of the neutral and charged fluorophores.

H ₂ O (%) in THF	$\lambda_{\text{abs}}^{\text{a}}$				$\lambda_{\text{em}}^{\text{b}}$				Φ (%) ^c			
	AIMF	AIMF –	AzMF +	AIMF +-	AIMF	AIMF –	AzMF +	AIMF +-	AIMF	AIMF –	AzMF +	AIMF +-
0	390	388	396	396	463	473	484	482	78	49	59	41
1	391	/	/	/	479	/	/	/	84	/	/	/
2	392	389	401	399	487	487	507	504	91	59	53	63
4	394	390	405	400	497	495	519	513	85	57	41	69
6	395	/	/	/	503	/	/	/	74	/	/	/
8	397	391	408	403	508	501	525	520	65	46	20	29
10	398	/	/	/	510	/	/	/	55	/	/	/
15	400	394	410	405	514	508	530	526	42	31	11	15
20	401	/	/	/	516	/	/	/	36	/	/	/
30	404	/	/	/	520	/	/	/	23	/	/	/
40	407	401	415	412	524	517	536	531	18	14	5	6
50	410	/	/	/	527	/	/	/	13	/	/	/
60	414	408	420	417	529	524	542	538	9	7	3	4
80	ns	416	428	426	ns	533	552	548	ns	2	2	2
90	ns	417	426	425	ns	538	551	553	ns	1	1	1
100	ns	413 421 ^d	422 428 ^d	421 432 ^d	ns	556	564	563	ns	>1	>1	>1

Footnotes: a) Position of the absorption band maximum; b) position of the emission band maximum; c) quantum yield determined using *p*-dimethylaminoflavone (dMAF) in EtOH ($\Phi = 0.27$) as a reference;² d) value extracted from the excitation spectrum at the maximum absorption wavelength. *ns* stands for not soluble.

Figure S4. Hydration study of AIMF⁻: normalized absorption (left) and fluorescence (right) spectra.



Footnotes: Titration performed by adding water to a THF solution containing the dye. A different solution was done for each percentage of water to keep the same concentration for each experiment (2 μM).

Figure S5. Hydration study of AzMF⁺: normalized absorption (left) and fluorescence (right) spectra.

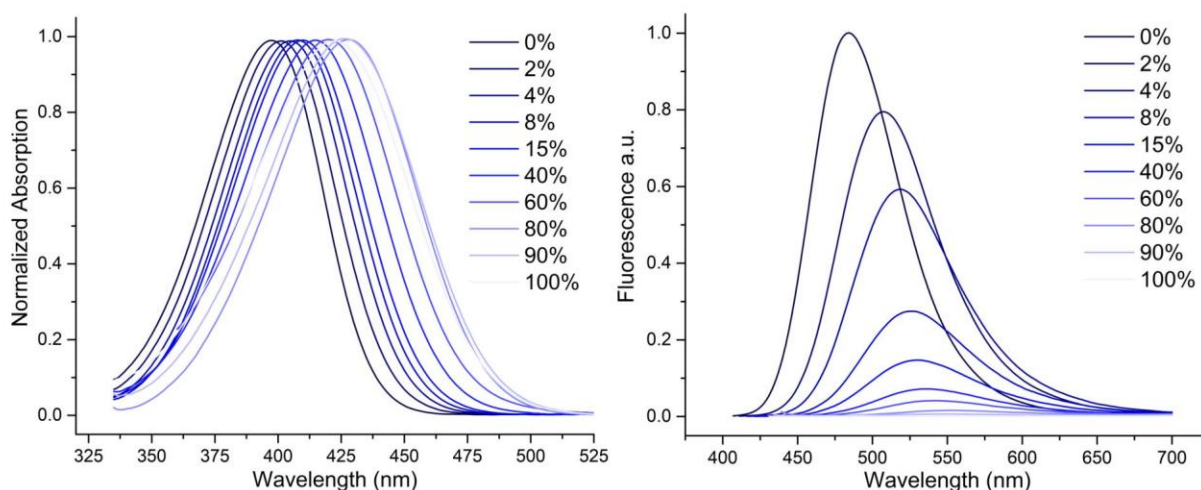
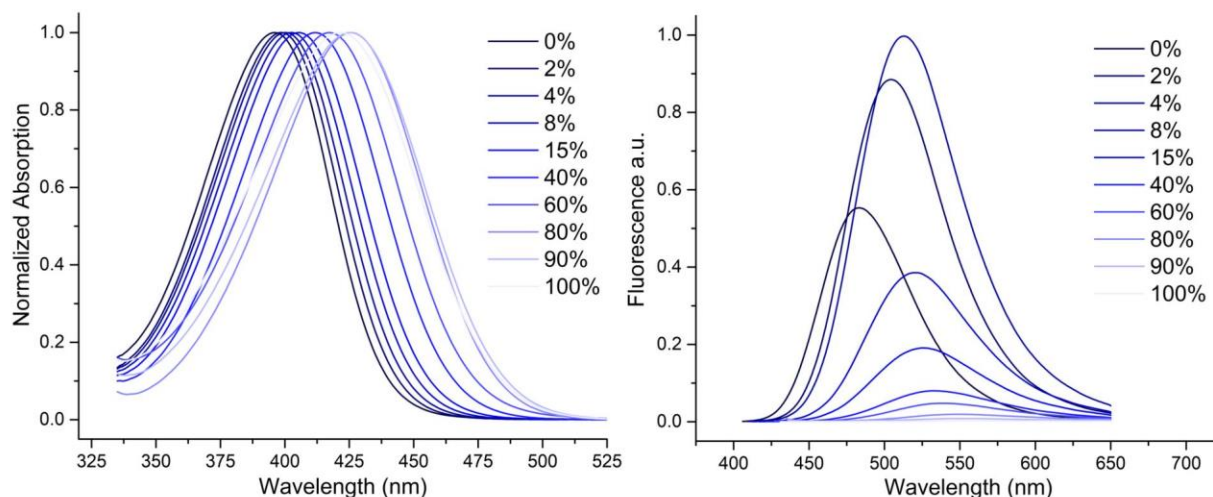


Figure S6. Hydration study of AIMF⁺⁻: normalized absorption (left) and fluorescence (right) spectra.



2.6 Steady-state fluorescence measurements of charged labels

Table S3. Spectroscopic properties of the charged analogs AIMF⁻, AzMF⁺ and AIMF⁺⁻.

Solvent	$E_T(30)^a$	λ_{abs}^b			λ_{em}^c			Φ (%) ^d		
		AIMF ⁻	AzMF ⁺	AIMF ⁺⁻	AIMF ⁻	AzMF ⁺	AIMF ⁺⁻	AIMF ⁻	AzMF ⁺	AIMF ⁺⁻
H ₂ O	63.1	421 ↑ ^e	428 ↑	432 ↑	556 =	564 ↑	563 ↑	>1 =	>1 =	>1 =
MeOH	55.4	402 =	414 ↑	412 ↑	524 =	543 ↑	539 ↑	10 ↑	2 ↓	3 ↓
BuOH	49.7	400 =	417 ↑	412 ↑	505 ↓	533 ↑	529 ↑	72 =	30 ↓↓	43 ↓↓
CH ₃ CN	45.6	392 =	401 ↑	400 ↑	494 ↓	516 ↑	515 ↑	63 =	58 ↓	59 ↓
DMSO	45.1	400 ↓	409 =	407 =	510 ↓	527 ↑	525 ↑	91 ↑↑	61 ↓	59 ↓
THF	36.2	389 =	397 ↑	397 ↑	475 ↑	487 ↑	487 ↑	55 ↓↓	54 ↓	45 ↓↓
Toluene	33.9	396 =	402 ↑	404 ↑	459 ↑	464 ↑	462 ↑	41 =	40 =	7 ↓↓

Footnotes: a) Reichardt's empirical solvent polarity index;¹ b) position of the absorption band maximum; c) position of the emission band maximum; d) quantum yield determined using *p*-dimethylaminoflavone (dMAF) in EtOH ($\Phi = 0.27$) as a reference;² e) arrows and equals refer to an increase, decrease or similarity in the value of the neutral dyes AIMF or AzMF.

2.7 Absorption & emission spectra of charged labels

Figure S7. Absorbance (left) & fluorescence (right) spectra of AIMF⁻.

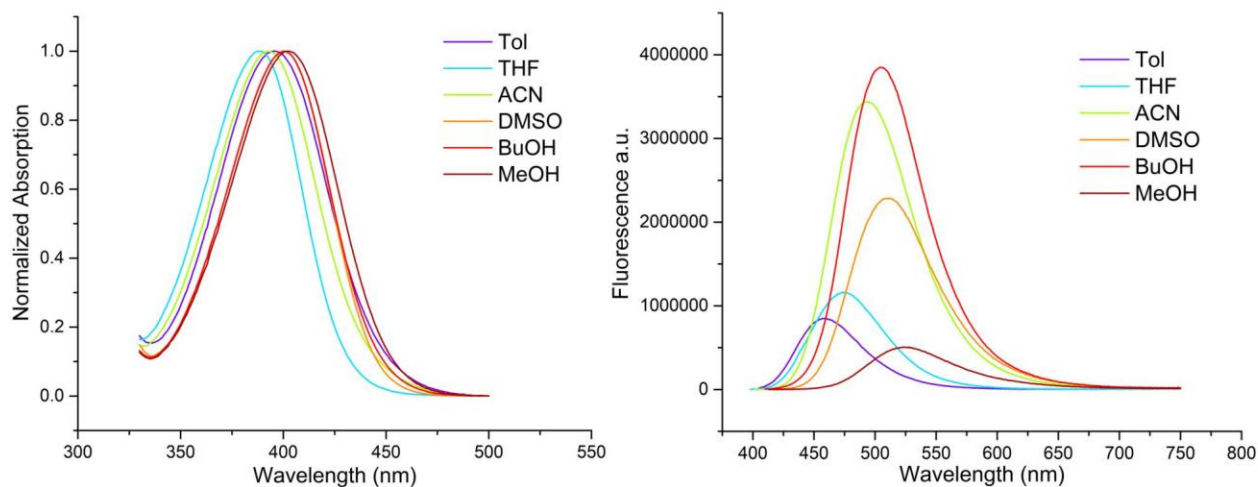


Figure S8. Absorbance (left) & fluorescence (right) spectra of AzMF⁺.

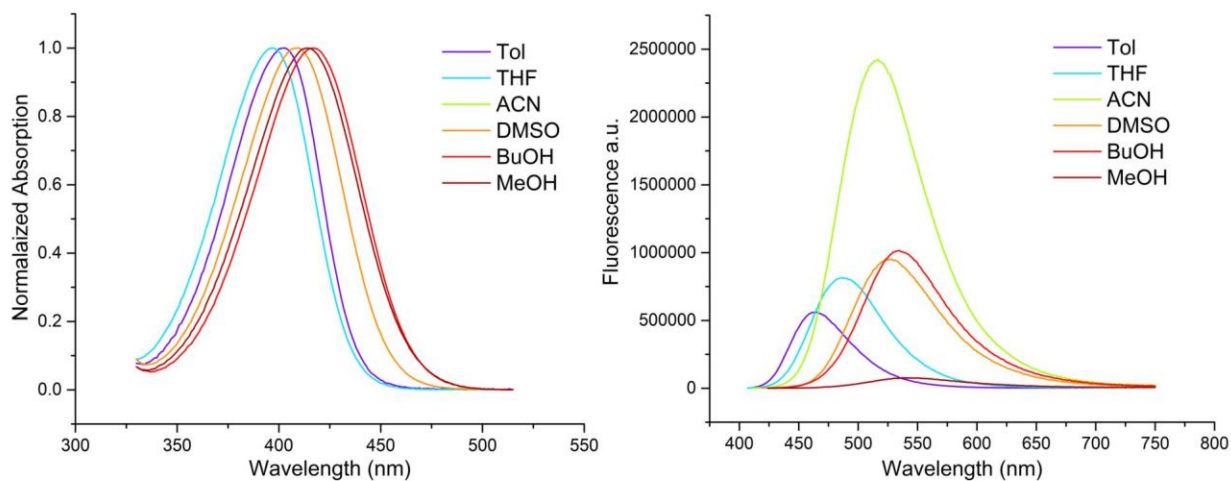
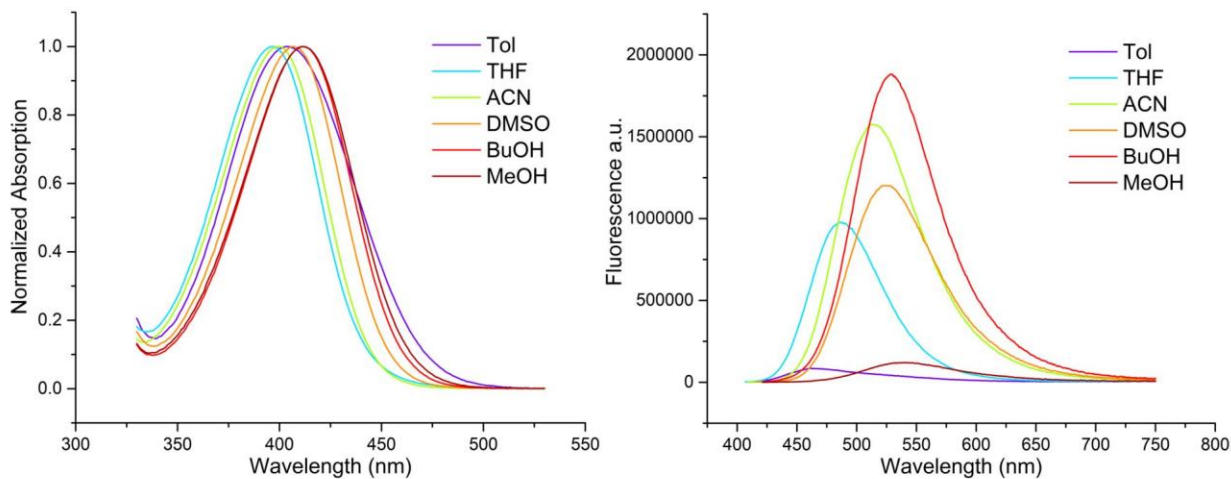


Figure S9. Absorbance (left) & fluorescence (right) spectra of AIMF^{+·}.



3. SPECTROSCOPIC STUDIES OF MODEL ODNs

3.1 ODN synthesis and purification

General method:

Wild-type and clickable ODNs were purchased from Microsynth AG. ODNs were ordered purified and ready to use.

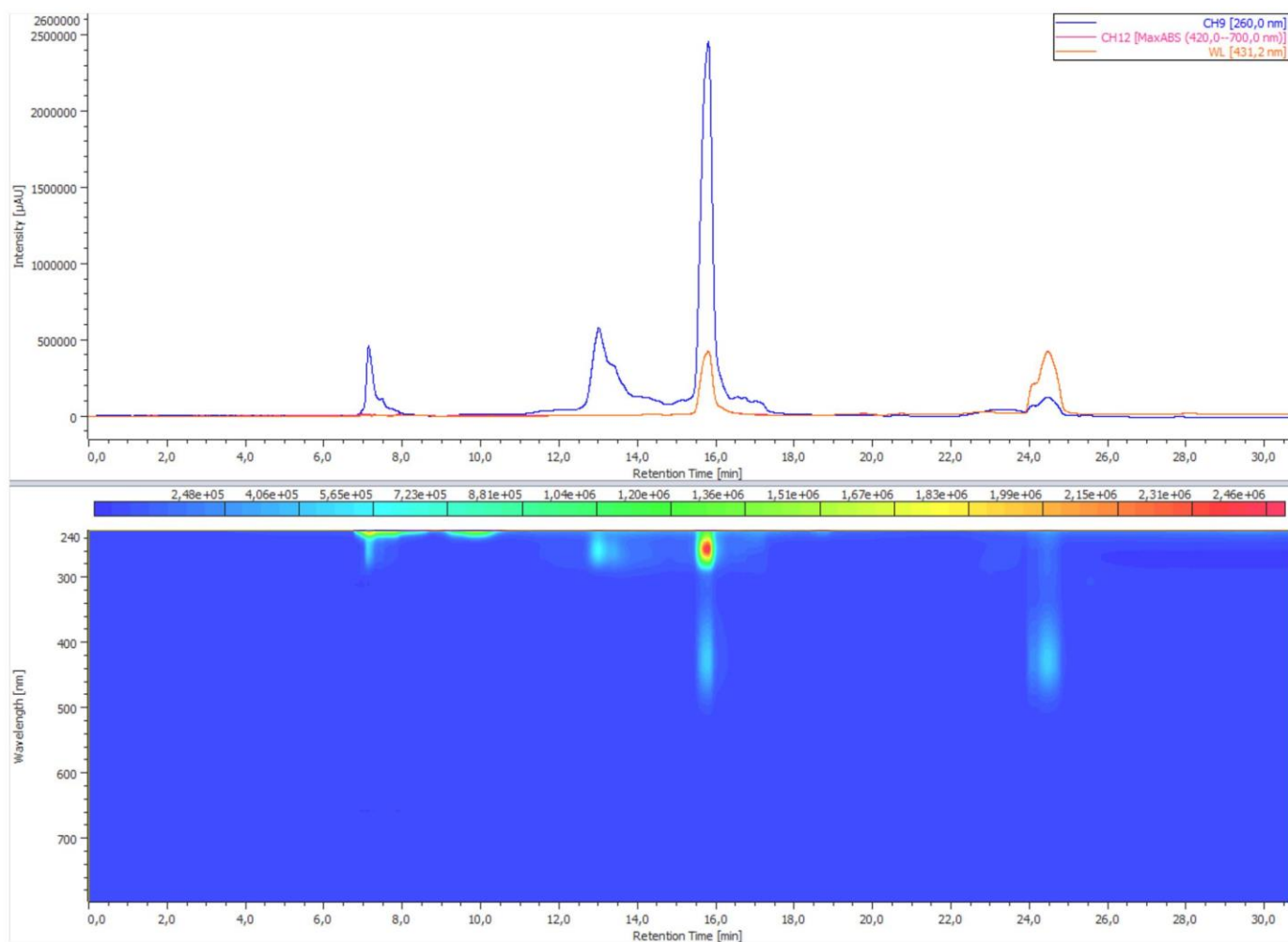
Typical labeling procedure:

First, a 5mM aq. solution of $\text{CuSO}_4 \cdot 5\text{H}_2\text{O}$ and the BTES ligand is prepared.

In a 200- μL vial, were sequentially added the ODN sequence (0.2mM aq. solution, 50 μL , 10 nmol, 1 eq.), DMSO (20 μL), dye (5 mM in DMSO, 10 μL , 50 nmol, 5 eq.), sodium ascorbate (5mM aq. solution, 10 μL , 50 nmol, 5 eq.), and finally the $\text{CuSO}_4/\text{BTES}$ mixture (5mM aq. solution, 10 μL , 50 nmol, 5 eq.). The mixture was vortexed overnight at rt. The solution was then recovered, and the vial was washed with minimal of H_2O and DMSO. Thus, the whole mixture was then purified by RP-HPLC.

ODNs were analyzed (0.5 mL/min) and purified (2.0 mL/min) by RP-HPLC (HPLC apparatus: WatersTM 600 Controller with WatersTM 996 Photodiode Array Detector. Columns: analytical, 300 \times 4.60 mm, 5 μm particle size, Clarity[®] 100 \AA , Phenomenex[®]; semi-preparative, Clarity[®] 5u Oligo-RP column 250 \times 10 mm Phenomenex[®]).

Figure S10. Representative 2D (top) and 3D (bottom) HPLC profiles of a crude mixture after post-synthetic click labeling reaction at two different wavelengths (260 & 430 nm).



Gradient: 100% A for 2 min \rightarrow 40% A: 60% B during 10 min then keep it for 2 min, \rightarrow 10% A: 90% B during 2 min then keep it for 14 min. A = Buffer pH 7.0 (90% TEAB buffer 100 mM:10% CH_3CN) and B = 90% CH_3CN :10% Buffer A. Peak at 8 min: starting clickable ODN; peak at 15 min: clicked ODN; peak at 24 min: starting clickable label.

Figure S11. Representative 2D HPLC profiles of purified ODN sequences: *TXT* labeled with *AIMF* (left) and *AWA* labeled with *AzMF* (right)

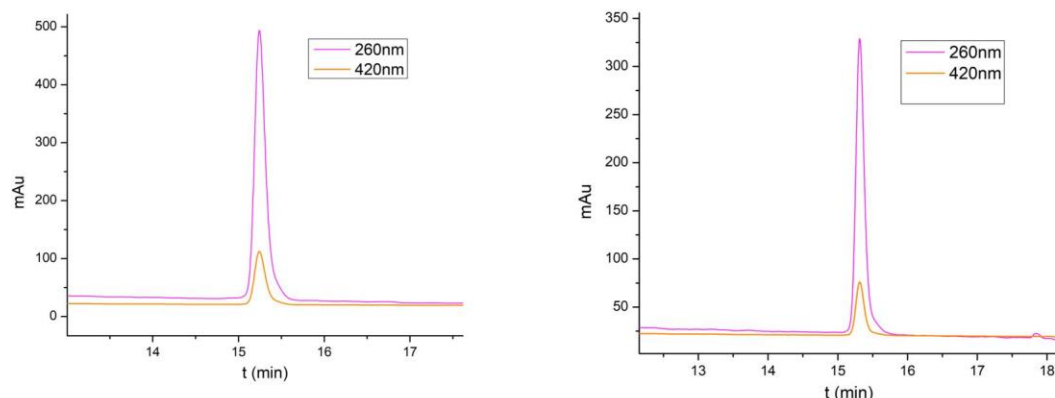


Table S4. Nature, absorptivity, and linker chemical structure of the ODNs to be labeled.

Sequence	Extinction coefficient ($L \cdot mol^{-1} \cdot cm^{-1}$)	Linker
5'- YCAG TCG CTC GCT GAC-3'	133,100	
5'- YGCA AAA TTT AAA ACG-3'	158,100	
5'-CAG TCG CXC GCT GAC-3'	133,100	
5'-GCA AAA TXT AAA ACG-3'	157,400	
5'-GCA AAA AAA AXA AAA AAA ACG-3'	238,600	
5'-GCA AAA TXsT AAA ACG-3'	157,400	
5'- VGCA AAA TTT AAA ACG-3'	158,100	
5'-GCA AAA TZT AAA ACG-3'	157,400	
5'-GCA AAA TWT AAA ACG-3'	149,600	
5'-GCA AAA AAA AWA AAA AAA ACG-3'	255,800	

3.2 HRMS analysis of labeled ODNs

Table S5. Mass of the single-stranded DNA tagged with AIMF.

ODN	Sequence	HRMS found (calc.) [M+H] ⁺
		Labeled with AIMF
YCAG	5'- YCAG TCG CTC GCT GAC-3'	5165.0580 (5165.0597)
YGCA	5'- YGCA AAA TTT AAA ACG-3'	5229.1165 (5229.1148)
CXC	5'-CAG TCG CXC GCT GAC-3'	5140.1009 (5140.0992)
TXT	5'-GCA AAA TXT AAA ACG-3'	5204.1559 (5204.1543)
AXA	5'-GCA AAA AAA AXA AAA AAA ACG-3'	6753.3779 (6753.3751)
TXsT	5'-GCA AAA TXsT AAA ACG-3'	5148.0899 (5148.0917)

Table S6. Mass of the single-stranded DNA tagged with AzMF.

ODN	Sequence	HRMS found (calc.) [M+H] ⁺
		Labeled with AzMF
VGCA	5'- VGCA AAA TTT AAA ACG-3'	5131.1129 (5131.1152)
TZT	5'-GCA AAA TZT AAA ACG-3'	5061.1361 (5061.1333)
TWT	5'-GCA AAA TWT AAA ACG-3'	4871.0616 (4871.0590)
AWA	5'-GCA AAA AAA AWA AAA AAA ACG-3'	6767.4341 (6767.4359)

3.3 Temperature-induced denaturation studies

Preparation of the ODN duplex solution: In a 500- μ L cuvette, were sequentially added the clicked ss-ODN probe solution (4 μ M aq. solution, 250 μ L) and its complementary wild-type ss-ODN solution (200 μ M aq. solution, 5 μ L), and PBS solution (250 μ L, [Na] = 300 mM, [P] = 25 mM). Melting curves were monitored by following the temperature-dependence of the absorbance changes at 260 nm of the sample (2 μ M concentration of each strand). Absorption spectra were recorded in a Peltier-thermostatted cell holder on a Cary 100 Bio UV-Vis spectrophotometer (Varian/Agilent) using Suprasil[®] quartz cuvettes with 1-cm path length. The temperature range for denaturation measurement was 20–75 °C. Speed of heating was 0.3 °C/min.

Table S7. Melting temperatures of duplexes labeled with AIMF.

Duplex	T_m (°C)		
	AIMF	Wild Type ^a	ΔT_m AIMF (°C) ^b
YCAG ·GTC	69.9	65.8 [61.6]	+ 4.1
YGCA ·CGT	47.8	48.1 [45.9]	- 0.3
CXC ·GAG	58.8	65.8 [61.6]	- 7.0
TXT ·AAA	44.6	48.1 [45.9]	- 3.5
TXsT ·AAA	43.2	48.1 [45.9]	- 4.9

^a T_m of the corresponding duplex formed from unmodified ODNs and its theoretical values given in square brackets. ^b ΔT_m refers to the difference of T_m between the labeled and wild type ODNs.

Table S8. Melting temperatures of duplexes labeled with AzMF+, AIMF+-, & AIMF-.

Duplex	T_m (°C)							
	AzMF+	AIMF+-	AIMF-	Wild Type ^a	ΔT_m AzMF+ (°C) ^b	ΔT_m AIMF+- (°C) ^b	ΔT_m AIMF- (°C) ^b	
TXT ·AAA	/	40.3	38.9	48.1	/	- 7.8	- 9.2	
VGCA ·CGT	47.0	/	/	48.1	- 1.1	/	/	
TWT ·AAA	34.3	/	/	48.1	- 13.8	/	/	
TZT ·AAA	41.7	/	/	48.1	- 6.4	/	/	

^a T_m of the corresponding duplex formed from unmodified ODNs and its theoretical values given in square brackets. ^b ΔT_m refers to the difference of T_m between the labeled and wild type ODNs.

Figure S12. Melting temperature curves of duplexes tagged with AIMF.

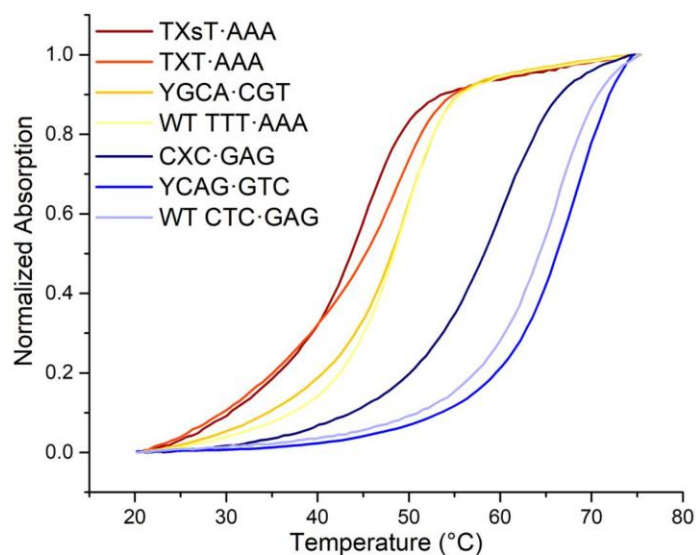


Figure S13. Melting temperature curves of duplexes tagged with AzMF+.

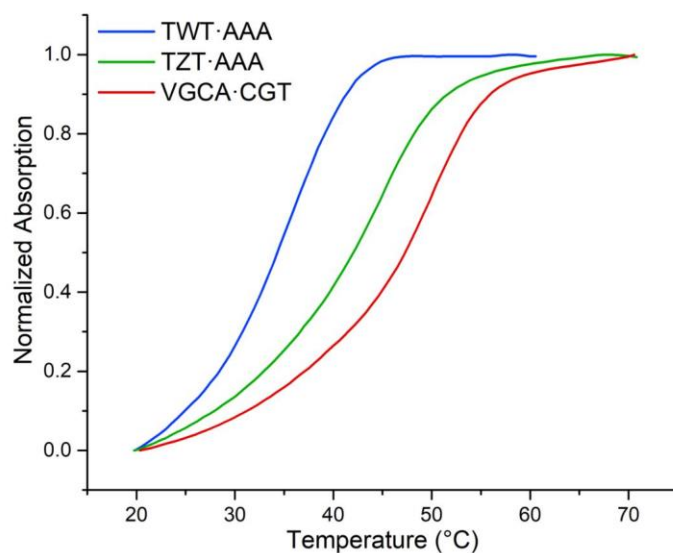
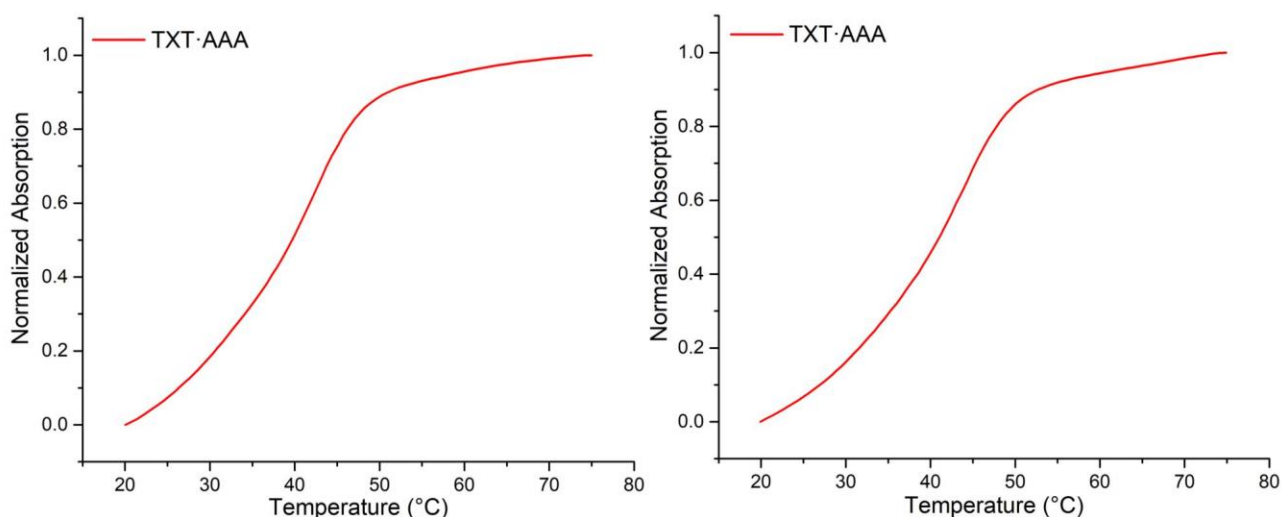


Figure S14. Melting temperature curves of duplexes tagged with AIMF⁻ (left) & AIMF⁺⁻ (right).



3.4 Steady-state fluorescence measurements

Absorption and fluorescence experiments were performed in duplicate in pH 7.0 phosphate-buffered saline (12 mM PBS, 120 mM NaCl). Absorption spectra were recorded at 25°C on a Cary 100 Bio UV-Vis spectrophotometer (Varian/Agilent) using Suprasil[®] quartz cuvettes with 1-cm path length. Fluorescence spectra were recorded on a FluoroMax 4.0 spectrofluorometer (Jobin Yvon, Horiba) with a 2x2 aperture slit and were corrected at excitation and emission. Measured solutions were prepared with absorbance of about 0.05 at 25 °C at the excitation wavelength mentioned in the corresponding experiments. Quantum yields were corrected according to the variation of the refractive index of the different solvents and were determined using *p*-dimethylaminoflavone (dMAF) in EtOH ($\lambda_{\text{ex}} = 404 \text{ nm}$, $\Phi = 0.27$) as a standard reference.²

Table S9. Spectroscopic properties of ODNs labeled with AzMF⁺, AIMF⁺⁻, & AIMF⁻.

Sequence	$\lambda_{\text{abs}} \text{ (nm)}^a$			$\lambda_{\text{em}} \text{ (nm)}^b$			$\Phi \text{ (%) }^c$		
	AzMF ⁺	AIMF ⁺⁻	AIMF ⁻	AzMF ⁺	AIMF ⁺⁻	AIMF ⁻	AzMF ⁺	AIMF ⁺⁻	AIMF ⁻
TXT	/	436	430	/	550	539	/	11	11
TXT·AAA	/	439	438	/	551	540	/	19	18
YGCA	/	442	431	/	551	541	/	9	10
YGCA·CGT	/	437	428	/	549	543	/	5	7
TWT	441	/	/	555	/	/	7	/	/
TWT·AAA	442	/	/	543	/	/	16	/	/
VGCA	436	/	/	550	/	/	9	/	/
VGCA·CGT	431	/	/	550	/	/	5	/	/

^a Position of the absorption band maximum. ^b Position of the emission band maximum. ^c Quantum yield determined using *p*-dimethylaminoflavone (dMAF) in EtOH ($\Phi = 0.27$).²

Table S10. Spectroscopic properties of AXA and AXA·TAT labeled with AIMF.

$\lambda_{\text{ex}} \text{ (nm)}^a$	AXA	AXA · TAT	Absorptivity ratio ^c	Fluorescence intensity ratio ^d
	Brightness (L.mol ⁻¹ .cm ⁻¹) ^b			
440	4510	13940	1.08	3.4
450	3583	13263	1.20	3.8
460	2730	11430	1.35	4.3
470	1814	8777	1.57	5.0
488	651	4237	2.1	6.3

^a Screening of the excitation wavelength. ^b Brightness calculation: absorptivity at the excitation wavelength*Quantum Yield; ^c Absorbance of ds/Absorbance of ss; ^d Fluorescence intensity of ds/Fluorescence intensity of ss.

3.5 Absorbance & fluorescence spectra

Figure S15. Absorption (left) and emission (right) spectra of ss- and ds-ODNs labeled with AzMF⁺.

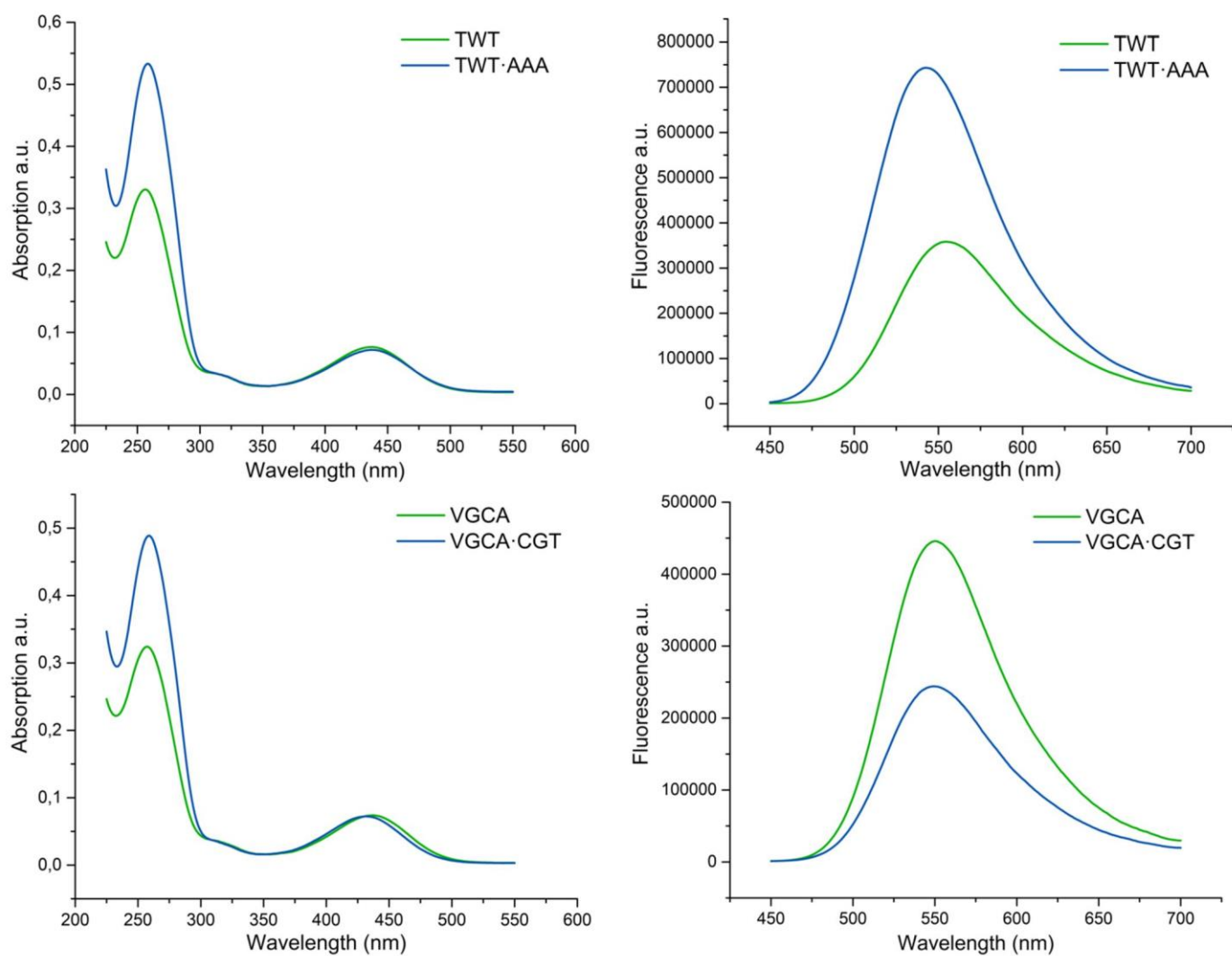
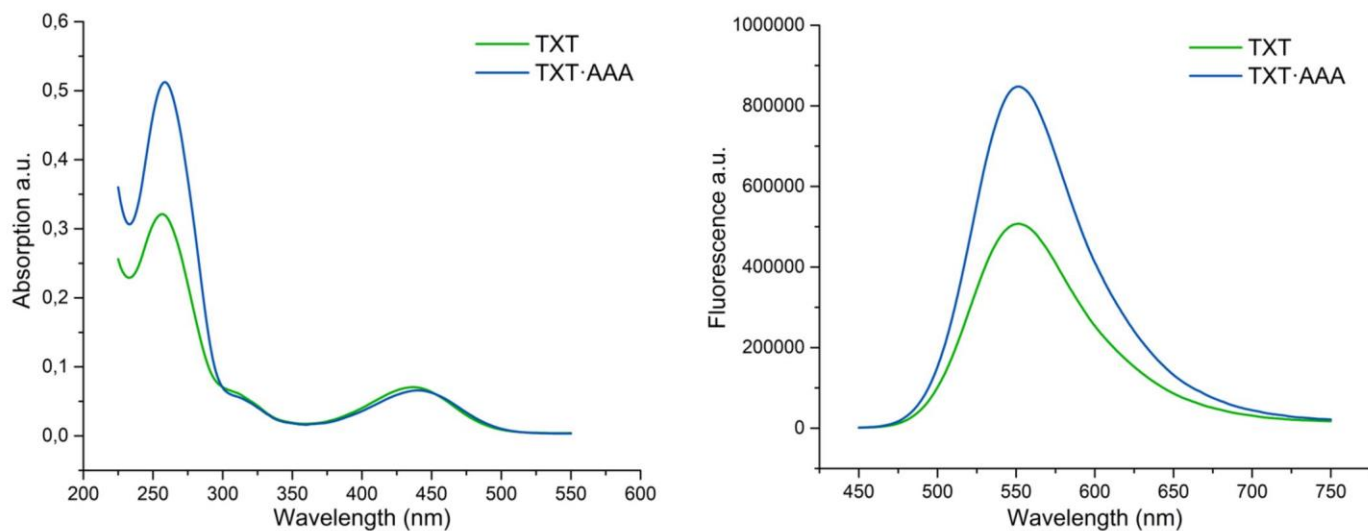


Figure S16. Absorption (left) and emission (right) spectra of ss- and ds-ODNs labeled with AIMF⁺.



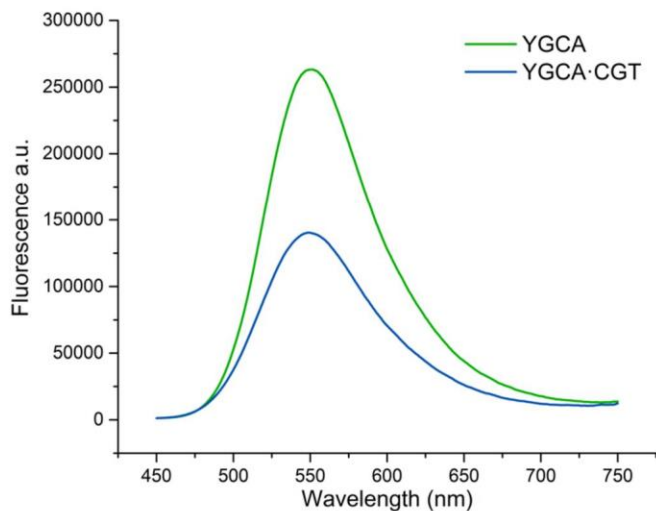
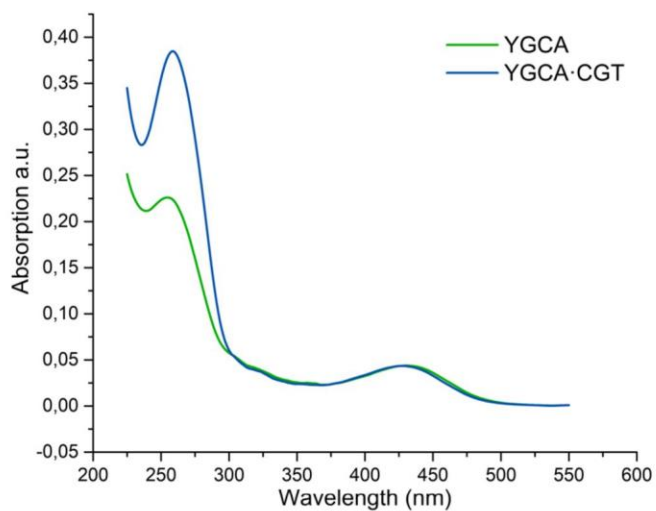


Figure S17. Absorption (left) and emission (right) spectra of ss- and ds-ODNs labeled with AIMF⁻.

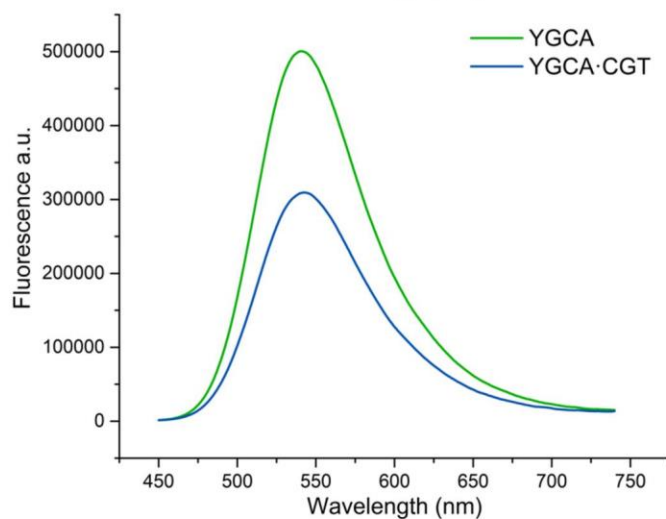
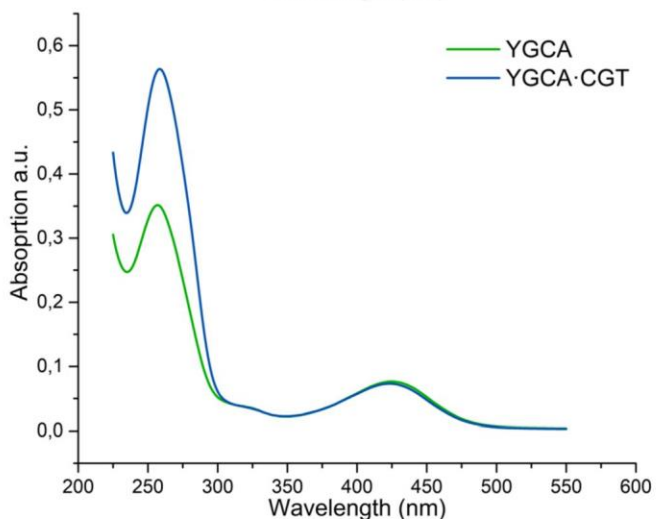
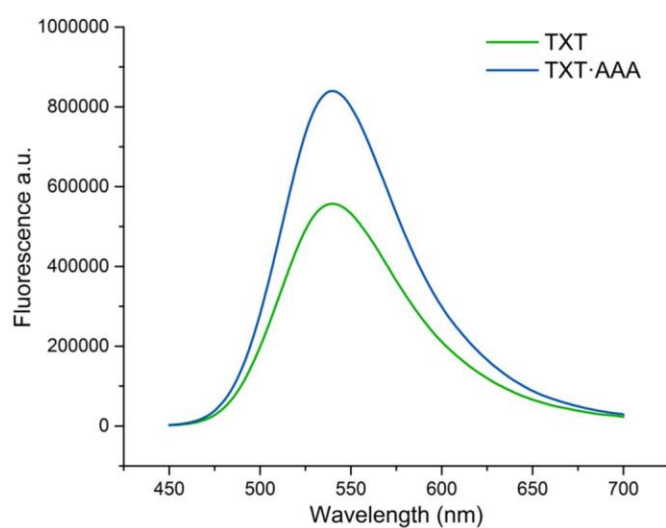
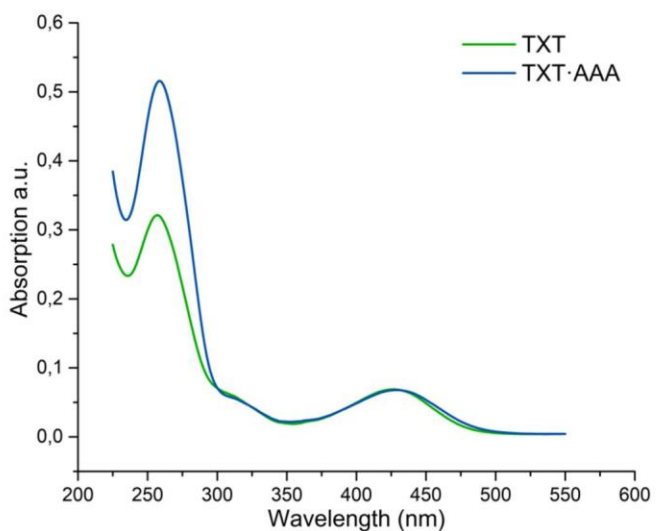
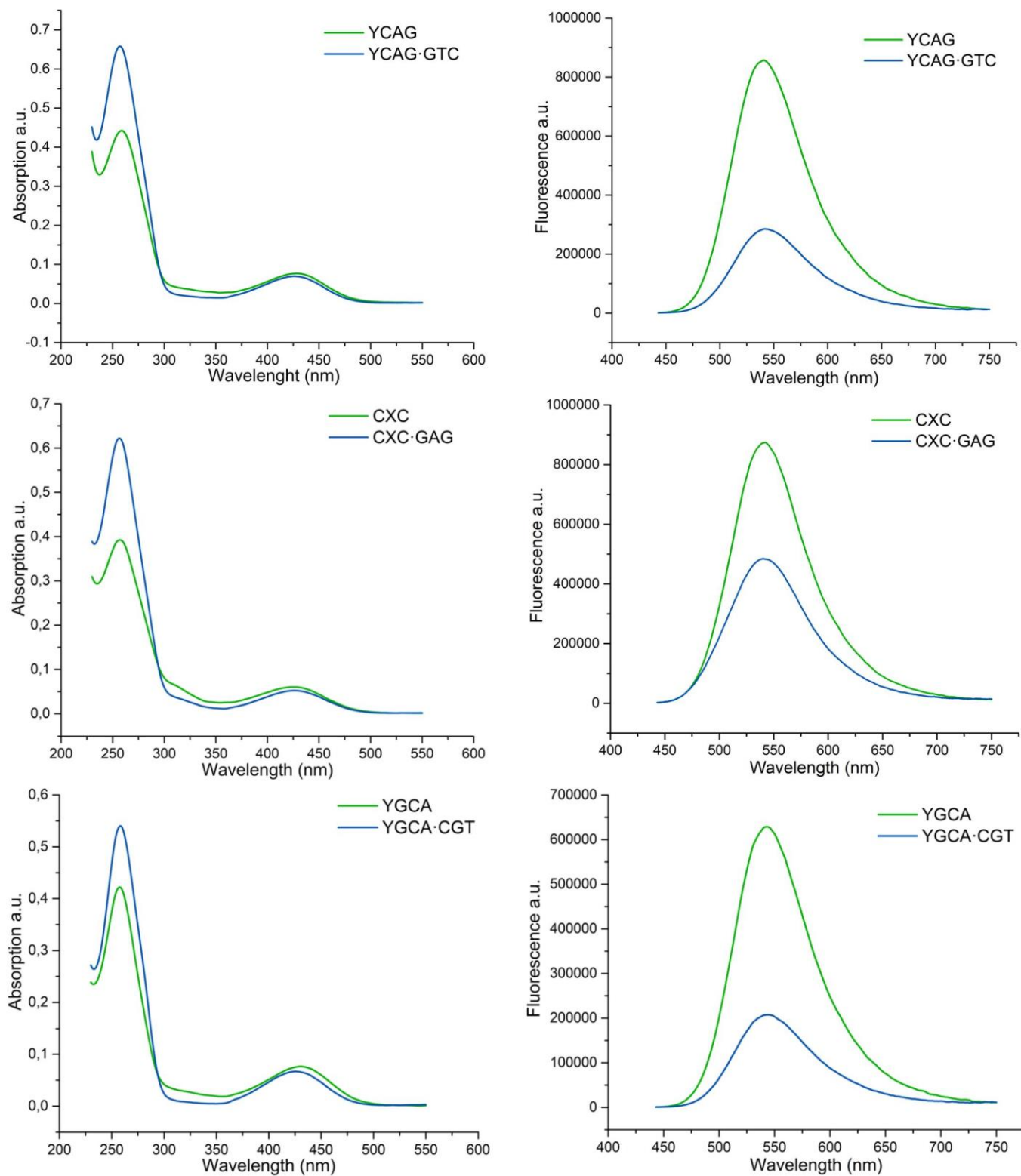


Figure S18. Absorption (left) and emission (right) spectra of ss- and ds-ODNs labeled with AIMF.



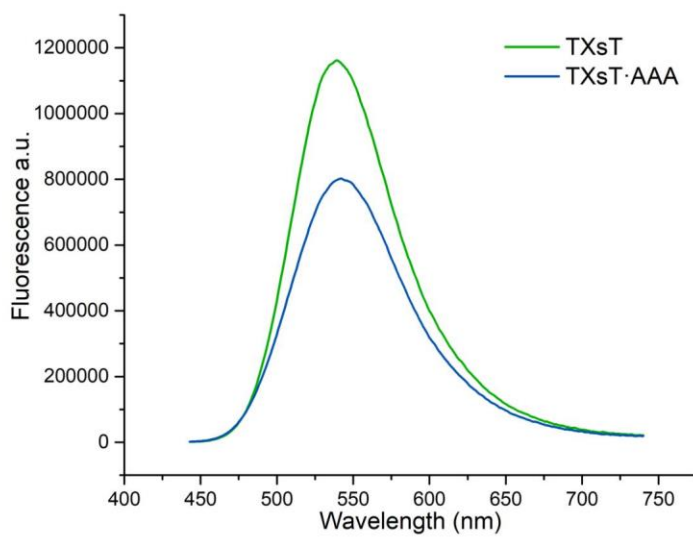
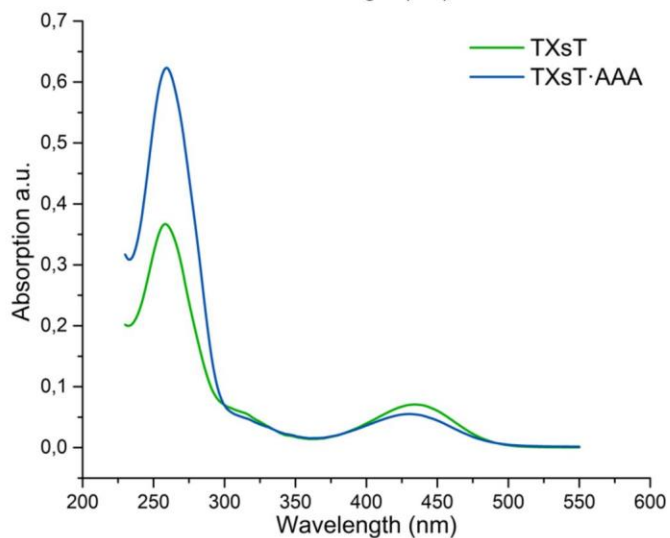
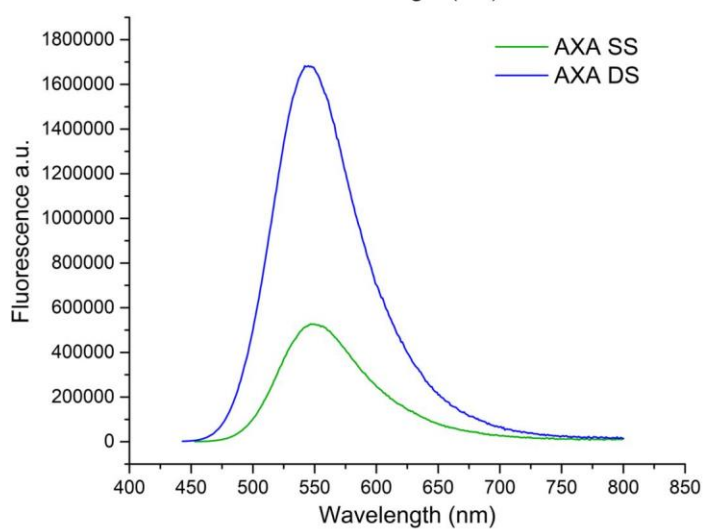
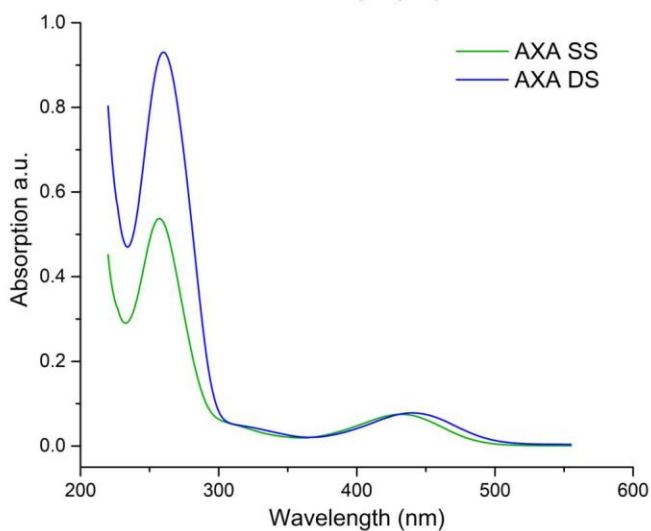
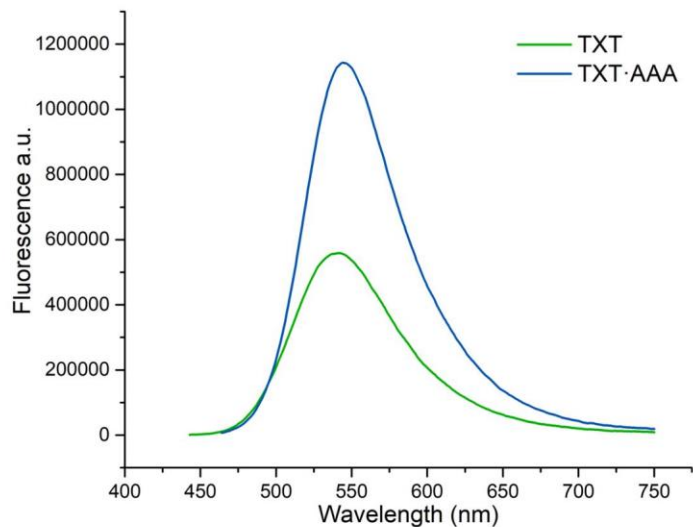
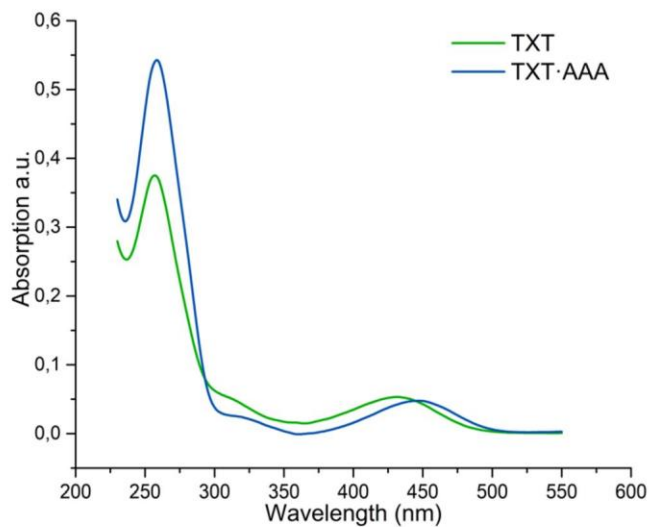
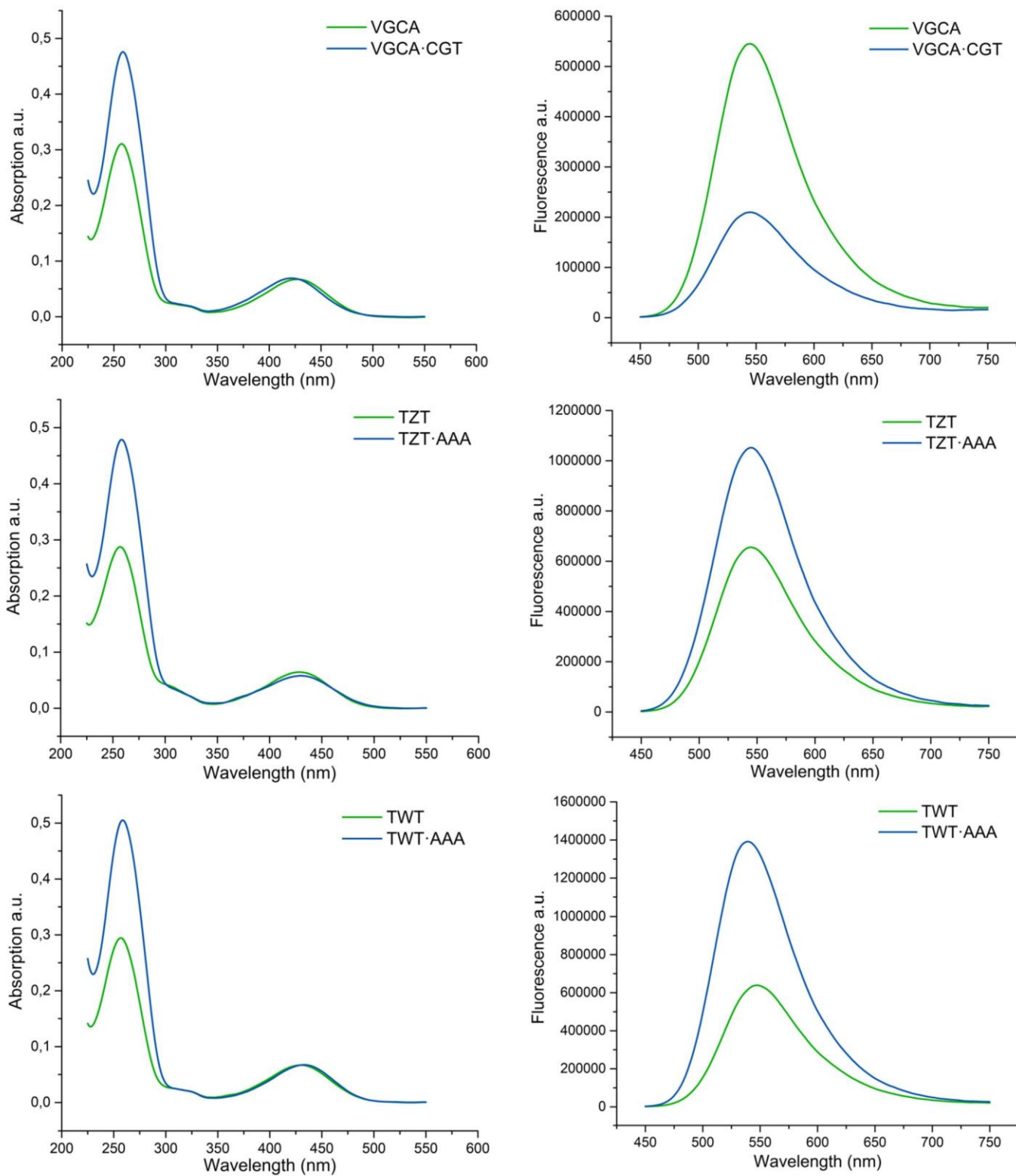


Figure S19. Absorption (left) and emission (right) spectra of ss- and ds-ODNs labeled with AzMF.



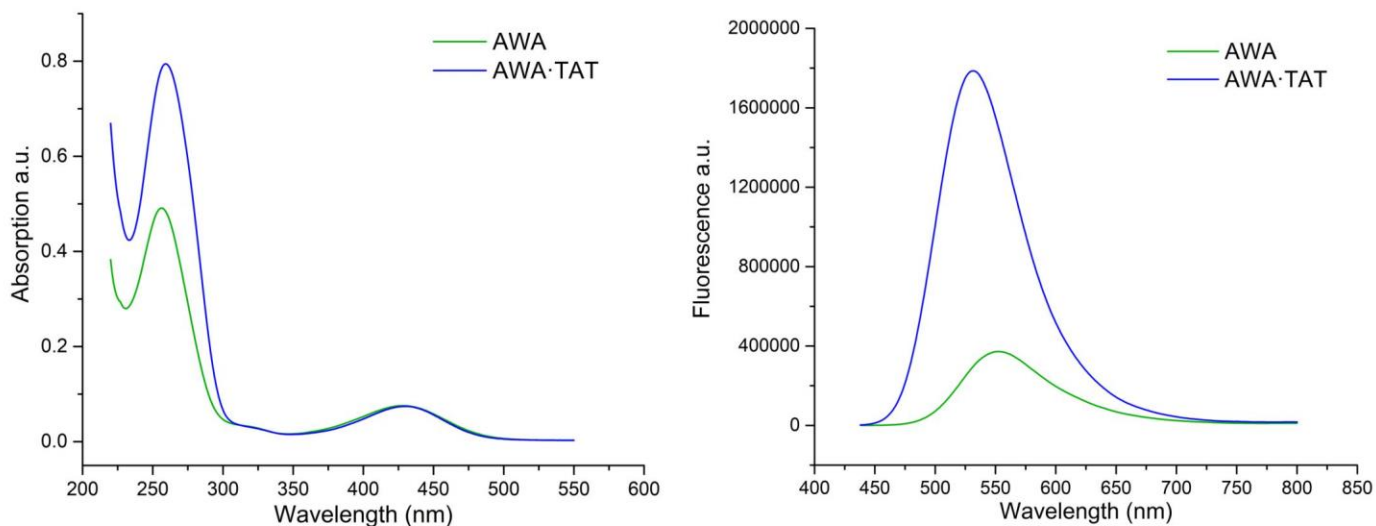
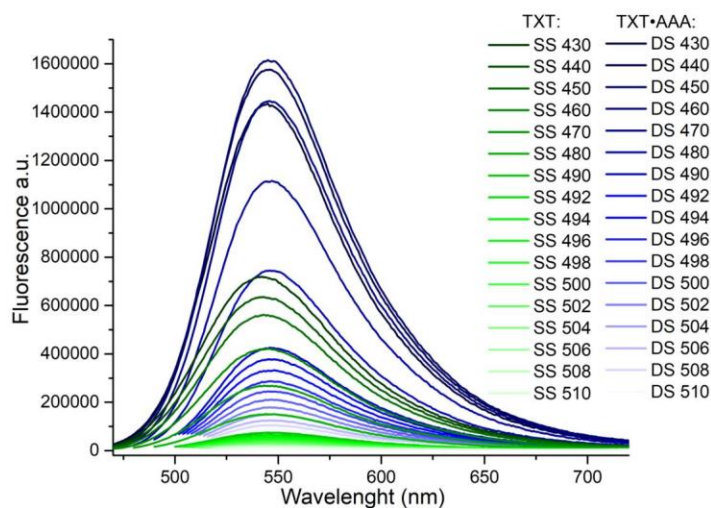
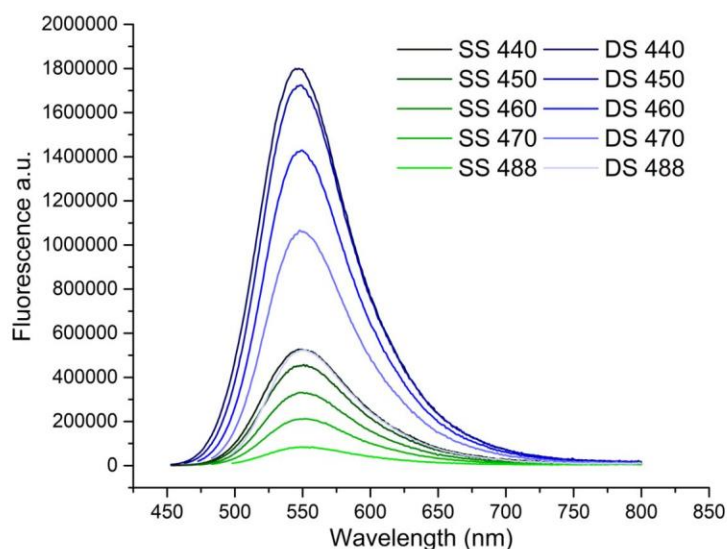


Figure S20. Fluorescence spectra of TXT and TXT·AAA labeled with AIMF at different excitation wavelengths.



Footnotes: Fluorescence spectra obtained by screening the excitation wavelength (values reported in Table 3).

Figure S21. Fluorescence spectra of AXA and AXA·TAT labeled with AIMF at different excitation wavelengths.



Footnotes: Fluorescence spectra obtained by screening the excitation wavelength (values reported in Table S10).

III. Publication 3

Supporting Information to:

A Fluorogenic Covalent Chromone-Based Intercalator with mega-Stokes Shift for Sensing DNA Hybridization

Steve Vincent, Suman Mallick, Guillaume Barnoin, Hoang-Ngoan Le, Alain Burger,* and Benoît Y. Michel*[^a]

[^a] Institut de Chimie de Nice, CNRS UMR 7272, Université Côte d'Azur, Parc Valrose, 06108 Nice cedex 2, France.

*Correspondence:

alain.burger@univ-cotedazur.fr , benoit.michel@univ-cotedazur.fr

Table of contents

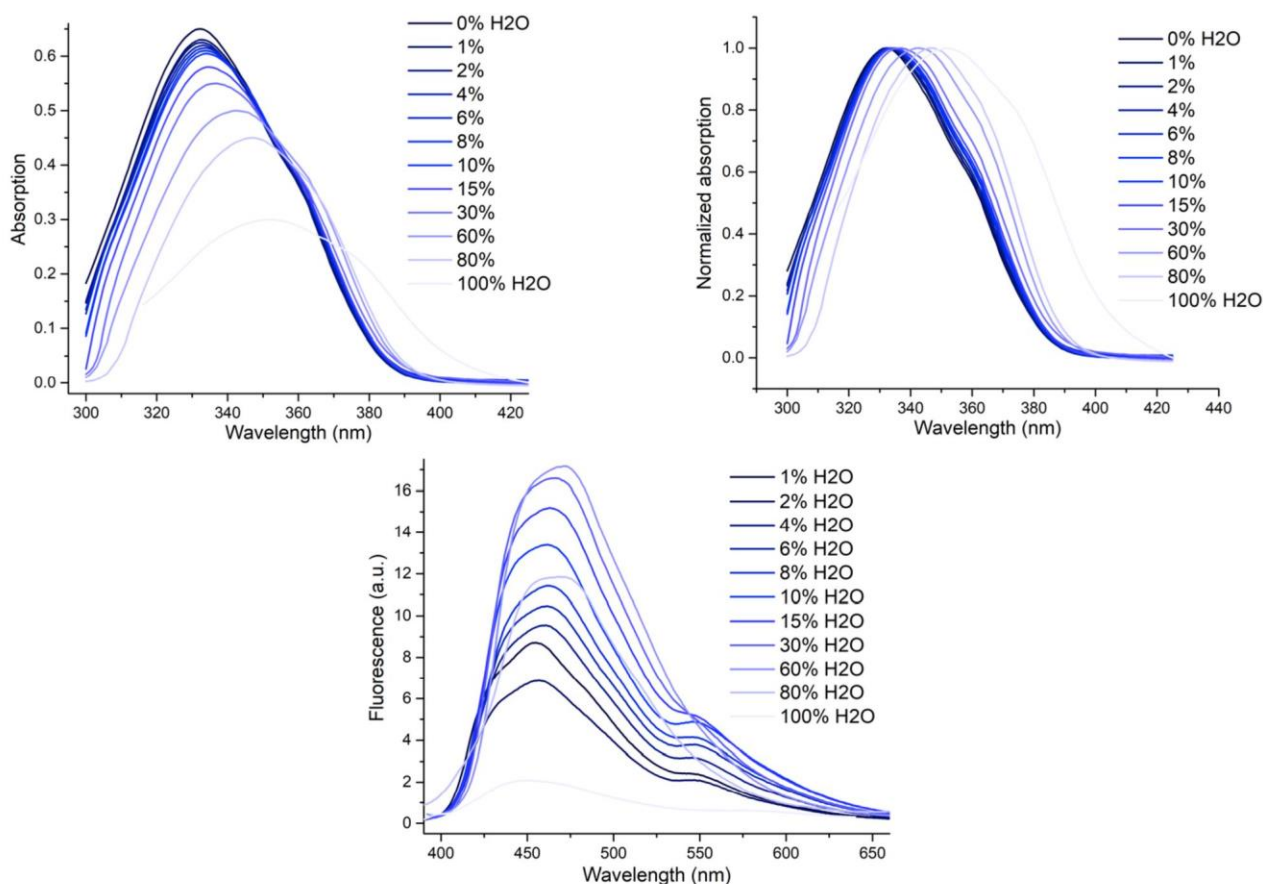
EXPERIMENTAL SECTION	3
1. PHOTOPHYSICAL CHARACTERIZATION	3
1.1 Hydration study	3
1.2 Photostability studies	3
1.3 Glycerol titration	4
2. SPECTROSCOPIC STUDIES of ss- & ds-ODNs	4
2.1 ODN synthesis and purification	4
2.2 HRMS analysis of labeled ODNs	5
2.3 Steady-state photophysical measurements	6
2.4 Temperature-induced denaturation studies	7
2.5 Circular dichroism	7
NMR SPECTRA	8

Experimental Section

1. PHOTOPHYSICAL CHARACTERIZATION

1.1 Hydration study

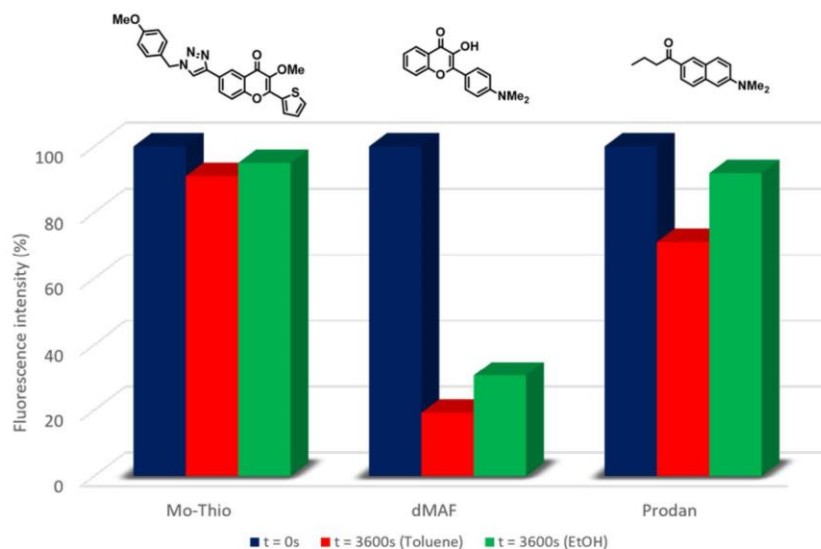
Figure S1. Hydration study of the clicked model compound, Mo-Thio: raw and normalized absorption spectra (top) and the corresponding fluorescence observables (bottom).



Footnotes: Titration was performed by adding water to a THF solution containing the dye. A different solution was made for each percentage of water to keep the same concentration for each experiment ($2 \mu\text{M}$).

1.2 Photostability studies

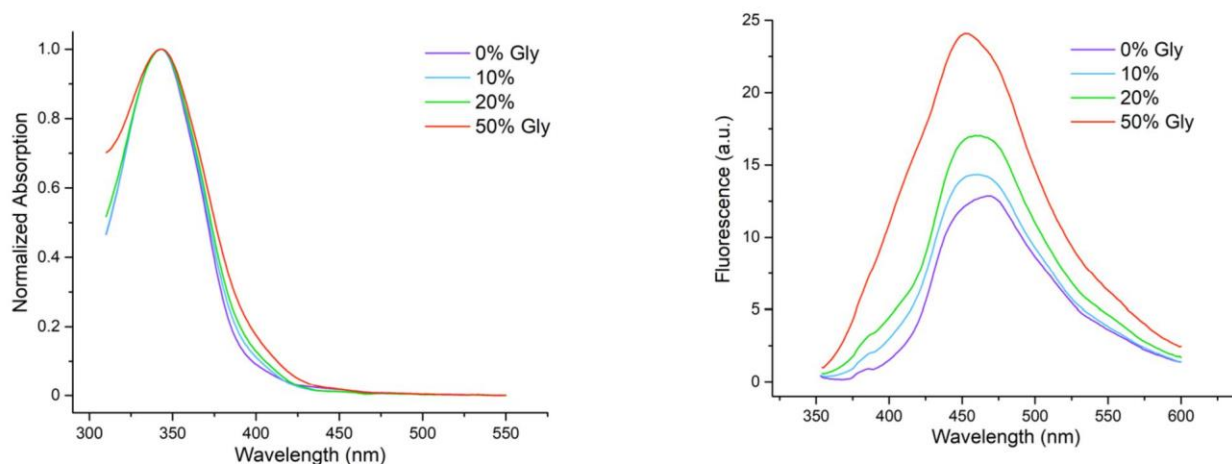
Figure S2. Photobleaching evolution of Mo-Thio and push-pull references (dMAF and Prodan), over the course of a one-hour experiment in toluene and EtOH.



Footnotes: For a $2 \mu\text{M}$ dye solution in a cuvette, with an 8×8 aperture slit, the evolution of the emission intensity was monitored over 1 hour. The fluorescence signal is recorded at its maximum intensity (453 nm in toluene, 437 nm in EtOH) with an excitation wavelength corresponding to the absorption maximum in the considered solvent (338 nm in toluene, 342 nm in EtOH).

1.3 Glycerol titration

Figure S3. Glycerol titration of the clicked model compound, Mo-Thio: normalized absorption (left) and fluorescence (right) spectra.



Footnotes: Titration was performed by adding glycerol to a methanolic solution of the dye. A different solution was made for each percentage of water to keep the same concentration for each experiment (2 μ M).

2. SPECTROSCOPIC STUDIES of ss- & ds-ODNS

2.1 ODN synthesis and purification

General method:

Wild-type and clickable ODNs were ordered purified and ready-to-use (Microsynth AG, Balgach, Switzerland).

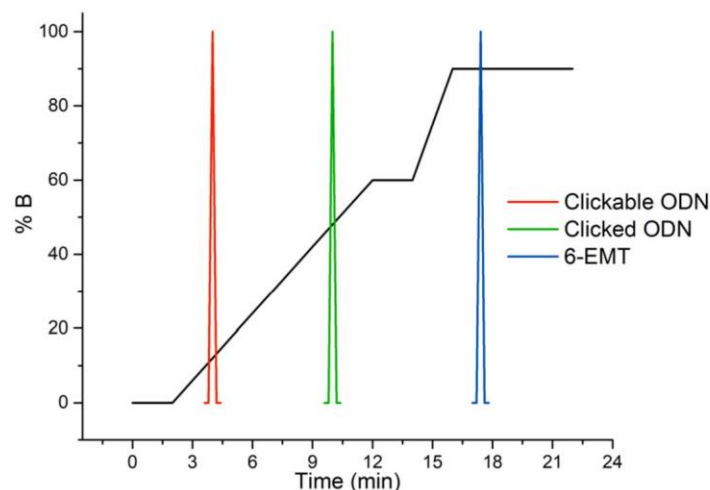
Typical post-synthetic labeling procedure:

First, a 5mM aq. solution of $\text{CuSO}_4 \cdot 5\text{H}_2\text{O}$ and the BTES ligand^[1] was freshly prepared. In a 200- μ L vial, were sequentially added the ODN sequence to be labeled (0.2mM aq. solution, 50 μ L, 10 nmol, 1 eq.), DMSO (20 μ L), 6-EMT label (5 mM in DMSO, 10 μ L, 50 nmol, 5 eq.), sodium ascorbate (5mM aq. solution, 10 μ L, 50 nmol, 5 eq.), and finally the 5mM CuSO_4 /BTES aq. solution (10 μ L, 50 nmol, 5 eq.). The reaction mixture was vortexed overnight at room temperature. The resulting solution was removed from the vial, which was then rinsed with minimal H_2O and DMSO. The combined solution was passed through a 0.22- μ m H-PTFE syringe filter before being analyzed (0.5 mL/min) by RP-HPLC.

Labeled ODNs were purified (2.0 mL/min) by RP-HPLC—including the following apparatus: WatersTM 600 Controller with WatersTM 996 Photodiode Array Detector (Waters, Milford, MA, USA)—using analytical and semi-preparative Clarity[®] Oligo-RPTM C18 columns with the respective dimensions: 300 \times 4.60 mm and 250 \times 10 mm, 5- μ m particle size, 100 \AA (Phenomenex, Torrance, CA, USA). The corresponding gradient system was employed: 100% A (kept 2 min) — (10 min) \rightarrow 40% A/60% B (kept 2 min) — (2 min) \rightarrow 10% A/90% B (kept 6 min) — (5 min) \rightarrow 100% A with A = 0.9 TEAB buffer 100 mM pH 7.8: 0.1 CH_3CN and B = 0.9 CH_3CN : 0.1 TEAB (Figure S4). To prepare a 100mM triethylamine bicarbonate (TEAB) buffer [(Et_3NH) HCO_3]: pass CO_2 into a 0.1M Et_3N deionized aq. solution until the pH reaches about 7.8 and store at 4 $^\circ\text{C}$.

¹ I. Ivancová, D.-L. Leone, M. Hocek, *Curr. Opin. Chem. Biol.* **2019**, 52, 136–144.

Figure S4. HPLC gradient and retention time of derivatives from the post-synthetic click reaction.



Footnotes: Depicted peaks at 4, 10, and 17 min represent, respectively, the starting clickable ODN, the labeled ODN ("clicked sequence"), and the clickable 6-EMT label.

Table S1. Nature, absorptivity, and linker chemical structure of the ODNs to be labeled.

Sequence	Extinction coefficient ($L \cdot mol^{-1} \cdot cm^{-1}$)	Azide linker
5'- Y -GCA AAA TTT AAA ACG-3'	158,100	
5'-GCA AAA TX T AAA ACG-3'	157,400	
5'-GCA AAA TXs T AAA ACG-3'	157,400	

2.2 HRMS analysis of labeled ODNs

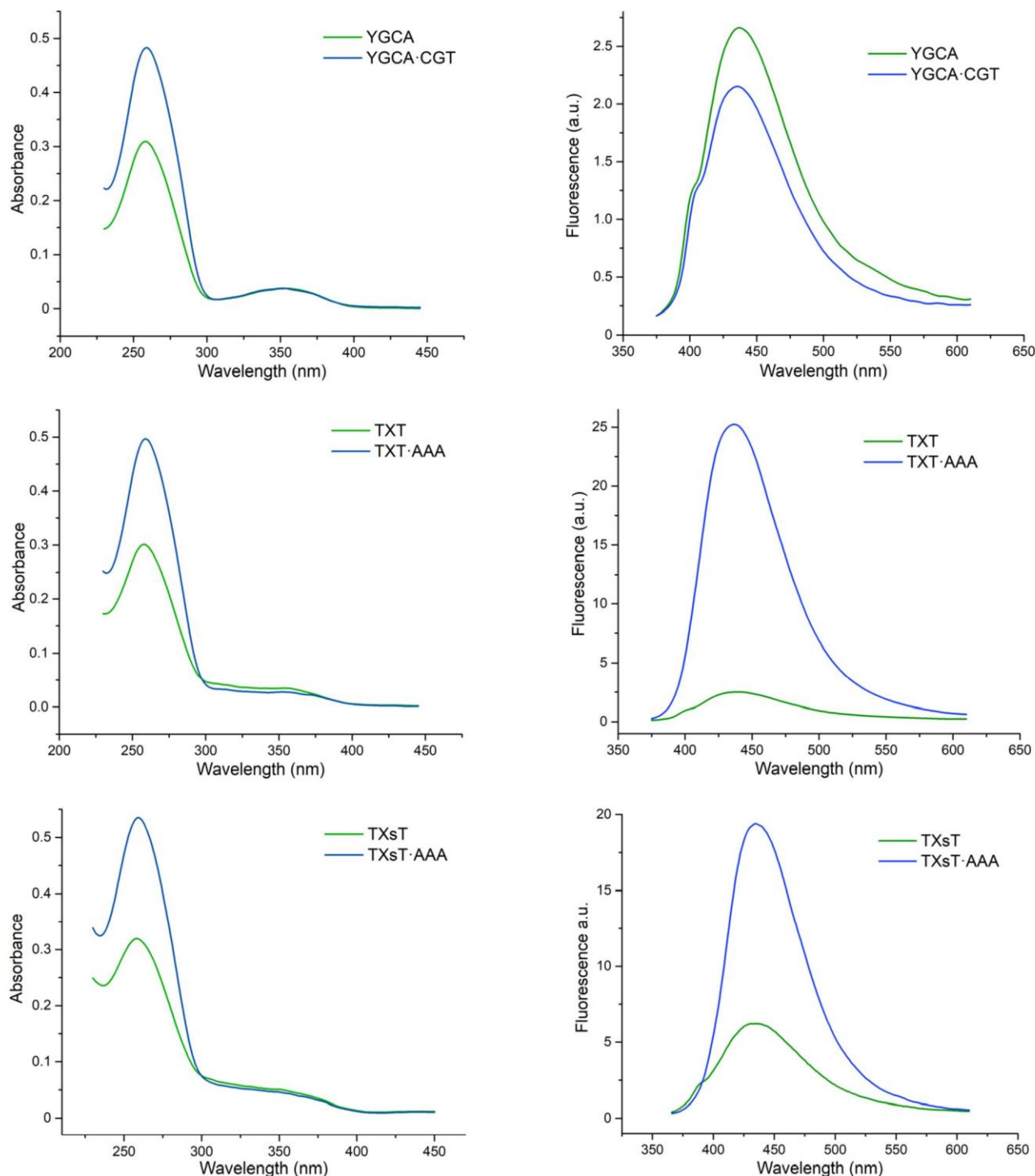
Table S2. Mass of the single-stranded DNA tagged with 6-EMT.

ODN	Sequence	HRMS found (calc.) [M+H] ⁺
		Labeled with 6-EMT
Y-GCA	5'- Y -GCA AAA TTT AAA ACG-3'	5163.9958 (5163.9977)
TX T	5'-GCA AAA TX T AAA ACG-3'	5219.0023 (5219.0035)
TXs T	5'-GCA AAA TXs T AAA ACG-3'	5162.9419 (5162.9409)

2.3 Steady-state photophysical measurements

Absorbance spectra were recorded on a Cary 100 Bio UV–Vis spectrophotometer (Varian/Agilent, Palo Alto, CA, USA) using 500- μ L cuvettes (Hellma, Müllheim, Germany) in Suprasil[®] quartz (Heraeus, Hanau, Germany) with 1-cm path length. The ODN stock solutions were prepared using Milli-Q[®] water (Merck Millipore, Burlington, MA, USA). Fluorescence measurements were conducted on a FluoroMax 4.0 spectrofluorometer (Jobin Yvon, Horiba, Kyoto, Japan) in a cell compartment thermostated at 20 ± 0.5 °C with a 2x2 aperture slit and were excitation and emission corrected. Measured solutions were prepared with absorbance of about 0.05 at the excitation wavelength mentioned in the corresponding experiments. Reported values are the average of two or more independent and reproducible measurements; ± 1 nm for wavelengths. Quantum yields were corrected according to the variation of the refractive index of the different solvents. They were determined by comparing the integrated area of the corrected emission spectrum of the sample with that of 4'-(*N,N*-dimethylamino)-3-hydroxyflavone (dMAF, $\lambda_{\text{Ex}} = 407$ nm, $\Phi = 27\%$) used as a reference,^[2] with $\pm 10\%$ mean standard deviation.

Figure S5. Absorption (left) and emission (right) spectra of ss- and ds-ODNs labeled with 6-EMT.



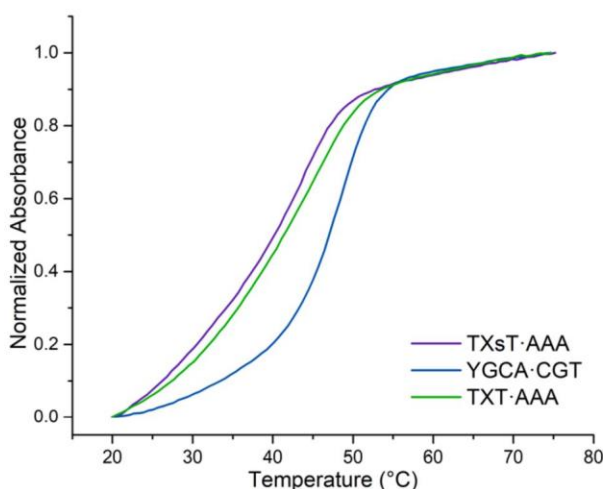
² S. M. Ormson, R. G. Brown, F. Vollmer, W. Rettig, *J. Photochem. Photobiol. A: Chem.* **1994**, *81*, 65–72.

2.4 Temperature-induced denaturation studies

Preparation of a 2 μ M ODN duplex solution (pH 7.4, [P] = 12 mM and [Na] = 170 mM):

In a 500- μ L quartz cuvette, sample was prepared by mixing the solutions of the modified ss-ODN (8 μ M, 125 μ L) and its complementary wild-type sequence (8 μ M, 125 μ L) with a PBS solution (250 μ L containing 24mM sodium phosphate and 300mM NaCl). To ensure reproducibility of hybridization and thus measurements, the double-stranded samples were first denatured and then cooled to room temperature. Melting curves were recorded in duplicate in a Peltier-thermostatted cell holder by following the temperature-dependence of absorbance changes at 260 nm of the sample (2 μ M concentration of each strand). The temperature range for the denaturation measurement was 5–80 °C. Speed of heating was 0.3 °C/min. Melting observables were converted to a plot of α versus temperature, where α represents the fraction of single strands in the duplex state. Melting temperatures (T_m) were extracted from these curves after differentiation as described.^[3] Reported values are the average of two or more independent and reproducible measurements; ± 0.5 °C for T_m .

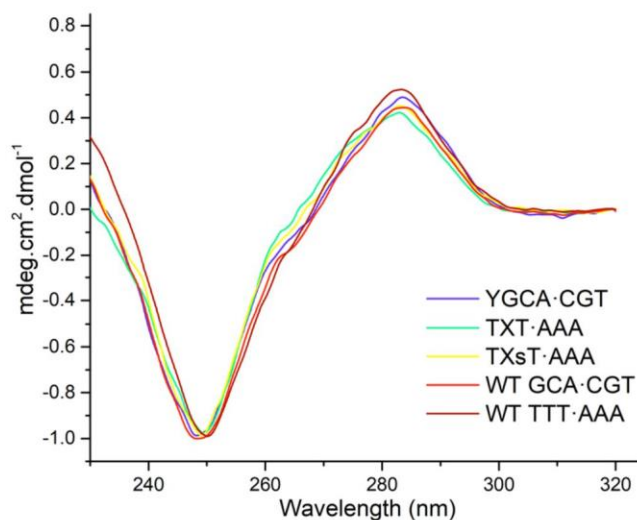
Figure S6. Melting temperature curves of duplexes tagged with 6-EMT.



2.5 Circular Dichroism

All spectra were run in duplicate with 2 μ M solution of the canonical and labeled duplexes (**X**, **Xs**, and **Y** opposite **A**) in PBS pH 7.4 ([P] = 12 mM and [Na] = 170 mM). Two maxima were observed in CD spectra: one negative at ~250 nm and the other positive at ~280 nm.

Figure S7. CD spectra of wild-type and labeled ds-ODNs normalized on their negative maximum.



³ K. J. Breslauer, *Methods Enzymol.* **1995**, 259, 221–242.

IV. Malachite Green

Partie Expérimentale du Chapitre 3 : II. Malachite Green

Table of contents

EXPERIMENTAL SECTION	2
1. SYNTHETIC PROCEDURES	2
2. SPECTROSCOPIC STUDIES OF MODEL ODNs	3
2.1 ODNs synthesis and purification	3
2.2 Steady-state fluorescence measurements	4
2.3 Absorbance & Fluorescence spectra	5
REFERENCES	15

Experimental Section

1. Synthetic Procedures

Figure S1: Synthetic scheme of the alkyne Malachite Green.

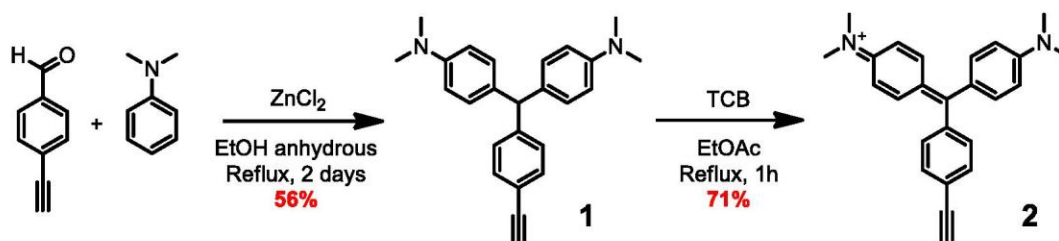
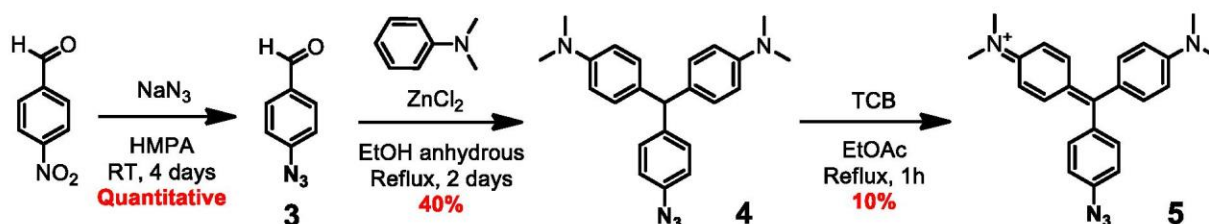


Figure S2: Synthetic scheme of the azide Malachite Green.



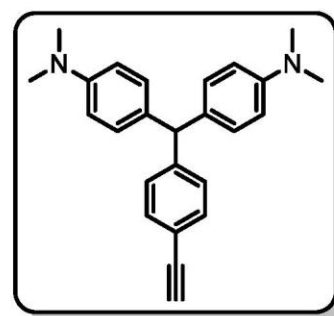
4,4'-((4-ethynylphenyl)methylene)bis(N,N-dimethylaniline): 1

N,N-dimethylaniline (292 μL , 2.28 mmol, 3 eq.) was added slowly to a stirred mixture of ethynylbenzaldehyde (100 mg, 0.76 mmol, 1 eq.) and ZnCl_2 (524 mg, 3.80 mmol, 5 eq.) in dry ethanol (7.6 mL, 0.1 M). The mixture was refluxed and stirred for 2 days (green color). After returned to RT, the mixture was extracted with water and DCM. The combined organic layers were dried (MgSO_4), filtered and concentrated under reduced pressure. The crude residue was purified by flash chromatography on silica gel eluted with Cyclohexane/EtOAc (95/5 \rightarrow 85/15, v/v) to give the desired product as a yellow solid (150 mg, 0.42 mmol, 56%).

$^1\text{H NMR}$ (CDCl_3 , 400 MHz): δ (ppm): 2.92 (s, 12H), 3.02 (s, 1H), 5.37 (s, 1H), 6.67 (d, $^3J = 8.8$ Hz, 4H), 6.96 (d, $^3J = 8.8$ Hz, 4H), 7.09 (d, $^3J = 8.2$ Hz, 2H), 7.39 (d, $^3J = 8.2$ Hz, 2H).

$^{13}\text{C-NMR}$ (CDCl_3 , 101 MHz): δ (ppm): 148.3, 144.3, 135.5, 133.0, 128.6, 127.6, 118.1, 110.7, 82.0, 77.0, 54.5, 37.1.

MS (ESI⁺): m/z calc for $\text{C}_{25}\text{H}_{26}\text{N}_2\text{H}^+$: 355.216 $[\text{M}+\text{H}]^+$; found: 355.216 $[\text{M}+\text{H}]^+$



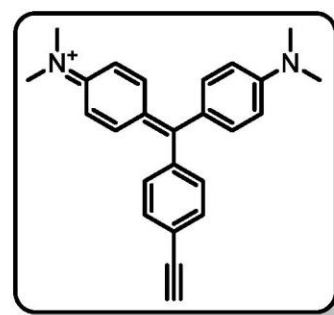
N-(4-((4-(dimethylamino)phenyl)(4-ethynylphenyl)methylene)cyclohexa-2,5-dien-1-ylidene)-N-methylmethanaminium: 2

1 (109 mg, 0.3 mmol) was dissolved in 25 mL ethyl acetate. Tetrachloro-p-benzoquinone (157 mg, 0.61 mmol, 2 eq.) was added and the reaction mixture was refluxed for 1 hr. The reaction mixture was cooled to RT. Ethyl acetate (20 mL) was added and the product was extracted with water (5 x 50 mL). The combined aqueous layers were washed with ethyl acetate (2 x 50 mL) and concentrated to give 2 (77 mg, 0.22 mmol, 72 %).

$^1\text{H NMR}$ (MeOD, 400 MHz): δ (ppm): 3.35 (s, 12H), 3.88 (s, 1H), 7.07 (d, $^3J = 9.5$ Hz, 4H), 7.37 (d, $^3J = 8.4$ Hz, 2H), 7.44 (d, $^3J = 9.5$ Hz, 4H), 7.68 (d, $^3J = 8.4$ Hz, 2H).

$^{13}\text{C-NMR}$ (MeOD, 101 MHz): δ (ppm): 176.1, 154.5, 141.5, 136.4, 135.4, 132.8, 129.3, 122.4, 114.7, 83.7, 82.7, 40.7.

MS (ESI⁺): m/z calc for $\text{C}_{25}\text{H}_{25}\text{N}_2^+$: 353.201 $[\text{M}]^+$; found: 353.203 $[\text{M}]^+$



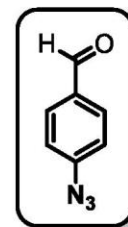
4-azidobenzaldehyde: 3

Done by following the protocol described in: *Org. Biomol. Chem.*, **2013**, 11, 3297-3306.

4-nitro-benzaldehyde (200 mg, 1.31 mmol, 1 eq.) and NaN₃ (1.6 g, 24.61 mmol, 2 eq.) were dissolved in HMPA (3.3 ml). The forming 4-azido-benzaldehyde is UV-sensitive so the reaction flask was covered with an aluminum foil to protect **3** from light. The reaction mixture was stirred for 4 days at RT. Thereafter, water (15 mL) was added, and the aqueous mixture was extracted with Et₂O (3×40 mL). The combined organic phases were washed with water (3×70 mL), dried over MgSO₄ and filtered. The solvent was evaporated to give an orange-yellow oil (quantitative).

Characterized by GC-MS: *m/z* calc for C₇H₅N₃O⁺: 147,043 [M]⁺; found: 147,043[M]⁺

¹H NMR (CDCl₃, 200 MHz): δ (ppm): 9.94 (s, 1H), 7.72 (d, ³J = 7.9 Hz, 2H), 7.12 (s, 1H).



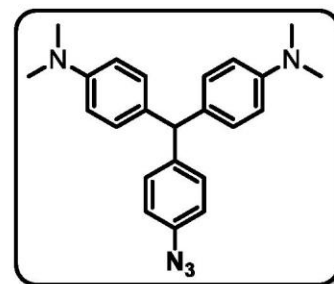
4,4'-((4-azidophenyl)methylene)bis(N,N-dimethylaniline): 4

To a solution of azidobenzaldehyde (27.5 mg, 0.19 mmol, 1 eq.) and ZnCl₂ (127.4 mg, 0.93 mmol, 5 eq.) in dry ethanol (1.85 mL, 0.1 M), N,N-dimethylaniline (71 μL, 0.56 mmol, 3 eq.) was slowly added, the reaction flask was covered with an aluminum foil and the mixture was stirred under reflux for 2 days. The mixture was cooled to RT, it was extracted with water and DCM. The combined organic layers were concentrated under reduced pressure and purified by flash chromatography on silica gel eluted with Cyclohexane/EtOAc (100/0 → 85/15, v/v) to give the desired product as a brownish oil (27.2 mg, 0,073 mmol, 40%).

¹H NMR (CDCl₃, 200 MHz): δ (ppm): 2.92 (s, 12H), 5.36 (s, &H), 6.67 (d, ³J = 8.8 Hz, 4H), 6.93 (d, ³J = 8.5 Hz, 2H), 6.96 (d, ³J = 8.8 Hz, 4H), 7.12 (d, ³J = 8.5 Hz, 2H).

¹³C-NMR (CDCl₃, 101 MHz): δ (ppm): 149.7, 140.4, 139.8, 136.3, 129.6, 129.1, 119.5, 111.8, 57.3, 41.3.

MS (ESI⁺): *m/z* calc for C₂₃H₂₅N₃H⁺: 372.218 [M+H]⁺; found: 372.221 [M+H]⁺



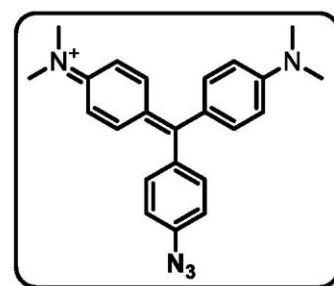
N-(4-((4-azidophenyl)(4-(dimethylamino)phenyl)methylene)cyclohexa-2,5-dien-1-ylidene)-N-methylmethanaminium: 5

4 (27.2 mg, 0.073 mmol, 1 eq.) was dissolved in ethyl acetate (1.45mL). Tetrachloro-p-benzoquinone (37.5 mg, 0.145 mmol, 2 eq.) was added and the reaction mixture was refluxed for 1 hr. The reaction mixture was cooled to RT. Ethyl acetate (20 mL) was added and the product was extracted with water (5 x 50 mL). The combined aqueous layers were washed with ethyl acetate (2 x 50 mL) and concentrated to give the crude desired product (2,43 mg, 10%).

¹H NMR (CDCl₃, 400 MHz): δ (ppm): 3.35 (s, 12H), 6.99 (d, ³J = 8.8 Hz, 2H), 7.07 (d, ³J = 9.4 Hz, 4H), 7.32 (d, ³J = 8.8 Hz, 2H), 7.45 (d, ³J = 9.4 Hz, 4H).

¹³C-NMR (CDCl₃, 101 MHz): 174.6, 151.1, 140.9, 137.5, 133.4, 127.8, 123.3, 117.3, 39.7.

MS (ESI⁺): *m/z* calc for C₂₃H₂₄N₅⁺: 370.202 [M]⁺; found: 370.208 [M]⁺



2. Spectroscopic studies of Model ODNs

2.1 ODNs synthesis and purification

General method:

Wild-type and clickable ODNs were purchased from Microsynth AG. ODNs were ordered purified and ready to use.

Typical labeling procedure:

First, a stock aq. solution of CuSO₄·5H₂O and BTES (5mM each) was prepared.

In a 200-μL vial, were sequentially added the ODN sequence (0.2mM aq. solution, 50 μL, 10 nmol, 1 eq.), DMSO (20 μL), dye (5 mM in DMSO, 10 μL, 50 nmol, 5 eq.), sodium ascorbate (5mM aq. solution, 10 μL, 50 nmol, 5 eq.), and finally the CuSO₄/BTES mixture (5mM aq. solution, 10 μL, 50 nmol, 5 eq.). The mixture was vortexed overnight at RT. The solution was then recovered, and the vial was washed with a minimum of H₂O and DMSO. Thus, the whole mixture was then purified by RP-HPLC. ODNs were analyzed (0.5 mL/min) and purified (2.0 mL/min) by RP-HPLC (HPLC apparatus: WatersTM 600 Controller with WatersTM 996 Photodiode Array Detector. Columns: analytical, 300 × 4.60 mm, 5μm particle size, Clarity[®] 100Å, Phenomenex[®]; semi-preparative, Clarity[®] 5u Oligo-RP column 250 x 10 mm Phenomenex[®]).

Table S1: Sequence, Nature, Name and linker of the ODNs to be labeled.

Sequence	Name	Linker
5'- YCAG TCG CTC GCT GAC-3'	YCAG	
5'- YGCA AAA TTT AAA ACG-3'	YGCA	
5'-CAG TCG CXC GCT GAC-3'	CXC	
5'-GCA AAA TXT AAA ACG-3'	TXT	
5'-GCA AAA TXsT AAA ACG-3'	TXsT	
5'- VGCA AAA TTT AAA ACG-3'	VGCA	
5'-GCA AAA TZT AAA ACG-3'	TZT	
5'-GCA AAA TWT AAA ACG-3'	TWT	

2.2 Steady-state fluorescence measurements

Absorption and fluorescence experiments were performed in duplicate in pH 7.0 phosphate-buffered saline (12 mM PBS, 120 mM NaCl). Absorption spectra were recorded at 25°C on a Cary 100 Bio UV–Vis spectrophotometer (Varian/Agilent) using Suprasil® quartz cuvettes with 1-cm path length. Fluorescence spectra were recorded on a FluoroMax 4.0 spectrofluorometer (Jobin Yvon, Horiba) with a 2x2 aperture slit and were corrected at excitation and emission. Measured solutions were prepared with absorbance of about 0.05 at 25 °C at the excitation wavelength mentioned in the corresponding experiments. Quantum yields were corrected according to the variation of the refractive index of the different solvents and were determined using Cresyl violet in EtOH ($\lambda_{\text{ex}} = 570 \text{ nm}$, $\Phi = 0.54$) as a standard reference^{1,2}.

Table S2: Spectroscopic properties of ODNs labeled with 2.

Sequence	$\lambda_{\text{abs}} (\text{nm})^a$		$\lambda_{\text{em}} (\text{nm})^b$	$\Phi (\%)^c$
	S_2	S_1		
YCAG	450	633	668	0,12
YCAG ·GTC	450	630	668	0,09
CXC	449	634	662	0,23
CXC ·GAG	451	635	667	0,17
YGCA	448	632	665	0,10
YGCA ·CGT	449	628	667	0,06
TXT	450	632	666	0,11
TXT ·AAA	450	635	674	0,12
TXsT	451	632	669	0,10
TXsT ·AAA	456	636	677	0,10

^a Position of the absorption band maximum for the S1 and S2. ^b Position of the emission band maximum. ^c Quantum yield determined using Cresyl-violet in EtOH ($\lambda_{\text{ex}} = 570 \text{ nm}$, $\Phi = 0.54$)^{1,2}.

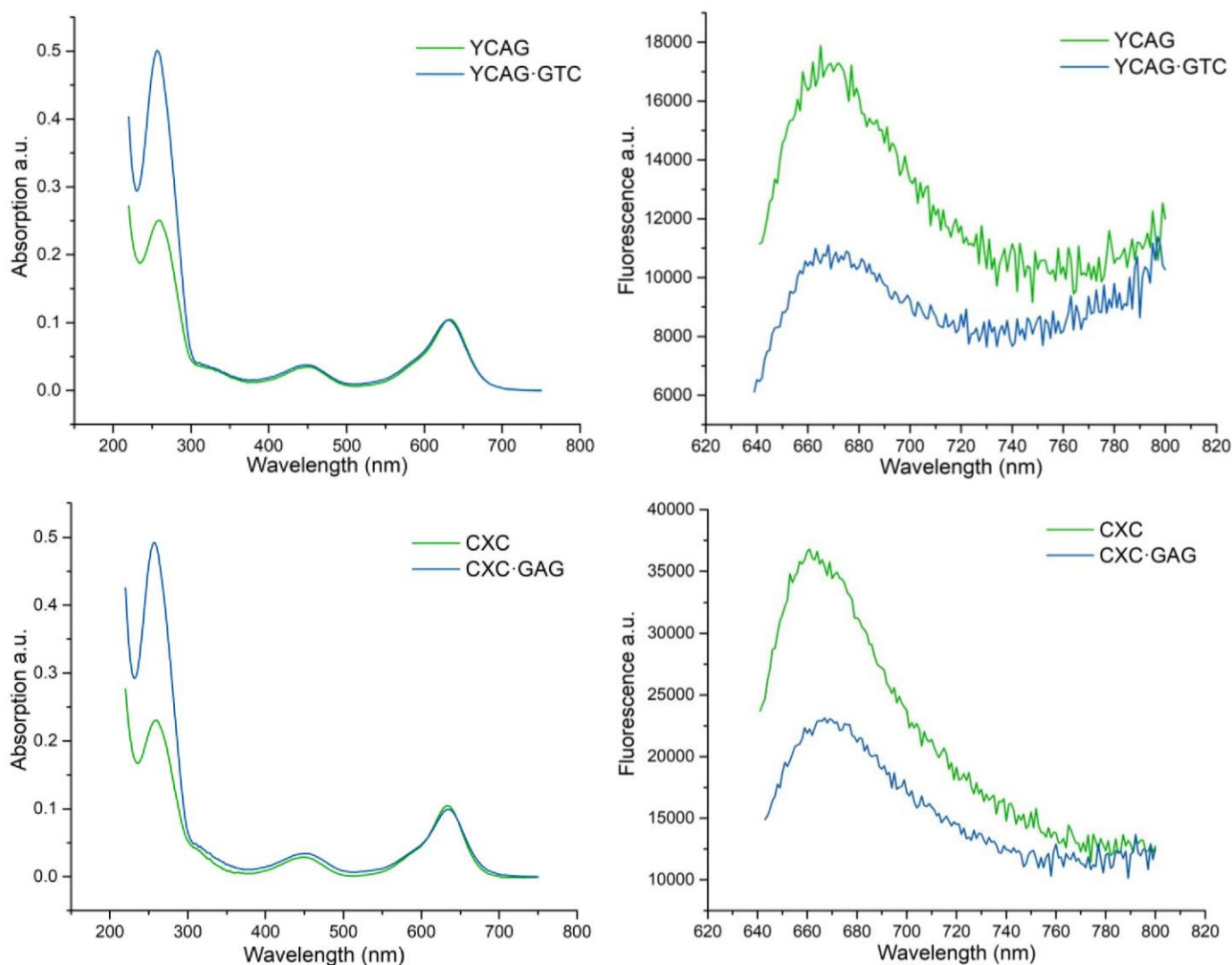
Table S3: Spectroscopic properties of ODNs labeled with 5.

Sequence	$\lambda_{\text{abs}} \text{ (nm)}^a$		$\lambda_{\text{em}} \text{ (nm)}^b$	$\Phi \text{ (\%)}^c$
	S ₂	S ₁		
VGCA	438	634	675	0.05
VGCA·CGT	438	634	675	0.04
TZT	436	634	673	0.06
TZT·AAA	439	639	681	0.07
TWT	436	636	680	0.05
TWT·AAA	439	639	680	0.06

^a Position of the absorption band maximum for the S1 and S2. ^b Position of the emission band maximum. ^c Quantum yield determined using Cresyl-violet in EtOH ($\lambda_{\text{ex}} = 570 \text{ nm}$, $\Phi = 0.54$)^{1,2}.

2.3 Absorbance & Fluorescence spectra

Figure S3: Absorption (left) and emission (right) spectra of ss- and ds-ODNs labeled with 2.



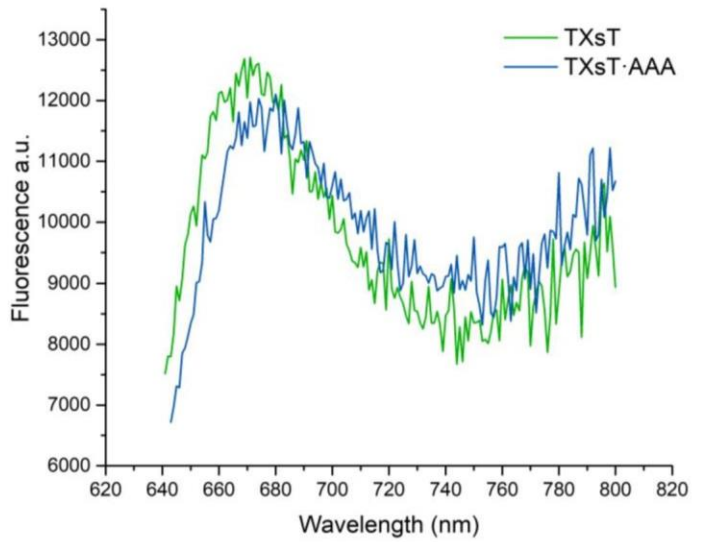
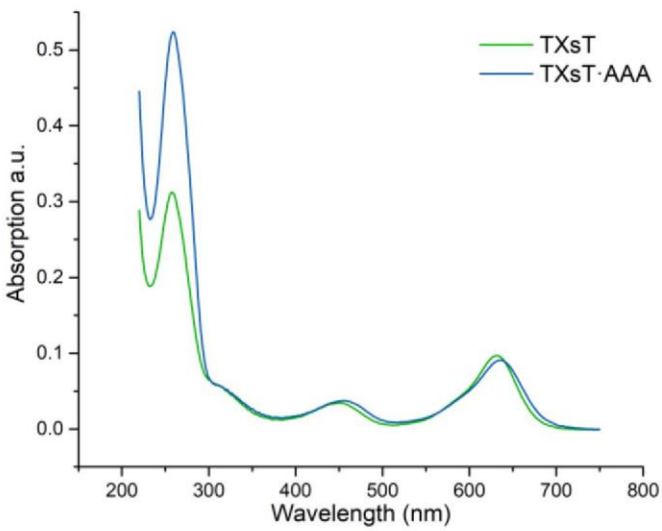
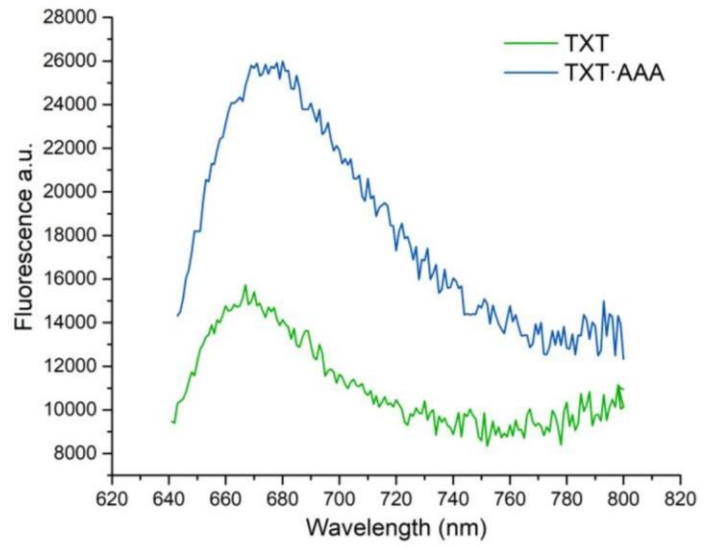
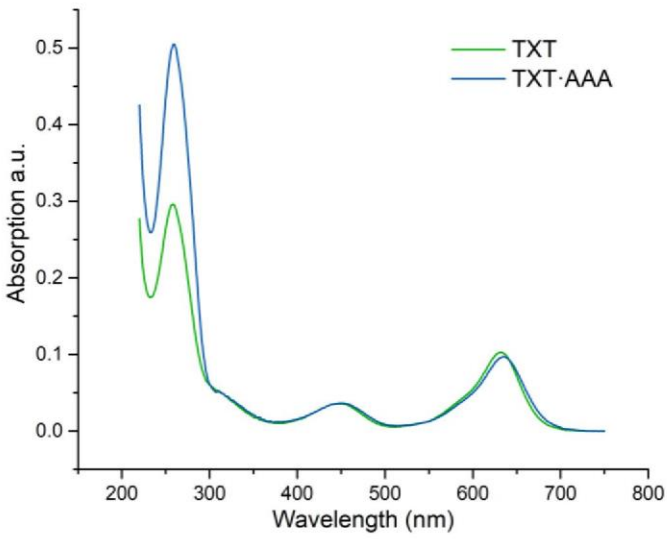
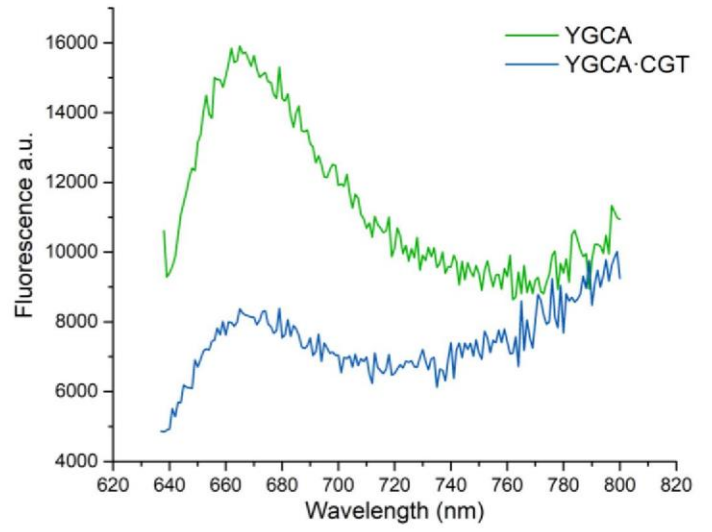
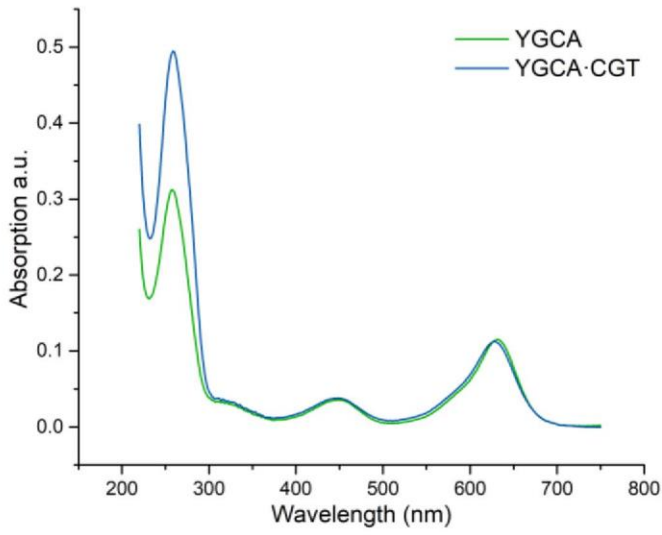


Figure S4: Absorption (left) and emission (right) spectra of ss- and ds-ODNs labeled with 5.

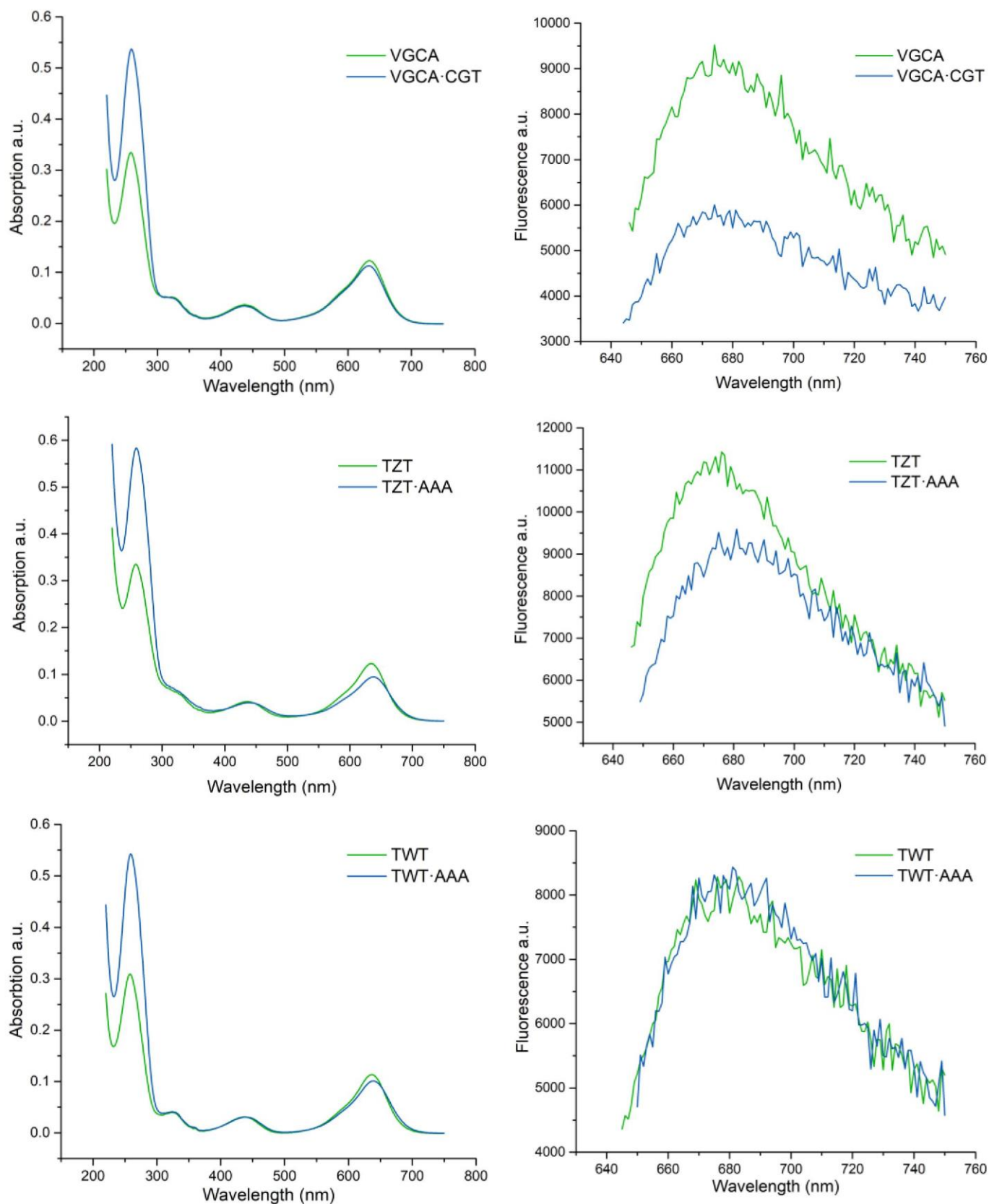


Figure S5: Absorption (left) spectra of ss- and ds-ODNs and emission (right) spectra of the Cy5 cross-excitation and ds-ODNs labeled with 2.

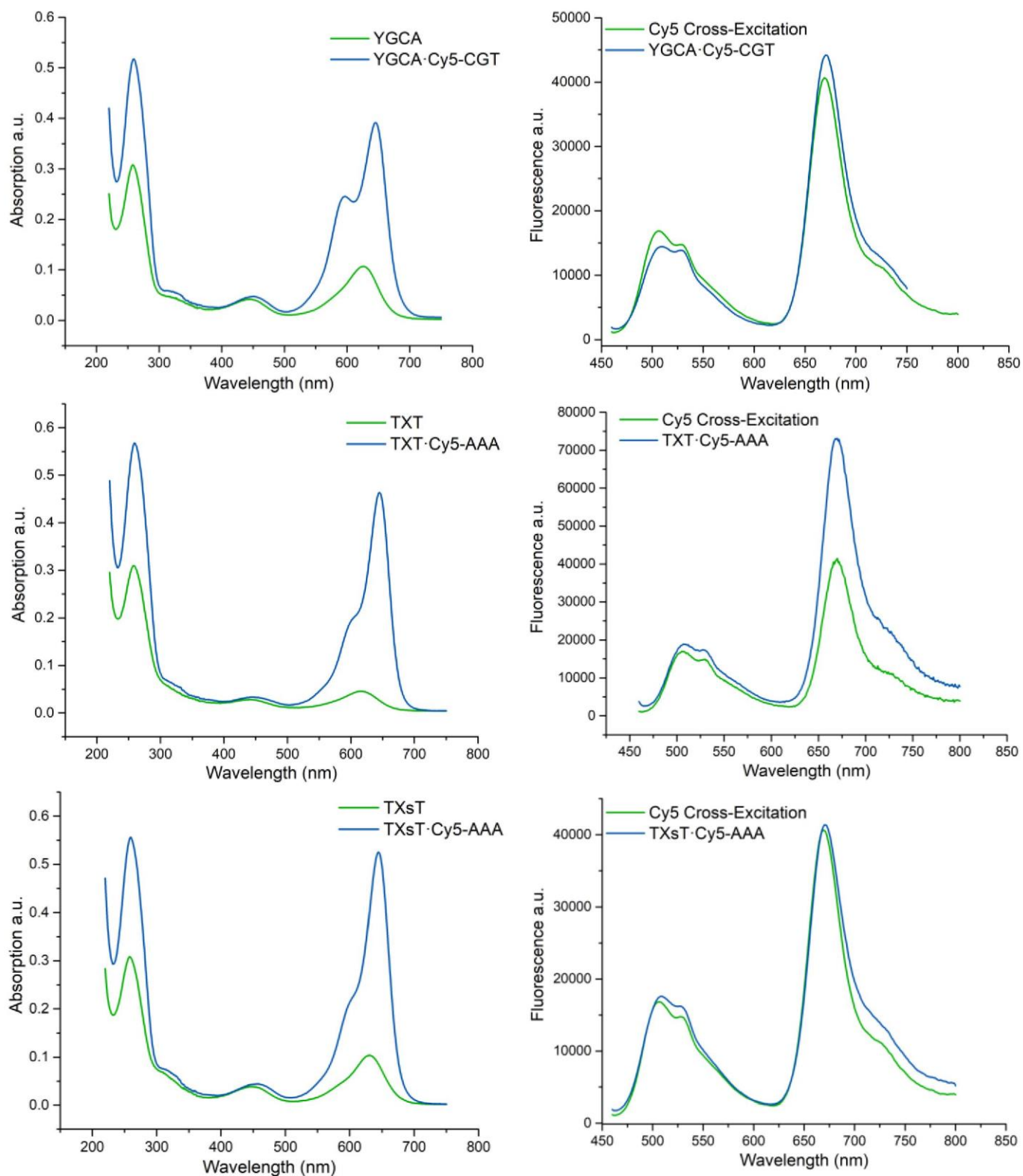


Table S4: Sequence, Nature, Name and linker of the ODNs to be labeled for G quadruplexes structures.

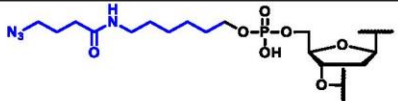
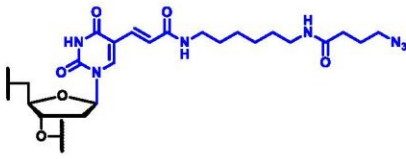
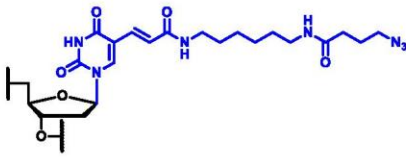
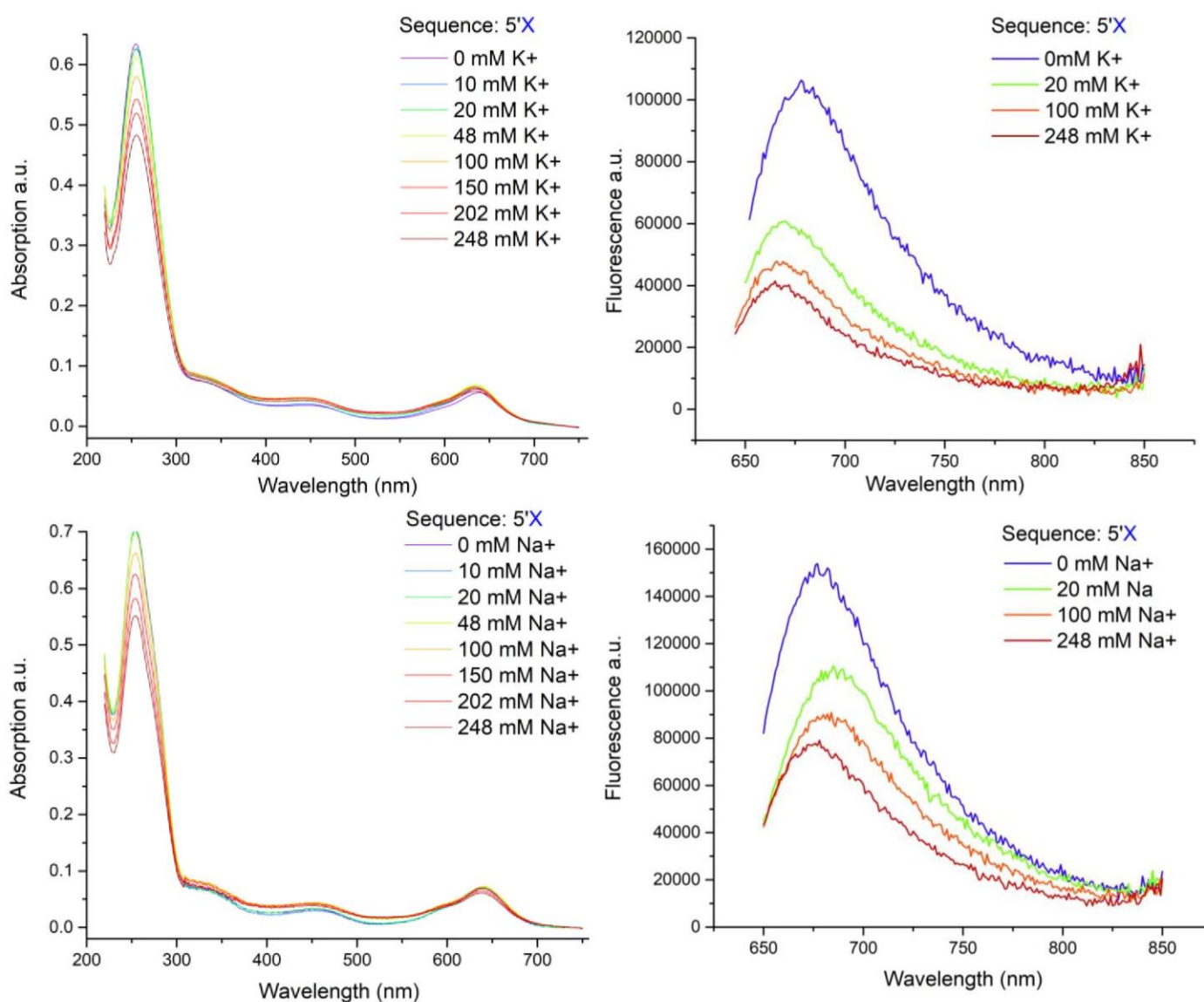
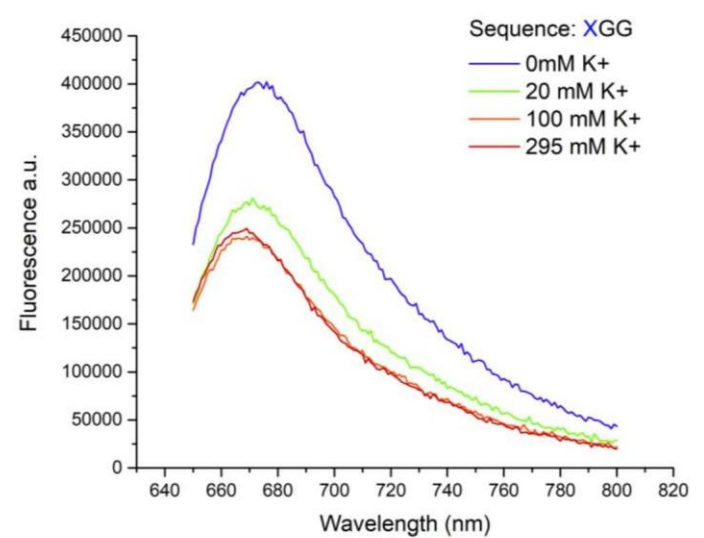
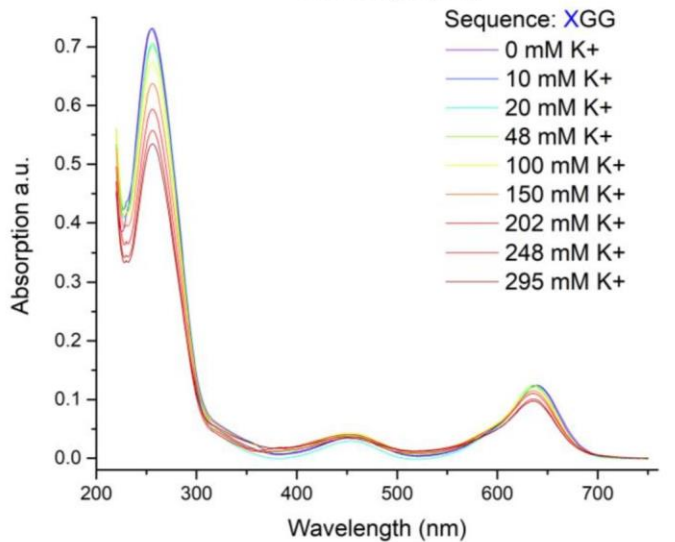
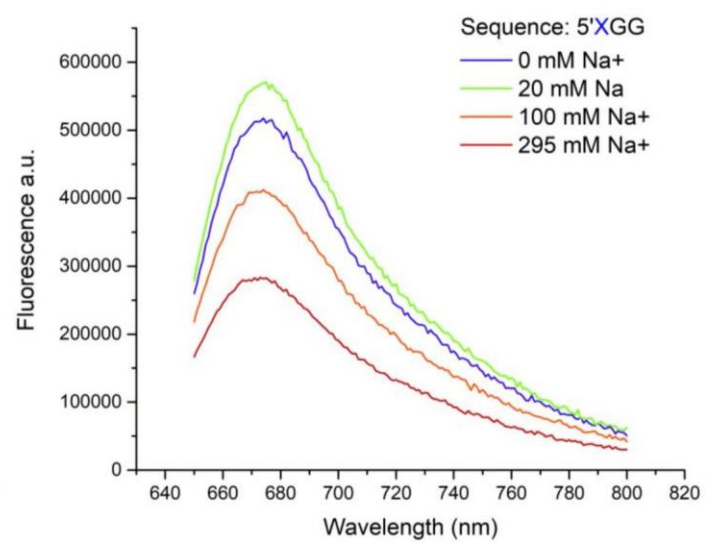
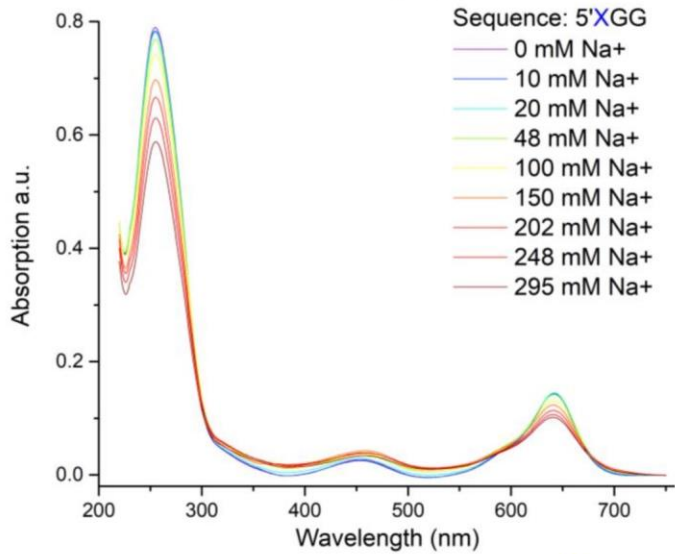
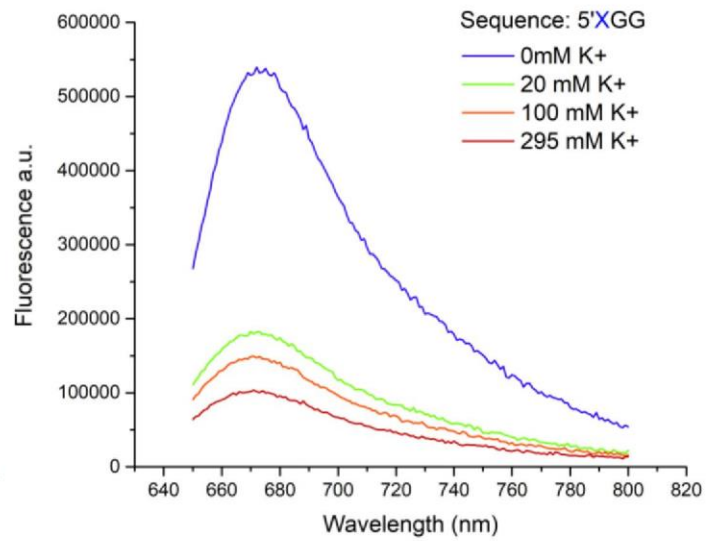
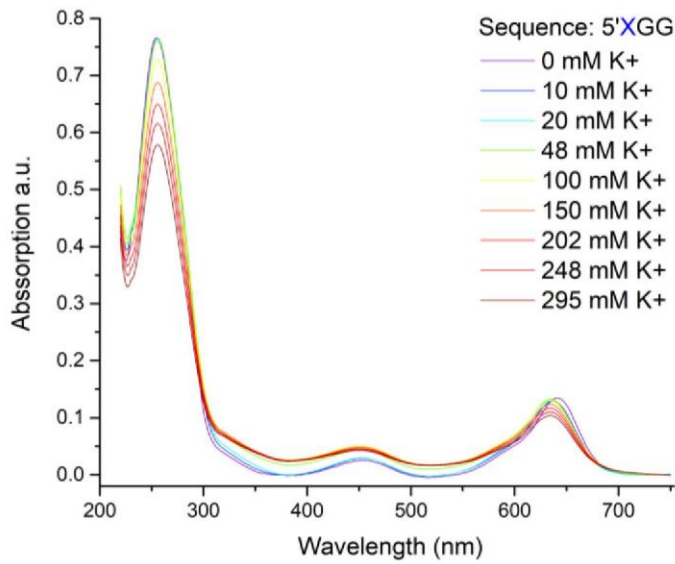
Sequence	Name	Linker
X GGG TGG TGG TGG TGG TGG TGG TGG TGG TGG TGG TGG TGG TG	5' X	
GGG XGG TGG TGG TGG TGG TGG TGG TGG TGG TGG TGG TGG TG	5' XGG	
GGG TGG TGG TGG TGG TGG TGG XGG TGG TGG TGG TGG TGG TG	XGG	

Figure S6: Absorption (left) and emission (right) spectra of the titration of ss-ODNs sequences with K⁺ or Na⁺ salt labeled with 2.





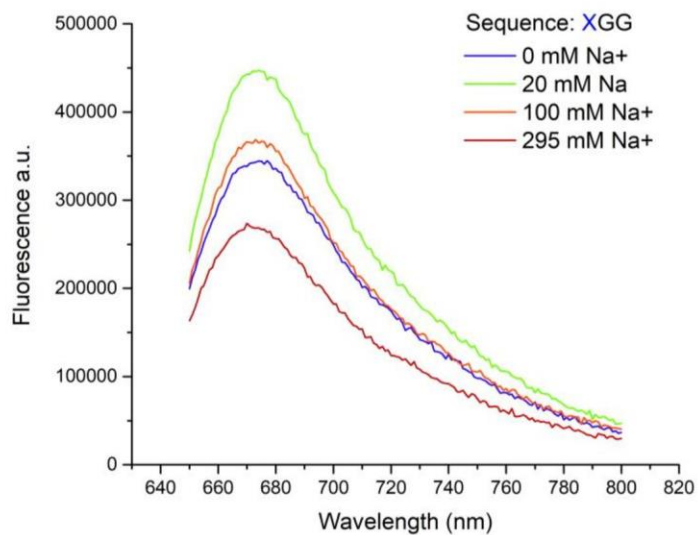
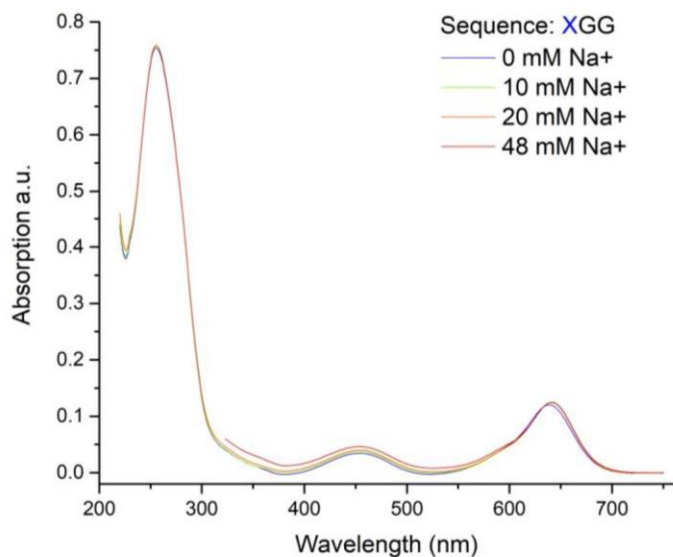
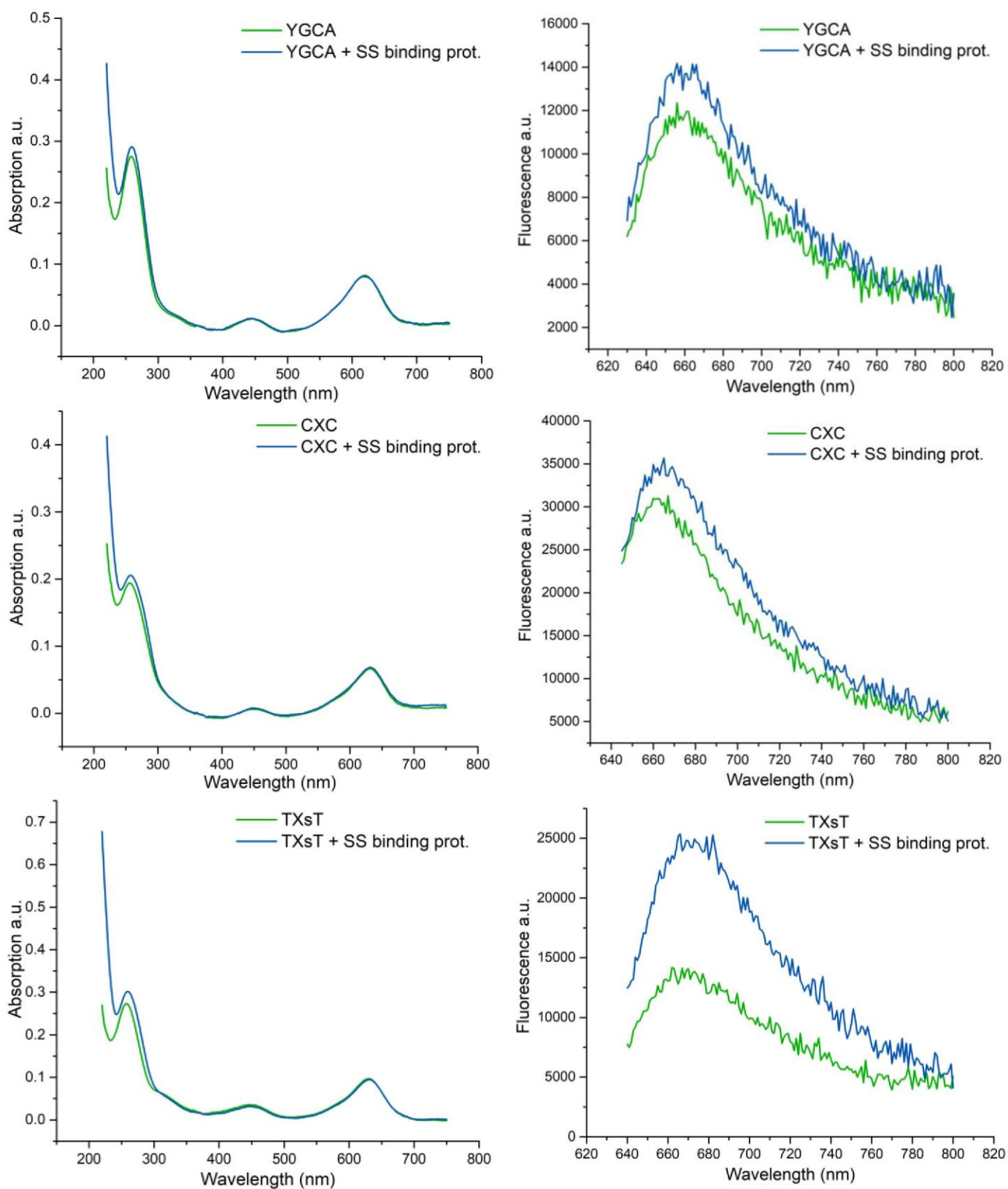


Table S5: : Sequence, Nature, Name and linker of the labeled ODNs with 2 or 5 used for the studies with the single strand binding protein.

Sequence	Name	Linker
5'- YGCA AAA TTT AAA ACG-3'	YGCA	
5'-CAG TCG CXC GCT GAC-3'	CXC	
5'-GCA AAA TXsT AAA ACG-3'	TXsT	
GGG TGG TGG TGG TGG TGG TGG XGG TGG TGG TGG TGG TGG TG	XGG	
5'-GCA AAA TWT AAA ACG-3'	TWT	

Figure S7: Absorption (left) and emission (right) spectra of the ssODNs and ssODNs with an excess of SS binding protein.



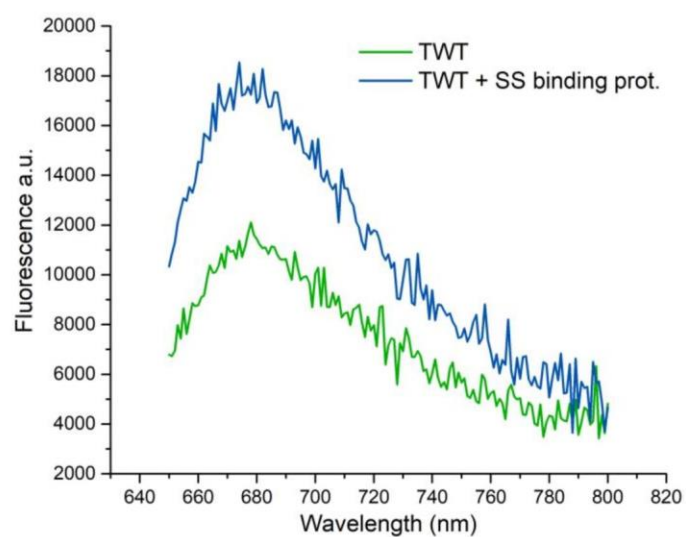
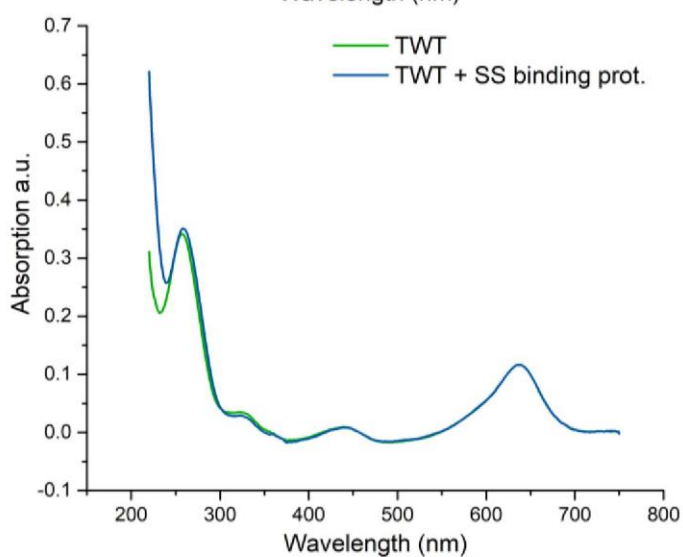
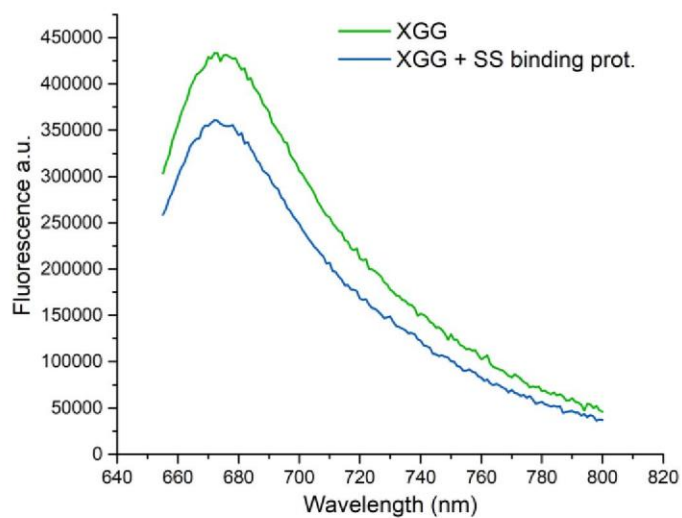
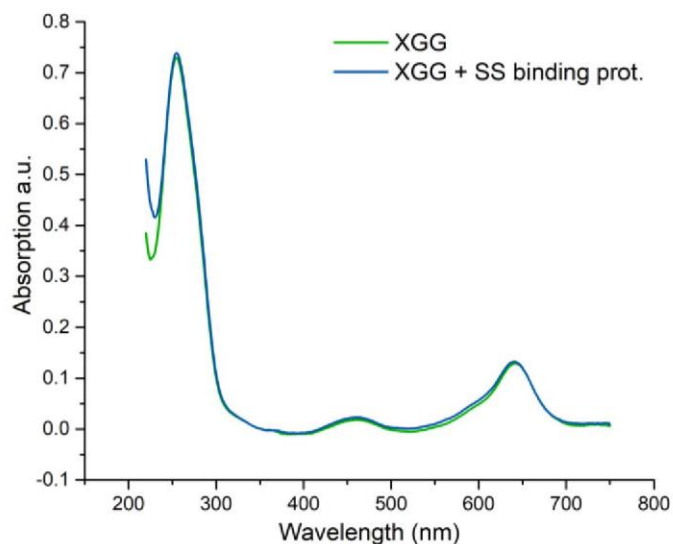


Table S6: Sequence, Nature, Name and linker of the labeled ODNs with 2 or 5 used for the studies with the single strand binding protein.

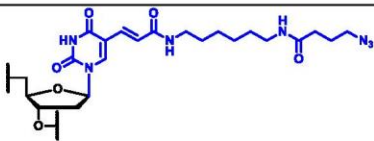
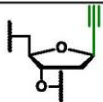
Sequence	Name	Linker
5'-CAG TCG CXC GCT GAC-3'	CXC	
5'-GCA AAA TWT AAA ACG-3'	TWT	

Figure S8: Absorption (left) and emission (right) spectra of the dsODNs and dsODNs with an excess of DS binding protein.

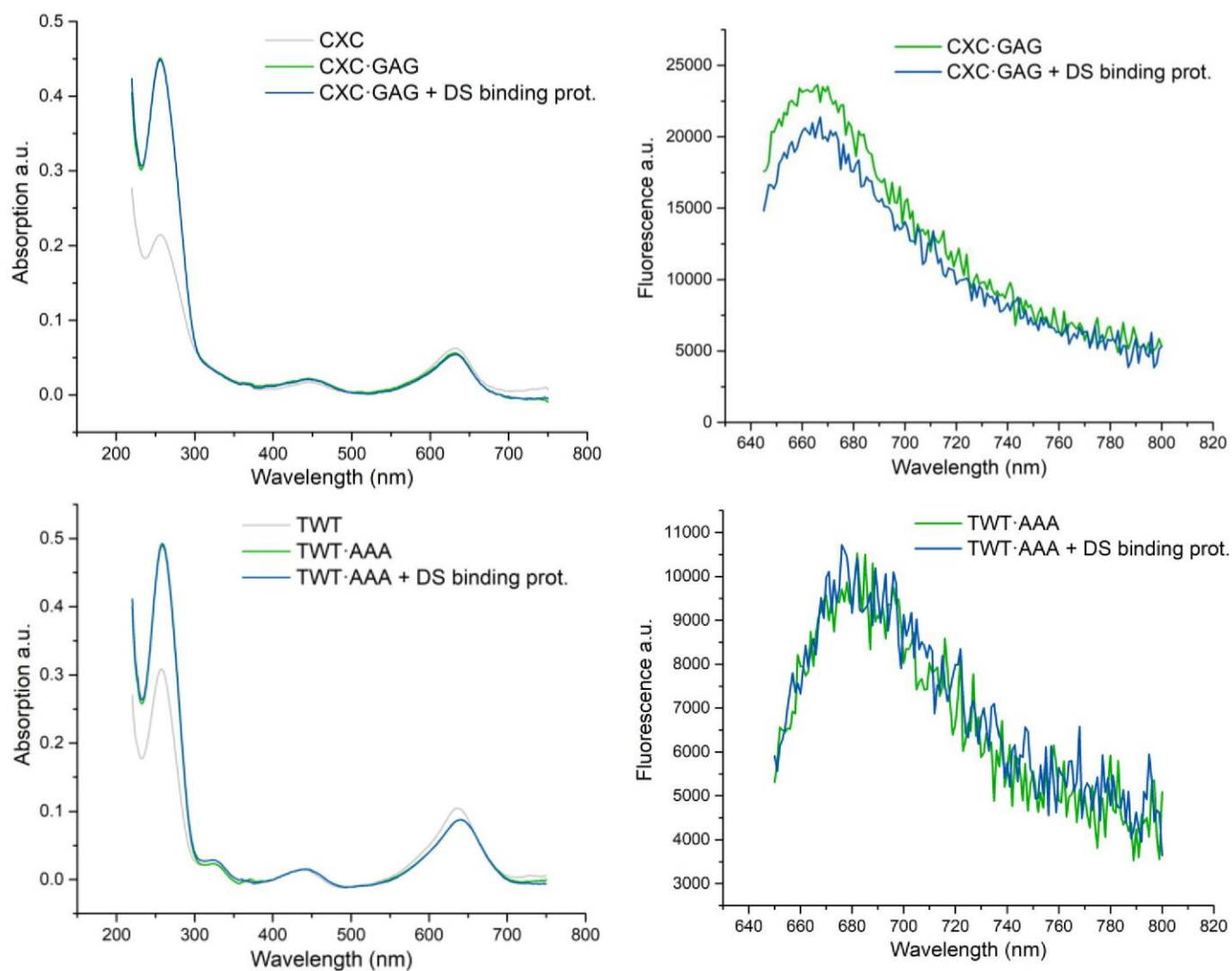


Table S7: Sequence, Nature, Name and linker of the labeled ODNs with 2 used for the studies with BSA.

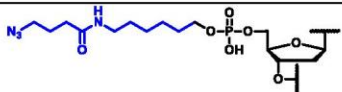
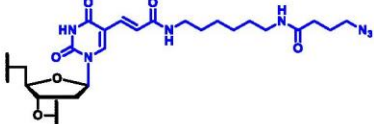
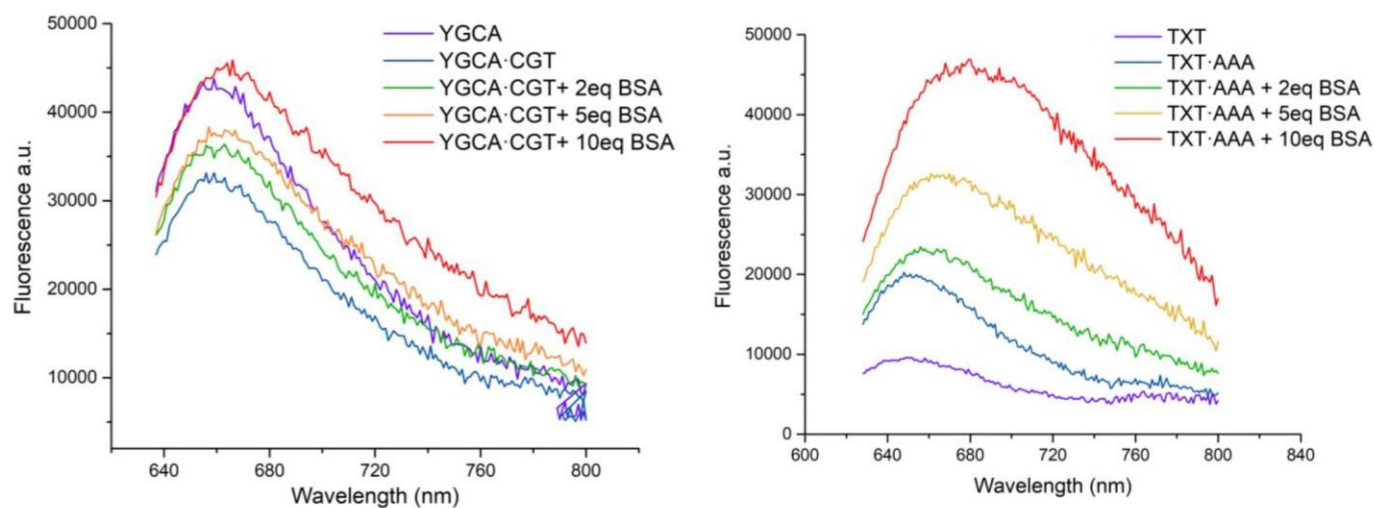
Sequence	Name	Linker
5'-YGCA AAA TTT AAA ACG-3'	YGCA	
5'-GCA AAA TXT AAA ACG-3'	TXT	

Figure S9: Emission spectra of the dsODNs and dsODNs with an excess of BSA protein.



References

1. Rurack, K. & Spies, M. Fluorescence Quantum Yields of a Series of Red and Near-Infrared Dyes Emitting at 600–1000 nm. *Anal. Chem.* **83**, 1232–1242 (2011).
2. Isak, S. J. & Eyring, E. M. Fluorescence quantum yield of cresyl violet in methanol and water as a function of concentration. *J. Phys. Chem.* **96**, 1738–1742 (1992).

V. Miami

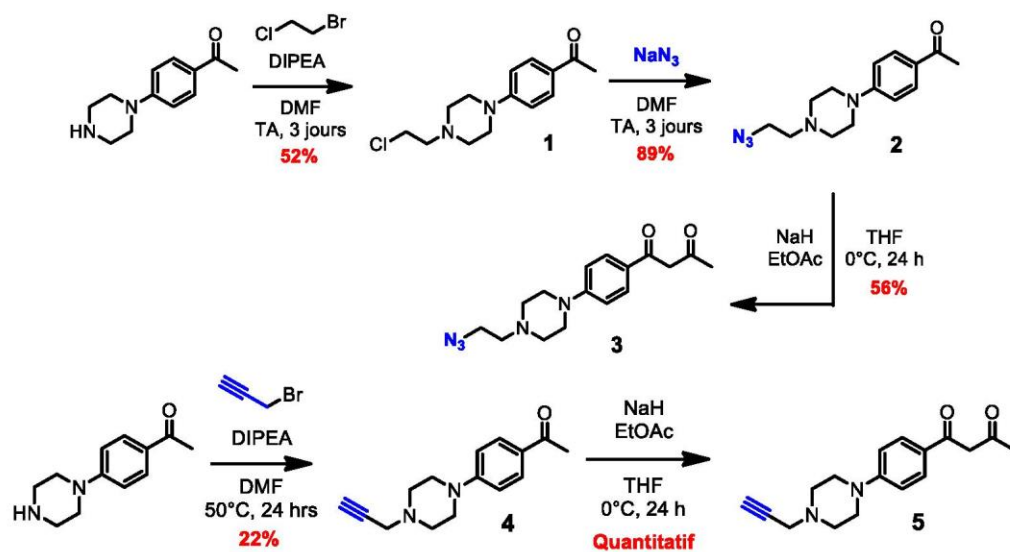
Partie Expérimentale du Chapitre 4 : Sondes Miami – Ligand et intercalant

Table of contents

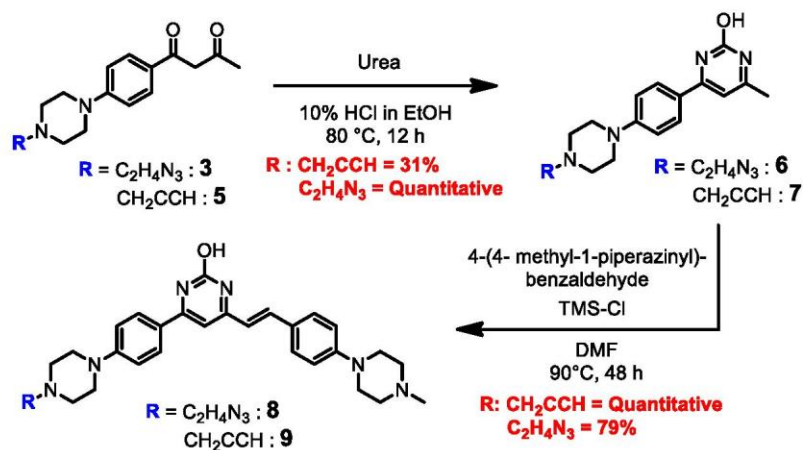
EXPERIMENTAL SECTION	2
1. SYNTHETIC PROCEDURES	2
2. PHOTOPHYSICAL CHARACTERIZATION	7
2.2 Hydration Study	7
2.3 pK_a Study	7
2.4 Emission Fluorescence Spectra	7
2.5 Photobleaching studies	8
3. MODEL ODNs SPECTROSCOPIC STUDIES	9
3.1 ODNs synthesis and purification	9
3.2 HRMS analysis of ODNs	10
3.3 Temperature-induced denaturation studies	10
3.4 Circular Dichroism	11
3.4 UV/visible & Fluorescence spectra	12
4. BIOLOGICAL APPLICATION	17
4.1 Steady-state fluorescence measurements	17
4.2 UV/visible & Fluorescence spectra of labeled ODNs before and after hybridization with the RNA or DNA target	19
4.3 UV & Fluorescence spectra for DNA target analog	21
NMR SPECTRA	25
REFERENCES	39

Experimental Section

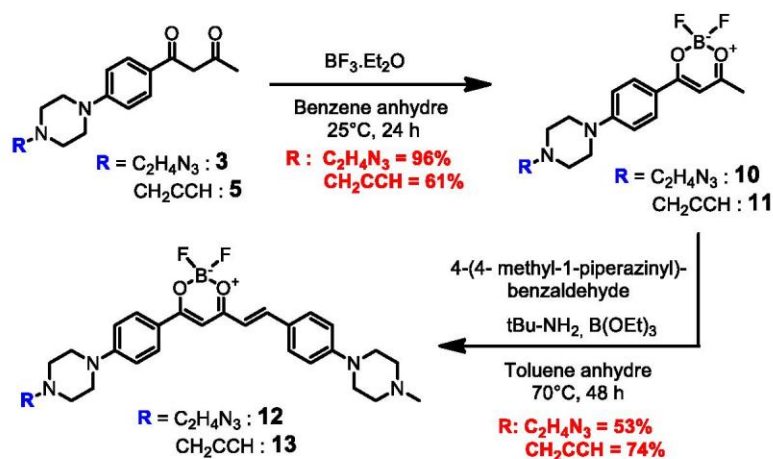
1. Synthetic Procedures



Scheme 1. Synthetic scheme of the intermediates



Scheme 2. Synthetic scheme of pyrimidine derivatives



Scheme 3. Synthetic scheme of organoborane derivatives

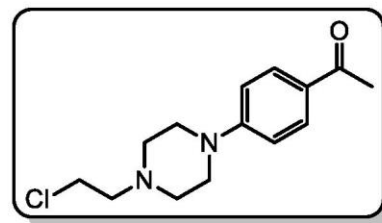
1-(4-(4-(2-chloroethyl)piperazin-1-yl)phenyl)ethenone: 1

1-Bromo-2-chloroethane (326 μL , 3.92 mmol, 1.60 eq.) and DIPEA (704 μL , 4.04 mmol, 1.65 eq.) were added to a solution 1-(4-(piperazin-1-yl)phenyl)ethanone (500 mg, 2.45 mmol, 1 eq.) in DMF (12 mL, 0.2 M) were), which was then stirred at RT for 3 days. The mixture was extracted with an aq. solution of LiCl (10% w/w) and DCM. The combined organic layers were dried over MgSO_4 , filtered, and concentrated under vacuum. The crude residue was purified by flash chromatography over silica gel (Cyclo/EtOAc, 90/10 \rightarrow 10/90) to give the desired product **1** as a white powder (337.6 mg, 1.26 mmol, 52%).

^1H NMR (CDCl_3 , 400 MHz): δ (ppm): 7.89 (d, $^3J = 9.0$ Hz, 2H), 6.88 (d, $^3J = 8.9$ Hz, 2H), 3.64 (t, $^3J = 6.9$ Hz, 2H), 3.44 – 3.34 (m, 4H), 2.81 (t, $^3J = 6.9$ Hz, 2H), 2.74 – 2.63 (m, 4H), 2.53 (s, 2H).

^{13}C -NMR (CDCl_3 , 101 MHz): δ (ppm): 196.7, 154.2, 130.5, 127.9, 113.6, 59.8, 52.9, 47.4, 41.0, 26.3.

HRMS (ESI $^+$): m/z calc for $\text{C}_{14}\text{H}_{19}\text{ClN}_2\text{OH}^+$: 267.1258 [M+H] $^+$; found: [M+H] $^+$: 267.12601 [M+H] $^+$



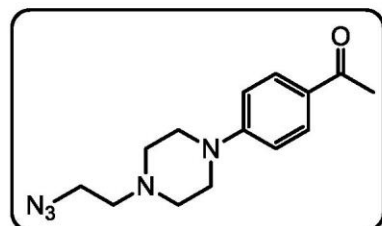
1-(4-(4-(2-azidoethyl)piperazin-1-yl)phenyl)ethenone: 2

A solution of compound of ketone **1** (200 mg, 0.75 mmol, 1 eq.) and NaN_3 (100 mg, 251 mg, 3.75 mmol, 5 eq.) in DMF (7.5 mL, 0.1 M) was stirred at RT for 3 days. Then the solution was extracted an aq. solution of LiCl (10% w/w) and DCM. The organic layers were dried over MgSO_4 , filtered, and concentrated under vacuo. The residue was purified by flash chromatography (SiO_2 , Cyclohexane/EtOAc, 90/10 \rightarrow 40/60) to give the desired product as a yellow oil (183 mg, 0.67 mmol, 89%).

^1H NMR (CDCl_3 , 400 MHz): δ (ppm): 7.87 (d, $^3J = 8.7$ Hz, 2H), 6.86 (d, $^3J = 8.7$ Hz, 2H), 3.38 (m, 6H), 2.65 (m, 6H), 2.52 (s, 3H).

^{13}C -NMR (CDCl_3 , 101 MHz): δ (ppm): 196.6, 154.2, 130.5, 127.8, 113.6, 57.3, 52.9, 48.3, 47.4, 26.2.

HRMS (ESI $^+$): m/z calc for $\text{C}_{14}\text{H}_{19}\text{N}_5\text{OH}^+$: 274.16624 [M+H] $^+$; found: [M+H] $^+$: 274.16691 [M+H] $^+$



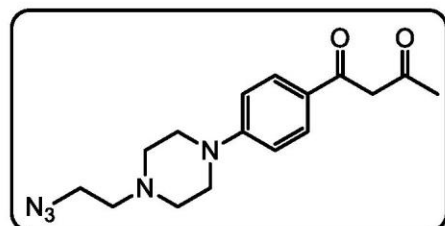
1-(4-(4-(2-azidoethyl)piperazin-1-yl)phenyl)butane-1,3-dione: 3

To a solution of ketone **2** (205 mg, 0.75 mmol, 1 eq.) in THF (2.5 mL, 0.3 M) at 0°C was added NaH (150 mg, 3.75 mmol, 5 eq.). The mixture was stirred for 15 min, cooled to 0°C before EtOAc (293 μL , 3.00 mmol, 4 eq.) was added dropwise. It was then stirred at RT for 24h and quenched with ice. The pH was raised to 7 by adding an aq. solution of HCl (1%). The mixture was extracted with DCM. The organic layers were combined, dried, filtered, and concentrated under vacuum. The crude extract was purified by flash chromatography over silica gel (Cyclohexane/EtOAc, 90/10 \rightarrow 10/90) to give the desired product **3** as a yellowish powder (132 mg, 0.42 mmol, 56%).

^1H NMR (CDCl_3 , 400 MHz): δ (ppm): 7.82 (d, $^3J = 8.9$ Hz, 2H), 6.89 (d, $^3J = 9.0$ Hz, 2H), 6.10 (s, 1H), 3.38 (m, 6H), 2.67 (m, 6H), 2.16 (s, 3H).

^{13}C -NMR (CDCl_3 , 101 MHz): δ (ppm): 190.7, 184.5, 153.9, 129.0, 124.7, 113.9, 95.4, 57.2, 52.9, 48.2, 47.5, 25.2.

HRMS (ESI $^+$): m/z calc for $\text{C}_{16}\text{H}_{21}\text{N}_5\text{O}_2\text{H}^+$: 316.17680 [M+H] $^+$; found: [M+H] $^+$: 316.17619 [M+H] $^+$



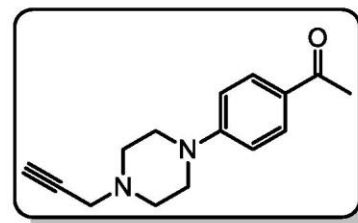
1-(4-(4-(prop-2-yn-1-yl)piperazin-1-yl)phenyl)ethenone: 4

Propargyl bromide (80% in toluene) (872 μL , 7.83 mmol, 1.6 eq.) and DIPEA (1.41 mL, 8.08 mmol, 1.65 eq.) were added to a solution of 1-(4-(piperazin-1-yl)phenyl)ethenone (1.0 g, 4.90 mmol, 1 eq.) in DMF (24.5 mL, 0.2 M) were added.), which was then stirred at 50°C for 24h. The mixture was cooled to RT, extracted with an aq. solution of LiCl (10% w/w) and DCM. The combined organic layers were dried over MgSO_4 , filtered, and concentrated under vacuum. The crude extract was purified by flash chromatography (SiO_2 , Cyclohexane/EtOAc, 90/10 \rightarrow 10/90) to give the desired product **4** as a white crystalline powder (288 mg, 1.08 mmol, 22%).

^1H NMR (CDCl_3 , 400 MHz): δ (ppm): 7.87 (d, $^3J = 9.0$ Hz, 1H), 6.87 (d, $^3J = 9.0$ Hz, 1H), 3.43 – 3.38 (m, 2H), 3.37 (d, $^4J = 2.4$ Hz, 1H), 2.78 – 2.66 (m, 2H), 2.28 (t, $^4J = 2.4$ Hz, 1H).

^{13}C -NMR (CDCl_3 , 101 MHz): δ (ppm): 196.5, 154.1, 130.4, 127.7, 113.5, 78.3, 73.6, 51.5, 47.3, 46.9, 26.1.

HRMS (ESI $^+$): m/z calc for $\text{C}_{15}\text{H}_{18}\text{N}_2\text{OH}^+$: 243.14919 [M+H] $^+$; found: [M+H] $^+$: 243.14992 [M+H] $^+$



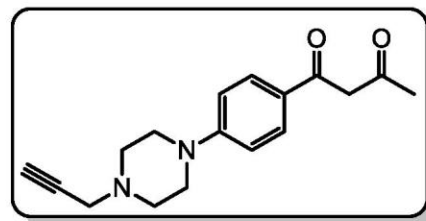
1-(4-(4-(prop-2-yn-1-yl)piperazin-1-yl)phenyl)butane-1,3-dione: 4

To a solution of ketone **4** (260 mg, 1.07 mmol, 1 eq.) in THF (3.6 mL, 0.3 M) at 0°C was added NaH (215 mg, 5.36 mmol, 5 eq.). The mixture was stirred for 15 min., cooled to 0°C before EtOAc (419 μ L, 4.29 mmol, 4 eq.) was added dropwise. After 24h stirring at RT, the mixture was quenched with ice and the pH was raised to 7 by adding an aq. solution of HCl (1%). The mixture was extracted with DCM. The organic layers were combined, dried, filtered, and concentrated under vacuum. The crude extract was purified by flash chromatography (SiO₂, Cyclohexane/EtOAc, 90/10 \rightarrow 10/90) to give the desired product **5** as a yellowish powder (Quantitative).

¹H NMR (CDCl₃, 400 MHz): δ (ppm): 7.81 (d, ³J = 9.0 Hz, 2H), 6.89 (d, ³J = 9.1 Hz, 2H), 6.08 (s, 1H), 3.39 (m, 6H), 2.91 – 2.62 (m, 4H), 2.28 (t, ⁴J = 2.4 Hz, 1H), 2.15 (s, 1H).

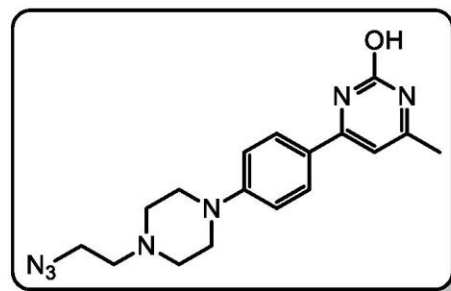
¹³C-NMR (CDCl₃, 101 MHz): δ (ppm): 190.8, 184.5, 153.9, 129.1, 124.9, 114.1, 95.5, 78.4, 73.7, 51.6, 47.5, 47.0, 25.3.

HRMS (ESI⁺): *m/z* calc for C₁₇H₂₀N₂O₂H⁺: 285.15975 [M+H]⁺; found: [M+H]⁺: 285.15886 [M+H]⁺



4-(4-(4-(2-azidoethyl)piperazin-1-yl)phenyl)-6-methylpyrimidin-2-ol: 6

In a 10 mL pressure tube equipped with a stirring bar, HCl (1.25 M in EtOH, 100 μ L) and urea (63 mg, 1.05 mmol, 6 eq.) were added to a solution of diketone **3** (55 mg, 0.17 mmol, 1 eq.) in *i*PrOH (0.5 mL, 0.38 M). The sealed tube was heated at 80°C and the mixture was stirred overnight. After completion of the reaction (checked by TLC), the reaction was cooled to RT and quenched with concentrated sodium hydroxide; to give a yellow precipitate, which was filtered and dried under vacuum (65mg, quantitative) to give **6**. Crude directly engaged in the next step.



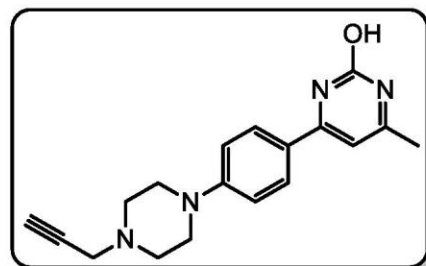
4-methyl-6-(4-(4-(prop-2-yn-1-yl)piperazin-1-yl)phenyl)pyrimidin-2-ol: 7

In a 10 mL pressure tube equipped with a stirring bar, urea (131.9 mg, 2.2 mmol, 5.6 eq.) and HCl (1.25 M in EtOH, 206 mL) were added to a solution of diketone **5** (112 mg, 0.39 mmol, 1 eq.) in *i*PrOH (1.1 mL, 0.38 M). The sealed tube was heated to 80°C under stirring. After overnight stirring (TLC monitoring), the reaction was cooled to room temperature and quenched with concentrated sodium hydroxide to give a precipitate, which was filtered and dried under vacuum to give the crude product **7** (38 mg, 0.123 mmol, 31%).

¹H NMR (CDCl₃, 400 MHz): δ (ppm): 11.57 (s, 1H), 7.96 (d, ³J = 8.8 Hz, 2H), 7.01 (d, ³J = 9.1 Hz, 2H), 6.78 (s, 1H), 3.34 (m, 6H), 3.18 (t, ³J = 2.4 Hz, 1H), 2.65 – 2.54 (m, 4H), 2.23 (s, 3H).

¹³C-NMR (DMSO-d₆, 101 MHz): 186.4, 181.4, 156.1, 149.2, 129.0, 126.7, 113.5, 104.0, 80.6, 72.2, 51.5, 49.0, 47.0, 25.4.

HRMS (ESI⁺): *m/z* calc for C₁₈H₂₀N₄O₄H⁺: 309.17099 [M+H]⁺; found: [M+H]⁺: 309.17167 [M+H]⁺



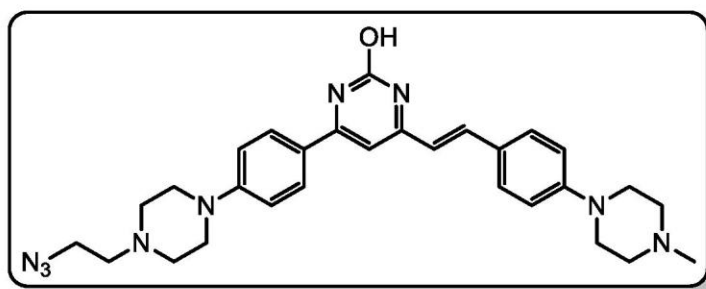
4-(4-(4-(2-azidoethyl)piperazin-1-yl)phenyl)-6-(4-(4-methylpiperazin-1-yl)styryl)pyrimidin-2-ol: 8

In a 10 mL pressure tube under Ar equipped with a stirring bar, 4-(4-methyl-1-piperazinyl)-benzaldehyde (27.4 mg, 0.13 mmol, 1.3 eq.) and TMSCl (249 μ L, 1.96 mmol, 19 eq.) were added to a solution of pyrimidinol **6** (35 mg, 0.10 mmol, 1 eq.) in dry DMF (1.0 mL, 0.1 M). The tube was sealed, the mixture was heated to 90 °C and stirred for 2 days under an Ar atmosphere. After cooling to room temperature, the volatiles were evaporated. The resulting solid was washed with Et₂O and several times with ACN (x5). The solid was washed several times with THF under sonication and centrifuged to give the clean desired product **8** as a purple solid (43 mg, 0.082 mmol, 79%).

¹H NMR (CDCl₃, 400 MHz): δ (ppm): 7.78 (d, ³J = 9.0 Hz, 2H), 7.67 (d, ³J = 16.0 Hz, 1H), 7.52 (d, ³J = 8.8 Hz, 2H), 7.09 (d, ³J = 9.1 Hz, 2H), 6.92 – 6.85 (m, 3H), 6.50 (d, ³J = 16.0 Hz, 1H), 3.86 (m, 6H), 3.51 (m, 4H), 3.39 – 3.33 (m, 2H), 3.05 (m, 6H), 2.87 (m, 5H).

¹³C-NMR (DMSO-d₆, 101 MHz): 183.2, 175.7, 156.1, 151.5, 145.1, 133.4, 129.6, 129.2, 129.2, 128.7, 128.6, 117.2, 114.0, 113.0, 59.1, 56.8, 52.2, 46.9, 46.0, 45.2, 41.9.

HRMS (ESI⁺): *m/z* calc for C₂₉H₃₅N₉O₄H⁺: 526.30373 [M+H]⁺; found: 526.30408 [M+H]⁺



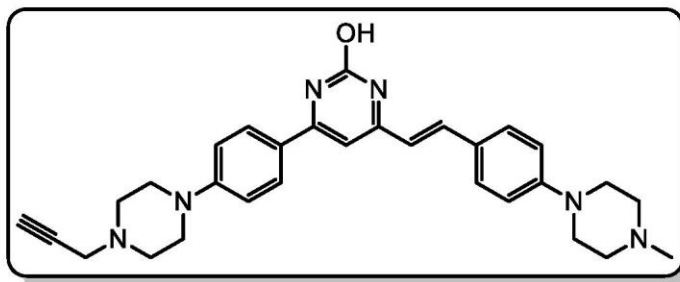
4-(4-(4-methylpiperazin-1-yl)styryl)-6-(4-(4-(prop-2-yn-1-yl)piperazin-1-yl)phenyl)pyrimidin-2-ol: 9

In a 10 mL pressure tube equipped with a stirring bar, 4-(4-methyl-1-piperazinyl)-benzaldehyde (32.7 mg, 0.16 mmol, 1.3 eq.) and TMSCl (297 μ L, 2.34 mmol, 19 eq.) were added to a solution of pyrimidinol 7 (38 mg, 0.12 mmol, 1 eq.) in dry DMF (1.23 mL, 0.1 M). The tube was sealed, and the mixture was heated to 90°C and stirred for 2 days. The reaction was cooled to room temperature and quenched with a minimum of concentrated sodium hydroxide solution. The mixture was then dry concentrated and the residue purified over flash chromatography column (SiO₂, DCM/MeOH/TEA, 100/0/0 --> 80/20/1) to give the desired product 9 as an orange solid (Quantitative).

¹H NMR (Acetic Acid-d⁴, 400 MHz): δ (ppm): 8.03 (d, ³J = 9.0 Hz, 2H), 7.91 (d, ³J = 16.1 Hz, 1H), 7.69 (d, ³J = 9.0 Hz, 2H), 7.14 (s, 1H), 7.10 (m, 4H), 6.92 (d, ³J = 16.1 Hz, 1H), 3.73 (m, 4H), 3.71 (d, ⁴J = 2.5 Hz, 2H), 3.66 (m, 4H), 3.44 (m, 4H), 3.11 (m, 4H), 2.96 (s, 3H), 2.75 (t, ⁴J = 2.5 Hz, 1H).

¹³C-NMR (DMSO-d₆, 101 MHz): δ (ppm): 163.8, 157.1, 154.3, 152.9, 150.6, 133.9, 129.7, 129.5, 128.1, 127.9, 126.8, 113.8, 112.92, 112.6, 79.4, 73.3, 55.9, 55.1, 50.2, 49.8, 46.8, 46.5.

HRMS (ESI⁺): *m/z* calc for C₃₀H₃₄N₆OH⁺: 495.28668 [M+H]⁺; found: 495.28668 [M+H]⁺; 495.28627 [M+H]⁺



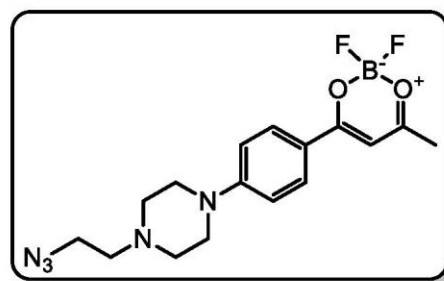
4-(4-(4-(2-azidoethyl)piperazin-1-yl)phenyl)-2,2-difluoro-6-methyl-2H-1,3,2-dioxaborinin-1-ium-2-uide: 10

In a 10 mL pressure tube, boron trifluoride diethyl etherate (861 μ L, 6.98 mmol, 11 eq.) was added slowly to a solution of diketone 3 in benzene (1.7 mL, 0.38 M). The tube was sealed. The mixture was stirred at RT for 24h. During the addition a precipitate formed that dissolved during the reaction time. Then the excess of boron trifluoride diethyl etherate was let evaporated by itself for 15 min under the hood. When the tube is not fuming anymore, benzene was evaporated. The residue was triturated with Et₂O to precipitate the product. If product purity is insufficient after precipitation, the precipitate was purified by flash chromatography (SiO₂, DCM/MeOH, 100/0 \rightarrow 95/5) to give the desired product 10 as an orange solid (220.9 mg, 0.608 mmol, 96%).

¹H NMR (DMSO-d₆, 400 MHz): δ (ppm): 8.50 (d, ³J = 9.2 Hz, 2H), 7.59 (d, ³J = 9.2 Hz, 2H), 7.46 (s, 1H), 4.70 (m, 2H), 4.30 (m, 2H), 4.03 (m, 4H), 3.78 (m, 4H), 2.76 (s, 2H).

¹³C-NMR (DMSO-d₆, 101 MHz): δ (ppm): 188.51, 179.77, 154.44, 131.77, 113.76, 96.16, 59.75, 54.21, 50.70, 44.79, 23.79.

HRMS (ESI⁺): *m/z* calc for C₁₆H₂₀BF₂N₅O₂H⁺: 364.17509 [M+H]⁺; found: [M+H]⁺: 364.17479 [M+H]⁺



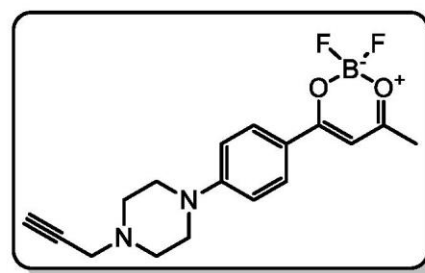
2,2-difluoro-6-methyl-4-(4-(4-(prop-2-yn-1-yl)piperazin-1-yl)phenyl)-2H-1,3,2-dioxaborinin-1-ium-2-uide: 11

In a 10 mL pressure tube, boron trifluoride diethyl etherate (819 μ L, 6.64 mmol, 11 eq.) slowly was added slowly to a solution of diketone 5 (171.6 mg, 0.60 mmol, 1 eq.) in benzene (1.72 mL, 0.35 M). The tube was sealed. The mixture was stirred at RT for 24h. During the addition a precipitate formed that dissolved during the reaction time. Then the excess of boron trifluoride diethyl etherate was let evaporated by itself for 15 min under the hood. When the tube is not fuming anymore, benzene was evaporated. The residue was triturated with Et₂O to precipitate the product. If product purity is insufficient after precipitation, the precipitate was purified by flash chromatography (SiO₂, DCM/MeOH, 100/0 \rightarrow 95/5) to give the desired product 11 as an orange solid (122.2 mg, 0.368 mmol, 61%).

¹H NMR (CDCl₃, 400 MHz): δ (ppm): 8.01 (d, ³J = 9.3 Hz, 1H), 7.08 (d, ³J = 9.3 Hz, 1H), 6.95 (s, 1H), 3.68 – 3.46 (m, 2H), 3.35 (d, ⁴J = 2.2 Hz, 2H), 3.19 (t, ⁴J = 2.2 Hz, 1H), 2.67 – 2.51 (m, 2H), 2.30 (s, 1H).

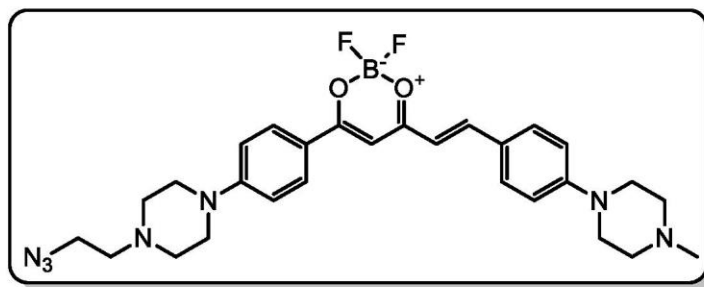
¹³C-NMR (CDCl₃, 101 MHz): δ (ppm): 186.94 (s), 179.41 (s), 155.40 (s), 131.94 (s), 117.21 (s), 113.12 (s), 95.76 (s), 78.94 (s), 76.05 (s), 50.71 (s), 45.89 (s), 45.83 (s), 23.62 (s).

HRMS (ESI⁺): *m/z* calc for C₁₇H₁₉BF₂N₂O₂H⁺: 333.15804 [M+H]⁺; found: [M+H]⁺: 333.15833 [M+H]⁺



4-(4-(4-(2-azidoethyl)piperazin-1-yl)phenyl)-2,2-difluoro-6-(4-(4-methylpiperazin-1-yl)styryl)-2H-1,3,2-dioxaborinin-1-ium-2-uide: 12

In a 10 mL pressure tube, 4-(4-methyl-1-piperazinyl)-benzaldehyde (124 mg, 0.61 mmol, 1.1 eq.), triisopropyl borate (146 μ L, 0.63 mmol, 1.15 eq.) and then tert-butylamine (64 μ L, 0.61 mmol, 1.1 eq.) were added to a solution of compound **10** (200 mg, 0.55 mmol, 1 eq.) in dry toluene (1.84 mL, 0.3 M). The tube was sealed. The mixture was stirred at 70°C for 24h. After cooling to RT the reaction



was concentrated under reduced pressure. The resulting residue was purified by flash chromatography over silica gel (DCM/MeOH, 100/0 \rightarrow 90/10) to give the desired product **12** as a purple solid (159.4 mg, 0.29 mmol, 53%).

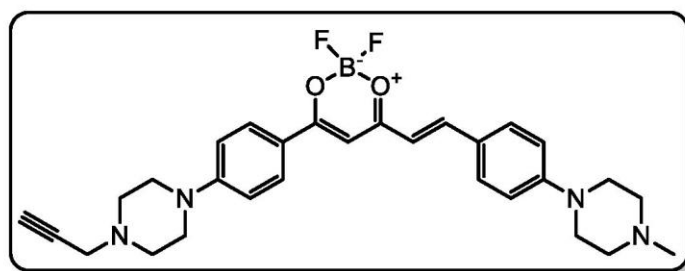
$^1\text{H NMR}$ (CD_2Cl_2 , 400 MHz): δ (ppm): 7.97 (d, $^3J = 9.2$ Hz, 2H), 7.90 (d, $^3J = 15.5$ Hz, 1H), 7.55 (d, $^3J = 8.9$ Hz, 2H), 6.93 – 6.89 (m, 4H), 6.61 (d, $^3J = 15.4$ Hz, 1H), 6.45 (s, 1H), 3.50 – 3.47 (m, 4H), 3.40 – 3.35 (m, 8H), 2.67 – 2.63 (m, 8H), 2.58 – 2.56 (m, 4H).

$^{13}\text{C-NMR}$ (CD_2Cl_2 , 101 MHz): δ (ppm): 178.85 (s), 177.49 (s), 155.19 (s), 153.21 (s), 145.30 (s), 131.06 (s), 130.95 (s), 124.33 (s), 120.15 (s), 116.61 (s), 114.35 (s), 113.10 (s), 95.81 (s), 57.02 (s), 54.51 (s), 52.60 (s), 48.18 (s), 47.02 (s), 46.69 (s), 45.62 (s).

HRMS (ESI $^+$): m/z calc for $\text{C}_{28}\text{H}_{34}\text{BF}_2\text{N}_7\text{O}_2\text{H}^+$: 550.29079 [M+H] $^+$; found: 550.29108 [M+H] $^+$

2,2-difluoro-6-(4-(4-methylpiperazin-1-yl)styryl)-4-(4-(4-(prop-2-yn-1-yl)piperazin-1-yl)phenyl)-2H-1,3,2-dioxaborinin-1-ium-2-uide: 13

In a 10 mL pressure tube, 4-(4-methyl-1-piperazinyl)-benzaldehyde (81 mg, 0.40 mmol, 1.1 eq.), triisopropyl borate (96 μ L, 0.42 mmol, 1.15 eq.) and then tert-butylamine (42 μ L, 0.40 mmol, 1.1 eq.) were added to a solution of compound **11** (120 mg, 0.36 mmol, 1 eq.) in dry toluene (1.20 mL, 0.3 M). The tube was sealed. The mixture was stirred at 70°C for 24h.



After cooling to RT the solution was concentrated under reduced pressure. The resulting residue was purified by flash chromatography over silica gel (DCM/MeOH, 100/0 \rightarrow 90/10) to give the desired product **13** as a purple powder (139.1 mg, 0.268 mmol, 74%).

$^1\text{H NMR}$ (CD_2Cl_2 , 400 MHz): δ (ppm): 7.97 (d, $^3J = 9.2$ Hz, 1H), 7.90 (d, $^3J = 15.4$ Hz, 1H), 7.55 (d, $^3J = 8.9$ Hz, 1H), 6.91 (m, 2H), 6.61 (d, $^3J = 15.4$ Hz, 1H), 6.45 (s, 1H), 3.53 – 3.47 (m, 2H), 3.36 (m, 3H), 2.73 – 2.65 (m, 2H), 2.56 – 2.48 (m, 2H), 2.32 (t, $^4J = 2.5$ Hz, 1H), 2.30 (s, 1H).

$^{13}\text{C-NMR}$ (CD_2Cl_2 , 101 MHz): δ (ppm): 179.39 (s), 178.13 (s), 155.72 (s), 153.93 (s), 145.98 (s), 131.62 (s), 131.55 (s), 124.74 (s), 120.77 (s), 117.04 (s), 114.82 (s), 113.72 (s), 96.35 (s), 78.96 (s), 73.74 (s), 55.26 (s), 51.73 – 51.07 (m), 47.78 (s), 47.25 (s), 47.21 (s), 46.42 (s).

HRMS (ESI $^+$): m/z calc for $\text{C}_{29}\text{H}_{33}\text{BF}_2\text{N}_4\text{O}_2\text{H}^+$: 519.27374 [M+H] $^+$; found: 519.27521 [M+H] $^+$

2. Photophysical characterization

2.2 Hydration Study

Table S1. Hydration study.

Hydration rate (%)	$\lambda_{\text{abs}}^{\text{b}}$ (nm)		$\lambda_{\text{em}}^{\text{c}}$ (nm)		Stokes shift (nm)		Φ (%) ^d	
	8	12	8	12	8	12	8	12
0	392	516	521	601	129	85	25	87
1	396	517	546	605	150	88	24	73
2	402	-	555	-	153	-	23	-
5	414	519	572	615	158	96	19	42
10	419	521	583	620	164	99	17	30
15	-	522	-	623		101	-	26
20	423	523	589	625	166	102	14	23
50	429	526	599	633	170	107	10	14
75	427	524	607	631	180	107	4	7
90	420	517	601	622	181	105	2	5

^aPosition of the absorption band maximum; ^bPosition of the emission maximum; ^cQuantum yield determined using *Nile Blue* in EtOH ($\Phi = 0.27$) as reference¹.

2.3 pK_a Study

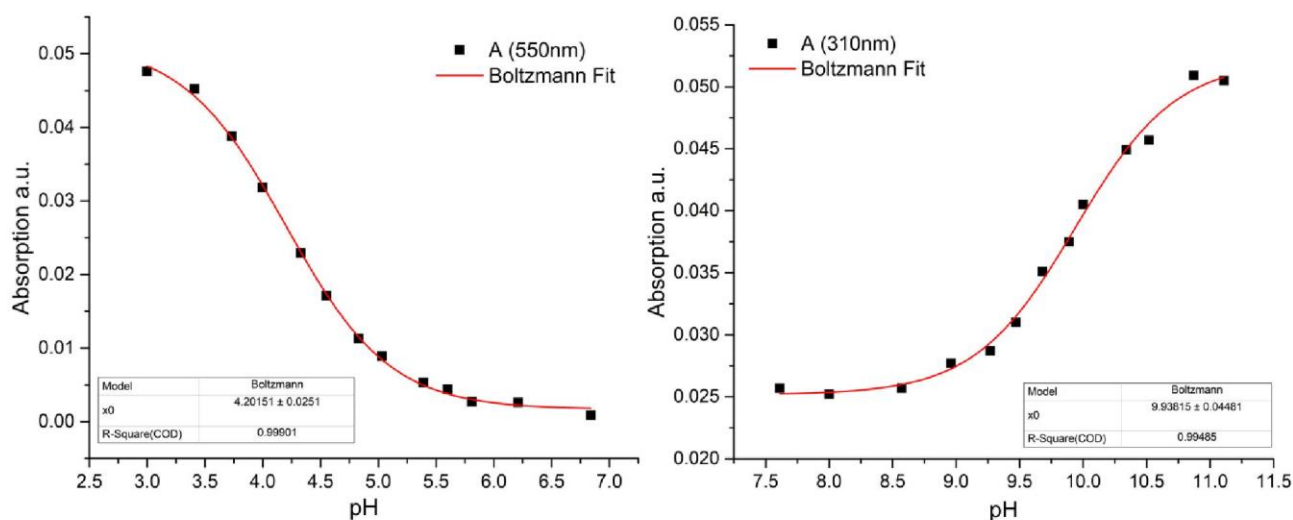


Figure S1. pH titration curves of 8: Acidic pH (left), basic pH (right).

2.4 Emission Fluorescence Spectra

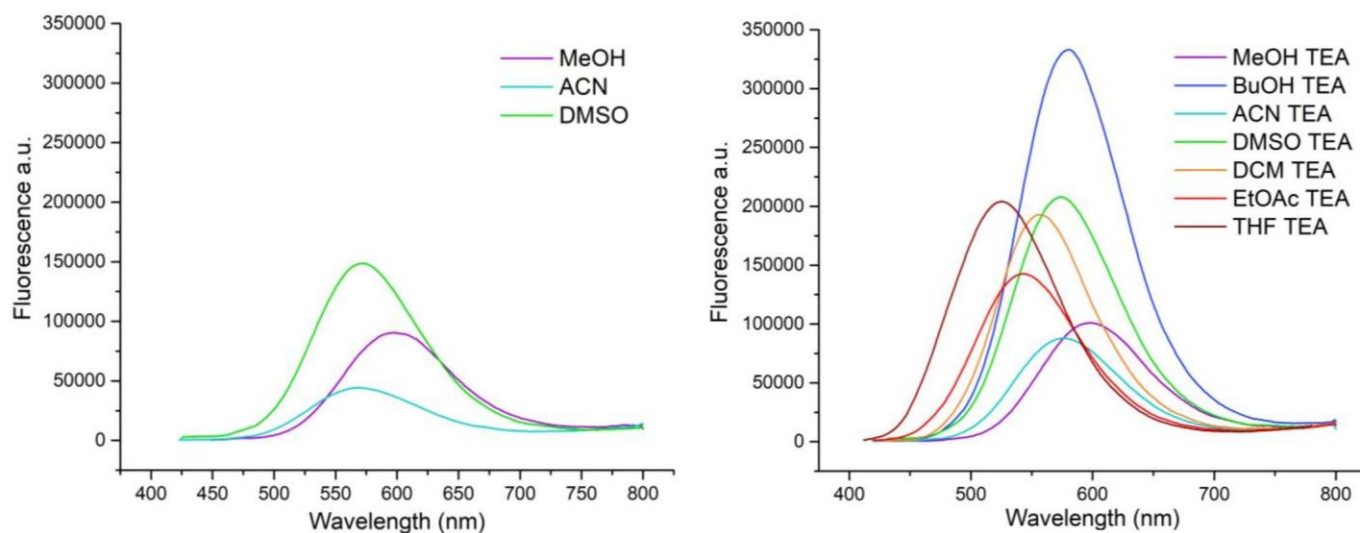


Figure S2. Fluorescence emission spectra of 8 without TEA (left) and with TEA (right)

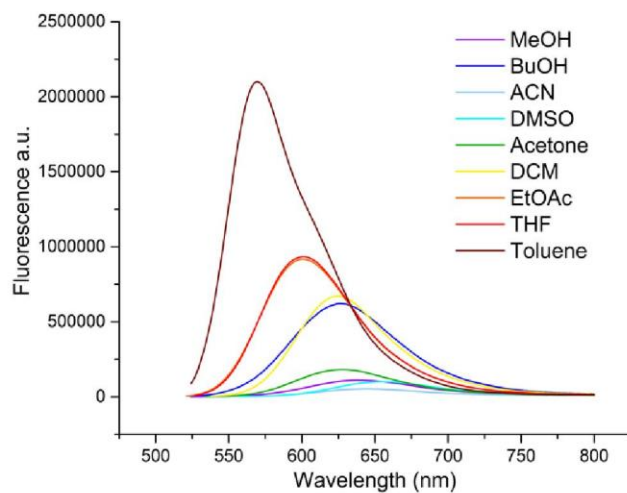


Figure S3. Fluorescence emission spectra of 12

2.5 Photobleaching studies

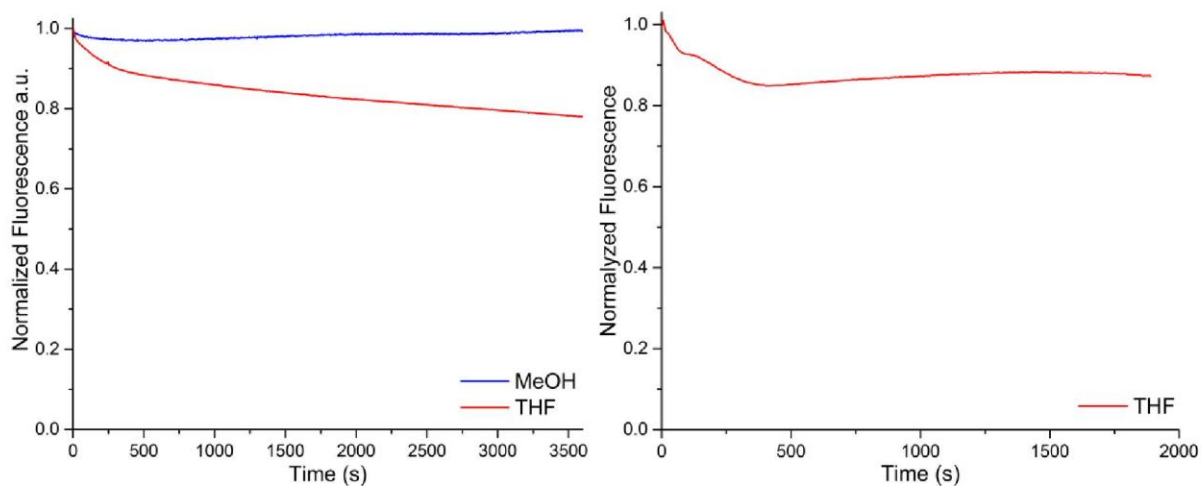


Figure S4. Photobleaching studies of 8 (left) & 9 (right)

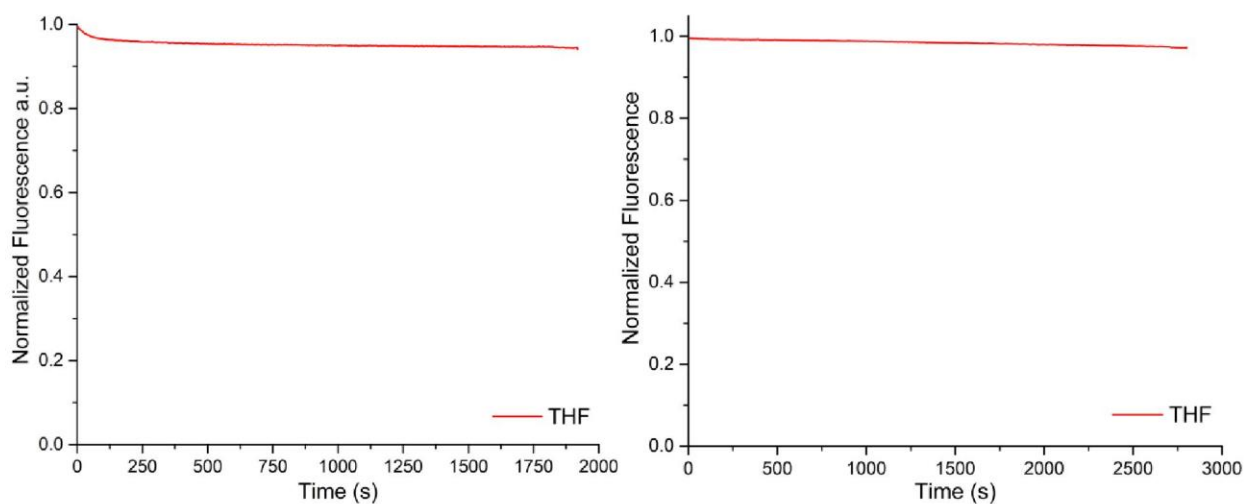


Figure S5. Photobleaching studies of 12 (left) & 13 (right)

3. Model ODNs spectroscopic studies

3.1 ODNs synthesis and purification

General method:

Wild-type and clickable ODNs were purchased from Microsynth AG and IBA Lifesciences. The ODNs were ordered purified and ready to use.

Typical procedure:

Firstly, a 5 mM stock solution (in H₂O) of CuSO₄·5H₂O and BTTES ligand was made.

In a 200 μL vial was added sequentially the ODN sequence (0.2 mM (in H₂O), 50 μL, 10 nmol, 1 eq.), DMSO (20 μL), probe (10 μL (5.0 mM in DMSO), 50 nmol, 5 eq.), sodium ascorbate (10 μL (5.0 mM in H₂O), 50 nmol, 5 eq.) and finally CuSO₄/BTTES mixture (10 μL (5 mM each in H₂O), 50 nmol, 5 eq.). The mixture was agitated on a Vortex overnight at room temperature. The solution was then recovered, and the vial was washed with a minimum of H₂O and DMSO. The whole was combined for HPLC purification. The ODNs were analyzed (0.5 mL/min) and purified (2.0 mL/min) by RP HPLC (Apparatus: Waters™ 600 Controller with Waters™ 996 Photodiode Array Detector. Columns: analytical, 300 × 4.60 mm, 5 μm particle size, Clarity® 100Å, Phenomenex®, semi-preparative, Clarity® 5u Oligo-RP column 250 x 10 mm Phenomenex®). The following gradient system was used:

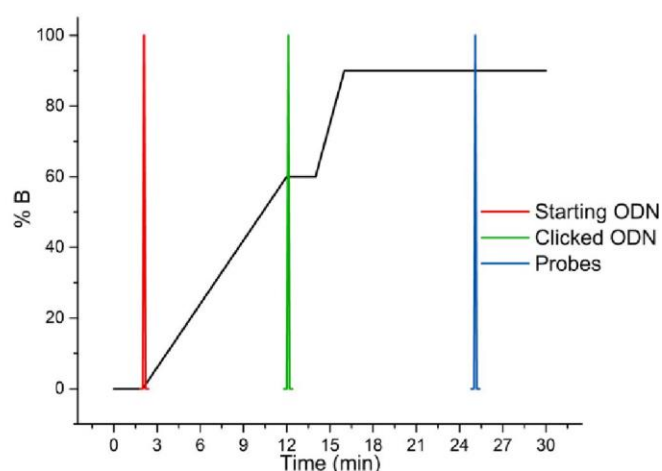
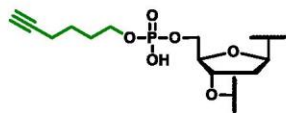
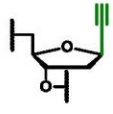
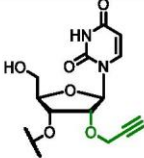
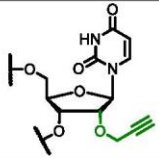


Figure S6. HPLC gradient and retention times of the compounds from the click reaction.

Gradient: 100% A for 2 min → 40% A: 60% B during 10min then keep it for 2 min → 10% A: 90% B during 2 min then keep it for 14 min. A = Buffer pH 7.0 (90% TEAB buffer 100nM:10% CH₃CN) and B = 90% CH₃CN:10% Buffer A

Table S2. Sequence, name, extinction coefficient and chemical structures of the purchased ODN.

Sequences	Names	Extinction coefficient (L.mol ⁻¹ .cm ⁻¹)	Base modification
5'-YGCA AAA TTT AAA ACG-3'	YGCA	158,100	
5'-GCA AAA TXT AAA ACG-3'	TXT	157,400	
5'-GCA AAA AAA AXA AAA AAA ACG-3'	AXA	238,600	
5'-GCA AAA TXsT AAA ACG-3'	TXsT	157,400	

5'- VGCA AAA TTT AAA ACG-3'	VGCA	158,100	
5'-GCA AAA TWT AAA ACG-3'	TWT	149,600	
5'-GCA AAA AAA AWA AAA AAA ACG-3'	AWA	255,800	
5'- SGCA AAA TTT AAA ACG-3'	SGCA	146,600	
5'-GCA AAA TST AAA ACG-3'	TST	133,200	

3.2 HRMS analysis of ODNs

Table S3. Masses of single strands DNA tagged with 9 & 13.

ODN	Sequence	HRMS found (calc) [M-H] ⁻	
		9	13
YGCA	5'- YGCA AAA TTT AAA ACG-3'	1791.41101(1791.40655)	1799.40601(1799.40224)
TXT	5'-GCA AAA TXT AAA ACG-3'	1783.08496(1783.08638)	1791.08423(1791.08206)
AXA	5'-GCA AAA AAA AXA AAA AAA ACG-3'	2414.86098(2414.87755)	2422.84976(2422.87324)
TXsT	5'-GCA AAA TXsT AAA ACG-3'	(1764.39885)	(1772.06008)

Table S4. Masses of single strands DNA tagged with 8 & 12

ODN	Sequence	HRMS found (calc) [M-H] ⁻	
		8	12
VGCA	5'- VGCA AAA TTT AAA ACG-3'	(1758.04930)	1766.04834(1766.04498)
TWT	5'-GCA AAA TWT AAA ACG-3'	(1666.69201)	(1674.68769)
AWA	5'-GCA AAA AAA AWA AAA AAA ACG-3'	2303.47424(2303.48952)	2311.46980(2311.48520)
SGCA	5'- SGCA AAA TTT AAA ACG-3'	1819.72180(1819.72109)	1827.71814(1827.71677)
TST	5'-GCA AAA TST AAA ACG-3'	1718.03979(1718.03796)	1726.03503(1726.03364)

3.3 Temperature-induced denaturation studies

Table S5. T_ms of labeled duplexes compare to wild types

Duplexe	T _m (°C)	ΔT _m (°C) ^b
AWA 8	48.4	-6.4
AWA 12	49.9	-4.9
AXA 9	50.8	-4.0
AXA 13	53.1	-1.7
Wild Type ^a	[54.8]	/

^a T_m of the corresponding duplex formed from unmodified ODNs and its theoretical values given in square brackets. ^b ΔT_m refers to the difference of T_m between the labeled and wild type dsODNs.

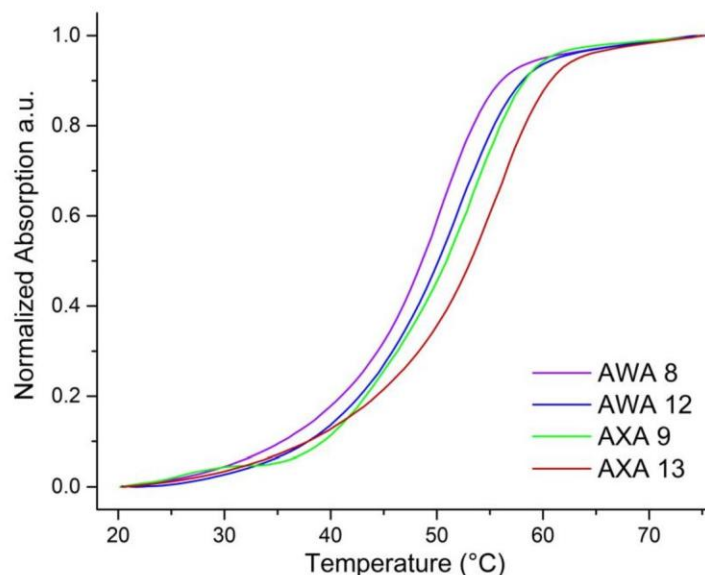


Figure S7. Melting curves

3.4 Circular Dichroism

Circular dichroism spectra were recorded in duplicate with 2 μM solution of the canonical dsDNA and labelled dsDNA in buffer pH 7.0 (PBS buffer, 150 mM NaCl) at 20 $^{\circ}\text{C}$ on a Jasco J-810 spectropolarimeter. Two maxima, typical for B-DNA duplexes, were observed in CD spectra: one negative at 249 nm and the other positive at 282 nm.

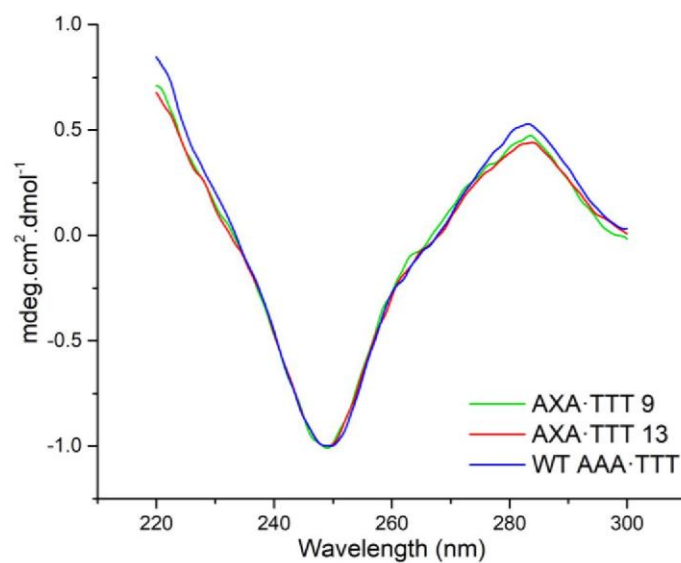
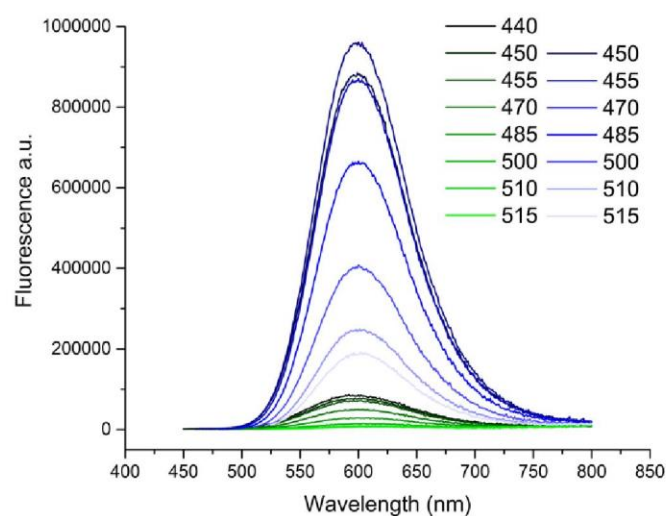
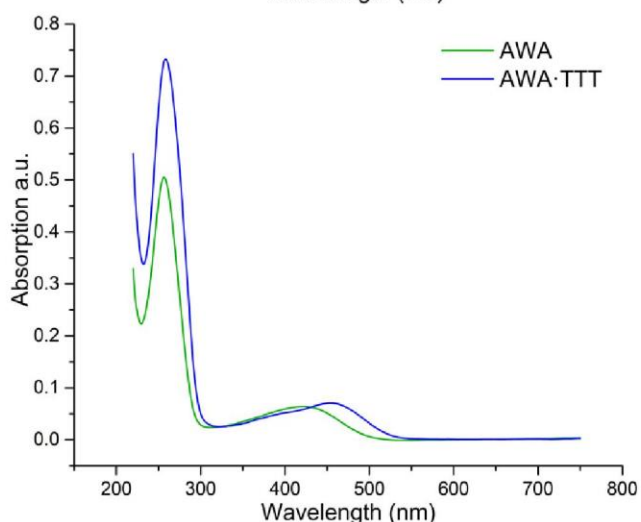
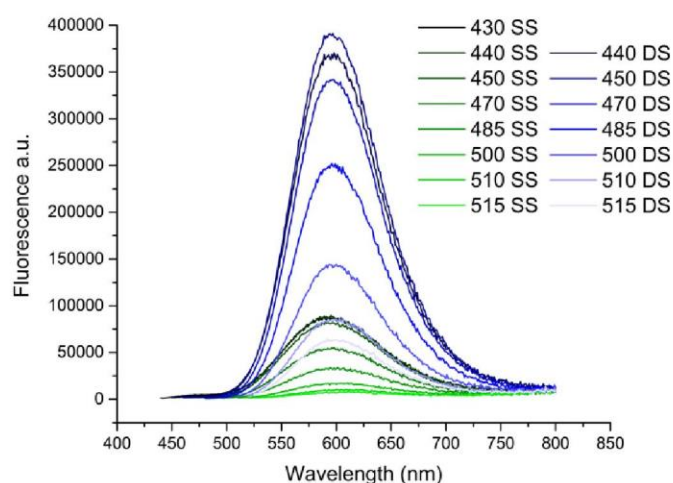
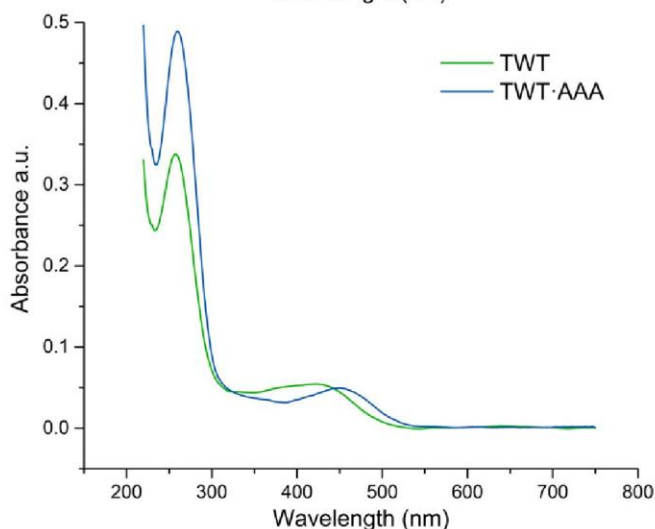
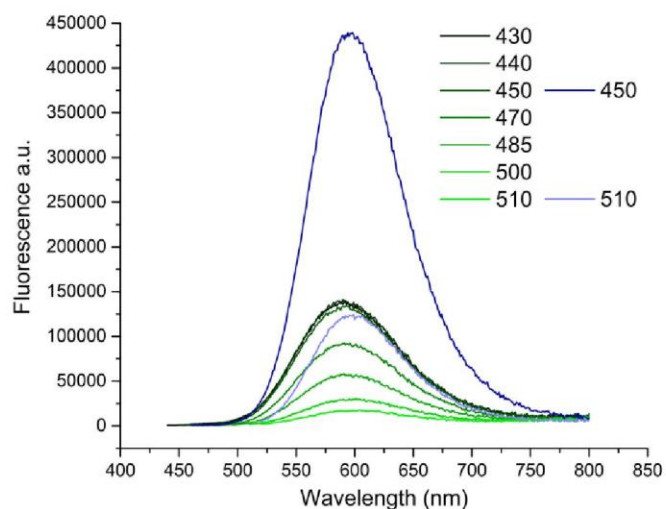
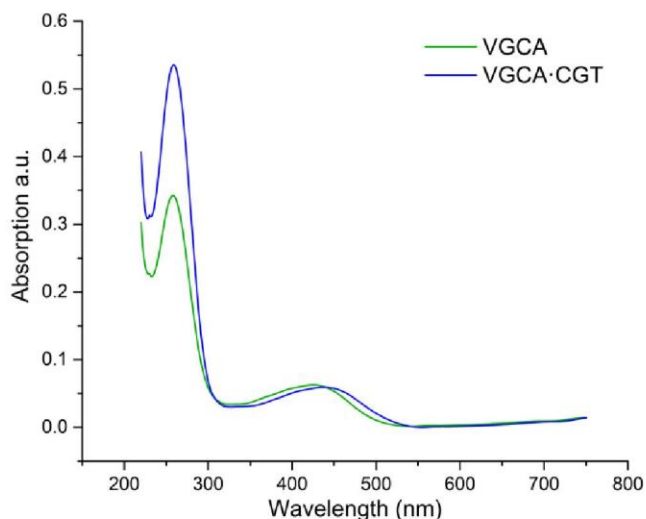


Figure 8: Representative CD spectra of the AXA-TTT duplex labeled with 9 or 13 compared to the wild type duplex AAA-TTT.

3.4 UV/visible & Fluorescence spectra

The absorption and fluorescence experiments were realized in duplicate in solvent of spectroscopic grade. The absorption spectra were recorded on a Cary 300 Scan spectrophotometer (Varian) using 1cm quartz cells at 25°C. The fluorescence spectra were recorded on a FluoroMax 4.0 spectrofluorometer (Jobin Yvon, Horiba) by using excitation and emission slits of 2 nm and were corrected at excitation and emission. They were taken with absorbance of about 0.05 at 25°C at the excitation wavelength mentioned in the corresponding experiments. The quantum yields were corrected according to the variation of the refractive index of the different solvents. Quantum yields were determined by using *Nile Blue* in EtOH ($\Phi = 0.27$) as reference¹.



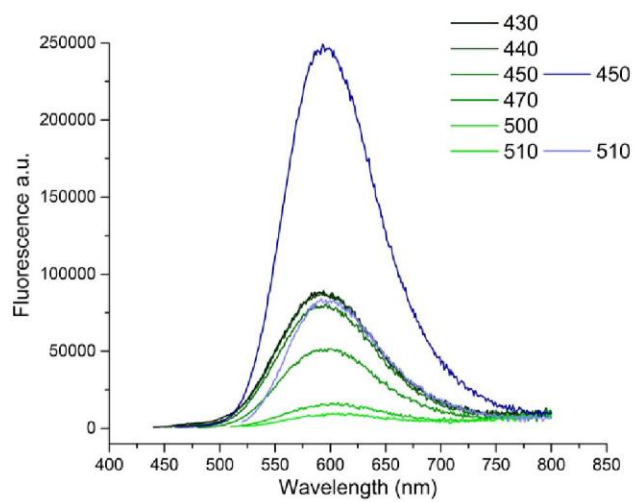
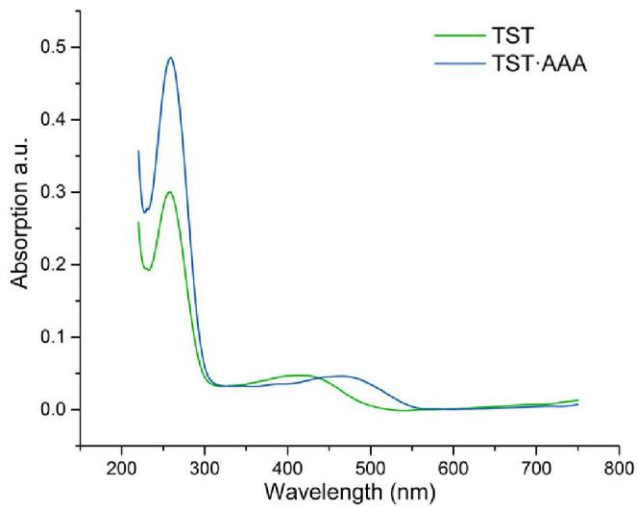
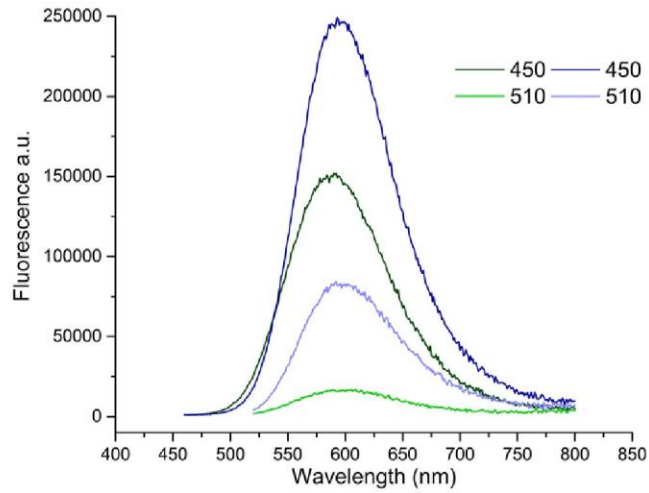
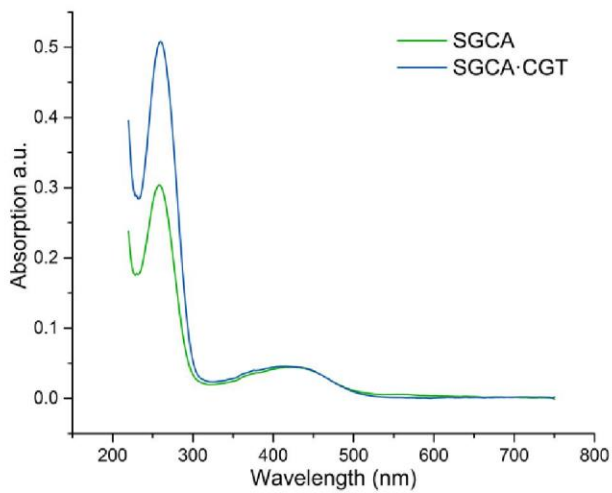
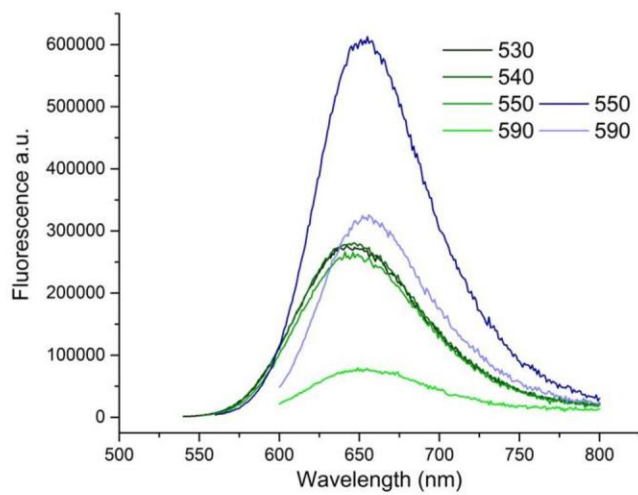
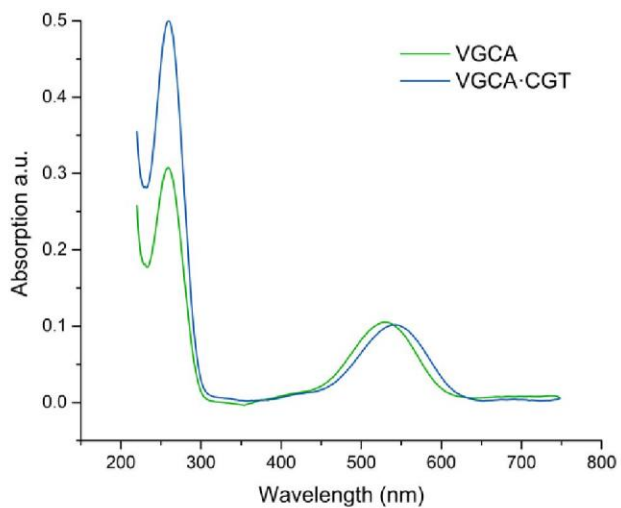
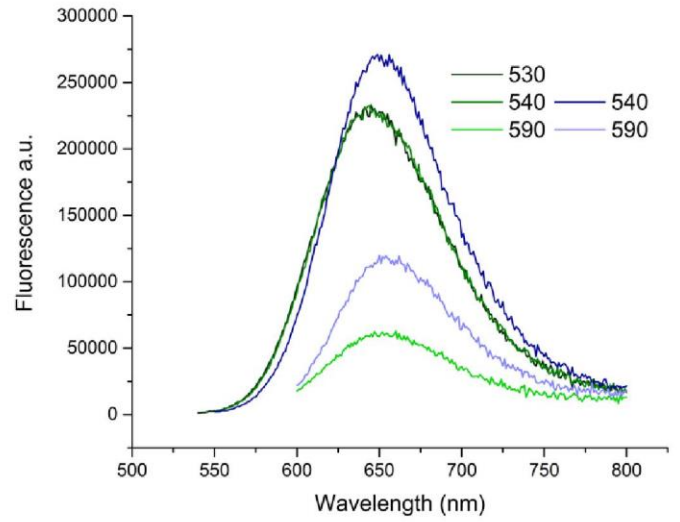
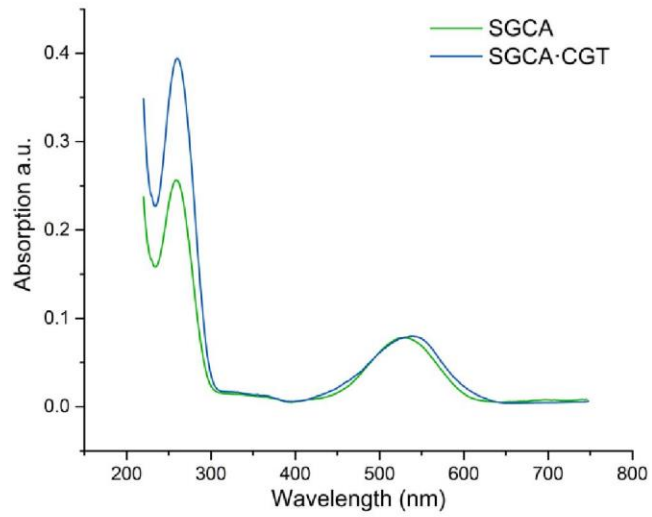
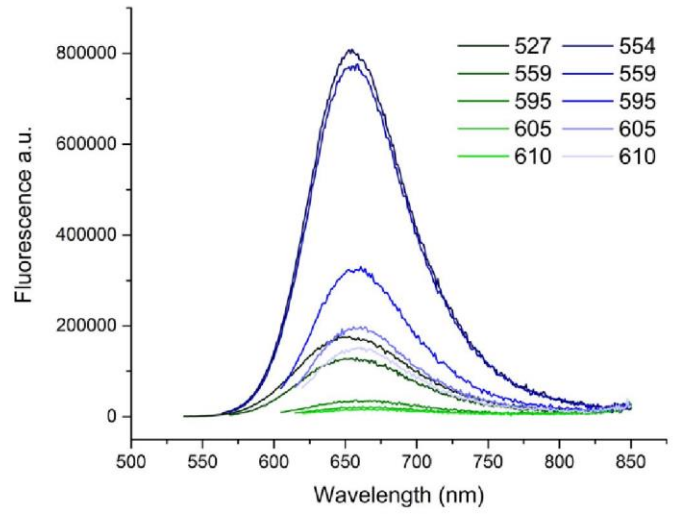
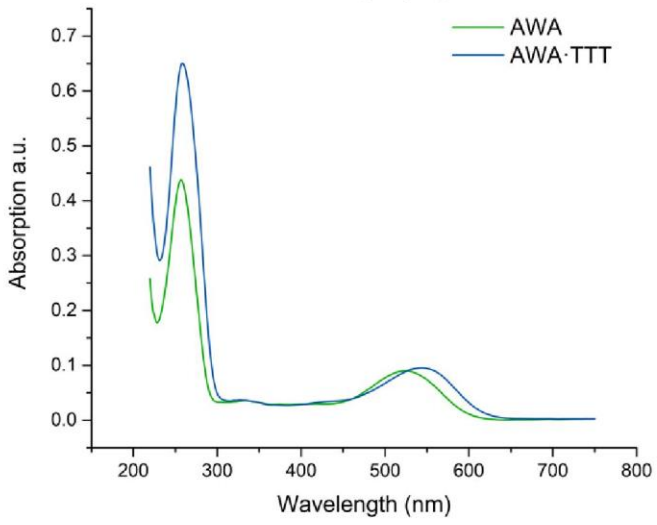
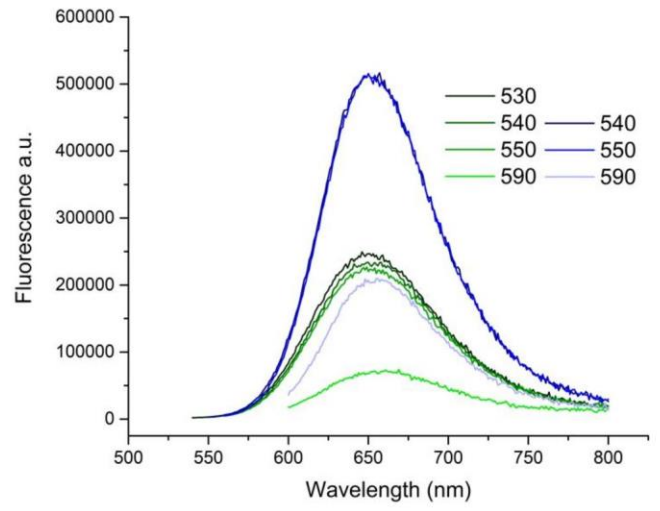
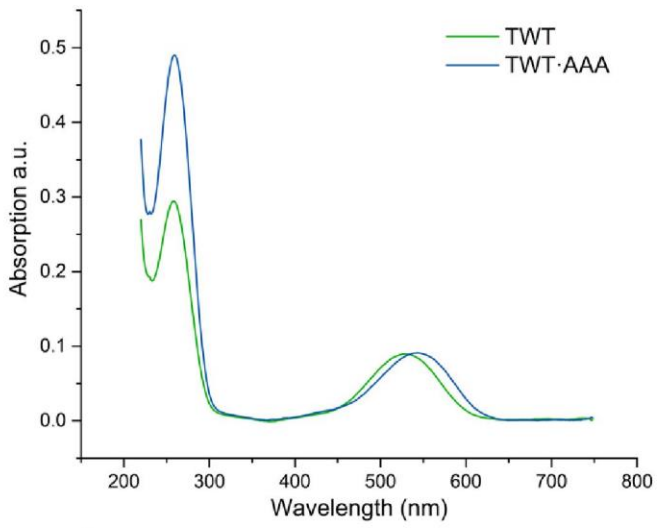


Figure S9. UV/visible and Fluorescence spectra of ss- and dsODNs labeled with 8





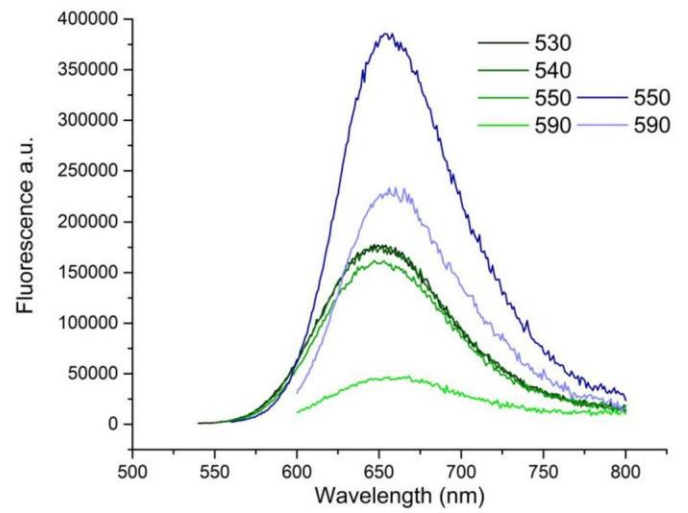
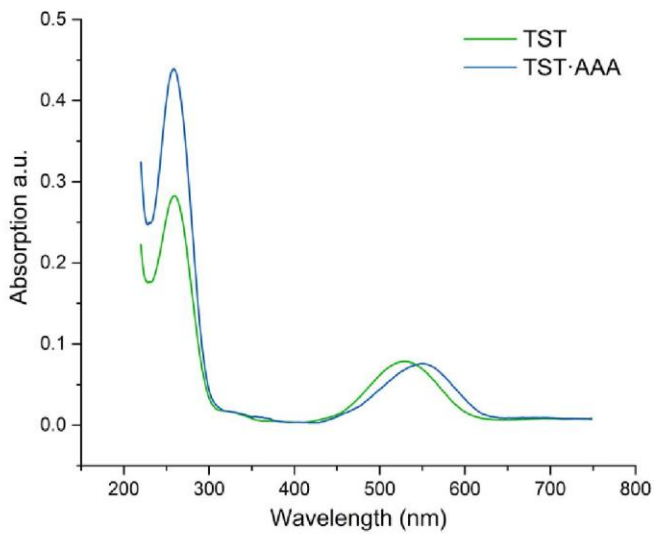
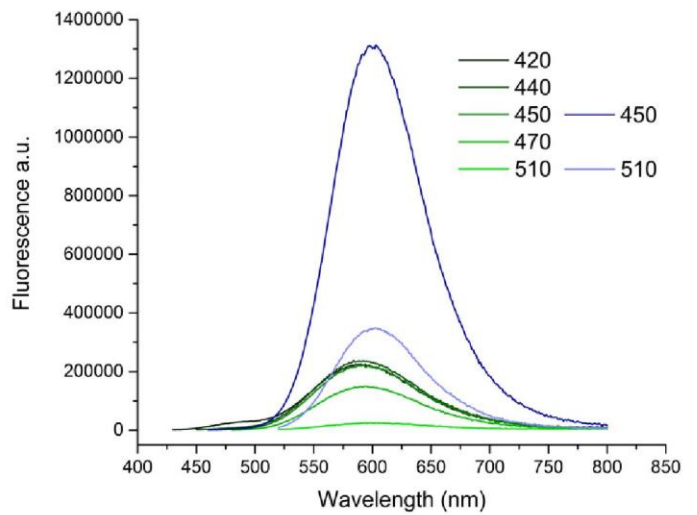
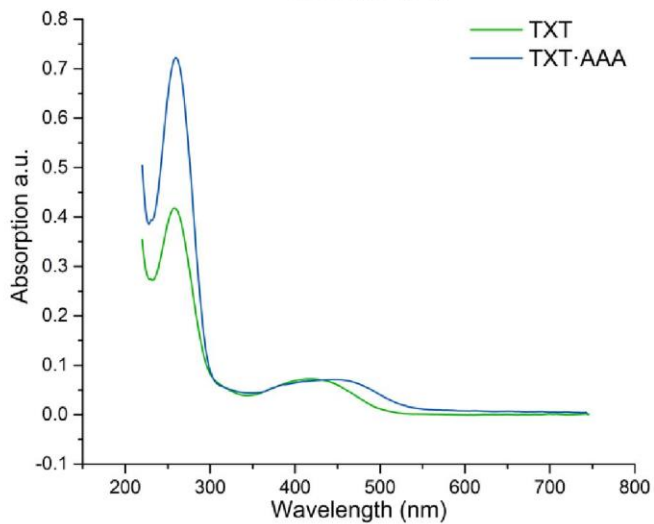
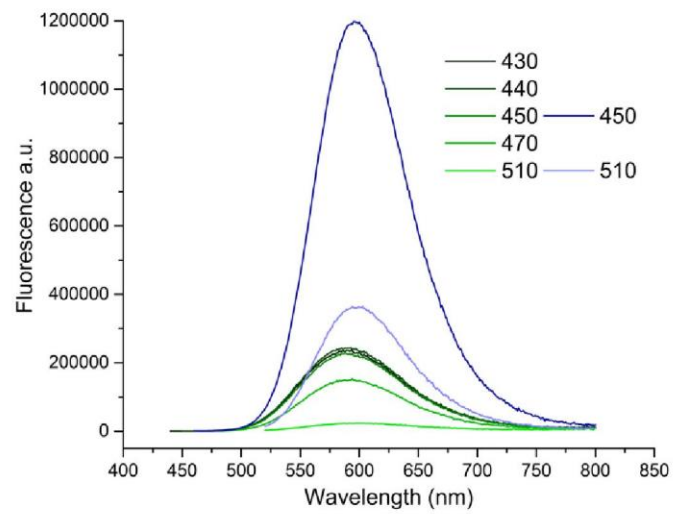
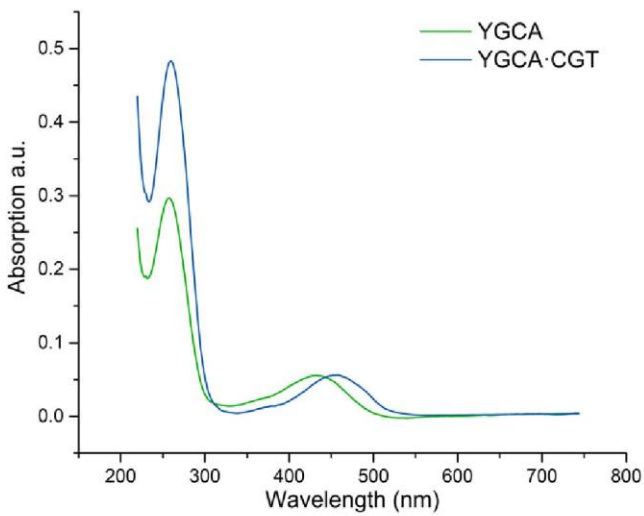


Figure S10. UV/visible and Fluorescence spectra of ss- and dsODNs labeled with 12



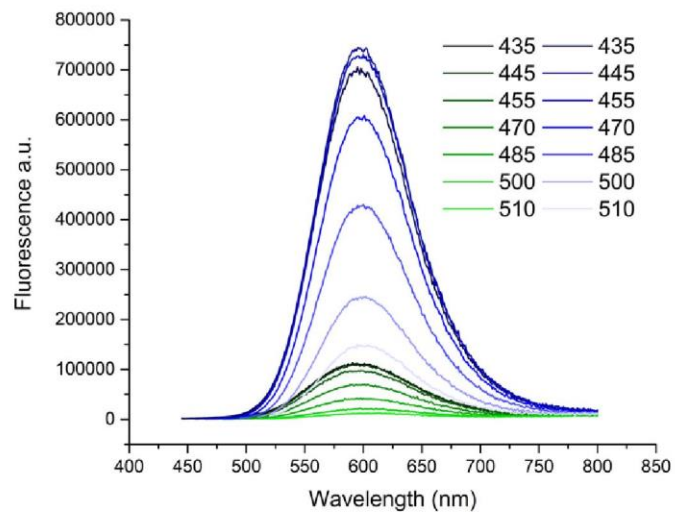
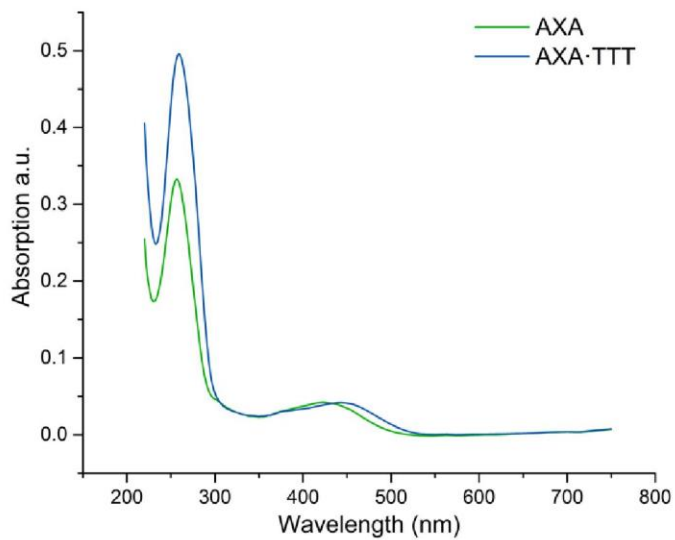
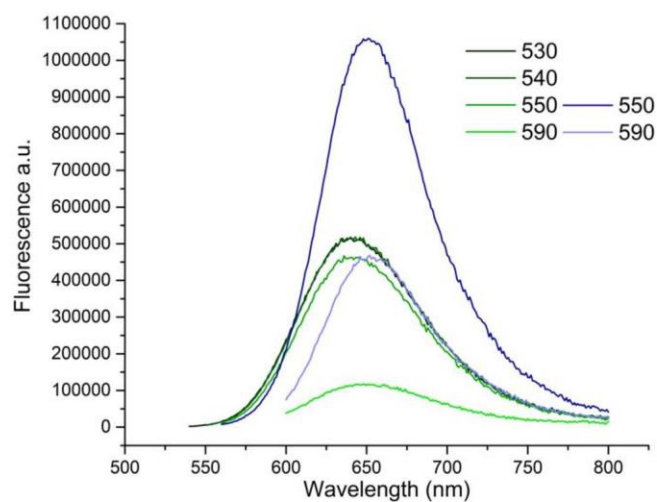
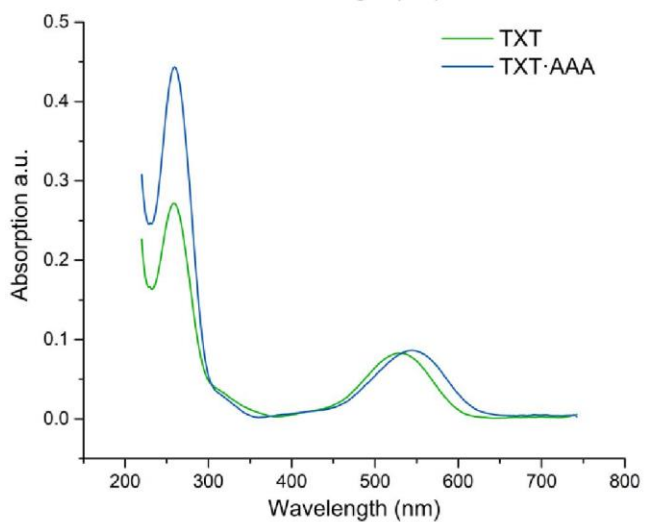
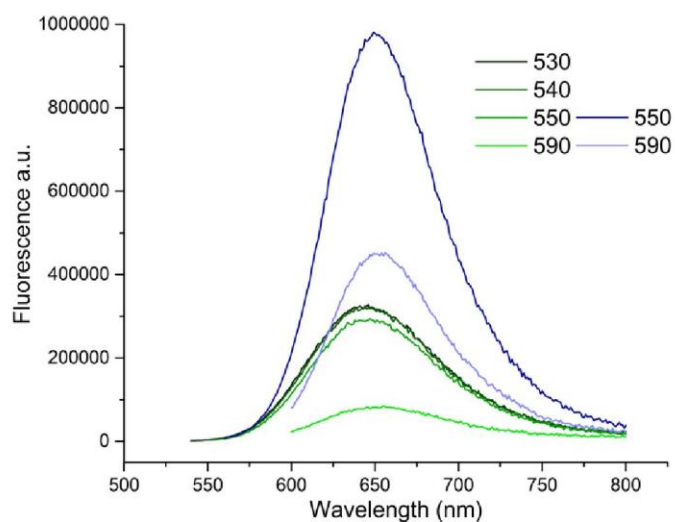
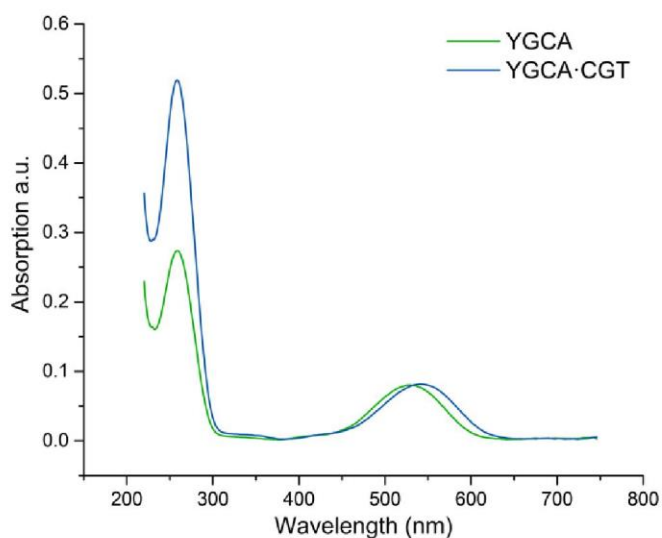


Figure S11. UV/visible and Fluorescence spectra of ss- and dsODNs labeled with 9



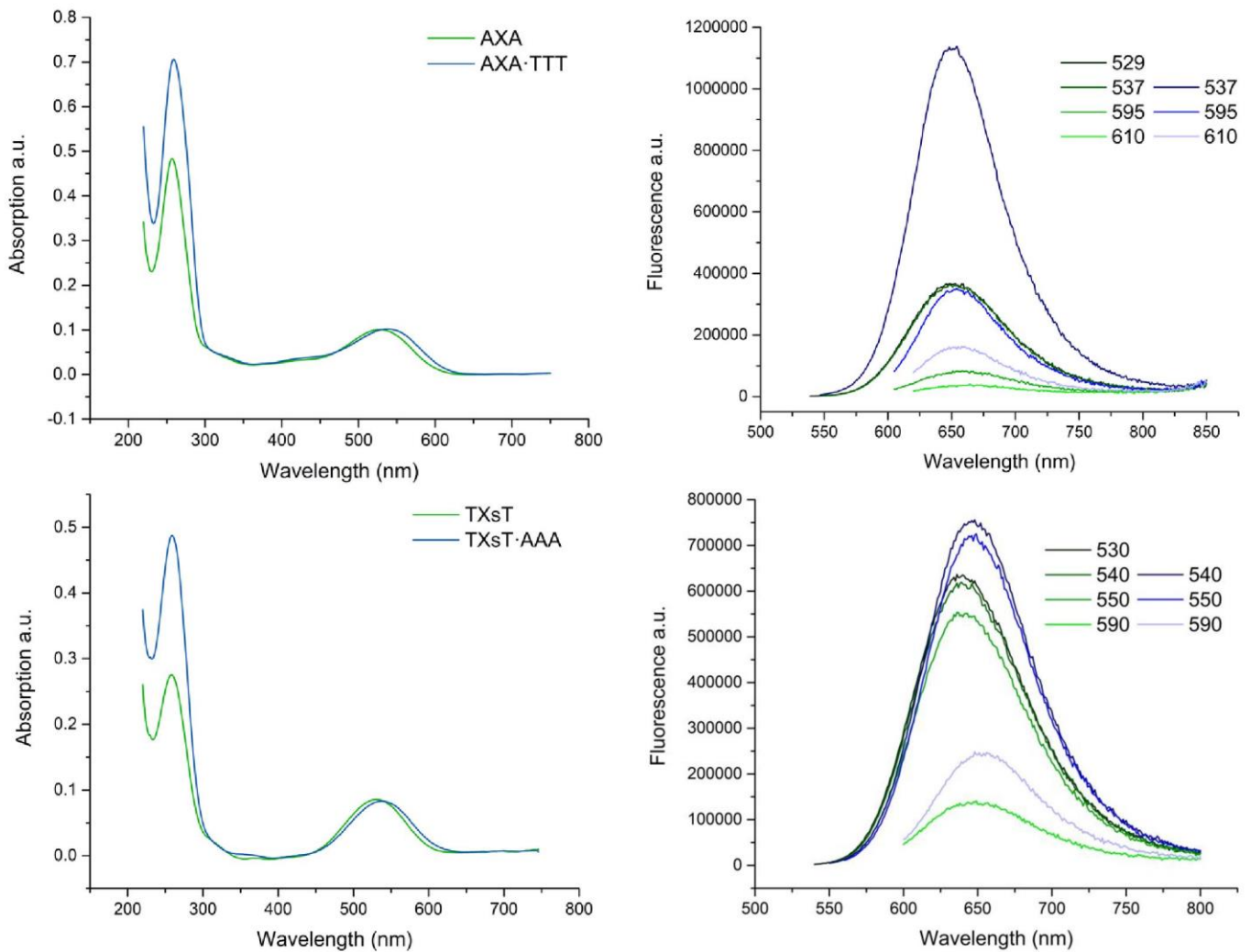
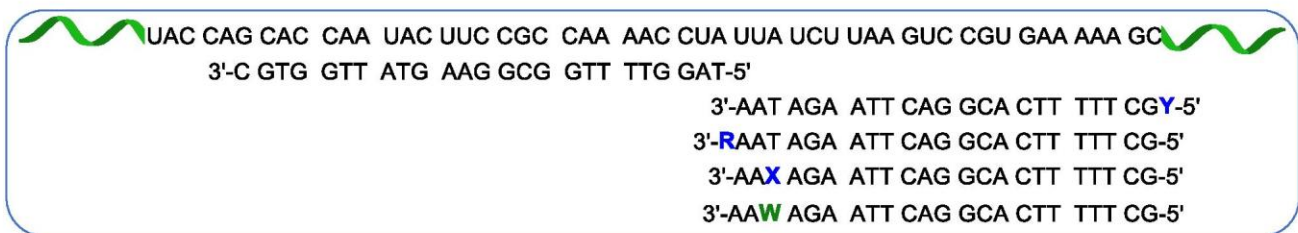


Figure S12. UV/visible and Fluorescence spectra of ss- and dsODNs labeled with 13

4. Biological Application

Figure S13: Summary of the sequences used for hybridization, of the RNA or DNA target



4.1 Steady-state fluorescence measurements

The absorption and fluorescence experiments were realized in duplicate in phosphate buffer pH 7.0 as described above. In these experiments, 3rd is corresponding to the *Wild-type* third partner ODN used to make a more stable duplex.

Table S6: Spectroscopic properties of 8 & 9 labeled ODNs

Sequences	λ_{Abs}^a (nm)		λ_{Em}^b (nm)		Φ (%) ^c		Intensity ratio ^d	
	RNA	DNA	RNA	DNA	RNA	DNA	RNA	DNA
YGCT	433	435	585	585	18	17		
YGCT·CGA	431	443 ↑	582	600 ↑	23	37 ↑	1.3	3.0 ↑
YGCT·CGA+3 rd	431	443 ↑	582	600 ↑	21	45 ↑		
AAR	433	433	585	585	25	20		
AAR·TT	431	442 ↑	585	590 ↑	23	59 ↑	1.2	3.7 ↑
AAR·TT+3 rd	433	442 ↑	584	588 ↑	30	56 ↑		
GAX	431	431	581	583	22	19		
GAX·CTA	431	432	585	587	26	25	1.5	1.7
GAX·CTA+3 rd	431	432	585	587	32	28		
WAT	434	436	585	583	10	7		
WAT·CTA	432	444 ↑	585	596 ↑	9	20 ↑	0.9	3.8 ↑
WAT·CTA+3 rd	432	444 ↑	585	596 ↑	9	19 ↑		

^aPosition of the absorption band maximum; ^bPosition of the emission maximum; ^cQuantum yield determined using *Nile Blue* in EtOH ($\Phi = 0.27$) as reference¹; ^dFluorescence intensity ratio at the maximum value of the DS: I(DS)/I(SS).

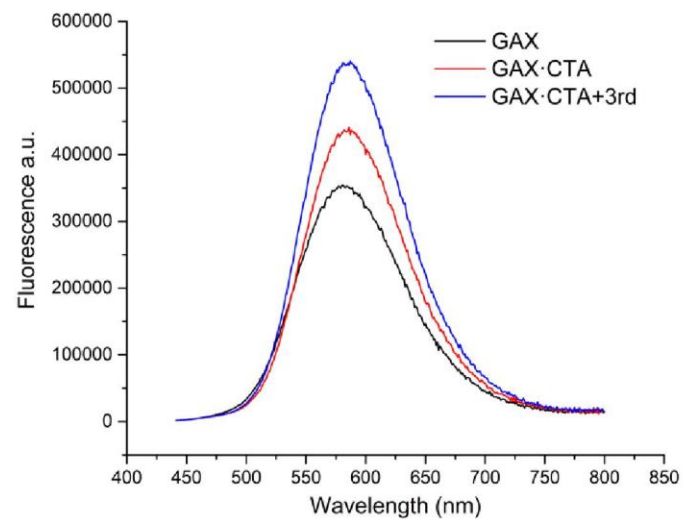
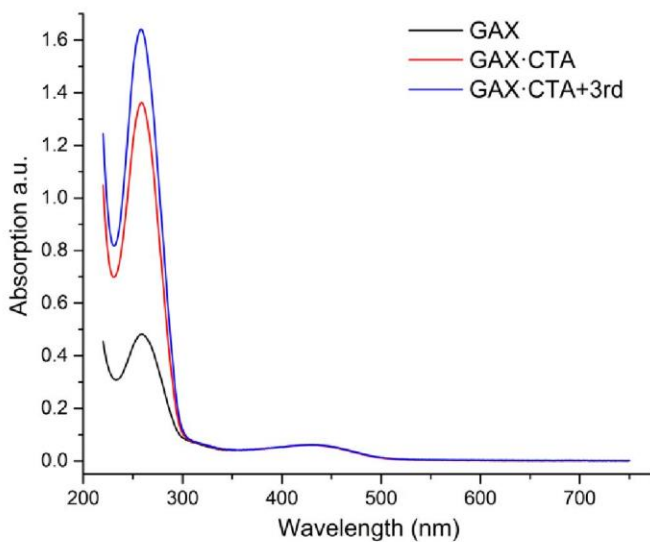
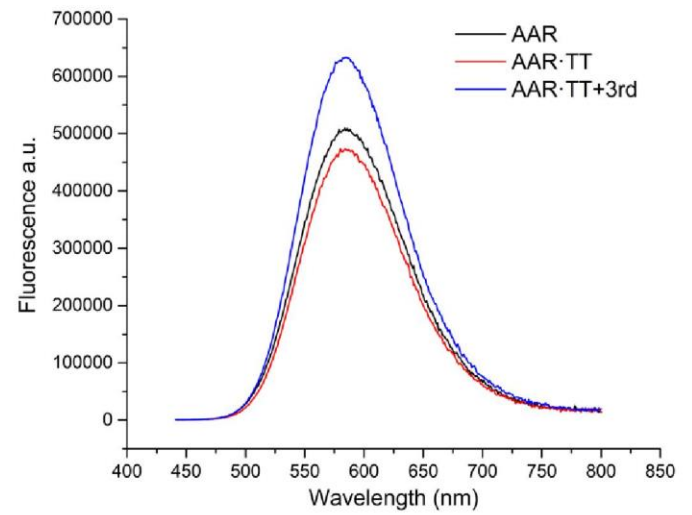
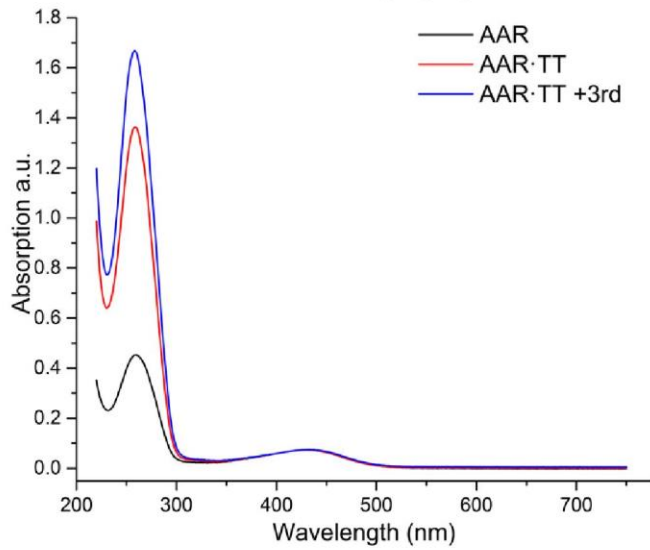
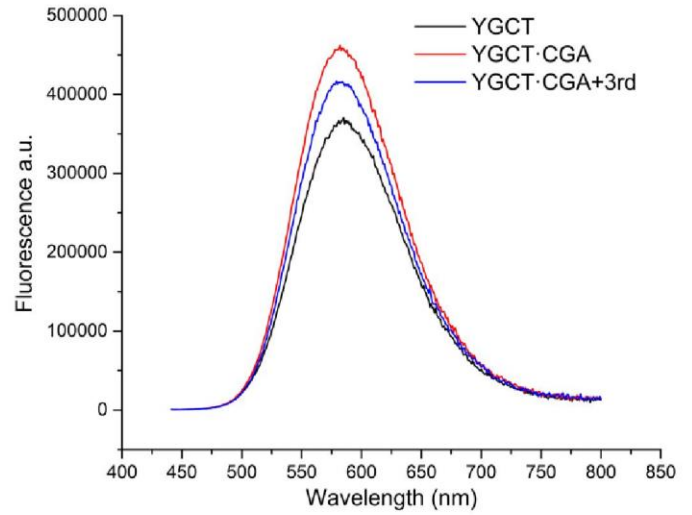
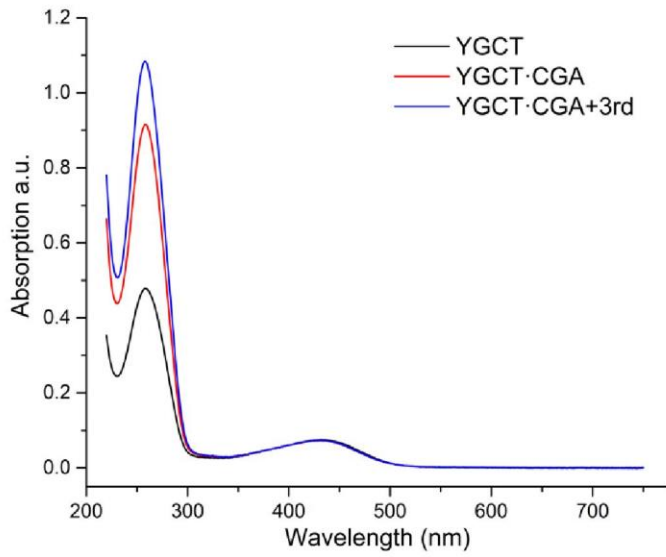
Table S7: Spectroscopic properties of 12 & 13 labeled ODNs

Sequences	λ_{abs}^a (nm)		λ_{N}^b (nm)		Φ (%) ^c		Intensity ratio ^d	
	RNA	DNA	RNA	DNA	RNA	DNA	RNA	DNA
YGCT	528	530	640	640	16	15		
YGCT·CGA	523	542 ↑	638	653 ↑	14	21 ↑	0.9	1.7 ↑
YGCT·CGA+3 rd	523	542 ↑	638	652 ↑	14	21 ↑		
AAR	527	527	642	642	20	18		
AAR·TT	525	536 ↑	642	652 ↑	19	29 ↑	1.3	2.0 ↑
AAR·TT+3 rd	523	539 ↑	639	652 ↑	27	27		
GAX	530	530	639	639	26	24		
GAX·CTA	528	531	640	644	25	28	1.1	1.2
GAX·CTA+3 rd	526	531	638	644	29	30		
WAT	530	532	641	639	15	12		
WAT·CTA	526	540 ↑	642	655 ↑	12	14 ↑	0.8	1.4 ↑
WAT·CTA+3 rd	526	540 ↑	642	655 ↑	11	14 ↑		

^aPosition of the absorption band maximum; ^bPosition of the emission maximum; ^cQuantum yield determined using *Nile Blue* in EtOH ($\Phi = 0.27$) as reference¹; ^dFluorescence intensity ratio at the maximum value of the DS: I(DS)/I(SS).

4.2 UV/visible & Fluorescence spectra of labeled ODNs before and after hybridization with the RNA or DNA target

In these experiments, 3rd is corresponding to the *Wild-type* third partner ODN used to make a more stable duplex.



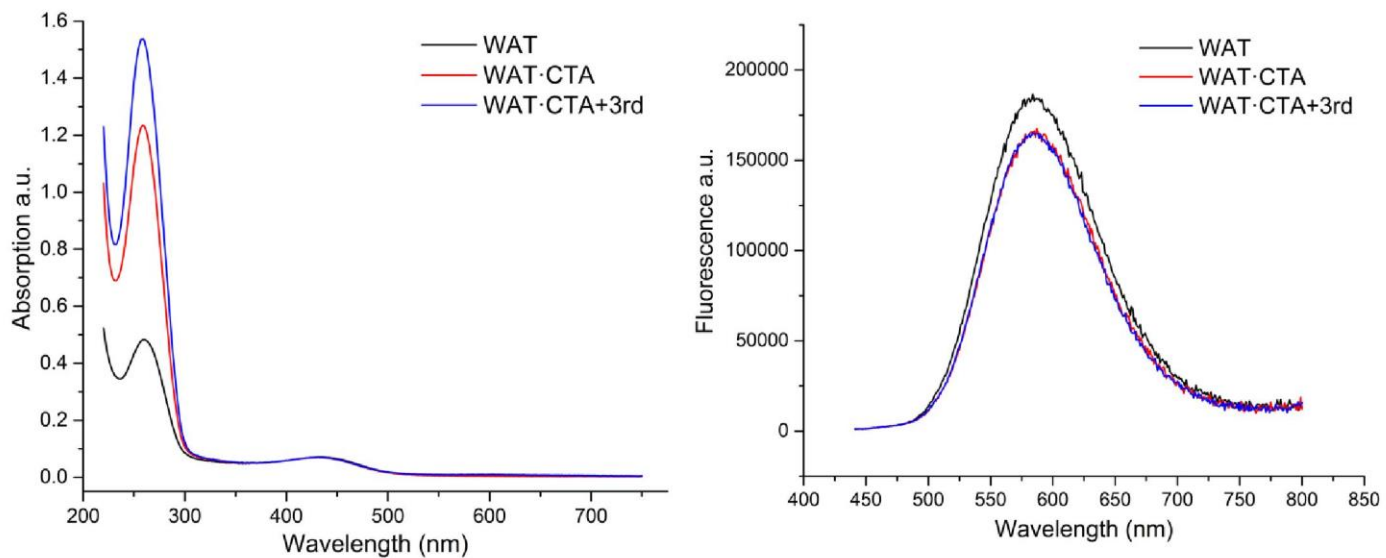
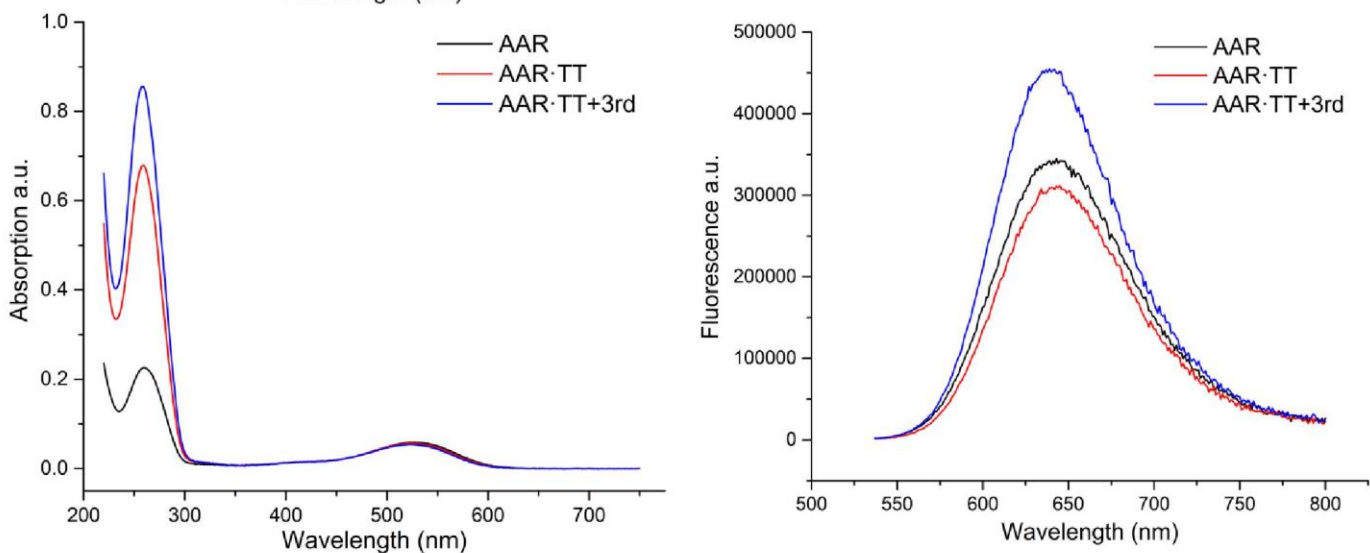
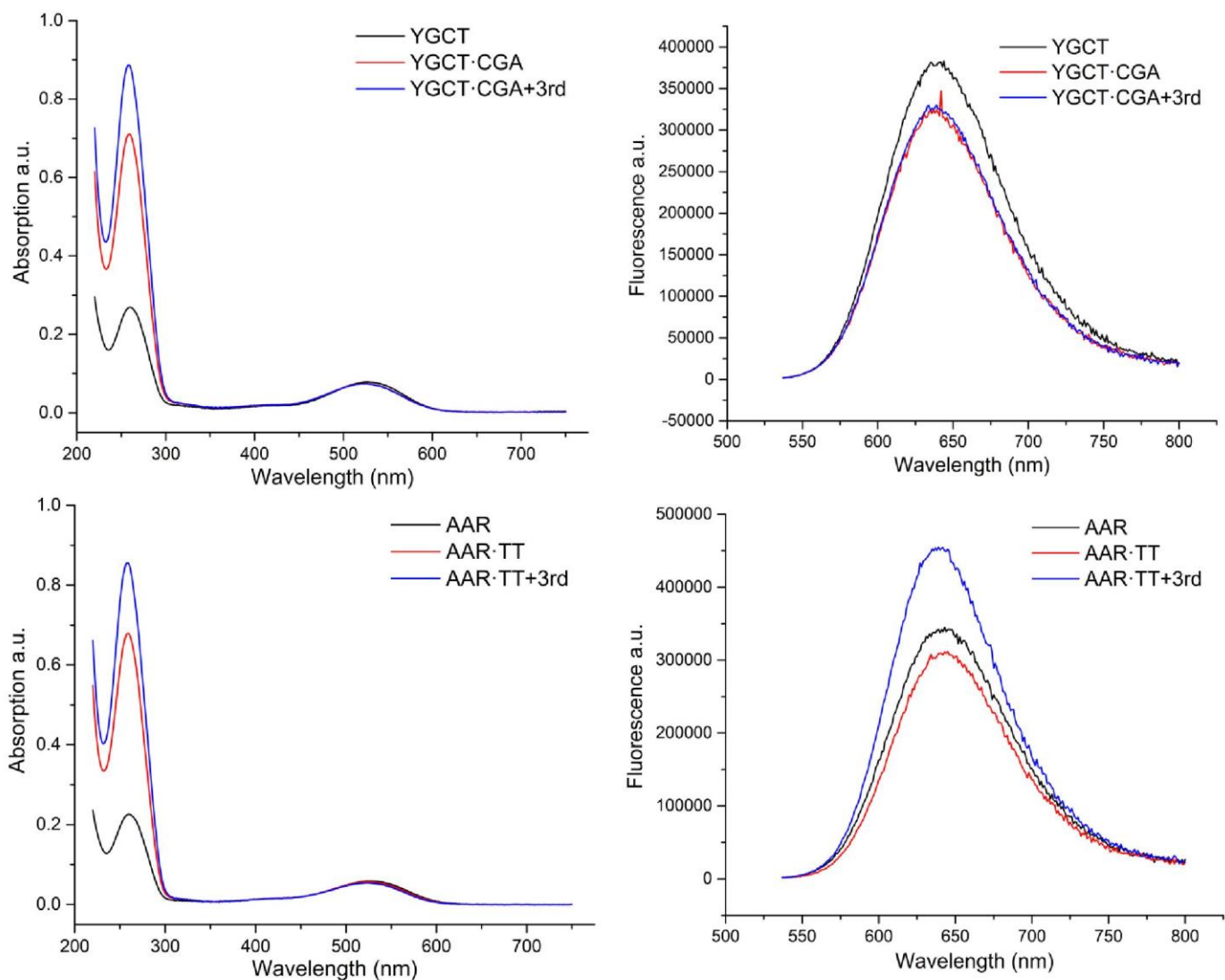


Figure S14. UV/visible and Fluorescence spectra of ODNs labeled with 8 & 9 before and after hybridization with the RNA target



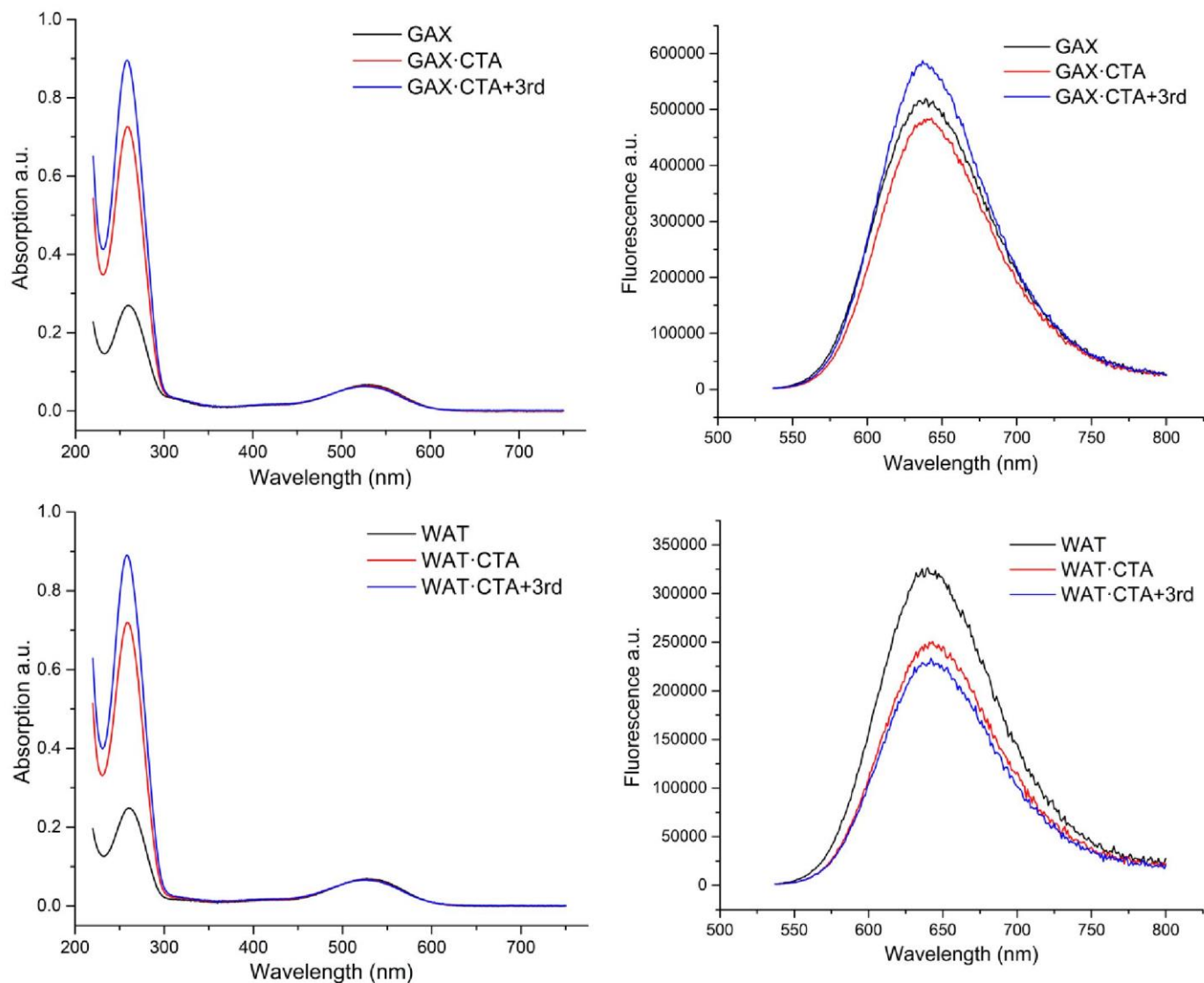
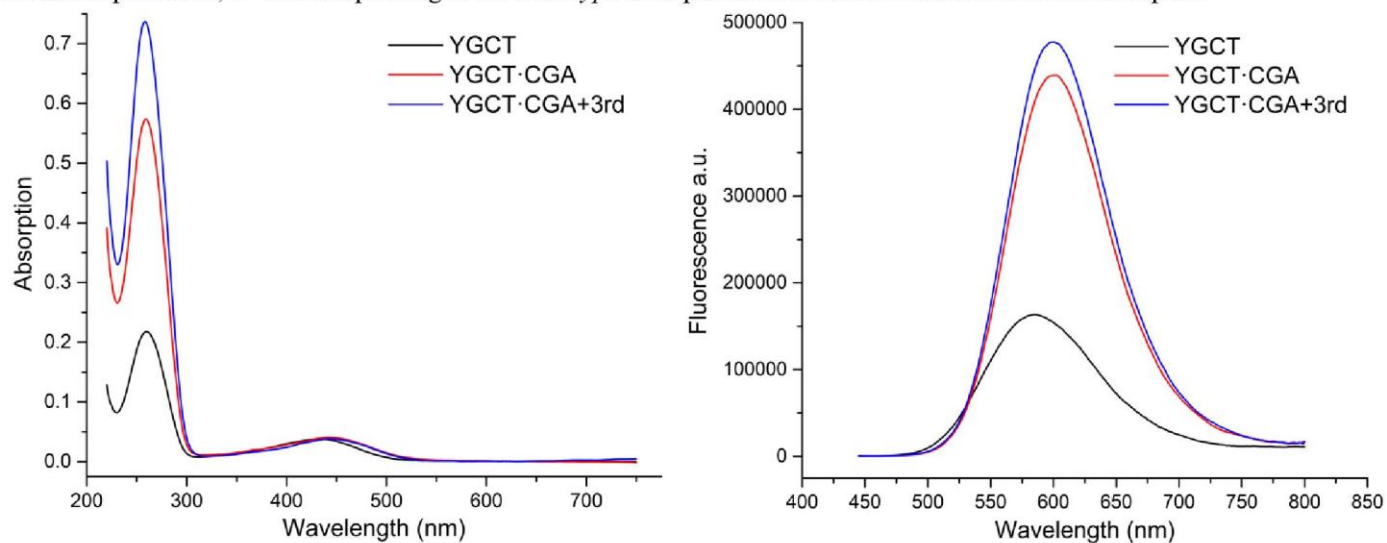


Figure S15. UV/visible and Fluorescence spectra of ODNs labeled with 12 & 13 before and after hybridization with the RNA target

4.3 UV & Fluorescence spectra for DNA target analog

In these experiments, 3rd is corresponding to the *Wild-type* third partner ODN used to make a more stable duplex.



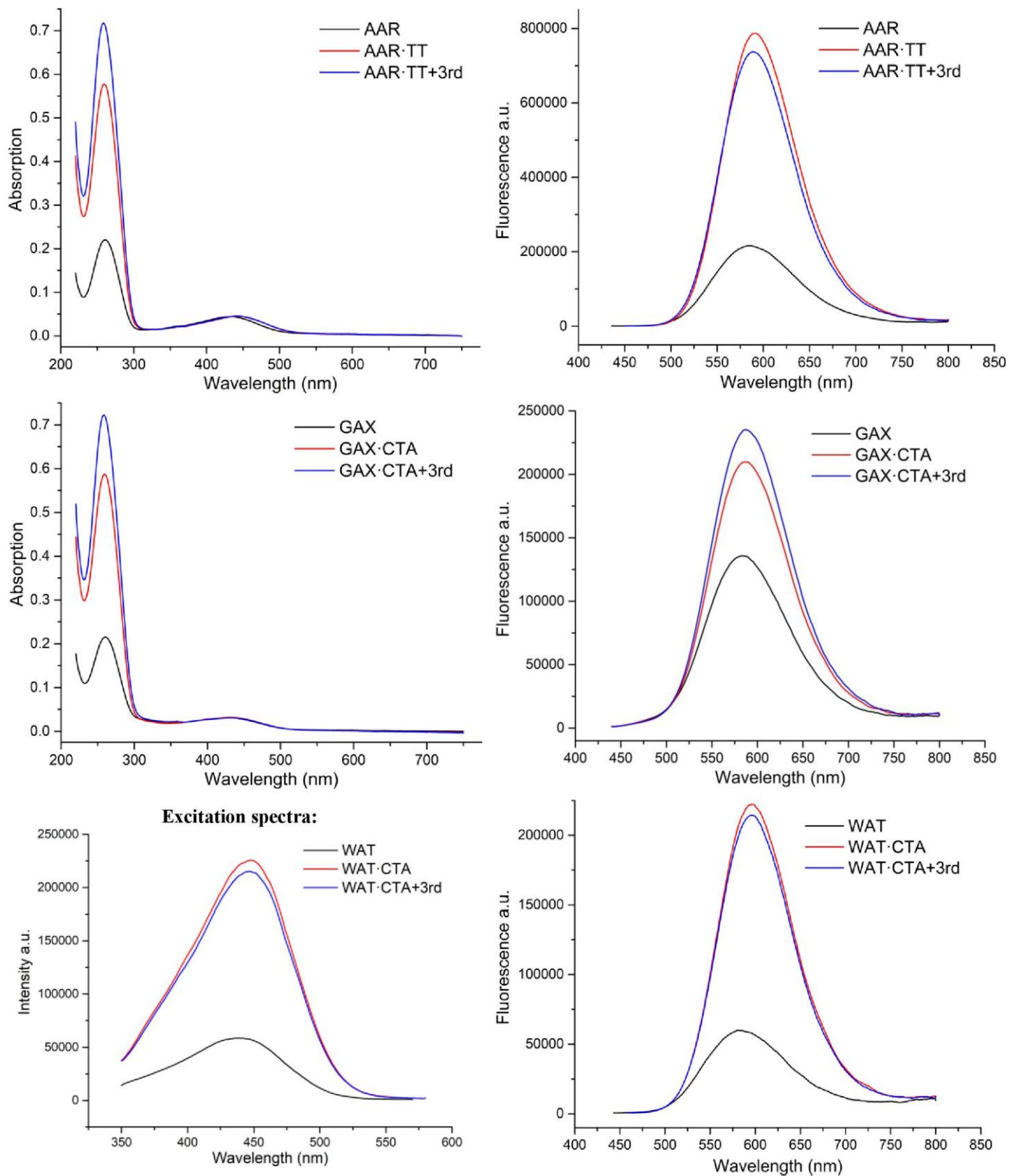
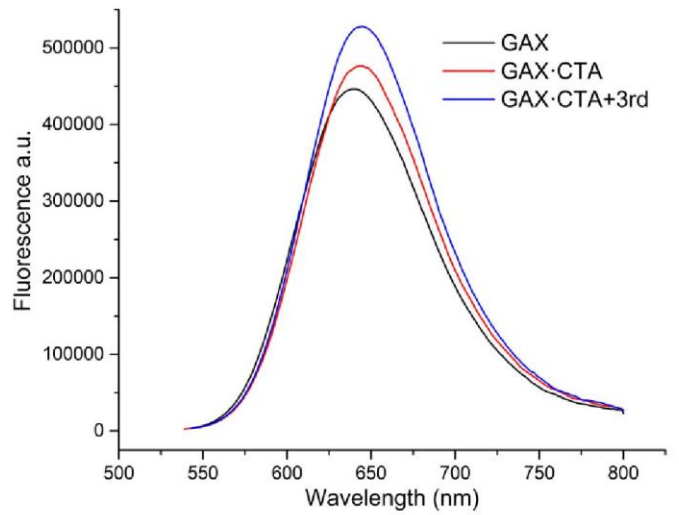
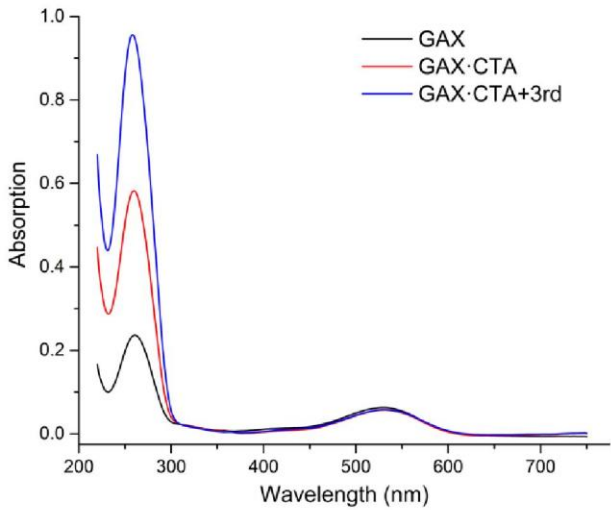
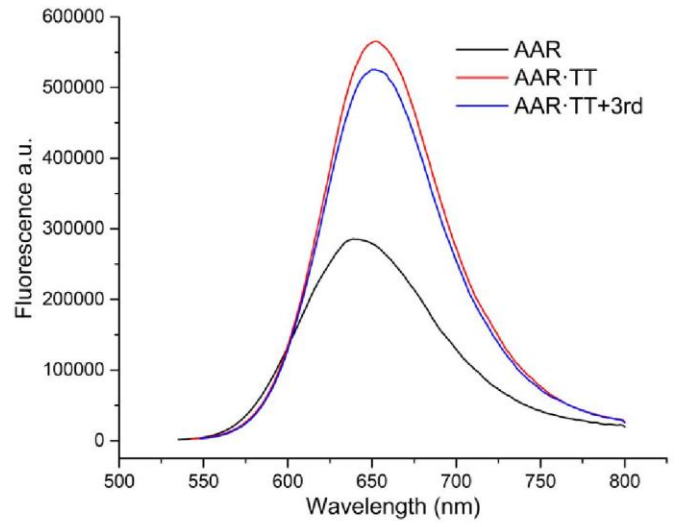
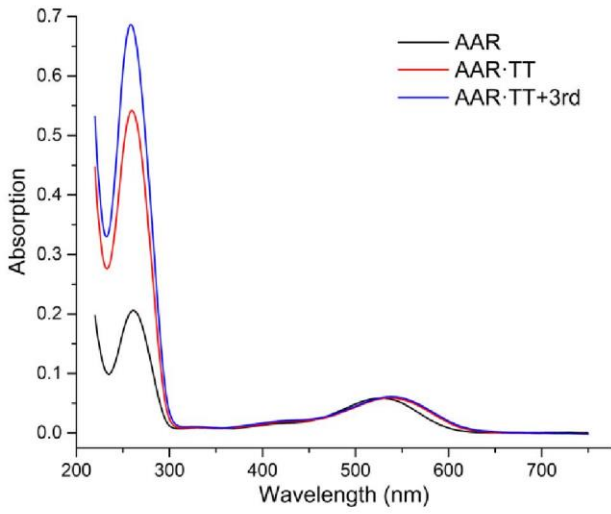
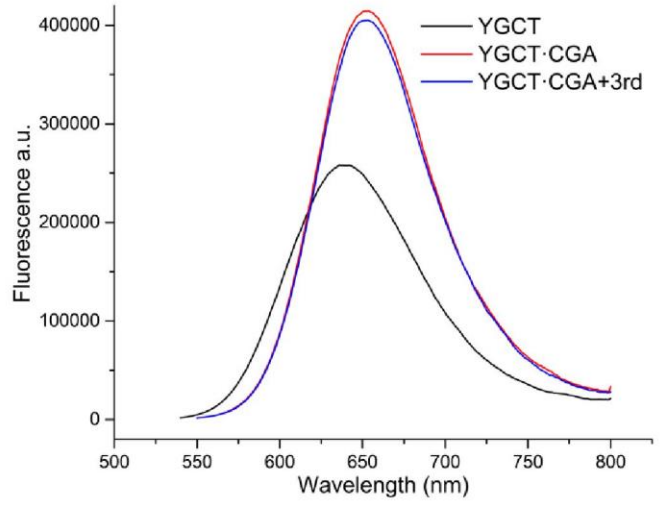
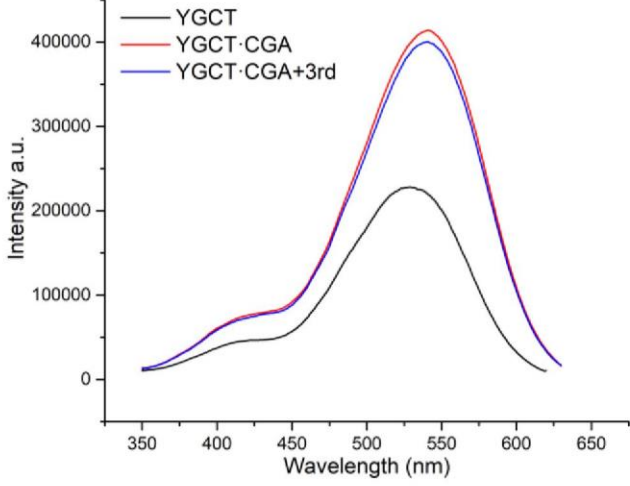


Figure S16. UV and Fluorescence spectra of ODNs labeled with 8 & 9 before and after hybridization with the DNA target

Excitation spectra:



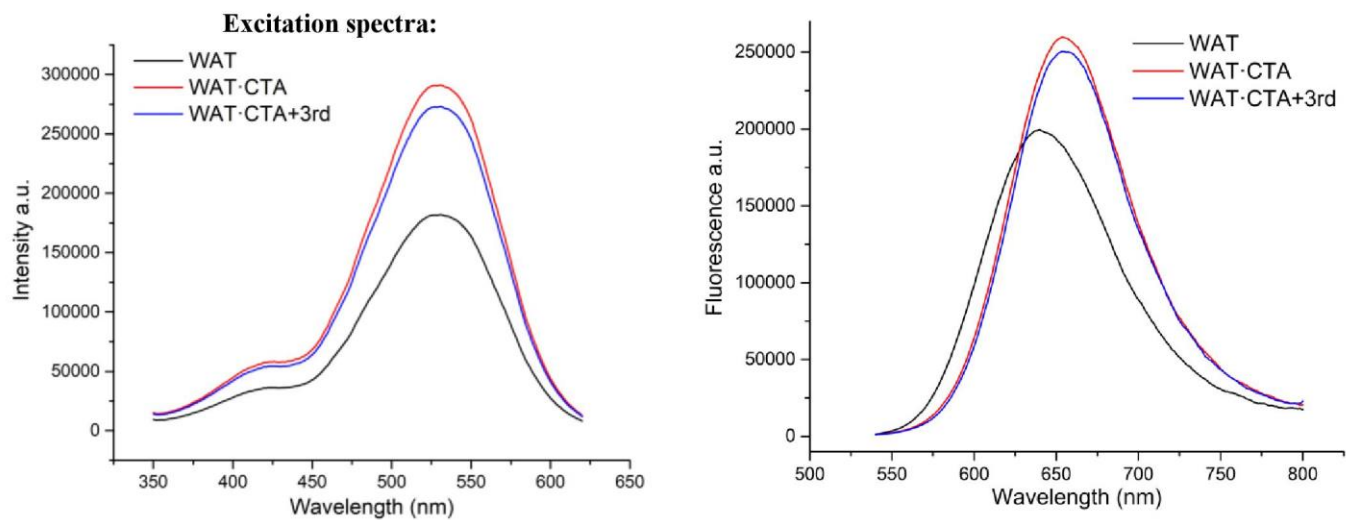


Figure S17. Fluorescence spectra of ODNs labeled with 12 & 13 before and after hybridization with the DNA target

References

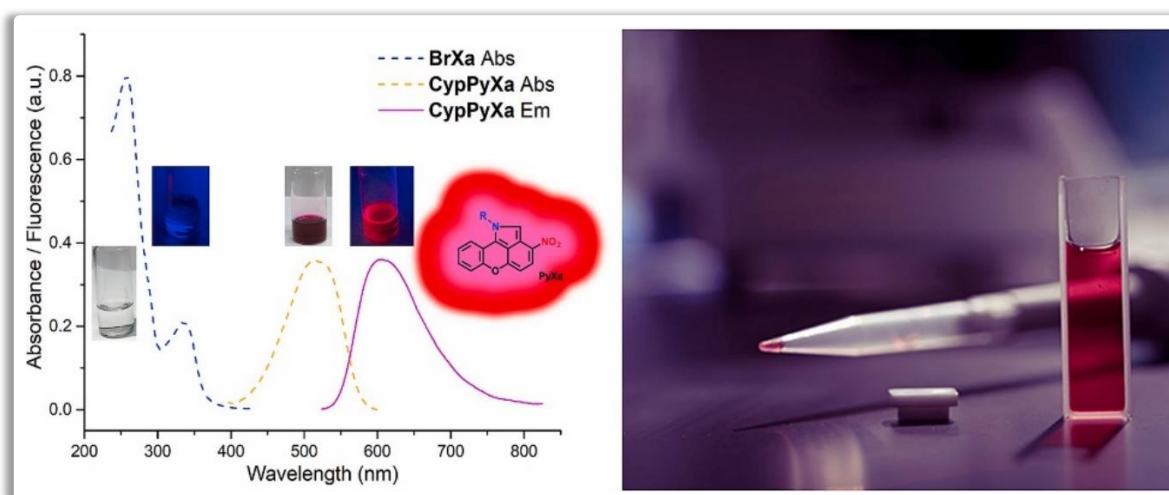
1. Jose, J., Ueno, Y. & Burgess, K. Water-Soluble Nile Blue Derivatives: Syntheses and Photophysical Properties. *Chem. - A Eur. J.* **15**, 418–423 (2009).

Annexes

Les publications suivantes, exposées dans cette partie annexes, sont des projets auxquels j'ai participé en dehors de mon sujet principal de thèse.

Publication 4

Publication réalisée en partenariat avec l'équipe du Dr. I. K. Kostakis de l'Université d'Athènes.



Dans celle-ci, nous décrivons la synthèse et l'analyse photophysique d'un dérivé de xanthène. Ce dernier, au contact d'une amine primaire uniquement se dérivatise en un composé fluorescent. Dans cet article publié dans *Dyes and Pigments* en 2021 nous décrivons le degré de sensibilité de ce réactif spécifique sur de multiples amines.



Synthesis, spectroscopic and computational evaluation of a xanthene-based fluorogenic derivatization reagent for the determination of primary amines

Amalia D. Kalampaliki^{a,1}, Steve Vincent^{b,1}, Suman Mallick^b, Hoang-Ngoan Le^b,
Guillaume Barnoin^b, Yogesh W. More^b, Alain Burger^b, Yannis Dotsikas^c, Evangelos Gikas^{d,**},
Benoît Y. Michel^{b,*}, Ioannis K. Kostakis^{a,***}

^a Department of Pharmacy, Division of Pharmaceutical Chemistry, National and Kapodistrian University of Athens, Panepistimiopolis, Zografou, 157 71, Athens, Greece

^b Université Côte d'Azur, CNRS, Institut de Chimie de Nice, UMR 7272 – Parc Valrose, Nice cedex 2, 06108, France

^c Laboratory of Pharmaceutical Analysis, Department of Pharmacy, National and Kapodistrian University of Athens, Panepistimiopolis, Zografou, 157 71, Athens, Greece

^d Laboratory of Analytical Chemistry, Department of Chemistry, National and Kapodistrian University of Athens, Panepistimiopolis, Zografou, 157 71, Athens, Greece

ARTICLE INFO

Keywords:

Amine derivatization
Colorimetric detection
Fluorogenic sensing
Chromatographic analysis
Quantum calculations

ABSTRACT

To detect an analyte, typically at the sub-nanomolar scale, extremely sensitive analytical tools are required. Fluorescence is the spectroscopy of choice to achieve such a level due to its non-invasive nature and efficiency in accurately probing the sub-nanomolar concentration range. Here, we report the design, synthesis and photo-physical characterization of a fluorogenic derivatization reagent with exclusive selectivity for primary amines. This xanthene-based dye owns an exacerbated fluorogenic character making the derivatized amine absorbing in yellow and emitting in the vermilion edge. In addition to being fluorogenic, this derivatization method also has the crucial advantage of being chromogenic (colorless => fuchsia). Chemical quantum calculations give an insight into the dye's molecular properties, while the development of an LC analytical method provides proof of concept regarding its application for the analysis of primary amines in a complex matrix.

1. Introduction

Modern analytical chemistry continuously pushes the limits of ultrasensitive analysis towards lower levels of detection [1]. Among all sensing methods, fluorescence spectroscopy appears to be the technique of choice because of its non-destructive character and its high sensitivity of response, especially for an extremely low concentration of analyte ($<10^{-9}$ M) [2,3]. Traditionally, there are two approaches for fluorescence-based sensing. One consists in turning on the fluorescence in the presence of a specific analyte while the other is to turn it off. Unequivocally, the turn-on method is significantly superior due to its high contrast to the background and the negligible risk of false positives, since most organic compounds are not intrinsically fluorescent [4].

In the case of turn-on sensing, the simplest strategy is the fluorescence derivatization, *i.e.* the transformation of a non-emissive analyte into a fluorescent molecule, based in most cases on a chemical reaction

[5]. The most frequently used methodology is the fluorescent labeling corresponding to the covalent attachment of an emissive dye (Scheme 1). The strong extrinsic fluorescence – brought by the coupled bright fluorophore – allows an efficient detection of the analyte with high sensitivity [6].

A myriad of fluorescent derivatization reagents has been synthesized; many of them being employed for quantitative purposes in analytical chemistry, generally for chromatography-based separations where exquisite sensitivity is required [7–10]. The derivatization and sensing of amines have been the subject of intense research as this functional group is found in many biomolecules including amino acids, proteins and nucleic acids [11–17]. A wide variety of reagents for amine derivatization was reported, mainly based on the classical families of dyes (coumarin [18–20], Bodipy [21–23], fluorescein [24,25], rhodamine [26], cyanine [27]) bearing an amine-reactive function such as succinimidyl and sulfosuccinimidyl esters (Scheme 1). To a lower extent,

* Corresponding author.

** Corresponding author.

*** Corresponding author.

E-mail address: benoit.michel@univ-cotedazur.fr (B.Y. Michel).

¹ These authors contributed equally to this work.

<https://doi.org/10.1016/j.dyepig.2021.109798>

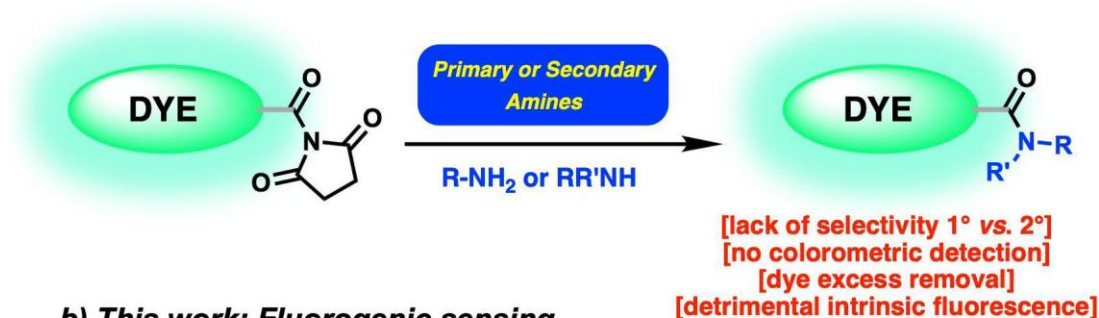
Received 4 May 2021; Received in revised form 4 September 2021; Accepted 6 September 2021

Available online 11 September 2021

0143-7208/© 2021 Elsevier Ltd. All rights reserved.

a) Classical approach for amine derivatization:

- Fluorescent dye bearing NHS ester

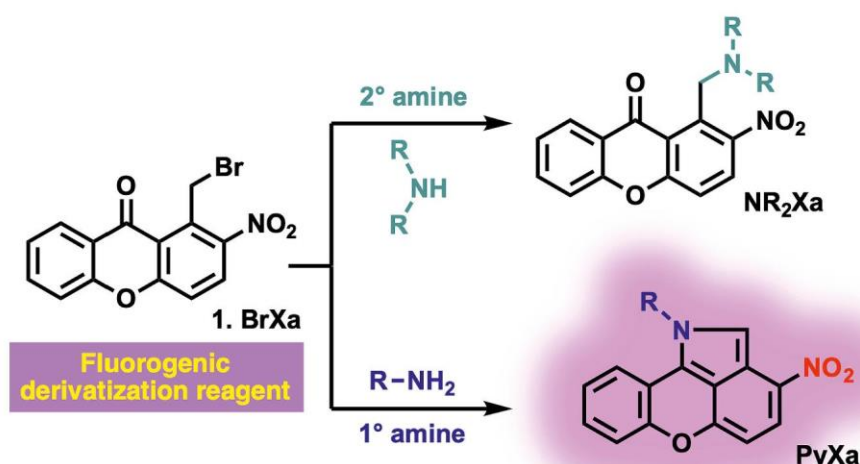


b) This work: Fluorogenic sensing

- Selective reaction towards 1° amines



Scheme 1. State-of-the-art labeling for the amine fluorescent derivatization vs. rational design for the engineering of the targeted fluorogenic reagent 1. *LG* denotes leaving group.



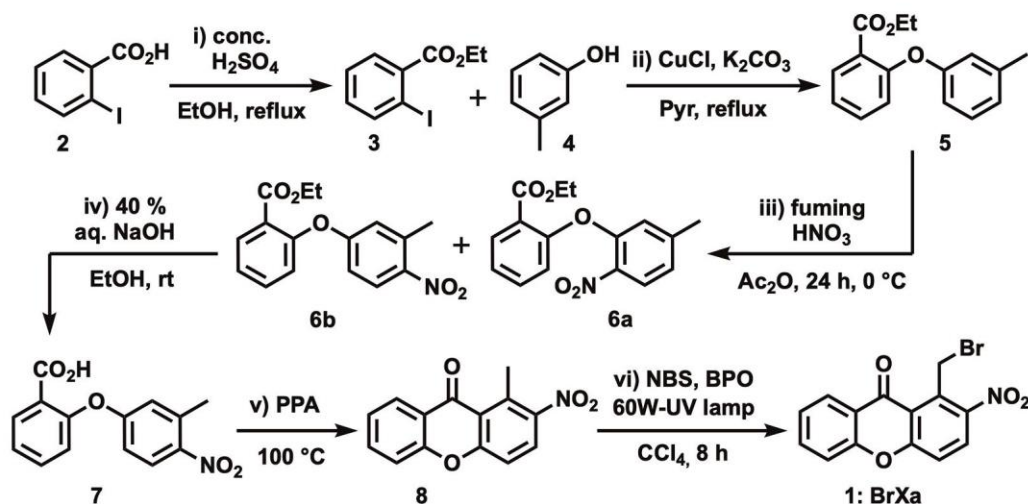
Scheme 2. Fluorogenic sensing using chemoselective reactivity of the derivatization reagent 1 towards primary amines. Donor and acceptor groups involved in the push-pull relationship are depicted in blue and red, respectively.

carbonyl azides, isothiocyanates, sulfonylchlorides and tetrafluorophenyl esters were proposed as an alternative amine-reactive group [7].

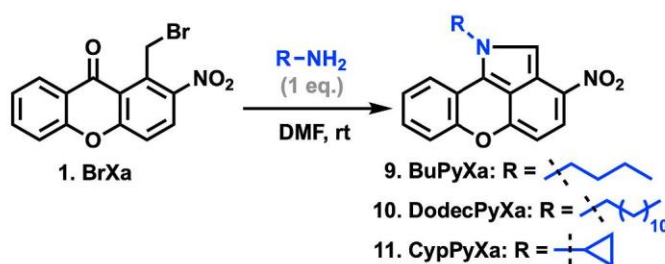
A major drawback of this technique is the fluorescence cross-contamination due to the large excess of the derivatization reagent used to drive the reaction kinetics to completion. Classically, this excess must either be chromatographically separated or removed by some pre-treatment procedures, as the intrinsic fluorescence of the reagent will interfere with both absorption and emission of the derivatized analyte and may contaminate the resulting fluorescent signal.

To overcome this, the ideal solution would be a “fluorogenic” reagent, *viz.* which fluoresces only after the derivatization reaction, thus avoiding both cross-contamination during the spectroscopic measurements and the implementation of extensive purification processes [28–33]. In that respect, innovative reagents such as quinolinizinium [34],

thiazolo-isoquinoline [35], DOOB – 2,2-diphenyl-1-oxa-3-oxonia-2-b oratanaphthalene [36], catechol [37], stilbene trifluoroacetate [38], and ylidenemalononitrile enamines [39] were alternatively developed to sense fluorogenically various types of amines by derivatization. For that purpose, the most widely used fluorogenic derivatization reagent is *ortho*-phthalaldehyde, which intrinsically exhibits no fluorescence [40]. In the presence of 2-mercaptoethanol, it reacts chemoselectively with primary amines to afford emissive isoindoles [40–42]. The requirement for a large excess of this thiol additive combined with the blue fluorescence of the product, severely limits the usage of this system; especially for derivatization of amino-based biomolecules accompanied by strong background fluorescence. Indeed, besides demonstrating negligible fluorescence in the emission range of the derivatization reaction product, a fundamental property of a successful reagent should be its ability to emit an intense signal in the red or NIR region to avoid the



Scheme 3. Synthetic pathway leading to the derivatization reagent BrXa.

Scheme 4. Implementation of the derivatization reaction for primary amines including aliphatic and saturated cyclic R-NH₂ derivatives.

auto-fluorescence from biological media. This could be achieved either through the significant rearrangement of the reagent scaffold or via its extension with a conjugate π -system [43]. It is expressly on this precise point of “fluorogenicity” that our research program has focused [44–46].

Previously, we reported the synthesis and biological activities of a series of pyrroloxanthones exhibiting substantial cytotoxicity against several cancer cell lines [47,48]. Interestingly, these compounds of the general formula PyXa, showed a bright fuchsia color in contrast to their starting material with a *pseudo* benzyl bromide **1** (BrXa), which presents the dramatic advantage of being completely colorless (Scheme 2). Noticeably, the Bischler-type reaction employed for the synthesis of PyXa proceeds only with primary amines, since secondary amines afford the amino-substituted compounds NR₂X₂, with no color and fluorescence detected.

Prompted by these findings, we decided to further explore the potential of the above-mentioned scaffold as a fluorescent derivatization reagent for the colorimetric/fluorometric detection of primary amines. The chromogenic and fluorogenic sensing method would rely on the *in-situ* formation of an expanded pyrrole ring, thus extending the conjugation and concomitantly introducing a push–pull relationship between the electron-donating nitrogen of the sensed amine and the electron-withdrawing nitro group (Scheme 2). Therefore, the imposed structural changes are expected to shift the absorption maximum towards the red region of the electromagnetic spectrum, rendering BrXa an ideal candidate for amine derivatization. Additionally, the architecture obtained with a Donor- π -Acceptor (D- π -A) relationship should allow a larger dipole moment to be established in the excited state, which should be reflected in an enhanced sensitivity with the increasing polarity,

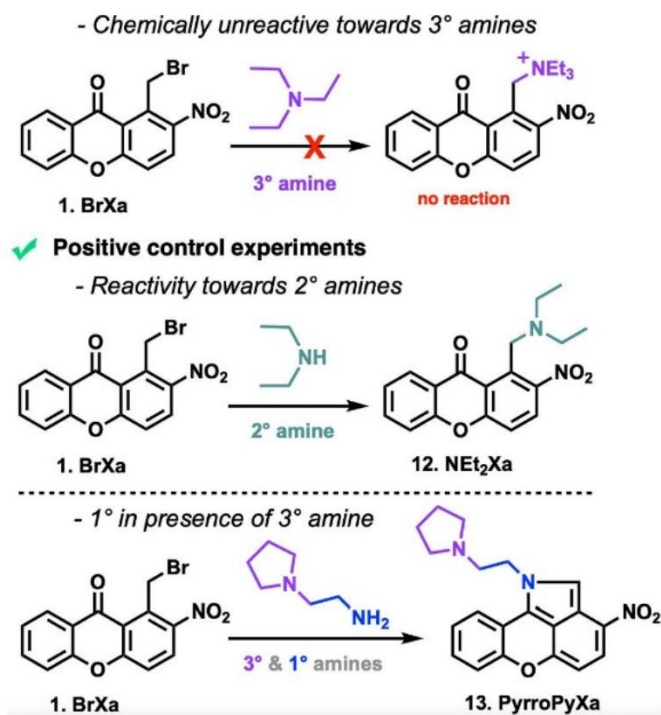
resulting in a λ -shift to the lower energetic wavelength. This operating redshift should greatly facilitate amine detection by avoiding potential fluorescent cross-contamination from the extracts.

Herein, we report the synthesis of a novel xanthene-based reagent BrXa for the fluorogenic derivatization of primary amines. The implementation of this derivatization reaction will be described, as well as the photophysics of the product *i.e.* the newly formed fluorescent pyrroloxanthone. Its application to the derivatization of cyclopropylamine by the development of an LC analytical method will be provided. Correlation between the establishment of a push–pull relationship into the derivatized amine scaffold and the resulting environment sensitivity will be further evidenced by employing quantum mechanics calculations.

2. Experimental section

2.1. Material and methods

All commercially available chemicals and solvents were purchased from Alfa Aesar and used as received without any further purification. Melting points were determined on a Büchi apparatus and were uncorrected. All NMR spectra (¹H, ¹³C, 2D) were recorded on 200, 400 or 600 MHz Bruker spectrometers respectively AC, Avance™ DRX and III instruments (Bruker BioSpin GmbH – Rheinstetten, Germany). ¹H NMR (200, 400 and 600 MHz) and ¹³C{¹H}NMR (50, 101 and 151 MHz, recorded with complete proton decoupling) spectra were obtained with samples dissolved in CDCl₃ or DMSO-*d*₆ with the residual solvent signals used as internal references: 7.26 ppm for CHCl₃, and 2.50 ppm for (CD₃)₂(CD₂H)S(O) regarding ¹H NMR experiments; 77.2 ppm for CDCl₃ and 39.4 ppm for (CD₃)₂S(O) concerning ¹³C NMR experiments [49,50].



Scheme 5. Negative (*top*) and positive (*bottom*) control experiments performed for the engineering of the derivatization reaction.

Chemical shifts (δ) are given in ppm to the nearest 0.01 (^1H) or 0.1 ppm (^{13}C). The coupling constants (J) are given in Hertz (Hz). The signals are reported as follows: (s = singlet, d = doublet, t = triplet, m = multiplet, br = broad). Assignments of ^1H and ^{13}C NMR signals were unambiguously achieved with the help of D/H exchange and 2D techniques: COSY, NOESY, HMQC, and HMBC experiments. Systematic xanthene nomenclature is used below for the assignment of each spectrum. Flash chromatography was performed on Merck silica gel (40–63 μm) with the indicated solvent system using gradients of increasing polarity in most cases (Merck KGaA – Darmstadt, Germany) [51]. The reactions were monitored by analytical thin-layer chromatography (Merck pre-coated silica gel 60 F254 TLC plates, 0.25-mm layer thickness). Compounds were visualized on TLC plates by both UV radiation (254 and 365 nm) and spraying with a staining agent (vanillin, PMA, KMnO_4 or ninhydrin) followed by subsequent warming with a heat gun. All solvents for absorption and fluorescence experiments were of spectroscopic grade. Absorption spectra were recorded on a Cary 100 Bio UV–Vis spectrophotometer (Varian/Agilent) using Suprasil® quartz cuvettes with 1-cm path length. Stock solutions of investigated dyes were prepared using dimethylformamide. The samples used for spectroscopic measurements contained $\approx 0.2\%$ v/v of solvents of the stock solution. Fluorescence spectra were recorded on a FluoroMax 4.0 spectrofluorometer (Jobin Yvon, Horiba) with a thermostatically controlled cell compartment at 20 ± 0.5 °C with slits open to 2 nm and were corrected for Raman scattering, lamp fluctuations and instrumental wavelength-dependent bias. Excitation wavelengths were set at the absorption maxima except when mentioned in the corresponding experiments. A Waters Acquity UPLC system (Waters Corporation – Manchester, UK), comprising a solvent manager module connected to an autosampler, was employed for the analytical chromatography. Spectrophotometric detection was performed using an Acquity PDA detector. Chromatographic separation was achieved on a C18 BEH column (Waters Acquity, 50 mm \times 2.1 mm, 1.7 μm). Mass spectra were recorded on a hybrid LTQ™ Orbitrap

Discovery XL instrument (Thermo Fisher Scientific – Bremen, Germany), coupled to an Accela HPLC system (Thermo Fisher Scientific) equipped with a binary pump, an autosampler, and Xcalibur 2.1 as a software.

2.2. Ethyl 2-iodobenzoate (3)

A suspension of 2-iodobenzoic acid **2** (50 g, 0.20 mol) and conc. H_2SO_4 (4.5 mL) in ethanol (200 mL) was refluxed for 24 h. The progress of the reaction was monitored using TLC. After completion of the reaction, volatiles were removed under reduced pressure and the resulting mixture was diluted with dichloromethane (500 mL) and neutralized with 10% Na_2CO_3 (50 mL). The organic layer was separated using a separating funnel, then dried over Na_2SO_4 and evaporated to dryness to afford 52 g (94%) of the ester **3**, which was used without further purification for the next reaction. MS (ESI⁺, MeOH): m/z : 277.0 $[\text{M}+\text{H}]^+$.

2.3. Ethyl 2-(3-methylphenoxy)benzoate (5)

A suspension of *m*-cresol **4** (35.55 g, 0.33 mol), **3** (45.43 g, 0.17 mol), K_2CO_3 (45.33 g, 0.33 mol) and CuCl (6.45 g, 0.028 mol) in dry pyridine (250 mL) was heated at 120 °C for 24 h under argon atmosphere. After completion of the reaction as indicated by TLC, volatiles were removed under reduced pressure and the residue was diluted in CH_2Cl_2 (100 mL). The organic layer was washed subsequently with 3 M aq. HCl solution (3 \times 50 mL), water (3 \times 50 mL), brine (3 \times 50 mL), dried over Na_2SO_4 , and evaporated to dryness. Flash chromatography on silica gel using a mixture of cyclohexane/EtOAc (20:1, v/v) afforded **5** as an oil (40.04 g, 92%). ^1H NMR (400 MHz, CDCl_3): δ 1.21 (t, $J = 7.1$ Hz, 3H, CH_3CH_2), 2.29 (s, 3H, CH_3), 4.25 (q, $J = 7.1$ Hz, 2H, CH_2CH_3), 6.72–6.75 (m, 2H, H-2', H-6'), 6.86 (d, $J = 7.6$ Hz, 1H, H-4'), 6.98 (dd, $J = 8.3, 0.8$ Hz, 1H, H-3), 7.16 (m, 2H, H-5', H-5), 7.43 (td, $J = 8.3, 1.8$ Hz, H-4), 7.9 (dd, $J = 7.8, 1.8$ Hz, 1H, H-6). ^{13}C NMR (50 MHz, CDCl_3): δ 14.1 (CH_3CH_2), 21.4 (CH_3), 61.0 (CH_3CH_2), 114.9 (C-6'), 118.5 (C-2'), 121.2 (C-3), 123.6 (C-

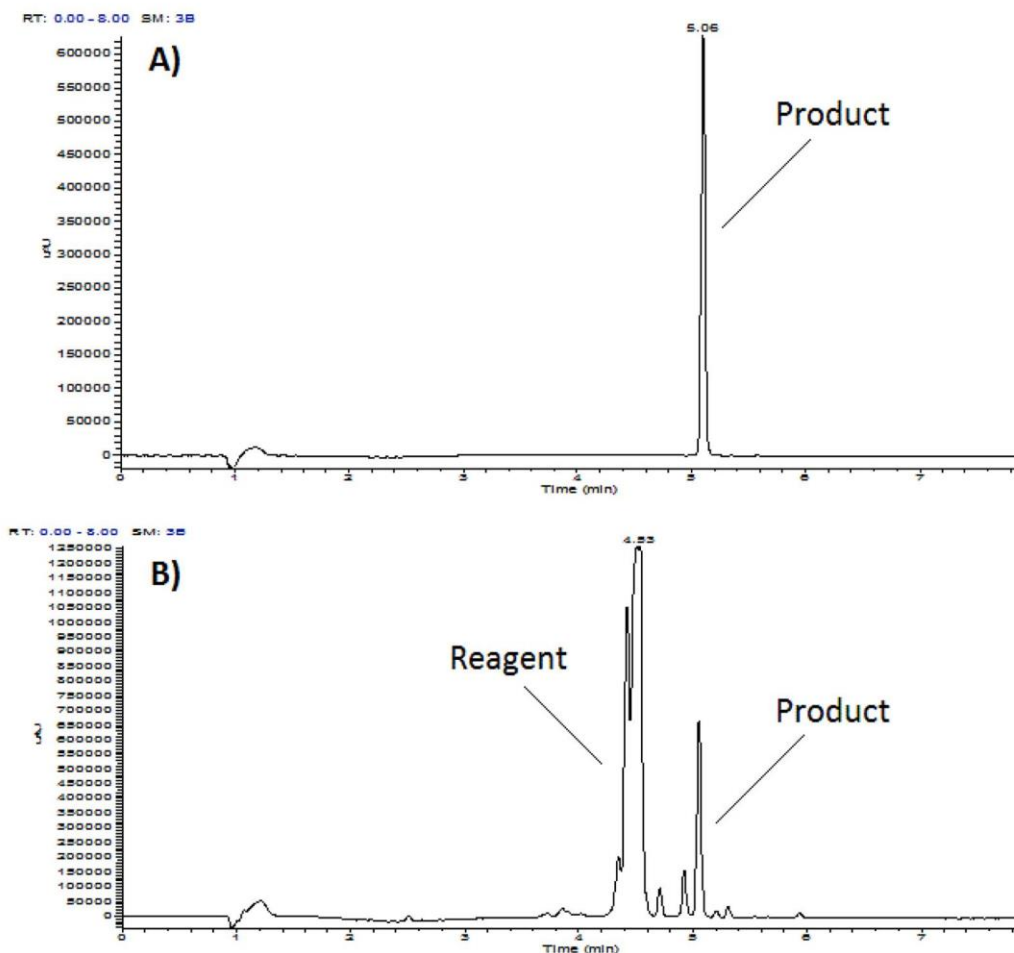


Fig. 1. Representative chromatograms of the HPLC purification process recorded by the PDA detector set at A) 537 nm and B) 280 nm.

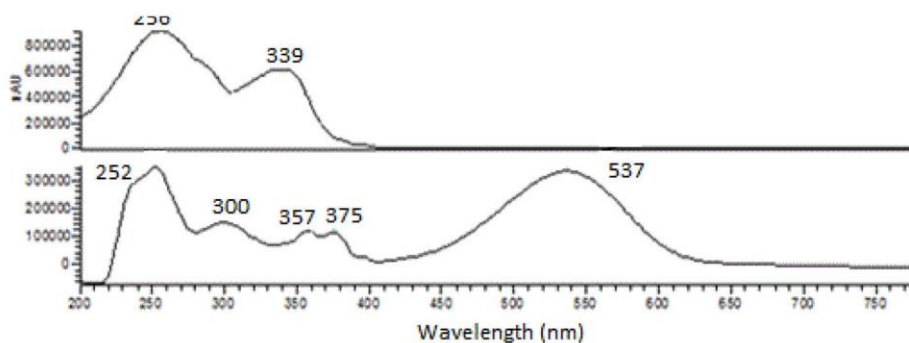


Fig. 2. UV-Vis spectra of the peaks, respectively assigned to the derivatization reagent **BrXa** (top) and the derivatized cyclopropylamine **CypPyXa** (bottom). Snapshots collected by the PDA detector.

5), 123.7 (C-4'), 123.9 (C-1), 129.4 (C-5'), 131.8 (C-6), 133.5 (C-4), 139.7 (C-3'), 155.9 (C-1'), 157.9 (C-2), 165.6 (CO). MS (ESI⁺, MeOH): *m/z*: 257.1 [M+H]⁺; HRMS (ESI⁺): *m/z* calcd for C₁₆H₁₇O₃: 257.1172 [M+H]⁺; found 257.1177.

2.4. Ethyl 2-(3-methyl-4-nitrophenoxy)benzoate (**6b**)

To a suspension of ester **5** (39.46 g, 0.15 mol) in acetic anhydride (93.4 mL, 0.99 mol), previously cooled down to 0 °C, was added

dropwise a solution of fuming HNO₃ (6.7 mL, 0.16 mol) in acetic anhydride (23.3 mL, 0.25 mol). The resulting mixture was stirred at rt for 24 h. After completion of the reaction, the mixture was poured into ice-water bath, basified with 15% NaOH aq. solution (pH ~ 9) and extracted with CH₂Cl₂ (3 × 30 mL). The combined organic layers were dried over anhydrous Na₂SO₄ and evaporated to dryness. The residue was purified by column chromatography on silica gel, using petroleum ether/EtOAc (30:1), to afford **6a** as the major regioisomer (29.28 g, 63%) and **6b** (9.76 g, 21%) as the minor one. *Ethyl 2-(5-methyl-2-nitrophenoxy)*

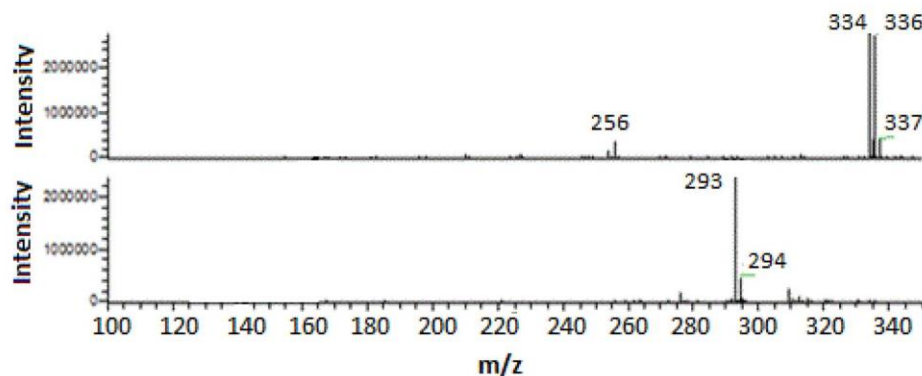


Fig. 3. Mass spectrograms of the peaks assigned to the derivatization reagent (top) and derivatized cyclopropylamine (bottom). The expected theoretical m/z values for the $[M+H]^+$ molecular ions of both compounds are respectively: **BrXa** ($C_{14}H_8O_4BrN$) = 333.971 & 335.969; and **CypPyXa** ($C_{17}H_{12}O_2N_2$) = 293.092.

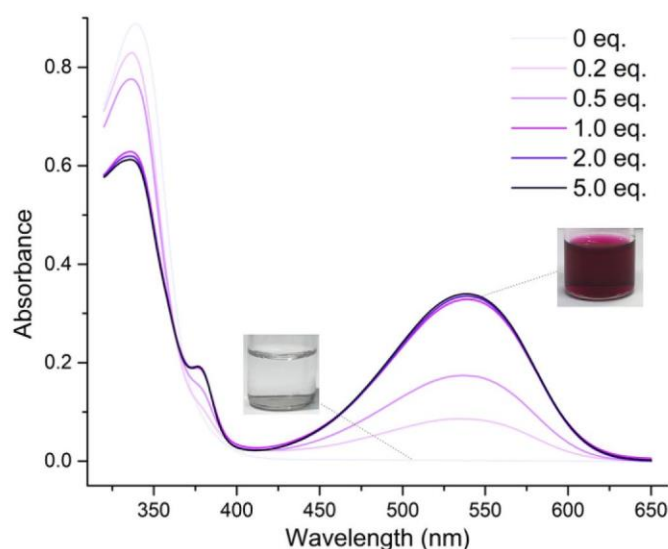


Fig. 4. Investigation of the colorimetric sensing: spectrophotometric titration of **BrXa** with Cyp-NH₂ leading to **CypPyXa**. Inserts represent the initial (left) and ending (right) solutions.

benzoate 6a: oil. ¹H NMR (400 MHz, CDCl₃): δ 1.16 (t, J = 7.1 Hz, 3H, CH₂CH₃), 2.30 (s, 3H, CH₃), 4.22 (q, J = 7.1 Hz, 2H, CH₂CH₃), 6.58 (s, 1H, H-6'), 6.95 (d, J = 8.3 Hz, 1H, H-4'), 7.11 (d, J = 8.2 Hz, 1H, H-3), 7.33 (td, J = 8.2, 2.1 Hz, 1H, H-5), 7.58 (td, J = 8.2, 2.1 Hz, 1H, H-4), 7.92 (d, J = 8.3 Hz, 1H, H-3'), 8.03 (dd, J = 8.2, 2.1 Hz, 1H, H-6). ¹³C NMR (50 MHz, CDCl₃): δ 13.8 (CH₂CH₃), 21.6 (CH₃), 61.2 (CH₂CH₃), 118.5 (C-6'), 122.1 (C-3), 123.1 (C-4'), 124.0 (C-1), 125.2 (C-5), 125.8 (C-3'), 132.3 (C-6), 133.9 (C-4), 137.8 (C-2'), 145.9 (C-5'), 151.7 (C-1'), 153.8 (C-2), 164.9 (CO). **6b:** white solid, m. p. = 63–64 °C (Et₂O/*n*-hexane). ¹H NMR (400 MHz, CDCl₃): δ 1.18 (t, J = 7.3 Hz, 3H, CH₂CH₃), 2.56 (s, 3H, CH₃), 4.20 (q, J = 7.3 Hz, 2H, CH₂CH₃), 6.75 (d, J = 8.2 Hz, 1H, H-6'), 6.8 (s, 1H, H-2'), 7.15 (d, J = 8.3 Hz, 1H, H-3), 7.36 (t, J = 8.3 Hz, 1H, H-5), 7.62 (t, J = 8.3 Hz, 1H, H-4), 8.03 (d, J = 8.3 Hz, 1H, H-6), 8.05 (d, J = 8.2 Hz, 1H, H-5'). ¹³C NMR (50 MHz, CDCl₃): δ 14.0 (CH₂CH₃), 21.5 (CH₃), 61.2 (CH₂CH₃), 113.9 (C-6'), 119.4 (C-2'), 123.1 (C-3), 124.5 (C-1), 125.7 (C-5), 127.4 (C-5'), 132.3 (C-6), 134.1 (C-4), 137.0 (C-3'), 143.1 (C-4'), 153.4 (C-2), 162.0 (C-1'), 164.7 (CO). MS (ESI⁺, MeOH): m/z : 302.1 [M+H]⁺; HRMS (ESI⁺): m/z calcd for C₁₆H₁₆NO₅: 302.1023 [M+H]⁺; found 302.1019.

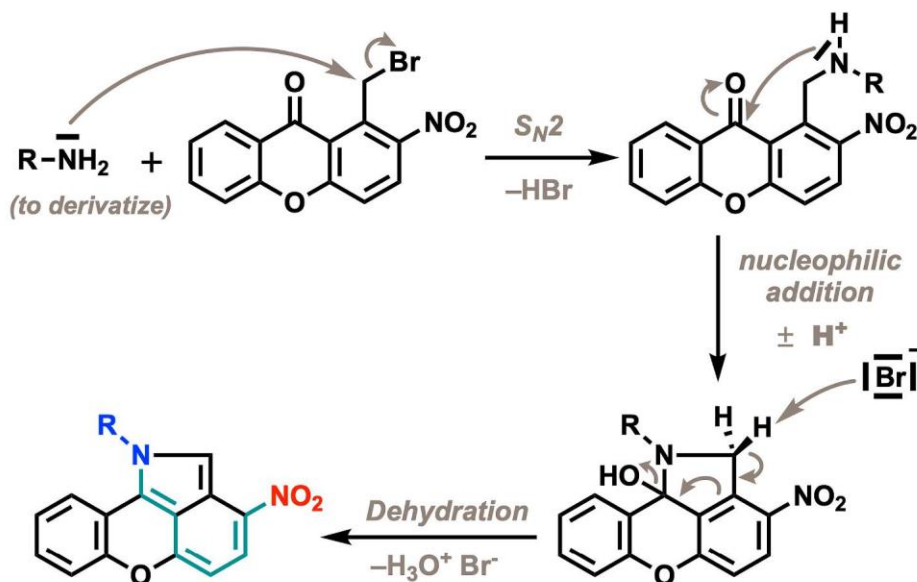
2.5. 2-(3-Methyl-4-nitrophenoxy)benzoic acid (**7**)

To a solution of ester **6b** (9.4 g, 30 mmol) in ethanol at rt, a cold 15% NaOH aq. solution (10 mL, 100 mmol) was added dropwise. The reaction mixture was stirred at rt for 1.5 h, before being poured into water

and acidified with 6 M HCl aq. solution (pH ~ 2). The resulting white precipitate was filtered and dried over phosphorus pentoxide (glass desiccator) to afford **7** (8.13 g, 96%), which was used for the next step without any further purification. M. p. = 144–145 °C (EtOAc). ¹H NMR (400 MHz, CDCl₃): δ 2.43 (s, 3H, CH₃), 6.90 (s, 1H, H-2'), 6.94 (d, J = 8.2 Hz, 1H, H-6'), 7.15 (d, J = 8.1 Hz, 1H, H-3), 7.26 (t, J = 8.1 Hz, 1H, H-5), 7.57 (td, J = 8.1, 1.9 Hz, H-4), 8.04 (d, J = 8.2 Hz, 1H, H-5'), 8.22 (dd, J = 8.1, 1.9 Hz, H-6). ¹³C NMR (50 MHz, CDCl₃): δ 21.7 (CH₃), 120.2 (C-6'), 120.7 (C-2'), 121.4 (C-3), 124.7 (C-1), 124.8 (C-5), 126.1 (C-5'), 133.3 (C-6), 135.0 (C-4), 138.6 (C-3'), 146.6 (C-4'), 150.1 (C-2), 155.6 (C-1'), 168.9 (CO). MS (ESI⁺, MeOH): m/z : 274.1 [M+H]⁺; HRMS (ESI⁺): m/z calcd for C₁₄H₁₂NO₅: 274.0710 [M+H]⁺; found 274.0713.

2.6. 1-Methyl-2-nitro-9H-xanthen-9-one (**8**)

A suspension of acid **7** (6.20 g, 0.023 mol) in polyphosphoric acid (15 mL) was stirred at 100 °C for 2 h. After cooling, the mixture was poured into crushed-ice bath. The resulting precipitate was filtered, washed with 10% Na₂CO₃ solution and water, and air-dried. Flash chromatography on silica gel, using a mixture of cyclohexane/CH₂Cl₂ (12:1 → 5:1, v/v) afforded **8** as a white solid (5.4 g, 92%). M. p. = 206–207 °C (EtOH) (lit. 205–207 °C) [47]. ¹H NMR (400 MHz, DMSO-*d*₆): δ 2.85 (s, 3H, CH₃), 7.50 (td, J = 7.9, 0.8 Hz, 1H, H-7), 7.64 (d, J = 9.0 Hz, 1H, H-4), 7.68 (d, J = 7.9 Hz, 1H, H-5), 7.88 (td, J = 7.9 Hz, 0.8 Hz, 1H, H-6), 8.13 (dd, J = 7.9, 0.8 Hz, 1H, H-8), 8.23 (d, J = 9.0



Scheme 6. Hypothetical mechanism of the derivatization reaction using one equivalent of primary amine. The push–pull relationship, involving the donor (blue) and acceptor (red) groups, is depicted in green.

Table 1
Photophysical properties of CypPyXa in various solvents, representative of a wide range of polarity.^[a]

Solvent	$E_T^{N(30)}$ ^[b]	$\epsilon_{\max}(\text{MeOH}) = 13$ ^[c]			ϕ ^[g]
		λ_{Abs} ^[d]	λ_{Em} ^[e]	$\Delta\lambda$ ^[f]	
EtOH	0.65	528	656	128	1
CH ₃ CN	0.46	531	654	123	4
DMSO	0.44	544	666	122	4
DMF	0.39	535	635	100	12
DCE	0.33	533	631	98	15
EtOAc	0.23	514	611	97	22
THF	0.21	514	607	93	65
Toluene	0.10	510	584	74	91

^a Reported values are the average of two or more independent and reproducible measurements, ± 1 nm for wavelengths. Excitation wavelength was at the corresponding absorption maximum. ^b Normalized Reichardt's solvent polarity index [52]. ^c Molar extinction coefficient in $10^3 \text{ M}^{-1} \text{ cm}^{-1}$ was determined in methanol; relative standard deviations are lower or equal to 5%. ^d Position of the absorption maximum in nm. ^e Wavelength of the emission maximum in nm. ^f For convenience, Stokes shifts are expressed in nm for $\Delta\lambda = \lambda_{\text{Em}} - \lambda_{\text{Abs}}$ (difference in cm^{-1}). ^g Fluorescence quantum yields ϕ were determined by performing an excitation at the corresponding absorption maximum of the reference standard in the considered solvent: Nile blue perchlorate in EtOH ($\lambda_{\text{Ex}} = 321 \text{ nm}$, $\phi = 27\%$) [53], $\pm 10\%$ mean standard deviation.

Hz, 1H, H-3). ¹³C NMR (50 MHz, DMSO-*d*₆): δ 16.9 (CH₃), 118.0 (C-5), 118.1 (C-4), 120.1 (C-9a), 122.2 (C-8a), 125.2 (C-7), 126.4 (C-8), 129.6 (C-3), 135.4 (C-1), 136.0 (C-6), 147.6 (C-2), 154.5 (C-10a), 158.5 (C-4a), 177.7 (CO). MS (ESI⁺, MeOH): m/z : 256.1 [M+H]⁺; HRMS (ESI⁺): m/z calcd for C₁₄H₁₀NO₄: 256.0604 [M+H]⁺; found 256.0609.

2.7. 1-(bromomethyl)-2-nitro-9H-xanthene-9-one (1-BrXa)

A suspension of xanthone **8** (2.86 g, 11 mmol), NBS (1.96 g, 11 mmol) and BPO (dibenzoyl peroxide, 286 mg, 1.18 mmol) in CCl₄ (100 mL) was refluxed for 8 h under UV irradiation (compact fluorescent lamp – CFL 150 W). After completion of the reaction, the mixture was washed with 5% NaHCO₃ aq. solution (3 × 20 mL), 5% Na₂S₂O₄ aq. solution (3 × 20 mL), water (3 × 50 mL), dried over Na₂SO₄, and evaporated to dryness. Flash chromatography on silica gel using a mixture of cyclohexane/CH₂Cl₂ (10:1 → 5:1, v/v) as the eluent afforded **1** (3.01 g, 82%). M. p. = 179–181 °C (EtOH) [47]. ¹H NMR (400 MHz,

CDCl₃): δ 5.29 (s, 2H, CH₂), 7.41–7.48 (m, 2H, H-7, H-5), 7.53 (d, $J = 8.4 \text{ Hz}$, 1H, H-4), 7.77 (td, $J = 8.7, 1.7 \text{ Hz}$, 1H, H-6), 8.17 (d, $J = 8.4 \text{ Hz}$, 1H, H-3), 8.29 (dd, $J = 8.7, 1.7 \text{ Hz}$, 1H, H-8). ¹³C NMR (50 MHz, CDCl₃): δ 23.3 (CH₂Br), 117.6 (C-5), 119.0 (C-9a), 120.3 (C-4), 122.8 (C-8a), 125.1 (C-7), 127.2 (C-8), 129.8 (C-3), 135.3 (C-6), 136.2 (C-1), 146.5 (C-2), 155.5 (C-10a), 159.6 (C-4a), 177.8 (CO). MS (ESI⁺, MeOH): m/z : 334.0, 336.0 [M+H]⁺; HRMS (ESI⁺): m/z calcd for C₁₄H₉BrNO₄: 333.9709 [M+H]⁺; found 333.9711.

2.8. 1-Butyl-3-nitro-1H-chromeno[4,3,2-cd]isoindole (9)

To a suspension of compound **1** (35 mg, 0.10 mmol) in dry MeOH (2 mL), *n*-butylamine (20 eq.) was added. The resulting mixture was stirred at rt for 2 h and the progress of the reaction was monitored by TLC. After the completion of the reaction, the precipitate was filtered off and then recrystallized with CH₂Cl₂/Et₂O to afford **9** (29 mg, 94%). M. p. = 198–199 °C (CH₂Cl₂/Et₂O). ¹H NMR (400 MHz, CDCl₃): δ 0.94 (t, $J = 7.3 \text{ Hz}$, 3H, CH₃), 1.35–1.49 (m, 2H, CH₂CH₂CH₃), 1.85–1.97 (m, 2H, CH₂CH₂CH₃), 4.40 (d, $J = 7.4 \text{ Hz}$, 2H, N-CH₂), 6.11 (d, $J = 8.4 \text{ Hz}$, 1H, H-5), 7.14–7.25 (m, 3H, H-7, H-9, H-8), 7.40 (s, 1H, H-2), 7.48 (dd, $J = 7.6, 1.5 \text{ Hz}$, 1H, H-10), 8.07 (d, $J = 8.4 \text{ Hz}$, 1H, H-4). ¹³C NMR (101 MHz, CDCl₃): δ 13.7 (CH₃), 19.9 (CH₂CH₂CH₃), 32.8 (CH₂CH₂CH₃), 50.0 (N-CH₂), 98.1 (C-5), 115.0 (C-2a), 116.4 (C-2), 118.2 (C-10a), 118.6 (C-7), 119.3 (C-10b), 120.5 (C-2a¹), 120.5 (C-10), 125.3 (C-9), 128.0 (C-8), 130.1 (C-4), 131.7 (C-3), 152.9 (C-6a), 157.6 (C-5a). MS (ESI⁺, MeOH): m/z : 309.1 [M+H]⁺; HRMS (ESI⁺): m/z calcd for C₁₈H₁₇N₂O₃: 309.1234 [M+H]⁺; found 309.1233.

2.9. 1-Dodecyl-3-nitro-1H-chromeno[4,3,2-cd]isoindole (10)

This compound **10** was synthesized following a similar procedure as described for **9**, using dodecylamine as the proper amine of the reaction. Yield: 95%. M. p. = 113–114 °C (CH₂Cl₂/Et₂O). ¹H NMR (600 MHz, CDCl₃): δ 0.87 (t, $J = 7.3 \text{ Hz}$, 3H, CH₃), 1.25–1.30 (m, 12H, dodecyl), 1.35 (m, 2H, dodecyl), 1.44 (p, $J = 7.3 \text{ Hz}$, 2H, dodecyl), 1.56–1.66 (m, 2H, dodecyl), 1.94–2.01 (m, 2H, dodecyl), 4.44 (t, $J = 7.4 \text{ Hz}$, 2H, N-CH₂), 6.19 (dd, $J = 8.6, 1.8 \text{ Hz}$, 1H, H-5), 7.19–7.26 (m, 2H, H-7, H-9), 7.29 (dd, $J = 8.1, 1.7 \text{ Hz}$, 1H, H-8), 7.47 (s, 1H, H-2), 7.53 (dd, $J = 7.7, 1.8 \text{ Hz}$, 1H, H-10), 8.15 (dd, $J = 8.6, 1.7 \text{ Hz}$, 1H, H-4). ¹³C NMR (151 MHz, CDCl₃): δ 14.23 (CH₃), 22.8 (dodecyl), 26.8 (dodecyl), 29.3 (dodecyl), 29.5 (dodecyl), 29.5 (dodecyl), 29.7 (2 x dodecyl), 29.7

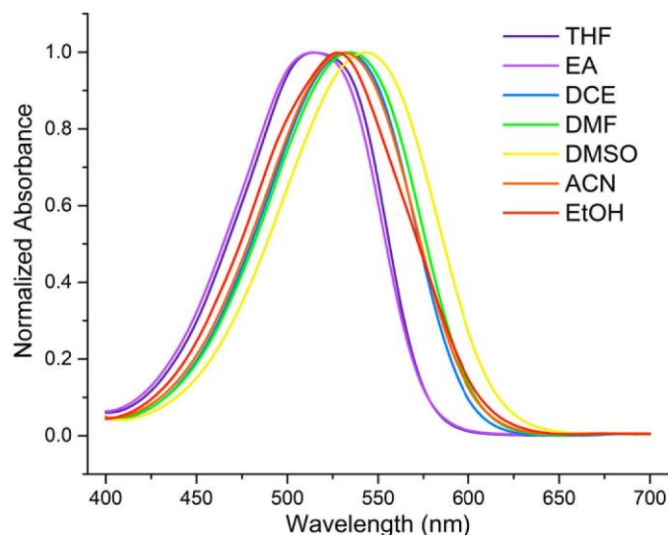


Fig. 5. Absorption observables of the derivatized adduct CypPyXa, illustrating solvatochromic characteristics.

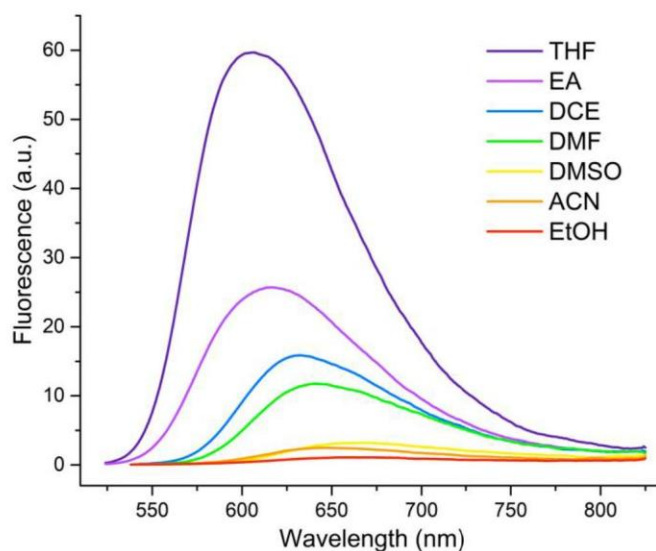


Fig. 6. Emission spectra of the derivatized adduct CypPyXa, demonstrating fluorescence quenching over the increasing polarity.

(dodecyl), 31.0 (dodecyl), 32.0 (dodecyl), 50.5 (N-CH₂), 98.2 (C-5), 115.3 (C-2a), 116.5 (C-2), 118.5 (C-10a), 118.8 (C-7), 119.4 (C-10b), 120.6 (C-2a¹), 120.6 (C-10), 125.4 (C-9), 128.1 (C-8), 130.2 (C-4), 132.1 (C-3), 153.2 (C-6a), 157.7 (C-5a). MS (ESI⁺, MeOH): *m/z*: 421.2 [M+H]⁺; HRMS (ESI⁺): *m/z* calcd for C₂₆H₃₃N₂O₃: 421.2486 [M+H]⁺; found 421.2490.

2.10. 1-Cyclopropyl-3-nitro-1H-chromeno[4,3,2-cd]isoindole (11)

This compound **11** was synthesized following a similar procedure as described for **9**, using cyclopropylamine as the proper amine of the reaction. Yield: 93%. ¹H NMR (400 MHz, CDCl₃): δ 1.31–1.41 (m, 4H, CH₂), 3.80 (m, 1H, CH-cyclopropyl), 6.18 (d, *J* = 8.3 Hz, 1H, H-5), 7.20–7.33 (m, 3H, H-7, H-9, H-8), 7.54 (s, 1H, H-2), 8.04 (dd, *J* = 7.4, 1.8 Hz, 1H, H-10), 8.15 (d, *J* = 8.3 Hz, 1H, H-4). ¹³C NMR (101 MHz, CDCl₃): δ 8.9 (CH₂), 31.3 (CH-cyclopropyl), 98.1 (C-5), 114.7 (C-2a), 115.7 (C-2), 118.3 (C-10a), 118.3 (C-7), 120.1 (C-10b), 121.5 (C-2a¹),

121.8 (C-10), 125.0 (C-9), 128.0 (C-8), 130.5 (C-4), 131.9 (C-3), 153.0 (C-6a), 157.7 (C-5a). MS (ESI⁺, MeOH): *m/z*: 293.1 [M+H]⁺; HRMS (ESI⁺): *m/z* calcd for C₁₇H₁₃N₂O₃: 293.0921 [M+H]⁺; found 293.0923.

2.11. 1-((diethylamino)methyl)-2-nitro-9H-xanthen-9-one (12)

This compound **12** was synthesized following a similar procedure as described for **9**, using diethylamine as the proper amine of the reaction. Yield: 89%. ¹H NMR (600 MHz, CDCl₃): δ 0.90 (t, *J* = 7.1 Hz, 6H, CH₂CH₃), 2.47 (q, *J* = 7.1 Hz, 4H, CH₂CH₃), 4.70 (s, 2H, CH₂), 7.41 (dd, *J* = 8.1, 1.1 Hz, 1H, H-5), 7.44–7.48 (m, 2H, H-7, H-4), 7.74 (dd, *J* = 8.1, 1.1 Hz, 1H, H-6), 7.82 (d, *J* = 9.0 Hz, 1H, H-3), 8.26 (dd, *J* = 8.0, 1.1 Hz, 1H, H-8). ¹³C NMR (151 MHz, CDCl₃): δ 11.2 (CH₂CH₃), 46.8 (CH₂CH₃), 50.3 (CH₂), 117.6 (C-5), 117.9 (C-9a), 121.0 (C-4), 122.8 (C-8a), 124.8 (C-7), 127.2 (C-8), 129.2 (C-3), 135.4 (C-6), 141.3 (C-1), 148.5 (C-2), 154.9 (C-10a), 157.8 (C-4a), 178.5 (CO). MS (ESI⁺, MeOH): *m/z*: 327.1 [M+H]⁺; HRMS (ESI⁺): *m/z* calcd for C₁₈H₁₉N₂O₄: 327.1339 [M+H]⁺;

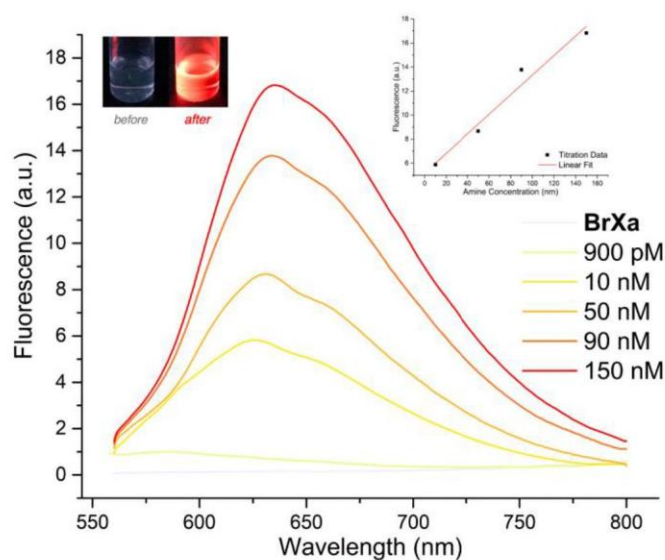


Fig. 7. Fluorogenic sensing of Cyp-NH₂: determination of the sensitivity limit of CypPyXa by fluorescence titration of BrXa. Inserts represent the starting (left) and final (right) solutions, respectively non-emissive and strongly red fluorescent.

found 327.1334.

2.12. 3-Nitro-1-(2-(pyrrolidin-1-yl)ethyl)-1H-chromeno[4,3,2-cd]isoindole (13)

To a suspension of **1** (70 mg, 0.20 mmol) in abs. EtOH (3 mL), was added 2-propylaminoethylamine (20 eq.). The reaction mixture was stirred at rt for 2 h, before being reduced under vacuum, taken over with CH₂Cl₂, washed with H₂O, dried over Na₂SO₄, and filtered. The volatiles were removed *in vacuo* and the resulting crude was purified by flash chromatography on silica gel eluted with CH₂Cl₂/MeOH (97:3, v/v) to afford **13** as an oil (66 mg, 94%) [48]. ¹H NMR (400 MHz, CDCl₃): δ 1.76 (br. s, 4H, (CH₂CH₂)₂N-), 2.56 (br. s, 4H, (CH₂CH₂)₂N), 2.91 (t, *J* = 7.5 Hz, 2H, (CH₂CH₂)₂NCH₂), 4.45 (t, *J* = 7.5 Hz, 2H, (CH₂CH₂)₂NCH₂CH₂), 6.00 (d, *J* = 8.3 Hz, 1H, H-5), 7.15–7.17 (m, 3H, H-7, H-9, H-8), 7.32 (s, 1H, H-2), 7.48 (d, *J* = 7.3 Hz, 1H, H-10), 7.97 (d, *J* = 8.3 Hz, 1H, H-4). ¹³C NMR (50 MHz, CDCl₃): δ 23.6 ((CH₂CH₂)₂NCH₂CH₂), 49.4 ((CH₂CH₂)₂NCH₂CH₂), 54.5 ((CH₂CH₂)₂NCH₂CH₂), 56.3 ((CH₂CH₂)₂NCH₂CH₂), 98.0 (C-5), 115.0 (C-2a), 116.4 (C-2), 117.9 (C-10a), 118.5 (C-7), 119.5 (C-10b), 120.1 (C-2a¹), 120.5 (C-10), 125.3 (C-9), 128.0 (C-8), 130.1 (C-4), 131.6 (C-3), 152.8 (C-6a), 157.5 (C-5a). MS (ESI⁺, MeOH): *m/z*: 350.1 [M+H]⁺; HRMS (ESI⁺): *m/z* calcd for C₂₀H₂₀N₃O₃: 350.1499 [M+H]⁺; found 350.1496.

3. Results and discussion

3.1. Preparation of the derivatization reagent

Our efforts were initially focused on the development of a reliable procedure for the scalable synthesis of the proposed reagent BrXa. To overcome previous difficulties such as the number of steps and overall yield [47,48], we considered a more convergent approach based on a copper-catalyzed coupling reaction (Scheme 3).

Commercially available 2-iodobenzoic acid **2** was used as a starting material which, upon esterification in ethanol, yielded almost quantitatively the corresponding ethyl ester **3**. Ullmann condensation of *m*-cresol **4** with the aryl iodide **3** efficiently afforded the coupling product

5. Nitric acid treatment in acetic anhydride of the biaryl ether **5**, led to a mixture of nitro-isomeric compounds **6a** and **6b**, separable by silica gel chromatography and identifiable by 2D-NMR. More specifically, structural discrimination resulted from the observation of ³*J* couplings between the methyl group and two aromatic CH carbons in *ortho* in the case of **6a**, against a single correlation for **6b**. Subsequently, saponification under mild conditions of the ester **6b** provided the carboxylic acid **7**, which was ring-closed upon treatment with PPA to give the xanthere **8**. The bromomethyl target **1** was finally obtained from **8** upon free-radical bromination with NBS under UV irradiation.

It is worth mentioning that the overall yield of the newly developed synthesis is >40%, *i.e.*, thrice higher than the precedent approach. In a nutshell, an original and straightforward synthetic approach has been developed for the preparation of the derivatization reagent BrXa, using practical, inexpensive and scalable procedures with purification processes remaining simple.

3.2. Derivatization reaction

To develop suitable conditions for this derivatization in order to make it an effective detection tool, a certain set of specifications have to be met. First of all, the reaction must be performed at room temperature to be truly practical. Another prerequisite is to find a solvent in which both the derivatization reagent BrXa and the targeted amines are fully soluble and also remains reactive. Protic solvents such as methanol and ethanol – typical for this kind of reaction – revealed to be not enough solvating in the concentration range routinely used for spectroscopic measurements. The chosen solvent has to be polar to allow the first step (S_N2) to be conducted, but the *pseudo* benzylic bromide – known to be reactive – must be stable during the reaction time. Dimethylformamide proved to be the one that ticks all the boxes.

Using DMF as a solvent at room temperature, first attempts on selected primary amines were carried out in batch. Derivatization reaction proceeded smoothly on aliphatic amines with side chains of different sizes (*butyl* and *dodecyl*) to quantitatively furnish the corresponding pyrroloxanthenes, **9 BuPyXa** and **10 DodecPyXa**, respectively (Scheme 4). Several observations could be made: *i*) a clear magenta

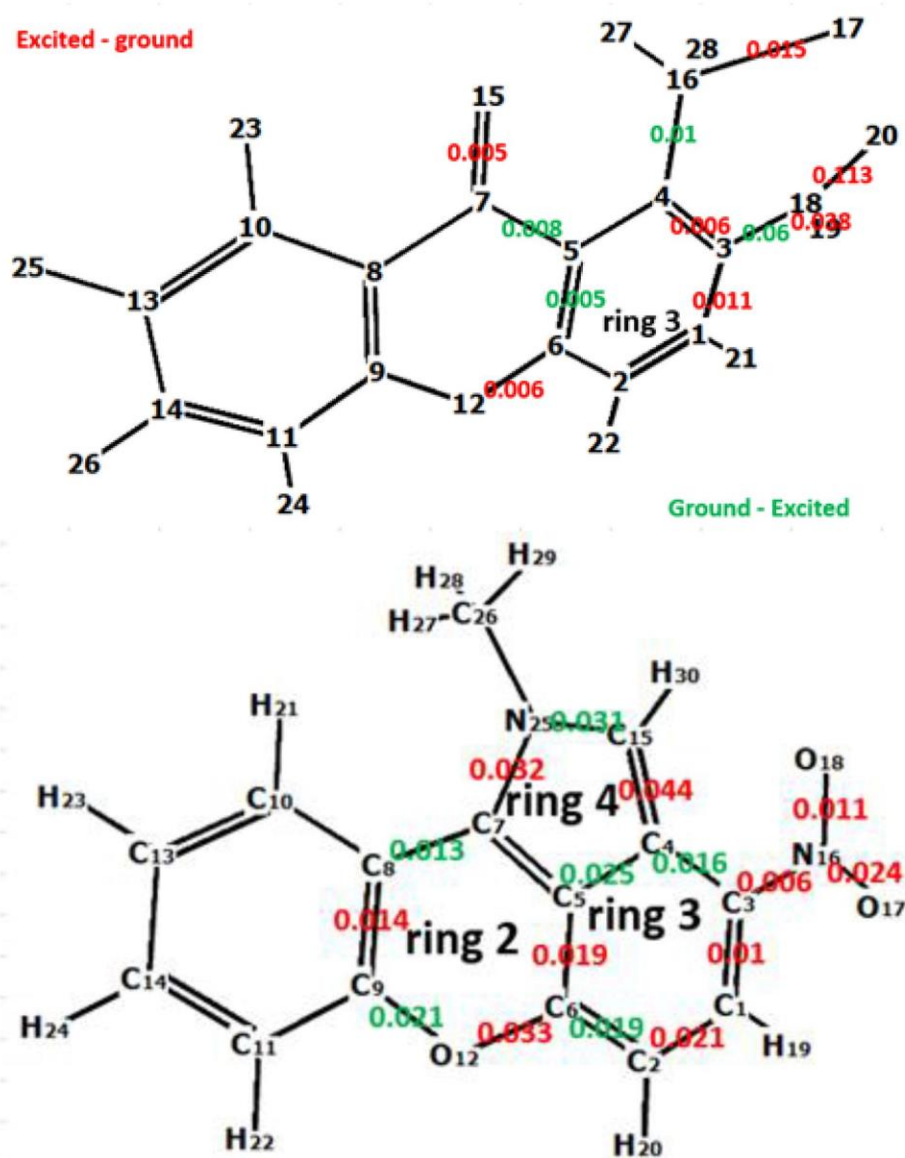


Fig. 8. Bond elongation features upon excitation for **BrXa** (top) and **MePyXa**, the methylamine-derivatized product (bottom). Only bond length differences larger than 0.005 Å were reported.

color appears along the derivatization process, offering an easy readout *ii*) a distinct vermilion fluorescence emerges upon excitation with any type of laser ranging from blue to yellow, allowing the sensitivity of the reaction to be substantially increased. As a consequence, these properties make the detection chromogenic and fluorogenic. Moreover, the simplicity of the method is clearly an asset, since there is no requirement of anhydrous conditions, temperature or precise order in the addition of the reagent.

Then, to establish the selectivity towards the order (1°, 2° & 3°) of the amines to be derivatized, different types of amines were chosen. Triethylamine was first screened as a negative control, and as expected, no reaction was observed with this tertiary amine (Scheme 5). This chemical inertia bodes well for the development of analytical methods with amine-based buffers. Thereafter, the reactivity of secondary amines was tested using diethylamine. As suspected, the first S_N2-type step

worked normally to provide **12**, but no further cyclization could take place due to the formation of an unstable ammonium intermediate (Scheme S1). Advantageously, **NEt₂Xa** has an electronic π-scaffold similar to that of the reagent, meaning therefore that it will be both colorless and devoid of fluorescence. Thus, derivatized secondary amines should not cross-contaminate the colorimetric detection of the amines of interest during the derivatization of a complex matrix.

Eventually, using 2-(pyrrolidinyl)ethylamine explicitly showed both the lack of reactivity of tertiary amines and the versatility of primary R-NH₂ for this derivatization procedure. Thence, this test exclusively produced the pyrrolidinyl-pyrroloxanthone **13**, **PyrrroPyXa**. Furthermore, a competition experiment using *N*-methylethylenediamine demonstrated the superior reactivity of the 1° amine at the expense of the 2° one towards **BrXa** (Figs. S7–9).

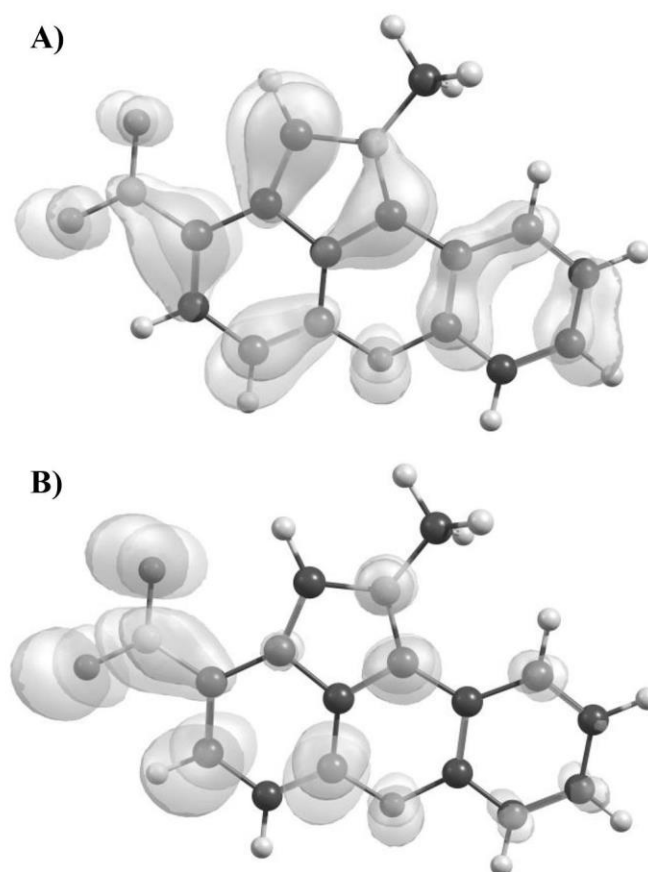


Fig. 9. HOMO (A) and LUMO (B) of the derivatization product of methylamine.

3.3. Chromatographic and mass spectrometry analysis

In order to apply the novel derivatization reagent to chromatographic analysis, cyclopropylamine was selected as a model analyte. The derivatization of the saturated cyclic primary amine with **BrXa** proceeded smoothly in acetonitrile to yield **11 CypPyXa**, as the derivatized product (Scheme 4). Triethylamine was used as a base to scavenge HBr formed *in situ* during the reaction process.

An analytical method was developed to separate the product from the excess of the derivatization reagent, using H₂O and acetonitrile, as solvents A & B, respectively. The total analysis time, including column equilibration, was 5 min per injection and the flow rate was set at 0.5 mL/min. The gradient elution program used was as follows: from 10% to 100% B in 3.0 min => 0.5 min at 100% B => from 100% to 10% B in 0.2 min => equilibration at 10% B for 1.3 min. The injection volume was adjusted to 5 μ L and the column temperature was maintained at 40 °C throughout all experiments.

The chromatograms depicted in Fig. 1 demonstrate that a baseline separation was obtained (Fig. 1B). The derivatized product is the only one that can be detected in the yellow range (Fig. 1A) due to its extended π -conjugation induced by the formation of an additional ring.

Absorbance spectra – illustrated in Fig. 2 – confirmed this increase of conjugation occurring through the derivatizing reaction, even in presence of a chromophore-free amine. Indeed, an intense and broad absorption band centered around 540 nm clearly appears, as a result of the important electronic conjugation being established between the pyrrolo donor (D) and nitro acceptor (A) groups. On another note, even in case

of contamination by traces of reagent, these observables substantiate that no cross-excitation can take place given the λ -shift of *ca.* 200 nm offered by the derivatized product. This bodes well for the photophysical characterization of the sensing reaction.

Transferring this liquid chromatographic analysis to an MS detector provides a more reliable characterization. Both analytes were precisely identified in the presented MS spectra obtained from the respective chromatographic peaks (Fig. 3). Typically, the two molecular ion isotopes observed with similar abundance were attributed to the presence of bromine in the reagent structure.

3.4. Photophysical characterization

To study this derivatization reaction in detail from a photophysical point of view, cyclopropylamine (Cyp-NH₂) was selected again, this time for the electron-releasing character of its saturated three-membered ring. Indeed, this inductive + I effect should enhance the donor strength in the push-pull relationship operating in the excited state with the nitro acceptor.

To check the chromogenic detection, the derivatization reagent was titrated with this challenging primary amine, and the formation of the resulting **CypPyXa** was monitored by UV-Vis spectroscopy (Fig. 4). For this purpose, **BrXa** was dissolved in DMF in the mM range, and changes in absorption were recorded upon the gradual addition of Cyp-NH₂. Since the xanthone core of **BrXa** absorbs at approx. 340 nm, and thus outside the visible range, the starting solution is completely colorless (*insert* in Fig. 4). As soon as the primary amine is added, an absorption

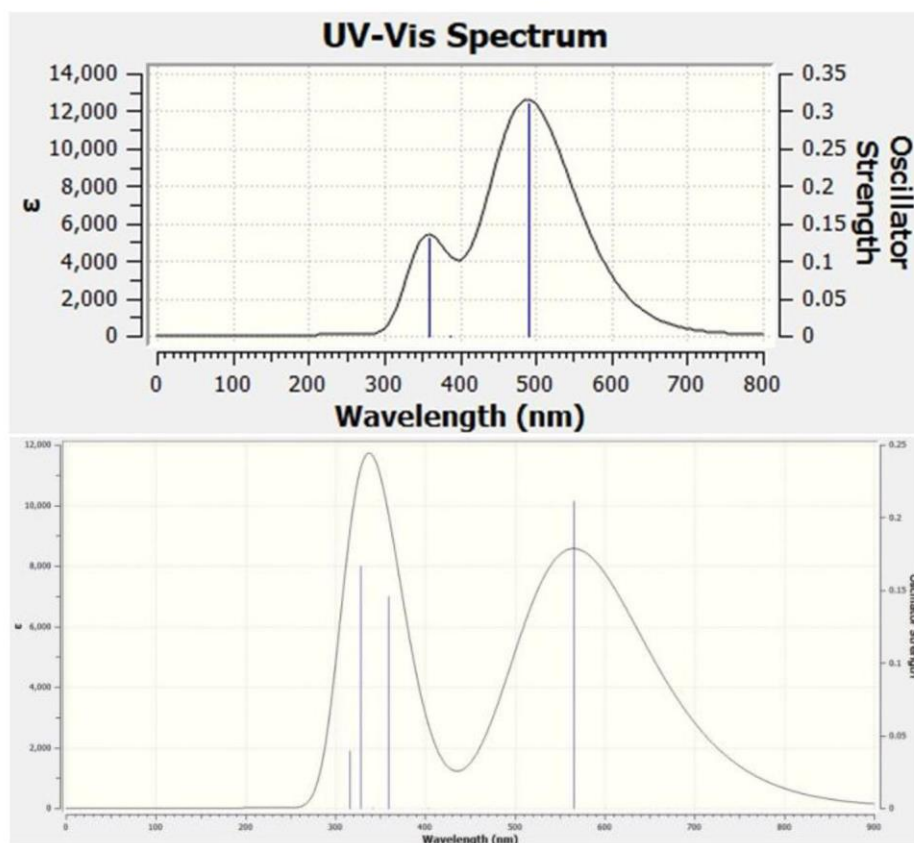


Fig. 10. Theoretical excitation (top) and emission (bottom) spectra of the derivatized amine.

band emerges in the yellow range (ca. 535 nm), transducing the appearance of the fuchsia color observed for the reaction mixture. Once an equivalent is reached, the yellow absorbance of **CypPyXa** no longer seems to change, and the solution turns into a persistent dark magenta (insert in Fig. 4). A similar observation could be made during the fluorescence titration where the emission signal does not fluctuate after the addition of one equivalent of 1° amine (Fig. S1). Therefore, these results highlight a 1:1 stoichiometry for the derivatization reaction, as reflected by the mechanism hypothesized herein in Scheme 6.

To provide further insights into the spectroscopic features of **CypPyXa**, absorption measurements were conducted in a set of solvents of increasing polarity, as transcribed by the Dimroth-Reichardt $E_T^N(30)$ parameter [52]. This empirical scale takes into account the dielectric constant and the H-bond donating ability of the solvent. It is normalized from TMS (0) to water (1). Absorption spectra displayed a certain solvatochromism (about 35 nm) since the maxima vary from 510 nm in toluene to 544 nm for DMSO (Table 1 & Fig. 5). This moderate dependency on solvent polarity revealed that charge transfer between the donor and acceptor groups is already operating in the ground state. This results in a color change from crimson red to purplish blue, respectively for apolar and strongly polar media. In protic EtOH, it is noteworthy that H-bonding with the NO_2 acceptor group induced a hypsochromic shift of the absorption band.

The molar absorptivity of **CypPyXa** was determined to be approx. $13,000 \text{ M}^{-1} \text{ cm}^{-1}$ in DMF, almost twice as high as that of **BrXa** ($\epsilon = 7000 \text{ M}^{-1} \text{ cm}^{-1}$). That observation is consistent with the extension of the π -system occurring during derivatization due to the pyrrole ring

formation [43]. This augurs well for fluorogenic sensing, given that brightness is the product of the molar extinction coefficient and the quantum yield.

Fluorescence measurements were performed in the same set of solvents (Table 1 & Fig. 6). After selective excitation, **CypPyXa** exhibited significant positive solvatochromism ($\sim 70 \text{ nm}$) with maxima oscillating from 584 to 656 nm and an emission color varying over yellow \leftrightarrow orange \leftrightarrow red (Fig. S2). Mega-Stokes shifts ($>100 \text{ nm}$) were even observed in polar solvents, attesting to the strong dependence of the excited-state dipole along with the increasing polarity; typical of push-pull fluorophores. In parallel, quantum yields fluctuate over the entire range, making the dye extremely bright in toluene (91%) and strongly quenched in protic medium, like EtOH (1%). Such a fluorescence quenching – resulting from the steady increase of polarity – is characteristic of a substantial push-pull relationship being established between the pyrrole donor (D) and the nitro acceptor (A) groups. In terms of solubility, reactivity and brightness, DMF appeared to be the best compromise for this derivatization reaction.

Lastly, the sensitivity limit was determined in order to define the scope of applicability of this derivatization process. By exciting at the absorption maximum of **CypPyXa** (535 nm), the initial **BrXa** solution proved to be completely “dark” (flat curve and insert, Fig. 7). This is an essential prerequisite for the development of a fluorogenic derivatization method. The increasing addition of **Cyp-NH₂** made emanate a bright red emission (insert in Fig. 7) resulting from the formation of **CypPyXa**. Plotting the fluorescence intensity as a function of the incremental concentration allowed us to estimate that the sensitivity limit was

located at the nanomolar scale (insert in Fig. 7, Fig. S3). Such a low level of detection combined with the colorimetric and fluorogenic character of this simple procedure, constitute as many assets to promote this derivatization method of primary amines.

To prove the potential applicability of **BrXa** to the study of biological samples, additional reactions were conducted with various thiols. Indeed, this class of compounds is known to include the strongest nucleophiles in biological media. Control experiments were performed with 2-mercaptoethanol and a L-cysteine derivative (Figs. S4–5). As expected, the substitution product was mainly formed but no color and fluorescence appearance was detected (Figs. S6–9). This confirms that the chromogenic and fluorogenic character of this derivatization is directly related to the sensing of 1° amines. Competition reactions between thiol vs. amine were also carried out to demonstrate that only a small excess of **BrXa** allows the detection of a primary amine even in the presence of a reactive thiol. Since only the 1° amine derivatization products generate colored and fluorescent products, the slight excess of this “completely transparent” reagent should not interfere with spectrophotometric detection.

3.5. Quantum calculations

Gaussian 09 was employed for calculating the theoretical optical and quantum chemical properties of **BrXa** and the derivatized amino product as well as for determining their geometry in both ground and excited states. To simplify the calculations, methylamine was chosen as the reacting species leading to **MePyXa**. DFT and TD-DFT were used at the B3LYP/6-311+G(d) level of theory for the geometry optimization of both molecules in their ground and excited states, respectively, verified by Hessian analysis. Calculations of the electronic absorption spectra were completed by selecting singlet vertical excitation energies and their oscillator strengths were determined by TD-DFT. It was found that the first excited state would fluoresce, therefore the IROOT = 1 keyword was utilized. Fluorescence spectra were calculated at the single point level of the optimized geometry in the excited state.

Fig. 8 shows the differentiation of the bond lengths upon excitation. For the reagent, the differentiation is associated with the benzene ring 3, with the largest elongation and de-conjugation of the aromatic ring being apparent for the two nitro group oxygens (Table S1). Similarly, but to a far lesser extent, the carbonyl oxygen partially lost its double bond character. **MePyXa** exhibits a similar trend, but the main geometric changes are expanded to rings 2 and 4, in addition to ring 3. As the structure of this derivative presents more extended π -delocalization and consequently increased rigidity, it should induce larger Stokes shifts and enhanced fluorescence quantum efficiency regarding its emission properties. The nitro group does show an important geometrical alteration in both cases, but to a lesser extent for **BrXa** (Fig. 8). All the dihedral angles of **BrXa** and **MePyXa** are $>177^\circ$, pointing out high aromaticity, both in the ground and excited states.

The HOMO and LUMO orbitals of **MePyXa** are delocalized, highlighting the aromatic character of the substance. Apparently, the LUMO orbital is more localized on certain atoms compared to the more widespread HOMO. This observation is also reflected in the distribution of the Mulliken charges (Table S2). Since the calculated HOMO–LUMO energy difference turns out to be small (2.76 eV), this indicates that the derivative is highly conjugated. Excitation occurs from HOMO (Fig. 9A) towards LUMO (Fig. 9B), which corresponds to $\lambda = 490$ nm affording an oscillator strength of $f = 0.31$. A second, less intense excitation ($f = 0.13$) is predicted from HOMO to the second, lower lying LUMO with an energy gap of 3.46 eV, which corresponds to $\lambda = 358$ nm. Finally, the dipole moment lies on the long axis of the compound showing a total

magnitude of 9.6 D. The emission from the geometry-optimized excitation level between HOMO and LUMO occurs with an orbital state difference of 2.46 eV corresponding to an emission $\lambda = 565$ nm with an oscillator strength of $f = 0.21$ (Fig. 10). Smaller oscillator strength transitions were observed at 359 nm ($f = 0.146$), 328 nm ($f = 0.167$) and 316 nm ($f = 0.04$). The dipole moment was calculated mainly along the x axis, affording a value of 8.8 D, attesting to significant charge separation in the excited state. Thus, the derivatization product becomes noticeably polarized upon photon absorption, which is characteristic of molecules interacting efficiently with light.

On the other hand, the direction and magnitude of the dipole moment vector reveal that the nitro group is essential for the fluorescence emission by establishing a push–pull relationship with the electron-donating *N*-methylpyrrole. This was verified experimentally by the reduction of the nitro group to an amine, yielding derivatives practically devoid of fluorescence. Specifically, this chemical reduction converts initially D- π -A fluorophores into D- π -D, known to exhibit a strongly quenched and blue-shifted emission.

4. Concluding remarks

Since amines are present in many naturally occurring molecules – including proteins, peptides, nucleic acids, or alkaloids – fishing for this functional group in a complex mixture at low concentrations, represents a major challenge. In this context, a xanthene-based derivatization reagent **BrXa** was engineered, which combines both colorimetric and fluorogenic sensing, exclusively for primary amines. Its preparation relies on an efficient and scalable synthesis. Given that the detection reaction is based on a pyrrole formation, its selectivity towards primary at the expense of secondary and tertiary amines was revealed to be extremely high. As the process is chromogenic (colorless \Rightarrow magenta), this should interestingly make the method more accessible and enable it to reach a wider audience. Besides the appearance of an easily detectable fluorescent color (dark \Rightarrow red), the fluorogenic nature of this detection turns out to be a real asset. As a matter of fact, it allows to benefit from the exquisite sensitivity of the fluorescence spectroscopy, making it possible to achieve the nanomolar range. Supported by quantum calculations and photophysical characterization, the push–pull relationship from which the red fluorescence originates, was clearly evidenced. Combining all these attractive features with the development of a robust LC analytical method, offers a unique turnkey solution for the derivatization of primary amines.

Declaration of competing interest

The authors declare that they have no known competing financial interests or personal relationships that could have appeared to influence the work reported in this paper.

Acknowledgements

We thank the Agence Nationale de la Recherche (PFPImaging – 18-CE09-0020-01, UCA^{JEDI} project: ANR-15-IDEX-01), the LIFE graduate school (UCA) and the French Government, for the PhD grants of S.V., H.-N.L., Y.W.M., G.B., respectively. We are grateful to the CNRS Emergence@INC2020 program for both the financial support and the post-doctoral fellowship of S.M. This research work was also funded by the Hellenic Foundation for Research and Innovation (HFRI) under the HFRI PhD Fellowship grant of A.D.K. (Fellowship Number: 1559/27.04.2018).

Appendix A. Supplementary data

Supplementary data to this article can be found online at <https://doi.org/10.1016/j.dyepig.2021.109798>.

Credit authorship contribution statement

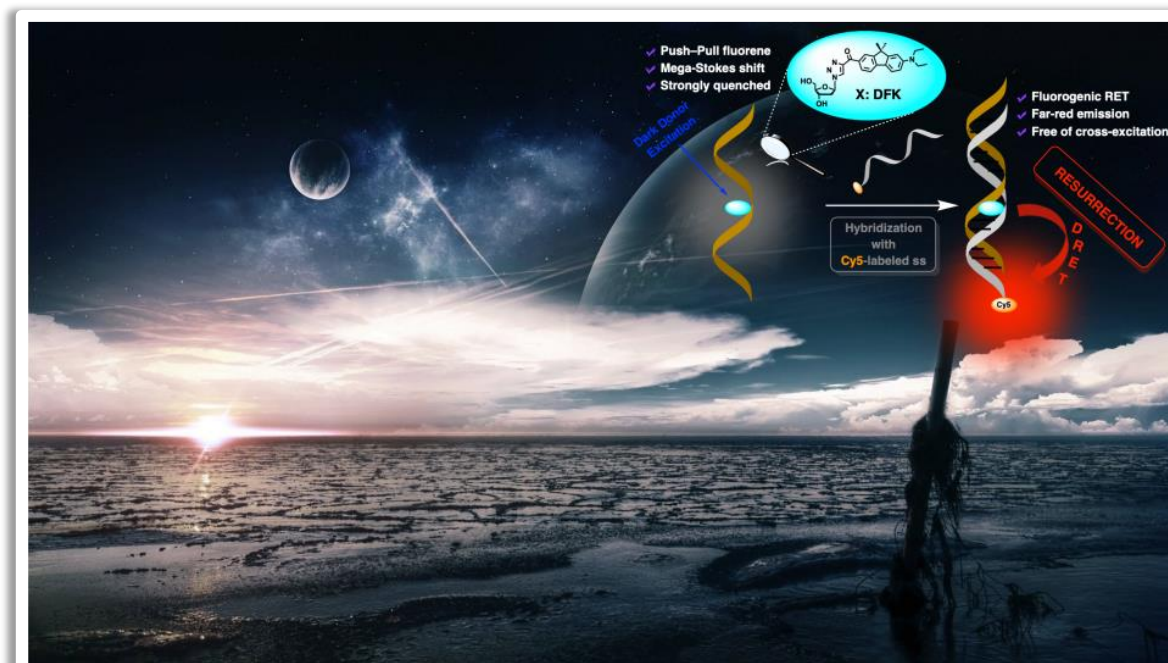
Amalia D. Kalampaliki: Methodology, Formal analysis, Investigation. Steve Vincent: Methodology, Formal analysis, Investigation. Suman Mallick: Methodology, Investigation, Review. Hoang-Ngoan Le: Visualization, Project administration. Guillaume Barnoin: Visualization, Validation. Yogesh W. MORE: Validation, Data curation. Alain BURGER: Funding acquisition, Review. Yannis Dotsikas: Conceptualization, Investigation. Evagelos Gikas: Funding acquisition, Writing – review & editing. Benoît Y. MICHEL: Funding acquisition, Writing – review & editing, Supervision. Ioannis K. Kostakis: Funding acquisition, Writing – review & editing, Supervision.

References

- Valcarcel Cases M, López Lorente ÀI, López Jiménez MA. Foundations of analytical chemistry. Cham, Switzerland: Springer; 2018. p. 487. <https://doi.org/10.1007/978-3-319-62872-1>.
- Lakowicz JR. Principles of fluorescence spectroscopy. third ed. New York, NY: Springer; 2006. p. 954. <https://doi.org/10.1007/978-0-387-46312-4>.
- Valeur B, Berberan-Santos MN. Molecular fluorescence: principle and applications. second ed. Weinheim, Germany: Wiley-VCH; 2013. p. 569. <https://doi.org/10.1002/9783527650002>.
- Jameson DM. Introduction to fluorescence. Boca Raton, FL: CRC Press; 2014. p. 313. <https://doi.org/10.1201/b16502>.
- Demchenko AP. Introduction to fluorescence sensing. Materials and devices. third ed., vol. 1. Cham, Switzerland: Springer; 2020. p. 657. <https://doi.org/10.1007/978-3-030-60155-3>.
- Lavis LD, Raines RT. Bright ideas for chemical biology. ACS Chem Biol 2008;3:142–55. <https://doi.org/10.1021/cb700248m>.
- Gonçalves MST. Fluorescent labeling of biomolecules with organic probes. Chem Rev 2009;109:190–212. <https://doi.org/10.1021/cr0783840>.
- Numasawa Y, Okabe K, Uchiyama S, Snata T, Imai K. Fluorescence characteristics of ionic benzofurazans, 7-substituted-2,1,3-benzoxadiazole-4-sulfonates. Dyes Pigments 2005;67:189–95. <https://doi.org/10.1016/j.dyepig.2004.12.014>.
- Sheshashena Reddy T, Ram Reddy A. Synthesis and fluorescence study of 6,7-diaminocoumarin and its imidazole derivatives. Dyes Pigments 2013;96:525–34. <https://doi.org/10.1016/j.dyepig.2012.08.021>.
- Nanda JS, Lorsch JR. Labeling of a protein with fluorophores using maleimide derivatization. Methods Enzymol 2014;536:79–86. <https://doi.org/10.1016/B978-0-12-420070-8.00007-6>.
- Peixoto PA, Boulangé A, Ball M, Naudin B, Alle T, Cosette P, et al. Design and synthesis of epicoconone analogues with improved fluorescence properties. J Am Chem Soc 2014;136:15248–56. <https://doi.org/10.1021/ja506914p>.
- Sutariya PG, Pandya A, Lodha A, Menon SK. A unique fluorescence biosensor for sensitive detection of tryptophan and histidine. Analyst 2014;139:4794–8. <https://doi.org/10.1039/C4AN00829D>.
- Fu Y, Yao J, Xu W, Fan T, He Q, Zhu D, et al. Reversible and “fingerprint” fluorescence differentiation of organic amine vapours using a single conjugated polymer probe. Polym Chem 2015;6:2179–82. <https://doi.org/10.1039/C4PY01793E>.
- Mallick S, Chandra F, Koner AL. A ratiometric fluorescent probe for detection of biogenic primary amines with nanomolar sensitivity. Analyst 2016;141:827–31. <https://doi.org/10.1039/C5AN01911G>.
- Cabanes J, Gandía-Herrero F, Escribano J, García-Carmona F, Jiménez-Atiéndar M. Fluorescent bioinspired protein labeling with betalamic acid. Derivatization and characterization of novel protein-betaxanthins. Dyes Pigments 2016;133:458–66. <https://doi.org/10.1016/j.dyepig.2016.06.037>.
- Saravanakumar M, Umamahesh B, Selvakumar R, Dhanapal J, Ashok kumar SK, Sathiyarayanan KI. A colorimetric and ratiometric fluorescent sensor for biogenic primary amines based on dicyanovinyl substituted phenanthridine conjugated probe. Dyes Pigments 2020;178. <https://doi.org/10.1016/j.dyepig.2020.108346>.
- Abbas JM, Stortz M, Rodríguez HB, Levi V, Wolosiuk A, Spagnuolo CC. The intramolecular self-healing strategy applied to near infrared fluorescent aminotriarocyanines. Dyes Pigments 2021;186. <https://doi.org/10.1016/j.dyepig.2020.109040>.
- Gikas E, Parissi-Poulou M, Kazanis M, Vavagianis A. MOZPhCSE, a new coumarin based fluorescent derivatization reagent. J Liq Chromatogr Relat Technol 2004;27:2699–713. <https://doi.org/10.1081/JLC-200029226>.
- Mertens MD, Gütschow M. Synthesis and evaluation of two coumarin-type derivatization reagents for fluorescence detection of chiral amines and chiral carboxylic acids. Chirality 2013;25:957–64. <https://doi.org/10.1002/chir.22240>.
- Li J, Zhang C, Wu S, Wen X, Xi Z, Yi L. Facile synthesis of green-light and large Stokes-shift emitting coumarins for bioconjugation. Dyes Pigments 2018;151:303–9. <https://doi.org/10.1016/j.dyepig.2018.01.016>.
- Ulrich G, Ziesel R, Harriman A. The chemistry of fluorescent body dye: versatility unsurpassed. Angew Chem Int Ed 2008;47:1184–201. <https://doi.org/10.1002/anie.200702070>.
- Sekhar AR, Kaloo MA, Sankar J. Aliphatic amine discrimination by pentafluorophenyl dibromo BODIPY. Chem Asian J 2014;9:2422–6. <https://doi.org/10.1002/asia.201402389>.
- Kaloo MA, Sekhar AR, Reddy RVR, Raman RS, Sankar J. A facile and visual approach for the detection of trace level ammonia vapours under ambient conditions. J Mater Chem C 2016;4:2452–6. <https://doi.org/10.1039/c6tc00426a>.
- Okorochenkova Y, Hlaváč J. Novel ratiometric xanthene-based probes for protease detection. Dyes Pigments 2017;143:232–8. <https://doi.org/10.1016/j.dyepig.2017.04.039>.
- Michel BY, Dziuba D, Benhida R, Demchenko AP, Burger A. Probing of nucleic acid structures, dynamics, and interactions with environment-sensitive fluorescent labels. Front Chem 2020;8:112. <https://doi.org/10.3389/fchem.2020.00112>.
- Lavis LD, Raines RT. Bright building blocks for chemical biology. ACS Chem Biol 2014;9:855–66. <https://doi.org/10.1021/cb500078u>.
- Shao F, Yuan H, Josephson L, Weissleder R, Hilderbrand SA. Facile synthesis of monofunctional pentamethine carbocyanine fluorophores. Dyes Pigments 2011;90:119–22. <https://doi.org/10.1016/j.dyepig.2010.12.008>.
- Martínez-Mañez R, Sancenón F. Fluorogenic and chromogenic chemosensors and reagents for anions. Chem Rev 2003;103:4419–76. <https://doi.org/10.1021/cr010421e>.
- Wu J, Kwon B, Liu W, Anslyn EV, Wang P, Kim JS. Chromogenic/fluorogenic ensemble chemosensing systems. Chem Rev 2015;115:7893–943. <https://doi.org/10.1021/cr500553d>.
- Li P, Zhu Y, He S, Fan J, Hu Q, Cao Y. Development and validation of a high-performance liquid chromatography method for the determination of diacetyl in beer using 4-nitro-o-phenylenediamine as the derivatization reagent. J Agric Food Chem 2012;60:3013–9. <https://doi.org/10.1021/jf3007163>.
- Feng TT, Xu XB, Du M, Tan MQ, Qin L, Zhu BW. Simultaneous determination of glyoxal, methylglyoxal and diacetyl in beverages using vortex-assisted liquid-liquid microextraction coupled with HPLC-DAD. Anal Methods 2017;9:2445–51. <https://doi.org/10.1039/c7ay00180k>.
- Marchetti M, Ronda L, Faggiano S, Luzzi A, Percudani R, Bettati S. Fluorescence quantification of allantoin in biological samples by cap-immobilized allantoinase/resorcinol assay. Sens Actuators, B 2018;255:2820–8. <https://doi.org/10.1016/j.snb.2017.09.099>.
- Nasirian A, Tikum AF, Fortibui MM, Lee S, Kim J. Naphthalimide-based fluorescent probe for selective and sensitive sensing of formaldehyde and biological applications. Dyes Pigments 2021;188. <https://doi.org/10.1016/j.dyepig.2021.109156>.
- Martín MA, del Castillo B. 2,3-Diphenylquinolinizinium bromide as a fluorescent derivatization reagent for amines. Anal Chim Acta 1991;245:217–23. [https://doi.org/10.1016/S0003-2670\(00\)80225-1](https://doi.org/10.1016/S0003-2670(00)80225-1).
- Steinert J, Khalaf H, Keese W, Rimpler M. Sensitive liquid chromatographic determination of hydrophobic primary and secondary amines by derivatization to form highly fluorescent thiazoles. Anal Chim Acta 1996;327:153–9. [https://doi.org/10.1016/0003-2670\(96\)00075-X](https://doi.org/10.1016/0003-2670(96)00075-X).
- Sanchez-Rodas D, Hohaus E, Wenclawiak B. High-performance liquid chromatographic determination of primary amines in aqueous solutions after extraction and derivatization with 2,2-diphenyl-1-oxa-3-oxonia-2-boratanaphthalene (DOOB). Anal Bioanal Chem 1996;355:187–9. <https://doi.org/10.1007/s0021663550187>.
- Kabashima T, Yu Z, Tang C, Nakagawa Y, Okumura K, Shibata T, et al. A selective fluorescence reaction for peptides and chromatographic analysis. Peptides 2008;29:356–63. <https://doi.org/10.1016/j.peptides.2007.11.014>.
- Körsten S, Mohr GJ. Star-shaped tripodal chemosensors for the detection of aliphatic amines. Chem Eur J 2011;17:969–75. <https://doi.org/10.1002/chem.201000787>.
- Longstreet AR, Jo M, Chandler RR, Hanson K, Zhan N, Hrudka JJ, et al. Ylidenemalononitrile enamines as fluorescent “turn-on” indicators for primary amines. J Am Chem Soc 2014;136:15493–6. <https://doi.org/10.1021/ja509058u>.
- Simons SS, Johnson DF. Reaction of o-phthalaldehyde and thiols with primary amines: fluorescence properties of 1-alkyl(and aryl)thio-2-alkylisoindoles. Anal Biochem 1978;90:705–25. [https://doi.org/10.1016/0003-2697\(78\)90163-X](https://doi.org/10.1016/0003-2697(78)90163-X).
- Benson JR, Hare PE. O-phthalaldehyde: fluorogenic detection of primary amines in the picomole range. Comparison with fluorescamine and ninhydrin. Proc Natl Acad Sci U S A 1975;72:619–22. <https://doi.org/10.1073/pnas.72.2.619>.
- Moliner Martínez Y, Campíns Falcó P, Herráez Hernández R, Verdú Andrés J. Evaluation of C18 adsorbent cartridges for sampling and derivatization of primary amines in air. Anal Chim Acta 2004;502:235–9. <https://doi.org/10.1016/j.aca.2003.10.008>.
- Shi W, Ma H. Spectroscopic probes with changeable π -conjugated systems. Chem Commun 2012;48:8732–813. <https://doi.org/10.1039/c2cc33366j>.
- Jullien L, Gautier A. Fluorogen-based reporters for fluorescence imaging: a review. Methods Appl Fluoresc 2015;3. <https://doi.org/10.1088/2050-6120/3/4/042007>.
- Klymchenko AS. Solvatochromic and fluorogenic dyes as environment-sensitive probes: design and biological applications. Acc Chem Res 2017;50:366–75. <https://doi.org/10.1021/acs.accounts.6b00517>.
- Kozma E, Kele P. Fluorogenic probes for super-resolution microscopy. Org Biomol Chem 2019;17:215–33. <https://doi.org/10.1039/C8OB02711K>.

- [47] Hadjipavlou C, Kostakis IK, Pouli N, Marakos P, Mikros E. 1-Ethyl-1H-3-nitrobenzopyrano[4,3,2-cd]isoindole: a novel heterocyclic ring system bearing an unusually labile deuterium-exchangeable aromatic proton. *Tetrahedron Lett* 2006; 47:3681–4. <https://doi.org/10.1016/j.tetlet.2006.03.130>.
- [48] Hadjipavlou C, Kostakis IK, Pouli N, Marakos P, Pratsinis H, Kletsas D. Synthesis and antiproliferative activity of substituted benzopyranoisoindoles: a new class of cytotoxic compounds. *Bioorg Med Chem Lett* 2006;16:4822–5. <https://doi.org/10.1016/j.bmcl.2006.06.074>.
- [49] Gottlieb HE, Kotlyar V, Nudelman A. NMR chemical shifts of common laboratory solvents as trace impurities. *J Org Chem* 1997;62:7512–5. <https://doi.org/10.1021/jo971176v>.
- [50] Fulmer GR, Miller AJM, Sherden NH, Gottlieb HE, Nudelman A, Stoltz BM, et al. NMR chemical shifts of trace impurities: common laboratory solvents, organics, and gases in deuterated solvents relevant to the organometallic chemist. *Organometallics* 2010;29:2176–9. <https://doi.org/10.1021/om100106e>.
- [51] Still WC, Kahn M, Mitra A. Rapid chromatographic technique for preparative separations with moderate resolution. *J Org Chem* 1978;43:2923–5. <https://doi.org/10.1021/jo00408a041>.
- [52] Reichardt C. Solvatochromic dyes as solvent polarity indicators. *Chem Rev* 1994; 94:2319–58. <https://doi.org/10.1021/cr00032a005>.
- [53] Sens R, Drexhage KH. Fluorescence quantum yield of oxazine and carbazine laser dyes. *J Lumin* 1981;24–25:709–12. [https://doi.org/10.1016/0022-2313\(81\)90075-2](https://doi.org/10.1016/0022-2313(81)90075-2).

Publication 5



Dans cet article publié dans *Nucleic Acids Research* en 2021, nous décrivons le fonctionnement ainsi que l'application d'un nouveau système fluorogénique, le DRET intramoléculaire, en comparaison de l'incontournable système FRET. Cet article a servi de fondement pour l'écriture de la partie introductive du DRET dans le **Chapitre 1 : II.2.4.**

Intermolecular dark resonance energy transfer (DRET): upgrading fluorogenic DNA sensing

Guillaume Barnoin¹, Janah Shaya¹, Ludovic Richert², Hoang-Ngoan Le¹, Steve Vincent¹, Vincent Guérineau³, Yves Mély^{1b,2}, Benoît Y. Michel^{1b,*} and Alain Burger^{1b,1,*}

¹Université Côte d'Azur, CNRS, Institut de Chimie de Nice, UMR 7272 – Parc Valrose, 06108 Nice cedex 2, France, ²Laboratoire de Biophotonique et Pharmacologie, UMR 7213 CNRS, Université de Strasbourg, Faculté de pharmacie, 74 Route du Rhin, 67401 Illkirch, France and ³Université Paris-Saclay, CNRS, Institut de Chimie des Substances Naturelles, UPR 2301, 91198 Gif-sur-Yvette, France

Received January 27, 2021; Revised March 01, 2021; Editorial Decision March 22, 2021; Accepted April 08, 2021

ABSTRACT

The sensitivity of FRET-based sensing is usually limited by the spectral overlaps of the FRET donor and acceptor, which generate a poor signal-to-noise ratio. To overcome this limitation, a quenched donor presenting a large Stokes shift can be combined with a bright acceptor to perform Dark Resonance Energy Transfer (DRET). The consequent fluorogenic response from the acceptor considerably improves the signal-to-noise ratio. To date, DRET has mainly relied on a donor that is covalently bound to the acceptor. In this context, our aim was to develop the first intermolecular DRET pair for specific sensing of nucleic acid sequences. To this end, we designed DFK, a push-pull probe based on a fluorenyl π -platform that is strongly quenched in water. DFK was incorporated into a series of oligonucleotides and used as a DRET donor with Cy5-labeled complementary sequences. In line with our expectations, excitation of the dark donor in the double-labeled duplex switched on the far-red Cy5 emission and remained free of cross-excitation. The DRET mechanism was supported by time-resolved fluorescence measurements. This concept was then applied with binary probes, which confirmed the distance dependence of DRET as well as its potency in detecting sequences of interest with low background noise.

INTRODUCTION

Since its introduction in the 1950s, Förster resonance energy transfer (FRET) has become an inescapable tool in the life sciences (1–3). Because FRET is distance dependent, it has been used to efficiently probe interactions between biomolecules and a large variety of ligands (4). Due to the predictable distances in nucleic acid (NA) duplexes, studies using FRET-based hybridization probes to detect NAs have been particularly productive (5). Numerous FRET probes have been designed with the aim to specifically detect target sequences (6) in molecular diagnostics (e.g. SNP, genotyping and PCR), screening and interrogation of NAs in living cells (1). Conventional FRET uses bright donor-acceptor pairs based on organic fluorophores. In particular, binary probes were developed that result in FRET when both probes bind to the target and the donor and acceptor come within 10 nm of each other (Figure 1A) (7,8). This reduces the donor emission with a concomitant increase in the red-shifted emission of the acceptor. A common drawback of binary probes is that they generally suffer from cross-excitation of the acceptor at the excitation wavelength of the donor as well as spectral overlap between the donor and acceptor emission (*cross-emission*) (1), because of the small Stokes shifts generally exhibited by FRET dyes (Figure 2A). All these factors contribute to increase the detection limit and also cause false positives. This is particularly critical in homogeneous solutions where the excess of probe cannot be removed, and the emission of the targeted sequence thus corresponds to only a small fraction of the total emission.

One solution to minimize direct excitation of the acceptor is to use a system of three partners, where an intermediate dye serves as a relay to transfer the energy of a donor to an acceptor. This provides a large apparent Stokes shift, but a

*To whom correspondence should be addressed. Tel: +33 4 89 15 01 65; Fax: +33 4 89 15 01 01; Email: alain.burger@univ-cotedazur.fr
Correspondence may also be addressed to Benoît Y. Michel. Email: benoit.michel@univ-cotedazur.fr

Dedicated to the memory of Dr Bang Luu.

Present addresses:

Janah Shaya, College of Medicine and Health Sciences, Khalifa University, Abu Dhabi, P.O. Box 127788, UAE.

Hoang-Ngoan Le, Department of Chemistry and Chemical Engineering, Chemistry and Biochemistry, Chalmers University of Technology, SE-41296 Gothenburg, Sweden.

© The Author(s) 2021. Published by Oxford University Press on behalf of Nucleic Acids Research.

This is an Open Access article distributed under the terms of the Creative Commons Attribution-NonCommercial License

(<http://creativecommons.org/licenses/by-nc/4.0/>), which permits non-commercial re-use, distribution, and reproduction in any medium, provided the original work is properly cited. For commercial re-use, please contact journals.permissions@oup.com

FRET vs. DRET

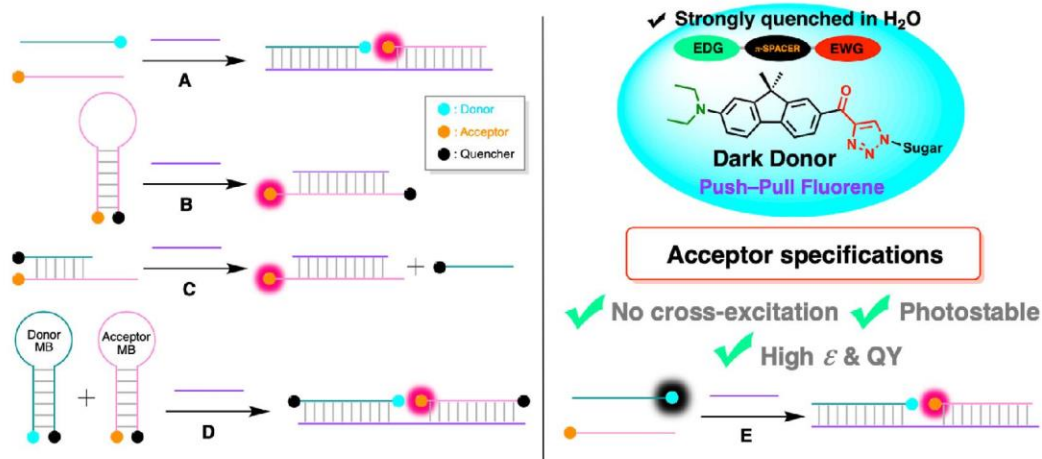


Figure 1. Main strategies implemented for specific sensing of nucleic acids. (*Left*) FRET-based approaches: (A) binary probes, (B) molecular beacon, (C) displacing probe and (D) double molecular beacons. (*Right*) Proposed DRET-based approach and (E) its application in fluorogenic binary probes.

FRET vs. DRET

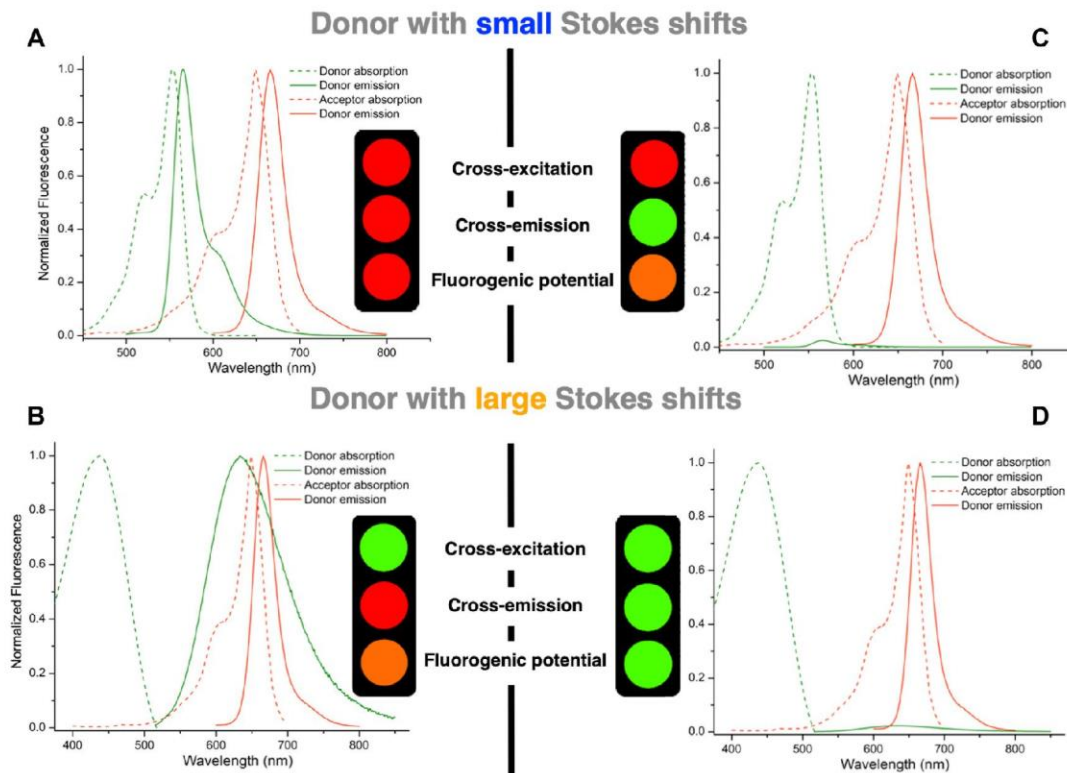


Figure 2. Direct comparison of 'FRET versus DRET' in two different contexts: donor with small (*top*) or large (*bottom*) Stokes shifts, illustrated by representative absorption and emission spectra (compare A & C and B & D). The traffic lights indicate the advantages and disadvantages in each case.

less efficient FRET (9). Another effective strategy is to use fluorescence quenchers in place of the acceptor, such as in the popular molecular beacons (MB) introduced by Tyagi and Kramer (Figure 1B). MBs consist of a stem-loop with 5' and 3' ends coupled to a fluorophore and a quencher (Q) (10,11). In their closed form, MBs barely fluoresce due to the close proximity of the fluorophore with the quencher, which is essential to reduce the signal-to-noise ratio (S/N). In contrast, binding of the complementary target sequence to the loop opens the stem and removes the dye from its quencher generating a turn-on emission signal. Thus, MBs enable a target-specific, background-free detection with a simple protocol that does not require one to wash out the excess of reagents. This highly efficient turn-on response is especially useful for imaging NAs in cells, where the excess unbound probe cannot be washed out. As an alternative to MB, displacement hybridization probes have also been developed (Figure 1C, 12). In the absence of the target, the donor is quenched by the close proximity of the quencher in the duplex. In the presence of the target, the single strand overhang in the duplex initiates annealing to the target, resulting in an efficient displacement of the quencher strand that switches on the donor emission. It is important to note that MBs or displacement hybridization probes can produce background signals in cells as a result of non-specific interactions with cellular components and/or metabolic degradation (13). To prevent false positives for mRNA imaging in cells, binary probes composed of two MBs were conceived to make the system more specific (Figure 1D, 14,15). Nevertheless, the resulting dual FRET MBs failed to suppress the problems of cross-excitation and cross-emission. Thus, poor S/N remains a critical issue in fluorogenic sensing of NAs, especially in cells where autofluorescence of cellular components can further contaminate the fluorescence signal.

In this context, we hypothesized that binary probes that couple a strongly quenched donor with a large Stokes shift to a bright acceptor might be an attractive solution for fluorogenic sensing of NAs with low cross-excitation and cross-emission. The use of a quenched donor for FRET was recently introduced by Chang *et al.* who built advanced fluorophores with large apparent Stokes shifts by tethering a quenched donor to a bright acceptor (16). This tether led to a highly efficient non-radiative process, called Dark-RET (DRET). The quenching of dark donors in DRET relies mainly on non-radiative intramolecular rotation (17–22). To date, all DRET studies were performed with a donor covalently bound to the acceptor. Our objective was to design, for the first time, a dynamic system with a non-covalently bound DRET pair for fluorogenic sensing of NAs. For the dark donor, we designed the push-pull fluorene DFK (DiethylaminoFluoreneKetotriazolyl) as a nucleobase surrogate with large Stokes shift to minimize cross-emission (Figures 2C, D and 3A, B). As a suitable acceptor, we used the bright Cy5 dye that shows minimal cross-excitation and perfect absorption overlap with DFK emission (Figures 2D and 3B, C). The proof of principle for the intermolecular DRET mechanism was demonstrated by the fluorogenic turn-on of Cy5 emission upon hybridization of DFK-labeled oligodeoxynucleotides with complementary sequences that were Cy5-labeled at either their 5'

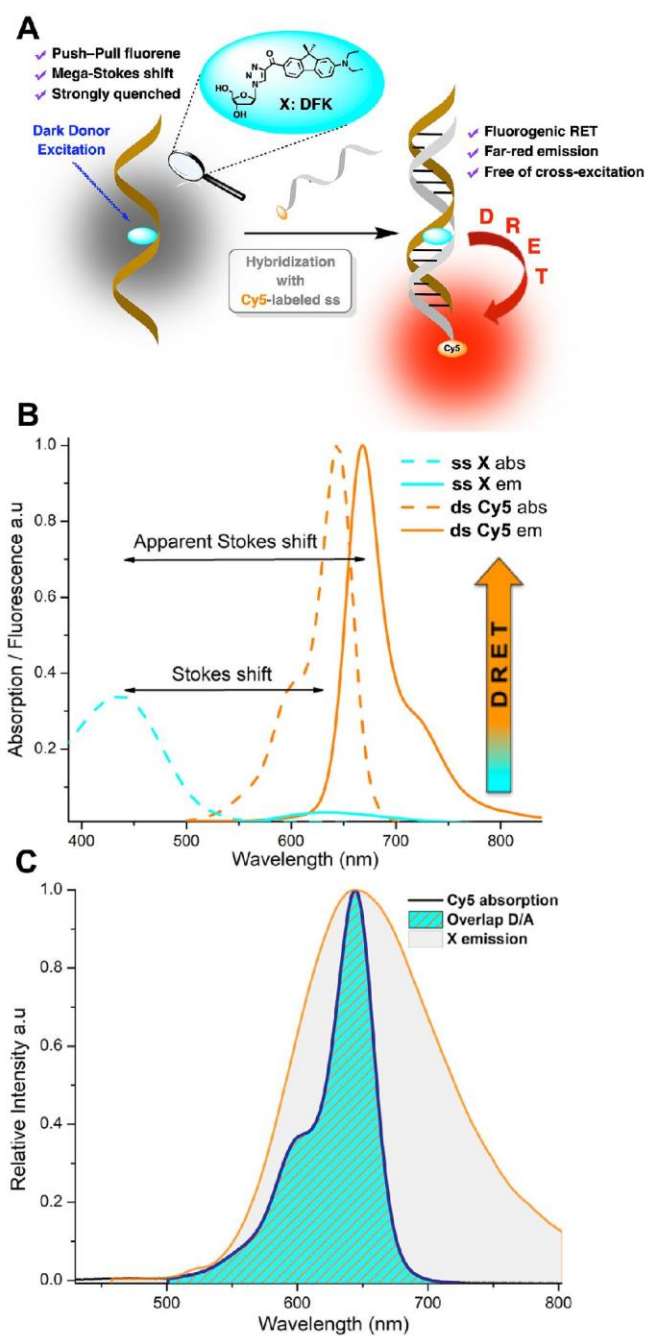


Figure 3. Intermolecular DRET monitored on annealing of a DFK-containing oligonucleotide with its Cy5-labeled complementary sequence. (A) Schematic representation of the intermolecular DRET between the push-pull DFK fluorophore used as a quenched donor and Cy5, employed as a bright acceptor. (B) DRET-associated photophysics. Absorption (dashed lines) and emission (solid) spectra of X-labeled single strand (cyan) or annealed with its Cy5-labeled complementary sequence (orange), highlighting the fluorogenic DRET process coupled with a large apparent Stokes shift. (C) Normalized absorption and emission spectra of the respective mono-labeled ds [comp-AGA + TCT-Cy5 (orange) and comp-AXA + TCT (indigo)] emphasizing the full overlap (cyan) of the X-Cy5 RET pair.

or 3' end. Time-resolved fluorescence measurements confirmed the DRET mechanism. Finally, this intermolecular DRET mechanism was used in the context of binary probes for the recognition of a specific sequence while maintaining low background noise (Figure 1E).

MATERIALS AND METHODS

Synthesis and spectrometry characterization

All reactions involving air- and water-sensitive conditions were performed in oven-dried glassware under argon by using Schlenk techniques employing a dual vacuum/argon manifold system and dry solvents. The synthetic intermediates were initially co-evaporated twice with toluene and dried *in vacuo* before use. All chemical reagents were purchased from commercial sources (Sigma-Aldrich, Acros, Alfa Aesar) and were used as supplied. Anhydrous solvents were obtained according to standard procedures (23). The reactions were monitored simultaneously by liquid chromatography–mass spectrometry (LC–MS) and thin-layer chromatography (TLC, silica gel 60 F254 plates). Compounds were visualized on TLC plates by both UV radiation (254 and 365 nm) and spraying with a staining agent (KMnO₄ or ninhydrin) followed by subsequent warming with a heat gun. Column chromatography was performed with flash silica gel (40–63 μm) with the indicated solvent system using gradients of increasing polarity in most cases (24). All NMR spectra (¹H, ¹³C, ²D) were recorded on 200 or 400 MHz Bruker Advance Spectrometers. ¹H NMR (200 and 400 MHz), ¹³C{¹H}NMR (50 and 101 MHz, recorded with complete proton decoupling), and ³¹P NMR (160 MHz, *proton decoupling*) spectra were obtained with samples dissolved in CDCl₃, CD₂Cl₂ or CD₃OD, with the residual solvent signals used as internal references: 7.26 ppm for CHCl₃, 5.32 ppm for CDHCl₂, and 3.31 ppm for CD₂HOD regarding ¹H NMR experiments, and 77.2 ppm for CDCl₃, 53.8 ppm for CD₂Cl₂ and 49.0 ppm for CD₃OD concerning ¹³C NMR experiments (25). Chemical shifts (δ) are given in ppm to the nearest 0.01 (¹H) or 0.1 ppm (¹³C and ³¹P). The coupling constants (*J*) are given in hertz (Hz). The signals are reported as follows: (s = singlet, d = doublet, t = triplet, m = multiplet, br = broad). Assignments of ¹H and ¹³C NMR signals were achieved with the help of D/H exchange, COSY, HMQC, HSQC, NOESY and HMBC experiments. LC–MS spectra were recorded using an ion trap Esquire 3000 Plus mass spectrometer equipped with an electrospray ionization (ESI) source in both positive and negative modes. High-resolution mass spectrometry (HRMS) was conducted with a hybrid ion trap–Orbitrap Thermo Scientific™ mass spectrometer (combining quadrupole precursor selection with high-resolution and accurate-mass Orbitrap detection) using ESI techniques.

ODN synthesis, purification and mass characterization

Solid-phase oligonucleotide (ODN) syntheses were performed both on an Expedite 8900 (Applied Biosystem) and H-8 (K&A) DNA synthesizers using the 'trityl off' mode and ultra-mild Pac phosphoramidite chemistry on 1 μmol scale. Reagents and solvents, as well as dT, Ac-dC, Pac-dA and iPr-Pac-dG (or dmf-dG) phosphoramidites were

purchased from Link Technologies (LGC) and Chemgenes. Standard DNA assembly 'DMT-off' protocol was employed except for the following modifications: 5-ethylthio-1H-tetrazole (ETT) was used as activating agent; Pac-anhydride was used for capping; a longer coupling time (1200 s) was applied to the fluorenyl phosphoramidite. Labeled ODNs were cleaved from the solid support and deprotected with concentrated aqueous ammonia at room temperature for 12 h. ODNs were analyzed (0.5 ml/min) and purified (2.5 ml/min) by RP-HPLC (HPLC apparatus: Waters™ 600 Controller including Waters™ 996 Photodiode Array Detector and Jasco LC-Net II with ADC) using analytical and semi-preparative C18 columns (Phenomenex™ Clarity® 300 × 4.60 mm and 250 × 10 mm, 5 μm particle size, 100 Å). The following gradient system was used: 100% A – (30 min) → 60% A/40% B – (5 min) → 100% B – (5 min) → 100% A with A = 0.9 TEAB Buffer 100 mM pH 7.8: 0.1 CH₃CN – B = 0.8 CH₃CN: 0.2 TEAB. 100 mM-triethylamine bicarbonate (TEAB) buffer (Et₃NH)HCO₃: prepare 0.1 M Et₃N in Milli-Q® water and pass CO₂ into the solution until the pH reaches about 7.8. Store at 4°C. Non-labeled ODNs (used as wild-type sequences) as well as Cy5-labeled ODNs (employed as DRET acceptor sequences) were purchased from Microsynth AG. Dibasic Ammonium Citrate (DAC) (98% capillary GC) and acetonitrile (HPLC grade) were purchased from Sigma-Aldrich. Ultrapure 3-hydroxypicolinic acid (3-HPA) MALDI matrix was obtained from Protea Biosciences. C4 pipette tips (Zip-Tip) were from Millipore. Samples (500 pmol) were diluted to 10 μl of water and were desalted with a C4 pipette Tips (Zip-tip). Zip-tip was activated before use with 2 × 5 μl of water:CH₃CN (50:50) and 2 × 5 μl of DAC (50 mg/ml diluted in water). 10 μl of the ODN solution were loaded on Zip-tip by drawing and expelling ten times. Next, the zip-tip was washed with 3 × 5 μl of DAC (50 mg/ml) and 3 × 5 μl of water. Elution was performed with 1.5 μl of 3-HPA matrix (80 mg/ml, 50:50 CH₃CN:DAC) directly on MALDI plate. MALDI-TOF/TOF-MS analysis: MS spectra were recorded manually in a mass range of 500–6000 Da resulting from 400 laser shots of constant intensity fixed at 6200. Data were collected using 4000 series Explorer (AB Sciex) experiments.

Photophysical characterization (UV–Vis and fluorescence measurements)

All solvents for absorption and fluorescence experiments were of spectroscopic grade. Absorption spectra were recorded at 20°C, on a Cary 100 Bio UV–vis spectrophotometer (Varian/Agilent) using Suprasil® quartz 500 μl cuvettes with 1-cm path length. Stock solutions of DFK or ODNs were prepared using THF or Milli-Q® water. The DFK samples used for spectroscopic measurements contained ≈0.2% (v/v) of solvents of the stock solution. Fluorescence measurements were conducted on a FluoroMax 4.0 spectrofluorometer (Jobin Yvon, Horiba) with a thermostatically controlled cell compartment at 20 ± 0.5°C with slits open to 2 nm and were corrected for Raman scattering, lamp fluctuations and instrumental wavelength-dependent bias. Emission spectra were performed with an absorbance of about 0.05. The excitation wavelength cor-

responds to the absorption maximum of the considered sample.

Quantum yields were corrected according to the variation of the refractive index of the different solvents. They were determined by using 7-(dimethylamino)-fluorene-2-carbaldehyde in MeOH ($\lambda_{\text{Ex}} = 385 \text{ nm}$, $\Phi = 0.46$) as a reference (26), with $\pm 10\%$ mean standard deviation. DFK was analyzed in duplicate at 10 and 2 μM , respectively for UV-Vis and fluorescence measurements. Labeled ODNs were analyzed in duplicate at 2 μM in phosphate-buffered saline pH 7.4 (50 mM sodium phosphate, 150 mM NaCl). In order to ensure reproducibility of hybridization and therefore of measurements, the double-stranded samples were first denatured and then cooled to rt. To estimate the sensitivity of the DRET probe, fluorescence signal amplification was determined according to the following equation $S/N = (F_{\text{hybrid}} - F_{\text{buffer}})/(F_{\text{ss}} - F_{\text{buffer}})$ (27).

Additional optical characterization (thermal denaturation and CD spectroscopy)

As previously described, PBS pH 7.4 (50 mM sodium phosphate, 150 mM NaCl) was used as a buffer for each type of experiment. Melting curves were recorded in duplicate by following the temperature-dependence of absorbance changes at 260 nm of the sample (2 μM concentration of each strand). Absorption spectra were recorded in a Peltier-thermostatted cell holder on a Cary 100 Bio UV-Vis spectrophotometer (Varian/Agilent) using Suprasil[®] quartz cuvettes with 1-cm path length. The temperature range for denaturation measurement was 20–70°C. Speed of heating was 1°C/min. Melting curves were converted into a plot of α versus temperature, where α represents the fraction of single strands in the duplex state. The melting temperatures were extracted from these curves after differentiation as reported (28). Circular dichroism experiments were recorded at 20°C on a Jasco J-810 spectropolarimeter. The wavelength range for CD measurements was 230–320 nm. Spectra were recorded from samples with a concentration of 2 μM for each strand.

Time-resolved fluorescence spectroscopy (TCSPC)

Time-resolved fluorescence measurements were performed using the time-correlated single-photon counting technique (TCSPC). Excitation pulses were generated by a pulse-picked supercontinuum laser (EXR-20, NKT photonics) with superK EXTEND-UV module. Excitation wavelength was set at 430 or 600 nm, with a repetition rate of 10 MHz. The fluorescence emission was collected through a polarizer set at magic angle and a 16-mm band-pass monochromator (H10 Jobin Yvon). The single-photon events were detected with a micro-channel plate photomultiplier (R3809, Hamamatsu) coupled to a pulse pre-amplifier HFAC (Becker-Hickl GmbH) and recorded on a time-correlated single-photon counting board (SPC-130, Becker-Hickl GmbH). The instrumental response function (IRF) was recorded using a polished aluminum reflector, and its full width at half-maximum was ~ 50 ps. Experimentally measured fluorescence decays were deconvoluted with the instrumental response function and fitted to retrieve the most probable

lifetime distribution using the maximum entropy method (Pulse 5 software) (29). Global fit analysis was performed with the DecayFit software (www.FluorTools.com). In all cases, the χ^2 values were close to 1, indicating an optimal fit. The mean lifetime $\langle \tau \rangle$ was calculated from the individual fluorescence lifetimes (τ_i) and their relative amplitudes (α_i) according to $\langle \tau \rangle = \sum \alpha_i \tau_i$.

RET-related parameters

RET parameters (including energy transfer efficiency and rate constant, spectral overlap integral and Förster distance) were calculated according the definitions and Equations (1-5), herein (4). The RET efficiency (E in %) was measured from the donor fluorescence quenching profile according to Equation (1):

$$E = \left(1 - \frac{F_{\text{DA}}}{F_{\text{D}}}\right) \times 100 \quad (1)$$

where F_{D} and F_{DA} are respectively, the relative fluorescence intensities in the absence and presence of the acceptor.

The spectral overlap integral ($J(\lambda)$ in $\text{M}^{-1} \cdot \text{cm}^{-1} \cdot \text{nm}^4$) of the donor emission and the acceptor absorption were determined by using Equation (2):

$$J(\lambda) = \frac{\int_0^\infty F_{\text{D}}(\lambda) \varepsilon_{\text{A}}(\lambda) \lambda^4 d\lambda}{\int_0^\infty F_{\text{D}}(\lambda) d\lambda} \quad (2)$$

where $F_{\text{D}}(\lambda)$ is the fluorescence intensity of the donor in the wavelength range $[\lambda; \lambda + \Delta\lambda]$ and ε_{A} is the extinction coefficient of the acceptor at λ .

Förster distance (R_0), corresponding to the distance where the RET is 50% efficient, was estimated according to Equations (3 and 4):

$$R_0 = 0.211 \sqrt[6]{(\kappa^2 n^{-4} Q_{\text{D}} J(\lambda))} \quad (3)$$

$$R_0 = \sqrt[6]{\left(\frac{E}{1-E}\right) r^6} \quad (4)$$

where κ^2 describes the relative orientation in space of the transition dipoles of the donor and acceptor (usually assumed to be equal to 2/3, which is appropriate for dynamic random averaging of the donor and acceptor); n is the refractive index of the medium (1.4 for biomolecules in aqueous solution) and Q_{D} is the quantum yield of the donor in the absence of acceptor.

r is the donor-to-acceptor distance and it was measured from Equation (5):

$$r = R_0 \sqrt[6]{\frac{(1-E)}{E}} \quad (5)$$

RESULTS AND DISCUSSION

Synthesis of DFK and the corresponding amidite

Previous examples of push-pull fluorophores have been designed by conjugating both a dialkylamino group as an electron-donating group (EDG) and a ketotriazolyl moiety as an electron-withdrawing group (EWG) to a π -fluorene

Table 1. Labeled single-stranded ODNs considered in this study with their respective mass and molar extinction coefficient

ODN ^a	Sequence	[M+H] ⁺ observed (calcd)	ϵ (M ⁻¹ ·cm ⁻¹) ^b
TXT	5'-CGT TTT TXT TTT TGC-3'	4756.2 (4756.2)	137 800
AXA	5'-CGT TTT AXA TTT TGC-3'	4775.2 (4774.2)	151 000
CXC	5'-CGT TTT CXC TTT TGC-3'	4726.1 (4726.2)	136 600
GXG	5'-CGT TTT GXG TTT TGC-3'	4806.6 (4806.2)	142 200
comp-GXG	5'-GCA AAA GXG AAA ACG-3'	4877.1 (4878.3)	174 000
comp-AXA	5'-GCA AAA AXA AAA ACG-3'	4847.4 (4846.2)	178 200
ret-AXA	5'-GCA AAA GTG AXA ACG-3'	4868.7 (4869.3)	174 200
ret-XCG	5'-GCA AAA GTG AAA XCG -3'	4869.4 (4869.3)	170 510
TCT-Cy5	5'- Cy5 -CGT TTT TCT TTT TGC-3'	5150.8 (5150.9)	130 000
comp-GCG-Cy5	5'- Cy5 -GCA AAA GCG AAA ACG-3'	5281.5 (5273.1)	182 700
comp-TCT-Cy5	5'- Cy5 -GCA AAA TCT AAA ACG-3'	5223.7 (5223.0)	177 500

^a ODNs were named according to their central codon.

^b Molar absorptivity of modified ODNs was calculated from www.atdbio.com/tools/oligo-calculator by considering $\epsilon_{260} = 20\,000$ and $12\,500\text{ M}^{-1}\cdot\text{cm}^{-1}$ for respectively X and Cy5 (with X = DFK and Cy5 = Cyanine-5).

scaffold (30–32). To introduce this fluorene dye as a base surrogate in NAs, we used our previous convergent approach (30,31) to assemble the naked nucleoside DFK via CuAAC between the 1'-azidodeoxyribose unit and diethylaminofluorenyl ynone (Schemes S1–2, Supplementary Figure S1). The dye could also be introduced into DNA through a linker. Although this solution allows easier access to the labeled ODNs, it was preferred to couple the dye to the 1'-azidodeoxyribose unit in order to make its photophysics more sensitive to the surrounding bases. The photophysical features of this nucleobase mimic were investigated in a wide range of solvents (Supplementary Table S1). DFK absorbed strongly around 410 nm ($\epsilon = 42\,000\text{ M}^{-1}\cdot\text{cm}^{-1}$ in acetonitrile) and displayed moderate solvatochromism ($\Delta\lambda = 15\text{ nm}$, Supplementary Figure S2). In contrast, fluorescence emission exhibited strong solvatofluorochromism along the polarity scale with mega-Stokes shifts exceeding 240 nm (Supplementary Figure S3). According to the Lippert–Mataga model (4), the calculation of the transition dipole moment (14.2 D, Supplementary Figures S4 and S5) confirmed the potent push–pull character of DFK. The quantum yield (QY) of DFK was found to strongly decrease with the proticity of the solvent; thus, the dye shows an exacerbated sensitivity to hydration with a turn-off emission shifted to far-red (Supplementary Table S2, Supplementary Figure S6). The pK_a of the amino group (~ 5.8) indicated that the push–pull property is maintained at physiological pH (Supplementary Figure S7). Thus, DFK demonstrates all the prerequisites for being a suitable DRET donor.

Labeled ODNs and their photophysics

DFK was then incorporated in model 15-mer ODNs (Table 1) differing by their contexts (YXY' with Y and Y' = A, T, C or G and X = DFK). The labeled single-stranded sequences (ss-ODNs) were obtained via solid-phase synthesis, purified by RP-HPLC and characterized by UV-vis spectroscopy and MALDI-TOF mass spectrometry (Table 1, Supplementary Figures S8–S16). Each ss-ODN was annealed to its complementary sequence containing a natural base (A, T, C and G) or an abasic site (Ab) at the position opposite X giving 28 duplexes of different compositions (Table 2).

As a first step, the effect of X on the stability and conformation of the duplexes (ds-ODNs) was studied by ther-

mal denaturation and CD spectroscopy (33). With the opposite A, C, G or T, the DFK nucleobase decreased the duplex stability by 3–9°C (Table 2, Supplementary Figure S17), but preserved the canonical B-helical conformation (Supplementary Figure S18). When an abasic site was opposite X, the duplexes were more stable, by 4 to 6°C, than the corresponding wild-type sequences (where G substitutes X). The stability data suggest that the moderate length ($\sim 10\text{ \AA}$) and aromatic character (Supplementary Figure S4) of the fluorescent nucleobase probably enable its correct accommodation into the double helix.

In single strands, the excitation maximum of X is red shifted to 430 nm, independently of the adjacent bases (Table 2, Supplementary Figure S19). Upon hybridization, a further bathochromic shift was observed, reaching 24 nm in the most discriminating case. This result confirmed the propensity of the aromatic fluorophore to stack with the neighboring base pairs (34). Given that the emission is in the red edge of the visible spectrum (649–680 nm for ss-ODNs, 634–659 nm for ds-ODNs), mega-Stokes shifts ranging from 184–247 nm were observed in all cases (Table 2, Supplementary Figures S20–S22). QYs were low and thus, suited for DRET (0.7–6.7%, Table 2). The low QYs and far-red emissions of labeled ODNs were clearly consistent with the results obtained for DFK in highly hydrated media (Supplementary Figures S6 and S23). Hence, the most quenched ODNs displayed the most red-shifted emissions. Altogether, our data suggest that the hydration of X is mainly responsible for its quenching, likely due to the carbonyl group acting as an efficient H-bonding acceptor in ODNs.

Selective excitation and turn-on emission

Proof of concept. The commonly used Cy5 dye was selected as DRET acceptor due to its well-matched properties, such as high brightness ($\epsilon = 250,000\text{ M}^{-1}\cdot\text{cm}^{-1}$; $\Phi = 28\%$) (35), perfect overlap with X donor emission (Figure 3C), and absence of absorption in the 420–480 nm range for Cy5, which avoids cross-excitation. To show the proof of principle of intermolecular DRET, X-labeled ss-ODNs were annealed with their complementary sequences labeled with Cy5 at 5'-position through a flexible linker (Table 1, Chart S2). Among all the studied sequences (Table 2), we

Table 2. Spectroscopic properties of X-labeled ODNs^a

ss & ds-ODNs	T_m (°C)			λ_{Abs} (nm) ^c	λ_{Em} (nm) ^d	$\Delta\lambda$ ^e	Φ (%) ^f
	Labeled	Wild type ^b	ΔT_m (°C)				
TXT	-	-	-	429 ^{uv}	654	-	1.8
TXT + comp-AAA	33.7	[42.0]	-8.3	435	654	219	2.2
TXT + comp-ATA	35.6	[42.0]	-6.4	435	654	219	2.0
TXT + comp-ACA	36.9	[44.7]	-7.8	441	652	211	2.4
TXT + comp-AGA	36.2	[44.7]	-8.5	438	654	216	2.1
TXT + comp-AAbA	37.9	32.3	+5.8	439	654	215	2.1
AXA	-	-	-	429	660	231	1.8
AXA + comp-TAT	37.4	[42.0]	-4.6	444	649	205	2.7
AXA + comp-TTT	36.4	[42.0]	-5.6	447	648	201	3.1
AXA + comp-TCT	39.6	[44.7]	-5.1	453	637	184	5.6
AXA + comp-TGT	37.3	[44.7]	-7.4	444	649	205	3.0
AXA + comp-TAbT	38.0	31.9	+6.1	450	650	200	3.5
CXC	-	-	-	432	649	217	2.7
CXC + comp-GAG	39.6	[47.5]	-7.9	437	659	222	1.6
CXC + comp-GTG	38.7	[47.5]	-8.8	437	652	215	1.9
CXC + comp-GCG	41.3	[50.2]	-8.9	437	655	218	1.4
CXC + comp-GGG	41.3	[50.2]	-8.9	437	651	214	2.0
CXC + comp-GAbG	43.3	39.3	+4.0	437	652	215	1.5
GXG	-	-	-	434	653	219	2.4
GXG + comp-CAC	44.9	[47.5]	-2.6	444	641	197	3.7
GXG + comp-CTC	44.9	[47.5]	-2.6	447	640	193	5.0
GXG + comp-CCC	45.8	[50.2]	-4.4	448	641	193	4.8
GXG + comp-CGC	45.9	[50.2]	-4.3	439	653	214	2.4
GXG + comp-CAbC	45.0	40.2	+4.8	446	647	201	3.8
comp-GXG	-	-	-	433	673	240	1.2
comp-GXG + CTC	44.5	[47.5]	-3.0	443	637	194	5.6
comp-GXG + CCC	45.8	[50.2]	-4.4	443	640	197	4.7
comp-GXG + CAbC	44.0	39.9	+4.1	443	645	202	3.7
comp-AXA	-	-	-	433	680	247	0.7
comp-AXA + TCT	41.9	[44.7]	-2.8	448	634	186	6.7
comp-AXA + TAbT	40.2	33.9	+6.3	445	648	203	2.7
ret-XCG	-	-	-	440	666	226	1.7
ret-XCG + CAC	46.7	[47.5]	-0.8	441	644	203	3.3
ret-AXA	-	-	-	427	671	244	0.7
ret-AXA + CAC	42.4	[47.5]	-5.1	446	647	201	2.9
comp-GXG + CAC	44.7	[47.5]	-2.8	440	639	199	2.8

^a Reported values are the average of two or more independent and reproducible measurements, ± 1 nm for wavelengths.

^b Theoretical T_m value of the corresponding duplex formed from unmodified ODNs (calculated from www.atd.bio.com/tools/oligo-calculator); given in square brackets.

^c Position of the absorption maximum in nm. Excitation wavelength was at the corresponding absorption maximum.

^d Emission maximum in nm.

^e For convenience, Stokes shifts are expressed in nm for $\Delta\lambda = \lambda_{Em} - \lambda_{Abs}$ (difference in cm^{-1}).

^f Fluorescence quantum yields Φ were determined using an excitation at the corresponding absorption maximum of X, $\pm 10\%$ mean standard deviation. 7-(dimethylamino)-fluorene-2-carbaldehyde in MeOH ($\lambda_{Ex} = 385$ nm, $\Phi = 0.46$) was used as a reference (26).

selected the X-labeled ds-ODNs with the lowest and highest QYs (CXC + *comp-GCG*: $\Phi = 1.4\%$ and *comp-AXA* + *TCT*: $\Phi = 6.7\%$). Assuming a 3.4 Å gap per base pair for B-DNA and a random orientation of the donor and acceptor, the distance between X and tethered Cy5, which is known to stack at the end of the duplex (36), should be around ≈ 30 Å (3,37–39). This distance is favorable for RET as the calculated Förster distances, R_0 (distance at which RET efficiency is 50%) were found to be 33 and 46 Å for the darkest and brightest duplexes, respectively (4).

Comparison of the fluorescence spectra of the ds *comp-AXA* + *TCT* with *comp-AXA* + *TCT-Cy5* indicated an almost complete disappearance of the X donor emission coupled to a very strong increase in the emission of Cy5 acceptor, which are evident signatures of RET (Figure 4A). Transfer efficiency was determined to be 83%. The strong increase in Cy5 fluorescence is clearly not related to a direct excitation of Cy5, as can be seen from the very low

emission of the *comp-AGA* + *TCT-Cy5* duplex (black curve, Figure 4A) and the low increment in fluorescence when the Cy5-labeled complementary strand was added in 10 eq. excess to the duplex *comp-AXA* + *TCT-Cy5* (green versus magenta spectra, Figure 4A). In comparison with ss *comp-AXA*, a 100-fold amplification was observed in the emission of Cy5 at 665 nm for the *comp-AXA* + *TCT-Cy5* duplex. Very similar observations were made for the comparison of the CXC + *comp-GCG-Cy5* duplex with the CXC + *comp-GCG* duplex and the ss CXC oligonucleotide (Figure 4B). Due to a smaller R_0 (33 Å), a lower transfer efficiency of 55% was calculated. An 8-fold increase in the fluorescence signal was observed at the emission maximum of Cy5 (665 nm) after hybridization of CXC to *comp-GCG-Cy5* demonstrating the sequence dependence of the system. Nevertheless, the strong increase in Cy5 was again unrelated to cross-excitation but was caused by RET between X and Cy5. The RET mechanism was further supported by the anisotropy

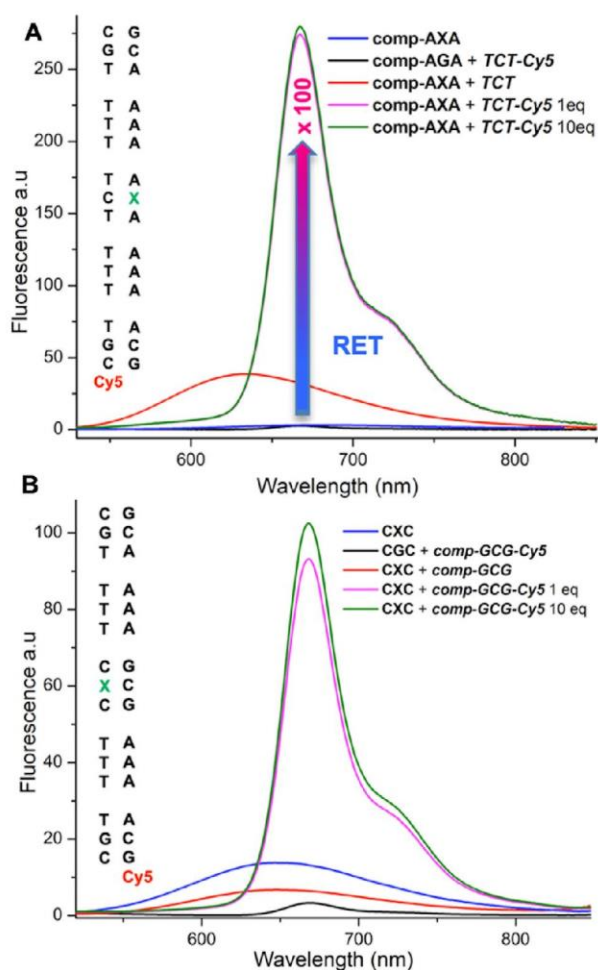


Figure 4. Emission spectra of the (A) comp-AXA + TCT and (B) CXC + comp-GCG ds-constructs in presence or absence of Cy5 acceptor on the complementary strands. In A) the RET between X and Cy5 led to a 100-fold increase in the fluorescence signal. Samples were recorded at 2 μ m, in pH 7.4 PBS and excitation was performed at the donor absorption maximum.

measurement of the acceptor at 667 nm, showing that excitation through RET at 430 nm leads to strong depolarization ($r \approx 0.04$) as compared to direct excitation at 600 nm ($r = 0.26$) (40). To complete our understanding of this fluorogenic process, time-resolved measurements were also performed.

Time-correlated single photon counting. For the free nucleoside DFK, a monoexponential decay was obtained in THF, with a fluorescence lifetime $\tau_{\text{THF}} = 2.8$ ns (Supplementary Figure S24). In EtOH, the lifetime decay dropped ($\tau_{\text{EtOH}} = 0.3$ ns) in agreement with the decrease in QY (Supplementary Table S1). Excitation at the absorption maximum (430 nm) of comp-AXA in its ss-form resulted in a biexponential decay with a major component (94%) at 0.23 ns and a minor component at 0.65 ns (Supplementary Figure S25). The value of 0.23 ns is close to the lifetime of X in EtOH, which is consistent with the known polar surroundings of nucleotides in ss-ODNs. Interestingly, once the

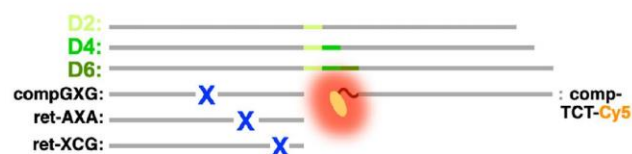


Figure 5. Gapped-junction-based system for distance-dependence DRET investigations: D2, D4 and D6 correspond to the target DNAs with a gap junction of two, four and six nucleotides, respectively. Binary probes labeled with X and Cy5 are complementary to D2, D4 and D6 on both sides of the gapped junction.

duplex is formed with TCT, the fluorescence decay became monoexponential with a lifetime of 0.64 ns (Supplementary Figure S25). This 2.5-fold increase in lifetime is fully consistent with the more apolar environment around X after hybridization.

In the next step, we investigated the time-resolved fluorescence decays of the same duplex, but this time, in presence of Cy5. First, the decay of the acceptor was recorded in the duplex by exciting at 630 nm where only Cy5 absorbs. A monoexponential decay was monitored with a lifetime $\tau_{\text{Cy5}} = 1.28$ ns at both 675 and 730-nm emission wavelengths (Supplementary Figure S26). Next, the emission decay of comp-AXA + TCT-Cy5 was measured, by exciting at 430 nm where Cy5 absorption is negligible (Supplementary Figure S27). The emission decay was first recorded at 600 nm (Supplementary Figure S27), where only X emits (Supplementary Figure S28). The fluorescence decay was well fitted with a major (96%) component at 0.12 ± 0.01 ns and a minor one (4%) at 0.69 ± 0.05 ns. This biexponential decay with a minor component – identical to the lifetime of X in duplex in absence of Cy5 – together with a short-lived lifetime is typical of a RET donor (4, 41).

To confirm the RET between X and Cy5, the emission decay of the doubly labeled duplex was monitored at 675 and 730 nm (Supplementary Figure S29) where the emission is largely dominated by Cy5 (Supplementary Figure S28). As Cy5 cannot be directly excited at 430 nm, its excitation ought to predominantly occur through RET from X. Accordingly, the acceptor decay function is expected to be the convolution of the fast decay of X with the natural decay function of Cy5. As a result, the decay function of comp-AXA + TCT-Cy5 should have a rising component with a time constant equal to the RET lifetime of the donor (42, <http://www.becker-hickl.de/pdf/SPC-handbook-6ed-12-web.pdf>). In fluorescence decays, rise components, which are commonly associated with excited-state reactions, appear with a negative amplitude and can therefore be easily identified. To demonstrate the presence of this rise component, we first fitted the decay at 675 nm with only positive components. Even when using 3 components, the fits of the fluorescence decay were poor as shown by the high χ^2 value and the non-random distribution of residuals, especially for the first channels of the decay curve (Supplementary Figures S29A and B). Inclusion of a rise component was found to substantially improve the fit and the distribution of residuals (43). An optimal fit was obtained when the rise component was associated with two positive components, one (1.28 ns) being the lifetime of Cy5

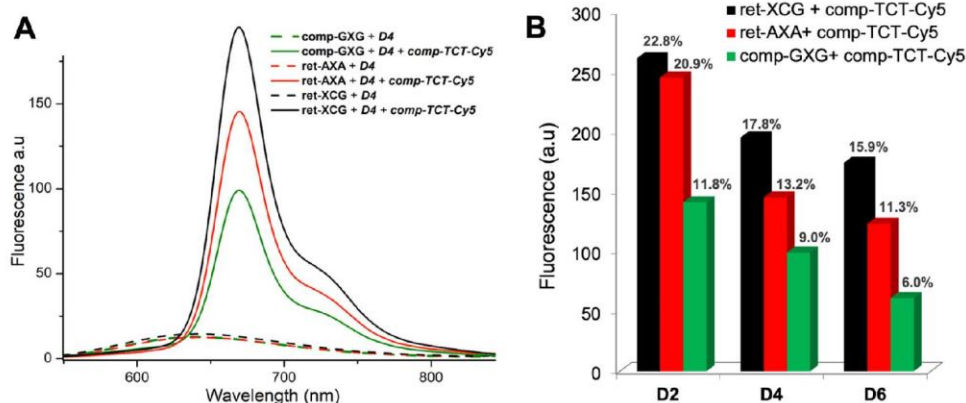


Figure 6. Distance impact on DRET: (A) emission spectra displaying distance dependent changes in fluorescence with gaps of two, four and six nucleotides for the D4 system (B) Histogram comparing the relative fluorescence intensity of the three considered ternary D2, D4 and D6 systems. Pseudo quantum yields of the DNA constructs undergoing RET were mentioned on the top of their relative bar. Sample concentration was 2 μ M in pH 7.4 PBS, and excitation was set at the donor absorption maximum.

(Supplementary Figure S29C). Similar outcomes were observed with an emission at 730 nm (*data not shown*).

To further validate our conclusions and to find the optimal values of fluorescence lifetimes, a global analysis was performed by simultaneously fitting the fluorescence decays of comp-AXA + TCT-Cy5 recorded at the three wavelengths, by constraining the decay times to be the same for all decays but allowing their amplitudes to vary (4). Using this approach, the best fits were obtained with the following three lifetimes: $\tau_1 = 90$ ps, $\tau_2 = 560$ ps, and $\tau_3 = 1.28$ ns (Supplementary Table S3). The value of the rise component ($\tau_1 = 90$ ps) is fully consistent with the RET-associated short-lived lifetime ($\tau_1 = 120$ ps) of the donor X in the comp-AXA + TCT-Cy5 duplex (*vide supra*), as expected for RET between X and Cy5. From the RET-associated short-lived lifetime of the donor X ($\tau_1 = 120$ ps) and a Förster distance of 46 Å for the X/Cy5 pair, a RET efficiency of 81% and a distance r of 36 Å was calculated between the two dyes (Equations 1–5). This distance is in accordance with the theoretical 30 Å distance (*vide supra*). Moreover, the RET efficiency determined from lifetime ($E = 81\%$) and steady-state ($E = 83\%$) experiments fully converged, which further confirms the consistency of the data.

Altogether, our data indicate that DRET turns on Cy5 emission with high amplification and is free of cross-excitation (Figure 4).

Application. To demonstrate the potential for intermolecular DRET in DNA sensing, we designed a set of binary probes labeled with X and Cy5, respectively, that are complementary to a long target sequence. The annealing of the binary probes with the target sequence leads to a gap of two, four or six nucleotides (D2, D4 and D6) (Figure 5, Supplementary Figure S30). A gap of at least two nucleotides between the probes is thought to avoid problems related to dipole orientation (44). Moreover, to further vary the distance between X and Cy5 in their ternary complexes with their target sequences, the position of X was changed in the X-labeled probe.

The donor was found to show a similar QY upon hybridization (close to 3%) with the target sequence in the absence of Cy5-labeled probe in all the constructs (Supplementary Figure S31). As a result, R_0 is constant ($R_0 \approx 40$ Å) in all systems and the distance effect in the RET process can be easily deduced from comparison of the spectra. In the ternary complexes, by reducing the distance between the donor and the acceptor – either by shortening the gap D6 \rightarrow D2 or moving X – a gradual increase in Cy5 fluorescence intensity was observed as expected for RET (Figure 6 & Supplementary Figure S32). The brightest signals were obtained for ret-XCG and ret-AXA in association with D2 + comp-TCT-Cy5 where the donor-to-acceptor distance is the shortest. If we define the ratio of the number of photons emitted by the acceptor to that absorbed by the donor as a *pseudo* quantum yield, Φ_{ps} , the values of Φ_{ps} (21–23%, Figure 6B) are comparable to the quantum yield of Cy5 ($\Phi = 28\%$) indicating an almost quantitative energy transfer from the donor to the acceptor. For both D4 and D6 systems, a progressive decrease of Φ_{ps} was observed when R_{D-A} increased as well as a strong depolarization of the Cy5 emission, which are consistent with a RET mechanism (Figure 6 & Supplementary Figure S33). Most importantly, photon collection at the emission maximum of Cy5 (667 nm) revealed a 90-fold enhancement of the fluorescence signal after hybridization of ret-XCG and comp-TCT-Cy5 to the D2 target, illustrating the exquisite sensitivity of the hybridization test with these binary probes.

CONCLUSION

In this study, our aim was to harness the potential of quenched push–pull probes to switch on a fluorescence signal through intermolecular DRET. To this end, we have developed a suitable DRET pair where the dark donor consists of a fluorene π -scaffold conjugating in a push–pull relationship, a diethylamino with a ketotriazolyl group. The acceptor was Cy5. In addition to offering far-red emission, the selected acceptor avoids detrimental cross-excitation. Once incorporated into DNAs, the fluorene derivative displayed mega-Stokes shifts (>200 nm) associated with low

quantum yields. Using DNA as a platform to control the distance, the combination of both probes allowed us to turn on the Cy5 fluorescence signal in a distance-dependent manner as expected for RET. The distance dependence of the intermolecular DRET could be exploited to accurately measure inter-chromophore distance in DNA duplexes. The performance of the X/Cy5 pair as a suitable ruler for distance measurements in DNA is currently being further explored. Combining a dark donor with mega-Stokes shifts and a bright acceptor free of cross-excitation, this DRET pair provides a fluorescence turn-on with minimal contamination. DRET probes are easy to implement and capitalize on the advantages of both MBs and binary probes. The amplification of S/N in the far-red was up to 100-fold and compares favorably with those reported for MBs (10,11,13). In order to increase it even more, the donor QY must be reduced. In the case of donor- π -acceptor dyes, this could be done by making them more sensitive to water by enhancing their push-pull character. Donors quenched by other non-radiative processes may also be considered. Screening the acceptor is an alternative and complementary approach. The S/N is directly correlated with the quantum efficiency of the acceptor, which is only 28% for Cy5. Therefore, an acceptor demonstrating a higher QY should improve the S/N. By using appropriate bandpass filters, the lack of spectral crosstalk should allow us to further optimize the collection of photons from the acceptor. As parent push-pull fluorophores exhibit a high two-photon absorption cross-section (45), the fluorene label could also be an attractive candidate for two-photon excitation in the NIR. Therefore, new opportunities for the construction of binary probes are expected for sensing applications in life sciences and detection in the far-red with minimal background fluorescence (46,47).

SUPPLEMENTARY DATA

Supplementary Data are available at NAR Online.

ACKNOWLEDGEMENTS

We thank the French Government for the PhD grants of G.B. and J.S.

FUNDING

French 'Agence Nationale de la Recherche' [PFPIImaging - 18-CE09-0020-01]; Y.M. is grateful to the 'Institut Universitaire de France (IUF)'. Funding for open access charge: Agence Nationale de la Recherche; Ministère de l'Enseignement Supérieur et de la Recherche.

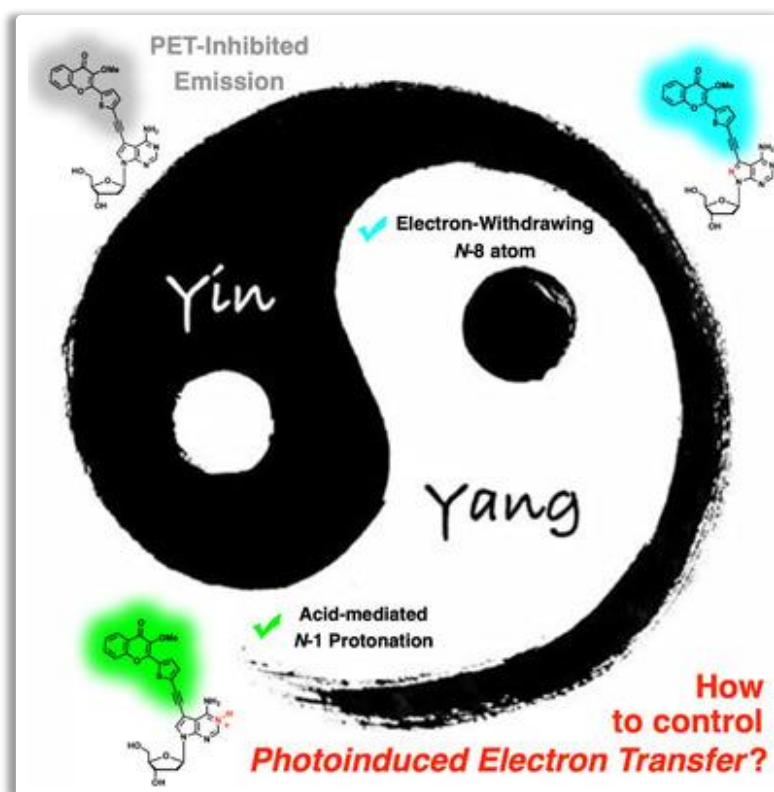
Conflict of interest statement. None declared.

REFERENCES

- Medintz,I. and Hildebrandt,N. (eds.) (2013) In: *FRET – Förster Resonance Energy Transfer: From Theory to Applications*. Wiley-VCH, Weinheim, p. 791.
- Mergny,J.-L., Boutorine,A.S., Garestier,T., Belloc,F., Rougée,M., Bulychev,N.V., Koshkin,A.A., Bourson,J., Lebedev,A.V., Valeur,B. et al. (1994) Fluorescence energy transfer as a probe for nucleic acid structures and sequences. *Nucleic Acids Res.*, **22**, 920–928.
- Preus,S., Kilsa,K., Miannay,F.A., Albinsson,B. and Wilhelmsson,L.M. (2012) FRETmatrix: a general methodology for the simulation and analysis of FRET in nucleic acids. *Nucleic Acids Res.*, **41**, e18.
- Lakowicz,J.R. (2006) In: *Principles of Fluorescence Spectroscopy*. 3rd edn., Springer, NY, p. 954.
- Wilhelmsson,L.M. and Tor,Y. (eds.) (2016) In: *Fluorescent Analogues of Biomolecular Building Blocks: Design and Applications*. John Wiley & Sons Inc., Hoboken, NJ, p. 448.
- Yuan,L., Lin,W., Zheng,K. and Zhu,S. (2013) FRET-based small-molecule fluorescent probes: rational design and bioimaging applications. *Acc. Chem. Res.*, **46**, 1462–1473.
- Cardullo,R.A., Agrawal,S., Flores,C., Zamecnik,P.C. and Wolf,D.E. (1988) Detection of nucleic acid hybridization by nonradiative fluorescence resonance energy transfer. *Proc. Natl. Acad. Sci. U.S.A.*, **85**, 8790–8794.
- Kolpashchikov,D.M. (2010) Binary probes for nucleic acid analysis. *Chem. Rev.*, **110**, 4709–4723.
- Marti,A.A., Jockusch,S., Stevens,N., Ju,J. and Turro,N.J. (2007) Fluorescent hybridization probes for sensitive and selective DNA and RNA detection. *Acc. Chem. Res.*, **40**, 402–409.
- Tyagi,S. and Kramer,F.R. (1996) Molecular beacons: probes that fluoresce upon hybridization. *Nat. Biotech.*, **14**, 303–308.
- Tyagi,S., Marras,S. and Kramer,F.R. (2000) Wavelength-shifting molecular beacons. *Nat. Biotech.*, **18**, 1191–1196.
- Li,Q., Luan,G., Guo,Q. and Liang,J. (2002) A new class of homogeneous nucleic acid probes based on specific displacement hybridization. *Nucleic Acids Res.*, **30**, e5.
- Han,S.-X., Jia,X., Ma,J.-L. and Zhu,Q. (2013) Molecular beacons: a novel optical diagnostic tool. *Arch. Immunol. Ther. Exp.*, **61**, 139–148.
- Santangelo,P.J. (2004) Dual FRET molecular beacons for mRNA detection in living cells. *Nucleic Acids Res.*, **32**, e57.
- Bratu,D.P., Cha,B.-J., Mhlanga,M.M., Kramer,F.R. and Tyagi,S. (2003) Visualizing the distribution and transport of mRNAs in living cells. *Proc. Natl. Acad. Sci. U.S.A.*, **100**, 13308–13313.
- Su,D., Oh,J., Lee,S.-C., Lim,J.M., Sahu,S., Yu,X., Kim,D. and Chang,Y.-T. (2014) Dark to light! A new strategy for large Stokes shift dyes: coupling of a dark donor with tunable high quantum yield acceptors. *Chem. Sci.*, **5**, 4812–4818.
- Su,D., Teoh,C.L., Sahu,S., Das,R.K. and Chang,Y.-T. (2014) Live cells imaging using a turn-on FRET-based BODIPY probe for biothiols. *Biomaterials*, **35**, 6078–6085.
- Su,D., Teoh,C.L., Kang,N.-Y., Yu,X., Sahu,S. and Chang,Y.-T. (2015) Synthesis and systematic evaluation of dark resonance energy transfer (DRET)-based library and its application in cell imaging. *Chem. Asian J.*, **10**, 581–585.
- Şen,E., Meral,K. and Atılgan,S. (2016) From dark to light to fluorescence resonance energy transfer (FRET): polarity-sensitive aggregation-induced emission (AIE)-active tetraphenylethene-fused BODIPY dyes with a very large pseudo-Stokes shift. *Chem. - Eur. J.*, **22**, 736–745.
- Lin,L., Lin,X., Guo,H. and Yang,F. (2017) Diphenylacrylonitrile-connected BODIPY dyes: fluorescence enhancement based on dark and AIE resonance energy transfer. *Org. Biomol. Chem.*, **15**, 6006–6013.
- Yu,Y., Yang,B., Yuan,Y. and Zhang,H. (2019) Novel side-chain alternative copolymer combined FRET and DRET with large pseudo-Stokes shift and polarity-sensitive fluorescence behavior. *J. Mater. Chem. C*, **7**, 11285–11292.
- Wang,X., Zhang,L., Zhuang,S., Huang,M. and Gao,Y. (2019) A novel fluorescent sensor for Sn⁴⁺ detection: Dark resonance energy transfer from silole to rhodamine. *Appl. Organometal. Chem.*, **114**, 590–597.
- Armarego,W.L.F. and Chai,C.L.L. (2012) In: *Purification of Laboratory Chemicals*. 7th edn., Butterworth-Heinemann, Oxford, p. 1024.
- Still,W.C., Kahn,M. and Mitra,A. (1978) Rapid chromatographic technique for preparative separations with moderate resolution. *J. Org. Chem.*, **43**, 2923–2925.
- Fulmer,G.R., Miller,A.J.M., Sherden,N.H., Gottlieb,H.E., Nudelman,A., Stoltz,B.M., Bercaw,J.E. and Goldberg,K.I. (2010) NMR chemical shifts of trace impurities: common laboratory solvents, organics, and gases in deuterated solvents relevant to the organometallic chemist. *Organometallics*, **29**, 2176–2179.

26. Sasaki,S., Niko,Y., Klymchenko,A.S. and Konishi,G.-I. (2014) Design of donor–acceptor geometry for tuning excited-state polarization: fluorescence solvatochromism of push–pull biphenyls with various torsional restrictions on their aryl–aryl bonds. *Tetrahedron*, **70**, 7551–7559.
27. Marras,S.A.E., Kramer,F.R. and Tyagi,S. (2003) Genotyping SNPs with molecular beacons. *Methods Mol. Biol.*, **212**, 111–128.
28. Breslauer,K.J. (1995) Extracting thermodynamic data from equilibrium melting curves for oligonucleotide order-disorder transitions. *Methods Enzymol.*, **259**, 221–242.
29. Brochon,J.C. (1994) Maximum entropy method of data analysis in time-resolved spectroscopy. *Methods Enzymol.*, **240**, 262–311.
30. Shaya,J., Collot,M., Bénailly,F., Mahmoud,N., Mély,Y., Michel,B.Y., Klymchenko,A.S. and Burger,A. (2017) Turn-on fluorene push-pull probes with high brightness and photostability for visualizing lipid order in biomembranes. *ACS Chem. Biol.*, **12**, 3022–3030.
31. Shaya,J., Fontaine-Vive,F., Michel,B.Y. and Burger,A. (2016) Rational design of push-pull fluorene dyes: synthesis and structure-photophysics relationship. *Chem. - Eur. J.*, **22**, 10627–10637.
32. Shaya,J., Deschamps,M.-A., Michel,B.Y. and Burger,A. (2016) Air-Stable Pd catalytic systems for sequential one-pot synthesis of challenging unsymmetrical aminoaromatics. *J. Org. Chem.*, **81**, 7566–7573.
33. Kyrp,J., Kejnovska,I., Renciuik,D. and Vorlickova,M. (2009) Circular dichroism and conformational polymorphism of DNA. *Nucleic Acids Res.*, **37**, 1713–1725.
34. Hainke,S. and Seitz,O. (2009) Binaphthyl-DNA: stacking and fluorescence of a nonplanar aromatic base surrogate in DNA. *Angew. Chem. Int. Ed.*, **48**, 8250–8253.
35. Dempsey,G.T., Vaughan,J.C., Chen,K.H., Bates,M. and Zhuang,X. (2011) Evaluation of fluorophores for optimal performance in localization-based super-resolution imaging. *Nat. Methods*, **8**, 1027–1036.
36. Moreira,B.G., You,Y. and Owczarzy,R. (2015) Cy3 and Cy5 dyes attached to oligonucleotide terminus stabilize DNA duplexes: Predictive thermodynamic model. *Biophys. Chem.*, **198**, 36–44.
37. Iqbal,A., Arslan,S., Okumus,B., Wilson,T.J., Giraud,G., Norman,D.G., Ha,T. and Lilley,D.M.J. (2008) Orientation dependence in fluorescent energy transfer between Cy3 and Cy5 terminally attached to double-stranded nucleic acids. *Proc. Natl. Acad. Sci. U.S.A.*, **105**, 11176–11181.
38. Börjesson,K., Preus,S., El-Sagheer,A.H., Brown,T., Albinsson,B. and Wilhelmsson,L.M. (2009) Nucleic acid base analog FRET-pair facilitating detailed structural measurements in nucleic acid containing systems. *J. Am. Chem. Soc.*, **131**, 4288–4293.
39. Preus,S. and Wilhelmsson,L.M. (2012) Advances in quantitative FRET-based methods for studying nucleic acids. *ChemBioChem*, **13**, 1990–2001.
40. Weber,G. and Shinitzky,M. (1970) Failure of energy transfer between identical aromatic molecules on excitation at the long wave edge of the absorption spectrum. *Proc. Natl. Acad. Sci. U.S.A.*, **65**, 823–830.
41. de Rocquigny,H., El Meshri,S.E., Richert,L., Didier,P., Darlix,J.-L. and Mély,Y. (2014) Role of the nucleocapsid region in HIV-1 Gag assembly as investigated by quantitative fluorescence-based microscopy. *Virus Res.*, **193**, 78–88.
42. Becker,W. (2012) *The Bh TCSPC Handbook: Time-correlated Single Photon Counting Modules SPC-130, SPC-134, SPC-130 EM, SPC-134 EM, SPC-140, SPC-144, SPC-150, SPC-154, SPC-630, SPC-730, SPC-830; Simple-Tau Systems, SPCM Software, SPCImage Data Analysis*. Becker et Hickl.
43. Borst,J.W., Laptinok,S.P., Westphal,A.H., Kühnemuth,R., Hornen,H., Visser,N.V., Kalinin,S., Aker,J., van Hoek,A., Seidel,C.A.M. and Visser,A.J.W.G. (2008) Structural changes of yellow cameleon domains observed by quantitative FRET analysis and polarized fluorescence correlation spectroscopy. *Biophys. J.*, **95**, 5399–5411.
44. Kashida,H., Kurihara,A., Kawai,H. and Asanuma,H. (2017) Orientation-dependent FRET system reveals differences in structures and flexibilities of nicked and gapped DNA duplexes. *Nucleic Acids Res.*, **45**, e105.
45. Kucherak,O.A., Didier,P., Mély,Y. and Klymchenko,A.S. (2010) Fluorene analogues of prodan with superior fluorescence brightness and solvatochromism. *J. Phys. Chem. Lett.*, **1**, 616–620.
46. Jin,Z., Geißler,D., Qiu,X., Wegner,K.D. and Hildebrandt,N. (2015) A rapid, amplification-free, and sensitive diagnostic assay for single-step multiplexed fluorescence detection of MicroRNA. *Angew. Chem. Int. Ed.*, **54**, 10024–10029.
47. Sharma,K.K., Przybilla,F., Restle,T., Godet,J. and Mély,Y. (2016) FRET-based assay to screen inhibitors of HIV-1 reverse transcriptase and nucleocapsid protein. *Nucleic Acids Res.*, **44**, e74.

Publication 6



Cette publication décrit l'utilisation et le fonctionnement d'un mécanisme de PET intermoléculaire sur des analogues de bases nucléique fluorescente pour permettre le développement de senseur du double brin d'ADN.

Electron Transfer | Hot Paper |

Control of Intermolecular Photoinduced Electron Transfer in Deoxyadenosine-Based Fluorescent Probes

Hoang-Ngoan Le,^[a] Johanna Brazard,^[b, c] Guillaume Barnoin,^[a] Steve Vincent,^[a] Benoît Y. Michel,^{*[a]} Jérémie Leonard,^[b] and Alain Burger^{*[a]}

Abstract: In this work, we report on the Photoinduced Electron Transfer (PET) reaction between a donor (adenine analogue) and an acceptor (3-methoxychromone dye, **3MC**) in the context of designing efficient fluorescent probes as DNA sensors. Firstly, Gibbs energy was investigated in disconnected donor–acceptor systems by Rehm–Weller equation. The oxidation potential of the adenine derivative was responsible for exergonicity of the PET reaction in separated combinations. Then, the PET reaction in donor– π -acceptor conjugates was investigated using steady-state fluorescence spectroscopy, acid-mediated PET inhibition and transient absorption techniques. In conjugated systems, PET is a favorable

pathway of fluorescent quenching when an electron-rich adenine analogue (**d7A**) was connected to the fluorophore (**3MC**). We found that formation of ground-state complexes even at nM concentration range dominated the dye photo-physics and generated poorly emissive species likely through intermolecular PET from **d7A** to **3MC**. On the other hand, solution acidification disrupts complexation and turns on the dye emission. Bridging an electron-poor adenine analogue with high oxidation potential (**8d7A**) to **3MC** presenting low reduction potential is another alternative to prevent complex formation and produce highly emissive monomer conjugates.

Introduction

Redesigning the structure of nucleosides to generate environment-sensitive fluorescent analogues and incorporating them into nucleic acids (NA) is a leading approach for the development of NA-related advanced sensors for sequencing and probing NA conformations, dynamics and interactions.^[1–3] A common strategy is grafting a chromophore to the nucleobase preferentially on a position not affecting Watson–Crick base pairing. In term of biocompatibility, extension at positions 5 and 7 of pyrimidine and purine rings, respectively, is the most favorable.^[1,4,5] Connecting a fluorophore is attractive as it opens the route to the development of emissive probes based on sensing parameters of the original dye.^[6,7] Extension of elec-

tronic nucleobase π -scaffolds to construct push–pull systems is particularly interesting since it could generate probes with unique photophysical properties including sensitivity to polarity and red-shifted absorption and emission.^[8] The responsiveness of the fluorescence reporter can be greatly increased if the emissive signal is based on the change between two spectrally resolved forms.^[9,10] In order to achieve this, we have selected fluorophores of the 3-hydroxychromone (**3HC**) family that can exist in two excited-state forms—the normal and tautomer ones—due to an excited-state intramolecular proton transfer (ESIPT). Both forms fluoresce at different wavelengths and thus generate a dual emission proving sensitive to H-bonding and electric field of the environment for which the intensity ratio of the two bands can be used as the reporting unit. In this context, we first reported push-pull probes with advanced features, elaborate from **dU** and **3HC**. These probes were characterized by a two-color emission (cyan and yellow), good quantum yields in different solvents including water and especially high sensitivity to hydration and NA conformations.^[11,12] The possibility to connect the **3HC** moiety to adenine nucleobases for NA labeling was next explored by electronically coupling 7-deazadeoxyadenosine (**d7A**) with **3HC** dyes (Figure 1. **FCA** and **TCA**).^[13] The new conjugates showed several improvements in the photophysical properties of **3HC** as evidenced by red-shifted absorptions from UV to the violet range, up to 1.5-fold increase in absorptivity and strong sensitivity to environmental changes. However, they revealed to be strongly quenched in polar protic solvents and almost non-emissive in water. Thus, the access of fluorescent purine-based nucleosides for NA labeling turned out to be more problematic

[a] H.-N. Le, G. Barnoin, S. Vincent, Dr. B. Y. Michel, Prof. Dr. A. Burger
Université Côte d'Azur, Institut de Chimie de Nice
UMR 7272, CNRS
Parc Valrose, 06108 Nice cedex 2 (France)
E-mail: benoit.michel@univ-cotedazur.fr
alain.burger@univ-cotedazur.fr

[b] Dr. J. Brazard, Dr. J. Leonard
Université de Strasbourg, Institut de Physique et Chimie
des Matériaux de Strasbourg and Labex NIE
UMR 7504, CNRS
67200 Strasbourg (France)

[c] Dr. J. Brazard
Present address: Université de Genève
Département de Chimie Physique
1211 Genève (France)

Supporting information and the ORCID identification number(s) for the author(s) of this article can be found under:
<https://doi.org/10.1002/chem.202003456>.

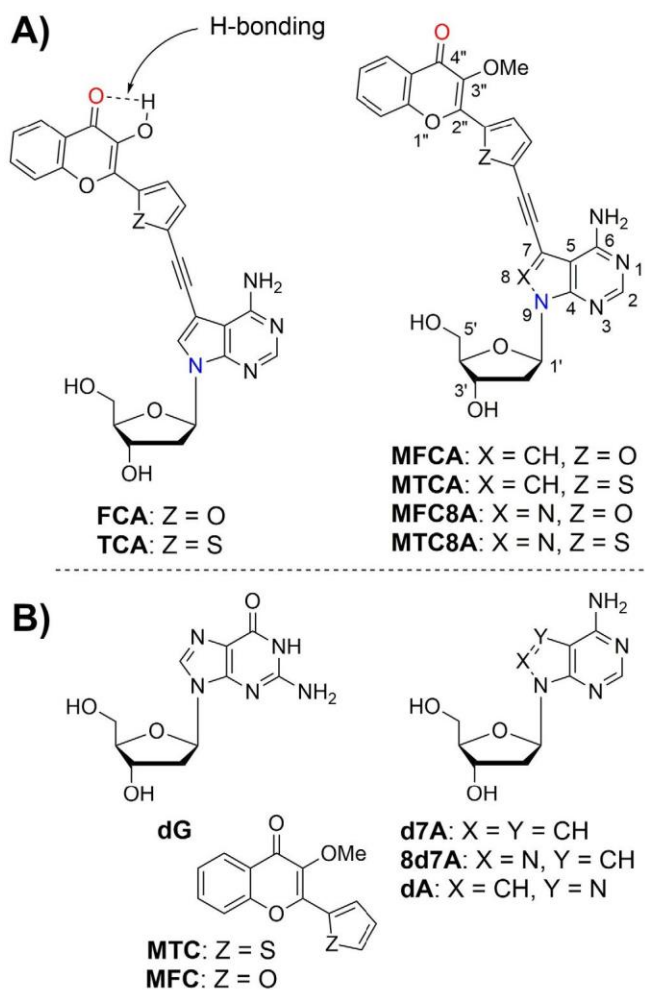


Figure 1. A) Synthesized push-pull conjugated systems investigated here: electron donors and acceptors are depicted in blue and red, respectively. B) Structures of separated donors (**dG**, **dA** and analogues) and acceptors (**3MC** derivatives).

than for the pyrimidine nucleobase. Since **7dA** is a potent donor for photoinduced electron transfer (PET), we hypothesized that a proton-coupled PET^[14] from the **7dA** fragment to the **3HC** could be a plausible mechanism to account for fluorescence quenching of **FCA** and **TCA**. Proposing such a process also raises the question of whether the electron transfer is intramolecular or intermolecular?

It is often difficult to prove the mechanism of quenching. The mechanism may not be exclusive and can be a combination of different processes (e.g. internal conversions, Dexter energy transfer, or twisted intramolecular charge transfer (TICT) conformation) making the task even more difficult.^[15] To have more convincing evidences, we carried out several experiments with 3-methoxychromones (**3MCs**) to avoid spectroscopic and kinetic complications due to the ESPT reaction (H-bond, Figure 1A). Herein, we report on our investigation of push-pull systems between **dA** analogues and **3MCs**. First, the energetic aspect of the PET reaction was studied between the separated **d7A** electron donor and **3MC** electron acceptor using cyclic voltammetry to demonstrate whether **d7A** can be oxidized

and **3MC** reduced. Given that **dG** has the lowest oxidation potential (*E*) and that incorporation of an *N* atom at position 8 of the purine increases this value ($E(\text{dG}) \sim E(7\text{dA}) < E(8\text{d7A}) \sim E(\text{dA})$),^[16–18] comparison experiments were implemented with positive (**dG**) and negative controls (**dA** and **8d7A** (8-aza-7-deaza-2'-deoxyadenosine)). Secondly, the photophysical investigations of the single-band emissive conjugates (**MFCA** and **MTCA**) and their corresponding negative controls (**MFC8A**, **MTC8A** and acidification) were performed to verify quenching of **MFCA** and **MTCA** in polar protic solvents. Lastly, UV/Vis transient absorption (TA) spectroscopy was performed on the conjugates to establish direct evidence of PET for **MFCA** and **MTCA** in methanol. This study not only provides a better understanding of the PET quenching reaction in separated as well as conjugated systems of **dA** analogues and chromones but also brings useful information for the design of fluorescent DNA sensors. Noticeably, fluorescence could be switched ON/OFF by using the suitable **dA** analogue or simply by fine tuning the medium pH.

Results and Discussion

Separated donors and acceptors, and conjugated deoxyadenosine analogues

The compounds required for the photophysics were synthesized (**MTCA**, **MFCA**, **MTC8A**, and **MFC8A**) or obtained from commercial sources (**MFC**, **dG**, **d7A**, **8d7A**, and **dA**). The synthesis of **MTC** was recently reported by our group.^[19] Synthesis of conjugates were adapted from Seela's previous works.^[17,20] The full details of their preparation and characterization are given in the Supporting Information.

Standard free energy changes of PET reaction between separated donors and acceptors

PET is the most common mechanism proposed to account for quenching of fluorophores by nucleobases.^[9] Upon PET, the **3MC** fluorophore can be reduced by the nucleobase to form a radical ion pair, which can further undergo radiationless relaxation to the ground state. Comparison of the redox potentials of the fluorophore and nucleobase allows us to examine the possibility for PET.^[16] Among the canonical nucleobases, guanine is the most potent electron donor with the lowest oxidation potential.^[16,21] The redox potential of **7dA**, a prospective nucleobase moiety to engineer adenosine-based probes, is close to that of guanosine.^[16] One strategy to raise the oxidation potential of **7dA** is to incorporate an endocyclic nitrogen in position 8 of the purine framework. Seela et al. exploited this approach and demonstrated its efficiency to affect the oxidation potential, placing **8d7A** in the range comparable to **dA**.^[17]

To determine if PET is energetically favorable, we have correlated fluorescence quenching of the bridged donor-acceptor systems with the redox potentials of the separated donors and acceptors and their corresponding Gibbs energies calculated from the Rehm–Weller equation [Eq. (1)].^[15,22] Based on the

latter, one could predict whether the electron transfer process is exergonic or endergonic.

$$\Delta G_{et}^{\circ} = E^{\text{ox}}(D) - E^{\text{red}}(A) - E_{00}(A) + \Delta G^{\circ}(\epsilon) \quad (1)$$

Where $E^{\text{ox}}(D)$ is the oxidation potential of the donor (purine base); $E^{\text{red}}(A)$ is the reduction potential of acceptor (**3MC** derivative); $E_{00}(A)$ is the zero-zero transition energy ($1240/\lambda$ (nm) in eV), where λ is the intersection of the normalized absorption and emission spectra of the acceptor.^[15] $\Delta G^{\circ}(\epsilon)$ is the solvent term contribution and depends on the dielectric constant of the solvent. It was estimated to be 0.1 eV in H₂O.^[16]

In this study, we assumed that **dA** analogues (**d7A** and **8d7A**) being the electron donors, and **3MCs**, the electron acceptors (Figure 1B). In order to compare with **dA** analogues, natural **dG** and **dA** were investigated as positive and negative controls, respectively.^[21] Oxidation and reduction potentials (Figure S1), as well as calculated Gibbs energies are reported in Table 1.

Analysis of these data allows several conclusions to be drawn. First, the oxidation potentials obtained for the known purine compounds were comparable to the reported values highlighting the consistency of our data (e.g. compare +1.46 V with +1.48 V for **d7A**, for the other compounds see Table S2).^[17] The oxidation potential of **d7A** (+1.46 V) is close to that of **dG** (+1.42 V); similarly, **8d7A** (+1.81 V) is comparable to **dA** (+1.85 V).

According to the Rehm–Weller equation, ΔG_{et}° depends on three main parameters. Firstly, it depends on the oxidation and reduction potentials of the donor and acceptor, respectively. Table 1 shows that the reduction potentials of the two chromones are identical; by contrast, the oxidation potentials of the purine bases are discriminant (compare **d7A** vs. **dG** with **8d7A** vs. **dA**). Hence, ΔG_{et}° of any pair between donor (**d7A** or **dG**) and acceptor (**MTC** or **MFC**) will be about 0.35–0.43 eV smaller than that of **8d7A** or **dA** as the donor. Basically, oxida-

tion of the donor and reduction of the acceptor in a PET process requires energy. Therefore, this energy contributes a positive value to the ΔG_{et}° of the PET reaction. Secondly, ΔG_{et}° depends on the zero-zero transition energy (E_{00}) of the fluorophore (**3MC**). E_{00} is the energy gain of the photoexcited **3MC**, it contributes a negative value to the free energy. The zero-zero transition energy of the furyl chromone (**MFC**, +3.18 eV) is just slightly higher than that of thiophene-containing chromone (**MTC**, +3.16 V). This result is consistent with the fact that the larger sulfur atom probably decreases of the HOMO–LUMO energy gap compared to the smaller oxygen atom due to resonance effects.^[23,24] Lastly, the solvent term contribution $\Delta G^{\circ}(\epsilon)$ depends on the dielectric constant of the solvent. Generally, it decreases with increasing permittivity; however, its contribution to the total energy is small. According to ΔG_{et}° , electron transfer from **d7A** to **MFC** and **MTC** is exergonic with –0.30 eV; while, it is slightly endergonic from **8d7A** to the chromones **MTC** and **MFC** with +0.05 eV. Assuming that $\Delta G_{et}^{\circ} = -0.30$ eV is in the normal region according to the Marcus theory,^[25–27] our results suggest that the electron transfer from **d7A** to the chromone should be faster and more favorable than that from **8d7A**.

General photophysical characterization

The photophysics of the newly synthesized push-pull nucleosides were characterized in a set of four protic solvents (water, methanol, ethanol, and *i*-propanol) of different polarities, and the results are summarized in Table 2 (Figures S3–S6). The Dimroth–Reichardt polarity index parameter^[28] is used to rank the solvents. This empirical scale takes into account the dielectric constant and H-bonding ability of the medium. The solvent acidity (SA) according to the Catalán scale is also given for comparison and discussion.^[29]

The **MFCA** and **MTCA** exhibit similar absorptivity and little variation of absorption maxima whatever the solvent studied. The maxima are centered near the visible range (377–379 and 388–391 nm, respectively). Both conjugates displayed a 35–41 nm bathochromic shift of their absorption by comparison to the parent **MFC** and **MTC** chromones (Figure S2 and ref. [19]) as expected for dyes with extended conjugation. The same conclusion can be deduced from the UV/Vis spectra of **MFC8A** and **MTC8A**, albeit with slightly blue-shifted absorption maxima (362–383 nm). Unsurprisingly, substitution of the 3-hydroxyl proton by the methyl group in the chromone inhibits ESIPT and thus, the dual emission. **MFCA** and **MTCA** displayed bathochromic shifts of their emission maxima with the increase in solvent polarity (e.g., from 534 nm in *i*PrOH to 571 nm in MeOH for **MFCA**, Table 2), as illustrated in Figure 2. Their quantum yields gradually drop as the polarity increases (Figure 3). For chromones, it is known that in the excited state, the electron-enriched 4'-carbonyl oxygen (Figure 1) is particularly sensitive to H-bonding for which H-bond interactions are all the stronger as the acidity of the solvent increases.^[31–33] There are many examples in chemistry and biology supporting that intermolecular site-specific interactions through H-bonding can increase PET.^[14,16,34] As with **FCA** and **TCA** compared to

Table 1. Oxidation potentials of donors, reduction potentials of acceptors and Gibbs energies.

Donor	Acceptor	$E^{\text{ox}}(D)^{[a]}$ vs. NHE [V]	$E^{\text{red}}(A)^{[a]}$ vs. NHE [V]	$E_{00}(A)^{[b]}$ [eV]	ΔG_{et}° [eV]
dG	MTC	+1.42	–1.50	+3.16	–0.33
d7A	MTC	+1.46	–1.50	+3.16	–0.30
8d7A	MTC	+1.81	–1.50	+3.16	+0.05
dA	MTC	+1.85	–1.50	+3.16	+0.10
dG	MFC	+1.42	–1.50	+3.18	–0.33
d7A	MFC	+1.46	–1.50	+3.18	–0.30
8d7A	MFC	+1.81	–1.50	+3.18	+0.05
dA	MFC	+1.85	–1.50	+3.18	+0.10

[a] Cyclic voltammetry was conducted against Ag/AgCl (KCl saturated) in acetonitrile containing 1 M tetra-*n*-butylammonium hexafluorophosphate (TBAPF₆) as the electrolyte, and saturated solution of the purine base or 1 mM **3MC**. Data were converted into normal hydrogen electrode (NHE) for comparison. Scan speed was 100 mVs^{–1}. [b] $E_{00}(A)$ values were obtained from absorption and emission spectra of the corresponding fluorophore in water (see Figure S2).

Table 2. Photophysical properties of nucleoside analogues in different solvents.						
ε_{\max} [$10^3 \text{ M}^{-1} \text{ cm}^{-1}$] ^[a]	—	40	40	34	37	
Solvent	$E_T^N(30)$ ^[b] SA ^[c]	λ [nm] ^[d] Φ [%] ^[e]	MFCA (10)	MTCA (11)	MFC8A (12)	MTC8A (13)
H ₂ O ^[f]	1.00	λ_{Abs}	378	388	372	366
	1.062	λ_{Em}	567	579	472	479
		Φ	0.2	0.7	30	NA ^[g]
H ₂ O–TFA 5% ^[f]		λ_{Abs}	377	384		
		λ_{Em}	521	527		
		Φ	6.0	6.0		
MeOH ^[f]	0.76	λ_{Abs}	378	388	372	366
	0.605	λ_{Em}	571	580	464	469
		Φ	1.3	0.9	38	36
MeOH ^[h]		λ_{Em}	512	512	464	469
MeOH–TFA 5% ^[f]		λ_{Abs}	371	382		
		λ_{Em}	501	508		
		Φ	41	35		
EtOH ^[f]	0.65	λ_{Abs}	378	390	368	379
	0.400	λ_{Em}	555	564	458	464
		Φ	6	4.2	33	30
iPrOH ^[f]	0.57	λ_{Abs}	379	391	368	379
	0.283	λ_{Em}	534	546	453	459
		Φ	19	18	29	26

[a] Molar extinction coefficient was determined in MeOH; relative standard deviations are $\leq 5\%$. [b] Reichardt's empirical solvent polarity index.^[28] [c] Acidity scale.^[29] [d] Wavelength of absorption (λ_{Abs}) and emission maxima (λ_{Em}) in nm. [e] Fluorescence quantum yields (Φ) were determined using an excitation at the corresponding absorption maximum of each compound in the considered solvent. *p*-Dimethylaminoflavone (DMAF) in EtOH ($\lambda_{\text{Abs}}=404 \text{ nm}$, $\Phi=27\%$)^[30] was used as the standard reference, $\pm 10\%$ mean standard deviation. [f] Absorption and emission spectra were recorded at concentrations of 11 and 1.1 μM , respectively. [g] Not investigated due to very low solubility. [h] Emission maximum obtained for solution at concentration $< 10 \text{ nM}$.

TCU, the corresponding methylated derivatives behave differently. They turn almost non-emissive in MeOH and H₂O (e.g. compare $\Phi=0.9\%$ for **MTCA** in MeOH with $\Phi=49\%$ for **MTCU**) and show larger bathochromic shifts, which can be seen from the shifts in emission since the compounds have close absorption maxima (e.g. compare 501 nm for **MTCU** in MeOH with 580 nm for **MTCA**).^[19]

Why do these compounds demonstrate such large spectral shifts and drop in quantum yields in protic solvents? Are these variations due to solvent specific effects, conformational changes generating a TICT conformer or probe-probe interactions? To address these questions, we examined the emission spectra recorded at different concentrations ranging from 60 μM to 1.25 nM as shown in Figure 4 (see also Figure S8) and observed concentration-dependent spectral shifts.

For example, the emission maximum of **MTCA** in MeOH was gradually blue-shifted from 580 nm (at concentrations larger than 0.5 μM) to 512 nm ($[\text{C}] < 2 \text{ nM}$). At concentrations as low as 5 nM, we have already detected a contribution of the 580-nm emissive species (see Figure 4, top). The high-energy emis-

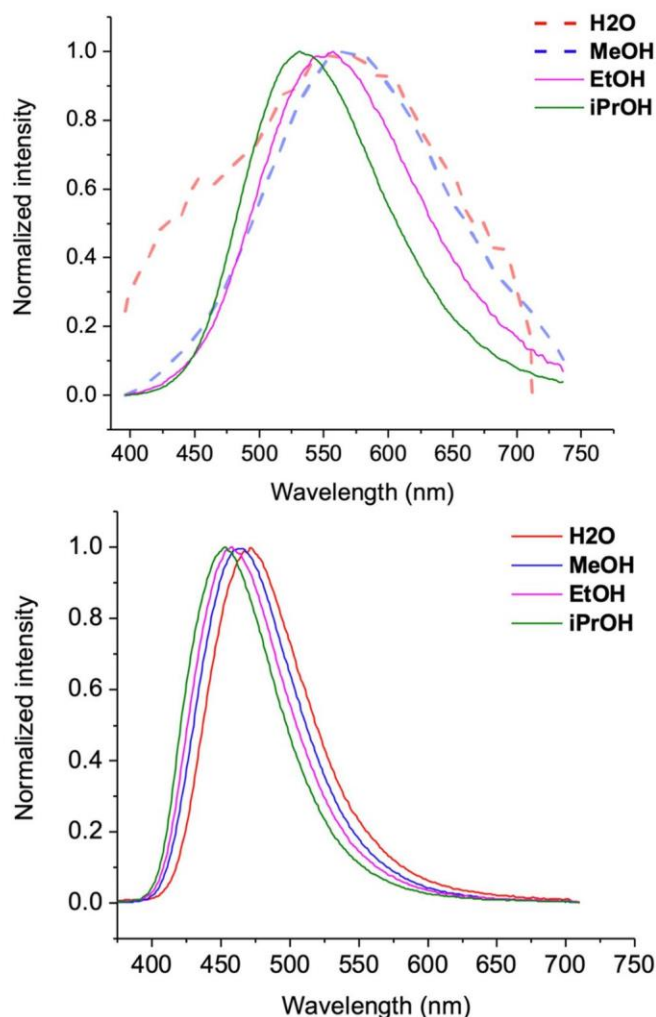


Figure 2. Normalized emission spectra of MFCA (top) and MFC8A (bottom) at 1.1 μM , in a set of protic solvents of increasing polarity. Excitation wavelength was set at the absorption maximum (Table 2).

sion band was close to that of **MTCU**. We therefore attribute the 512-nm emission band to the monomer dye, and that at 580 nm to a complex. Excimers are typically observed as a broad emission band, red-shifted relative to that of the fluorophore monomer. Excimer is a complex formed between two monomers when at least one component is in the excited state. Noticeably, the changes in the emission spectra of **MTCA** and **MFCA** clearly showed that the complexes are formed at concentrations as low as few nM, which are far below the mM-concentration range for which excimers are typically observed.^[15,35]

Indeed at 2 μM concentration, the average distance between solute molecules of $d \approx 0.1 \mu\text{M}$ corresponds to a typical diffusion time $\tau=d^2/D$ in the 20- μs range for two molecules to encounter (assuming $D=500 \mu\text{m}^2 \text{s}^{-1}$ for the diffusion coefficient),^[36,37] which is 4 orders of magnitude longer than the excited-state lifetime. Thus, the emission spectra observed at concentrations of 0.5 μM or larger are attributed to a complex resulting from ground-state interactions. Analyzing the excitation spectra recorded at different concentrations further supports this interpretation as the existence of two absorbing spe-

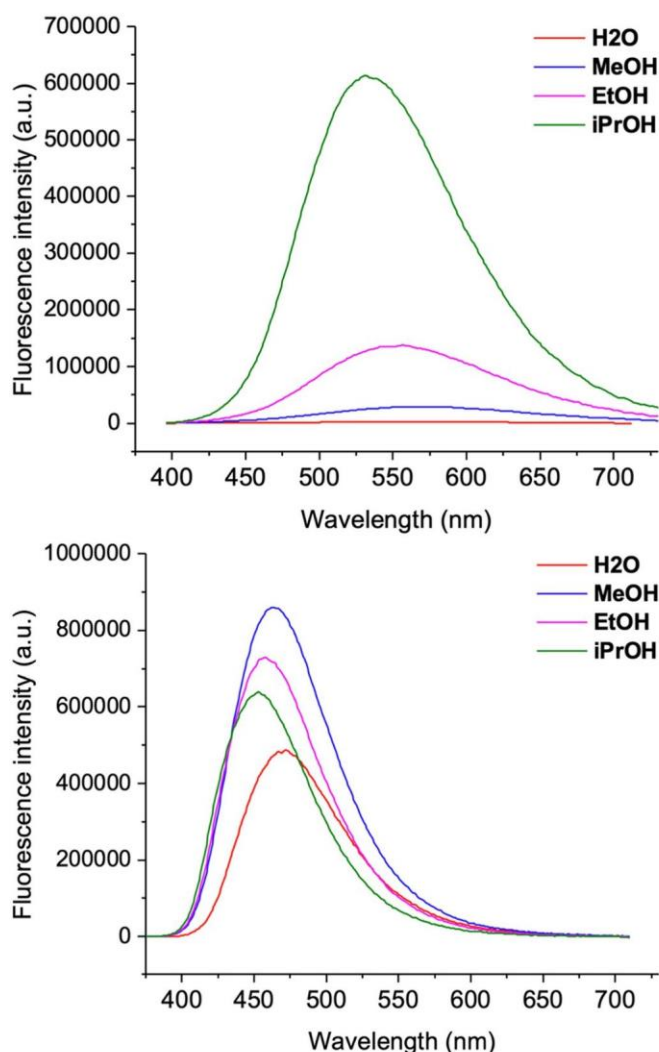


Figure 3. Fluorescence spectra of **MFCA** (top) and **MFC8A** (bottom) at 1.1 μM , in a set of protic solvents of increasing polarity. Excitation wavelength was set at the absorption maximum (Table 2).

cies was evidenced at low concentration (Figures S7 and S8). Formation of ground-state complexes of acceptor–donor pairs is known.^[38,39] The close association of both species favors PET affording radical ion pairs. The radical ion pair generated from the charge-transfer complex can be compared to the well-known poorly emissive geminate radical ion pairs for exciplexes, although the latter, as for the excimer, generally refer to bimolecular contacts of the excited dye and a quencher.^[40–43] The peculiarity of our compounds is that they formed complexes even at very low concentrations. We are not aware of other examples of such intermolecular tight interactions reported in the literature. In the case of **MTCA** and **MFC8A**, their complexation could be favored in polar solvents due to the hydrophobic nature of the extended flat fluorophore, favorable π -stacking and van der Waals interactions as well as a quadrupole arrangement allowing strong Coulombic coupling. A head-to-tail orientation of the two dyes should favor intermolecular PET, because the nucleobase donor in one specie would be in contact with the chromone acceptor of the other specie (Figure 5). Thus, the complexation of **MTCA** and **MFC8A** and photoinduced

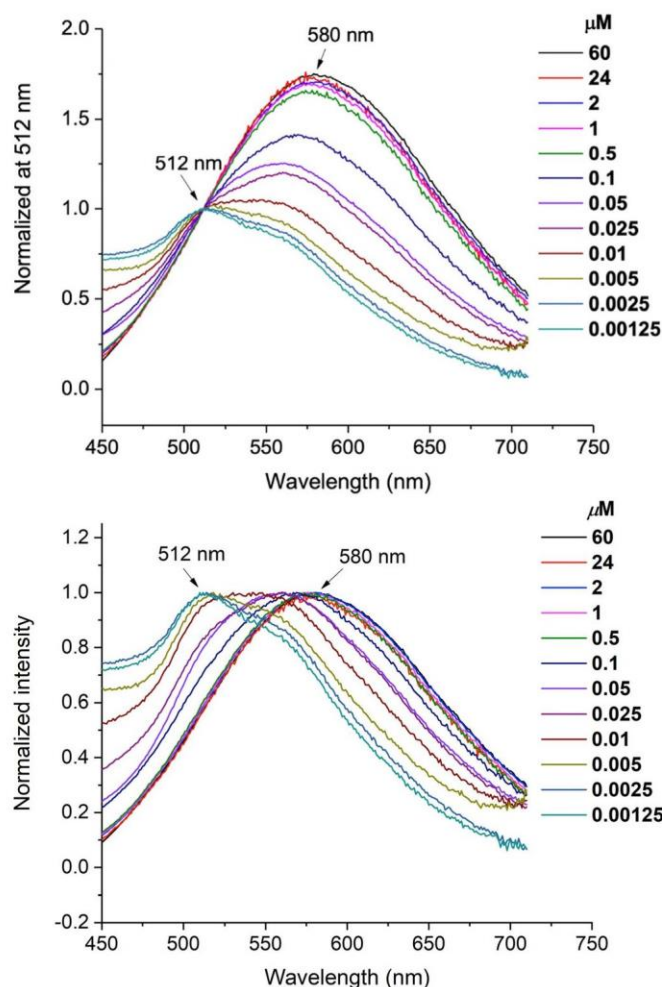


Figure 4. Emission spectra of **MTCA** for different concentrations in MeOH, normalized at 512 nm (top) and on their maximum (bottom). Excitation wavelength was set at 370 nm.

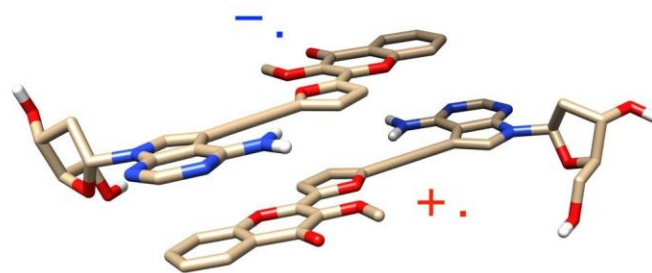


Figure 5. Proposed representation of the complexed, radical pair structure (generated from Chimera).

formation of poorly emissive radical ion pairs likely dominate the photophysics of these dyes in polar protic solvents.

The 8-aza series (**MTC8A** and **MFC8A**) behave differently. They showed reduced redshifts of their emission maxima along with the increase in solvent polarity (e.g. from 453 nm in *i*PrOH to 474 nm in MeOH for **MFC8A**) and bright emissions in polar protic solvents (e.g. 30% in water for **MFC8A**). Importantly, the emission spectra remain unchanged even down to the 1–2 nM range for both dyes by contrast to **MTCA** and **MFC8A** (Figures S11, S12). These results suggest that the **MTC8A** and

MFC8A were observed as monomers in MeOH solution at all studied concentrations from nM to μM . Since both types of dyes have the same size and area, the only difference between them is the introduction of an electron-withdrawing nitrogen at the 8 position on the nucleobase. This considerably reduces the electron-donating ability of **8d7A** as evidenced by the increased of the oxidation potential (Table 1, compare 1.81 and 1.46 V for **8d7A** and **d7A**, respectively). Therefore, the difference between the oxidation potential of the donor and the reduction potential of the acceptor increases. As a consequence, the propensity to form charge-transfer complexes between the **8d7A** donor and the **MTC** or **MFC** acceptor should be greatly affected by contrast to that formed with **d7A**. Previous reports have shown that the association constant of donor/acceptor complexes decreases as the difference in the redox potential increases,^[38,39] albeit they form at concentrations several orders of magnitude higher than those required for **MFCA** and **MTCA**. Our data highlights that the difference in the redox potential is one important contributor to the complex association for our dyes.

Acid-mediated inhibition of the PET process

Protonation of amines linked to weakly emissive systems is a common way to switch on their fluorescence.^[44] The purine bases have 2-electron-rich centers at N3 and N1 atoms with pK_a of around 4.3.^[45] In acidic media, the most basic nitrogen N1 will be protonated. Protonation of the purine base should therefore reduce its electron-donating ability and disrupt both the complex formation and electron transfer process (Figure 6). To check this hypothesis, the absorption and emission spectra of **MFCA** and **MTCA** in MeOH and H₂O, with and without adding TFA (0.5% v/v), were investigated. Upon addition of this strong Brønsted acid, turn-on emissions were recorded (Figures 6 and S13). For instance, the poor quantum yields (< 1%) of **MTCA** increased to 35% and 6% for acidified MeOH and H₂O solutions, respectively. Analysis of the excitation and emission spectra of **MFCA** and **MTCA** in acidified MeOH (TFA, 0.5% v/v) at different concentrations led to the same conclusion, as for **MTC8A** and **MFC8A** (Figures S9, S10), that only the monomer spectra are observed at all concentrations employed here.

Direct observation of PET on conjugated systems using UV/Vis TA spectroscopy

To further support the proposed PET reaction and observe the corresponding reaction kinetics, femtosecond UV/Vis transient absorption (TA) spectroscopy was used. Methanolic solutions of **MTCA**, **MTC8A** and **MFC8A** with TFA (0.5% v/v)—as well as **MFCA**, **MFC8A** and **MFC8A** with TFA (0.5% v/v)—were prepared at a concentration of 330 μM and investigated by TA, with a 60 to 70-fs time resolution, using a 370-nm pump pulse, and a white-light probe pulse offering an absorption detection window spanning from 330 to 700 nm. The experimental set-up is the same as previously described (see General methods, Experimental Section).^[33] Quantitative analysis of the TA data is

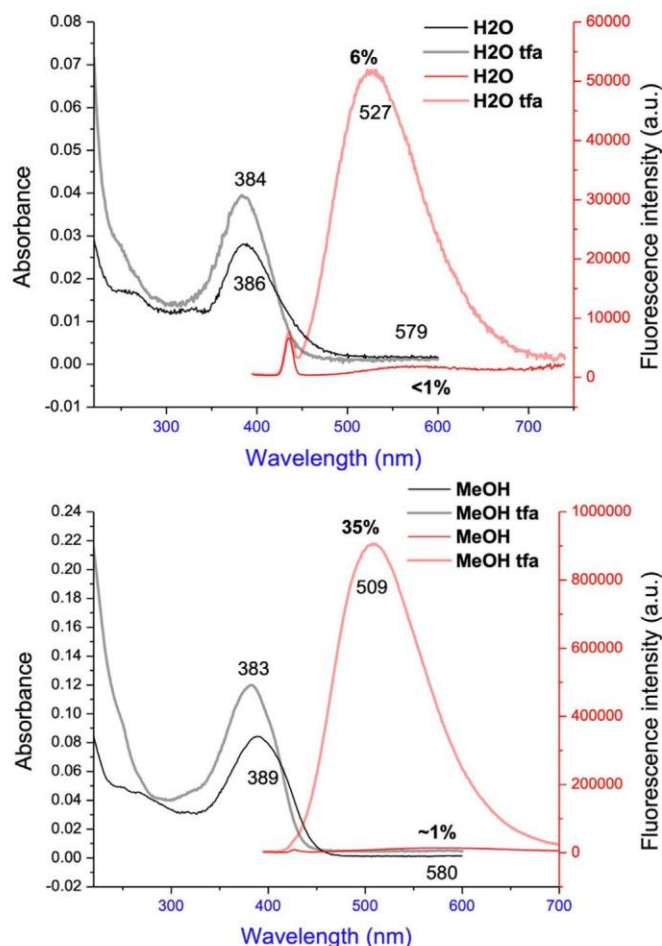


Figure 6. Substantial fluorescent turn-on signal of **MTCA** upon TFA addition recorded in H₂O (top) and MeOH (bottom). Absorption (grey and black) and emission (pink and red) spectra were measured at 2 μM . Maxima are given in nm and quantum yields mentioned above, in %. Their determination took into account the change in absorbance at the excitation wavelength of 370 nm.

performed by global analysis and illustrated by presenting the so-called decay-associated spectra (DAS, Figures 7 and S14–S18), which reveal the time scales and associated spectral modifications characterizing the TA decay kinetics recorded across the entire UV/Vis observation window.

Immediately after excitation, the early signature of the first excited state S_1 is similar in the three samples (0.2-ps spectra in Figure 7a, d, and g). We identify the ground-state bleach (GSB) as a negative signal around 380 nm, a stimulated emission (SE) band—also negative—around 450 nm, and a positive excited-state absorption at wavelengths > 500 nm. Early spectral relaxation occurs in all three samples already within the instrument response function, and with a 0.5 to 0.6-ps time scale (Figure S16), likely due to the fast solvent relaxation^[46] and possibly to the early vibrational relaxation out of the Franck–Condon (FC) region. Then, in the case of **MTCA**, the early SE and an excited-state absorption (ESA) band decay on the 2.8-ps time scale, corresponding to the formation of a first transient state that we named **U**, which is still an excited state (possibly the **MTCA** complex in a different conformation), since the GSB does not recover on this time scale (Figure 7a and b). This

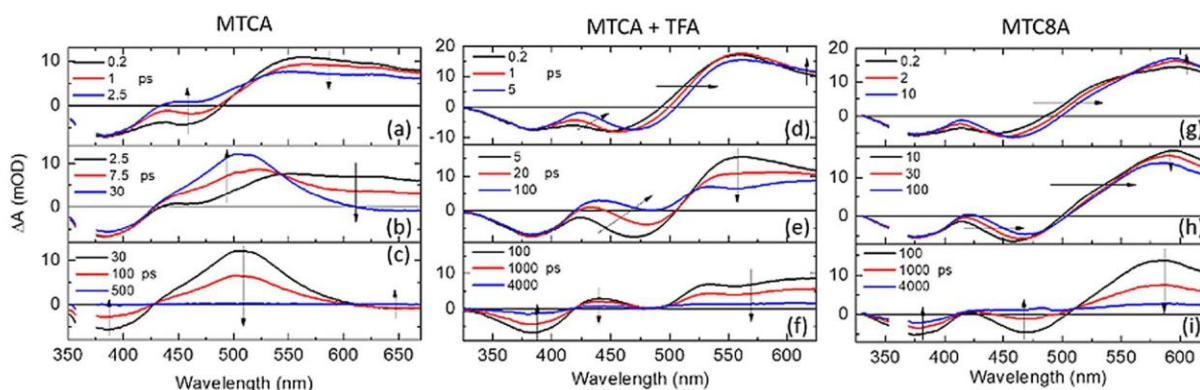


Figure 7. TA data (ΔA) measured upon 370-nm excitation of methanolic solutions of **MTCA** (left), **MTCA + TFA** (middle), and **MTC8A** (right). A selection of transient spectra at early (first line: panels a, d, and g), intermediate (second line: panels b, e, and h) and later (third line: panels c, f, and i) pump-probe time delays are displayed to illustrate the spectral evolutions observed on different times (highlighted by the black arrows).

state then decays on the 12-ps time scale to form a new state, that we name **V**, characterized by an intense absorption band around 510 nm and a new, weak (negative) SE band at $\lambda > 610$ nm (see the 30-ps spectrum in panel b), while still hardly any recovery of the GSB signal occurs. The **V** state then decays with a 100-ps time scale, with the TA signal decaying completely to zero while keeping the same shape (see panel c), thus indicating the reformation of the original ground state on this time scale. The two successive SE bands observed here—at 450 nm with a 2.8-ps lifetime, and > 610 nm with a 100-ps lifetime—must be closely related to the emission spectrum displayed for the same compound in Figure S4. In the observed spectroscopic signatures of the transient **V** state, the intense (positive) 510-nm ESA band overlaps and masks the (negative, less intense) SE band which is expected to be maximum at 580 nm, according to the steady-state spectrum (see Table 2). Due to this spectral overlap and larger intensity of the ESA signal, we actually only observe the red tail of the **V** emission in the TA data. The short-lived 450-nm SE band of the initially populated S_1 state is very short-lived and its contribution to the steady-state emission spectrum—expected in its high-energy tail—is strongly quenched.

In the case of **MTC8A**, following the early, sub-ps kinetics attributed to solvation and early relaxation away from the FC region, the SE and ESA bands both redshift with a 7-ps time constant (Figure S16). Further redshift of the SE band towards 470 nm occurs together with a slight decay of the ESA band on the 30-ps time scale (Figure S16). This overall multiexponential spectral relaxation is possibly due to structural reorganization of the **MTC8A** monomer excited state, resulting in the formation of the 469-nm emissive state detected by steady-state emission (Table 2), that we named **U'**. Here, the long-lived 470-nm SE band is not hidden by any ESA overlapping and therefore in perfect agreement with the observed steady-state emission. No strong ESA band at 510 nm corresponding to the **MTCA V** state is observed here.

The **U'** lifetime is measured to be 1.0 ns (Figure S16). Unlike for **MTCA**, the TA signal of **MTC8A** does not return to zero within the maximum 5-ns time scale achievable in our TA experimental set-up, meaning that the **U'** state does not decay

back to the original ground state, but to a long-lived (≥ 5 ns) photoproduct (PP) state. Specifying the nature of this PP would require complementary investigations and is beyond the scope of this work.

Upon acidification by addition of TFA, the TA signal of **MTCA + TFA** resembles that of **MTC8A**, with no intense ESA band at 510 nm, but a multiexponential spectral relaxation, resulting in the redshift of the initial SE band towards 490 nm. The slowest component of this multiexponential relaxation is found to be 23 ps (Figure S16) and characterizes a decay of the SE and ESA bands while the GSB remains constant. The time scale is similar to that of the formation of the **U'** intermediate in **MTC8A**, we therefore also name **U'** the transient state formed on the 23-ps time scale in **MTCA** in the presence of TFA. Importantly, **MTCA** is strongly fluorescent in the presence of TFA (with $\lambda_{Em} = 509$ nm and $\Phi = 35\%$, Table 2). Therefore, we must describe the apparent decay of SE on the 23-ps time scale as the rise of an underlying ESA, leading to a net decay of the TA signal to zero at 480 nm, as a result of two significant but cancelling positive (ESA) and negative (SE) contributions. This emissive **U'** state is then observed to decay on the 2.2-ns time scale, with no further spectral modification, to reform the original ground state, as indicated by the TA signal decaying fully to zero on this time scale. The same TA data, analysis and interpretation hold for the **MFCA**, **MFC8A** and **MFCA + TFA** methanol solutions (Figures S17, S18).

All together our data are consistent with the following plausible scenario (Figure 8). In polar protic solvents, **MTCA** or **MFCA** exist in their ground states most likely as face-to-face complexes in head-to-tail relative orientation (vide supra). Light absorption of these complexes generates a first transient **U** state within the first 3 ps (vibrational relaxation), which rapidly (12 ps) leads to the **V** state characterized by a strong absorption band at 510 nm (**MTCA**, Figure 7c) or 490 nm (**MFCA**, Figure S17) and weak emission band at 580 nm (**MTCA**, Table 2) or 571 nm (**MFCA**, Table 2). Based on the relative redox potentials and accompanying the discussion above, we interpret the **V** state as resulting from an intermolecular electron transfer from the **d7A** donor part of one molecule to the **MTC** or **MFC** acceptor part of the other molecule of a ground-

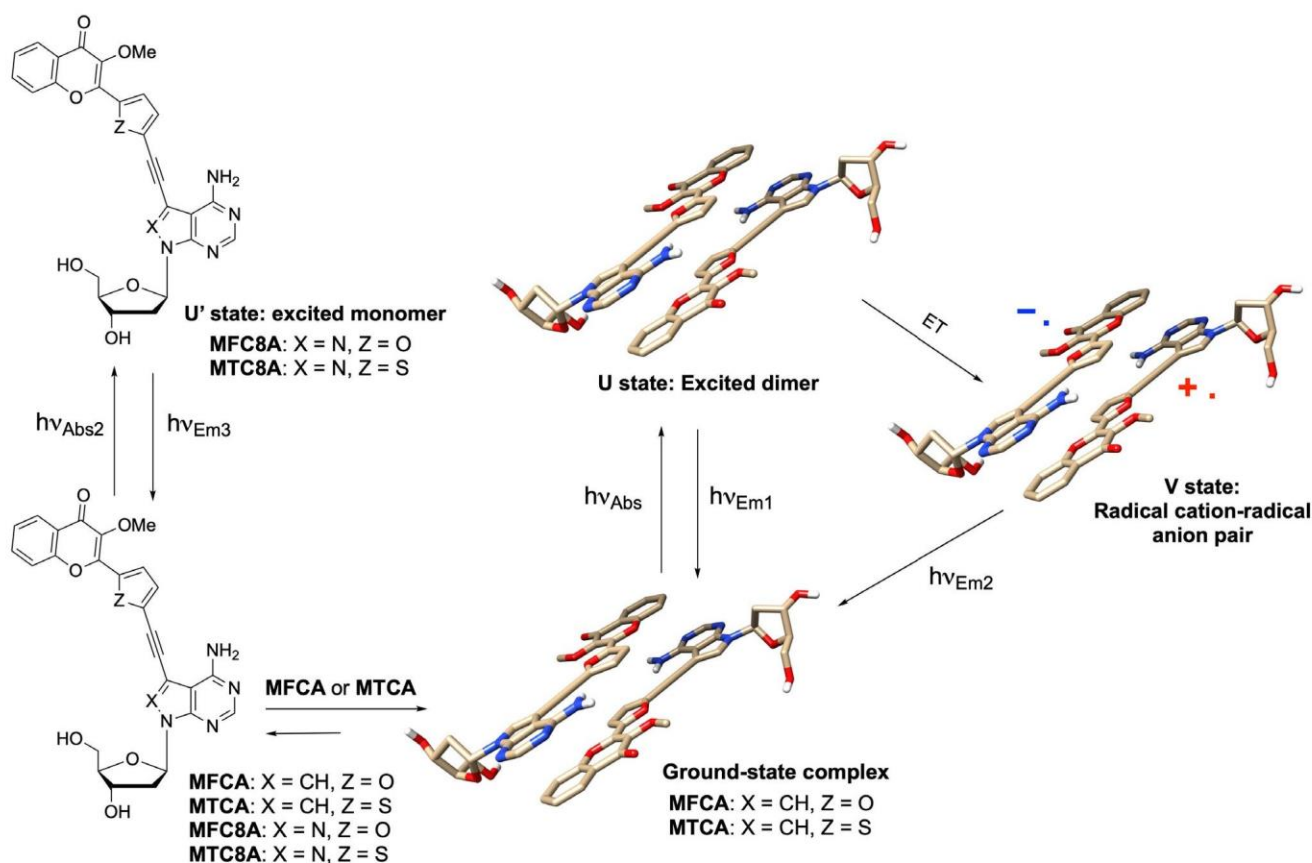


Figure 8. Schematic representation illustrating the formation of ground-state complexes favorable only for **MFCA** and **MTCA**, PET and radical ion pair products. For clarity, H-bonding with the protic solvent was not presented. The proposed representation of the dimer structure was generated from Chimera.^[47]

state preformed complex. On the 100-ps time scale, this geminate radical ion pair would recombine so as to reform to the ground state, therefore quenching the already weak 580/571 emission and explaining the very low quantum yield ($\approx 1\%$) of these species.

On the other hand, our data did not bring any evidence of the existence of ground-state complexes for **MTC8A** or **MFC8A**. After excitation of **MTC8A** or **MFC8A**, a multiexponential spectral relaxation is assigned to excited-state conformational relaxation producing the **U'** excited state characterized by an emission spectrum centered at 469/464 nm and a 1-ns-long lifetime in good agreement with a high quantum yield of these nucleoside analogues in MeOH (36–38%). Interestingly, acidified solutions of **MTCA** or **MFCA** (0.5% v/v of TFA in MeOH) show results similar to those of **MTC8A** or **MFC8A**. A strong spectral relaxation on a comparable time scale yields to a 2-ns long-lived **U'** state emitting fluorescence around 508/501 nm, with no sign of the 510 nm absorption characterizing the **V** state in the absence of TFA (Figures 7 and S17). As the introduction of an electron-withdrawing nitrogen at position 8, protonation of **d7A** reduces the electron-rich properties of the nucleobase, which should raise its oxidation potential. As a consequence, no ground-state complexation occurs, and the monomer keeps a long lifetime explaining the quantum yields (35–41%) of **MTCA** and **MFCA** upon acidification with TFA in MeOH (Figure 6).

Conclusions

In the field of fluorescent sensors based on donor-bridge-acceptor fluorophores, intramolecular PET is generally proposed to account for fluorescence quenching.^[48–50] Our data are consistent with a different scenario. **MFCA** and **MTCA** likely form head-to-tail complexes in the ground state in polar protic solvents. Upon excitation, such configuration should be favorable for intermolecular proton-coupled PET from the electron-donor nucleobase to the electron-acceptor chromone. Photoexcitation of these complexes produces a weakly emissive and short-lived state that we assigned to a radical ion pair generated by PET, responsible for low-emission quantum yields. The question of whether the monomer itself is quenched by the intramolecular PET remains in abeyance as the photophysics of these compounds was dominated by the formation of ground-state complexes even at very low concentrations. Will through-bound electron transfer be competitive in this case?^[49,50] Incorporation of **MFCA** and **MTCA** into double-stranded DNA may help to answer this question because adjacent natural nucleobases should shield the **7dA** base from complex formation while exposing the electronically coupled chromone to the major groove and water.^[51] In the light of our results, it would be interesting to know if formation of poorly emissive charge-transfer complexes is particular to our compounds or more common to donor electronically coupled to acceptor.^[52–54] Ad-

addressing this question could help reconsidering conjugates that may have been eliminated too quickly as fluorescent probes of biomolecular structures and interactions. On the other hand, protonation of the purine base or introduction of an electron-withdrawing nitrogen at position 8 of the nucleobase are expected to disfavor the putative electron transfer. Both approaches may certainly prevent the formation of such a complex and thus, make the monomers highly fluorescent. Introduction of the new conjugates into DNA and photophysical characterization of the labeled sequences are currently in progress.

Experimental Section

General methods

All reactions involving air- and water-sensitive conditions were performed in oven-dried glassware under argon by using Schlenk techniques employing a dual vacuum/argon manifold system and dry solvents. The synthetic intermediates were initially co-evaporated twice with toluene and dried in vacuo before use. All chemical reagents were purchased from commercial sources (Sigma–Aldrich, Acros, Alfa Aesar) and were used as supplied. Anhydrous solvents were obtained according to standard procedures.^[55] The reactions were monitored simultaneously by liquid chromatography–mass spectrometry (LC-MS) and thin-layer chromatography (TLC, silica gel 60 F254 plates). Compounds were visualized on TLC plates by both UV radiation (254 and 365 nm) and spraying with a staining agent (vanillin, PMA, KMnO_4 or ninhydrin) followed by subsequent warming with a heat gun. Column chromatography was performed with flash silica gel (40–63 μm) with the indicated solvent system using gradients of increasing polarity in most cases.^[56] All NMR spectra (^1H , ^{13}C , ^2D) were recorded on 200, 400 or 500 MHz Bruker Advance Spectrometers. ^1H NMR (200, 400 and 500 MHz) and $^{13}\text{C}\{^1\text{H}\}$ NMR (50, 101 and 126 MHz, recorded with complete proton decoupling) spectra were obtained with samples dissolved in CDCl_3 , CD_2Cl_2 , CD_3OD , $[\text{D}_6]\text{DMSO}$, $[\text{D}_6]\text{acetone}$, CD_3CN or $\text{C}_5\text{D}_5\text{N}$ with the residual solvent signals used as internal references: 7.26 ppm for CHCl_3 , 5.32 ppm for CDHCl_2 , 3.31 ppm for CD_2HOD , 2.50 ppm for $(\text{CD}_3)(\text{CD}_2\text{H})\text{S}(\text{O})$, 2.05 ppm for $(\text{CD}_3)(\text{CD}_2\text{H})\text{C}(\text{O})$, 1.94 ppm for CD_2HCN , 8.74 ppm for $\text{C}_5\text{D}_4\text{HN}$ regarding ^1H NMR experiments, and 77.2 ppm for CDCl_3 , 53.8 ppm for CD_2Cl_2 , 49.0 ppm for CD_3OD , 39.4 ppm for $(\text{CD}_3)_2\text{S}(\text{O})$, 30.8 ppm for $(\text{CD}_3)_2\text{C}(\text{O})$, 118.7 ppm for CD_3CN , 150.3 ppm for $\text{C}_5\text{D}_5\text{N}$ concerning ^{13}C NMR experiments.^[57,58] Chemical shifts (δ) are given in ppm to the nearest 0.01 (^1H) or 0.1 ppm (^{13}C). The coupling constants (J) are given in Hertz (Hz). The signals are reported as follows: (s=singlet, d=doublet, t=triplet, m=multiplet, br=broad). Assignments of ^1H and ^{13}C NMR signals were achieved with the help of D/H exchange, COSY, DEPT, APT, HMQC, HSQC, TOCSY, NOESY, and HMBC experiments. LC-MS spectra were recorded using an ion trap Esquire 3000 Plus mass spectrometer equipped with an electrospray ionization (ESI) source in both positive and negative modes. High-resolution mass spectrometry (HRMS) was conducted with a hybrid ion trap-Orbitrap Thermo Scientific™ mass spectrometer (combining quadrupole precursor selection with high-resolution and accurate-mass Orbitrap detection) using ESI techniques. Systematic flavone and nucleoside nomenclatures are used in the Supporting Information for the assignment of each spectrum. All solvents for absorption and fluorescence experiments were of spectroscopic grade. Absorption spectra were recorded on a Cary 100 Bio UV/Vis spectrophotometer (Varian/Agilent) using Suprasil® quartz cuvettes with 1-cm path

length. Stock solutions of dyes **MFCA**, **MTCA**, **MFC8A**, and **MTC8A** were prepared using DMSO. The samples used for spectroscopic measurements contained $\approx 0.2\%$ v/v of solvents of the stock solution. Fluorescence spectra were recorded on a FluoroMax 4.0 spectrofluorometer (Jobin Yvon, Horiba) with a thermostatically controlled cell compartment at $20 \pm 0.5^\circ\text{C}$ with slits open to 2 nm and were corrected for Raman scattering, lamp fluctuations and instrumental wavelength-dependent bias. Excitation wavelengths were set at the absorption maxima except when mentioned in the corresponding experiments. Redox potentials were recorded on EG&G Princeton Applied Research Model 273A. A three-electrode cell system was used for the measurements. The working, reference, and auxiliary electrodes were glassy carbon, Ag/AgCl, and platinum foil, respectively. Concerning the transient absorption (TA) experiments, the pump-probe setup for TA spectroscopy and data analysis methods have already been described elsewhere.^[33,59–61] In brief, a 40-fs pulses of a Ti: sapphire regenerative amplifier (5 kHz) is used to pump a commercial optical parametric amplifier (TOPAS; Light Conversion) followed by 4th harmonic generation to produce pulses at 370 nm. The probe white-light continuum is generated in a 2-mm thick CaF_2 crystal. The polarization of the pump beam is set at the magic angle (54.7°) with respect to that of the probe. The samples were circulated through a 0.5-mm-path-length, fused silica, flow cell using a peristaltic pump. Data sets were acquired displaying the spectrally resolved (350 to 700 nm) pump-induced absorbance change ΔA as a function of pump-probe delay. All TA data presented here are post-processed in order to (i) subtract the “solvent” signal around time-zero resulting from the coherent interaction of pump and probe laser fields, and (ii) compensate for the group velocity dispersion in the probe beam—independently determined from the pure solvent signal—so as to define time-zero accurately (within ≈ 20 fs) at all wavelengths. Singular value decomposition (SVD) was used for data reduction and noise filtering. Global fitting of the 5 dominant singular traces was performed. The fitting function was a sum of exponential decaying functions convolved with a normalized Gaussian curve of standard deviation σ standing for the temporal instrument response function (IRF). The residuals of the fits of the 5 dominating singular transients were structureless, and of amplitude similar to or larger than that of the 6th and 7th singular transients, justifying that only the first five singular transients were considered as significant in this global analysis. The result of the global fitting was analyzed by computing and displaying the Decay-Associated Spectra (DAS). Each decay time constant is associated to a DAS representing the spectral dependence of the prefactor of this decay component in the original 2D data set. The DAS reveal the spectral evolution occurring within their associated time constant, along the course of the molecule photoreaction. Supplementary data associated with this article, including the experimental protocols of intermediates and target compounds, some ^1H , ^{13}C , ^1H – ^1H COSY, ^1H – ^1H NOESY, ^1H – ^{13}C HSQC, and ^1H – ^{13}C HMBC NMR spectra of derivatives previously mentioned as well as additional photophysical characterization, can be consulted in the Supporting Information.

Acknowledgements

We thank Dr. Sandra Olivero for her support to cyclic voltammetry. We are grateful for the ANR (UCAJEDI project: ANR-15-IDEX-01; ANR-12-BS08-0003-02) and the French Government concerning the PhD grants of H.-N.L., S.V. and G.B., respectively. This research program was financially supported by the ANR

(ANR-12-BS08-0003-02, ANR-15-CE11-0006 "PICO2", ANR-11-LABX-0058_NIE) and PACA region (DNAfix-2014-02862).

Conflict of interest

The authors declare no conflict of interest.

Keywords: deoxyadenosine probes · fluorescence · ground-state complexes · photoinduced electron transfer · push–pull dyes

- [1] K. Nakatani, Y. Tor in *Modified nucleic acids, nucleic acids and molecular biology series, Vol. 31* (Eds.: K. Nakatani, Y. Tor), Springer International Publishing, Cham **2016**, p. 276.
- [2] M. S. Gonçalves, *Angew. Chem. Int. Ed.* **2017**, *56*, 4655; *Angew. Chem.* **2017**, *129*, 4727.
- [3] W. Xu, K. M. Chan, E. T. Kool, *Nat. Chem.* **2017**, *9*, 1043–1055.
- [4] S. De Ornellas, J. M. Slattery, R. M. Edkins, A. Beeby, C. G. Baumann, I. J. S. Fairlamb, *Org. Biomol. Chem.* **2015**, *13*, 68–72.
- [5] H. Cahová, R. Pohl, L. Bednářová, K. Nováková, J. Cvačka, M. Hocek, *Org. Biomol. Chem.* **2008**, *6*, 3657–4.
- [6] L. M. Wilhelmsson, *Q. Rev. Biophys.* **2010**, *43*, 159–183.
- [7] A. M. Agafontsev, A. Ravi, T. A. Shumilova, A. S. Oshchepkov, E. A. Kataev, *Chem. Eur. J.* **2019**, *25*, 2684–2694.
- [8] A. Dumas, G. Mata, N. W. Luedtke in *Fluorescent Analogues of Biomolecular Building Blocks: Design and Applications*. Hoboken, Wiley, Hoboken, **2016**, pp. 242–275.
- [9] B. Y. Michel, D. Dziuba, R. Benhida, A. P. Demchenko, A. Burger, *Front. Chem.* **2020**, *8*, 112.
- [10] V. G. Pivovarenko, O. Bugera, N. Humbert, A. S. Klymchenko, Y. Mély, *Chem. Eur. J.* **2017**, *23*, 11927–11934.
- [11] N. P. F. Barthes, I. A. Karpenko, D. Dziuba, M. Spadafora, J. Auffret, A. P. Demchenko, Y. Mély, R. Benhida, B. Y. Michel, A. Burger, *RSC Adv.* **2015**, *5*, 33536–33545.
- [12] N. P. F. Barthes, K. Gavvala, D. Dziuba, D. Bonhomme, I. A. Karpenko, A. S. Dabert-Gay, D. Debayle, A. P. Demchenko, R. Benhida, B. Y. Michel, A. Burger, *J. Mater. Chem. C* **2016**, *4*, 3010–3017.
- [13] H.-N. Le, C. Zilio, G. Barnoin, N. P. F. Barthes, J.-M. Guignonis, N. Martinet, B. Y. Michel, A. Burger, *Dyes Pigm.* **2019**, *170*, 107553.
- [14] D. R. Weinberg, C. J. Gagliardi, J. F. Hull, C. F. Murphy, C. A. Kent, B. C. Westlake, A. Paul, D. H. Ess, D. G. McCafferty, T. J. Meyer, *Chem. Rev.* **2012**, *112*, 4016–4093.
- [15] J. R. Lakowicz in *Principles of fluorescence spectroscopy*, 3rd ed, Springer, New York, **2006**, p. 954.
- [16] C. A. M. Seidel, A. Schulz, M. H. M. Sauer, *J. Phys. Chem.* **1996**, *100*, 5541–5553.
- [17] F. Seela, S. S. Pujari, *Bioconjugate Chem.* **2010**, *21*, 1629–1641.
- [18] T. Aso, K. Saito, A. Suzuki, Y. Saito, *Org. Biomol. Chem.* **2015**, *13*, 10540–10547.
- [19] D. Dziuba, I. A. Karpenko, N. P. F. Barthes, B. Y. Michel, A. S. Klymchenko, R. Benhida, A. P. Demchenko, Y. Mély, A. Burger, *Chem. Eur. J.* **2014**, *20*, 1998–2009.
- [20] F. Seela, M. Zulauf, *Synthesis* **1996**, 726–730.
- [21] M. Torimura, S. Kurata, K. Yamada, T. Yokomaku, Y. Kamagata, T. Kanagawa, R. Kurane, *Anal. Sci.* **2001**, *17*, 155–160.
- [22] D. Rehm, A. Weller, *Isr. J. Chem.* **1970**, *8*, 259–271.
- [23] B. Calitree, D. J. Donnelly, J. J. Holt, M. K. Gannon, C. L. Nygren, D. K. Sukumaran, J. Autschbach, M. R. Detty, *Organometallics* **2007**, *26*, 6248–6257.
- [24] Y. Koide, Y. Urano, K. Hanaoka, T. Terai, T. Nagano, *ACS Chem. Biol.* **2011**, *6*, 600–608.
- [25] R. A. Marcus, *J. Chem. Phys.* **1956**, *24*, 966–978.
- [26] R. A. Marcus, *Can. J. Chem.* **1959**, *37*, 155–163.
- [27] N. J. Turro, V. Ramamurthy, J. C. Scaiano, *Principles of Molecular Photochemistry: an Introduction*, University Science Books, Philadelphia, **2009**.
- [28] C. Reichardt, *Chem. Rev.* **1994**, *94*, 2319–2358.
- [29] J. Catalán, *J. Phys. Chem. B* **2009**, *113*, 5951–5960.
- [30] S. M. Ormson, R. G. Brown, F. Vollmer, W. Rettig, *J. Photochem. Photobiol. A* **1994**, *81*, 65–72.
- [31] V. V. Shynkar, A. S. Klymchenko, E. Piémont, A. P. Demchenko, Y. Mély, *J. Phys. Chem. A* **2004**, *108*, 8151–8159.
- [32] A. Sougnabé, D. Lissouck, F. Fontaine-Vive, M. Nsangou, Y. Mély, A. Burger, C. A. Kenfack, *RSC Adv.* **2020**, *10*, 7349–7359.
- [33] A. I. Skilitsi, D. Agathangelou, I. Shulov, J. Conyard, S. Haacke, Y. Mély, A. Klymchenko, J. Léonard, *Phys. Chem. Chem. Phys.* **2018**, *20*, 7885–7895.
- [34] M. H. V. Huynh, T. J. Meyer, *Chem. Rev.* **2007**, *107*, 5004–5064.
- [35] B. Ma, P. I. Djurovich, M. E. Thompson, *Coord. Chem. Rev.* **2005**, *249*, 1501–1510.
- [36] P.-O. Gendron, F. Avaltroni, K. J. Wilkinson, *J. Fluoresc.* **2008**, *18*, 1093–1101.
- [37] T. Dertinger, V. Pacheco, I. von der Hocht, R. Hartmann, I. Gregor, J. Enderlein, *ChemPhysChem* **2007**, *8*, 433–443.
- [38] I. R. Gould, R. H. Young, R. E. Moody, S. Farid, *J. Phys. Chem.* **1991**, *95*, 2068–2080.
- [39] I. R. Gould, R. H. Young, L. J. Mueller, S. Farid, *J. Am. Chem. Soc.* **1994**, *116*, 8176–8187.
- [40] I. R. Gould, D. Noukakis, L. Gomez-Jahn, R. H. Young, J. L. Goodman, S. Farid, *Chem. Phys.* **1993**, *176*, 439–456.
- [41] K. K. Mentel, R. M. D. Nunes, C. Serpa, L. G. Arnaut, *J. Phys. Chem. B* **2015**, *119*, 7571–7578.
- [42] J. Eriksen, C. S. Foote, *J. Phys. Chem.* **1978**, *82*, 2659–2662.
- [43] A. R. Melnikov, E. V. Kalneus, V. V. Korolev, I. G. Dranov, A. I. Kruppa, D. V. Stass, *Photochem. Photobiol. Sci.* **2014**, *13*, 1169–1179.
- [44] J. Qi, D. Liu, X. Liu, S. Guan, F. Shi, H. Chang, H. He, G. Yang, *Anal. Chem.* **2015**, *87*, 5897–5904.
- [45] S. Chatterjee, W. Pathmasiri, O. Plashkevych, D. Honcharenko, O. P. Varghese, M. Maiti, J. Chattopadhyaya, *Org. Biomol. Chem.* **2006**, *4*, 1675–1686.
- [46] M. L. Horng, J. A. Gardecki, A. Papazyan, M. Maroncelli, *J. Phys. Chem.* **1995**, *99*, 17311–17337.
- [47] E. F. Pettersen, T. D. Goddard, C. C. Huang, G. S. Couch, D. M. Greenblatt, E. C. Meng, T. E. Ferrin, *J. Comput. Chem.* **2004**, *25*, 1605–1612.
- [48] D. Escudero, *Acc. Chem. Res.* **2016**, *49*, 1816–1824.
- [49] A. C. Benniston, A. Harriman, *Chem. Soc. Rev.* **2006**, *35*, 169–179.
- [50] G. L. Closs, J. R. Miller, *Science* **1988**, *240*, 440–447.
- [51] F. Seela, H. Xiong, P. Leonard, S. Budow, *Org. Biomol. Chem.* **2009**, *7*, 1374–1387.
- [52] P. Trojanowski, J. Plötner, C. Grünwald, F. F. Graupner, C. Slavov, A. J. Reuss, M. Braun, J. W. Engels, J. Wachtveitl, *Phys. Chem. Chem. Phys.* **2014**, *16*, 13875–13888.
- [53] Y. Saito, R. H. E. Hudson, *J. Photochem. Photobiol. C* **2018**, *36*, 48–73.
- [54] P. Leonard, D. Kondhare, X. Jentgens, C. Daniliuc, F. Seela, *J. Org. Chem.* **2019**, *84*, 13313–13328.
- [55] W. L. F. Armarego, C. L. L. Chai in *Purification of Laboratory Chemicals*, 7th ed., Butterworth-Heinemann, Oxford, **2012**, p. 1024.
- [56] W. C. Still, M. Kahn, A. Mitra, *J. Org. Chem.* **1978**, *43*, 2923–2925.
- [57] H. E. Gottlieb, V. Kotlyar, A. Nudelman, *J. Org. Chem.* **1997**, *62*, 7512–7515.
- [58] G. R. Fulmer, A. J. M. Miller, N. H. Sherden, H. E. Gottlieb, A. Nudelman, B. M. Stoltz, J. E. Bercaw, K. I. Goldberg, *Organometallics* **2010**, *29*, 2176–2179.
- [59] J. Briand, O. Bräm, J. Réhault, J. Léonard, A. Cannizzo, M. Chergui, V. Zanirato, M. Olivucci, J. Helbing, S. Haacke, *Phys. Chem. Chem. Phys.* **2010**, *12*, 3178–3187.
- [60] C. García-Iriepa, M. Gueye, J. Léonard, D. Martínez-López, P. J. Campos, L. M. Frutos, D. Sampedro, M. Marazzi, *Phys. Chem. Chem. Phys.* **2016**, *18*, 6742–6753.
- [61] M. Paolino, M. Gueye, E. Pieri, M. Manathunga, S. Fusi, A. Cappelli, L. Latzerini, D. Pannacci, M. Filatov, J. Léonard, M. Olivucci, *J. Am. Chem. Soc.* **2016**, *138*, 9807–9825.

Manuscript received: July 23, 2020

Accepted manuscript online: August 6, 2020

Version of record online: December 7, 2020

Références bibliographiques

1. Demchenko, A. P. *Introduction to Fluorescence Sensing*. (Springer International Publishing, 2015). doi:10.1007/978-3-319-20780-3.
2. Van De Linde, S. & Sauer, M. How to switch a fluorophore: From undesired blinking to controlled photoswitching. *Chem. Soc. Rev.* **43**, 1076–1087 (2014).
3. Klymchenko, A. S. Solvatochromic and Fluorogenic Dyes as Environment-Sensitive Probes: Design and Biological Applications. *Acc. Chem. Res.* **50**, 366–375 (2017).
4. Bureš, F. Fundamental aspects of property tuning in push–pull molecules. *RSC Adv.* **4**, 58826–58851 (2014).
5. Demchenko, A. P., Mély, Y., Duportail, G. & Klymchenko, A. S. Monitoring Biophysical Properties of Lipid Membranes by Environment-Sensitive Fluorescent Probes. *Biophys. J.* **96**, 3461–3470 (2009).
6. Grabowski, Z. R., Rotkiewicz, K. & Rettig, W. Structural Changes Accompanying Intramolecular Electron Transfer: Focus on Twisted Intramolecular Charge-Transfer States and Structures. *Chem. Rev.* **103**, 3899–4032 (2003).
7. Sasaki, S., Drummen, G. P. C. & Konishi, G. Recent advances in twisted intramolecular charge transfer (TICT) fluorescence and related phenomena in materials chemistry. *J. Mater. Chem. C* **4**, 2731–2743 (2016).
8. Le, H. *et al.* Control of Intermolecular Photoinduced Electron Transfer in Deoxyadenosine-Based Fluorescent Probes. *Chem. – A Eur. J.* **27**, 1364–1373 (2021).
9. Klymchenko, A. S. & Mely, Y. Fluorescent environment-sensitive dyes as reporters of biomolecular interactions. in *Progress in Molecular Biology and Translational Science* vol. 113 35–58 (Elsevier Inc., 2013).
10. Dziuba, D. *et al.* A Universal Nucleoside with Strong Two-Band Switchable Fluorescence and Sensitivity to the Environment for Investigating DNA Interactions. *J. Am. Chem. Soc.* **134**, 10209–10213 (2012).
11. Enander, K. *et al.* A peptide-based, ratiometric biosensor construct for direct fluorescence detection of a protein analyte. *Bioconjug. Chem.* **19**, 1864–1870 (2008).
12. Postupalenko, V. Y. *et al.* Dual-fluorescence l -amino acid reports insertion and orientation of melittin peptide in cell membranes. *Bioconjug. Chem.* **24**, 1998–2007 (2013).
13. Sedgwick, A. C. *et al.* Excited-state intramolecular proton-transfer (ESIPT) based fluorescence sensors and imaging agents. *Chem. Soc. Rev.* **47**, 8842–8880 (2018).
14. Haidekker, M. A. & Theodorakis, E. A. Molecular rotors - Fluorescent biosensors for viscosity

- and flow. *Org. Biomol. Chem.* **5**, 1669–1678 (2007).
15. Haidekker, M. A. & Theodorakis, E. A. Environment-sensitive behavior of fluorescent molecular rotors. *J. Biol. Eng.* **4**, 1–14 (2010).
 16. Sutharsan, J. *et al.* Rational design of amyloid binding agents based on the molecular rotor motif. *ChemMedChem* **5**, 56–60 (2010).
 17. Amdursky, N., Erez, Y. & Huppert, D. Molecular rotors: What lies behind the high sensitivity of the thioflavin-T fluorescent marker. *Acc. Chem. Res.* **45**, 1548–1557 (2012).
 18. Sunahara, H., Urano, Y., Kojima, H. & Nagano, T. Design and synthesis of a library of BODIPY-based environmental polarity sensors utilizing photoinduced electron-transfer-controlled fluorescence ON/OFF switching. *J. Am. Chem. Soc.* **129**, 5597–5604 (2007).
 19. Kuimova, M. K., Yahioğlu, G., Levitt, J. A. & Suhling, K. Molecular rotor measures viscosity of live cells via fluorescence lifetime imaging. *J. Am. Chem. Soc.* **130**, 6672–6673 (2008).
 20. Lukinavičius, G. *et al.* A near-infrared fluorophore for live-cell super-resolution microscopy of cellular proteins. *Nat. Chem.* **5**, 132–139 (2013).
 21. Lukinavičius, G. *et al.* Fluorogenic Probes for Multicolor Imaging in Living Cells. *J. Am. Chem. Soc.* **138**, 9365–9368 (2016).
 22. Uno, S. N. *et al.* A spontaneously blinking fluorophore based on intramolecular spirocyclization for live-cell super-resolution imaging. *Nat. Chem.* **6**, 681–689 (2014).
 23. Han, J. & Burgess, K. Fluorescent indicators for intracellular pH. *Chem. Rev.* **110**, 2709–2728 (2010).
 24. Mizusawa, K., Takaoka, Y. & Hamachi, I. Specific cell surface protein imaging by extended self-assembling fluorescent turn-on nanoprobe. *J. Am. Chem. Soc.* **134**, 13386–13395 (2012).
 25. Zong, L. *et al.* From ACQ to AIE: The suppression of the strong π - π Interaction of naphthalene diimide derivatives through the adjustment of their flexible chains. *Chem. Commun.* **52**, 11496–11499 (2016).
 26. Hestand, N. J. & Spano, F. C. Expanded Theory of H- and J-Molecular Aggregates: The Effects of Vibronic Coupling and Intermolecular Charge Transfer. *Chem. Rev.* **118**, 7069–7163 (2018).
 27. Würthner, F., Kaiser, T. E. & Saha-Möller, C. R. J-Aggregates: From Serendipitous Discovery to Supramolecular Engineering of Functional Dye Materials. *Angew. Chemie Int. Ed.* **50**, 3376–3410 (2011).
 28. Klymchenko, A. Emerging field of self-assembled fluorescent organic dye nanoparticles. *J.*

- Nanosci. Lett* **3**, 21 (2013).
29. Würthner, F. Aggregation-Induced Emission (AIE): A Historical Perspective. *Angew. Chemie - Int. Ed.* **59**, 14192–14196 (2020).
 30. Peng, Q. & Shuai, Z. Molecular mechanism of aggregation-induced emission. *Aggregate* **2**, 1–20 (2021).
 31. Qian, J. & Tang, B. Z. AIE Luminogens for Bioimaging and Theranostics: From Organelles to Animals. *Chem* **3**, 56–91 (2017).
 32. Suzuki, S. *et al.* Principles of Aggregation-Induced Emission: Design of Deactivation Pathways for Advanced AIEgens and Applications. *Angew. Chemie* **132**, 9940–9951 (2020).
 33. Leung, N. L. C. *et al.* Restriction of Intramolecular Motions: The General Mechanism behind Aggregation-Induced Emission. *Chem. - A Eur. J.* **20**, 15349–15353 (2014).
 34. Kwok, R. T. K., Leung, C. W. T., Lam, J. W. Y. & Tang, B. Z. Biosensing by luminogens with aggregation-induced emission characteristics. *Chem. Soc. Rev.* **44**, 4228–4238 (2015).
 35. Kumpulainen, T., Lang, B., Rosspeintner, A. & Vauthey, E. Ultrafast Elementary Photochemical Processes of Organic Molecules in Liquid Solution. *Chem. Rev.* **117**, 10826–10939 (2017).
 36. Xu, W., Chan, K. M. & Kool, E. T. Fluorescent nucleobases as tools for studying DNA and RNA. *Nat. Chem.* **9**, 1043–1055 (2017).
 37. Michel, B. Y., Dziuba, D., Benhida, R., Demchenko, A. P. & Burger, A. Probing of Nucleic Acid Structures, Dynamics, and Interactions With Environment-Sensitive Fluorescent Labels. *Front. Chem.* **8**, (2020).
 38. Crespo-Hernández, C. E., Close, D. M., Gorb, L. & Leszczynski, J. Determination of redox potentials for the Watson-crick base pairs, DNA nucleosides, and relevant nucleoside analogues. *J. Phys. Chem. B* **111**, 5386–5395 (2007).
 39. Koide, Y., Urano, Y., Hanaoka, K., Terai, T. & Nagano, T. Evolution of group 14 rhodamines as platforms for near-infrared fluorescence probes utilizing photoinduced electron transfer. *ACS Chem. Biol.* **6**, 600–608 (2011).
 40. Greene, L. E., Lincoln, R. & Cosa, G. Tuning Photoinduced Electron Transfer Efficiency of Fluorogenic BODIPY- α -Tocopherol Analogues. *Photochem. Photobiol.* **95**, 192–201 (2019).
 41. Bordello, J. *et al.* Fluorescence-Labeled Bis-benzamidines as Fluorogenic DNA Minor-Groove Binders: Photophysics and Binding Dynamics. *Chem. - A Eur. J.* **21**, 1609–1619 (2015).

42. van der Meer, B. W. Förster Theory. in *FRET – Förster Resonance Energy Transfer* 23–62 (Wiley, 2013). doi:10.1002/9783527656028.ch03.
43. Sahoo, H. Förster resonance energy transfer - A spectroscopic nanoruler: Principle and applications. *J. Photochem. Photobiol. C Photochem. Rev.* **12**, 20–30 (2011).
44. Bajar, B. T., Wang, E. S., Zhang, S., Lin, M. Z. & Chu, J. A guide to fluorescent protein FRET pairs. *Sensors (Switzerland)* **16**, 1–24 (2016).
45. Kang, J. S., Piszczek, G. & Lakowicz, J. R. Enhanced Emission Induced by FRET from a Long-Lifetime, Low Quantum Yield Donor to a Long-Wavelength, High Quantum Yield Acceptor. *J. Fluoresc.* **12**, 97–103 (2002).
46. Barnoin, G. *et al.* Intermolecular dark resonance energy transfer (DRET): upgrading fluorogenic DNA sensing. *Nucleic Acids Res.* **49**, e72–e72 (2021).
47. WATSON, J. D. & CRICK, F. H. C. Molecular Structure of Nucleic Acids: A Structure for Deoxyribose Nucleic Acid. *Nature* **171**, 737–738 (1953).
48. Sinden, R. R., Pearson, C. E., Potaman, V. N. & Ussery, D. W. DNA: Structure and function. in *Advances in Genome Biology* vol. 5 1–141 (1998).
49. Victor, J. La structure de l'ADN en double hélice. 0–12 <http://journals.openedition.org/bibnum/503> (2012).
50. Saenger, W. *Principles of Nucleic Acid Structure. Principles of Nucleic Acid Structure* (Springer New York, 1984). doi:10.1007/978-1-4612-5190-3.
51. García-ramos, J. C. *et al.* Metal-Based Drug-DNA Interactions. *J. Mex. Chem. Soc.* **57**, 245–259 (2013).
52. Potaman, V. N. & Sinden, R. R. DNA. in *DNA: Conformation and Transcription* 3–17 (Springer US, 2005). doi:10.1007/0-387-29148-2_1.
53. Kaushik, M. *et al.* A bouquet of DNA structures: Emerging diversity. *Biochem. Biophys. Reports* **5**, 388–395 (2016).
54. Wright, E. P. *et al.* Mitoxantrone and analogues bind and stabilize i-motif forming DNA sequences. *Sci. Rep.* **6**, 4–10 (2016).
55. Fedoroff, O. Y., Rangan, A., Chemeris, V. V. & Hurley, L. H. Cationic porphyrins promote the formation of i-motif DNA and bind peripherally by a nonintercalative mechanism. *Biochemistry* **39**, 15083–15090 (2000).
56. Robidoux, S., Klinck, R., Gehring, K. & Damha, M. J. Association of branched oligonucleotides into the i-motif. *J. Biomol. Struct. Dyn.* **15**, 517–527 (1997).

57. Debnath, M., Fatma, K. & Dash, J. Chemical Regulation of DNA i-Motifs for Nanobiotechnology and Therapeutics. *Angew. Chemie* **131**, 2968–2983 (2019).
58. Davis, J. T. G-Quartets 40 Years Later: From 5'-GMP to Molecular Biology and Supramolecular Chemistry. *Angew. Chemie - Int. Ed.* **43**, 668–698 (2004).
59. Huppert, J. L. Structure, location and interactions of G-quadruplexes. *FEBS J.* **277**, 3452–3458 (2010).
60. Choi, J. & Majima, T. Conformational changes of non-B DNA. *Chem. Soc. Rev.* **40**, 5893–5909 (2011).
61. Brooks, T. A., Kendrick, S. & Hurley, L. Making sense of G-quadruplex and i-motif functions in oncogene promoters. *FEBS J.* **277**, 3459–3469 (2010).
62. Brooks, T. A. & Hurley, L. H. The role of supercoiling in transcriptional control of MYC and its importance in molecular therapeutics. *Nat. Rev. Cancer* **9**, 849–861 (2009).
63. Hanahan, D. & Weinberg, R. A. The Hallmarks of Cancer. *Cell* **100**, 57–70 (2000).
64. Manna, S. & Srivatsan, S. G. Fluorescence-based tools to probe G-quadruplexes in cell-free and cellular environments. *RSC Adv.* **8**, 25673–25694 (2018).
65. Lepecq, J. B. & Paoletti, C. A fluorescent complex between ethidium bromide and nucleic acids. Physical-Chemical characterization. *J. Mol. Biol.* **27**, 87–106 (1967).
66. Larsson, A., Carlsson, C., Jonsson, M. & Albinsson, B. Characterization of the binding of the fluorescent dyes YO and YOYO to DNA by polarized light spectroscopy. *Doktorsavhandlingar vid Chalmers Tek. Högsk.* 8459–8465 (1997).
67. Fürstenberg, A. *et al.* Ultrafast excited-state dynamics of DNA fluorescent intercalators: New insight into the fluorescence enhancement mechanism. *J. Am. Chem. Soc.* **128**, 7661–7669 (2006).
68. Biancardi, A., Biver, T., Secco, F. & Mennucci, B. An investigation of the photophysical properties of minor groove bound and intercalated DAPI through quantum-mechanical and spectroscopic tools. *Phys. Chem. Chem. Phys.* **15**, 4596 (2013).
69. Kapuscinski, J. DAPI: a DNA-Specific Fluorescent Probe. *Biotech. Histochem.* **70**, 220–233 (1995).
70. Suseela, Y. V., Narayanaswamy, N., Pratihari, S. & Govindaraju, T. Far-red fluorescent probes for canonical and non-canonical nucleic acid structures: Current progress and future implications. *Chem. Soc. Rev.* **47**, 1098–1131 (2018).
71. Köhler, O. *et al.* Forced intercalation as a tool in gene diagnostics and in studying DNA–

- protein interactions. *Pure Appl. Chem.* **77**, 327–338 (2005).
72. Ottaviani, M. F. *et al.* Nitroxide-labeled ruthenium(II)-polypyridyl complexes as EPR probes to study organized systems. 2. Combined photophysical and EPR investigations of B-DNA. *J. Am. Chem. Soc.* **114**, 8946–8952 (1992).
 73. Ishiguro, T. *et al.* Fluorescence Detection of Specific Sequence of Nucleic Acids by Oxazole Yellow-Linked Oligonucleotides. Homogeneous Quantitative Monitoring of In Vitro Transcription. *Nucleic Acids Res.* **24**, 4992–4997 (1996).
 74. Dziuba, D., Pohl, R. & Hocek, M. Bodipy-Labeled Nucleoside Triphosphates for Polymerase Synthesis of Fluorescent DNA. *Bioconjug. Chem.* **25**, 1984–1995 (2014).
 75. Stengel, G., Urban, M., Purse, B. W. & Kuchta, R. D. Incorporation of the Fluorescent Ribonucleotide Analogue tCTP by T7 RNA Polymerase. *Anal. Chem.* **82**, 1082–1089 (2010).
 76. Beaucage, S. L. & Caruthers, M. H. Deoxynucleoside phosphoramidites—A new class of key intermediates for deoxypolynucleotide synthesis. *Tetrahedron Lett.* **22**, 1859–1862 (1981).
 77. McBride, L. J. & Caruthers, M. H. An investigation of several deoxynucleoside phosphoramidites useful for synthesizing deoxyoligonucleotides. *Tetrahedron Lett.* **24**, 245–248 (1983).
 78. Link Technologies. *Guidebook for the Synthesis of Oligonucleotides*. (2016).
 79. Fantoni, N. Z., El-Sagheer, A. H. & Brown, T. A Hitchhiker’s Guide to Click-Chemistry with Nucleic Acids. *Chem. Rev.* **121**, 7122–7154 (2021).
 80. Weisbrod, S. H. & Marx, A. Novel strategies for the site-specific covalent labelling of nucleic acids. *Chem. Commun.* 5675 (2008) doi:10.1039/b809528k.
 81. Oliveira, B. L., Guo, Z. & Bernardes, G. J. L. Inverse electron demand Diels–Alder reactions in chemical biology. *Chem. Soc. Rev.* **46**, 4895–4950 (2017).
 82. Diels, O. & Alder, K. Synthesen in der hydroaromatischen Reihe. *Justus Liebig’s Ann. der Chemie* **460**, 98–122 (1928).
 83. Staudinger, H. & Hauser, E. Über neue organische Phosphorverbindungen IV Phosphinimine. *Helv. Chim. Acta* **2**, 635–646 (1919).
 84. Prescher, J. A. & Bertozzi, C. R. Chemistry in living systems. *Nat. Chem. Biol.* **1**, 13–21 (2005).
 85. Sletten, E. M. & Bertozzi, C. R. Bioorthogonal Chemistry: Fishing for Selectivity in a Sea of Functionality. *Angew. Chemie Int. Ed.* **48**, 6974–6998 (2009).
 86. Okamoto, A., Taiji, T., Tainaka, K. & Saito, I. Oligonucleotides containing 7-vinyl-7-

- deazaguanine as a facile strategy for expanding the functional diversity of DNA. *Bioorganic Med. Chem. Lett.* **12**, 1895–1896 (2002).
87. Weisbrod, S. H., Baccaro, A. & Marx, A. Site-Specific DNA Labeling by Staudinger Ligation. in *A Law Unto Herself* vol. 751 195–207 (2011).
 88. Kolb, H. C., Finn, M. G. & Sharpless, K. B. Click Chemistry: Diverse Chemical Function from a Few Good Reactions. *Angew. Chemie Int. Ed.* **40**, 2004–2021 (2001).
 89. Huisgen, R. 1,3-Dipolar Cycloadditions. Past and Future. *Angew. Chemie Int. Ed. English* **2**, 565–598 (1963).
 90. Agard, N. J., Prescher, J. A. & Bertozzi, C. R. A strain-promoted [3 + 2] azide-alkyne cycloaddition for covalent modification of biomolecules in living systems. *J. Am. Chem. Soc.* **126**, 15046–15047 (2004).
 91. Laughlin, S. T., Baskin, J. M., Amacher, S. L. & Bertozzi, C. R. In Vivo Imaging of Membrane-Associated Glycans in Developing Zebrafish. *Science* **320**, 664–667 (2008).
 92. Porte, K., Riomet, M., Figliola, C., Audisio, D. & Taran, F. Click and Bio-Orthogonal Reactions with Mesoionic Compounds. *Chem. Rev.* **121**, 6718–6743 (2021).
 93. Devaraj, N. K., Weissleder, R. & Hilderbrand, S. A. Tetrazine-Based Cycloadditions: Application to Pretargeted Live Cell Imaging. *Bioconjug. Chem.* **19**, 2297–2299 (2008).
 94. Blackman, M. L., Royzen, M. & Fox, J. M. Tetrazine Ligation: Fast Bioconjugation Based on Inverse-Electron-Demand Diels–Alder Reactivity. *J. Am. Chem. Soc.* **130**, 13518–13519 (2008).
 95. Song, W., Wang, Y., Qu, J. & Lin, Q. Selective Functionalization of a Genetically Encoded Alkene-Containing Protein via “Photoclick Chemistry” in Bacterial Cells. *J. Am. Chem. Soc.* **130**, 9654–9655 (2008).
 96. Shelbourne, M., Chen, X., Brown, T. & El-Sagheer, A. H. Fast copper-free click DNA ligation by the ring-strain promoted alkyne-azide cycloaddition reaction. *Chem. Commun.* **47**, 6257 (2011).
 97. Meldal, M. & Tornøe, C. W. Cu-Catalyzed Azide–Alkyne Cycloaddition. *Chem. Rev.* **108**, 2952–3015 (2008).
 98. Besanceney-Webler, C. *et al.* Increasing the Efficacy of Bioorthogonal Click Reactions for Bioconjugation: A Comparative Study. *Angew. Chemie* **123**, 8201–8206 (2011).
 99. Presolski, S. I., Hong, V. P. & Finn, M. G. Copper-Catalyzed Azide–Alkyne Click Chemistry for Bioconjugation. *Curr. Protoc. Chem. Biol.* **3**, 153–162 (2011).

100. Presolski, S. I., Hong, V., Cho, S. H. & Finn, M. G. Tailored ligand acceleration of the copper-catalyzed azide-alkyne cycloaddition reaction: Practical and mechanistic implications. *J. Am. Chem. Soc.* **132**, 14570–14576 (2010).
101. Fomich, M. A. *et al.* Azide Phosphoramidite in Direct Synthesis of Azide-Modified Oligonucleotides. *Org. Lett.* **16**, 4590–4593 (2014).
102. Markey, F. B., Parashar, V. & Batish, M. Methods for spatial and temporal imaging of the different steps involved in RNA processing at single-molecule resolution. *Wiley Interdiscip. Rev. RNA* **12**, 1–20 (2021).
103. Rentmeister, A., Mannack, L. V. J. C. & Eising, S. Current techniques for visualizing RNA in cells. *F1000Research* **5**, 1–8 (2016).
104. Driever, W. & Nüsslein-Volhard, C. The bicoid protein determines position in the *Drosophila* embryo in a concentration-dependent manner. *Cell* **54**, 95–104 (1988).
105. Bertrand, E. *et al.* Localization of ASH1 mRNA Particles in Living Yeast. *Mol. Cell* **2**, 437–445 (1998).
106. Park, H. Y. *et al.* Visualization of Dynamics of Single Endogenous mRNA Labeled in Live Mouse. *Science* **343**, 422–424 (2014).
107. George, L., Indig, F. E., Abdelmohsen, K. & Gorospe, M. Intracellular RNA-tracking methods. *Open Biol.* **8**, 180104 (2018).
108. Garcia, J. F. & Parker, R. MS2 coat proteins bound to yeast mRNAs block 5' to 3' degradation and trap mRNA decay products: implications for the localization of mRNAs by MS2-MCP system. *RNA* **21**, 1393–1395 (2015).
109. Wu, B., Chao, J. A. & Singer, R. H. Fluorescence Fluctuation Spectroscopy Enables Quantitative Imaging of Single mRNAs in Living Cells. *Biophys. J.* **102**, 2936–2944 (2012).
110. Famulok, M., Hartig, J. S. & Mayer, G. Functional Aptamers and Aptazymes in Biotechnology, Diagnostics, and Therapy. *Chem. Rev.* **107**, 3715–3743 (2007).
111. Bhadra, S. & Ellington, A. D. A Spinach molecular beacon triggered by strand displacement. *RNA* **20**, 1183–1194 (2014).
112. Paige, J. S., Wu, K. Y. & Jaffrey, S. R. RNA Mimics of Green Fluorescent Protein. *Science* **333**, 642–646 (2011).
113. Autour, A. *et al.* Fluorogenic RNA Mango aptamers for imaging small non-coding RNAs in mammalian cells. *Nat. Commun.* **9**, 656 (2018).
114. Cawte, A. D., Unrau, P. J. & Rueda, D. S. Live cell imaging of single RNA molecules with

- fluorogenic Mango II arrays. *Nat. Commun.* **11**, 1283 (2020).
115. Crockett, A. O. & Wittwer, C. T. Fluorescein-Labeled Oligonucleotides for Real-Time PCR: Using the Inherent Quenching of Deoxyguanosine Nucleotides. *Anal. Biochem.* **290**, 89–97 (2001).
116. Vaughn, C. P. & Elenitoba-Johnson, K. S. J. Hybridization-Induced Dequenching of Fluorescein-Labeled Oligonucleotides. *Am. J. Pathol.* **163**, 29–35 (2003).
117. Hövelmann, F., Gaspar, I., Ephrussi, A. & Seitz, O. Brightness Enhanced DNA FIT-Probes for Wash-Free RNA Imaging in Tissue. *J. Am. Chem. Soc.* **135**, 19025–19032 (2013).
118. Hövelmann, F. *et al.* Brightness through Local Constraint-LNA-Enhanced FIT Hybridization Probes for In Vivo Ribonucleotide Particle Tracking. *Angew. Chemie Int. Ed.* **53**, 11370–11375 (2014).
119. Jarikote, D. V., Krebs, N., Tannert, S., Röder, B. & Seitz, O. Exploring Base-Pair-Specific Optical Properties of the DNA Stain Thiazole Orange. *Chem. - A Eur. J.* **13**, 300–310 (2007).
120. Okamoto, A. ECHO probes: a concept of fluorescence control for practical nucleic acid sensing. *Chem. Soc. Rev.* **40**, 5815 (2011).
121. Jean, J. M. & Hall, K. B. 2-Aminopurine fluorescence quenching and lifetimes: Role of base stacking. *Proc. Natl. Acad. Sci.* **98**, 37–41 (2001).
122. Shin, D., Sinkeldam, R. W. & Tor, Y. Emissive RNA Alphabet. *J. Am. Chem. Soc.* **133**, 14912–14915 (2011).
123. Sholokh, M. *et al.* Conquering 2-Aminopurine's Deficiencies: Highly Emissive Isomorphic Guanosine Surrogate Faithfully Monitors Guanosine Conformation and Dynamics in DNA. *J. Am. Chem. Soc.* **137**, 3185–3188 (2015).
124. Dziuba, D. *et al.* Fundamental photophysics of isomorphic and expanded fluorescent nucleoside analogues. *Chem. Soc. Rev.* **50**, 7062–7107 (2021).
125. Hawkins, M. E. Use of pteridine nucleoside analogs as hybridization probes. *Nucleic Acids Res.* **32**, e62–e62 (2004).
126. Okamoto, A., Tainaka, K. & Saito, I. Clear Distinction of Purine Bases on the Complementary Strand by a Fluorescence Change of a Novel Fluorescent Nucleoside. *J. Am. Chem. Soc.* **125**, 4972–4973 (2003).
127. Okamoto, A., Tainaka, K. & Saito, I. Detection of A/G Single Nucleotide Alteration in RNA Using Base-discriminating Fluorescent Oligodeoxynucleotides. *Chem. Lett.* **32**, 684–685 (2003).

128. Okamoto, A., Tainaka, K. & Saito, I. Synthesis and properties of a novel fluorescent nucleobase, naphthopyridopyrimidine. *Tetrahedron Lett.* **44**, 6871–6874 (2003).
129. Okamoto, A., Tanaka, K., Fukuta, T. & Saito, I. Design of Base-Discriminating Fluorescent Nucleoside and Its Application to T/C SNP Typing. *J. Am. Chem. Soc.* **125**, 9296–9297 (2003).
130. Miyata, K. *et al.* Synthesis and Properties of a New Fluorescent Bicyclic 4- N - Carbamoyldeoxycytidine Derivative. *Org. Lett.* **8**, 1545–1548 (2006).
131. Wojciechowski, F. & Hudson, R. H. E. Fluorescence and Hybridization Properties of Peptide Nucleic Acid Containing a Substituted Phenylpyrrolocytosine Designed to Engage Guanine with an Additional H-Bond. *J. Am. Chem. Soc.* **130**, 12574–12575 (2008).
132. Mayer, E. *et al.* 1-Ethynylpyrene as a Tunable and Versatile Molecular Beacon for DNA. *ChemBioChem* **5**, 865–868 (2004).
133. Seo, Y. J., Ryu, J. H. & Kim, B. H. Quencher-Free, End-Stacking Oligonucleotides for Probing Single-Base Mismatches in DNA. *Org. Lett.* **7**, 4931–4933 (2005).
134. Kaura, M. & Hrdlicka, P. J. Locked nucleic acid (LNA) induced effect on the hybridization and fluorescence properties of oligodeoxyribonucleotides modified with nucleobase-functionalized DNA monomers. *Org. Biomol. Chem.* **13**, 7236–7247 (2015).
135. Hwang, G. T., Seo, Y. J. & Kim, B. H. A Highly Discriminating Quencher-Free Molecular Beacon for Probing DNA. *J. Am. Chem. Soc.* **126**, 6528–6529 (2004).
136. Dziuba, D. *et al.* Solvatochromic fluorene-linked nucleoside and DNA as color-changing fluorescent probes for sensing interactions. *Chem. Sci.* **7**, 5775–5785 (2016).
137. Le, H.-N. *et al.* Rational design, synthesis, and photophysics of dual-emissive deoxyadenosine analogs. *Dye. Pigment.* **170**, 107553 (2019).
138. Tsuji, A. *et al.* Direct Observation of Specific Messenger RNA in a Single Living Cell under a Fluorescence Microscope. *Biophys. J.* **78**, 3260–3274 (2000).
139. Okabe, K. *et al.* Real time monitoring of endogenous cytoplasmic mRNA using linear antisense 2'-O-methyl RNA probes in living cells. *Nucleic Acids Res.* **39**, e20–e20 (2011).
140. Matsuo, T. In situ visualization of messenger RNA for basic fibroblast growth factor in living cells. *Biochim. Biophys. Acta - Gen. Subj.* **1379**, 178–184 (1998).
141. Sokol, D. L., Zhang, X., Lu, P. & Gewirtz, A. M. Real time detection of DNA-RNA hybridization in living cells. *Proc. Natl. Acad. Sci.* **95**, 11538–11543 (1998).
142. Kang, W. J. *et al.* Molecular beacon-based bioimaging of multiple microRNAs during myogenesis. *Biomaterials* **32**, 1915–1922 (2011).

143. Tyagi, S., Bratu, D. P. & Kramer, F. R. Multicolor molecular beacons for allele discrimination. *Nat. Biotechnol.* **16**, 49–53 (1998).
144. Peng, X., Draney, D. R. & Volcheck, W. M. Quenched near-infrared fluorescent peptide substrate for HIV-1 protease assay. in *Optical Molecular Probes for Biomedical Applications* (eds. Achilefu, S., Bornhop, D. J. & Raghavachari, R.) vol. 6097 60970F (2006).
145. Bunt, G. & Wouters, F. S. FRET from single to multiplexed signaling events. *Biophys. Rev.* **9**, 119–129 (2017).
146. Bohländer, P. R., Abba, M. L., Bestvater, F., Allgayer, H. & Wagenknecht, H. A. Two wavelength-shifting molecular beacons for simultaneous and selective imaging of vesicular miRNA-21 and miRNA-31 in living cancer cells. *Org. Biomol. Chem.* **14**, 5001–5006 (2016).
147. Chung, K. K. H. *et al.* Fluorogenic DNA-PAINT for faster, low-background super-resolution imaging. *Nat. Methods* **19**, 554–559 (2022).
148. Vangindertael, J. *et al.* An introduction to optical super-resolution microscopy for the adventurous biologist. *Methods Appl. Fluoresc.* **6**, 022003 (2018).
149. Huang, B., Bates, M. & Zhuang, X. Super-Resolution Fluorescence Microscopy. *Annu. Rev. Biochem.* **78**, 993–1016 (2009).
150. Heintzmann, R. & Huser, T. Super-Resolution Structured Illumination Microscopy. *Chem. Rev.* **117**, 13890–13908 (2017).
151. Gustafsson, M. G. L. Nonlinear structured-illumination microscopy: Wide-field fluorescence imaging with theoretically unlimited resolution. *Proc. Natl. Acad. Sci. U. S. A.* **102**, 13081–13086 (2005).
152. Blom, H. & Widengren, J. Stimulated Emission Depletion Microscopy. *Chemical Reviews* vol. 117 7377–7427 at <https://doi.org/10.1021/acs.chemrev.6b00653> (2017).
153. Vicidomini, G., Bianchini, P. & Diaspro, A. STED super-resolved microscopy. *Nature Methods* vol. 15 173–182 at <https://doi.org/10.1038/nmeth.4593> (2018).
154. Müller, T., Schumann, C. & Kraegeloh, A. STED Microscopy and its Applications: New Insights into Cellular Processes on the Nanoscale. *ChemPhysChem* **13**, 1986–2000 (2012).
155. Samanta, S. *et al.* Organic fluorescent probes for stochastic optical reconstruction microscopy (STORM): Recent highlights and future possibilities. *Coord. Chem. Rev.* **380**, 17–34 (2019).
156. Van De Linde, S. *et al.* Direct stochastic optical reconstruction microscopy with standard fluorescent probes. *Nat. Protoc.* **6**, 991–1009 (2011).
157. Bates, M., Jones, S. A. & Zhuang, X. Stochastic optical reconstruction microscopy (STORM):

- A method for superresolution fluorescence imaging. *Cold Spring Harb. Protoc.* **8**, 498–520 (2013).
158. Rust, M. J., Bates, M. & Zhuang, X. Sub-diffraction-limit imaging by stochastic optical reconstruction microscopy (STORM). *Nat. Methods* **3**, 793–795 (2006).
 159. Jungmann, R. *et al.* Single-molecule kinetics and super-resolution microscopy by fluorescence imaging of transient binding on DNA origami. *Nano Lett.* **10**, 4756–4761 (2010).
 160. Nieves, D., Gaus, K. & Baker, M. DNA-Based Super-Resolution Microscopy: DNA-PAINT. *Genes* **9**, 621 (2018).
 161. Lin, R., Clowsley, A. H., Lutz, T., Baddeley, D. & Soeller, C. 3D super-resolution microscopy performance and quantitative analysis assessment using DNA-PAINT and DNA origami test samples. *Methods* **174**, 56–71 (2020).
 162. Schnitzbauer, J., Strauss, M. T., Schlichthaerle, T., Schueder, F. & Jungmann, R. Super-resolution microscopy with DNA-PAINT. *Nat. Protoc.* **12**, 1198–1228 (2017).
 163. Gimber, N., Strauss, S., Jungmann, R. & Schmoranzler, J. Simultaneous Multicolor DNA-PAINT without Sequential Fluid Exchange Using Spectral Demixing. *Nano Lett.* **22**, 2682–2690 (2022).
 164. Jungmann, R. *et al.* Quantitative super-resolution imaging with qPAINT. *Nat. Methods* **13**, 439–442 (2016).
 165. Jungmann, R. *et al.* Multiplexed 3D cellular super-resolution imaging with DNA-PAINT and Exchange-PAINT. *Nat. Methods* **11**, 313–318 (2014).
 166. Auer, A., Strauss, M. T., Schlichthaerle, T. & Jungmann, R. Fast, Background-Free DNA-PAINT Imaging Using FRET-Based Probes. *Nano Lett.* **17**, 6428–6434 (2017).
 167. Barthes, N. P. F. *et al.* Dual emissive analogue of deoxyuridine as a sensitive hydration-reporting probe for discriminating mismatched from matched DNA and DNA/DNA from DNA/RNA duplexes. *J. Mater. Chem. C* **4**, 3010–3017 (2016).
 168. Szent-Gyorgyi, C. *et al.* Fluorogen-activating single-chain antibodies for imaging cell surface proteins. *Nat. Biotechnol.* **26**, 235–240 (2008).
 169. Xu, S. & Hu, H. Y. Fluorogen-activating proteins: beyond classical fluorescent proteins. *Acta Pharm. Sin. B* **8**, 339–348 (2018).
 170. Yan, Q. *et al.* Localization microscopy using noncovalent fluorogen activation by genetically encoded fluorogen-activating proteins. *ChemPhysChem* **15**, 687–695 (2014).
 171. Gallo, E. Fluorogen-Activating Proteins: Next-Generation Fluorescence Probes for Biological

- Research. *Bioconjug. Chem.* **31**, 16–27 (2020).
172. Cheng, D. & Li, B. Simple and sensitive fluorometric sensing of malachite green with native double-stranded calf thymus DNA as sensing material. *Talanta* **78**, 949–953 (2009).
173. Hu, X., Jiao, K., Sun, W. & You, J. Y. Electrochemical and spectroscopic studies on the interaction of malachite green with DNA and its application. *Electroanalysis* **18**, 613–620 (2006).
174. MULLER, W. & GAUTIER, F. Interactions of Heteroaromatic Compounds with Nucleic Acids. A . T-Specific Non-Intercalating DNA Ligands. *Eur. J. Biochem.* **54**, 385–394 (1975).
175. Babendure, J. R., Adams, S. R. & Tsien, R. Y. Aptamers Switch on Fluorescence of Triphenylmethane Dyes. *J. Am. Chem. Soc.* **125**, 14716–14717 (2003).
176. Kolpashchikov, D. M. Binary malachite green aptamer for fluorescent detection of nucleic acids. *J. Am. Chem. Soc.* **127**, 12442–12443 (2005).
177. Bhasikuttan, A. C., Mohanty, J. & Pal, H. Interaction of malachite green with guanine-rich single-stranded DNA: Preferential binding to a G-quadruplex. *Angew. Chemie - Int. Ed.* **46**, 9305–9307 (2007).
178. Herner, A., Nikić, I., Kállay, M., Lemke, E. A. & Kele, P. A new family of bioorthogonally applicable fluorogenic labels. *Org. Biomol. Chem.* **11**, 3297–3306 (2013).
179. Sen, D. & Gilbert, W. A sodium-potassium switch in the formation of four-stranded G4-DNA. *Nature* **344**, 410–414 (1990).
180. Masiero, S. *et al.* A non-empirical chromophoric interpretation of CD spectra of DNA G-quadruplex structures. *Org. Biomol. Chem.* **8**, 2683 (2010).
181. Ashton, N. W., Bolderson, E., Cubeddu, L., O’Byrne, K. J. & Richard, D. J. Human single-stranded DNA binding proteins are essential for maintaining genomic stability. *BMC Mol. Biol.* **14**, 9 (2013).
182. Wang, W., Liu, J. & Zhou, X. Identification of single-stranded and double-stranded dna binding proteins based on protein structure. *BMC Bioinformatics* **15**, 1–9 (2014).
183. Dietz, S. *et al.* The double-stranded DNA-binding proteins TEBP-1 and TEBP-2 form a telomeric complex with POT-1. *Nat. Commun.* **12**, 2668 (2021).
184. Wilson, J. N. *et al.* Base pair sensitivity and enhanced ON/OFF ratios of DNA-binding: Donor-acceptor-donor fluorophores. *J. Phys. Chem. B* **117**, 12000–12006 (2013).
185. Pitter, D. R. G. *et al.* Turn-on, fluorescent nuclear stains with live cell compatibility. *Org. Lett.* **15**, 1330–1333 (2013).

186. Pitter, D. R. G., Brown, A. S., Baker, J. D. & Wilson, J. N. One probe, two-channel imaging of nuclear and cytosolic compartments with orange and red emissive dyes. *Org. Biomol. Chem.* **13**, 9477–9484 (2015).
187. Ryabukhin, S. V. *et al.* Combinatorial Knoevenagel Reactions. *J. Comb. Chem.* **9**, 1073–1078 (2007).
188. Ryabukhin, S. V., Plaskon, A. S., Tverdokhlebov, A. V. & Tolmachev, A. A. 2-Benzothiazolemethanol as Precursor of 2-Aryl-1-(2-benzothiazolyl)-1-ethanones. *Synth. Commun.* **34**, 1483–1487 (2004).
189. Bose, A. & Basu, S. Medium-dependent interactions of quinones with cytosine and cytidine: A laser flash photolysis study with magnetic field effect. *Biophys. Chem.* **140**, 62–68 (2009).
190. Alemán, C. The keto-amino/enol tautomerism of cytosine in aqueous solution. A theoretical study using combined discrete/self-consistent reaction field models. *Chem. Phys.* **253**, 13–19 (2000).
191. Chung, G., Oh, H. & Lee, D. Tautomerism and isomerism of guanine–cytosine DNA base pair: Ab initio and density functional theory approaches. *J. Mol. Struct. THEOCHEM* **730**, 241–249 (2005).
192. Nakamura, M., Murakami, Y., Sasa, K., Hayashi, H. & Yamana, K. Pyrene-Zipper Array Assembled via RNA Duplex Formation. *J. Am. Chem. Soc.* **130**, 6904–6905 (2008).
193. Bratu, D. P., Cha, B. J., Mhlanga, M. M., Kramer, F. R. & Tyagi, S. Visualizing the distribution and transport of mRNAs in living cells. *Proc. Natl. Acad. Sci. U. S. A.* **100**, 13308–13313 (2003).
194. Barnoin, G. Transfert d'énergie intermoléculaire par résonance à partir d'un donneur éteint (DRET). (Université Côte d'Azur, 2021).
195. Terrazas, M. *et al.* The Origins and the Biological Consequences of the Pur/Pyr DNA-RNA Asymmetry. *Chem* **5**, 1619–1631 (2019).
196. Ormson, S. M., Brown, R. G., Vollmer, F. & Rettig, W. Switching between charge- and proton-transfer emission in the excited state of a substituted 3-hydroxyflavone. *J. Photochem. Photobiol. A Chem.* **81**, 65–72 (1994).
197. Melhuish, W. H. Quantum efficiencies of fluorescence of organic substances: Effect of solvent and concentration of the fluorescent solute 1. *J. Phys. Chem.* **65**, 229–235 (1961).